

Entwicklung von Chelator-konjugierten Fibroblasten-Aktivierungsprotein-Inhibitoren für die Anwendung in der Theranostik

Dissertation

zur Erlangung des akademischen Grades
„Doktor der Naturwissenschaften (Dr. rer. nat.)“
im Promotionsfach Chemie

am Fachbereich Chemie, Pharmazie, Geographie und Geowissenschaften
der Johannes Gutenberg-Universität Mainz

vorgelegt von

Euy Sung Moon

geboren in Köln

Mainz, November 2021

Dekan: [REDACTED]

Erster Berichterstatter: [REDACTED]

Zweiter Berichterstatter: [REDACTED]

Tag der mündlichen Prüfung: 17.12.2021

Zusammenfassung

Das Fibroblasten-Aktivierungsprotein (FAP) ist eine Membran-gebundene Serinprotease (Glykoprotein Typ II). Es erlangt in der heutigen Nuklearmedizin immer mehr an Aufmerksamkeit zur gezielten Adressierung durch FAP-spezifische radiomarkierte Theranostika sowohl in der onkologischen Diagnostik als auch der Therapie verschiedener Krebsarten. Interessant ist das FAP als biologisches Zielmolekül dadurch, dass es als Biomarker in krebssassoziierten, aktivierten Fibroblasten (den sogenannten „cancer-associated fibroblasts“, CAF) vorliegt und die CAFs in über 90% der häufigsten menschlichen Epitheltumoren überexprimiert wird. Das Besondere dabei ist, dass die CAFs vermehrt in Tumoren und Krankheiten wie Wundheilung, chronischen Entzündungen, Leberzirrhosen, rheumatoider Arthritis, Lungenfibrose, Knochen- und Weichteilsarkomen vorkommen und in normalen, gesunden Geweben so gut wie nicht vorzufinden sind. Die CAFs weisen ein myofibroblastischen Phänotyp auf und sind eine entscheidende Komponente des Tumorstromas. Da die Stromazellen wiederum einen signifikanten Anteil der gesamten Tumormasse von bis zu 90% ausmachen, ermöglichen FAP-adressierende Radiopharmaka gezielte *in vivo*-Darstellungen in der molekularen Bildgebung mittels PET oder SPECT sowie therapeutische Anwendungen (Endoradiotherapie) zur Behandlung von verschiedenen Tumorerkrankungen.

Ein sehr wirksamer FAP-Inhibitor (FAPi), als UAMC1110 bezeichnet, basiert auf einer Chinolin-Glycin-4,4-difluoro-2-cyanopyrrolidin-Struktur und gilt als sehr FAP-spezifisch und -selektiv. In den letzten Jahren wurden auf Basis dieses Inhibitors FAPi-Radiopharmaka im Rahmen der radiopharmazeutischen Chemie entwickelt und in der Nuklearmedizin eingesetzt.

Das Ziel der Arbeit war die Entwicklung von verschiedenen Chelator-Linker-Konjugaten auf der Grundlage der FAP-Inhibitor-Einheit. Die Chelatoren dienen zur koordinativen Bindung verschiedener Radionuklide mit entweder bildgebenden Photonen und/oder ionisierende Teilchen. Die Entwicklung beinhaltet die Synthese der Chelator-Linker-FAPi-Derivate sowie weiterhin die Untersuchung in Hinblick auf die Radiokomplexierung, *in vitro*-Eigenschaften (Stabilität und Affinität) bis hin zu präklinischen und klinischen *in vivo*-Applikationen.

Im ersten Projekt wurden der makrozyklische Chelator DOTA sowie der hybridische Chelator DATA^{5m} über ein Quadratsäureamid (SA) als Linker an den Targetvektor FAPi gebunden. Unter der Bezeichnung DOTA.SA.FAPi und DATA^{5m}.SA.FAPi wurden beide Vorläufer synthetisiert, die Komplexbildungskinetiken mit Gallium-68 analysiert und ihre *in vitro*-Stabilität in verschiedenen Medien sowie ihre Affinität und Selektivität bzgl. FAP untersucht. Gute quantitative Radiomarkierungen, hohe Stabilitäten, sowie hohe FAP-Affinitäten mit hohen Selektivitäten gegenüber der verwandten Protease PREP, erlaubten erste

präklinische Anwendungen mit [⁶⁸Ga]Ga-DOTA.SA.FAPi in xenotransplantierten Mäusen mit dem humanen Kolonkarzinom HT-29. Die μ PET-Studie zeigte eine deutlich sichtbare und höchste Aufnahme im Tumor und ein insgesamt sehr gutes Tumor-zu-Organ-Verhältnis. Weiterführend wurden beide Radiopharmaka in ersten klinischen Studien untersucht. [⁶⁸Ga]Ga-DOTA^{5m}.SA.FAPi zeigte eine spezifische Tumoraufnahme bei einer Patientin mit fokalen nodulären Hyperplasie. In einer weiteren Studie konnte eine Korrelation zwischen [⁶⁸Ga]Ga-DOTA^{5m}.SA.FAPi positiver Tumorfraktion und dem Ki-67 in Lebermetastasen von neuroendokrinen Tumoren festgestellt werden. Humane PET/CT Studien zur Biodistribution, Pharmakokinetik und Dosimetrie von [⁶⁸Ga]Ga-DOTA.SA.FAPi bei Patienten mit verschiedenen Krebsarten im Endstadium wurden ebenfalls durchgeführt.

Der zweite Abschnitt befasst sich mit AAZTA⁵.SA.FAPi. Im Gegensatz zum DATA^{5m} ermöglicht der Hybridchelator AAZTA⁵ neben der Komplexierung von ⁶⁸Ga auch weitere Koordinationen mit Nukliden wie ⁴⁴Sc und ¹⁷⁷Lu. Das AAZTA⁵.SA.FAPi wurde hergestellt, radiochemisch mit ⁶⁸Ga, ⁴⁴Sc und ¹⁷⁷Lu evaluiert und die Bindungsaffinität bzgl. FAP und den konkurrierenden Proteasen DPPs und PREP charakterisiert und mit den Eigenschaften von DOTA.SA.FAPi verglichen. AAZTA⁵.SA.FAPi wies im Vergleich zu den anderen SA.FAPi-Liganden eine ähnlich gute inhibitorische Wirksamkeit auf. Die Markierung von AAZTA⁵.SA.FAPi mit allen drei Radiometallen resultierte in quantitativen radiochemischen Ausbeuten bei Raumtemperatur und war effizienter als die Komplexierung mit dem entsprechenden DOTA-Analogon. Insbesondere in der ⁴⁴Sc-Markierung erwies sich das AAZTA-Derivat mit besserer Komplexierung und Stabilität als Alternative zum DOTA.

Im dritten Abschnitt werden homodimere SA.FAPi-Konjugate behandelt. Durch die Entwicklung der homodimeren Systeme sollte eine Verbesserung der Tumorakkumulation und der Verweildauer erlangt werden. Zwei dimere Verbindungen mit Quadratsäureamid-konjugierten FAP-Inhibitoren wurden entwickelt, die über die bifunktionellen Chelatoren DOTA und DOTAGA eingeführt wurden. Die Homodimere DOTA.(SA.FAPi)₂ und DOTAGA.(SA.FAPi)₂ wurden synthetisiert, radiochemisch hinsichtlich der Komplexierung mit ⁶⁸Ga und *in vitro*-Stabilität des Komplexes evaluiert, sowie auf die inhibitorische Wirkung zu FAP und den konkurrierenden Proteasen untersucht. Erste klinische Patientenuntersuchungen via PET/CT mit [⁶⁸Ga]Ga-DOTAGA.(SA.FAPi)₂ im direkten Vergleich zum [⁶⁸Ga]Ga-DOTA.SA.FAPi zeigten sowohl eine höhere absolute Tumoraufnahme als auch eine verlängerte Tumorverweildauer nach der Injektion bei gleichbleibender Tumoranreicherung. Untersuchungen mit [¹⁷⁷Lu]Lu-DOTAGA.(SA.FAPi)₂ via SPECT/CT generierten eine signifikant höhere effektive Ganzkörperdosis und eine deutlich längere Tumorakkumulation sowie Retention in den Läsionen, die im Vergleich zum [¹⁷⁷Lu]Lu-DOTA.SA.FAPi noch nach 168 h zu beobachten war. In einer ersten Therapie-Pilotstudie wurden Patienten mit radiojodrefraktärem differenziertem Schilddrüsenkrebs (RR-DTC) im fortgeschrittenen Stadium über [¹⁷⁷Lu]Lu-DOTAGA.(SA.FAPi)₂ in verschiedenen Zyklen behandelt. Es konnte ein deutlicher Rückgang der Thyreoglobulin (Tg)-Werte

aller Patienten festgestellt werden mit einer signifikanten Besserung in der visuellen Analogskala (VAS) vor und nach der Therapie.

Im letzten Teil wurden verschiedene Linkereinheiten zwischen dem Chelator DATA^{5m} und dem den FAP-Inhibitor eingeführt. Der DATA Chelator ermöglicht durch die effiziente Radiokomplexierung mit ⁶⁸Ga bei milden Bedingungen eine „instant-kit“-Anwendung. Die DATA^{5m} basierenden FAPI-Moleküle, DATA^{5m}.NH.FAPi, DATA^{5m}.Pip.FAPi, DATA^{5m}.Pyr-N-CH₃.FAPi zeigten vielversprechende ⁶⁸Ga-Markierungs-, Stabilitäts- und Affinitätseigenschaften vergleichbar mit denen der SA.FAPi-Derivate. Abgesehen von [⁶⁸Ga]Ga-DATA^{5m}.NH-Pyr.FAPi bieten die drei weiteren Derivate vielversprechende Eigenschaften für potentielle Kit-Anwendungen in klinischen Studien.

Abstract

The fibroblast activation protein (FAP), a membrane-bound serine protease, is currently gaining increasing attention in nuclear medicine for targeting different cancer types with FAP-specific radiolabeled agents for both diagnostics and therapy. FAP is ubiquitous present in cancer-associated fibroblasts (CAFs) as a biomarker. The unique property of CAFs are the overexpression in over 90% of the most common human epithelial tumors and diseases such as wound healing, chronic inflammation, liver cirrhosis, rheumatoid arthritis, pulmonary fibrosis, bone and soft tissue sarcomas and in opposite almost absent in normal, healthy tissues. CAFs are a myofibroblastic phenotype and are found as one of the dominant components in the tumor stroma. Since stromal cells in turn can comprise up to 90% of the total tumor mass, FAP-targeting radiopharmaceuticals enable *in vivo* molecular imaging *via* PET or SPECT and treatment of various tumor diseases.

A very potent FAP inhibitor (FAPi), so-called UAMC1110, is based on a quinoline-glycine-4,4-difluoro-2-cyanopyrrolidine scaffold and demonstrates high FAP-specificity and -selectivity. Based on this inhibitor, FAPi-radiopharmaceuticals have recently been applied in nuclear medicine.

The aim of this work was to develop various chelator-linker-conjugates based on the FAP inhibitor moiety. The chelators are used to coordinate various radionuclides with either photons for imaging and/or ionizing particles for therapy. This work contains the synthesis of the chelator-linker-FAPi derivatives and further investigates the terms of complexation with different radiometals, *in vitro* properties (stability and affinity) as well as first preclinical and clinical *in vivo* applications.

In the first project, the macrocyclic chelator DOTA and the hybrid chelator DATA^{5m} were coupled to the FAPi moiety *via* a squaramide (SA)-linker. After synthesis of both precursors DOTA.SA.FAPi and DATA^{5m}.SA.FAPi, the complexation kinetics with gallium-68 were analyzed and evaluated for their *in vitro* stability in different media, as well as their *in vitro* affinity and selectivity for FAP. Quantitative radiolabeling, high stabilities and high FAP affinities in nanomolar IC₅₀ ranges led to first preclinical applications with [⁶⁸Ga]Ga-DOTA.SA.FAPi in tumor-bearing mice with HT-29 human colon carcinoma. The μ PET study showed clear and visible high uptake in the tumor and an overall very good tumor-to-organ ratio, which led to both radiotracer applications in first clinical studies. [⁶⁸Ga]Ga-DATA^{5m}.SA.FAPi showed specific liver uptake in a patient with focal nodular hyperplasia. Another study showed a correlation between [⁶⁸Ga]Ga-DATA^{5m}.SA.FAPi positive tumor fraction and Ki-67 in liver metastases of neuroendocrine tumors. Human PET/CT studies on the biodistribution, pharmacokinetics, and dosimetry of [⁶⁸Ga]Ga-DOTA.SA.FAPi in patients with various end-stage cancers were also performed.

The second part focused on AAZTA⁵.SA.FAPi. In contrast to DATA^{5m}, the hybrid chelator AAZTA⁵ allows labeling with radiometals such as ⁴⁴Sc and ¹⁷⁷Lu besides ⁶⁸Ga. The AAZTA⁵.SA.FAPi was synthesized, radiochemically evaluated with ⁶⁸Ga, ⁴⁴Sc, and ¹⁷⁷Lu, characterized for the FAP-affinity and against the competing proteases DPPs/ PREP and compared with the properties of DOTA.SA.FAPi. AAZTA⁵.SA.FAPi exhibited similar inhibitory efficacy compared with the other SA.FAPi ligands. Labeling of AAZTA⁵.SA.FAPi with all three radiometals resulted in quantitative radiochemical yields at room temperature and was more efficient than complexation with the corresponding DOTA analog.

In the third section, homodimeric SA.FAPi conjugates were introduced. Through the development of the homodimeric systems, an improvement in tumor accumulation and retention time should be obtained. Two dimeric compounds containing squaramide-conjugated FAP inhibitors were developed and introduced *via* the bifunctional chelators DOTA and DOTAGA. The homodimers DOTA.(SA.FAPi)₂ and DOTAGA.(SA.FAPi)₂ were synthesized and radiochemically evaluated for complexation with ⁶⁸Ga. They were analyzed for their *in vitro* stability and inhibitory efficacy to FAP and to the competing proteases DPPs and PREP. Initial clinical studies *via* PET/CT with the homodimer [⁶⁸Ga]Ga-DOTAGA.(SA.FAPi)₂ in direct comparison to the monomer [⁶⁸Ga]Ga-DOTA.SA.FAPi showed both higher absolute tumor uptake and prolonged tumor retention time for the dimeric compound. Studies with [¹⁷⁷Lu]Lu-DOTAGA.(SA.FAPi)₂ *via* SPECT/CT generated higher effective whole-body doses in patients and significantly longer tumor accumulation, as well as retention in lesions of at least 168 hours compared to [¹⁷⁷Lu]Lu-DOTA.SA.FAPi. In a first therapeutic pilot study, patients with radioiodine refractory differentiated thyroid cancer (RR-DTC) in an advanced stage were treated with [¹⁷⁷Lu]Lu-DOTAGA.(SA.FAPi)₂ through several cycles. A significant decrease in thyroglobulin (Tg) levels of all patients was observed with significant improvement in visual analog scale (VAS) before and after therapy.

In the last part, different linker units between the DATA^{5m} chelator and the FAP inhibitor were introduced. The DATA chelator enables "instant-kit" application due to its efficient radiocomplexation with ⁶⁸Ga at mild conditions. The DATA^{5m}-based FAPi molecules, DATA^{5m}.NH.FAPi, DATA^{5m}.Pip.FAPi, DATA^{5m}.Pyr-N-CH₃.FAPi showed promising ⁶⁸Ga-labeling, *in vitro* stability and affinity properties comparable to those of the SA.FAPi derivatives. Apart from [⁶⁸Ga]Ga-DATA^{5m}.NH-Pyr.FAPi, the other three derivatives offer promising properties for potential kit applications in clinical trials.

Meiner Familie

„Des Menschen Herz erdenkt sich seinen Weg;
aber der HERR allein lenkt seinen Schritt.“ (Sprüche 16,9)

Inhaltsverzeichnis

1.	Einleitung.....	19
1.1.	Diagnostik – Positronen-Emissions-Tomographie.....	20
1.2.	Radionuklide für die PET	23
1.2.1.	Gallium-68	25
1.2.2.	Scandium-44.....	27
1.3.	Therapie – Endoradiotherapie	28
1.4.	Radionuklide für die Therapie	29
1.4.1.	Lutetium-177	30
1.5.	Chelatorsysteme.....	31
1.5.1.	Bifunktionelle Chelatoren.....	33
1.5.2.	Azyklische Chelatoren	34
1.5.3.	Makrozyklische Chelatoren	35
1.5.4.	Hybridische Chelatoren	38
1.6.	Fibroblasten-Aktivierungsprotein (FAP) als Targetvektor	39
1.6.1.	FAP - Biologische Eigenschaften.....	40
1.6.2.	Adressierung von FAP für die Theranostik	42
2.	Problemstellung und Zielsetzung	47
3.	Manuskripte	63
A.	Targeting fibroblast activation protein (FAP): next generation PET radiotracers using squaramide coupled bifunctional DOTA and DATA ^{5m} chelators	65
A.1.	[⁶⁸ Ga]Ga-DOTA ^{5m} .SA.FAPi PET/CT: Specific Tracer-uptake in Focal Nodular Hyperplasia and potential Role in Liver Tumor Imaging	105
A.2.	Fibroblast activation protein inhibitor (FAPi) positive tumour fraction on PET/CT correlates with Ki-67 in liver metastases of neuroendocrine tumours.....	117
A.3.	Biodistribution, pharmacokinetics, dosimetry of [⁶⁸ Ga]Ga-DOTA.SA.FAPi and the head-to-head comparison with [¹⁸ F]F-FDG PET/CT in patients with various cancers.....	147
B.	In Vitro Evaluation of the Squaramide-Conjugated Fibroblast Activation Protein Inhibitor-Based Agents AAZTA ⁵ .SA.FAPi and DOTA.SA.FAPi.....	187
C.	Fibroblast Activation Protein (FAP) targeting homodimeric FAP inhibitor radiotheranostics: A step to improve tumor uptake and retention time.....	217
C.1.	First-in-human results on the Biodistribution, Pharmacokinetics, and Dosimetry of [¹⁷⁷ Lu]Lu-DOTA.SA.FAPi and [¹⁷⁷ Lu]Lu-DOTAGA.(SA.FAPi) ₂ in Patients with Various End-stage Cancers.....	251
C.2.	Novel Fibroblast Activation Protein Inhibitor-Based targeted Theranostics for Radioiodine Refractory differentiated Thyroid Cancer Patients: A Pilot Study.....	281

D. Development of DATA ^{5m} chelator-based Fibroblast Activation Protein Inhibitor small molecules for PET imaging	315
4. Zusammenfassung und Ausblick	349
5. Liste der Publikationen	371
Danksagung	373
Eidesstattliche Erklärung	375
Curriculum Vitae.....	377

1. Einleitung

Lag das Hauptaugenmerk der Nuklearmedizin in der Vergangenheit noch häufig in der getrennten Betrachtung von Diagnostik und Therapie, so hat sich in den vergangenen Jahren der Fokus immer weiter in Richtung „Theranostik“, also der Kombination aus beidem, verschoben [1,2]. Für die medizinische Diagnostik haben sich die Positronen-Emissions-Tomographie (PET) und Einzelphotonen-Emissionscomputertomographie (SPECT) als nicht-invasive, bildgebende Verfahren etabliert [3,4]. In Kombination mit der Computertomographie (CT) oder Magnetresonanztomographie (MRT) können gleichzeitig hochauflösende, sensitive Aufnahmen gemacht werden, die zusätzlich auch biologische Prozesse im Patienten visualisieren und dabei helfen, Erkrankungen *in vivo* gezielt zu diagnostizieren. Für die PET werden Positronen (β^+) emittierende Radionuklide benötigt und für die SPECT Nuklide verwendet, die γ -Strahlung aussenden. Bei der Endoradiotherapie (ERT), auch als Radionuklid-therapie bezeichnet, werden ionisierende Partikelstrahlungen wie α - oder β^- -Strahler genutzt, die die DNA-Stränge zerstören, dadurch die malignen Zellen abtöten und dabei umliegendes, gesundes Gewebe nur in geringem Ausmaß schädigen [5–7]. Häufig genutzte Radionuklide für die PET sind die β^+ -Emitter ^{18}F , ^{68}Ga und ^{89}Zr und in der ERT die β^- -Emitter ^{90}Y und ^{177}Lu sowie der α -Emitter ^{225}Ac [8].

Sowohl für die Diagnose als auch für die Therapie werden in der Nuklearmedizin Radiopharmaka eingesetzt, welche auf dem „Tracer-Prinzip“ von G. De Hevesy beruhen [9,10]. Hierbei werden kleinste Mengen radioaktiv markierter Wirkstoffe („radiotracer“) dem Patienten injiziert, welche am biochemischen und physiologischen Metabolismus im Körper teilnehmen, ohne dabei die pharmakologischen Wechselwirkungen *in vivo* zu beeinflussen.

Das wichtigste Element eines Radiopharmakons ist das Pharmakophor, welches hohe und selektive Bindungsaffinitäten zu den Zielstrukturen (z.B. Enzyme, Rezeptoren oder Antigene) besitzt und eine effiziente Anreicherung ermöglicht [11]. Solche biologisch aktiven Moleküle werden „Targetvektoren“ (TV) genannt und können z.B. Inhibitoren, Peptide, Antikörper oder Proteine sein. Bei der Nutzung von Radiometallen, wo eine direkte Bindungsknüpfung mit dem Pharmakophor bzw. Targetvektor nicht möglich ist, werden Chelatoren für die ionisch, koordinative Komplexierung des Metalls verwendet. Der Targetvektor wird mit einem bifunktionellen Chelator kovalent verknüpft und bildet ein Chelator-TV-Konjugat.

1.1. Diagnostik – Positronen-Emissions-Tomographie

Die Positronen-Emissions-Tomographie (PET) ist ein nicht-invasives, bildgebendes Verfahren und ermöglicht eine dreidimensionale Visualisierung der biochemischen Stoffwechselprozesse *in vivo*. Dabei nutzt die PET die β^+ -Umwandlung protonenreicher Radionuklide. Ein Proton wandelt sich in ein Neutron um, wodurch ein Positron β^+ und ein Elektron-Neutrino ν_e entstehen [12,13]. Die dabei freiwerdende (Zerfalls-)Energie ΔE ist die Massendifferenz der Kernumwandlung und wird als kinetische Energie zufällig auf das Positron und Elektron-Neutrino verteilt. Die zufällige Verteilung der Energie resultiert in einem kontinuierlichen Energiespektrum mit einer für jedes Radionuklid charakteristischen, maximalen β^+ -Energie [12].

Positronen haben eine sehr hohe kinetische Energie (bis zu einigen MeV) und durch verschiedene Wechselwirkungen mit der Umgebung verliert das Positron stetig an kinetischer Energie, bis es sich im thermischen Bereich (einige eV) befindet [14,15]. Die Reichweite (d) des β^+ ist proportional zur ursprünglichen kinetischen Energie und daher auch proportional zur durchschnittlichen β^+ -Energie des jeweiligen Nuklids [12,16]. Die Reichweite hängt weiterhin mit der Dichte des durchdringenden Materials zusammen und beträgt z.B. in Wasser etwa 1-2 mm [13,17].

Trifft das β^+ -Teilchen im thermischen Energiebereich auf ein Elektron e^- , so annihilieren sie entweder direkt oder erst nach Bildung eines instabilen, kurzlebigen Positroniums [14]. Bei dem Prozess der Annihilation werden Vernichtungsstrahlungen in Form von γ -Quanten mit einer entsprechenden Energie und Winkelverteilung ausgesendet.

Geschieht die Annihilation direkt, ohne Bildung eines intermediären Positroniums, hängt die Anzahl der ausgesendeten γ -Quanten vom Spinzustand des β^+ und e^- ab [14,18]. Im Fall des Singulett-Zustandes mit antiparallel ausgerichteten Spins kommt es durch Auswahlregeln für die Erhaltung von Impuls, Parität und Energie zur Aussendung von zwei γ -Quanten in einem Winkel von 180° mit einer jeweiligen Energie von 511 keV (aus $E = mc^2$, m = Ruhemasse eines Elektrons, c = Lichtgeschwindigkeit). Bei paralleler Ausrichtung der Spins kommt es zur Aussendung von meist drei γ -Quanten mit einer sehr komplexen Winkel- und Energieverteilung, welches als Triplett-Zustand bezeichnet wird. Das Verhältnis des Wirkungsquerschnitts zwischen antiparalleler zu paralleler Annihilation liegt bei 372 zu 1. Der Wirkungsquerschnitt für die direkte Annihilation des freien Positrons ist jedoch sehr viel kleiner als die Energieübertragung durch Ionisation oder Anregung und findet daher nur zu 5% statt.

Die zweite Möglichkeit der Annihilation ist die Bildung eines Positroniums, ein wasserstoffähnlicher Zustand von Positron und Elektron [12,14,16–18]. Bei diesem Annihilationsvorgang wird abhängig von

der Spin-Anordnung des β^+ und e^- zwischen der Aussendung von zwei oder drei γ -Quanten unterschieden. Bei antiparalleler Spinanordnung bildet sich das *para*-Positronium, welches zwei γ -Quanten mit einer Energie von jeweils 511 keV in 180° versetzter Richtung aussendet (Abbildung 1). Bei parallel ausgerichteten Spins entsteht das *ortho*-Positronium mit einer komplexeren Energie- und Winkelverteilung. Das für die PET relevante *para*-Positronium tritt zwar nur mit einer 25%-igen Wahrscheinlichkeit auf, stellt jedoch durch seine deutlich kürzere Lebensdauer von $1,25 \cdot 10^{-10}$ s und konstante Gleichgewichtsbildung aus dem längerlebigen *ortho*-Positronium ($1,4 \cdot 10^{-7}$ s) die dominante Umwandlungsart dar.

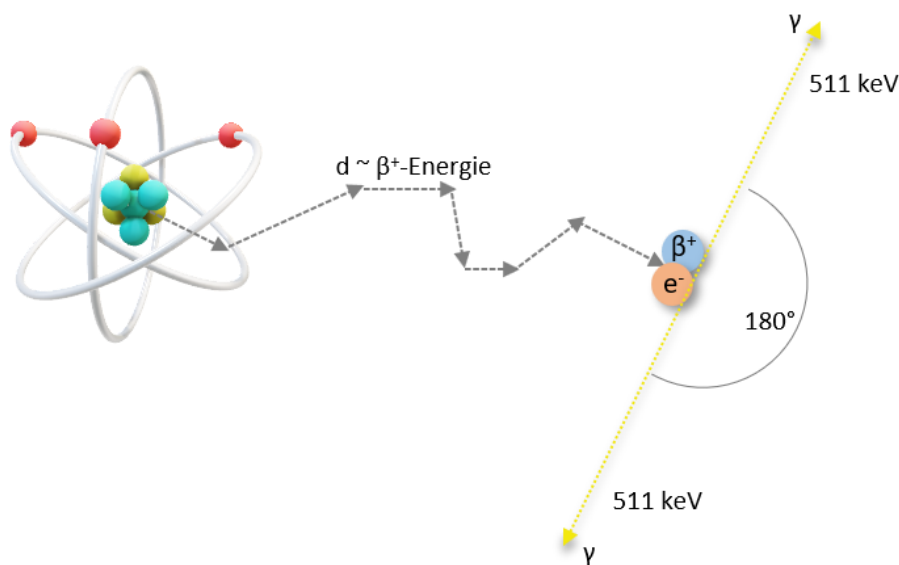


Abbildung 1: β^+ -Umwandlung und anschließende *para*-Positronium-Annihilation unter Aussendung von zwei γ -Quanten mit jeweils einer Energie von 511 keV in 180° versetzter Richtung. Die Reichweite d ist proportional zur β^+ -Energie. (Abb. in Anlehnung an [12,13]).

Die Detektion der Annihilationsstrahlung wird durch einen Detektorring mittels Koinzidenz-Registrierung realisiert (Abbildung 2). Die zwei ausgesendeten γ -Quanten werden von zwei gegenüber liegenden Detektoren gleichzeitig innerhalb eines festgelegten Koinzidenzfensters (im Nanosekunden-Bereich) detektiert [17,19,20]. Neben der normalen, wahren Koinzidenz können noch weitere gestreute und zufällige Koinzidenzen registriert werden. Durch Rekonstruktion werden die falsch positiven (gestreuten und zufälligen) Koinzidenzen korrigiert und aus der Auswertung der Messung herausgefiltert [15]. Der Ort der Annihilation liegt somit auf einer gedachten Linie zwischen den beiden Koinzidenz-Signalen (180°), welche als „line of response“ (LOR) bezeichnet wird. Durch Algorithmen können alle detektierten LORs rekonstruiert werden und ergeben ein dreidimensionales Bild.

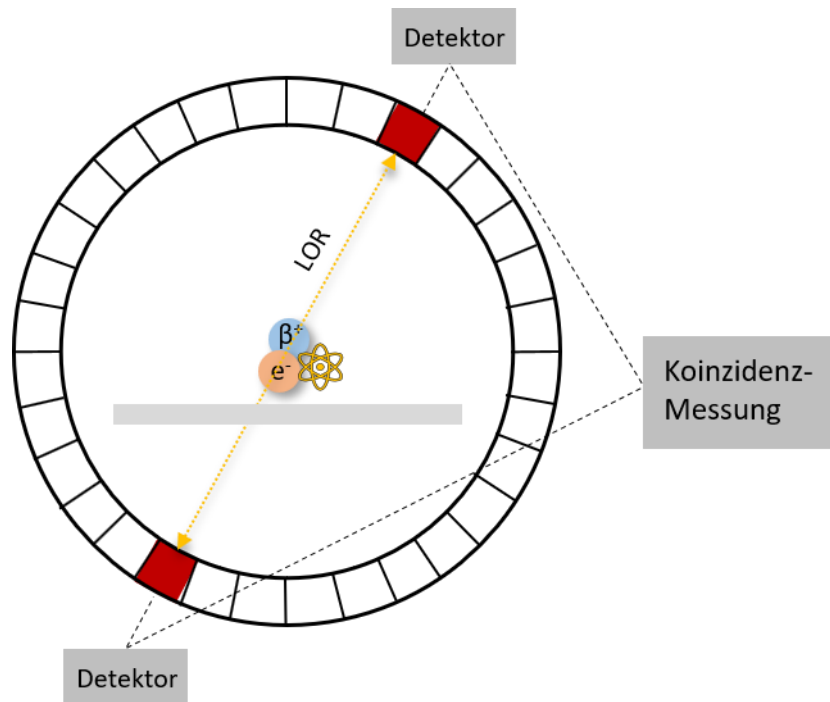


Abbildung 2: Schematische Darstellung der PET mit einem ringförmigen Detektor und der Messung der beiden Koinzidenzen in einem Winkel von 180° an der „line of response“ (LOR). (Abb. in Anlehnung an [3]).

Das Material des Detektorringes besteht aus Szintillationskristallen, wie Bismut-Germanat (BGO), Cer-dotiertem Lutetium-Oxyorthosilikat (LSO), Cer-dotiertem Gadolinium-Oxyorthosilikat (GSO) oder Thallium-dotierten Natriumiodid-Kristallen (NaI(Tl)) [12,17,20–22]. Der Detektor hat die Aufgabe, Informationen über die Energie, den physischen Ort und den Zeitpunkt der γ -Signale genauestens zu registrieren. Kriterien entscheidend bei der Materialauswahl sind Lichtintensität, Abklingzeit, Totzeit und die sog. „stopping power“ [23].

Die PET wird meist mit einer Computertomographie (CT) oder auch Magnetresonanztomographie (MRT) kombiniert [24]. Durch die vereinten Hybridsysteme PET/CT bzw. PET/MRT können die detektierten Ereignisse der Photonen mit der Morphologie des Körpers überlagert und somit die biochemischen und physiologischen Prozesse als auch die Anatomie dargestellt werden.

1.2. Radionuklide für die PET

Für die PET können verschiedene β^+ -emittierende Radionuklide verwendet werden. Die in der Nuklearmedizin meist verwendeten PET-Nuklide sind in der Tabelle 1 zu finden [25–27]. Für die Auswahl geeigneter Nuklide gilt es einige Kriterien zu beachten, wie die Halbwertszeit ($t_{1/2}$), die Zerfallsart, sprich der β^+ -Anteil bei der Umwandlung und die β -Energie des Nuklids.

Tabelle 1: PET relevante β^+ -emittierende Radionuklide und deren Eigenschaften (Halbwertszeit $t_{1/2}$, β^+ -Anteil, maximale β -Energie $E_{\beta,\max}$ und Herstellungsweg) [25–27].

Nuklid	$t_{1/2}$	β^+ -Anteil [%]	$E_{\beta,\max}$ [MeV]	Verfügbarkeit
^{11}C	20,3 min	100	0,97	$^{14}\text{N}(p,\alpha)^{11}\text{C}$
^{13}N	9,96 min	100	1,20	$^{16}\text{O}(p,\alpha)^{13}\text{N}$
^{15}O	2,04 min	100	1,73	$^{15}\text{N}(p,n)^{15}\text{O}$ bzw. $^{14}\text{N}(d,n)^{15}\text{O}$
^{18}F	110 min	100	0,63	$^{18}\text{O}(p,n)^{18}\text{F}$ bzw. $^{20}\text{Ne}(d,\alpha)^{18}\text{F}$
^{44}Sc	4,04 h	95	0,63	$^{44}\text{Ti}/^{44}\text{Sc}$ -Generator $^{44}\text{Ca}(p,n)^{44}\text{Sc}$
^{68}Ga	67,7 min	89	1,90	$^{68}\text{Ge}/^{68}\text{Ga}$ -Generator
^{64}Cu	12,7 h	18	0,66	$^{64}\text{Ni}(p,n)^{64}\text{Cu}$ bzw. $^{67}\text{Zn}(p,\alpha)^{64}\text{Cu}$
^{89}Zr	78,4 h	23	0,90	$^{89}\text{Y}(p,n)^{89}\text{Zr}$
^{86}Y	14,7 h	32	1,22	$^{86}\text{Sr}(p,n)^{86}\text{Y}$

Die Halbwertszeit (HWZ) der Nuklide muss lang genug sein, um die Radiosynthese sowie die Aufreinigung durchführen zu können und weiterhin den Transport und die Applikation *in vivo* abzudecken. Jedoch sollte die HWZ nicht zu lange sein, um die Strahlenbelastung für den Patienten so gering wie möglich zu halten. Die biologische Halbwertszeit des Radiopharmakons ist ein entscheidender Faktor, denn je nach Anreicherungskinetik der Targetvektoren müssen die Eigenschaften des Radionuklids entsprechend angepasst werden. ^{15}O als $[^{15}\text{O}]\text{H}_2\text{O}$ findet Anwendung als Perfusionstracer [28]. ^{11}C als $[^{11}\text{C}]\text{Methionin}$, wird zur Visualisierung von Hirntumoren verwendet [29]. Das wohl prominenteste PET-Nuklid in der nuklearmedizinischen Anwendung ist ^{18}F . Mit einer Halbwertszeit von 110 min bietet dieses Nuklid ausreichend Zeit für die Synthese/Aufreinigung und den Transport zum Patienten bis hin zur Injektion. Einsatz findet ^{18}F z.B. in Form von $[^{18}\text{F}]\text{F-DOPA}$ zur Visualisierung des dopaminergen Systems und dem wohl bekanntesten Radiopharmakon $[^{18}\text{F}]\text{FDG}$, welcher bei der Diagnose von Tumoren eingesetzt wird [13,28,30,31]. ^{68}Ga , mit einer HWZ von 68 min, zählt neben ^{18}F zu den meistgenutzten PET-Nukliden. Großes Interesse weckte zuletzt die Darstellung

neuroendokriner Tumore mittels [^{68}Ga]Ga-DOTATOC und [^{68}Ga]Ga-DOTATATE und die Visualisierung von Prostata-Karzinomen mit [^{68}Ga]Ga-PSMA-11 und [^{68}Ga]Ga-PSMA-617 [32]. Bei der Verwendung größerer Biomoleküle wie z.B. Antikörper(fragmenten) mit einer zeitlich längeren Pharmakokinetik und verlangsamten, biochemischen Prozessen werden dementsprechend langlebigere Nuklide wie ^{89}Zr ($t_{1/2} = 78 \text{ h}$) verwendet [19,25].

Für eine hohe Detektionsrate sollte die Hauptzerfallsart des Nuklids die β^+ -Umwandlung sein. Beim Konkurrenzprozess, dem Elektroneneinfang („electron capture“, EC), werden keine Positronen emittiert und der Annihilationsprozess wird dadurch erst gar nicht möglich. Daraus resultierend, sollten gut geeignete PET-Nuklide einen möglichst geringen EC-Anteil besitzen [33].

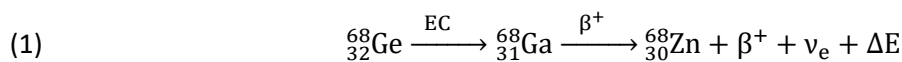
Die β^+ -Energie des Nuklids ist bestimmend für die Ortsauflösung der PET und sollte für eine verbesserte Auflösung möglichst klein sein [33]. Durch die kleine β^+ -Energie ist die Reichweite des β^+ -Teilchens geringer und ermöglicht einen kürzeren Weg bis zur Annihilation. Eine hohe Energie des Positrons hat eine größere Ortsunschärfe zur Folge.

Neben den Eigenschaften der Radionuklide spielt die Herstellung bzw. Verfügbarkeit eine große praktische Rolle. Dabei können die Nuklide mittels eines Zyklotrons oder einem Generator erhalten werden. Die Anschaffung eines Zyklotrons sowie die Produktion am Zyklotron sind mit sehr hohen Kosten verbunden. Die Verfügbarkeit des Nuklids ist am Standort des Zyklotrons begrenzt und nur wenige kernchemische und klinische Einrichtungen verfügen über ein Zyklotron. Eine einfachere, günstigere Alternative ist die Verwendung von Generatorsystemen, welche kostengünstiger und standortunabhängiger sind. Die Tochternuklide werden über Mutter-Tochter-Gleichgewichte aus den langlebigen Mutternukliden gewonnen und durch Nachbildung der Tochter können die Generatoren (mehrmals) täglich eluiert werden. Die verbreitetsten Generatorsysteme in der Nuklearmedizin sind $^{99}\text{Mo}/^{99\text{m}}\text{Tc}$ -Generatoren zur Herstellung des SPECT-Nuklids $^{99\text{m}}\text{Tc}$ und $^{68}\text{Ge}/^{68}\text{Ga}$ -Generatoren für die Gewinnung des PET-Nuklids ^{68}Ga [34–38].

1.2.1. Gallium-68

Gallium(III) ist eine harte Lewis-Säure mit einem Ionenradius von 47-62 pm. Für Komplexierungen werden sechsfache Koordinationen mit harten Lewis-Akzeptoren wie Stickstoff und Sauerstoff in einer pseudo-oktaedrischen Konformation bevorzugt [39].

Das Radiometall ^{68}Ga hat eine Halbwertszeit von 68 min und wird durch die Umwandlung des Mutternuklids ^{68}Ge durch Elektroneneinfang gewonnen. Das ^{68}Ge wird wiederum durch Bestrahlung mit hochenergetischen Protonen im Zyklotron in einer $^{69}\text{Ga}(p,2n)^{68}\text{Ge}$ -Reaktion hergestellt und besitzt eine Halbwertszeit von 271 Tagen [37,38,40]. Da die HWZ vom ^{68}Ge sehr viel länger ist als die des ^{68}Ga , handelt es sich hier um ein säkulares Gleichgewicht [41]. Die β^+ -Umwandlung von ^{68}Ga zum stabilen ^{68}Zn findet zu 89% statt (Gleichung 1):



Die maximale Energie des Positrons $E_{\beta,\text{max}}$ von ^{68}Ga beträgt 1,90 MeV und der EC-Anteil ist mit 11% gering [40].

Das ^{68}Ge wird auf einer anorganischen (z.B. Al_2O_3 , SnO_2 , ZrO_2 oder TiO_2) oder seltener auf einer organischen Matrix (z.B. Pyrogallol-Formaldehyd-Polymerharze) fixiert [36–38]. Die Abtrennung und Elution von ^{68}Ga vom Generator erfolgt mit verdünnter Salzsäure (0,05 – 0,6 M). Oft ist es nach der Elution noch notwendig, Fremdmetalle abzutrennen oder das Eluat zu konzentrieren. Hierfür kommen typischerweise 3 Verfahren zum Einsatz: die Fraktionierung, das kationische- und das anionische „post processing“ [36–38,40,41].

Bei der Fraktionierung wird das Eluat in kleine Volumina getrennt und die Fraktionen mit den höchsten Gallium-Aktivitäten für die weitere Aufbereitung gesammelt. Bei den beiden post processing-Methoden wird das Eluat vom Generator auf einem Anionen- oder Kationenaustauscher fixiert. Beim anionischen post processing werden die GaCl_4^- bzw. GaCl_6^{3-} Komplexe durch Verwendung einer salzsauren Lösung mit hoher Molarität $> 3 \text{ M}$ auf einem Anionenaustauscher fixiert und anschließend mit Wasser von der Säule in Form von GaCl_3 bzw. Ga^{3+} abgetrennt. Beim kationischen post processing mit Ethanol wird das $^{68}\text{Ga}^{3+}$ auf einem Kationenaustauscher fixiert und mit einer Kombination aus Ethanol und Salzsäure eluiert (Abbildung 3). Es gibt noch weitere kationische post processing Verfahren, welche das $^{68}\text{Ga}^{3+}$ mit Aceton/Salzsäure-Lösungen oder Natriumchlorid-Lösungen vom Kationenaustauscher abtrennen [42–44].

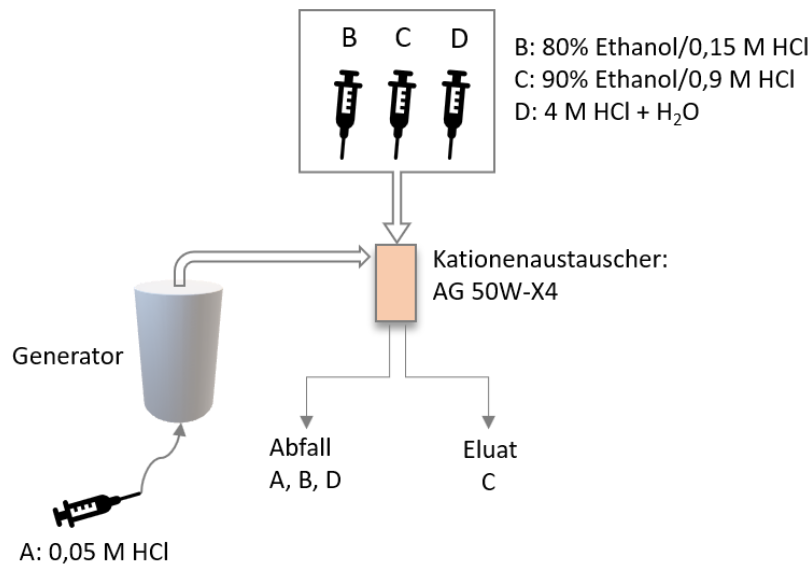


Abbildung 3: Schematischer Aufbau eines $^{68}\text{Ge}/^{68}\text{Ga}$ -Generators mit kationischem Ethanol-post processing, A: Elution des Galliums durch eine 0,05 M HCl-Lösung vom Generator und die anschließende Fixierung am Kationenaustauscher; B: Spülung mit einer 80% EtOH/0,15 M HCl-Lösung zur Entfernung von Verunreinigungen und Fremd-Ionen; C: Elution des ^{68}Ga ; D: Rekonditionierung des Austauschers mit 4 M HCl und H₂O. (Abb. in Anlehnung an [36–38]).

Bei der Fixierung des Galliums auf den Kationenaustauscher wird potenzieller Germanium-Durchbruch beinahe vollständig abgetrennt und eine ^{68}Ga -Reinheit von > 97% erhalten. Ein sehr geringer Anteil an Verunreinigungen wie Zn^{2+} , Fe^{3+} oder Trägermaterial-Ionen (Ti^{4+} oder Sn^{4+}) wird mit einer 80% Ethanol/0,15 M Salzsäure-Lösung vom Austauscher gespült. Das nun verbliebene, reine ^{68}Ga auf dem Austauscher wird mit einer 90% Ethanol/0,9 M HCl-Lösung eluiert und weist eine vernachlässigbar niedrige Metallverunreinigung auf [45].

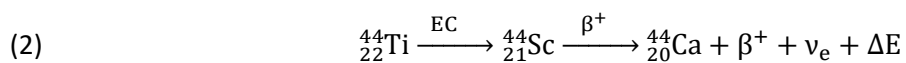
Gallium hat im wässrigen Medium lediglich eine stabile Oxidationsstufe von +III. Im schwach-sauren Milieu liegt es als $[\text{Ga}(\text{H}_2\text{O})_6]^{3+}$ hydratisiert vor und im neutralen Milieu als unlösliches Gallium(III)-hydroxid $\text{Ga}(\text{OH})_3$. Im Basischen bildet sich $[\text{Ga}(\text{OH})_4]^-$ [37]. Durch die Elution vom Generator mit verdünnter Salzsäure liegt das Gallium als Ga^{3+} vor. Die anschließende Komplexierung mit dem Chelator wird meist in einem schwach bis mäßig saurem Puffersystem (pH=3 – 5.5) durchgeführt, um die Bildung der unlöslichen Gallium(III)hydroxide zu vermeiden.

1.2.2. Scandium-44

Scandium(III) wird analog zum Gallium(III) als harte Lewis-Säure eingeordnet. Dadurch geht das Scandium bevorzugt Komplexbildungen mit harten Lewis-Basen bzw. Lewis-Akzeptoren ein und weist eine sechsfach bis achtfache Koordination auf [46].

Das Radiometall ^{44}Sc hat einen hohen Positronen-Anteil von 94% mit einer maximalen β^+ -Energie von 1,46 MeV. Es gibt zwei Wege das ^{44}Sc zu erhalten, einerseits über eine $^{44}\text{Ca}(p,n)^{44}\text{Sc}$ -Kernreaktion am Zyklotron und andererseits über einen $^{44}\text{Ti}/^{44}\text{Sc}$ -Generator [47–50]. Der erste, für die Praxis einsetzbare, $^{44}\text{Ti}/^{44}\text{Sc}$ -Generator hat seinen Ursprung an der Universität Mainz. In den letzten Jahren finden fortgeschrittene Ansätze statt, $^{44}\text{Ti}/^{44}\text{Sc}$ -Generatoren für den kommerziellen Gebrauch herzustellen [51–53].

Im $^{44}\text{Ti}/^{44}\text{Sc}$ -Generator generiert das langlebige Mutternuklid ^{44}Ti ($t_{1/2} = 60,6$ a) durch einen EC das im Verhältnis kurzlebiger Tochterkern ^{44}Sc ($t_{1/2} = 3,97$ h) [54]. Das ^{44}Sc wandelt sich anschließend unter der Aussendung von einem β^+ -Teilchen zum stabilen ^{44}Ca um (Gleichung 2):



Das ^{44}Ti wird durch eine $^{45}\text{Sc}(p,2n)^{44}\text{Ti}$ -Reaktion hergestellt und auf einem Anionenaustauscher fixiert. Durch die Elution des 5 mCi $^{44}\text{Ti}/^{44}\text{Sc}$ -Generators kann eine ^{44}Sc -Aktivität von 170-180 MBq pro Elution erhalten werden. Das Scandium wird mit einer 0,005 M $\text{H}_2\text{C}_2\text{O}_4/0,07$ M Salzsäure-Lösung vom Generator eluiert und auf einem Kationenaustauscher fixiert (Abbildung 4). Der ^{44}Ti -Durchbruch ist dabei mit < 200 Bq sehr gering. Die Elution des $^{44}\text{Sc}^{3+}$ vom Austauscher erfolgt mit einem 0,25 M Ammoniumacetat (AmAc)-Puffer (pH=4,0). Durch den Elutionsvorgang können bis zu 85% Scandium-44 (140-160 MBq) vom Kationenaustauscher gewonnen werden und der ^{44}Ti -Durchbruch ist nach post processing mit < 7 Bq vernachlässigbar gering [48].

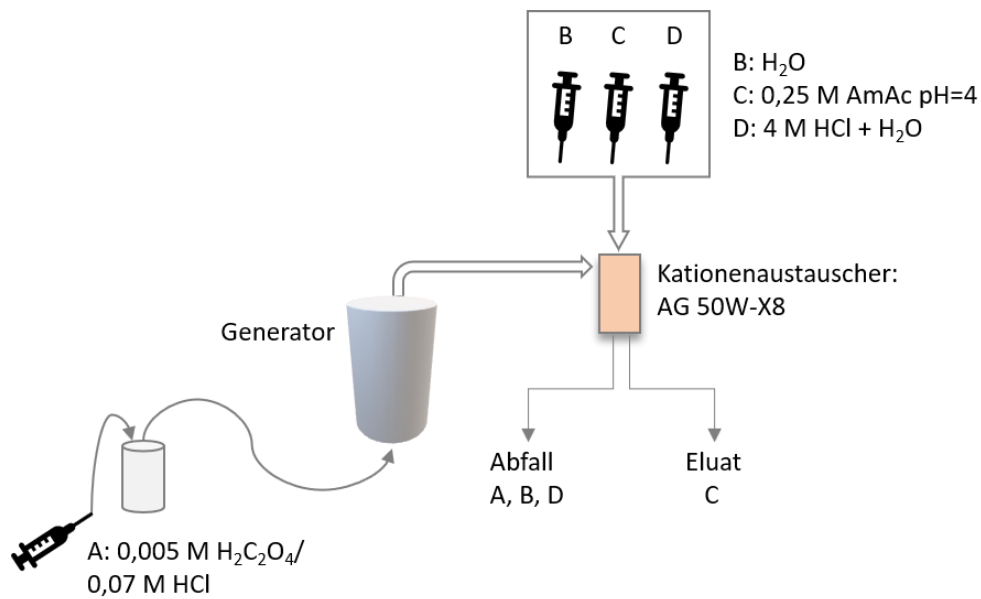


Abbildung 4: Schematischer Aufbau eines $^{44}\text{Ti}/^{44}\text{Sc}$ -Generators: A: Elution mit einer $0,005\text{ M H}_2\text{C}_2\text{O}_4/0,07\text{ M HCl}$ -Lösung und die anschließende Fixierung am Kationenaustauscher; B: Spülung mit H_2O ; C: Elution von $^{44}\text{Sc}^{3+}$ mit $0,25\text{ M Ammoniumacetat-Puffer pH}=4,0$; D: Rekonditionierung des Austauschers mit 4 M HCl und H_2O . (Abb. in Anlehnung an [48]).

1.3. Therapie – Endoradiotherapie

Für die Endoradiotherapie (ERT) werden in der heutigen Nuklearmedizin hauptsächlich α - und β -emittierende Radionuklide verwendet. Die ionisierenden Strahlungen zerstören die Tumorgewebe, wobei eine selektive und spezifische Zerstörung der Tumore gewährleistet werden muss um die gesunden Gewebe bzw. Organe so weit wie möglich nicht zu schädigen. Durch die selektive Anreicherung des Radiopharmakons, analog wie bei der Diagnostik mittels PET, und einer optimalen Strahlendosierung können Nebenwirkungen und Toxizität größtenteils vermieden werden [55]. Durch die Ionisation der Strahlungen, entweder direkt oder indirekt über Radikalbildung durch Radiolyse, werden DNA-(Doppel)-Strangbrüche verursacht, wodurch die Zellen irreparabel geschädigt werden und absterben [6].

Bei der Auswahl der Strahlungsart spielt der lineare Energietransfer (LET) eine entscheidende Rolle. Dieser ist ein Maß für die Wirkung der Strahlung und stellt die Energiemenge dar, die ein ionisierendes Teilchen pro Längeneinheit an die Umgebung abgibt [25,56]. Der LET ist abhängig von der Strahlungsart und vom durchdringenden Medium. α -Teilchen besitzen eine sehr geringe Reichweite von $< 100\ \mu\text{m}$ bei gleichzeitig hohem LET. Vorteil der α -Teilchen ist, dass diese durch ihre geringere Reichweite, weniger die umliegenden, gesunden Gewebe beschädigen (als „crossfire damage“ bezeichnet) als β -

Teilchen. Durch den sehr hohen LET der α -Partikeln (80 keV/ μ m) und eine höhere lokale Ionisierungsdichte können diese Teilchen vermehrt DNA-Doppelstrangbrüche verursachen [5,56,57]. Dafür müssen die α -Teilchen in die Tumorzelle eindringen bzw. sich nahezu homogen im Tumor verteilen. β^- -Teilchen haben einen geringeren LET (0,2 keV/ μ m), besitzen aber eine deutlich höhere Reichweite (0,5-10 mm) im Vergleich zu den α -Teilchen und eine homogene Gewebeverteilung ist nicht unbedingt notwendig für eine effektive Therapie [58]. Außerdem ermöglicht die längere Reichweite der β^- -Teilchen auch Bestrahlung von umliegenden, entfernteren Tumorgeweben.

1.4. Radionuklide für die Therapie

Analog zu den Kriterien für eine geeignete Wahl von PET-Nukliden, sind Halbwertszeiten, Energien, Zerfallsart der emittierten Teilchen sowie Kosten und Verfügbarkeit wichtige Punkte bei der Auswahl von Nukliden für die therapeutische Anwendung. Geeignete und meist verwendete Therapienuklide in der Nuklearmedizin sind in der Tabelle 2 zu finden [25,55,57,58].

Tabelle 2: α - und β^- -emittierende Radionuklide und deren Eigenschaften (Halbwertszeit $t_{1/2}$, Umwandlungsart und Anteil, maximale Energie E_{\max} und Herstellungsweg) [25,55,57,58].

Nuklid	$t_{1/2}$	Umwandlungsart, Anteil [%]	E_{\max} [MeV]	Verfügbarkeit
^{90}Y	64,1 h	β^- (100)	2,28	$^{90}\text{Sr}/^{90}\text{Y}$ -Generator
^{177}Lu	6,73 d	β^- (100)	0,50	$^{176}\text{Lu}(n,\gamma)^{177}\text{Lu}$ (c.a.) $^{176}\text{Yb}(n,\gamma,\beta^-)^{177}\text{Lu}$ (n.c.a.)
^{212}Pb	10,6 h	β^- (80)	0,57	^{224}Ra -Generator
^{131}I	8,02 d	β^- (89)	0,70	$^{130}\text{Te}(n,\gamma,\beta^-)^{131}\text{I}$
^{225}Ac	10,0 d	α (100 %)	5,93	^{229}Th -Generator
^{211}At	7,21 h	α (42 %)	5,87	$^{209}\text{Bi}(\alpha,2n)^{211}\text{At}$

Auch bei den Therapienukliden muss die Halbwertszeit lang genug sein damit eine Anreicherung im Zielgewebe stattfinden kann. Optimal sollte sich die HWZ daher nach der Pharmakokinetik des Targetvektors richten. Eine zu kurze HWZ führt zu einem verfrühten Zerfall des Nuklids, noch bevor das Radiopharmakon das Zielgewebe erreicht. Dadurch erhöht sich auch die Wahrscheinlichkeit einer höheren Strahlendosis im gesunden Gewebe.

Je nachdem, welche Art von Tumoren und Metastasen adressiert werden sollen, sind auch die Zerfallsart und die entsprechende Energie des Therapienuklids wichtig. Für eine maximale therapeutische Effizienz sollte die Energie und damit die Reichweite der emittierenden Teilchen an die Gegebenheiten des Tumors angepasst sein, um die Tumorzellen und dadurch die DNA-Stränge vollständig zu zerstören, aber umliegende gesunde Zellen so wenig wie möglich zu beschädigen. Wie in 1.3. erwähnt, besitzen α -Emitter eine sehr geringe Reichweite aber dafür einen sehr hohen LET. Die β -Emitter haben eine längere Reichweite, aber einen niedrigeren LET als die α -Teilchen.

Einige Radionuklide finden regelmäßig Anwendung in der nuklearmedizinischen ERT. ^{131}I ist bekannt für die Radioiodtherapie von Schilddrüsenerkrankungen und ^{90}Y wird z.B. bei Behandlungen von hepatozellulären Karzinomen eingesetzt [58–60]. Therapienuklide wie ^{90}Y und ^{177}Lu gewinnen immer mehr an Bedeutung in der Peptidrezeptorradiotherapie (PRRT) neuroendokriner Tumore (NET) und der Radioligandentherapie (RLT) von metastasierten Prostatakarzinomen [61–63]. Bekannt wurde vor allem die ^{177}Lu -Therapie mit [^{177}Lu]Lu-DOTATATE für die Therapiebehandlung von NET und [^{177}Lu]Lu-PSMA-617 sowie [^{177}Lu]Lu-PSMA-I&T für eine zielgerichtete Behandlung von Prostatakrebs [64–67].

Einige Therapienuklide geben im sekundären Umwandlungsprozess γ -Quanten ab und ermöglichen dadurch die Nachverfolgung der Therapieerfolge mittels SPECT/CT. Unter anderem wird bei der PSMA-617-Therapie das Radionuklidpaar $^{68}\text{Ga}/^{177}\text{Lu}$ für die Theranostik angewendet. Die Diagnose wird mittels ^{68}Ga -PET/CT durchgeführt und der Therapieverlauf mit ^{177}Lu -SPECT verfolgt [68,69].

1.4.1. Lutetium-177

^{177}Lu hat eine Halbwertszeit von 6,7 Tagen und einer maximalen β -Energie von 497 keV. Es gibt zwei Wege das ^{177}Lu herzustellen, entweder über die direkte oder indirekte Produktionsroute [70]. Der direkte Produktionsweg ist die Bestrahlung von natürlichem Lu_2O_3 (2,6% ^{176}Lu) oder angereichertem Lu_2O_3 (60,6% ^{176}Lu) mit thermischen Neutronen im Reaktor (Gleichung 3) [71]:

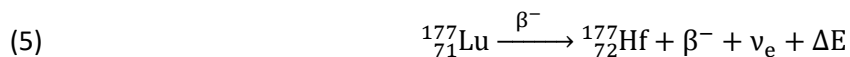


Der Nachteil des direkten Weges ist, dass in geringen Mengen das Nebenprodukt $^{177\text{m}}\text{Lu}$ mit einer $t_{1/2}$ von 160 d entsteht und das ^{177}Lu mit natürlichem ^{175}Lu bzw. ^{176}Lu geträgert ist („carrier added“, c.a.).

Eine alternative Variante, der indirekte Weg, bietet die Bestrahlung von angereichertem ^{176}Yb mit thermischen Neutronen [72]. Dabei entsteht zunächst das ^{177}Yb mit einer $t_{1/2}$ von 1,9 h und der anschließende β^- -Zerfall liefert das ^{177}Lu (Gleichung 4):



Der Vorteil dieser Methode ist, dass das ^{177}Lu chemisch vom Yb-Target abgetrennt werden kann und damit trägerfrei („non carrier added“, n.c.a.), sprich radionuklidisch rein ist. Durch eine β^- -Umwandlung bildet sich aus ^{177}Lu das stabile ^{177}Hf (Gleichung 5). Das ^{177}Lu weist nach der primären β^- -Umwandlung, als sekundären Umwandlungsprozess, niedrigerenergetische γ -Quanten auf. Durch die ausgesendeten γ -Strahlungen mit einer Energie von 113 keV und 208 keV ist die Bildgebung mittels SPECT möglich.



Das dreiwertige Kation Lutetium(III) hat einen Ionenradius von ~ 86 pm und kann Koordinationen von sechs bis neun eingehen, wobei gewöhnlich Koordinationen von acht bis neun bevorzugt werden [56]. Mit dem makrozyklischen DOTA-Chelator geht das Lutetium eine achtfache quadratisch-antiprismatische Komplexierung ein [73,74]. Wie bereits in 1.4 erwähnt sind die prominentesten Vertreter für die Lutetium-Therapie das Somatostatin-Octreotid-Analogon [^{177}Lu]Lu-DOTATATE für die ERT-NET Anwendung und die PSMA-Derivate [^{177}Lu]Lu-PSMA-617 und [^{177}Lu]Lu-PSMA-I&T für die Behandlung von Prostatakarzinomen.

1.5. Chelatorsysteme

Radionuklide werden in organische und metallische Nuklide unterteilt. Zu den organischen Nukliden zählen u.a. ^{11}C , ^{13}N , ^{15}O und ^{18}F . Die organischen Nuklide können kovalent an das Pharmakophor direkt gebunden werden. So kann z.B. das [^{18}F]F $^-$ über eine nukleophile Substitution eine OH-Gruppe ersetzen und in das Molekül eingeführt werden (wie z.B. bei der Herstellung von [^{18}F]FDG) [13,16,30,75]. Neben der direkten Einführung des ^{18}F besteht auch die Möglichkeit das Nuklid über eine prosthetische Gruppe (wie z.B. das [^{18}F]FETos zur Synthese von [^{18}F]FET) in das Molekül einzuführen. ^{68}Ga , ^{64}Cu und ^{89}Zr sind Vertreter der metallischen Nuklide, welche nicht kovalent, sondern über Chelatorsysteme koordinativ gebunden werden [25,39].

Für die koordinative Bindung von Radiometallen wie z.B. ^{68}Ga , ^{44}Sc , ^{64}Cu und ^{177}Lu werden Chelatoren, auch als Liganden bezeichnet, benötigt. Je nach Elektronenkonfiguration, Ionenladung des Metalls und Donoratomen des Liganden können sich verschiedene Bindungsgeometrien wie z.B. (verzerrt) tetraedrisch, quadratisch-planar oder oktaedrische Ligand-Metall-Koordinationen formen. Die koordinative Ligand-Metall-Bindung beruht auf der Donor-Akzeptor-Wechselwirkung. Geeignete funktionelle Donor-Gruppen der Liganden wie z.B. OH- und NH-Gruppen koordinieren mit dem Metallion (Akzeptor-Gruppe).

Die stabile Komplexbildung zwischen Chelator und Metallion ist verbunden mit der thermodynamischen und kinetischen Stabilität [76]. Die thermodynamische Stabilität gibt das Ligand-Metall-Gleichgewicht (Donor-Akzeptor-Wechselwirkung) an und wird durch die thermodynamische Stabilitätskonstante K_{ML} definiert. Je höher die Konstante ist umso stabiler ist auch der Ligand-Metall-Komplex. Neben der thermodynamischen Stabilität spielt in der Praxis die kinetische Stabilität eine wichtige Rolle. Diese gibt die Geschwindigkeit des Ligandenaustausches an, sprich die Tendenz zur Transchelatierung und Transmetallierung. Ein Ligand kann trotz einer geringen thermodynamischen Stabilität durch seine kinetische Stabilität einen stabilen Ligand-Metall-Komplex bilden. Andersherum können Liganden eine hohe thermodynamische Stabilität aufweisen, dennoch durch eine geringe kinetische Stabilität mit anderen Liganden transchelatiert oder durch andere Metallionen transmetalliert werden.

Es gibt verschiedene Arten von Chelatoren, die sich in azyklische, makrozyklische und hybridische Kategorien (siehe 1.5.2.–1.5.4.) einordnen lassen. Je nach Klasse haben die Chelatoren unterschiedliche Eigenschaften in Hinblick auf thermodynamische und kinetische Stabilität. Liganden können durch zusätzliche Modifikationen in der Struktur neben den Koordinationsstellen für das Metallion, auch weitere funktionalisierende Gruppen enthalten. Diese Chelatoren werden bifunktionelle Chelatoren genannt (s. 1.5.1.) und ermöglichen durch die zusätzlichen Bindungsstellen Kopplungen an Targetvektoren und dadurch auch die Anwendung in der Radiopharmazie und Nuklearmedizin.

1.5.1. Bifunktionelle Chelatoren

Chelatoren mit zusätzlichen, funktionalen Gruppen zur Kopplung von Targetvektoren werden „bifunktionelle Chelatoren“ (BFC) genannt. Der Chelator dient zur Komplexierung eines Radiometalls und die weitere Anbindungsstelle ermöglicht die Kopplung von Biomolekül-Konjugaten zur Bildung eines Radiopharmakons (Abbildung 5). Erst durch den Targetvektor erfolgt die selektive Adressierung und Bindung an die Zielstruktur. Meist sind zwischen dem Chelator und dem Targetvektor Linkereinheiten konjugiert, welche durch die Veränderung von z.B. Lipophilie, Gesamtladung, Abstand zwischen Chelator-TV und Molekulargewicht, Einflüsse auf das pharmakokinetische Verhalten des gesamten Radiopharmakons nehmen können [77]. Dadurch bedingt hat die Linkereinheit oft einen enormen Einfluss auf die Bindungsaffinität und auch das *in vivo*-Verhalten. Die Linkerbestandteile bestehen aus linearen oder (hetero-)zyklischen Strukturen, Aminosäure- sowie Peptidsequenzen, auch oft in vielfältigen Kombinationen. Die funktionalisierenden Stellen des BFCs sind meist Carboxyl- oder Aminogruppen, oft finden aber auch Konjugationen z.B. über NCS-, NHS-, Alkin- und Azidgruppen statt [76,78].

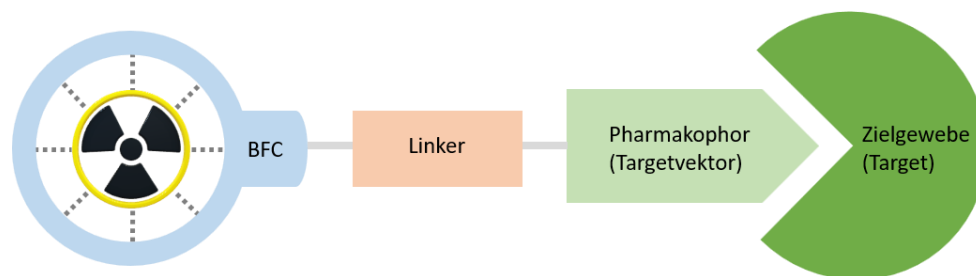


Abbildung 5: Schematische Darstellung eines bifunktionellen Chelators (BFC, blau) zur Koordination von Radiometallen und die zusätzliche Bindungsstelle zur Kopplung an ein Pharmakophor (hellgrün) über Linkereinheiten (orange). Das Radiopharmakon ermöglicht die selektive Anreicherung an das Zielgewebe (dunkelgrün). (Abb. in Anlehnung an [79]).

1.5.2. Azyklische Chelatoren

Azyklische Chelatoren sind offenkettige, meist lineare Liganden und weisen oft eine geringere Liganden-Metall-Stabilität auf als makrozyklische Chelatoren. Jedoch bieten die offenkettigen Liganden den großen Vorteil, dass eine relativ geringe Energiebarriere zur Ligand-Metall-Bindung überwunden werden muss und dadurch eine deutlich schnellere Komplexierung bei milden Reaktionsbedingungen möglich ist.

Die bekanntesten und meist verwendeten azyklischen Chelatoren in der radiopharmazeutischen Chemie sind EDTA (Ethyldiamintetraessigsäure), DTPA (Diethylentriaminpentaessigsäure), HBED (*N,N*-bis(2-hydroxybenzyl)ethyldiamin-*N,N*-diacetat) und DFO (Desferrioxamin) (Abbildung 6) [76,80]. DTPA ist ein sehr häufig genutzter azyklischer Chelator in der Onkologie. Durch die Zähigkeit von acht kann dieser eine Vielzahl von Radionukliden wie ^{68}Ga , ^{64}Cu , ^{90}Y , ^{111}In und ^{177}Lu komplexieren. In der Nuklearmedizin verwendete und zugelassene DTPA-Derivate sind [^{111}In]In-DTPA-octreotid und [^{111}In]In-capromab pendetid, welche für die Diagnose von NET und Prostatakarzinomen mittels SPECT verwendet werden [81]. Neben dem „klassischen“ DTPA-Liganden wurden viele weitere bifunktionelle Varianten des DTPAs entwickelt, die weitere Kopplungsmöglichkeiten von TVs am Ligandengerüst ermöglichen. Ein Beispiel ist das DTPA-*p*-Benzyl-NCS (Isothiocyanatobenzyl), welches eine weitere Anbindung von Linker-TV Konjugaten am NCS ermöglicht.

Ein weiterer, wichtiger azyklischer Chelator ist das DFO welcher insbesondere zur Komplexierung von ^{89}Zr genutzt wird. Mit entsprechender Funktionalisierung und Bindung an (monoklonale-) Antikörper(fragmente), findet das DFO seine Anwendung in der Diagnostik maligner Tumorgewebe mittels Immuno-PET. Die drei Hydroxamat-Gruppen des DFOs eignen sich sehr gut für die Komplexierung mit ^{89}Zr , aber durch die Besetzung von lediglich sechs von acht möglichen Koordinationsstellen kann es zu einer unerwünschten Freisetzung des Radionuklids kommen. Um die Stabilität zu erhöhen wurde das DFO* entwickelt, welches eine Hydroxamat-Einheit mehr besitzt und eine bessere Komplexstabilität aufweist [82,83].

Der HBED-Chelator und das bifunktionelle Analogon HBED-CC zeigen sehr gute Komplexierungseigenschaften mit ^{68}Ga . Immer wichtiger wurde der HBED-CC-Ligand in den letzten Jahren durch die Kopplung an einen Prostataspezifisches Membranantigen (PSMA)-Inhibitor und die gezielte Bildgebung von PSMA-exprimierenden Prostatakarzinomen. Das [^{68}Ga]Ga-PSMA-11 findet mittlerweile routinemäßig Anwendung in der nuklearmedizinischen Diagnostik mittels PET/CT [84,85].

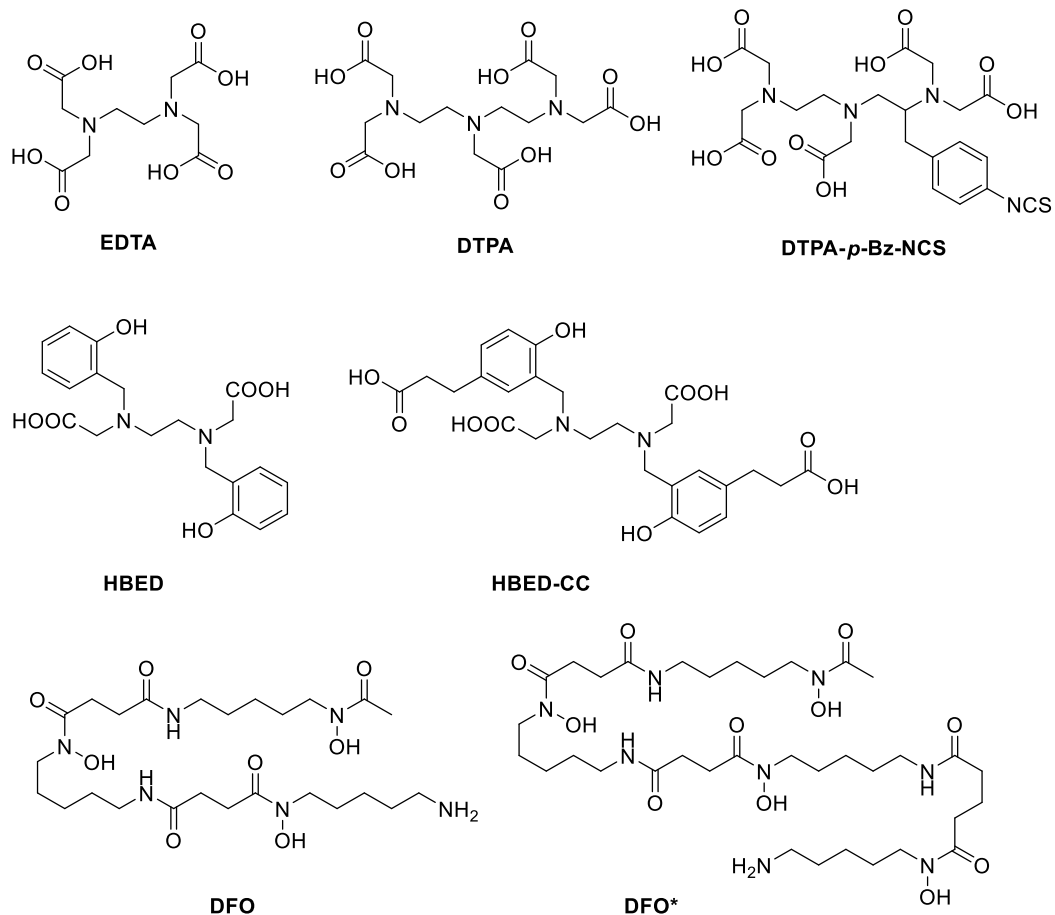


Abbildung 6: Beispiele für azyklische Chelatoren: EDTA, DTPA, DTPA-*p*-Bz-NCS, HBED, HBED-CC, DFO und DFO*.

1.5.3. Makrozyklische Chelatoren

Makrozyklische Chelatoren besitzen, im Gegensatz zu azyklischen Chelatoren, eine Art Käfiggerüst, welches die Metallionen im Zentrum koordinativ bindet. Die Ligand-Metall-Komplexe von makrozyklischen Chelatoren sind meist thermodynamisch und kinetisch stabiler als die der Azyklischen, da durch die zentrale Umschließung im zyklischen Gerüst das Metallion stärker gebunden ist und hierdurch die Dekomplexierung des Metalls erschwert wird. Andererseits erfordern die Komplexbildungen bei Makrozyklen durch die hohe kinetische Energiebarriere relativ harsche Bedingungen bei der Komplexbildung.

Die bekanntesten makrozyklischen Chelatoren, für Metalle mit der Koordinationszahl sechs oder höher, sind NOTA (1,4,7-Triazaacyclononan-1,4,7-triessigsäure), DOTA (1,4,7,10-Tetraazaacyclododecan-1,4,7,10-tetraessigsäure) und TRAP (1,4,7-Triazaacyclononan-1,4,7-tris(methyl(2-carboxyethyl)-phosphinsäure)) (Abbildung 7) [76,78,80].

Das NOTA mit einem Triazacyclononan-Gerüst eignet sich besonders gut für die Komplexierung von ^{68}Ga . Der Ionenradius des dreiwertigen Galliums passt sehr gut mit dem inneren Radius des NOTAs überein, während der des DOTAs etwas zu groß ist für Ga(III) . Jedoch ist die Komplexierung von NOTA, aufgrund der Zähnnigkeit von sechs und der kleinen Käfigstruktur, im Hinblick auf die Theranostik auf eine kleine Anzahl von Metallen begrenzt.

TRAP, welches auf dem NOTA-Gerüst basiert, bietet durch die drei PO_2H -Gruppen eine sechsfache Koordination mit ^{68}Ga und ermöglicht dennoch weitere Anbindungen an Biomolekülen durch die zusätzlichen Carbonsäure-Komponenten. Daher eignet sich der TRAP-Chelator vor allem für die Bildung von di- und trimeren Konjugaten [86,87].

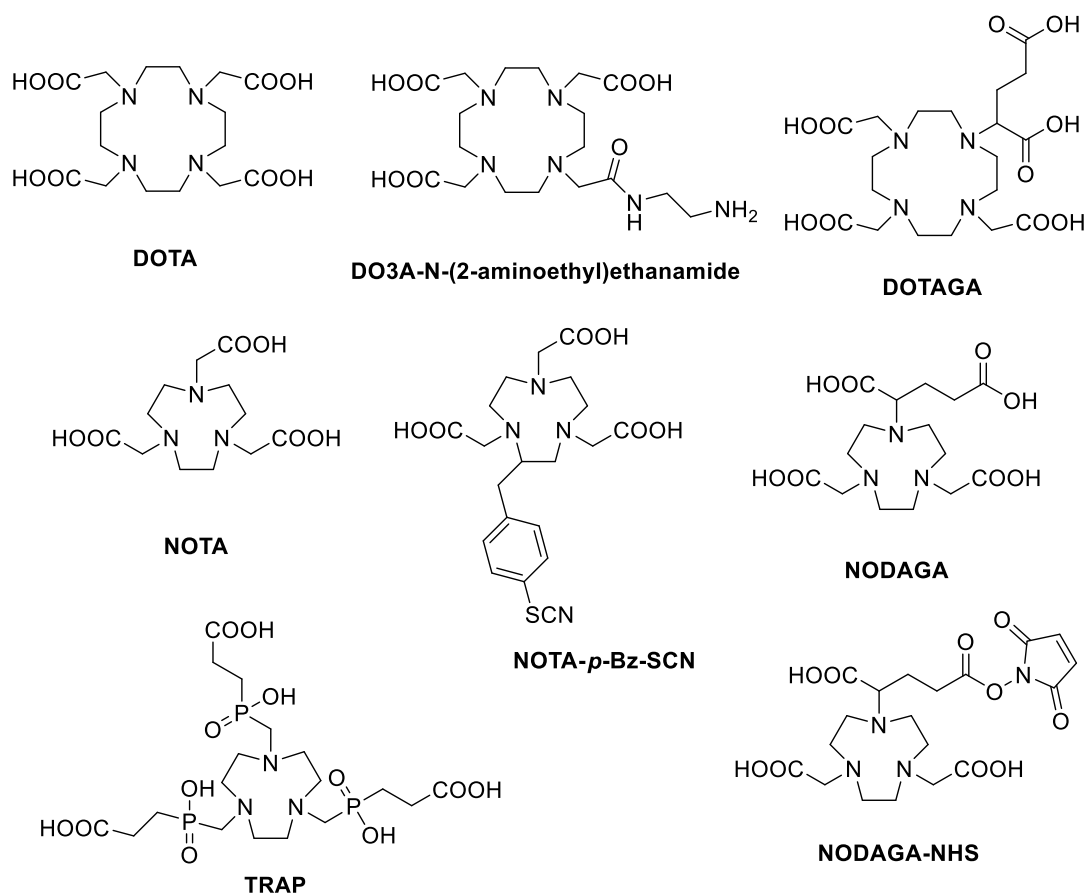


Abbildung 7: Beispiele für makrozyklische Chelatoren: DOTA, DO3A-N-(2-aminoethyl)ethanamide, DOTAGA, NOTA, NOTA-*p*-Bz-SCN, NODAGA, TRAP und NODAGA-NHS.

Der wohl meist genutzte, makrozyklische Chelator in der Nuklearmedizin ist DOTA, ein octadentaler Ligand. Trotz Funktionalisierung einer Carboxylgruppe bietet das DOTA immer noch eine heptadentale Koordination, wodurch eine Reihe von Ligand-Metall-Bindungen wie z.B. mit ^{68}Ga , ^{44}Sc , ^{90}Y , ^{111}In und ^{177}Lu möglich sind.

DOTA-basierte, radiokomplexierte Wirkstoffe gewinnen immer mehr an Bedeutung für die Anwendung in der Theranostik (Abbildung 8).

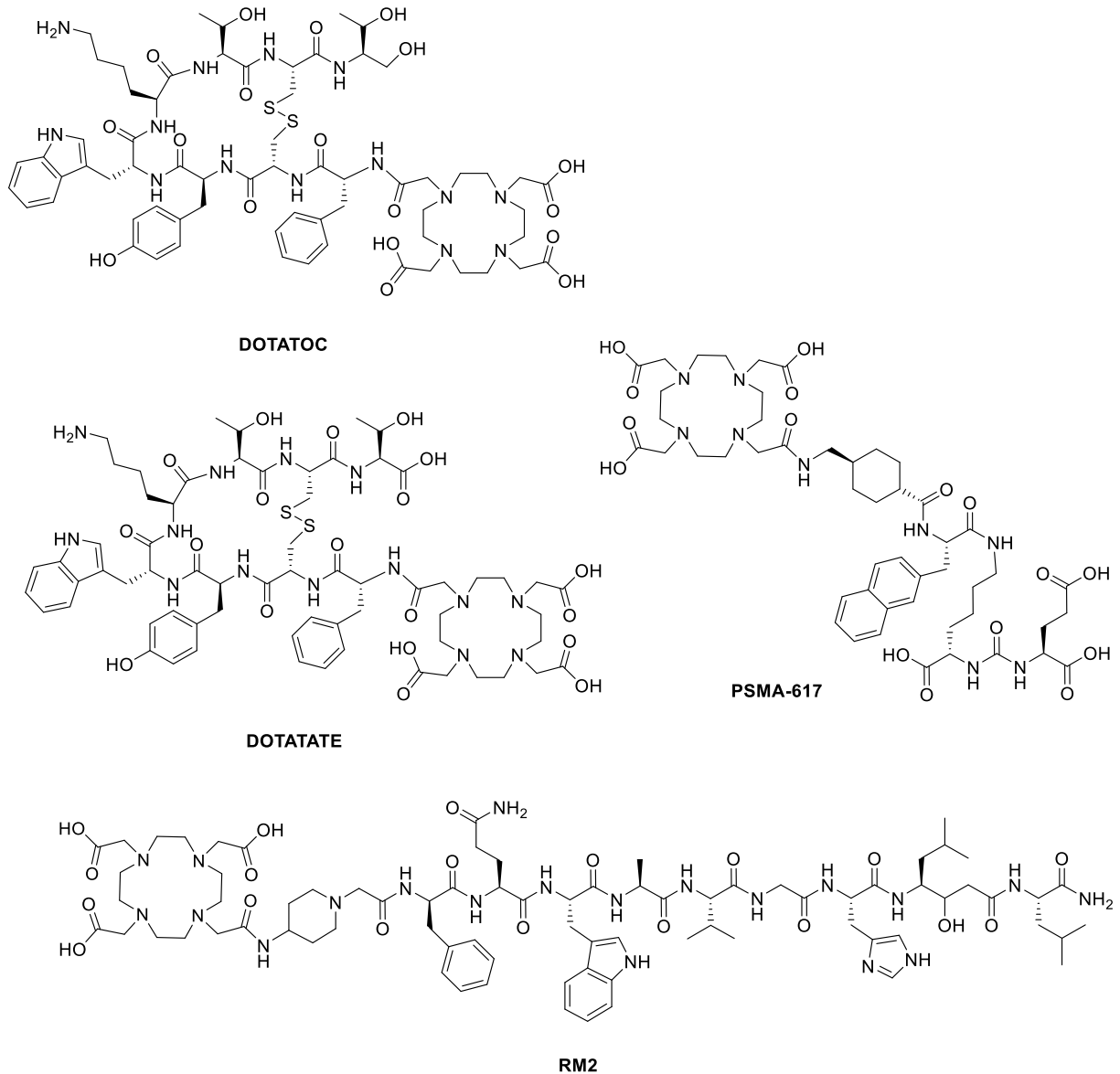


Abbildung 8: DOTA konjugierte Wirkstoffe: Somastatin-Analoga DOTATOC und DOTATATE, PSMA-617 (PSMA-Inhibitor gebundener DOTA Chelator) und GPRr-Antagonist RM2.

DOTA konjugierte Somastatin-Octreotid-Analoga $[^{68}\text{Ga}]\text{Ga-DOTATOC/DOTATATE}$ sowie $[^{90}\text{Y}]\text{Y-DOTATOC/DOTATATE}$ und $[^{177}\text{Lu}]\text{Lu-DOTATOC/DOTATATE}$ werden in der Theranostik von neuroendokrinen Tumoren eingesetzt. Für die diagnostische Bildgebung von PSMA wird zwar hauptsächlich das $[^{68}\text{Ga}]\text{Ga-PSMA-11}$ eingesetzt, für die Therapie kommt aber auch ein DOTA-Derivat, das $[^{177}\text{Lu}]\text{Lu-PSMA-617}$, zum Einsatz [8,88]. Auch werden Therapienuklide wie ^{90}Y und ^{225}Ac mit (DOTA)-PSMA-617 komplexiert und in der Therapie praktisch eingesetzt. Ein weiteres

Anwendungsbeispiel von DOTA konjugierten Radiopharmazeutika ist die klinische Applikation von „Gastrin Releasing Peptide receptor“ (GRPr, auch als BB₂ bekannt) basierten Antagonisten, wie das (DOTA)-RM2, welcher Verwendung mit ⁶⁸Ga und ¹⁷⁷Lu findet [89,90].

Ein Analogon von DOTA, der DOTAGA-Ligand (1,4,7,10-Tetraazacyclododecan-1-glutarsäure-4,7,10-triessigsäure) und ein Analogon von NOTA, der NODAGA-Chelator (1,4,7-Triazacyclononan-1-glutarsäure-4,7-diessigsäure) haben eine zusätzliche Carboxylseitenkette zur Verfügung. Daher ermöglichen die zwei Chelatoren eine sechsfache bzw. achtfache Koordination mit Metallen und zusätzlich eine Funktionalisierung an weitere Targetvektoren.

1.5.4. Hybridische Chelatoren

Hybridische Chelatoren vereinigen die Vorteile von zyklischen- und makrozyklischen Chelatoren. Die Komplexierung von Metallen kann wie bei den azyklischen Chelatoren unter milden Bedingungen ablaufen. Zusätzlich bilden, bedingt durch die zyklische Einheit, die hybridischen Chelatoren eine meist hohe Ligand-Metall-Stabilität. Die bekanntesten, in der Radiopharmazie eingesetzten Hybridchelatoren, sind das DATA^m (1,4-Diessigsäure-6-methyl-(amino(methyl)acetat)-perhydro-1,4-diazepan) und das AAZTA (1,4-Bis(hydroxy-carbonylmethyl)-6-[bis(hydroxycarbonylmethyl)]-amino-6-methylperhydro-1,4-diazepin) mit einem cyclischen 6-Amino-6-methylperhydro-1,4-diazepin Grundgerüst und einem azyklischen exo-Amin (Abbildung 9) [80,91–93]. Das hexadentale DATA^m eignet sich ausgezeichnet zur Komplexierung von Gallium(III) mit einer sechsfachen N₃O₃-Koordination in einer leicht verzerrt oktaedrischen Konformation [94,95]. Das AAZTA wurde zunächst für die MRT-Untersuchung zur Komplexierung von Gadolinium entwickelt [96]. Der heptadentale AAZTA-Chelator ermöglicht durch die zusätzliche Acetatgruppe am exo-Amin neben ⁶⁸Ga auch Komplexierungen mit z.B. ⁴⁴Sc, ⁶⁴Cu und ¹⁷⁷Lu [97–99].

Für die Anbindung an Targetvektoren wurden bifunktionelle Derivate wie das DATA^{5m} (5-[[6-(N-Essigsäure)(N'-methyl)amino]-1,4-diessigsäure-1,4-diazepan]-pentansäure) und das AAZTA⁵ (5-[[6-(N,N'-Diessigsäure)amino]-1,4-diessigsäure-1,4-diazepan]-pentansäure) entwickelt. Erste klinische Anwendungen wurden mit dem DATA^{5m} in Form von [⁶⁸Ga]Ga-DATA-TOC zur molekularen Bildgebung von NET durchgeführt [100,101].

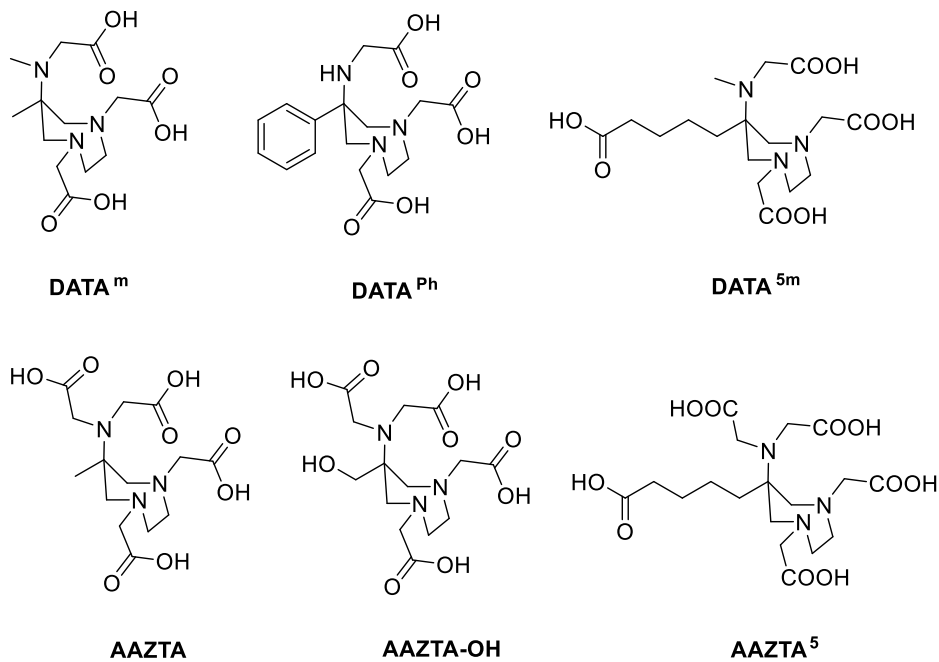


Abbildung 9: Hybridchelatoren: DATA^m, DATA^{Ph}, DATA^{5m}, AAZTA, AAZTA-OH und AAZTA⁵.

1.6. Fibroblasten-Aktivierungsprotein (FAP) als Targetvektor

Targetvektoren (TV), sind Biomoleküle, durch die das Radiopharmakon erst gezielt an die entsprechende biologische Zielstruktur bzw. das Zielgewebe (auch „Target“ genannt) transportiert werden kann. Dabei weist der TV optimalerweise eine sehr hohe Affinität und Selektivität zum Target auf. Es gibt hauptsächlich zwei Möglichkeiten, den TV in ein Radiopharmakon einzuführen. Eine Möglichkeit ist, dass das Pharmakophor, wie z.B. beim [¹⁸F]FDG, selbst als Targetvektor im physiologischen *in vivo*-Prozess mitwirkt. Die zweite Variante sind Chelator-basierte Radiopharmaka, indem die Targetvektoren an einen Chelator, meist über Linkereinheiten, verknüpft sind. Die bereits erwähnten [⁶⁸Ga]Ga-DOTATOC oder [⁶⁸Ga]Ga-PSMA-617 sind solche Beispiele. Es gibt verschiedene Arten von Targetvektoren, um spezifisch an das Target zu binden. Die gängigsten Formen in der Onkologie sind Verwendungen von Inhibitoren, (linearen oder cyclischen) Peptiden und (monoklonalen-)Antikörper(fragmenten).

1.6.1. FAP - Biologische Eigenschaften

Das Fibroblasten-Aktivierungsprotein (FAP) ist ein transmembranes Glykoprotein (Typ II), gehört es zur Familie der Serinproteasen und besteht aus 760 Aminosäuren [102]. Ein kleiner Teil der Aminosäuresequenzen (Sequenz 1-25) gehört den intrazellulären und transmembranen Domänen an und die restlichen 26-760 Aminosäuren liegen in der extrazellulären Domäne (Abbildung 10). Erst durch die Bildung eines FAP-Homodimers wird das Protein enzymatisch aktiv. Innerhalb der extrazellulären Domäne ergeben sich zwei Unterdomänen, die aus einer β -Propellerdomäne und einer α/β -Hydroxylasedomäne bestehen [102,103]. Die β -Propeller-Domäne besteht aus acht Blättern, die sich um eine zentrale Pore wickeln und dienen als eine Art Filter, um selektiv Peptide in das katalytische Zentrum passieren zu lassen [104]. Das FAP besitzt eine katalytische Triade aus Serin, Asparaginsäure und Histidin, welche sich an der Schnittstelle zwischen der β -Propeller- und der α/β -Hydroxylase-Domäne befindet.

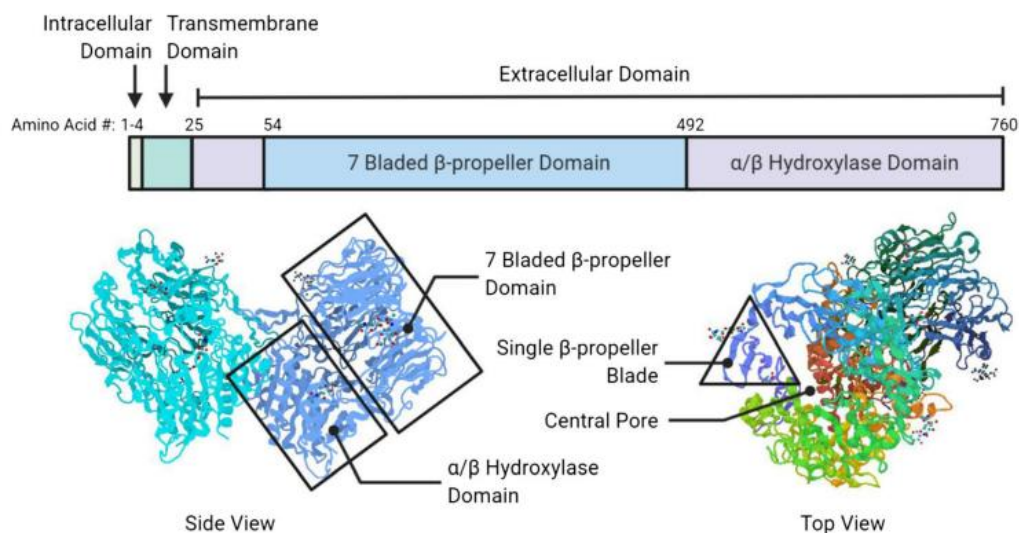


Abbildung 10: Schematische Darstellung und Unterteilung der FAP-Domänen (oben); Homodimere FAP-Struktur mit der siebenblättrigen β -Propellerdomäne und α/β -Hydroxylasedomäne (unten, Seitenansicht); β -Einzelpropellerdomäne und die zentrale Pore (unten, Draufsicht). (Abb. mit der Genehmigung von © Springer Nature Switzerland AG, Springer Nature aus [103] entnommen).

Das FAP gehört zur Gruppe der Dipeptidylpeptidasen (DPPs), zu welcher u.a. auch DPP4, DPP8 und DPP9 gehören. Die Hälfte der Aminosäuresequenzen und 70% der katalytischen Domäne von FAP ist mit DPP4 identisch [105,106]. Allerdings hat das FAP, im Gegensatz zu den DPPs, sowohl eine Dipeptidylpeptidase- als auch eine Endopeptidase-Aktivität. Durch die DPP-Aktivität kann ein Dipeptid am N-Terminus abgespalten werden, wobei die vorletzte Aminosäure eine Prolin-Einheit ist, während durch die Endopeptidase-Aktivität ein Peptid nach dem Prolin einer Glycin-Prolin (Gly-Pro)-Einheit

gespalten werden kann. (Abbildung 11) [107]. Die Endopeptidase-Aktivität ist jedoch weit effizienter und wird gegenüber der DPP-Aktivität bevorzugt. Dabei ist die Endopeptidase-Aktivität nach den Aminosäuresequenzen von Gly-Pro-Phe oder Gly-Pro-Met am effektivsten und bei Gly-Pro-His und Gly-Pro-Glu weniger effektiv [103].

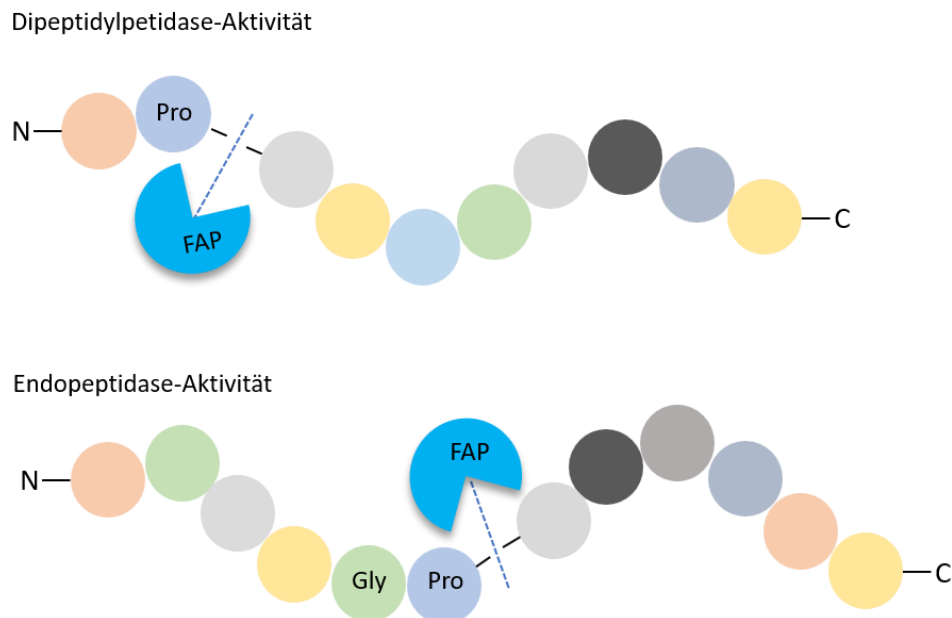


Abbildung 11: Doppelte Enzym-Aktivität von FAP, die Dipeptidylpeptidase-Aktivität mit der Spaltung von zwei Aminosäuren am N-Terminus nach der Prolin-Sequenz; die Endopeptidase-Aktivität nach Gly-Pro Sequenzen mit mehr als zwei Aminosäuren. (Abb. in Anlehnung an [107]).

Das Besondere von FAP ist, dass diese in gesunden Geweben, sowie gutartigen Tumoren nicht oder nur in minimalen Mengen vorhanden sind. Dahingegen ist das FAP in über 90% der häufigsten menschlichen Epitheltumoren wie z.B. Brust-, Pankreas-, Darm- und Lungenkrebs überexprimiert und ebenso bei Krankheiten wie Wundheilung, chronischen Entzündungen, Leberzirrhosen, rheumatoider Arthritis, Lungenfibrose, Knochen- und Weichteilsarkomen, Osteoarthritis und Morbus Crohn vorzufinden [103,104,108–111].

Beim Tumorwachstum ist das Fibroblasten-Aktivierungsprotein erheblich mitbeteiligt und beeinflusst u.a. die Förderung von Zellproliferation, Migration, Invasion und Angiogenese [103,104].

Das FAP hat Einfluss auf die Remodellierung der extrazellulären Matrix (ECM) und kann als Serinprotease direkt die ECM abbauen oder indirekt bei der Aktivierung und Modifikation der ECM als regulierende Protease wirken. Der Einfluss von FAP auf die Angiogenese konnte in FAP exprimierenden Brustkrebszellen identifiziert werden, wobei die Zellen mit FAP-Exprimierung eine dreimal höhere Mikrogefäßdichte zeigten als die Zellen ohne FAP-Exprimierung. Außerdem konnte bei einer Depletion von FAP eine Verringerung der Tumor-Blutgefäßdichte in Mäusen beobachtet werden [104].

Das FAP wird in epithelialen Tumoren nicht von den Krebszellen selbst, sondern in aktivierten Fibroblasten, den sogenannten krebssassoziierten Fibroblasten („cancer-associated fibroblasts“, CAFs), überexprimiert. Die CAFs sind Fibroblasten mit einem myofibroblastischen Phänotyp und befinden sich, als einer der dominierenden und wichtigsten Komponenten, in der Tumormikroumgebung [104,112]. Die CAFs haben verschiedene spezifische und selektive Biomarker zur Identifizierung mit u.a. α -SMA, PDGFR α/β , S100A4 und CD10 und FAP [113,114].

Die Zusammensetzung der Tumormikroumgebung ist sehr komplex und besteht aus der extrazellulären Matrix, Stromazellen (u.a. Fibroblasten), Myofibroblasten, Endothelzellen, Perizyten, verschiedenen Immunzellen, Lymphozyten und neuroendokrinen Zellen [104,112]. Die Tumormikroumgebung hat großen Einfluss auf die Entwicklung und Wachstum des Tumors (Karzinogenese), Initiierung und Metastasierung. Die Stromazellen (als Tumorstroma bezeichnet) machen den größten Teil der gesamten Tumormasse aus (über 90%), wodurch die CAFs und FAP als Biomarker eine große Bedeutung in Hinsicht auf Krebsentwicklung sowie Metastasierung haben und ein geeignetes Target für die medizinische Theranostik diverser Tumoren darstellen.

1.6.2. Adressierung von FAP für die Theranostik

Es gibt verschiedene Wege das FAP zu adressieren und mehrere FAP-adressierende Wirkstoffe befinden sich bereits in der Forschung und Anwendung. In der Onkologie liegt der Fokus vor allem auf der Entwicklung von Radiopharmazeutika unter Verwendung von FAP-Antikörpern, FAP-Inhibitoren und -Peptiden.

Das erste Mal wurden humane Fibroblasten-Aktivierungsproteine in kultivierten Fibroblasten unter Verwendung des monoklonalen Antikörpers (mAb) F19 entdeckt. Das murine anti-FAP mAb F19, markiert mit ^{131}I (^{131}I -mAbF19), zeigte in einer Phase-I-Studie eine hohe FAP-Tumorexpression in primären und metastasierten kolorektalen Karzinomen [115]. Es folgten zwei weitere Phase-I Studien, welche Pharmakokinetik und Dosimetrie von Patienten mit Lebermetastasen von kolorektalem Krebs und Weichteilsarkomen beinhalteten [116]. Weitere Untersuchungen mit einer humanisierten Version des F19 mAb, dem Sibrotuzumab, wurden als ^{131}I -Sibrotuzumab bei Patienten mit kolorektalem und nicht kleinzelligem Lungenkrebs (NSCLC) durchgeführt [117]. Zwar waren die Phase-I-Studienergebnisse vielversprechend, jedoch zeigten weitere Phase-II-Studien des F19 mAbs, mit metastasierenden Darmkrebspatienten, keine nutzbringenden Vorteile bzw. therapeutischen Erfolge

[118]. Die Gründe dafür sind, dass das Sibrotuzumab weder eine inhibitorische Aktivität für FAP aufweist noch eine zytotoxische oder zytostatische Wirksamkeit [108]. Weitere, bisher bekannte FAP-mAb-Untersuchungen beruhen auf präklinischen Studien, wie das FAP5-DM1 (ein anti-FAP mAb konjugiert an das zytostatische Maytansin-Derivat DM1), die humanen Fab-Fragmente ESC11 und ESC14 komplexiert mit ¹⁷⁷Lu und das Antikörper-Wirkstoff-Konjugat OMTX705 aus dem humanisierten anti-FAP monoklonalen Antikörper OMTX005 [119–121]. Alle Studien zeigen Verzögerungen bzw. Hemmungen des Tumorwachstums und verlängerte Tumorregressionen.

Die wohl fortgeschrittenste Entwicklung zur Adressierung von FAP, für die Anwendung in der Theranostik, ist die Nutzung von FAP-Inhibitoren (FAPi). Inhibitoren dienen der Blockierung und Hemmung von Enzymaktivitäten. In der Onkologie ist es eine gängige Methode, Inhibitoren zur Adressierung der Zielmoleküle zu verwenden und dadurch sowohl Diagnose mittels PET/CT als auch therapeutische Ansätze durchzuführen. Prominente Beispiele sind die bereits erwähnten PSMA-Inhibitoren zur Anreicherung am PSMA bei Prostatakarzinomen.

FAP-Inhibitoren besitzen reaktive Gruppen, die eine kovalente Bindung mit dem aktiven Zentrum des Zielenzym herstellen, sie werden als „warhead“ bezeichnet [122]. Die kovalenten FAPi können sowohl reversibel als auch irreversibel sein und enthalten eine funktionelle Gruppe, die eine Bindung mit dem Serin im aktiven Zentrum eingeht [123]. Reversible, kovalente Inhibitoren verfügen über Aldehyd-, Nitril-, Boronsäure- oder α -Ketoamid-Gruppen und irreversible kovalente Inhibitoren über Chlormethylketon-, Phosphorfluoridat- oder Phosphonatester-Gruppen. Vorteile kovalenter Inhibitoren gegenüber nicht-kovalenten Inhibitoren sind die Erhöhung der biochemischen Effizienz, geringere Empfindlichkeit von pharmakokinetischen Parametern, wie die Proteinbindung oder die Ausscheidung, und die tendenziell längere Verweildauer und Aktivität [124].

Vor allem ist die Selektivität und Spezifität für FAP und dahingegen die Nicht-Selektivität für die anderen Peptidasen der selbigen Gruppe (Dipeptidyl-Peptidasen DPPiV, DPP8, DPP9 und Prolyl-Endopeptidase (PREP)) bei FAP-Inhibitoren entscheidend, da diese immer in Konkurrenz zum FAP stehen. Daher muss bei der strukturellen Entwicklung neuartiger FAPi-Radiopharmaka eine selektive Affinität für FAP vorausgesetzt werden.

Die bisher bekanntesten FAP-Inhibitoren sind Boronsäure basierte- und Glycin-2-cyanopyrrolidin-basierte FAPi (Abbildung 12 und 13). Bei den Boronsäure-haltigen FAPi fungiert die Boronsäure als „warhead“ und bei den (Cyano)Prolin-basierten FAPi das Nitril am Pyrrolidin.

Die Boronsäure basierten Val-boroPro (Talabostat, PT-100) und D-Ala-boroPro-Inhibitoren haben sich in der Vergangenheit als nicht FAP-selektiv herausgestellt, da die Affinität bzw. Inhibition für FAP im

Gegensatz zu den DPPs und PREP nicht signifikant genug war (Abbildung 12) [123]. Eine weitere strukturelle Veränderung des D-Ala-boroPro-Inhibitors, das *N*-(Pyridin-4-carbonyl)-D-Ala-boroPro (ARI-3099), zeigte zwar eine deutlich höhere Selektivität gegenüber den DPPs und PREP, konnte bisher jedoch keine bedeutenden *in vivo*-Studien darlegen.

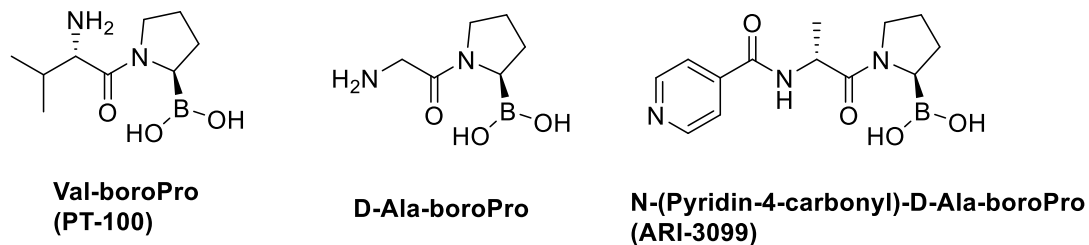


Abbildung 12: FAP-Inhibitoren: Boronsäure-basierte FAPis, Val-boroPro (Talabostat, PT-100), D-Ala-boroPro und *N*-(Pyridin-4-carbonyl)-D-Ala-boroPro (ARI-3099).

Die Gly-(2-cyano)Pro-Inhibitoren weisen demgegenüber eine sehr hohe Selektivität für FAP und zusätzlich eine zufriedenstellende Nicht-Spezifizität für die anderen Peptidasen auf [122,125,126]. Ausgehend von einer Naphthalin acylierten Glycin-2-cyanopyrrolidin-Struktur wurde in einer Reihe von Struktur-Wirkungsbeziehungen und pharmakokinetischen Untersuchungen die Affinität zu FAP weiter verbessert. Durch die Ersetzung von Naphthalin durch ein Chinolin konnte die Inhibition für FAP und die Selektivität gegenüber den DPPs und PREP deutlich optimiert werden. Die Substitution von Difluoro-Einheiten am Pyrrolidin-Gerüst verbesserte bedeutend die Bindungsaffinität für FAP und kristallisierte sich letztendlich als der potenteste FAP-Inhibitor heraus. Der (4-Chinolinyl)glycyl-4,4-difluoro-2-cyanopyrrolidin FAP-Inhibitor, bezeichnet als „UAMC1110“, enthält eine Difluoreinheit an der 4,4-Position am 2-Cyanopyrrolidin-Ring und ist über eine Glycin-Einheit an der 4-Position des Chinolins verbunden (Abbildung 13) [122].

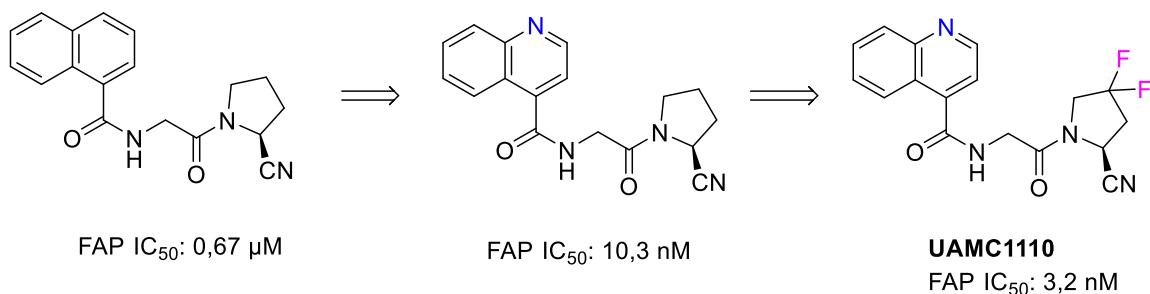


Abbildung 13: Entwicklung der Gly-2-cyanopyrrolidin-FAP-Inhibitoren: *N*-(1-naphthyl)-Gly-2-cyanopyrrolidin (FAP IC₅₀ Wert: 0,67 µM), (4-Chinolinyl)glycyl-2-cyanopyrrolidin (FAP IC₅₀ Wert: 10,3 nM) und der Chinolin-Gly-2-Cyano-4,4-difluoroPro-basierte FAPi, UAMC1110 (FAP IC₅₀ Wert: 3,2 nM). [IC₅₀ Wert gibt die Konzentration an, bei der ein Wirkstoff einen bestimmten biologischen Prozess um 50 % hemmen kann].

Interessant wurde die nuklearmedizinische Anwendung der FAPi durch die Einführung eines bifunktionellen DOTA-Chelators, verknüpft über einen Piperazin-Linker. Auf Basis des UAMC1110 FAP-Inhibitors wurden eine Vielzahl von FAPi-verknüpften DOTA-Varianten entwickelt mit diversen Modifikationen am Piperazinsystem [127–129]. In präklinischen Untersuchungen konnten sich die sogenannten FAPI-04- und FAPI-46-Konjugate hervorheben und erlangten die größte Aufmerksamkeit als die bisher vielversprechendsten, FAP-adressierenden Radiopharmaka (Abbildung 14). Seitdem befinden sich die FAPi-Derivate in etlichen klinischen Applikationen für verschiedenste Tumorarten. Hauptsächlich liegt der Fokus auf der Diagnose mittels ^{68}Ga -PET/CT, mittlerweile gibt es aber immer mehr Anwendungen mit anderen PET-Nukliden wie z.B. ^{18}F und ^{64}Cu sowie erste Therapieansätze mit beispielsweise ^{90}Y und ^{177}Lu [114,130–132].

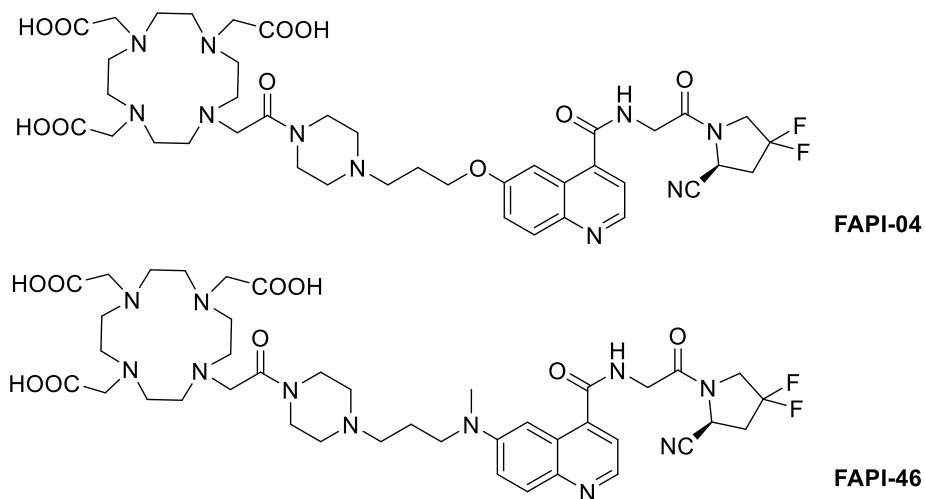


Abbildung 14: Die DOTA-konjugierten FAPi-Konjugate FAPI-04 und FAPI-46, verbunden über ein Piperazin-Linkersystem an den UAMC1110-Inhibitor.

Unabhängig davon wurde kürzlich die Verwendung von FAP-gebundenen Peptiden, als FAP-2286 bezeichnet, beschrieben. Die komplette Struktur des FAP-Peptids ist allerdings bisher noch nicht veröffentlicht. Das Peptid ist mit einem DOTA-Chelator konjugiert und wurde in ersten Patienten mit fortgeschrittene Adenokarzinome der Bauchspeicheldrüse, der Brust, des Rektums und der Eierstöcke mittels der Peptidrezeptor-Radionuklidtherapie (PRRT) untersucht. Die Diagnose der Adenokarzinome erfolgte über ^{68}Ga -FAP-2286 und ^{68}Ga -FAPI-04 PET/CT-Aufnahmen und die ersten Therapieansätze mit dem ^{177}Lu -FAP-2286 [133]. Dabei konnten über SPECT/CT-Aufnahmen gute Tumoranreicherungen beobachtet werden sowie lange Verweildauern in den primären und metastasierten Tumorerläsionen mit einem geringen Risiko für die Patienten.

2. Problemstellung und Zielsetzung

Die vorliegende Arbeit ist in vier Hauptabschnitte unterteilt. Eine Übersicht der Projekte ist in Abbildung 15 dargestellt. Der Fokus liegt auf der Entwicklung neuer Radiopharmaka zur Adressierung von FAP unter Verwendung von FAP-Inhibitor-konjugierten Chelator-Linker-Systemen. In allen vier Projekten A – D werden verschiedene Chelator-FAPi-Konjugate synthetisiert, radiochemisch evaluiert und die *in vitro*-Stabilitäten in verschiedenen Medien sowie die *in vitro*-Affinitäten bzgl. FAP und den verwandten Proteasen DPPs und PREP gemessen. Zusätzlich umfassen die Projekte A und C erste präklinische und klinische *in vivo*-Applikationen.

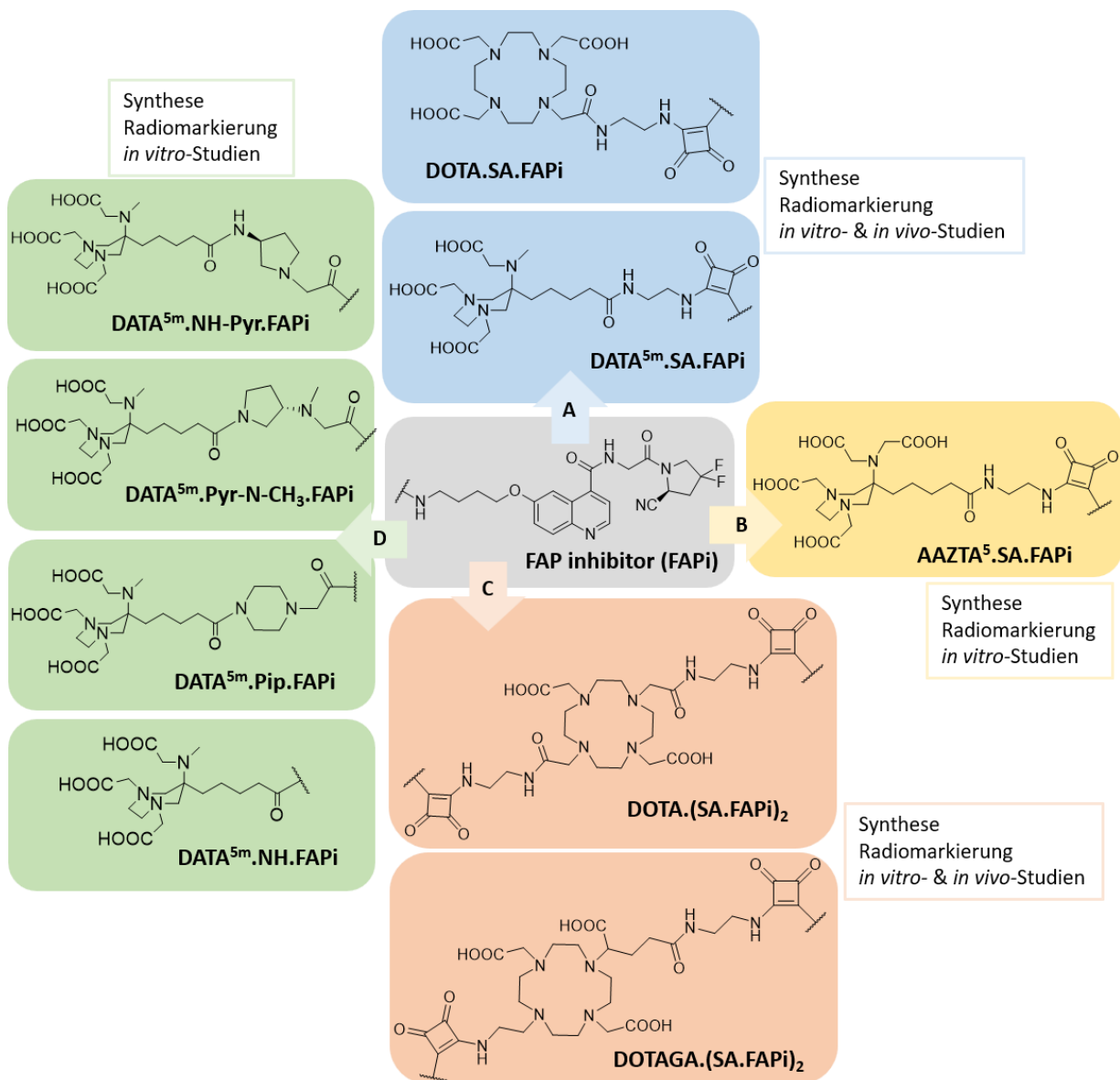


Abbildung 15: Übersicht der vier Hauptabschnitte A – D.: Abschnitt A: DOTA.SA.FAPi und DATA^{5m}.SA.FAPi; Abschnitt B: AAZTA⁵.SA.FAPi; Abschnitt C: DOTA.(SA.FAPi)₂ und DOTAGA.(SA.FAPi)₂; Abschnitt D: DATA^{5m}.NH-Pyr.FAPi, DATA^{5m}.Pyr-N-CH₃.FAPi, DATA^{5m}.Pip.FAPi und DATA^{5m}.NH.FAPi.

Hauptabschnitt A

In diesem Projekt sollen die zwei Chelatoren DOTA und DATA^{5m} zur Kopplung an den UAMC1110 FAP-Inhibitor untersucht werden. Die Konjugation zwischen Chelator und Targetvektor findet über die Quadratsäure, unter Bildung eines Quadratsäurediamids („squaramide“, SA), statt. Die Quadratsäure als Linkereinheit ermöglicht präparative Vorteile durch die pH-gesteuerte, selektive und schrittweise asymmetrische Amidierung von Quadratsäurediethylester ohne Bildung unerwünschter Nebenprodukte unter milden Bedingungen. Zusätzlich konnten in vorherigen Arbeiten pharmakokinetische Vorteile von SA-Konjugaten (z.B. PSMA-SA-Derivate) im Vergleich zu Verbindungen ohne SA bestätigt werden [134]. In der Anwendung der Quadratsäure-basierten PSMA-Tracer [⁶⁸Ga]Ga-NODAGA.SA.PSMA, [⁶⁸Ga]Ga-TRAM.SA.PSMA und [⁶⁸Ga]Ga-DOTAGA.SA.PSMA zeigten diese eine sehr gute Tumoranreicherung sowie hohe Tumor-zu-Organ-Verhältnisse in LNCaP-Tumor-tragenden Mäusen. Die Ergebnisse waren vergleichbar gut mit den klinischen Standards [⁶⁸Ga]Ga-PSMA-617 and [⁶⁸Ga]Ga-PSMA-11 [135].

Der Chelator DATA eignet sich besonders gut für die Komplexierung von ⁶⁸Ga, welches eine hexadentale Koordination mit der N₃O₃-Konformation des Chelators eingeht. Durch die schnelle und quantitative Komplexierung in wenigen Minuten unter milden Bedingungen ermöglicht dieser Chelator eine Art “instant-kit“-Markierung und -Anwendung. Daher bietet DATA eine Alternative zum DOTA, bei dem durch die relativ harschen Komplexierungsbedingungen eine instant-kit-Anwendung erschwert bzw. problematisch sind.

Die erfolgreich synthetisierten Vorläufer DOTA.SA.FAPi und DATA^{5m}.SA.FAPi werden radiochemisch mit ⁶⁸Ga in Hinblick auf die Komplexierungskinetik und *in vitro*-Komplexstabilität in humanen Serum (HS), Ethanol und isotonischer Kochsalzlösung und phosphatgepufferter Salzlösung (PBS) untersucht. Weiterhin werden *in vitro*-Affinitätsstudien für die beiden Vorläufer und deren natürliche Ga- und Lu-Komplexe durchgeführt. Dabei wird die Inhibitionseffizienz für FAP und gegenüber der Prolylendopeptidase PREP der Chelator-SA-FAPi-Konjugate überprüft. In einer ersten Tierstudie mit dem ⁶⁸Ga-DOTA-Derivat wird in HT-29 xenoplansplantierten Tumormäusen die *in vivo*-Verteilung im Tumor und normalen Organen gemessen. In weiterführenden Patientenstudien werden die beiden Derivate DOTA.SA.FAPi und DATA^{5m}.SA.FAPi auf deren pharmakologische Verteilungen im Tumor und Organen untersucht. In den Abschnitten A.1. und A.2. wird das DATA^{5m}.SA.FAPi klinisch mittels PET/CT angewendet. In A.1. wird die Anreicherung in fokal nodulärer Hyperplasie untersucht. Abschnitt A.2. gibt Erkenntnisse über etwaigen Zusammenhang zwischen dem PET-positiven Tumoranteil des [⁶⁸Ga]Ga-DATA^{5m}.SA.FAPi und dem Ki-67-Wert in Lebermetastasen neuroendokriner Tumore. In A.3.

wird das [^{68}Ga]Ga-DOTA.SA.FAPi in 54 Patienten mit diversen Tumorarten via PET/CT untersucht. Dabei werden Biodistribution, Pharmakokinetik und Dosimetrie analysiert sowie mit [^{18}F]FDG verglichen.

Hauptabschnitt B

Der Hybridchelator AAZTA ermöglicht, analog zum DATA-Chelator, Radiomarkierungen mit Nukliden unter milden Bedingungen. Meist sind quantitative Ausbeuten schon bei Raumtemperatur in wenigen Minuten erreicht. Außerdem verfügt AAZTA über eine Carboxylgruppe mehr als das DATA und kann durch die N_3O_4 -Koordinierung heptadentale Koordinationen mit dem entsprechenden Radiometall eingehen. Dies ermöglicht Komplexierungen mit Nukliden wie u.a. dem PET Nuklid ^{44}Sc als auch mit dem Therapienuklid ^{177}Lu . Dadurch kann AAZTA in einem theranostischen Rahmen eingesetzt werden, wodurch es eine Alternative zum DOTA bieten kann.

Der bifunktionelle Chelator AAZTA⁵ wird hergestellt und über SA mit FAPi verknüpft. Der Markierungsvorläufer AAZTA⁵.SA.FAPi wird anschließend in Markierungsstudien mit ^{68}Ga , ^{44}Sc und ^{177}Lu radiochemisch evaluiert und auf die Komplexstabilität in HS, PBS und isotonischer Kochsalzlösung überprüft. Parallel wird das DOTA.SA.FAPi als Vergleich in den Markierungs- und Stabilitätsstudien sowie Lipophiliemessungen untersucht. AAZTA⁵.SA.FAPi und die natürlichen $^{\text{nat}}\text{Sc}$ - und $^{\text{nat}}\text{Lu}$ -Derivate werden auf die Affinität für FAP und gegen PREP und die Dipeptidylpeptidasen (DPP4 und DPP9) untersucht.

Hauptabschnitt C

Durch Entwicklung homodimerer Systeme mit zwei FAP-Inhibitoren soll die Avidität für FAP und dadurch die Verweildauer und somit die intratumorale Halbwertszeit erhöht werden, bei gleichzeitig höherer Tumorakkumulation im Vergleich zu den monomeren SA.FAPi-Strukturen. Dadurch kann neben der Diagnostik auch eine effektive therapeutische Anwendung mit langlebigeren Therapienukliden ermöglicht werden. Die monomeren FAPi-Strukturen weisen tendenziell eine kurze Verweildauer im Tumor und eine schnelle renale Ausscheidung auf, wodurch ein Therapieansatz bedingt möglich ist. Abbildung 16 zeigt einen schematischen Vergleich für monomere und homodimere SA.FAPi-Moleküle.

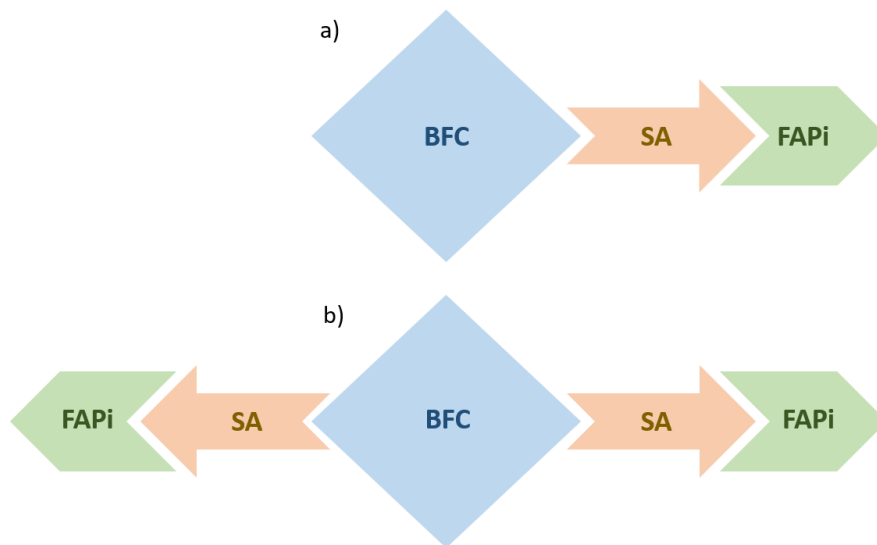


Abbildung 16: Schematischer Aufbau eines a) monomeren Chelator-SA-FAPi-Konjugats und b) eines homodimeren BFC-(SA.FAPi)₂-Derivats.

Die Homodimere mit zwei SA-gekoppelten FAP-Inhibitoren DOTA.(SA.FAPi)₂ und DOTAGA.(SA.FAPi)₂ werden synthetisiert und radiochemisch mit ⁶⁸Ga validiert. [⁶⁸Ga]Ga-DOTAGA.(SA.FAPi)₂ wird auf die Komplexstabilität in HS, PBS und isot. NaCl-Lösung überprüft. Lipophilien und Affinitäten für FAP werden bestimmt und mit denen des monomeren DOTA.SA.FAPi-Konjugats verglichen. Zusätzlich werden erste „proof-of-concept“-Patientenstudien mittels PET/CT durchgeführt und ein direkter Vergleich zwischen dem Dimer [⁶⁸Ga]Ga-DOTAGA.(SA.FAPi)₂, dem Monomer [⁶⁸Ga]Ga-DOTA.SA.FAPi und [¹⁸F]FDG generiert. [¹⁷⁷Lu]Lu-DOTAGA.(SA.FAPi)₂ wird im Abschnitt C.1. in Patienten mit verschiedenen Arten von Krebs im Endstadium untersucht. Biodistributions-, Pharmakokinetik- und Dosimetriemessungen werden analysiert und mit dem Monomer-Analogon [¹⁷⁷Lu]-Lu-DOTA.SA.FAPi verglichen. Eine erste klinische Therapieanwendung von [¹⁷⁷Lu]Lu-DOTAGA.(SA.FAPi)₂ in 15 Patienten wird im Kapitel C.2. behandelt. Dabei wird die Wirksamkeit und die Sicherheit in Patienten mit fortgeschrittenen differenzierten Schilddrüsenkarzinomen betrachtet.

Hauptabschnitt D

Im Abschnitt D werden vier DATA^{5m}-konjugierte FAPi-Derivate mit variierenden, heterozyklischen Linkersystemen hergestellt. Wie bereits im Hauptabschnitt A erwähnt, ist DATA durch die sehr schnelle Komplexierung mit ⁶⁸Ga in quantitativen radiochemischen Umsätzen unter milden Bedingungen bestens geeignet für eine instant-kit-Anwendung. Neben dem DATA^{5m}.SA.FAPi, aus Abschnitt A sollten weitere, alternative DATA^{5m}-Linker-FAPi-Derivate hergestellt werden. Durch die Variation der heterozyklischen Linkersysteme können die FAP-adressierenden DATA^{5m}-Verbindungen in deren radiochemischen und pharmakokinetischen Eigenschaften miteinander verglichen werden.

Das DATA^{5m}.Pip.FAPi beinhaltet das Piperazin, das DATA^{5m}.Pyr-N-CH₃.FAPi and DATA^{5m}.NH-Pyr.FAPi besitzen modifizierte Pyrrolidineinheiten als Linker. Das DATA^{5m}.NH.FAPi schließt eine direkte Kopplung zwischen dem bifunktionellen DATA^{5m}-Chelator und dem FAP-Inhibitor ein. Die vier synthetisierten DATA^{5m}-FAPi-Vorläufer werden mit ⁶⁸Ga markiert und auf Komplexstabilität in HS, Ethanol und NaCl getestet. Weiterhin wird die Lipophilie der DATA-Komplexe bestimmt, auf die Inhibitionsfähigkeit für FAP in einer *in vitro*-Affinitätsstudie hin untersucht und die Ergebnisse mit DATA^{5m}.SA.FAPi verglichen.

Referenzen

1. Kelkar, S.S.; Reineke, T.M. Theranostics: Combining imaging and therapy. *Bioconjug. Chem.* **2011**, *22*, 1879–1903, doi:10.1021/bc200151q.
2. Okamoto, S.; Shiga, T.; Tamaki, N. Clinical perspectives of theranostics. *Molecules* **2021**, *26*, 2232, doi:10.3390/molecules26082232.
3. Herzog, H.; Rösch, F. Chemie und physik der bildgebung: PET- und SPECT-technik. *Pharm. Unserer Zeit* **2005**, *34*, 468–473, doi:10.1002/pauz.200500144.
4. Rahmim, A.; Zaidi, H. Pet versus spect: Strengths, limitations and challenges. *Nucl. Med. Commun.* **2008**, *29*, 193–207, doi:10.1097/MNM.0b013e3282f3a515.
5. Kassis, A.I.; Adelstein, S.J. Radiobiologic principles in radionuclide therapy. *J. Nucl. Med.* **2005**, *46*, 4–12.
6. Zoller, F.; Eisenhut, M.; Haberkorn, U.; Mier, W. Endoradiotherapy in cancer treatment - Basic concepts and future trends. *Eur. J. Pharmacol.* **2009**, *625*, 55–62, doi:10.1016/j.ejphar.2009.05.035.
7. Nitipir, C.; Niculae, D.; Orlov, C.; Barbu, M.A.; Popescu, B.; Popa, A.M.; Pantea, A.M.S.; Stanciu, A.E.; Galateanu, B.; Ginghina, O.; et al. Update on radionuclide therapy in oncology. *Oncol. Lett.* **2017**, *14*, 7011–7015, doi:10.3892/ol.2017.7141.
8. Rangger, C.; Haubner, R. Radiolabelled peptides for positron emission tomography and endoradiotherapy in oncology. *Pharmaceuticals* **2020**, *13*, 22, doi:10.3390/ph13020022.
9. Hevesy, G. The Absorption and Translocation of Lead by Plants. *Biochem. J.* **1923**, *17*, 439–445, doi:10.1042/bj0170439.
10. Levi, H. George Hevesy and his concept of radioactive indicators-In retrospect. *Eur. J. Nucl. Med.* **1976**, *1*, 3–10, doi:10.1007/BF00253259.
11. Vermeulen, K.; Vandamme, M.; Bormans, G.; Cleeren, F. Design and Challenges of Radiopharmaceuticals. *Semin. Nucl. Med.* **2019**, *49*, 339–356, doi:10.1053/j.semnucl-med.2019.07.001.
12. Ganguly, B.N.; Mondal, N.N.; Nandy, M.; Roesch, F. Some physical aspects of positron annihilation tomography: A critical review. *J. Radioanal. Nucl. Chem.* **2009**, *279*, 685–698, doi:10.1007/s10967-007-7256-2.
13. Bauser, M.; Lehmann, L. Biochemie im Bild: Positronen-Emissions-Tomographie. *Chemie Unserer Zeit* **2012**, *46*, 80–99, doi:10.1002/ciuz.201200564.
14. Ache, H.J. Chemistry of the Positron and of Positronium. *Angew. Chemie Int. Ed. English* **1972**, *11*, 179–199, doi:10.1002/anie.197201791.
15. Humm, J.L.; Rosenfeld, A.; Del Guerra, A. From PET detectors to PET scanners. *Eur. J. Nucl. Med. Mol. Imaging* **2003**, *30*, 1574–1597, doi:10.1007/s00259-003-1266-2.
16. Ametamey, S.M.; Honer, M.; Schubiger, P.A. Molecular imaging with PET. *Chem. Rev.* **2008**, *108*, 1501–1516, doi:10.1021/cr0782426.
17. Fahey, F.H. Positron Emission Instrumentation. *Radiol. Clin. North Am.* **2001**, *39*, 919–929, doi:10.1016/s0033-8389(05)70320-1.

18. Tao, S.J. Positronium annihilation in molecular substances. *J. Chem. Phys.* **1972**, *56*, 5499–5510, doi:10.1063/1.1677067.
19. Tolmachev, V.; Stone-Elander, S. Radiolabelled proteins for positron emission tomography: Pros and cons of labelling methods. *Biochim. Biophys. Acta - Gen. Subj.* **2010**, *1800*, 487–510, doi:10.1016/j.bbagen.2010.02.002.
20. Zanzonico, P. Positron Emission Tomography: A Review of Basic Principles, Scanner Design and Performance, and Current Systems. *Semin. Nucl. Med.* **2004**, *34*, 87–111, doi:10.1053/j.sem-nuclmed.2003.12.002.
21. Melcher, C.L. Scintillation crystals for PET. *J. Nucl. Med.* **2000**, *41*, 1051–1055.
22. Ziegler, S.I. Positron emission tomography: Principles, technology, and recent developments. *Nucl. Phys. A* **2005**, *752*, 679–687, doi:10.1016/j.nuclphysa.2005.02.067.
23. Lewellen, T.K. Recent developments in PET detector technology Positron emission tomography—some of the basics. *Phys. Med. Biol.* **2010**, *53*, 1–46, doi:10.1088/0031-9155/53/17/R01.Recent.
24. Cherry, S.R. Multimodality Imaging: Beyond PET/CT and SPECT/CT. *Semin. Nucl. Med.* **2009**, *39*, 348–353, doi:10.1053/j.semnuclmed.2009.03.001.
25. Holland, J.P.; Williamson, M.J.; Lewis, J.S. Unconventional Nuclides for Radiopharmaceuticals. *Mol. Imaging* **2010**, *9*, 1–20, doi:10.2310/7290.2010.00008.
26. Cutler, C.S.; Hennkens, H.M.; Sisay, N.; Huclier-Markai, S.; Jurisson, S.S. Radiometals for combined imaging and therapy. *Chem. Rev.* **2013**, *113*, 858–883, doi:10.1021/cr3003104.
27. Talip, Z.; Favaretto, C.; Geistlich, S.; Van Der Meulen, N.P. A step-by-step guide for the novel radiometal production for medical applications: Case studies with ⁶⁸Ga, ⁴⁴Sc, ¹⁷⁷Lu and ¹⁶¹Tb. *Molecules* **2020**, *25*, 966, doi:10.3390/molecules25040966.
28. Gambhir, S.S. Molecular imaging of cancer with positron emission tomography. *Nat. Rev. Cancer* **2002**, *2*, 683–693, doi:10.1038/nrc882.
29. Glaudemans, A.W.J.M.; Enting, R.H.; Heesters, M.A.A.M.; Dierckx, R.A.J.O.; Van Rheenen, R.W.J.; Walenkamp, A.M.E.; Slart, R.H.J.A. Value of ¹¹C-methionine PET in imaging brain tumours and metastases. *Eur. J. Nucl. Med. Mol. Imaging* **2013**, *40*, 615–635, doi:10.1007/s00259-012-2295-5.
30. Jacobson, O.; Chen, X. PET Designated Flouride-18 Production and Chemistry. *Curr. Top. Med. Chem.* **2010**, *10*, 1048–1059, doi:10.2174/156802610791384298.
31. Kwee, T.C.; Kwee, R.M. Combined FDG-PET/CT for the detection of unknown primary tumors: Systematic review and meta-analysis. *Eur. Radiol.* **2009**, *19*, 731–744, doi:10.1007/s00330-008-1194-4.
32. Lenzo, N.; Meyrick, D.; Turner, J. Review of Gallium-68 PSMA PET/CT Imaging in the Management of Prostate Cancer. *Diagnostics* **2018**, *8*, 16, doi:10.3390/diagnostics8010016.
33. Conti, M.; Eriksson, L. Physics of pure and non-pure positron emitters for PET: A review and a discussion. *EJNMMI Phys.* **2016**, *3*, 8, doi:10.1186/s40658-016-0144-5.
34. Molinski, V.J. A review of ^{99m}Tc generator technology. *Int. J. Appl. Radiat. Isot.* **1982**, *33*, 811–819, doi:10.1016/0020-708X(82)90122-3.
35. Lagunas-Solar, M.C.; Kiefer, P.M.; Carvacho, O.F.; Lagunas, C.A.; Cha, Y.P. Cyclotron production of NCA ^{99m}Tc and ⁹⁹Mo. An alternative non-reactor supply source of instant ^{99m}Tc and

- $^{99}\text{Mo} \rightarrow ^{99\text{m}}\text{Tc}$ generators. *Int. J. Radiat. Appl. Instrumentation. Part* **1991**, *42*, 643–657, doi:10.1016/0883-2889(91)90035-Y.
36. Rösch, F. Past, present and future of $^{68}\text{Ge}/^{68}\text{Ga}$ generators. *Appl. Radiat. Isot.* **2013**, *76*, 24–30, doi:10.1016/j.apradiso.2012.10.012.
37. Roesch, F.; J. Riss, P. The Renaissance of the $^{68}\text{Ge}/^{68}\text{Ga}$ Radionuclide Generator Initiates New Developments in ^{68}Ga Radiopharmaceutical Chemistry. *Curr. Top. Med. Chem.* **2012**, *10*, 1633–1668, doi:10.2174/156802610793176738.
38. Roesch, F. Maturation of a Key Resource – The Germanium-68/Gallium-68 Generator: Development and New Insights. *Curr. Radiopharm.* **2012**, *5*, 202–211, doi:10.2174/18744-71011205030202.
39. Wadas, T.J.; Wong, E.H.; Weisman, G.R.; Anderson, C.J. Coordinating Radiometals of Copper, Gallium, Indium, Yttrium and Zirconium for PET and SPECT Imaging of Disease. *Chem. Rev.* **2010**, *110*, 2858–2902, doi:10.2174/15734005113096660013.
40. Fani, M.; André, J.P.; Maecke, H.R. ^{68}Ga -PET: A powerful generator-based alternative to cyclotron-based PET radiopharmaceuticals. *Contrast Media Mol. Imaging* **2008**, *3*, 53–63, doi:10.1002/cmml.232.
41. Velikyan, I. ^{68}Ga -based radiopharmaceuticals: Production and application relationship. *Molecules* **2015**, *20*, 12913–12943, doi:10.3390/molecules200712913.
42. Mueller, D.; Breeman, W.A.P.; Klette, I.; Gottschaldt, M.; Odparlik, A.; Baehre, M.; Tworowska, I.; Schultz, M.K. Radiolabeling of DOTA-like conjugated peptides with generator-produced ^{68}Ga and using NaCl-based cationic elution method. *Nat. Protoc.* **2016**, *11*, 1057–1066, doi:10.1038/nprot.2016.060.
43. Zhernosekov, K.P.; Filosofov, D. V.; Baum, R.P.; Aschoff, P.; Bihl, H.; Razbash, A.A.; Jahn, M.; Jennewein, M.; Rösch, F. Processing of generator-produced ^{68}Ga for medical application. *J. Nucl. Med.* **2007**, *48*, 1741–1748, doi:10.2967/jnumed.107.040378.
44. Seemann, J.; Eppard, E.; Waldron, B.P.; Ross, T.L.; Roesch, F. Cation exchange-based post-processing of ^{68}Ga -eluate: A comparison of three solvent systems for labelling of DOTATOC, NO2APBP and DATA^m. *Appl. Radiat. Isot.* **2015**, *98*, 54–59, doi:10.1016/j.apradiso.2015.01.023.
45. Eppard, E.; Wuttke, M.; Nicodemus, P.L.; Rösch, F. Ethanol-based post-processing of generator-derived ^{68}Ga Toward kit-type preparation of ^{68}Ga -radiopharmaceuticals. *J. Nucl. Med.* **2014**, *55*, 1023–1028, doi:10.2967/jnumed.113.133041.
46. Kerdjoudj, R.; Pniok, M.; Alliot, C.; Kubíček, V.; Havlíčková, J.; Rösch, F.; Hermann, P.; Huclier-Markai, S. Scandium(III) complexes of monophosphorus acid DOTA analogues: A thermodynamic and radiolabelling study with ^{44}Sc from cyclotron and from a $^{44}\text{Ti}/^{44}\text{Sc}$ generator. *Dalt. Trans.* **2016**, *45*, 1398–1409, doi:10.1039/c5dt04084a.
47. Filosofov, D. V.; Loktionova, N.S.; Rösch, F. A $^{44}\text{Ti}/^{44}\text{Sc}$ radionuclide generator for potential application of ^{44}Sc -based PET-radiopharmaceuticals. *Radiochim. Acta* **2010**, *98*, 149–156, doi:10.1524/ract.2010.1701.
48. Pruszyński, M.; Loktionova, N.S.; Filosofov, D. V.; Rösch, F. Post-elution processing of $^{44}\text{Ti}/^{44}\text{Sc}$ generator-derived ^{44}Sc for clinical application. *Appl. Radiat. Isot.* **2010**, *68*, 1636–1641, doi:10.1016/j.apradiso.2010.04.003.
49. Pniok, M.; Kubíček, V.; Havlíčková, J.; Kotek, J.; Sabatie-Gogová, A.; Plutnar, J.; Huclier-Markai, S.; Hermann, P. Thermodynamic and kinetic study of scandium(III) complexes of DTPA and DOTA: A step toward scandium radiopharmaceuticals. *Chem. - A Eur. J.* **2014**, *20*, 7944–7955,

doi:10.1002/chem.201402041.

50. Krajewski, S.; Cydzik, I.; Abbas, K.; Bulgheroni, A.; Simonelli, F.; Holzwarth, U.; Bilewicz, A. Cyclotron production of ^{44}Sc for clinical application. *Radiochim. Acta* **2013**, *101*, 333–338, doi:10.1524/ract.2013.2032.
51. Wittwer, D.; Dressler, R.; Eichler, R.; Gäggeler, H.W.; Piguet, D.; Serov, A.; Türler, A.; Vögele, A. The thermal release of scandium from titanium metal - A simple way to produce pure ^{44}Sc for PET application. *Radiochim. Acta* **2011**, *99*, 193–196, doi:10.1524/ract.2011.1832.
52. Radchenko, V.; Meyer, C.A.L.; Engle, J.W.; Naranjo, C.M.; Unc, G.A.; Mastren, T.; Brugh, M.; Birnbaum, E.R.; John, K.D.; Nortier, F.M.; et al. Separation of ^{44}Ti from proton irradiated scandium by using solid-phase extraction chromatography and design of $^{44}\text{Ti}/^{44}\text{Sc}$ generator system. *J. Chromatogr. A* **2016**, *1477*, 39–46, doi:10.1016/j.chroma.2016.11.047.
53. Radchenko, V.; Engle, J.W.; Medvedev, D.G.; Maassen, J.M.; Naranjo, C.M.; Unc, G.A.; Meyer, C.A.L.; Mastren, T.; Brugh, M.; Mausner, L.; et al. Proton-induced production and radiochemical isolation of ^{44}Ti from scandium metal targets for $^{44}\text{Ti}/^{44}\text{Sc}$ generator development. *Nucl. Med. Biol.* **2017**, *50*, 25–32, doi:10.1016/j.nucmedbio.2017.03.006.
54. Roesch, F. Scandium-44: Benefits of a Long-Lived PET Radionuclide Available from the $^{44}\text{Ti}/^{44}\text{Sc}$ Generator System. *Curr. Radiopharm.* **2012**, *5*, 187–201, doi:10.2174/1874471011205030187.
55. Gudkov, S. V.; Shilyagina, N.Y.; Vodeneev, V.A.; Zvyagin, A. V. Targeted radionuclide therapy of human tumors. *Int. J. Mol. Sci.* **2015**, *17*, 1–19, doi:10.3390/ijms17010033.
56. Banerjee, S.; Pillai, M.R.A.; Knapp, F.F. Lutetium-177 therapeutic radiopharmaceuticals: Linking chemistry, radiochemistry, and practical applications. *Chem. Rev.* **2015**, *115*, 2934–2974, doi:10.1021/cr500171e.
57. Makvandi, M.; Dupis, E.; Engle, J.W.; Nortier, F.M.; Fassbender, M.E.; Simon, S.; Birnbaum, E.R.; Atcher, R.W.; John, K.D.; Rixe, O.; et al. Alpha-Emitters and Targeted Alpha Therapy in Oncology: from Basic Science to Clinical Investigations. *Target. Oncol.* **2018**, *13*, 189–203, doi:10.1007/s11523-018-0550-9.
58. Das, T.; Pillai, M.R.A. Options to meet the future global demand of radionuclides for radionuclide therapy. *Nucl. Med. Biol.* **2013**, *40*, 23–32, doi:10.1016/j.nucmedbio.2012.09.007.
59. Goldsmith, S.J. Targeted Radionuclide Therapy: A Historical and Personal Review. *Semin. Nucl. Med.* **2020**, *50*, 87–97, doi:10.1053/j.semnuclmed.2019.07.006.
60. Ersahin, D.; Doddamane, I.; Cheng, D. Targeted radionuclide therapy. *Cancers* **2011**, *3*, 3838–3855, doi:10.3390/cancers3043838.
61. Van Essen, M.; Krenning, E.P.; Kam, B.L.R.; De Jong, M.; Valkema, R.; Kwekkeboom, D.J. Peptide-receptor radionuclide therapy for endocrine tumors. *Nat. Rev. Endocrinol.* **2009**, *5*, 382–393, doi:10.1038/nrendo.2009.105.
62. Cives, M.; Strosberg, J. Radionuclide Therapy for Neuroendocrine Tumors. *Curr. Oncol. Rep.* **2017**, *19*, 9, doi:10.1007/s11912-017-0567-8.
63. Kratochwil, C.; Haberkorn, U.; Giesel, F.L. Radionuclide Therapy of Metastatic Prostate Cancer. *Semin. Nucl. Med.* **2019**, *49*, 313–325, doi:10.1053/j.semnuclmed.2019.02.003.
64. Mitra, E.S. Neuroendocrine tumor therapy: ^{177}Lu -DOTATATE. *Am. J. Roentgenol.* **2018**, *211*, 278–285, doi:10.2214/AJR.18.19953.
65. Emmett, L.; Willowson, K.; Violet, J.; Shin, J.; Blanksby, A.; Lee, J. Lutetium-177 PSMA radionuclide therapy for men with prostate cancer: a review of the current literature and

- discussion of practical aspects of therapy. *J. Med. Radiat. Sci.* **2017**, *64*, 52–60, doi:10.1002/jmrs.227.
66. Iravani, A.; Violet, J.; Azad, A.; Hofman, M.S. Lutetium-177 prostate-specific membrane antigen (PSMA) theranostics: practical nuances and intricacies. *Prostate Cancer Prostatic Dis.* **2020**, *23*, 38–52, doi:10.1038/s41391-019-0174-x.
 67. Sun, M.; Niaz, M.O.; Nelson, A.; Skafida, M.; Niaz, M.J. Review of ¹⁷⁷Lu-PSMA-617 in Patients With Metastatic Castration-Resistant Prostate Cancer. *Cureus* **2020**, *12*, 10–17, doi:10.7759/cureus.8921.
 68. Werner, R.A.; Bluemel, C.; Allen-Auerbach, M.S.; Higuchi, T.; Herrmann, K. ⁶⁸Gallium- and ⁹⁰Yttrium-/¹⁷⁷Lutetium: “theranostic twins” for diagnosis and treatment of NETs. *Ann. Nucl. Med.* **2015**, *29*, 1–7, doi:10.1007/s12149-014-0898-6.
 69. Afshar-Oromieh, A.; Hetzheim, H.; Kratochwil, C.; Benesova, M.; Eder, M.; Neels, O.C.; Eisenhut, M.; Kübler, W.; Holland-Letz, T.; Giesel, F.L.; et al. The theranostic PSMA ligand PSMA-617 in the diagnosis of prostate cancer by PET/CT: Biodistribution in humans, radiation dosimetry, and first evaluation of tumor lesions. *J. Nucl. Med.* **2015**, *56*, 1697–1705, doi:10.2967/jnumed.115.161299.
 70. Dash, A.; Pillai, M.R.A.; Knapp, F.F. Production of ¹⁷⁷Lu for Targeted Radionuclide Therapy: Available Options. *Nucl. Med. Mol. Imaging* **2015**, *49*, 85–107, doi:10.1007/s13139-014-0315-z.
 71. Pillai, M.R.A.; Chakraborty, S.; Das, T.; Venkatesh, M.; Ramamoorthy, N. Production logistics of ¹⁷⁷Lu for radionuclide therapy. *Appl. Radiat. Isot.* **2003**, *59*, 109–118, doi:10.1016/S0969-8043(03)00158-1.
 72. Lebedev, N.A.; Novgorodov, A.F.; Misiak, R.; Brockmann, J.; Rösch, F. Radiochemical separation of no-carrier-added ¹⁷⁷Lu as produced via the ¹⁷⁶Yb(n,γ)¹⁷⁷Yb→¹⁷⁷Lu process. *Appl. Radiat. Isot.* **2000**, *53*, 421–425, doi:10.1016/S0969-8043(99)00284-5.
 73. Aime, S.; Barge, A.; Botta, M.; Fasano, M.; Ayala, J.D.; Bombieri, G. Crystal structure and solution dynamics of the lutetium(III) chelate of DOTA. *Inorganica Chim. Acta* **1996**, *246*, 423–429, doi:10.1016/0020-1693(96)05130-4.
 74. Parus, J.; Pawlak, D.; Mikolajczak, R.; Duatti, A. Chemistry and bifunctional chelating agents for binding ¹⁷⁷Lu. *Curr. Radiopharm.* **2015**, *8*, 86–94, doi:10.2174/1874471008666150312160440.
 75. Jacobson, O.; Kiesewetter, D.O.; Chen, X. Fluorine-18 radiochemistry, labeling strategies and synthetic routes. *Bioconjug. Chem.* **2015**, *26*, 1–18, doi:10.1021/bc500475e.
 76. Price, E.W.; Orvig, C. Matching chelators to radiometals for radiopharmaceuticals. *Chem. Soc. Rev.* **2014**, *43*, 260–290, doi:10.1039/c3cs60304k.
 77. Evans, B.J.; King, A.T.; Katsifis, A.; Matesic, L.; Jamie, J.F. Methods to enhance the metabolic stability of peptide-based PET radiopharmaceuticals. *Molecules* **2020**, *25*, 2314, doi:10.3390/molecules25102314.
 78. Okoye, N.C.; Baumeister, J.E.; Khosroshahi, F.N.; Hennkens, H.M.; Jurisson, S.S. Chelators and metal complex stability for radiopharmaceutical applications. *Radiochim. Acta* **2019**, *107*, 1087–1120, doi:10.1515/ract-2018-3090.
 79. Baranyai, Z.; Tircsó, G.; Rösch, F. The Use of the Macrocyclic Chelator DOTA in Radiochemical Separations. *Eur. J. Inorg. Chem.* **2020**, *2020*, 36–56, doi:10.1002/ejic.201900706.
 80. Spang, P.; Herrmann, C.; Roesch, F. Bifunctional Gallium-68 Chelators: Past, Present, and Future.

Semin. Nucl. Med. **2016**, *46*, 373–394, doi:10.1053/j.semnuclmed.2016.04.003.

81. Liu, S. The role of coordination chemistry in the development of target-specific radiopharmaceuticals. *Chem. Soc. Rev.* **2004**, *33*, 445–461, doi:10.1039/c0dt01075h.
82. Patra, M.; Bauman, A.; Mari, C.; Fischer, C.A.; Häussinger, D.; Gasser, G.; Mindt, T.L. An octadentate bifunctional chelating agent for the development of stable zirconium-89 based molecular imaging probes. *Chem. Commun.* **2014**, *50*, 11523–11525, doi:10.1039/c4cc05558f.
83. Chomet, M.; Schreurs, M.; Bolijn, M.J.; Verlaan, M.; Beaino, W.; Brown, K.; Poot, A.J.; Windhorst, A.D.; Gill, H.; Marik, J.; et al. Head-to-head comparison of DFO* and DFO chelators: selection of the best candidate for clinical ⁸⁹Zr-immuno-PET. *Eur. J. Nucl. Med. Mol. Imaging* **2021**, *48*, 694–707, doi:10.1007/s00259-020-05002-7.
84. Afshar-Oromieh, A.; Holland-Letz, T.; Giesel, F.L.; Kratochwil, C.; Mier, W.; Haufe, S.; Debus, N.; Eder, M.; Eisenhut, M.; Schäfer, M.; et al. Diagnostic performance of ⁶⁸Ga-PSMA-11 (HBED-CC) PET/CT in patients with recurrent prostate cancer: evaluation in 1007 patients. *Eur. J. Nucl. Med. Mol. Imaging* **2017**, *44*, 1258–1268, doi:10.1007/s00259-017-3711-7.
85. Bois, F.; Noirod, C.; Dietemann, S.; Mainta, I.C.; Zilli, T.; Garibotto, V.; Walter, M.A. [⁶⁸Ga]Ga-PSMA-11 in prostate cancer: a comprehensive review. *Am. J. Nucl. Med. Mol. Imaging* **2020**, *10*, 349–374.
86. Notni, J.; Šimeček, J.; Hermann, P.; Wester, H.J. TRAP, a powerful and versatile framework for gallium-68 radiopharmaceuticals. *Chem. - A Eur. J.* **2011**, *17*, 14718–14722, doi:10.1002/chem.-201103503.
87. Šimeček, J.; Zemek, O.; Hermann, P.; Wester, H.J.; Notni, J. A Monoreactive Bifunctional Triazacyclononane Phosphinate Chelator with High Selectivity for Gallium-68. *ChemMedChem* **2012**, *7*, 1375–1378, doi:10.1002/cmdc.201200261.
88. Ferro-Flores, G.; Ocampo-García, B.; Luna-Gutiérrez, M.; Santos-Cuevas, C.; Jiménez-Mancilla, N.; Azorín-Vega, E.; Meléndez-Alafort, L. Radiolabeled Protein-inhibitor Peptides with Rapid Clinical Translation towards Imaging and Therapy. *Curr. Med. Chem.* **2019**, *27*, 7032–7047, doi:10.2174/0929867327666191223121211.
89. Stoykow, C.; Erbes, T.; Maecke, H.R.; Bulla, S.; Bartholomä, M.; Mayer, S.; Drendel, V.; Bronsert, P.; Werner, M.; Gitsch, G.; et al. Gastrin-releasing peptide receptor imaging in breast cancer using the receptor antagonist ⁶⁸Ga-RM2 And PET. *Theranostics* **2016**, *6*, 1641–1650, doi:10.7150/thno.14958.
90. Kurth, J.; Krause, B.J.; Schwarzenböck, S.M.; Bergner, C.; Hakenberg, O.W.; Heuschkel, M. First-in-human dosimetry of gastrin-releasing peptide receptor antagonist [¹⁷⁷Lu]Lu-RM2: a radiopharmaceutical for the treatment of metastatic castration-resistant prostate cancer. *Eur. J. Nucl. Med. Mol. Imaging* **2020**, *47*, 123–135, doi:10.1007/s00259-019-04504-3.
91. Vágner, A.; D'Alessandria, C.; Gambino, G.; Schwaiger, M.; Aime, S.; Maiocchi, A.; Tóth, I.; Baranyai, Z.; Tei, L. A rigidified AAZTA-like ligand as efficient chelator for ⁶⁸Ga radiopharmaceuticals. *ChemistrySelect* **2016**, *1*, 163–171, doi:10.1002/slct.201500051.
92. Seemann, J.; Waldron, B.P.; Roesch, F.; Parker, D. Approaching “kit-type” labelling with ⁶⁸Ga: The DATA chelators. *ChemMedChem* **2015**, *10*, 1019–1026, doi:10.1002/cmdc.201500092.
93. Nagy, G.; Szikra, D.; Trencsényi, G.; Fekete, A.; Garai, I.; Giani, A.M.; Negri, R.; Masciocchi, N.; Maiocchi, A.; Uggeri, F.; et al. AAZTA: An Ideal Chelating Agent for the Development of ⁴⁴Sc PET Imaging Agents. *Angew. Chemie - Int. Ed.* **2017**, *56*, 2118–2122, doi:10.1002/anie.201611207.
94. Parker, D.; Waldron, B.P. Conformational analysis and synthetic approaches to polydentate

- perhydro-diazepine ligands for the complexation of gallium(III). *Org. Biomol. Chem.* **2013**, *11*, 2827–2838, doi:10.1039/c3ob40287h.
95. Parker, D.; Waldron, B.P.; Yufit, D.S. Crystallographic and solution NMR structural analyses of four hexacoordinated gallium(III) complexes based on ligands derived from 6-amino-perhydro-1,4-diazepine. *Dalt. Trans.* **2013**, *42*, 8001–8008, doi:10.1039/c3dt50287b.
96. Aime, S.; Calabi, L.; Cavallotti, C.; Gianolio, E.; Giovenzana, G.B.; Losi, P.; Maiocchi, A.; Palmisano, G.; Sisti, M. [Gd-AAZTA]: A new structural entry for an improved generation of MRI contrast agents. *Inorg. Chem.* **2004**, *43*, 7588–7590, doi:10.1021/ic0489692.
97. Waldron, B.P.; Parker, D.; Burchardt, C.; Yufit, D.S.; Zimny, M.; Roesch, F. Structure and stability of hexadentate complexes of ligands based on AAZTA for efficient PET labelling with gallium-68. *Chem. Commun.* **2013**, *49*, 579–581, doi:10.1039/c2cc37544c.
98. Sinnes, J.; Nagel, J.; Rösch, F. AAZTA⁵/AAZTA⁵-TOC: synthesis and radiochemical evaluation with ⁶⁸Ga, ⁴⁴Sc and ¹⁷⁷Lu. **2019**, *1*, 1–10.
99. Greifenstein, L.; Grus, T.; Nagel, J.; Sinnes, J.P.; Rösch, F. Synthesis and labeling of a squaric acid containing PSMA-inhibitor coupled to AAZTA⁵ for versatile labeling with ⁴⁴Sc, ⁶⁴Cu, ⁶⁸Ga and ¹⁷⁷Lu. *Appl. Radiat. Isot.* **2020**, *156*, 108867, doi:10.1016/j.apradiso.2019.108867.
100. Sinnes, J.P.; Nagel, J.; Waldron, B.P.; Maina, T.; Nock, B.A.; Bergmann, R.K.; Ullrich, M.; Pietzsch, J.; Bachmann, M.; Baum, R.P.; et al. Instant kit preparation of ⁶⁸Ga-radiopharmaceuticals via the hybrid chelator DATA: clinical translation of [⁶⁸Ga]Ga-DATA-TOC. *EJNMMI Res.* **2019**, *9*, 48, doi:10.1186/s13550-019-0516-7.
101. Yadav, D.; Ballal, S.; Yadav, M.P.; Tripathi, M.; Roesch, F.; Bal, C. Evaluation of [⁶⁸Ga]Ga-DATA-TOC for imaging of neuroendocrine tumours: comparison with [⁶⁸Ga]Ga-DOTA-NOC PET/CT. *Eur. J. Nucl. Med. Mol. Imaging* **2020**, *47*, 860–869, doi:10.1007/s00259-019-04611-1.
102. Aertgeerts, K.; Levin, I.; Shi, L.; Snell, G.P.; Jennings, A.; Prasad, G.S.; Zhang, Y.; Kraus, M.L.; Salakian, S.; Sridhar, V.; et al. Structural and kinetic analysis of the substrate specificity of human fibroblast activation protein α . *J. Biol. Chem.* **2005**, *280*, 19441–19444, doi:10.1074/jbc.C50-0092200.
103. Fitzgerald, A.A.; Weiner, L.M. The role of fibroblast activation protein in health and malignancy. *Cancer Metastasis Rev.* **2020**, *39*, 783–803, doi:10.1007/s10555-020-09909-3.
104. Liu, R.; Li, H.; Liu, L.; Yu, J.; Ren, X. Fibroblast activation protein: A potential therapeutic target in cancer. *Cancer Biol. Ther.* **2012**, *13*, 123–129, doi:10.4161/cbt.13.3.18696.
105. Jiang, G.-M.; Xu, W.; Du, J.; Zhang, K.-S.; Zhang, Q.-G.; Wang, X.-W.; Liu, Z.-G.; Liu, S.-Q.; Xie, W.-Y.; Liu, H.-F.; et al. The application of the fibroblast activation protein α -targeted immunotherapy strategy. *Oncotarget* **2016**, *7*, 33472–33482, doi:10.18632/oncotarget.8098.
106. Juillerat-Jeanneret, L.; Tafelmeyer, P.; Golshayan, D. Fibroblast activation protein- α in fibrogenic disorders and cancer: more than a prolyl-specific peptidase? *Expert Opin. Ther. Targets* **2017**, *21*, 977–991, doi:10.1080/14728222.2017.1370455.
107. Hamson, E.J.; Keane, F.M.; Tholen, S.; Schilling, O.; Gorrell, M.D. Understanding fibroblast activation protein (FAP): Substrates, activities, expression and targeting for cancer therapy. *Proteomics - Clin. Appl.* **2014**, *8*, 454–463, doi:10.1002/prca.201300095.
108. Puré, E. The road to integrative cancer therapies: Emergence of a tumor-associated fibroblast protease as a potential therapeutic target in cancer. *Expert Opin. Ther. Targets* **2009**, *13*, 967–973, doi:10.1517/14728220903103841.

109. Yu, D.M.T.; Yao, T.W.; Chowdhury, S.; Nadvi, N.A.; Osborne, B.; Church, W.B.; McCaughan, G.W.; Gorrell, M.D. The dipeptidyl peptidase IV family in cancer and cell biology. *FEBS J.* **2010**, *277*, 1126–1144, doi:10.1111/j.1742-4658.2009.07526.x.
110. Zi, F.; He, J.; He, D.; Li, Y.; Yang, L.; Cai, Z. Fibroblast activation protein α in tumor microenvironment: Recent progression and implications (Review). *Mol. Med. Rep.* **2015**, *11*, 3203–3211, doi:10.3892/mmr.2015.3197.
111. Busek, P.; Mateu, R.; Zubal, M.; Kotackova, L.; Sedo, A. Targeting Fibroblast activation protein in cancer - Prospects and caveats. *Front. Biosci. - Landmark* **2018**, *23*, 1933–1968, doi:10.2741/4682.
112. Wang, M.; Zhao, J.; Zhang, L.; Wei, F.; Lian, Y.; Wu, Y.; Gong, Z.; Zhang, S.; Zhou, J.; Cao, K.; et al. Role of tumor microenvironment in tumorigenesis. *J. Cancer* **2017**, *8*, 761–773, doi:10.7150/jca.17648.
113. Chen, X.; Song, E. Turning foes to friends: targeting cancer-associated fibroblasts. *Nat. Rev. Drug Discov.* **2019**, *18*, 99–115, doi:10.1038/s41573-018-0004-1.
114. Koustoulidou, S.; Hoorens, M.W.H.; Dalm, S.U.; Mahajan, S.; Debets, R.; Seimbille, Y.; de Jong, M. Cancer-associated fibroblasts as players in cancer development and progression and their role in targeted radionuclide imaging and therapy. *Cancers* **2021**, *13*, 1–19, doi:10.3390/cancers13051100.
115. Welt, S.; Divgi, C.R.; Scott, A.M.; Garin-Chesa, P.; Finn, R.D.; Graham, M.; Carswell, E.A.; Cohen, A.; Larson, S.M.; Old, L.J.; et al. Antibody targeting in metastatic colon cancer: A phase I study of monoclonal antibody F19 against a cell-surface protein of reactive tumor stromal fibroblasts. *J. Clin. Oncol.* **1994**, *12*, 1193–1203, doi:10.1200/JCO.1994.12.6.1193.
116. Tanswell, P.; Garin-Chesa, P.; Rettig, W.J.; Welt, S.; Divgi, C.R.; Casper, E.S.; Finn, R.D.; Larson, S.M.; Old, L.J.; Scott, A.M. Population pharmacokinetics of antifibroblast activation protein monoclonal antibody F19 in cancer patients. *Br. J. Clin. Pharmacol.* **2001**, *51*, 177–180, doi:10.1046/j.1365-2125.2001.01335.x.
117. Brennen, W.N.; Isaacs, J.T.; Denmeade, S.R. Rationale behind targeting fibroblast activation protein-expressing carcinoma-associated fibroblasts as a novel chemotherapeutic strategy. *Mol. Cancer Ther.* **2012**, *11*, 257–266, doi:10.1158/1535-7163.MCT-11-0340.
118. Hofheinz, R.D.; Al-Batran, S.E.; Hartmann, F.; Hartung, G.; Jäger, D.; Renner, C.; Tanswell, P.; Kunz, U.; Amelsberg, A.; Kuthan, H.; et al. Stromal antigen targeting by a humanised monoclonal antibody: An early phase II trial of sibrotuzumab in patients with metastatic colorectal cancer. *Onkologie* **2003**, *26*, 44–48, doi:10.1159/000069863.
119. Ostermann, E.; Garin-Chesa, P.; Heider, K.H.; Kalat, M.; Lamche, H.; Puri, C.; Kerjaschki, D.; Rettig, W.J.; Adolf, G.R. Effective immunoconjugate therapy in cancer models targeting a serine protease of tumor fibroblasts. *Clin. Cancer Res.* **2008**, *14*, 4584–4592, doi:10.1158/1078-0432.CCR-07-5211.
120. Fischer, E.; Chaitanya, K.; Wuëst, T.; Wadle, A.; Scott, A.M.; Van Den Broek, M.; Schibli, R.; Bauer, S.; Renner, C. Radioimmunotherapy of fibroblast activation protein positive tumors by rapidly internalizing antibodies. *Clin. Cancer Res.* **2012**, *18*, 6208–6218, doi:10.1158/1078-0432.CCR-12-0644.
121. Fabre, M.; Ferrer, C.; Domínguez-Hormaetxe, S.; Bockorny, B.; Murias, L.; Seifert, O.; Eisler, S.A.; Kontermann, R.E.; Pfizenmaier, K.; Lee, S.Y.; et al. OMTX705, a novel FAP-targeting ADC demonstrates activity in chemotherapy and pembrolizumab-resistant solid tumor models. *Clin. Cancer Res.* **2020**, *26*, 3420–3430, doi:10.1158/1078-0432.CCR-19-2238.

122. Jansen, K.; Heirbaut, L.; Verkerk, R.; Cheng, J.D.; Joossens, J.; Cos, P.; Maes, L.; Lambeir, A.M.; De Meester, I.; Augustyns, K.; et al. Extended structure-activity relationship and pharmacokinetic investigation of (4-quinolinoyl)glycyl-2-cyanopyrrolidine inhibitors of fibroblast activation protein (FAP). *J. Med. Chem.* **2014**, *57*, 3053–3074, doi:10.1021/jm-500031w.
123. Poplawski, S.E.; Lai, J.H.; Li, Y.; Jin, Z.; Liu, Y.; Wu, W.; Wu, Y.; Zhou, Y.; Sudmeier, J.L.; Sanford, D.G.; et al. Identification of selective and potent inhibitors of fibroblast activation protein and prolyl oligopeptidase. *J. Med. Chem.* **2013**, *56*, 3467–3477, doi:10.1021/jm400351a.
124. Johnson, D.S.; Weerapana, E.; Cravatt, B.F. Strategies for discovering and derisking covalent, irreversible enzyme inhibitors. *Future Med. Chem.* **2010**, *2*, 949–964, doi:10.4155/fmc.10.21.
125. Ryabtsova, O.; Jansen, K.; Van Goethem, S.; Joossens, J.; Cheng, J.D.; Lambeir, A.M.; De Meester, I.; Augustyns, K.; Van Der Veken, P. Acylated Gly-(2-cyano)pyrrolidines as inhibitors of fibroblast activation protein (FAP) and the issue of FAP/prolyl oligopeptidase (PREP)-selectivity. *Bioorganic Med. Chem. Lett.* **2012**, *22*, 3412–3417, doi:10.1016/j.bmcl.2012.03.107.
126. Jansen, K.; De Winter, H.; Heirbaut, L.; Cheng, J.D.; Joossens, J.; Lambeir, A.M.; De Meester, I.; Augustyns, K.; Van Der Veken, P. Selective inhibitors of fibroblast activation protein (FAP) with a xanthine scaffold. *Medchemcomm* **2014**, *5*, 1700–1707, doi:10.1039/c4md00167b.
127. Loktev, A.; Lindner, T.; Mier, W.; Debus, J.; Altmann, A.; Jaeger, D.; Giesel, F.; Kratochwil, C.; Barthe, P.; Roumestand, C.; et al. A Tumor-Imaging Method Targeting Cancer-Associated Fibroblasts. *J. Nucl. Med.* **2018**, *59*, 1423–1429, doi:10.2967/jnumed.118.210435.
128. Lindner, T.; Loktev, A.; Altmann, A.; Giesel, F.; Kratochwil, C.; Debus, J.; Jäger, D.; et al. Development of Quinoline-Based Theranostic Ligands for the Targeting of Fibroblast Activation Protein. *J. Nucl. Med.* **2018**, *59*, 1415–1422, doi:10.2967/jnu-med.118.210443.
129. Loktev, A.; Lindner, T.; Burger, E.-M.; Altmann, A.; Giesel, F.; Kratochwil, C.; Debus, J.; Marme, F.; Jaeger, D.; Mier, W.; et al. Development of novel FAP-targeted radiotracers with improved tumor retention. *J. Nucl. Med.* **2019**, *60*, 1421–1429, doi:10.2967/jnumed.118.224469.
130. Lindner, T.; Loktev, A.; Giesel, F.; Kratochwil, C.; Altmann, A.; Haberkorn, U. Targeting of activated fibroblasts for imaging and therapy. *EJNMMI Radiopharm. Chem.* **2019**, *4*, 1–15, doi:10.1186/s41181-019-0069-0.
131. Altmann, A.; Haberkorn, U.; Siveke, J. The latest developments in imaging of fibroblast activation protein. *J. Nucl. Med.* **2021**, *62*, 160–167, doi:10.2967/jnumed.120.244806.
132. Windisch, P.; Zwahlen, D.R.; Giesel, F.L.; Scholz, E.; Lugenbiel, P.; Debus, J.; Haberkorn, U.; Adeberg, S. Clinical results of fibroblast activation protein (FAP) specific PET for non-malignant indications: systematic review. *EJNMMI Res.* **2021**, *11*, 18, doi:10.1186/s13550-021-00761-2.
133. Baum, R.P.; Schuchardt, C.; Singh, A.; Chantadisai, M.; Robiller, F.C.; Zhang, J.; Mueller, D.; et al. Feasibility, Biodistribution and Preliminary Dosimetry in Peptide-Targeted Radionuclide Therapy (PTRT) of Diverse Adenocarcinomas using ¹⁷⁷Lu-FAP-2286: First-in-Human Results. *J. Nucl. Med.* **2021**, doi:10.2967/jnumed.120.259192.
134. Grus, T.; Lahnif, H.; Klasen, B.; Moon, E.S.; Greifenstein, L.; Roesch, F. Squaric Acid-Based Radiopharmaceuticals for Tumor Imaging and Therapy. *Bioconjug. Chem.* **2021**, *32*, 1223–1231, doi:10.1021/acs.bioconjchem.1c00305.
135. Greifenstein, L.; Engelbogen, N.; Lahnif, H.; Sinnes, J.-P.; Bergmann, R.; Bachmann, M.; Rösch, F. Synthesis, labeling and preclinical evaluation of a squaric acid containing PSMA-inhibitor labeled with ⁶⁸Ga – a comparison with PSMA-11 and PSMA-617. *ChemMedChem* **2020**, *15*, 695–704, doi:10.1002/cmcd.201900559.

3. Manuskripte

A. Targeting fibroblast activation protein (FAP): next generation PET radiotracers using squaramide coupled bifunctional DOTA and DATA^{5m} chelators

Moon, E.S.; [REDACTED]
[REDACTED]

[REDACTED] *EJNMMI Radiopharm. Chem.* **2020**, *5*, 19, doi:10.1186/s41181-020-00102-z.

A.1. [⁶⁸Ga]Ga-DATA^{5m}.SA.FAPi PET/CT: Specific Tracer-uptake in Focal Nodular Hyperplasia and potential Role in Liver Tumor Imaging

[REDACTED]
[REDACTED] Moon, E.S.; [REDACTED]

Nuklearmedizin **2020**, *59*, 387–389, doi:10.1055/a-1164-5667.

A.2. Fibroblast activation protein inhibitor (FAPi) positive tumour fraction on PET/CT correlates with Ki-67 in liver metastases of neuroendocrine tumours

[REDACTED] Moon, E.S.;
[REDACTED]

Nuklearmedizin **2021**, *60*, 344–354, doi:10.1055/a-1521-8604.

A.3. Biodistribution, pharmacokinetics, dosimetry of [⁶⁸Ga]Ga-DOTA.SA.FAPi, and the head-to-head comparison with [¹⁸F]F-FDG PET/CT in patients with various cancers

[REDACTED] Moon, E.S.; [REDACTED]
[REDACTED]

[REDACTED] *Eur. J. Nucl. Med. Mol. Imaging* **2021**, *48*, 1915–1931, doi:10.1007/s00259-020-05132-y.

B. In Vitro Evaluation of the Squaramide-Conjugated Fibroblast Activation Protein Inhibitor-Based Agents AAZTA⁵.SA.FAPi and DOTA.SA.FAPi

Moon, E.S.; [REDACTED]
[REDACTED]

[REDACTED] *Molecules* **2021**, *26*, 3482, doi:10.3390/molecules26123482.

**C. Fibroblast Activation Protein (FAP) targeting homodimeric FAP inhibitor radiotheranostics:
A step to improve tumor uptake and retention time**

Moon, E.S.; [REDACTED]
[REDACTED] *AJNMMI*, 2021, akzeptiert.

C.1. First-in-human results on the Biodistribution, Pharmacokinetics, and Dosimetry of [¹⁷⁷Lu]Lu-DOTA.SA.FAPi and [¹⁷⁷Lu]Lu-DOTAGA.(SA.FAPi)₂ in Patients with Various End-stage Cancers

[REDACTED] Moon, E.S.; [REDACTED] *Pharmaceuticals*, 2021, eingereicht.

C.2. Novel Fibroblast Activation Protein Inhibitor-Based targeted Theranostics for Radioiodine Refractory differentiated Thyroid Cancer Patients: A Pilot Study

[REDACTED] Moon, E.S.; [REDACTED]
[REDACTED] *Thyroid*, 2021, doi:10.1089/thy.2021.0412.

D. Development of DATA^{5m} chelator-based Fibroblast Activation Protein Inhibitor small molecules for PET imaging

Moon, E.S.; [REDACTED]
In Vorbereitung zur Veröffentlichung.

A. Targeting fibroblast activation protein (FAP): next generation PET radiotracers using squaramide coupled bifunctional DOTA and DATA^{5m} chelators

Veröffentlicht in *EJNMMI Radiopharmacy and Chemistry* **2020**, *5*, 19.

mit Genehmigung von © BioMed Central Ltd, Springer Nature

**Targeting fibroblast activation protein (FAP): Next generation PET
radiotracers using squaramide coupled bifunctional
DOTA and DATA^{5m} chelators**

Euy Sung Moon¹, [REDACTED]
[REDACTED]
[REDACTED]

¹ Department of Chemistry – TRIGA site, Johannes Gutenberg University Mainz, Mainz, Germany

² Department of Nuclear Medicine, Antwerp University Hospital (UZA), Edegem, Belgium

³ Department of Pharmaceutical Sciences, Laboratory of Medical Biochemistry, University of Antwerp, Wilrijk, Belgium

⁴ Positronpharma SA, Providencia, Santiago, Chile

⁵ Molecular Imaging Center Antwerp (MICA), University of Antwerp, Wilrijk, Belgium

*Corresponding author: [REDACTED]

Abstract

Background: Fibroblast activation protein (FAP) is a proline selective serine protease that is overexpressed in tumor stroma and in lesions of many other diseases that are characterized by tissue remodeling. In 2014, a most potent FAP-inhibitor (referred to as UAMC1110) with low nanomolar FAP-affinity and high selectivity toward related enzymes such as prolyl oligopeptidase (PREP) and the dipeptidyl-peptidases (DPPs): DPP4, DPP8/9 and DPP2 were developed. This inhibitor has been adopted recently by other groups to create radiopharmaceuticals by coupling bifunctional chelator-linker systems. Here, we report squaric acid (SA) containing bifunctional DATA^{5m} and DOTA chelators based on UAMC1110 as pharmacophor. The novel radiopharmaceuticals DOTA.SA.FAPi and DATA^{5m}.SA.FAPi with their non-radioactive derivatives were characterized for *in vitro* inhibitory efficiency to FAP and PREP, respectively and radiochemically investigated with gallium-68. Further, first proof-of-concept *in vivo* animal study followed by *ex vivo* biodistribution were determined with [⁶⁸Ga]Ga-DOTA.SA.FAPi.

Results: [⁶⁸Ga]Ga-DOTA.SA.FAPi and [⁶⁸Ga]Ga-DATA^{5m}.SA.FAPi showed high complexation > 97% radiochemical yields after already 10 minutes and high stability over a period of 2 h. Affinity to FAP of DOTA.SA.FAPi and DATA^{5m}.SA.FAPi and its ^{nat}Ga and ^{nat}Lu-labeled derivatives were excellent resulting in low nanomolar IC₅₀ values of 0.7 – 1.4 nM. Additionally, all five compounds showed low affinity for the related protease PREP (high IC₅₀ with 1.7 – 8.7 μM). First proof-of-principle *in vivo* PET-imaging animal studies of the [⁶⁸Ga]Ga-DOTA.SA.FAPi precursor in a HT-29 human colorectal cancer xenograft mouse model indicated promising results with high accumulation in tumor (SUV_{mean} of 0.75) and low background signal. *Ex vivo* biodistribution showed highest uptake in tumor (5.2 %ID/g) at 60 min post injection with overall low uptake in healthy tissues.

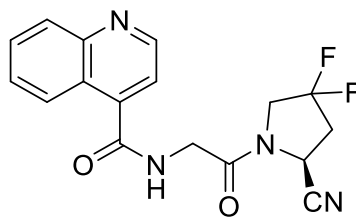
Conclusion: In this work, novel PET radiotracers targeting fibroblast activation protein were synthesized and biochemically investigated. Critical substructures of the novel compounds are a squaramide linker unit derived from the basic motif of squaric acid, DOTA and DATA^{5m} bifunctional chelators and a FAP-targeting moiety. In conclusion, these new FAP-ligands appear promising, both for further research and development as well as for first human application.

Keywords: DOTA, DATA^{5m}, gallium-68, FAP, PREP, squaric acid, squaramide, HT-29

Background

The proline-selective serine protease fibroblast activation protein (FAP) is a type II transmembrane glycoprotein with 760 amino acids. It is related to the dipeptidyl peptidases (DPPs) DPP2, DPP4, DPP8 and DPP9 and furthermore related to the endopeptidase prolyl oligopeptidase (PREP) [1,2]. FAP combines DPP and endopeptidase activities [3–6]. With respect to FAP's endopeptidase activity, a remarkable preference is present for cleavage after Gly-Pro motifs in peptides [7]. FAP is not detectable in most healthy adult tissues and therefore considered non-essential under normal circumstances. However, it is clearly expressed in pathophysiological lesions, characterized by tissue remodeling. Such lesions can be found in, e.g., cancer, atherosclerosis, arthritis and several fibrosis types [8,9]. Over the past two decades, significant attention has gone to FAP in solid tumors, where it is mainly expressed on so-called cancer associated fibroblasts (CAFs) [10,11]. These are activated fibroblasts with a myofibroblast phenotype [12]. There is growing evidence that CAFs have a regulatory role in tumor biology and extracellular matrix composition [13–15]. FAP⁺-CAFs are present in the stromal tissue of more than 90% of epithelial carcinomas, including pancreatic, colon, ovarian, lung and breast cancer [16,17]. Generally speaking, the tumor stroma contains a large part of the tumor mass (> 90% of tumor mass in carcinomas) and is therefore an attractive target for diagnostic and therapeutic radiopharmaceuticals. Conferring stroma affinity to these radiopharmaceuticals by incorporating a FAP-inhibitor moiety is, based on the presence of FAP⁺-CAFs, a potentially rewarding strategy.

Several highly potent FAP-inhibitors have been reported earlier [18,19]. First-generation compounds with a boronic acid warhead, however, are plagued by a lack of selectivity with respect to the related enzymes and are also characterized by lower chemical stability. More recently, compounds with a more stable carbonitrile warhead have been reported [20,21]. One of the most promising molecules to date is UAMC1110 (Figure 1). This molecule combines low nanomolar FAP affinity and high selectivity with respect to both the DPPs and PREP. The high FAP-selectivity of UAMC1110 is particularly attractive for tumor-targeting, when taking into account the near-ubiquitous expression of the DPPs and PREP in humans. In addition, this molecule possesses a satisfactory pharmacokinetic profile.



UAMC1110

Fig. 1 FAP-inhibitor lead structure UAMC 1110.

UAMC1110 is currently still under evaluation as a potential therapeutic in diseases characterized by FAP expression. At the same time, the molecule is being used as a FAP-targeting moiety in so-called activity-based probes that can be used to visualize and quantify FAP activity in tissues and organisms [22]. Highly relevant examples have also been published that rely on radionuclide-based reporter systems, such as XY-FAP-02 developed by Yang et al. [23]. They used a DOTAGA chelator combined with an alkyl chain as linker system bound to the FAP-inhibitor.

Further development of radiotracers by Lindner and Loktev et al. based on the FAP inhibitors from Antwerp have shown promising results in preclinical and first clinical patient studies. Applications of these molecules cover both diagnosis and therapy [24–29]. First, a DOTA-FAPI conjugate using piperazine as linker (referred to as FAPI-02 in the original reference) was synthesized and characterized with respect to binding, internalization, and efflux in cells expressing human and murine FAP as well as CD26. PET-imaging studies of HT-1080 tumor xenografts showed low [^{68}Ga]Ga-FAPI-02 accumulation in normal tissues and a rapid clearance from the blood via kidneys and bladder. In addition, a high tumor uptake resulting in high tumor-to-normal organ-ratio was determined. By structural variation, especially in the linker region, more analogous gallium-68 labeled compounds were obtained. Several of these had improved imaging parameters, with FAPI-04, FAPI-21 and FAPI-46 being relevant examples [25,26]. These compounds also had low nanomolar FAP-affinities, higher tumor uptakes *in vivo* and longer tumor retention times. First PET/CT imaging studies of patients diagnosed with different tumor entities were performed with the gallium-68 compounds indicating high tumor uptake and low background in healthy organs. As an example of a first therapeutic application, patients diagnosed with metastatic breast cancer were treated with [^{90}Y]Y-FAPI-04. The $^{68}\text{Ga}/^{90}\text{Y}$ -DOTA-derivatives represent promising tracers for both diagnostic imaging and, possibly, targeted therapy of malignant tumors with high accumulated activated fibroblasts.

In this work, novel FAP-targeting radiotracers were evaluated using bifunctional DOTA and DATA^{5m} chelators coupled by squaramide as linker moiety. The basic motif squaric acid (SA) is a cyclic aromatic diacid [30,31]. One advantage of SA is the simple chemistry regarding coupling to chelator and target vector including that no protecting groups are necessary due to its selectivity for primary amines.

Especially reactions with biomolecules are attractive and no side reactions are observed. The coupling with SA-diester is a highly selective, pH controlled asymmetric amidation under mild conditions [32]. In a neutral pH, only one ester of the SA-diester reacts with an amine and by increasing the pH to basic conditions, amidation of the second ester takes place. The use of SA as a linker unit between a chelator-biomolecule conjugate as a radiopharmaceutical was demonstrated using DFO and conjugation on a peptide to complex iron and using DFO-squaric acid coupled to antibodies for complexing zirconium-89 [33,34]. Recently, our group published the usage of SA as a linker forming a radiotracer with the bifunctional hybrid chelator AAZTA⁵ coupled to a PSMA inhibitor unit (KuE) and evaluated those AAZTA⁵.SA.PSMA conjugate with various radionuclides such as scandium-44, copper-64, gallium-68 and lutetium-177 [35]. Additionally, we indicate a second feature of SA beyond coupling chemistry. In several cases we could observe a positive impact on pharmacology of the final products. [⁶⁸Ga]Ga-NODAGA.SA.PSMA, [⁶⁸Ga]Ga-TRAM.SA.PSMA and [⁶⁸Ga]Ga-DOTAGA.SA.PSMA showed high tumor uptake and overall high tumor-to-organ ratio. [⁶⁸Ga]Ga-DOTAGA.SA.PSMA provided *in vivo* in LNCaP-tumor bearing mice comparable results to [⁶⁸Ga]Ga-PSMA-617 and [⁶⁸Ga]Ga-PSMA-11 with significant tumor accumulation [36].

Here, the preparative synthesis of DOTA.SA.FAPi and DATA^{5m}.SA.FAPi and the metal-analogs [^{nat}Ga]Ga-DOTA.SA.FAPi, [^{nat}Ga]Ga-DATA^{5m}.SA.FAPi and [^{nat}Lu]Lu-DOTA.SA.FAPi are described. The macrocyclic chelator DOTA was used to allow labeling with both gallium-68 and lutetium-177. However, one disadvantage of these chelator types are the requirement of high temperatures for complexation [37]. DATA^{5m}, a bifunctional version of the hybrid chelator DATA, was used to allow instant gallium-68 labeling at room temperature [38–40]. Radiochemical evaluation with regard to labeling and *in vitro* stability studies were performed with gallium-68 for DOTA.SA.FAPi and DATA^{5m}.SA.FAPi. For all the five cold compounds, inhibition assays were carried out and IC₅₀ values obtained for FAP and PREP. In a first proof-of-principle PET-study, [⁶⁸Ga]Ga-DOTA.SA.FAPi was tested *in vivo* using a FAP-expressing HT-29 human colorectal adenocarcinoma xenograft model.

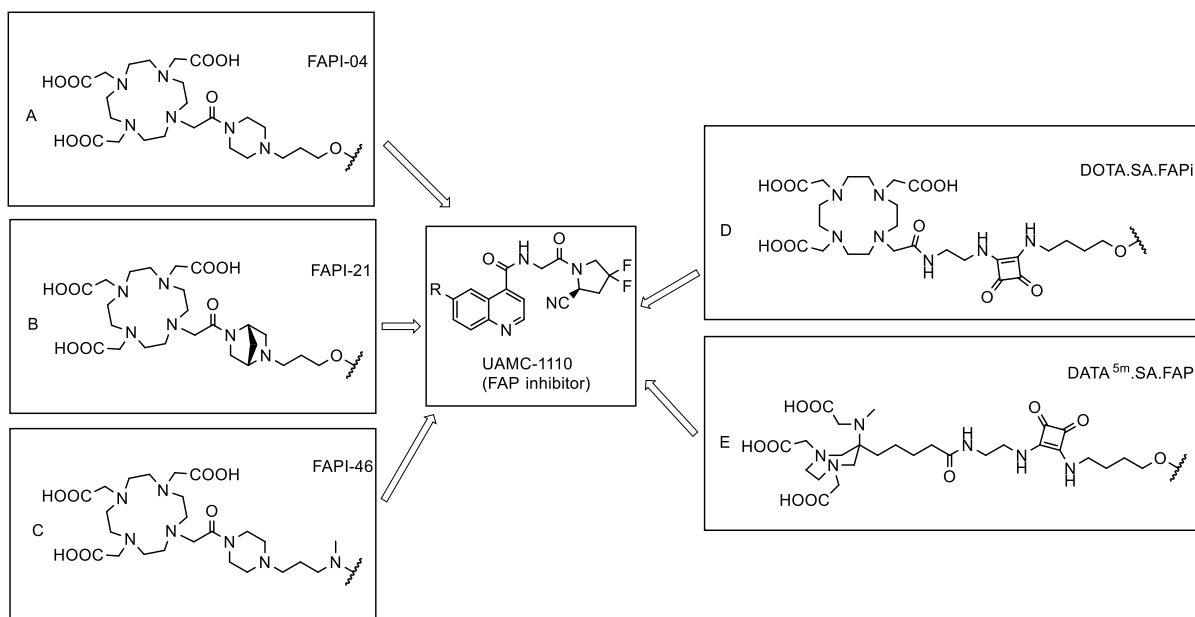


Fig. 2 structural comparison of chelator-linker conjugates coupled with UAMC1110 (FAP inhibitor). A) FAPI-04; B) FAPI-21; C) FAPI-46; D) DOTA.SA.FAPi; E) DATA^{5m}.SA.FAPi.

Results

Synthesis of DOTA.SA.FAPi

The commercially available DO3AtBu-*N*-(2-aminoethyl)ethanamide **1** was treated with TFA to deprotect the *tert*-butyl groups. Since the coupling of squaric acid diethyl ester (SADE) with primary amines is selective, no protective groups were necessary for the next synthesis steps. The deprotected DO3A-*N*-(2-aminoethyl)ethanamide was coupled to SADE in phosphate buffer (pH 7) at ambient temperature and purified via HPLC to receive DOTA.SA **2**. The free coupling side of **2** was afterwards coupled to (5)-6-(4-aminobutoxy)-*N*-(2-(2-cyano-4,4-difluoropyrrolidin-1-yl)-2-oxoethyl)-quinoline-4-carboxamide **3** (termed NH₂-UAMC1110) in phosphate buffer (pH 9) at room temperature. After successful HPLC purification, DOTA.SA.FAPi **4** was obtained (Figure 3).

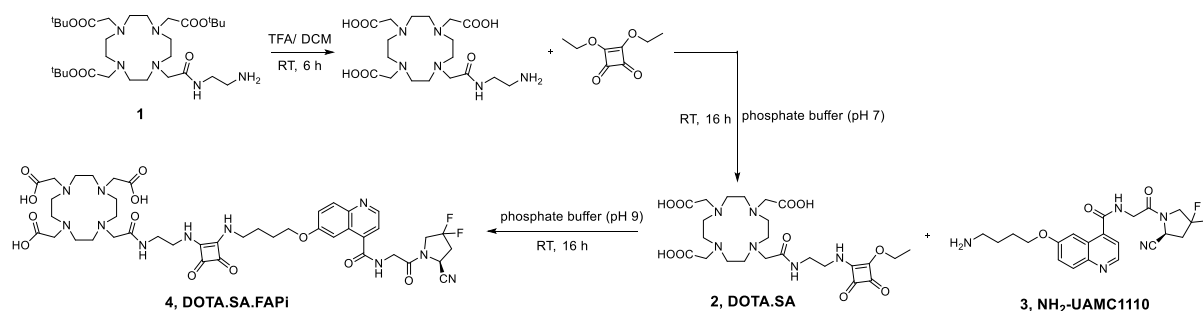


Fig. 3 synthesis scheme of DOTA.SA.FAPi **4**.

Synthesis of DATA^{5m}.SA.FAPi

DATA^{5m}-3^tBu **5** was synthesized as described by Seemann et al. (Figure 4) [38]. DATA^{5m}-3^tBu provides a bifunctional carbonyl group for further coupling with spacer molecules or target vectors. Terminal primary amines are required for binding to SA-diethylester. Therefore *N*-boc-ethylenediamine was attached to the carboxylic acid group of DATA^{5m} via common coupling reagents HATU in DIPEA and acetonitrile receiving **6**. Amidation of SA-monoester **7** with the terminal amine of NH₂-UAMC1110 was executed analogously to DOTA.SA.FAPi to receive DATA^{5m}.SA.FAPi **8**.

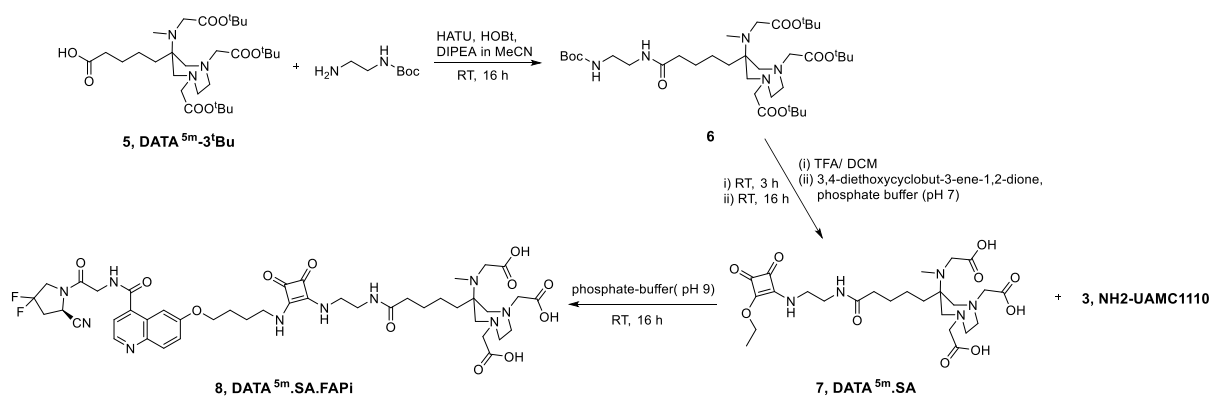


Fig. 4 synthesis scheme of DATA^{5m}.SA.FAPi **8**.

Synthesis of cold complexes and enzyme inhibition assays

Non-radioactive complexes of [^{nat}Ga]Ga-DOTA.SA.FAPi, [^{nat}Ga]Ga-DATA^{5m}.SA.FAPi and [^{nat}Lu]Lu-DOTA.SA.FAPi were synthesized. The corresponding precursors were reacted with a 10 mM solution of the metal chlorides or nitrates in 0.2 M sodium acetate (NaAc) buffer pH 4.5. The solutions of ^{nat}Ga

and ^{nat}Lu complexed DOTA.SA.FAPi were shaken for 3 h at 95 °C and the solution of ^{nat}Ga -metalled DATA^{5m}.SA.FAPi was shaken for 2 h at RT. Complexations were monitored by ESI LC-MS and the metal complexes were purified via HPLC.

In the inhibition assays, DOTA.SA.FAPi and DATA^{5m}.SA.FAPi, along with their non-radioactive, metal complexed analogues were characterized for inhibitory potency towards FAP and PREP. Earlier work had shown that the lack of a basic amine function in UAMC1110-based molecules, precludes DPP-affinity in this series [21,22]. Nonetheless, the FAP/PREP selectivity was shown to be a particularly important parameter to check. Obtained results are summarized in Table 1. Parent compound UAMC1110 was used as a reference in this assay. All the evaluated molecules displayed highly satisfactory, low nanomolar FAP potencies, in the same range as the parent inhibitor UAMC1110. This implies that introduction of a linker, a chelator and a metal ion at the selected position of the quinoline ring are tolerated by FAP and have no negative influence on target affinity. Likewise, equally satisfactory compound selectivities with respect to PREP were measured, again comparable with UAMC1110.

Tab. 1 IC₅₀-values of DOTA.SA.FAPi, the ^{nat}Ga and ^{nat}Lu -complexes and DATA^{5m}.SA.FAPi and the ^{nat}Ga -complex with regard to FAP and PREP. Selectivity index gives the ratio FAP to PREP.

	IC ₅₀ FAP (nM)	IC ₅₀ PREP (μM)	Selectivity index (IC ₅₀ (FAP/PREP))
DOTA.SA.FAPi – uncomplexed	0.9 ± 0.1	5.4 ± 0.3	6000
DOTA.SA.FAPi - ^{nat}Ga	1.4 ± 0.2	8.7 ± 0.9	6214
DOTA.SA.FAPi – ^{nat}Lu	0.8 ± 0.2	2.5 ± 0.4	3125
DATA ^{5m} .SA.FAPi – uncomplexed	0.8 ± 0.2	1.7 ± 0.1	2113
DATA ^{5m} .SA.FAPi – ^{nat}Ga	0.7 ± 0.1	4.7 ± 0.3	6714
FAP-inhibitor UAMC1110	0.43 ± 0.07 ^a	1.8 ± 0.2 ^b	4186

^a Determined under the conditions of this study. ^b data from Jansen et al. [21]

Radiochemical evaluations with gallium-68

Radiolabeling of DOTA.SA.FAPi with ^{68}Ga was performed with varying amounts of the precursor (11–42 nmol) and at 95 °C (Figure 5). Labeling was performed in 300 μl 1 M ammonium acetate (AmAc) buffer (pH 5.5) at 95 °C in triplicate n=3 with around 200 MBq of gallium-68. For precursor amounts of more than 16 nmol, a quantitative radiochemical yield (RCY) of > 97% could be achieved in less than

5 minutes. At 11 nmol a decreased RCY of 44 % after 15 minutes could be observed. HPLC retention time of free gallium-68: $t_R(^{68}\text{Ga})= 4$ min and the retention time of the complex $t_R ([^{68}\text{Ga}]\text{Ga-DOTA.SA.FAPi})= 9$ min. The R_f values of the radio-TLC were $R_f(^{68}\text{Ga})= 0.9$ and $R_f([^{68}\text{Ga}]\text{Ga-DOTA.SA.FAPi})= 0.1$ using citrate buffer pH 4 as mobile phase.

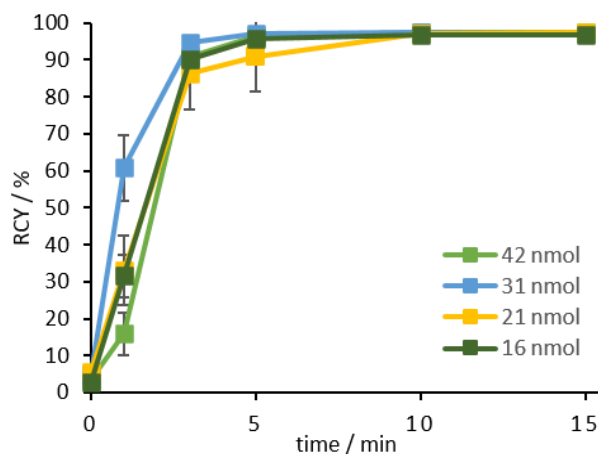


Fig. 5 radiolabeling kinetics for various amounts of $[^{68}\text{Ga}]\text{Ga-DOTA.SA.FAPi}$ complex at 95 °C, precursor amounts > 15 nmol result in RCY > 97% after 15 min.

Carrying out labeling of DOTA.SA.FAPi at different temperatures (70, 80 and 95 °C) with a defined precursor amount of 31 nmol resulted in quantitative RCYs > 97% at temperatures of 80 °C and 95 °C after 15 minutes. At 70 °C, complexation of gallium-68 via DOTA.SA.FAPi showed decreased radiolabeling efficiency, nevertheless resulting in > 83% after 15 min. (SI, Figure S3).

Stability studies were performed in ethanol (EtOH), human serum (HS) and saline 0.9% (NaCl) over a period of 2 h at 37 °C. In all three media, $[^{68}\text{Ga}]\text{Ga-DOTA.SA.FAPi}$ showed high stabilities over 98% intact conjugate (SI, Figure S4). In addition, stability against transmetallation and transchelation were carried out (SI, Figure S5, S6). Against DTPA and EDTA the stability values were > 98% and against Cu, Mg and Ca the stabilities were > 95% after 2 h. Stabilities against Fe showed > 95% after 90 minutes and a slightly lower value however still over 92 % after 2 h.

For radiolabeling of DATA^{5m}.SA.FAPi, various precursor amounts (1–21 nmol) in 300 μl 1 M AmAc buffer (pH 5.5) were labeled with gallium-68. The reaction mixture was shaken for 10 min at room temperature to afford $[^{68}\text{Ga}]\text{Ga-DATA}^{5m}.\text{SA.FAPi}$.

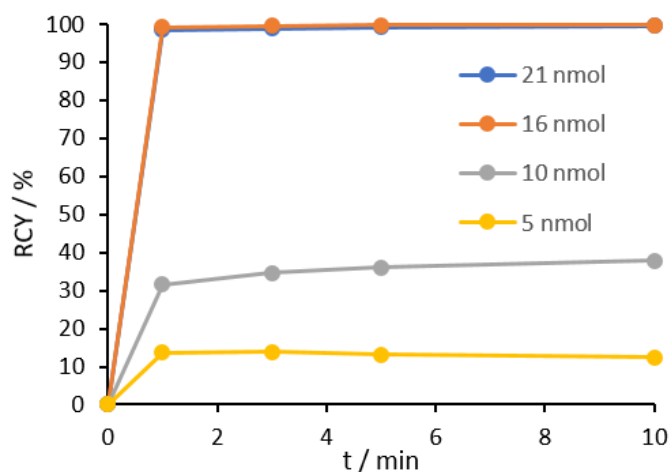


Fig. 6 radiolabeling kinetics of various amounts of $[^{68}\text{Ga}]\text{Ga-DOTA}^{5\text{m}}.\text{SA.FAPi}$ complex at RT, precursor amounts > 15 nmol result in RCY > 98% after 15 min.

First kinetic studies were performed with 200–230 MBq of gallium-68 in 1 M AmAc buffer (pH 5.5) at RT (n=1). Quantitative RCYs > 98% could be achieved for precursor amounts of 16 nmol and 21 nmol in less than 1 minute. Analogous to $[^{68}\text{Ga}]\text{Ga-DOTA.SA.FAPi}$, $[^{68}\text{Ga}]\text{Ga-DOTA}^{5\text{m}}.\text{SA.FAPi}$ also showed significantly lower RCY below 15 nmol. At 10 nmol only a RCY of 38% and for 5 nmol a RCY of just 12% after 10 minutes could be observed. HPLC retention times of free gallium-68 $t_R(^{68}\text{Ga})$ and of the complex $t_R([^{68}\text{Ga}]\text{Ga-DOTA}^{5\text{m}}.\text{SA.FAPi})$ were 4 min and 8.5 min, respectively. The R_f values of the radio-TLC were $R_f(^{68}\text{Ga})=0.9$ and $R_f([^{68}\text{Ga}]\text{Ga-DOTA}^{5\text{m}}.\text{SA.FAPi})=0.1$ using citrate buffer pH 4 as mobile phase. Stability of $[^{68}\text{Ga}]\text{Ga-DOTA}^{5\text{m}}.\text{SA.FAPi}$ was determined in phosphate buffered saline (PBS), HS and NaCl over a period of 120 min. In all three media, the stability of $[^{68}\text{Ga}]\text{Ga-DOTA}^{5\text{m}}.\text{SA.FAPi}$ remained > 95% (SI, Figure S7).

PET/CT-imaging and *ex vivo* biodistribution data of $[^{68}\text{Ga}]\text{Ga-DOTA.SA.FAPi}$

For investigation of the tumor uptake by $[^{68}\text{Ga}]\text{Ga-DOTA.SA.FAPi}$ HT-29 tumor-bearing mice (n=3) were sacrificed after PET/CT scans and an *ex vivo* biodistribution study was executed. In the PET images, the tumor accumulation is clearly visible (SUV_{mean} of 0.75 ± 0.09) and the ratio to nonspecific organs and tissues is very high (SUV_{mean} : 0.15 ± 0.01 in the heart, 0.18 ± 0.07 in the muscle, 0.37 ± 0.14 in the small intestine, 0.27 ± 0.11 in kidneys and 0.22 ± 0.08 in the liver)). Figure 7 shows the maximum intensity projection (MIP) images of three mice. *Ex vivo* biodistribution is shown in Figure 8a. The accumulation in the tumor at 60 min post injection (p.i.) as found in both the PET images and biodistribution with high with an overall uptake of 5.2 %ID/g. In general, the tumor-to-organ ratios are high after 1 h p.i. which is shown by, e.g., tumor-to-blood (9.2 ± 1.1), tumor-to-large intestine (24.9 ± 1.7) and tumor-to-

muscle (11.5 ± 2.2) ratios (Figure 8b). Uptake in other organs are also low such as in heart, lungs, liver, spleen, pancreas, stomach, fat and skin. In addition to the tumor accumulation, a slightly higher accumulation at the bones and small intestine were found, which cannot yet be fully explained. One suggestion could be that FAP is also expressed in these tissues. However, it is important that the main accumulation is located in the tumor and although the unexpected radiotracer uptake in bone and small intestine the tumor-to-bone (1.5 ± 0.2) and tumor-to-small intestine (2.9 ± 0.8) ratios are still high enough to provide high contrast PET images.

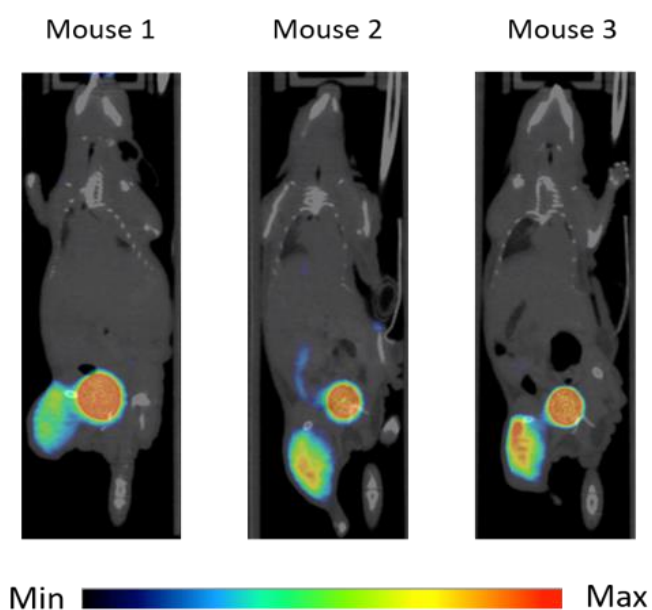


Fig. 7 *In vivo* evaluation of [^{68}Ga]Ga-DOTA.SA.FAPi uptake in a HT-29 xenograft mouse model. Representative coronal small-animal PET/CT images (MIP) 60 min after injection of [^{68}Ga]Ga-DOTA.SA.FAPi.

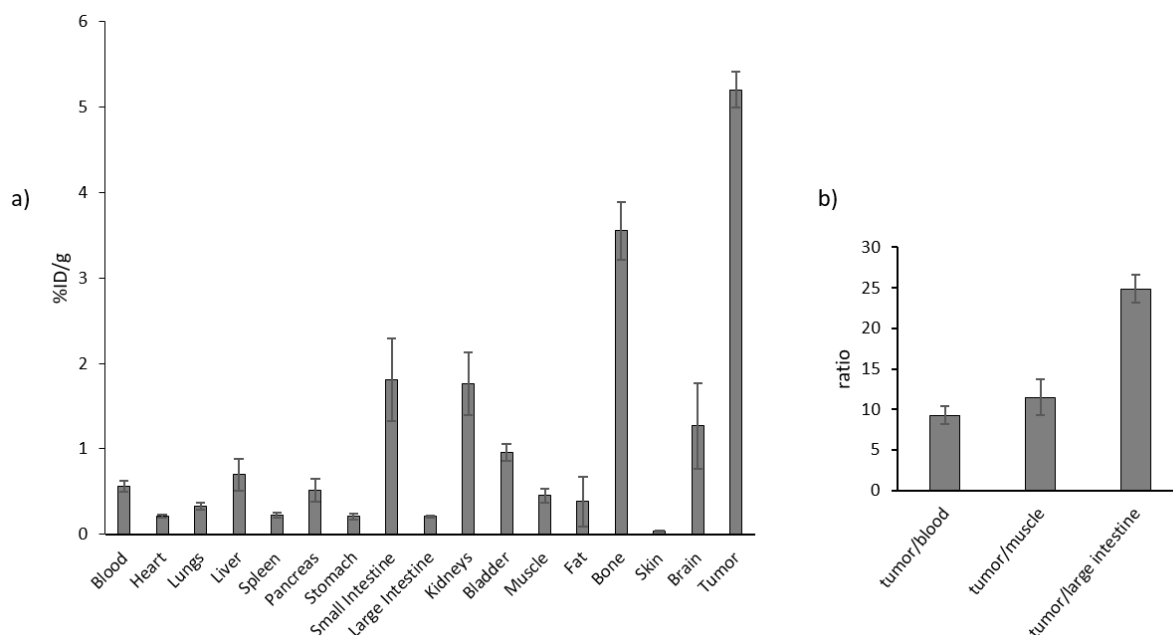


Fig. 8 a) *Ex vivo* biodistribution of $[^{68}\text{Ga}]\text{Ga-DOTA.SA.FAPi}$ in HT-29 xenograft mice (n=3) 1 h p.i. b) Tumor-to-organ ratios of $[^{68}\text{Ga}]\text{Ga-DOTA.SA.FAPi}$ in HT-29 xenograft mice (n=3) 1 h p.i.

Discussion

Two novel bifunctional chelator-linker conjugates based on the FAP inhibitor UAMC1110 were developed. As bifunctional chelators, macrocyclic DOTA as well as the hybrid chelator DATA^{5m} were used. DATA is well known for fast and stable complexation of gallium-68 and to show high stabilities over a long period of time. DOTA is interesting because of its ability to complex other radiometals preferring higher coordination numbers, e.g., the long-lived therapy radionuclide lutetium-177 but also shorter-lived therapeutic radionuclides such as bismuth-213, lead-210 and yttrium-90. DOTA.SA.FAPi allows to use the same precursor for both diagnosis with gallium-68 and therapy with lutetium-177 in nuclear medicine. SA is the main component of the linker system forming a squaramide unit and accordingly substitutes the heterocyclic nitrogen moieties in the structures reported by the Heidelberg group [24–26]. In recent works from our group, SA has shown good results, both in chemistry and physiologically, as a linker unit coupled with PSMA inhibitors [35,36]. The asymmetrically substituted squaramide unit in the target compounds was efficiently installed with SADE, relying on the latter's elegant pH-dependent chemistry and selectivity for primary amines. Due to this selectivity, no protecting groups are required. In addition, the pH dependent reactivity of SADE

is explained by changes of the aromatic stabilization energy in the ring system over the course of the sequential amidation steps [32]. After the first amidation, which is carried out at neutral pH, the obtained uncharged monoamide is characterized by a higher aromatic stabilization than the starting material, squaric acid diester. This stabilization prevents addition of a second amine molecule. By increasing the pH, the monoamide is deprotonated, loses aromatic stabilization, and this allows for addition of a second amine molecule to provide the diamide [30,41]. Correspondingly, C₂-symmetric diamide derivatives of SA can be obtained, if the reaction is performed at higher pH: in that case, two equivalents of amine will directly substitute the ethoxy groups in SADE.

Both DOTA.SA.FAPi and DATA^{5m}.SA.FAPi could be well used for radiolabeling with gallium-68. DATA has already demonstrated good complexation with gallium-68 and has the advantage of labeling even under mild conditions such as room temperature. Quantitative gallium-68 labeling results were observed for both FAPi-conjugates with gallium-68. The DOTA complex showed quantitative radiochemical yields at temperatures of 95 °C with precursor amounts of > 15 nmol. For the DATA^{5m} conjugate quantitative yields could be achieved at room temperature for amounts > 15 nmol. In addition, it could be seen that with lower competing cations of gallium-68, less precursor amount (≥ 10 nmol) is required to achieve quantitative complexation, whereas with higher gallium activity (> 200 MBq) more substance >15 nmol is needed for quantitative yields.

The stability for both derivatives against different media was high with > 95% intact conjugates. [⁶⁸Ga]Ga-DOTA.SA.FAPi proved stable in EtOH, HS and saline and was stable against transmetallation (Cu, Mg, Ca and Fe) and transchelation (DTPA and EDTA). Stability of [⁶⁸Ga]Ga-DATA^{5m}.SA.FAPi in HS, PBS and in saline is very high with > 95% intact conjugates over a period of 2 h.

All five measured compounds, DOTA.SA.FAPi, [^{nat}Ga]Ga-DOTA.SA.FAPi, [^{nat}Lu]Lu-DOTA.SA.FAPi, DATA^{5m}.SA.FAPi and [^{nat}Ga]Ga-DATA^{5m}.SA.FAPi demonstrated very high affinity to FAP with low nanomolar IC₅₀ values and high IC₅₀ values with respect to PREP. Therefore, all measured FAP inhibitors have a potency in the same order of magnitude as the original FAP inhibitor. In addition, they all presented excellent selectivity for FAP with regard to PREP.

Preclinical *in vivo* animal studies were performed with HT-29 xenograft mice. The HT-29 cancer cell line is a human colorectal adenocarcinoma cell line with epithelial morphology [42,43]. When inoculated into nude mice, they produce undifferentiated tumors with modest stroma. Significant FAP expression is present in this stroma, that typically trabeculates between nests of HT-29 cells. Notably, and similar to the situation in most tumor types, FAP staining is distinctly absent from the actual HT-29 cancer cells within the tumors [43].

The highest accumulation in the tumor was found in both the PET images with SUV_{mean} of 0.75 ± 0.09 60 min post injection and biodistribution with an overall uptake of 5.2 %ID/g. In addition, the tumor-to-organ ratios in the biodistribution data were quite high (tumor-to-blood (9.2 ± 1.1), tumor-to-large intestine (24.9 ± 1.7) and tumor-to-muscle (11.5 ± 2.2)), which is also reflected by the high contrast in the images. Besides the high tumor uptake, accumulation in the bladder could also be observed, suggesting renal clearance to be the predominant excretion.

The reference FAPI-04 could not be included in the experiments because it was not available yet. While head-to-head comparison with ^{68}Ga -FAPI-04 was not possible, we may compare the SUV_{mean} value data from reference publications. It should be noted, however, that different tumor models in different test series were used. Therefore, a direct comparison of the results is not advisable, but tendencies could still be observed. The tumor model used in Heidelberg are HT-1080-FAP cells (transfected fibrosarcoma cells) [25]. There is a recent publication from Watabe et al. on ^{64}Cu -, ^{68}Ga -, and ^{225}Ac -FAPI-04 in PANC-1 and MIA PaCa-2 (human pancreatic cancer cells) xenograft tumor mice [44]. Table 2 shows a summary of the different models with the corresponding gallium-68 tracer complex and the SUV_{mean} values of PET measurements at 60 min p.i.

Tab. 2 Comparison of [^{68}Ga]Ga-FAPI-04 and [^{68}Ga]Ga-DOTA.SA.FAPI: SUV_{mean} values of μPET measurements at 60 min p.i. with the corresponding tumor models. The values of the FAPI-04 component are obtained from the reference literatures [25,44].

Compound	[^{68}Ga]Ga-FAPI-04		[^{68}Ga]Ga-DOTA.SA.FAPI
Tumormodel	HT-1080 FAP	PANC-1 / MIA-PaCa-2	HT-29
	SUV_{mean} (60 min p.i.)		
Heart	0.16	0.17	0.15
Muscle	0.06	0.03	0.18
Kidney	0.33	0.36	0.27
Liver	0.11	0.67	0.22
Tumor	0.45	0.14 / 0.11	0.75

(The values from references were read from the graphs and therefore do not indicate precise values.)

Table 2 shows that comparable SUV_{mean} values can be found with [^{68}Ga]Ga-DOTA.SA.FAPi and [^{68}Ga]Ga-FAPi-04 in the HT-1080 FAP model. In both, tumor uptake is highest with overall low background in normal organs. The uptake in the tumor of ^{68}Ga -FAPi-04 in the models of Watabe et al. are marginal while liver shows slightly higher uptake.

Conclusion

In this work, two potential theranostic radiopharmaceuticals were successfully synthesized, based on the selective FAP-inhibitor UAMC1110. Key elements of these compounds are a squaramide motif (introduced via amidation of SADE) and a DOTA or DATA^{5m}-type chelator. Due to the unique chemistry of SADE, it was possible to avoid complex synthesis routes and protective group strategies. DOTA.SA.FAPi and DATA^{5m}.SA.FAPi showed very good *in vitro* complexations of gallium-68 and a very high stability in different media of more than 95% intact conjugate. In general, the hybrid chelator DATA^{5m} shows a quantitative complexation under mild conditions and is therefore very well suited to label temperature sensitive target molecules with radiometals.

Both FAPi-precursors as well as their gallium and lutetium versions showed excellent affinity and selectivity to FAP, in the low nanomolar range, with IC_{50} -values between 0.7 and 1.4 nM. Conversely, PREP IC_{50} -values were found to be in the μM -range, implying excellent FAP/PREP selectivity indices.

In the HT-29 colon cancer xenograft model, first proof-of-concept animal studies with [^{68}Ga]Ga-DOTA.SA.FAPi showed good tumoral accumulation with high uptake ($SUV_{\text{mean}} 0.75 \pm 0.09$) at 60 min p.i. Ex vivo biodistribution revealed 5.2 ± 0.2 % ID/g on average and low background activity, *i.e.* an overall good tumor-to-organ ratio. Comparison of the different tumor models with the reference compound FAPi-04 has shown that DOTA.SA.FAPi offers comparable results to FAPi-04. The values should not be compared in direct relation, as there are different test series as well as different tumor models, but nevertheless a tendency can be exhibited.

The potential of the novel compound family to target FAP could be clearly demonstrated. The introduction of squaric acid as linker forming a squaramide bond between bifunctional chelator and pharmacophore firstly simplified the preparative work and secondly showed pharmacological improvements due to the excellent *in vitro* binding affinities and the great *in vivo*/ *ex vivo* data. Further preclinical characterizations for both precursors are planned for publication at a later stage. In meantime, a first clinical trial was carried out in cooperation with the University Medical Center Bonn

showing specific uptake in focal nodular hyperplasia [45]. Further patient investigations are ongoing and we expect that our FAPi based radiotracers could be of importance characterize various malignant and benign tumor types in nuclear medicine.

Materials and Methods

Reagents and instrumentations for synthesis

All basic chemicals were acquired from Sigma-Aldrich (St. Louis, USA), Merck KGaA (Darmstadt, Germany), TCI Deutschland GmbH (Eschborn, Germany) and VWR International GmbH (Darmstadt, Germany). DOT3AtBu-*N*-(2-aminoethyl)ethanamide **1** was purchased from CheMatech (Dijon, France), (*S*)-6-(4-aminobutoxy)-*N*-(2-(2-cyano-4,4-difluoropyrrolidin-1-yl)-2-oxoethyl)-quinoline-4-carboxamide **3** was purchased from KE Biochem Co. (Shanghai, China). Thin-layer chromatography plates from Merck, Kieselgel 60 F254 coated aluminum plates, were used for the analysis. Detection was carried out by fluorescence extinction at $\lambda = 254$ nm and by staining with potassium permanganate. Silica gel 60 (core size 0.063 0.200 mm) from Acros Organics (Schwerte, Germany) was used for purification by column chromatography. The LC/MS spectra were measured on an Agilent Technologies 1220 Infinity LC system coupled to an Agilent Technologies 6130B Single Quadrupole LC/MS system. The ^1H and ^{13}C NMR measurements were performed at 400 MHz (400 MHz FT NMR spectrometer AC 400, Bruker Analytik GmbH). For analytical and semi-preparative HPLC a 7000 series Hitachi LaChrom with a Phenomenex (Aschaffenburg, Germany) Luna C18 (250 x 4.6 mm, 5 μ) column, a Phenomenex Luna C18 (250 x 10 mm, 10 μ) column and a Phenomenex Synergi C18 (250 x 10 mm, 4 μ) column were used.

Organic Synthesis

Synthesis of DOTA.SA.FAPi

DOTA.SA (2) [2,2',2''-(10-(2-((2-ethoxy-3,4-dioxocyclobut-1-en-1-yl)amino)ethyl)amino)-2-oxoethyl)-1,4,7,10-tetraazacyclododecane-1,4,7-triyl]triacetic acid]

1 (48.0 mg; 78.1 μmol) was reacted with 1 mL 80% TFA in DCM for 6 h at room temperature for deprotection of *tert*-butyl protecting groups. After evaporating TFA/DCM, the residue was reacted with 3,4-diethoxycyclobut-3-ene-1,2-dione (13.3 mg; 78.1 μmol) in 500 μL 0.5 M $\text{Na}_2\text{HPO}_4/\text{NaH}_2\text{PO}_4$

phosphate buffer pH 7 and shaken at room temperature overnight. The chelator-linker conjugate DOTA.SA **2** could be isolated via HPLC purification. After HPLC purification (Phenomenex® Luna® 10 µm C18 (2) 100 Å, gradient 6-8% MeCN (+0.1% TFA)/ 94-92% Water (+0.1% TFA) in 20 min with a 5 mL/min flow) and lyophilization the product was obtained as white powder (28.2 mg; 49.4 µmol; 63 %). ¹H-NMR (D₂O, 600 MHz, δ [ppm]): 4.64-4.53 (dq, 2 H); 3.93-2.89 (m, 28 H); 1.41-1.33 (m, 3 H). MS (ESI⁺): m/z (%): 571.3 (M+H⁺), 593.3 (M+Na); calculated for C₂₄H₃₈N₆O₁₀: 570.26

DOTA.SA.FAPi (4) [(S)-2,2',2''-(10-(2-((2-((4-((2-cyano-4,4-difluoropyrrolidin-1-yl)-2-oxoethyl)carbamoyl)quinolin-6-yl)oxy)butyl)amino)-3,4-dioxocyclobut-1-en-1-yl)amino)ethyl)amino)-2-oxoethyl)-1,4,7,10-tetraazacyclododecane-1,4,7-triyl]triacetic acid]

Coupling of DOTA.SA **2** (10.3 mg; 17.5 µmol) and NH₂-UAMC1110 **3** (11.4 mg; 26.3 µmol) to form DOTA.SA.FAPi **4** was performed by amidation at pH 9 in 500 µL 0.5 M Na₂HPO₄ phosphate buffer at room temperature. The reaction was shaken for 12 h. DOTA.SA.FAPi **4** was isolated via HPLC purification (Phenomenex® Luna® 10 µm C18(2) 100 Å) with a linear gradient condition of 15-20% MeCN (+0,1% TFA)/85-80% Water (+0,1% TFA) in 20 min with a 5 mL/min flow. After lyophilization the product was obtained as yellow powder (12.2 mg; 12.7 µmol, 73 %). MS (ESI⁺): m/z (%): 956.4 (M+H⁺), 978.4 (M+Na); calculated for C₄₃H₅₅F₂N₁₁O₁₂: 955.40

Synthesis of DATA^{5m}.SA.FAPi

DATA^{5m}-en (6) [1,4-Di(tert-butylacetate)-6-((5-(2-((tert-butoxy-carbonyl)aminoethyl)amino)-5-oxopentyl)-6-(amino(methyl)-tert-butylacetate)-perhydro-1,4-diazepane)]

5 (100 mg; 0.18 mmol) was added to 1 mL dry MeCN, HATU (66.3 mg; 0.18 mmol), HOBt (70.9 mg; 0.53 mmol) and DIPEA (89.3 µL; 0.53 mmol) were added and stirred for 1 h at room temperature. *N*-boc-ethylenediamine (56.1 mg; 0.35 mmol) was added to the solution and stirred overnight. After completion of the reaction, the solution was concentrated under vacuum and the residue was purified by column chromatography (CHCl₃/MeOH, 20:1, R_f= 0.23). The product was obtained as yellow oil (114 mg; 0.16 mmol; 91%). ¹H-NMR (DMSO, 400 MHz, δ [ppm]): 3.36 (s, 2 H); 3.23 (s, 4 H); 3.07-3.01 (m, 2 H); 2.97-2.91 (m, 2 H); 2.79 (d, J=13.7 Hz, 2 H); 2.72-2.67 (m, 2 H); 2.59-2.54 (m, 2 H); 2.51 (d, J=13.7 Hz, 2 H); 2.17 (s, 3 H); 2.03 (t, 2 H); 1.45-1.41 (m, 4 H); 1.40 (s, 18 H); 1.39 (s, 9 H); 1.37(s, 9 H); 1.22-1.18 (m, 2 H). ¹³C-NMR (CDCl₃, 100 MHz, δ [ppm]): 172.25 (s); 171.72 (s); 170.28 (s); 169.58 (s); 155.62 (s); 80.19 (s); 80.08 (s); 77.63 (s); 62.37 (s); 61.87 (s); 61.73 (s); 58.72 (s); 56.06 (s); 51.50 (s);

37.10 (s); 35.55 (s); 28.24 (s); 27.87 (s); 27.77 (s); 26.11 (s); 25.50 (s); 21.55 (s). MS (ESI⁺): m/z (%): 714.4 (M+H⁺); 736.5 (M+Na⁺); calculated for C₃₆H₆₇N₅O₉: 713.49

DATA^{5m}.SA (7) [1,4-Di(acetate)-6-((5-(2-((2-ethoxy-3,4-dioxo-cyclobut-1-en-1-yl)aminoethyl)amino)-5-oxo-pentyl)-6-(amino(methyl)-acetate)-perhydro-1,4-diazepane]

6 (100 mg; 0.14 mmol) was dissolved in DCM/TFA (1:1; vol%) and stirred for 3 hours. After complete deprotection of the *tert*-butyl groups, the solution was concentrated under vacuum and 3 mL 0.5 M phosphate buffer pH 7 was added to the residue. After adding 3,4-diethoxycyclobut-3-ene-1,2-dione (61.7 µL; 0.42 mmol) to the solution, the pH was adjusted again to pH 7 with 1 M NaOH and stirred overnight at room temperature. After completion, the reaction solution was purified by HPLC (Phenomenex[®] Luna[®] 10 µm C18(2) 100 Å) with a linear gradient condition of 8-12% MeCN (+0,1% TFA)/92-88% Water (+0,1% TFA) in 20 min with a 5 mL/min flow. After lyophilization the product was obtained as white powder (24.8 mg; 43.6 µmol, 31%). ¹H-NMR (D₂O, 600 MHz, δ [ppm]): 4.73-4.66 (m, 2 H); 3.79 (s, 2 H); 3.70 (s, 4 H), 3.67-3.47 (m, 6 H); 3.39-3.22 (m, 6 H); 2.98 (d, J=8.7 Hz, 3 H); 2.22 (t, 2 H); 1.71-1.68 (m, 2 H); 1.53-1.48 (m, 2 H); 1.43-1.38 (m, 2 H); 1.35-1.29 (m, 2 H). ¹³C-NMR (D₂O, 150 MHz, δ [ppm]): 188.70 (s); 183.25 (s); 177.21 (s); 176.42 (s); 173.82 (s); 170.00 (s); 117.19 (s); 115.26 (s); 70.66 (s); 68.77 (s); 54.14 (s); 43.89 (s); 39.22 (s); 37.76 (s); 35.09 (s); 29.53 (s); 25.69 (s); 25.54 (s); 22.09 (s); 15.03 (s); 14.94 (s). MS (ESI⁺): m/z (%): 570.3 (M+H⁺); 593.3 (M+Na⁺); calculated for C₂₅H₃₉N₅O₁₀: 569.27

DATA^{5m}.SA.FAPi (8) [(S)-2,2'-(6-((carboxymethyl)(methyl)amino)-6-(5-((2-((2-((4-((2-(2-cyano-4,4-difluoropyrrolidin-1-yl)-2-oxoethyl)carbamoyl)quinolin-6-yl)oxy)butyl)amino)-3,4-dioxocyclobut-1-en-1-yl)amino)ethyl)amino)-5-oxopentyl)-1,4-diazepane-1,4-diyl]diacetic acid]

DATA^{5m}.SA **7** (8.7 mg, 15.3 µmol) and NH₂-UAMC1110 **3** (19.8 mg, 45.9 µmol) were reacted to form DATA^{5m}.SA.FAPi **8** via amidation at pH 9 in 500 µL 0.5 M Na₂HPO₄ phosphate buffer at room temperature stirred overnight. DATA^{5m}.SA.FAPi was isolated via HPLC purification (Phenomenex[®] Luna[®] 10 µm C18(2) 100 Å) with a linear gradient condition of 18-20% MeCN (+0,1% TFA)/82-80% Water (+0,1% TFA) in 20 min. The product was obtained as yellowish powder (6.2 mg, 6.5 µmol; 42%). MS (ESI⁺): m/z (%): 955.4 (M+H⁺); calculated for C₄₄H₅₆F₂N₁₀O₁₂: 954.40

^{nat}Ga/^{nat}Lu-complexes of DOTA.SA.FAPi

The ^{nat}Ga-metallated species [^{nat}Ga]Ga-DOTA.SA.FAPi was obtained after treatment of DOTA.SA.FAPi (5.2 mg; 5.4 μmol) with stoichiometric amount (1 eq) of 10 mM ^{nat}Ga(NO₃)₂ in 1 mL 0.2 M AmAc buffer pH 4.5 shaken for 3 h at 80 °C. Complexation was confirmed by ESI-MS and HPLC-purification was performed (Phenomenex® Synergi® 10 μm (C18) 100 Å (250 mm × 10 mm, 10 μm), linear gradient of 5-95% MeCN (+0,1% TFA)/95-5% Water (+0,1% TFA) in 10 min. The product was obtained as yellowish powder (4.6 mg, 4.5 μmol; 83%). MS (ESI⁺): m/z (%): 1022.2 (M+H⁺), 1044.2 (M+Na); calculated for C₄₃H₅₃F₂GaN₁₁O₁₂: 1021.30

The ^{nat}Lu-metallated species [^{nat}Lu]Lu-DOTA.SA.FAPi was obtained after treatment of DOTA.SA.FAPi (6.0 mg; 6.3 μmol) with stoichiometric amount (1eq) of 1mM ^{nat}LuCl₃ in 1 mL 0.2 M AmAc buffer pH 4.5 shaken for 3 h at 80 °C. Complexation was confirmed by ESI-MS and HPLC purification was done analogously to the gallium species. The product was obtained as yellowish powder (5.5 mg, 4.9 μmol; 77%). MS (ESI⁺): m/z (%): 1028.3 (M+H⁺), 1051.2 (M+Na); calculated for C₄₃H₅₂F₂LuN₁₁O₁₂: 1027.32

^{nat}Ga-complexes of DATA^{5m}.SA.FAPi

The ^{nat}Ga-metallated species [^{nat}Ga]Ga-DATA^{5m}.SA.FAPi was obtained after treatment of DATA^{5m}.SA.FAPi (7.2 mg; 7.5 μmol) with stoichiometric amount of ^{nat}Ga(NO₃)₂ in 1 mL 0.2 M AmAc buffer pH 4.5 shaken for 2 h at 25 °C. Complexation was confirmed by ESI-MS and HPLC-purification was performed (Phenomenex® Luna® 10 μm (C18) 100 Å (250 mm × 10 mm, 10 μm), linear gradient of 5-95% MeCN (+0,1% TFA)/95-5% Water (+0,1% TFA) in 10 min. The product was obtained as yellowish powder (4.4 mg, 4.3 μmol; 57%). MS (ESI⁺): m/z (%): 1021.3 (M+H⁺), 1043.2 (M+Na); calculated for C₄₄H₅₃F₂GaN₁₀O₁₂: 1020.31

Inhibitory potency determination

Enzymes: A gateway-entry clone for human FAP was purchased from Dharmacon (Accession number DQ891423) and the human secretion signal was replaced with the HoneyBee mellitin secretion signal. For transfection and expression of FAP in Sf9 insect cells, the C-terminal BaculoDirect kit from LifeTechnologies was used. The enzyme was purified from the supernatant of the insect cells using immobilized Ni-chelating chromatography (GE healthcare, Diegem, Belgium), followed by anion-exchange chromatography using a 1 mL HiTrap Q (GE healthcare, Diegem, Belgium). Human recombinant PREP was expressed in BL21(DE3) cells and purified using immobilized Co-chelating

chromatography (GE healthcare) followed by anion-exchange chromatography on a 1 ml Mono Q column (GE healthcare).

FAP: IC₅₀ measurements of the inhibitors were carried out using Z-Gly-Pro-7-amino-4-methylcoumarine (AMC) (Bachem, Switzerland) as the substrate at a concentration of 50 μM at pH 8 (0.05 M Tris-HCl buffer with 0.1% glycerol, 1 mg/mL BSA and 140 mM NaCl). Eight concentrations of inhibitors were tested. The final DMSO concentration was kept constant during the experiment to exclude any solvent effects. Inhibitors were pre-incubated with the enzyme for 15 minutes at 37 °C, afterwards the substrate was added and the velocities of AMC release were measured kinetically at λ_{ex}= 380 nm, λ_{em}= 465 nm for at least 10 minutes at 37 °C. The Infinite 200 (Tecan Group Ltd.) micro-titer plate reader and the Magellan software were used for measurement and data processing respectively.

Note: a slightly different protocol, involving a different FAP substrate (Ala-Pro-pNA), was used to determine the originally published FAP IC₅₀-value for reference UAMC1110 (3.2 +/- 0.4 nM). This accounts for the non-identical value published here.

PREP: IC₅₀ measurements of the inhibitors were carried out using *N*-succinyl-Gly-Pro-AMC (Bachem, Switzerland) as the substrate at a concentration of 250 μM at pH 7.4 (0.1 M K-phosphate, 1 mM EDTA, 1 mM DTT). Eight concentrations of inhibitors were tested. The final DMSO concentration is kept constant during the experiment to exclude any effects. Inhibitors were pre-incubated with the enzyme for 15 minutes at 37 °C, afterwards the substrate was added and the velocities of AMC release were measured kinetically at λ_{ex}= 380 nm, λ_{em}= 465 nm for at least 10 minutes at 37 °C. The Infinite 200 (Tecan Group Ltd.) micro-titer plate reader and the Magellan software were used for measurement and data processing, respectively.

The data were fitted using a non-linear fit model in GraFit 7 software, according to the following equation:

$$y = \frac{range}{1 + \left(\frac{x}{IC_{50}}\right)^s}$$

where y is the value of the residual enzymatic activity compared to a non-inhibited sample, x is the final inhibitor concentration in the assay, s is the slope factor and the IC₅₀ is the half maximal inhibitory concentration.

Radiolabeling and stability studies with gallium-68

Gallium-68 was obtained manually utilizing ethanol-based post-processing from a $^{68}\text{Ge}/^{68}\text{Ga}$ -generator (ITG Garching, Germany). Elution process was performed following the protocol established by Eppard et al. [46]. After elution of gallium through the generator with a 0.05 M HCl (5 mL) solution gallium-68 was distributed on the microchromatography CEX column AG 50W-X4. The column was washed with 1 mL 80% EtOH/ 0.15 M HCl and the Ga(III) was eluted from the column with 400 μL 90% EtOH/0.9 M HCl. The washing step ensures that unwanted chemical and radiochemical impurities are separated and only $^{68}\text{Ga}^{3+}$ remains on the column.

Reaction controls for radiochemical purity were executed using radio-TLC (TLC Silica gel 60 F₂₅₄ Merck) with citrate buffer pH 4 and radio-HPLC using an analytical HPLC 7000 series Hitachi LaChrom with a Phenomenex (Aschaffenburg, Germany) Luna C18 column (250 x 4.6 mm, 5 μm), linear gradient of 5-95% MeCN (+0,1% TFA)/ 95-5% Water (+0,1% TFA) in 10 min). TLC's were measured in TLC imager CR-35 Bio Test-Imager from Duerr-ndt (Bietigheim-Bissingen, Germany) with the analysis software AIDA Elysia-Raytest (Straubenhardt, Germany). The citrate TLCs show free radio metal with a R_f value of 0.8–0.9. The labeled complexes are observed at a R_f value of 0.1–0.2.

Gallium-68 stability studies against transmetallation (Fe, Cu, Ca, Mg), transchelation (EDTA, DTPA) as well as in HS, EtOH and saline (0.9% isotone NaCl-solution) were performed. 50 μL of the [^{68}Ga]Ga-DOTA.SA.FAPI labeling solution with > 95% radiochemical purity were added to 1 mL of the respective media. The measured time points for gallium-68 were 15, 30, 45, 60, 90, 120 min. HS (human male AB plasma, USA origin) was bought from Sigma Aldrich, PBS was purchased from Sigma Aldrich and 0.9% saline from B. Braun Melsungen AG (Melsungen, Germany).

***In vivo* animal studies and *ex vivo* biodistributions**

After quantitative radiolabeling of [^{68}Ga]Ga-DOTA.SA.FAPI with a tracer amount of 20 nmol at 95 °C in 20 min. the solution was purified via C-18 column (Sep-Pak Light C18, Waters Corporation, Massachusetts, USA). Conditioning of the SPE was performed using 5 ml abs. ethanol and 5 mL water. Crude reaction mixture was pressed over the SPE and then washed with 5 ml water. Afterwards, the gallium-68 labeled product was eluted with 1 mL of 50 vol% ethanol. Finally, the ethanol was evaporated and the tracer was reformulated in 5 % ethanol in saline solution (500 μL total volume). The radiochemical purity was > 99% and no traces of free gallium could be detected by radio-TLC analysis (mobile phase: citrate buffer pH 4.0) and RP-HPLC (5-95% MeCN (+0,1% TFA)/95-5% Water (+0,1% TFA) in 10 min). The activity after purification process was 200 ± 10 MBq (10 GBq/ μmol) with a total RCY of 56%.

In vivo tumor model: HT-29 (human colon adenocarcinoma, ATCC, Rockville, Maryland) cells were routinely cultured in Dulbecco's Modified Eagle Medium supplemented with 10% heat inactivated foetal bovine serum (FBS), 2 mM glutamine, 1% sodium pyruvate and 1% penicillin/streptomycin (Gibco, Life technologies). After detaching the cells, the number of viable cells was counted with the automated Muse™ Cell Analyzer (Merck Millipore). For the HT-29 subcutaneous model, 10×10^6 viable cells, suspended in 100 μ l PBS, were inoculated in the right hind leg of female 6-week-old CD1^{-/-} Foxn1nu mice (n=3), obtained from Charles River Laboratories (L'Arbresle, France). The animals were kept under environmentally controlled conditions (12 h light/dark cycle, 20–24°C and 40–70% relative humidity) with food and water ad libitum. When tumors reached an approximate volume of 400 mm³, 3 mice underwent μ PET imaging. All experimental procedures and protocols were performed in accordance with European Directive 86/609/EEC Welfare and Treatment of Animals and were approved by the local ethical commission (2017-070, University of Antwerp, Belgium).

Micro-PET imaging: Micro-PET scans were carried out using an Inveon small-animal PET/CT scanner (Siemens), after i.v. injection of 4 nmol of [⁶⁸Ga]-DOTA.SA.FAPi (8.6 MBq, molar activity of 2.1 GBq/ μ mol) into tumor bearing mice (n=3), under isoflurane anesthesia (5% for induction, 2% for maintenance). Static whole-body PET images were acquired 60 min after injection of the radiotracer. Following each PET acquisition, a whole-body CT scan was acquired to obtain the animal's anatomical information individually.

For quantitative analysis, PET data were reconstructed using 3-dimensional ordered subset expectation maximization (OSEM3D, 16 subsets and 2 iterations) and 18 maximum a posteriori (MAP) iterations including scatter and attenuation correction (matrix size, 128 \times 128 \times 159; voxel size, 0.776 \times 0.776 \times 0.776 mm). Volumes of interest (VOIs) were manually drawn on the PET/CT images using PMOD (version 3.6; PMOD Technologies) to delineate the tumor, heart and muscle.

Ex vivo biodistribution: Immediately after the CT scans, the animals were sacrificed, the blood, tissues and organs were collected, weighed and the radioactivity was measured using an automatic γ -counter (Wizard² 2480, PerkinElmer). Values were expressed as percentage of the injected dose per gram (%ID/g).

List of abbreviations

DATA: 2,2'-(6-((carboxymethyl)amino)-1,4-diazepane-1,4-diyl)diacetic acid); DATA^{5m}-3^tBu: 5-[1,4-bis tertbutoxycarbonylmethyl-6-(tert-butoxycarbonylmethyl-methyl-amino)-[1,4]diazepan-6-yl]-pentanoic acid; DOTA: 1,4,7,10-Tetraazacyclododecane-1,4,7,10-tetraacetic acid; DTPA: cyclohexyldiethylene-triaminepentaacetic acid; EDTA: ethylenediaminetetraacetic acid; FAP: fibroblast activation protein; PREP: prolyl endopeptidase; DPP: dipeptidyl peptidase; CAF: cancer associated fibroblast; IC₅₀: Half-maximal inhibitory concentration; MIP: maximum intensity projection; PET: positron emission tomography; CT: computed tomography; Boc: *tert*-Butyloxycarbonyl; ^tBu: *tert*-Butyl; ESI: electrospray ionization; HS: human serum; HPLC: high-performance liquid chromatography; LC: liquid chromatography; MS: mass spectrometry; AmAc: ammonium acetate; NaAc: natrium acetate; NMR: nuclear magnetic resonance; PBS: phosphate buffered saline; RCY: radiochemical yield; RT: room temperature; SA: squaric acid; SADE: squaric acid diethyl ester; TLC: thin layer chromatography; AMC: Z-Gly-Pro-7-amino-4-methylcoumarine; FBS: foetal bovine serum; p.i.: post injection.

Declarations

Ethics approval and consent to participate: All experimental procedures and protocols were performed in accordance with European Directive 86/609/EEC Welfare and Treatment of Animals and were approved by the local ethical commission (2017-070, University of Antwerp, Belgium).

Consent for publication: Not applicable.

Availability of data and materials: Data sharing is not applicable to this article as no datasets were generated. Please contact authors for data request.

Competing interests: The authors declare that they have no competing interests.

Funding: No specific funding was received.

Authors contribution: EM carried out the preparative organic and radiochemical synthesis and evaluations, chemical separations, and analytics. Additionally, EM wrote the manuscript. ■ carried out the *in vitro* inhibitory studies and ■ is responsible for the expression of FAP and PREP. ■ and EM carried out the labeling for *in vivo* studies and ■ was responsible for analysis of the *in vivo* and *ex vivo* data. ■ was responsible for the tumor model and has carried out the animal handling and ■ was also involved in the organ/tumor manipulation during the biodistribution determination. ■ helped with radiochemical evaluation and ■ with organic synthesis. ■ and ■ directed the *in vitro* inhibitory and *in vivo/ex vivo* studies in Antwerp. ■ supervised the whole project. All authors read and approved the manuscript.

Acknowledgements: The authors thank the employees and technicians of the nuclear medicine (UZA) and the animal PET-team of the Molecular Imaging Center Antwerp (MICA). ■ is supported by the GOA BOF 2015 grant (No. 30729) of the University of Antwerp. Especially thanks to ■ (MICA) for the *in vivo* measurements, ■ and ■ (UZA) for helping with ⁶⁸Ga-elution for the *in vivo* studies.

References

1. Brennen, W.N.; Isaacs, J.T.; Denmeade, S.R. Rationale behind targeting fibroblast activation protein-expressing carcinoma-associated fibroblasts as a novel chemotherapeutic strategy. *Mol. Cancer Ther.* **2012**, *11*, 257–266, doi:10.1158/1535-7163.MCT-11-0340.
2. Dvořáková, P.; Bušek, P.; Knedlík, T.; Schimer, J.; Etrych, T.; Kostka, L.; Stollinová Šromová, L.; Šubr, V.; Šácha, P.; Šedo, A.; et al. Inhibitor-Decorated Polymer Conjugates Targeting Fibroblast Activation Protein. *J. Med. Chem.* **2017**, *60*, 8385–8393, doi:10.1021/acs.jmedchem.7b00767.
3. Aertgeerts, K.; Levin, I.; Shi, L.; Snell, G.P.; Jennings, A.; Prasad, G.S.; Zhang, Y.; Kraus, M.L.; Salakian, S.; Sridhar, V.; et al. Structural and kinetic analysis of the substrate specificity of human fibroblast activation protein α . *J. Biol. Chem.* **2005**, *280*, 19441–19444, doi:10.1074/jbc.C5000-92200.
4. Levy, M.T.; McCaughan, G.W.; Abbott, C.A.; Park, J.E.; Cunningham, A.M.; Muller, E.; Rettig, W.J.; Gorrell, M.D. Fibroblast activation protein: A cell surface dipeptidyl peptidase and gelatinase expressed by stellate cells at the tissue remodelling interface in human cirrhosis. *Hepatology* **1999**, *29*, 1768–1778, doi:10.1002/hep.510290631.
5. Park, J.E.; Lenter, M.C.; Zimmermann, R.N.; Garin-Chesa, P.; Old, L.J.; Rettig, W.J. Fibroblast activation protein, a dual specificity serine protease expressed in reactive human tumor stromal fibroblasts. *J. Biol. Chem.* **1999**, *274*, 36505–36512, doi:10.1074/jbc.274.51.36505.
6. Edosada, C.Y.; Quan, C.; Wiesmann, C.; Tran, T.; Sutherlin, D.; Reynolds, M.; Elliott, J.M.; Raab, H.; Fairbrother, W.; Wolf, B.B. Selective inhibition of fibroblast activation protein protease based on dipeptide substrate specificity. *J. Biol. Chem.* **2006**, *281*, 7437–7444, doi:10.1074/jbc.M511112200.
7. Bracke, A.; Van Elzen, R.; Van Der Veken, P.; Augustyns, K.; De Meester, I.; Lambeir, A.M. The development and validation of a combined kinetic fluorometric activity assay for fibroblast activation protein alpha and prolyl oligopeptidase in plasma. *Clin. Chim. Acta* **2019**, *495*, 154–160, doi:10.1016/j.cca.2019.04.063.
8. Hamson, E.J.; Keane, F.M.; Tholen, S.; Schilling, O.; Gorrell, M.D. Understanding fibroblast activation protein (FAP): Substrates, activities, expression and targeting for cancer therapy. *Proteomics - Clin. Appl.* **2014**, *8*, 454–463, doi:10.1002/prca.201300095.
9. Liu, R.; Li, H.; Liu, L.; Yu, J.; Ren, X. Fibroblast activation protein: A potential therapeutic target in cancer. *Cancer Biol. Ther.* **2012**, *13*, 123–129, doi:10.4161/cbt.13.3.18696.
10. Chen, X.; Song, E. Turning foes to friends: targeting cancer-associated fibroblasts. *Nat. Rev. Drug Discov.* **2019**, *18*, 99–115, doi:10.1038/s41573-018-0004-1.
11. Jiang, G.-M.; Xu, W.; Du, J.; Zhang, K.-S.; Zhang, Q.-G.; Wang, X.-W.; Liu, Z.-G.; Liu, S.-Q.; Xie, W.-Y.; Liu, H.-F.; et al. The application of the fibroblast activation protein alpha-targeted immunotherapy strategy. *Oncotarget* **2016**, *7*, 33472–33482, doi:10.18632/oncotarget.8098.
12. Liu, T.; Zhou, L.; Li, D.; Andl, T.; Zhang, Y. Cancer-associated fibroblasts build and secure the tumor microenvironment. *Front. Cell Dev. Biol.* **2019**, *7*, 1–14, doi:10.3389/fcell.2019.00060.
13. Zi, F.; He, J.; He, D.; Li, Y.; Yang, L.; Cai, Z. Fibroblast activation protein α in tumor microenvironment: Recent progression and implications (Review). *Mol. Med. Rep.* **2015**, *11*, 3203–3211, doi:10.3892/mmr.2015.3197.

14. De Vlieghere, E.; Verset, L.; Demetter, P.; Bracke, M.; De Wever, O. Cancer-associated fibroblasts as target and tool in cancer therapeutics and diagnostics. *Virchows Arch.* **2015**, *467*, 367–382, doi:10.1007/s00428-015-1818-4.
15. Tao, L.; Huang, G.; Song, H.; Chen, Y.; Chen, L. Cancer associated fibroblasts: An essential role in the tumor microenvironment (review). *Oncol. Lett.* **2017**, *14*, 2611–2620, doi:10.3892/ol.2017.6497.
16. Busek, P.; Mateu, R.; Zubal, M.; Kotackova, L.; Sedo, A. Targeting Fibroblast activation protein in cancer - Prospects and caveats. *Front. Biosci. - Landmark* **2018**, *23*, 1933–1968, doi:10.2741/4682.
17. Scanlan, M.J.; Raj, B.K.M.; Calvo, B.; Garin-Chesa, P.; Sanz-Moncasi, M.P.; Healey, J.H.; Old, L.J.; Rettig, W.J. Molecular cloning of fibroblast activation protein α , a member of the serine protease family selectively expressed in stromal fibroblasts of epithelial cancers. *Proc. Natl. Acad. Sci. U. S. A.* **1994**, *91*, 5657–5661, doi:10.1073/pnas.91.12.5657.
18. Poplawski, S.E.; Lai, J.H.; Li, Y.; Jin, Z.; Liu, Y.; Wu, W.; Wu, Y.; Zhou, Y.; Sudmeier, J.L.; Sanford, D.G.; et al. Identification of selective and potent inhibitors of fibroblast activation protein and prolyl oligopeptidase. *J. Med. Chem.* **2013**, *56*, 3467–3477, doi:10.1021/jm400351a.
19. Connolly, B.A.; Sanford, D.G.; Chiluwal, A.K.; Healey, S.E.; Peters, D.E.; Dimare, M.T.; Wu, W.; Liu, Y.; Maw, H.; Zhou, Y.; et al. Dipeptide boronic acid inhibitors of dipeptidyl peptidase IV: Determinants of potency and in vivo efficacy and safety. *J. Med. Chem.* **2008**, *51*, 6005–6013, doi:10.1021/jm800390n.
20. Jansen, K.; De Winter, H.; Heirbaut, L.; Cheng, J.D.; Joossens, J.; Lambeir, A.M.; De Meester, I.; Augustyns, K.; Van Der Veken, P. Selective inhibitors of fibroblast activation protein (FAP) with a xanthine scaffold. *Medchemcomm* **2014**, *5*, 1700–1707, doi:10.1039/c4md00167b.
21. Jansen, K.; Heirbaut, L.; Verkerk, R.; Cheng, J.D.; Joossens, J.; Cos, P.; Maes, L.; Lambeir, A.M.; De Meester, I.; Augustyns, K.; et al. Extended structure-activity relationship and pharmacokinetic investigation of (4-quinolinoyl)glycyl-2-cyanopyrrolidine inhibitors of fibroblast activation protein (FAP). *J. Med. Chem.* **2014**, *57*, 3053–3074, doi:10.1021/jm500031w.
22. De Decker, A.; Vliegen, G.; Van Rompaey, D.; Peeraer, A.; Bracke, A.; Verckist, L.; Jansen, K.; Geiss-Friedlander, R.; Augustyns, K.; De Winter, H.; et al. Novel Small Molecule-Derived, Highly Selective Substrates for Fibroblast Activation Protein (FAP). *ACS Med. Chem. Lett.* **2019**, *10*, 1173–1179, doi:10.1021/acsmchemlett.9b00191.
23. Yang, X.; Nimmagadda, S.; Rowe, S.; Slania, S.; Pomper, M.G. Imaging and Radiotherapeutics Agents Targeting Fibroblast-Activation Protein-Alpha (FAP-Alpha). Patent US/2020/0237936 A1, **2020**.
24. Loktev, A.; Lindner, T.; Mier, W.; Debus, J.; Altmann, A.; Jaeger, D.; Giesel, F.; Kratochwil, C.; Barthe, P.; Roumestand, C.; et al. A Tumor-Imaging Method Targeting Cancer-Associated Fibroblasts. *J. Nucl. Med.* **2018**, *59*, 1423–1429, doi:10.2967/jnumed.118.210435.
25. Lindner, T.; Loktev, A.; Altmann, A.; Giesel, F.; Kratochwil, C.; Debus, J.; Jäger, D.; Mier, W.; Haberkorn, U. Development of Quinoline-Based Theranostic Ligands for the Targeting of Fibroblast Activation Protein. *J. Nucl. Med.* **2018**, *59*, 1415–1422, doi:10.2967/jnu-med.118.210443.
26. Loktev, A.; Lindner, T.; Burger, E.M.; Altmann, A.; Giesel, F.; Kratochwil, C.; Debus, J.; Marmé, F.; Jäger, D.; Mier, W.; et al. Development of fibroblast activation protein-targeted radiotracers with improved tumor retention. *J. Nucl. Med.* **2019**, *60*, 1421–1429, doi:10.2967/jnu-

med.118.224469.

27. Giesel, F.L.; Kratochwil, C.; Lindner, T.; Marschalek, M.M.; Loktev, A.; Lehnert, W.; Debus, J.; Jäger, D.; Flechsig, P.; Altmann, A.; et al. ^{68}Ga -FAPI PET/CT: Biodistribution and preliminary dosimetry estimate of 2 DOTA-containing FAP-targeting agents in patients with various cancers. *J. Nucl. Med.* **2019**, *60*, 386–392, doi:10.2967/jnumed.118.215913.
28. Giesel, F.L.; Heussel, C.P.; Lindner, T.; Röhrich, M.; Rathke, H.; Kauczor, H.U.; Debus, J.; Haberkorn, U.; Kratochwil, C. FAPI-PET/CT improves staging in a lung cancer patient with cerebral metastasis. *Eur. J. Nucl. Med. Mol. Imaging* **2019**, *46*, 1754–1755, doi:10.1007/s00259-019-04346-z.
29. Kratochwil, C.; Flechsig, P.; Lindner, T.; Abderrahim, L.; Altmann, A.; Mier, W.; Adebeg, S.; Rathke, H.; Röhrich, M.; Winter, H.; et al. ^{68}Ga -FAPI PET/CT: Tracer uptake in 28 different kinds of cancer. *J. Nucl. Med.* **2019**, *60*, 801–805, doi:10.2967/jnumed.119.227967.
30. Wurm, F.R.; Klok, H.-A.A. Be squared: Expanding the horizon of squaric acid-mediated conjugations. *Chem. Soc. Rev.* **2013**, *42*, 8220–8236, doi:10.1039/c3cs60153f.
31. Ian Storer, R.; Aciro, C.; Jones, L.H. Squaramides: Physical properties, synthesis and applications. *Chem. Soc. Rev.* **2011**, *40*, 2330–2346, doi:10.1039/c0cs00200c.
32. Tietze, L.F.; Arlt, M.; Beller, M.; Glüsenkamp, K. -H; Jähde, E.; Rajewsky, M.F. Squaric Acid Diethyl Ester: A New Coupling Reagent for the Formation of Drug Biopolymer Conjugates. Synthesis of Squaric Acid Ester Amides and Diamides. *Chem. Ber.* **1991**, *124*, 1215–1221, doi:10.1002/cber.19911240539.
33. Yoganathan, S.; Sit, C.S.; Vederas, J.C. Chemical synthesis and biological evaluation of gallidermin-siderophore conjugates. *Org. Biomol. Chem.* **2011**, *9*, 2133–2141, doi:10.1039/c0ob00846j.
34. Rudd, S.E.; Roselt, P.; Cullinane, C.; Hicks, R.J.; Donnelly, P.S. A desferrioxamine B squaramide ester for the incorporation of zirconium-89 into antibodies. *Chem. Commun.* **2016**, *52*, 11889–11892, doi:10.1039/c6cc05961a.
35. Greifenstein, L.; Grus, T.; Nagel, J.; Sinnes, J.P.; Rösch, F. Synthesis and labeling of a squaric acid containing PSMA-inhibitor coupled to AAZTA⁵ for versatile labeling with ^{44}Sc , ^{64}Cu , ^{68}Ga and ^{177}Lu . *Appl. Radiat. Isot.* **2020**, *156*, 108867, doi:10.1016/j.apradiso.2019.108867.
36. Greifenstein, L.; Engelbogen, N.; Lahnif, H.; Sinnes, J.-P.; Bergmann, R.; Bachmann, M.; Rösch, F. Synthesis, labeling and preclinical evaluation of a squaric acid containing PSMA-inhibitor labeled with ^{68}Ga – a comparison with PSMA-11 and PSMA-617. *ChemMedChem* **2020**, *15*, 695–704, doi:10.1002/cmdc.201900559.
37. Price, E.W.; Orvig, C. Matching chelators to radiometals for radiopharmaceuticals. *Chem. Soc. Rev.* **2014**, *43*, 260–290, doi:10.1039/c3cs60304k.
38. Seemann, J.; Waldron, B.; Parker, D.; Roesch, F. DATATOC: a novel conjugate for kit-type ^{68}Ga labelling of TOC at ambient temperature. *EJNMMI Radiopharm. Chem.* **2017**, *1*, 4, doi:10.1186/s41181-016-0007-3.
39. Seemann, J.; Waldron, B.P.; Roesch, F.; Parker, D. Approaching “kit-type” labelling with ^{68}Ga : The DATA chelators. *ChemMedChem* **2015**, *10*, 1019–1026, doi:10.1002/cmdc.201500092.
40. Sinnes, J.P.; Nagel, J.; Waldron, B.P.; Maina, T.; Nock, B.A.; Bergmann, R.K.; Ullrich, M.; Pietzsch, J.; Bachmann, M.; Baum, R.P.; et al. Instant kit preparation of ^{68}Ga -radiopharmaceuticals via the hybrid chelator DATA: clinical translation of [^{68}Ga]Ga-DATA-TOC. *EJNMMI Res.* **2019**, *9*, 48, doi:10.1186/s13550-019-0516-7.

41. Quiñonero, D.; Frontera, A.; Ballester, P.; Deyà, P.M. A theoretical study of aromaticity in squaramide and oxocarbons. *Tetrahedron Lett.* **2000**, *41*, 2001–2005, doi:10.1016/S0040-4039(00)00084-8.
42. Henry, L.R.; Lee, H.O.; Lee, J.S.; Klein-Szanto, A.; Watts, P.; Ross, E.A.; Chen, W.T.; Cheng, J.D. Clinical implications of fibroblast activation protein in patients with colon cancer. *Clin. Cancer Res.* **2007**, *13*, 1736–1741, doi:10.1158/1078-0432.CCR-06-1746.
43. Cheng, J.D.; Dunbrack, R.L.; Valianou, M.; Rogatko, A.; Alpaugh, R.K.; Weiner, L.M. Promotion of tumor growth by murine fibroblast activation protein, a serine protease, in an animal model. *Cancer Res.* **2002**, *62*, 4767–4772.
44. Watabe, T.; Liu, Y.; Kaneda-Nakashima, K.; Shirakami, Y.; Lindner, T.; Ooe, K.; Toyoshima, A.; Nagata, K.; Shimosegawa, E.; Haberkorn, U.; et al. Theranostics Targeting Fibroblast Activation Protein in the Tumor Stroma: ⁶⁴Cu- and ²²⁵Ac-Labeled FAPI-04 in Pancreatic Cancer Xenograft Mouse Models. *J. Nucl. Med.* **2020**, *61*, 563–569, doi:10.2967/jnumed.119.233122.
45. Kreppel, B.; Gärtner, F.; Marinova, M.; Attenberger, U.; Meisenheimer, M.; Toma, M.; Kristiansen, G.; Feldmann, G.; Moon, E.; Roesch, F.; et al. [⁶⁸Ga]Ga-DATA^{5m}.SA .FAPI PET/CT : Specific Tracer-uptake in Focal Nodular Hyperplasia and potential Role in Liver Tumor Imaging. *Nuklearmedizin* **2020**, *59*, 387–389, doi: 10.1055/a-1164-5667.
46. Eppard, E.; Wuttke, M.; Nicodemus, P.L.; Rösch, F. Ethanol-based post-processing of generator-derived ⁶⁸Ga Toward kit-type preparation of ⁶⁸Ga-radiopharmaceuticals. *J. Nucl. Med.* **2014**, *55*, 1023–1028, doi:10.2967/jnumed.113.133041.

Supporting Information

Synthesis

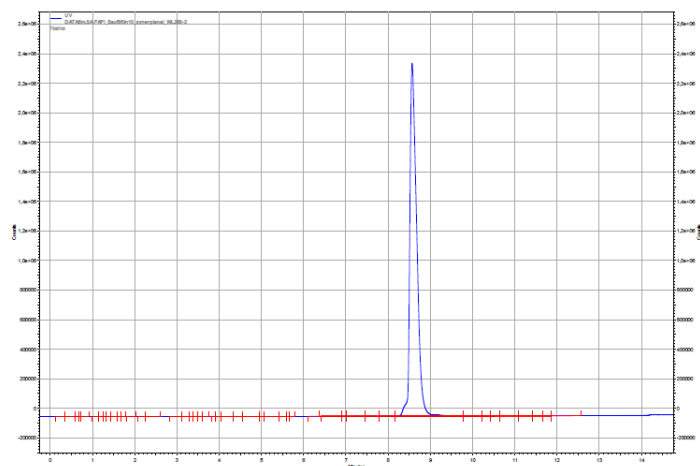


Fig. S1 HPLC spectra of DOTA.SA.FAPi with linear gradient condition of 5-95% MeCN (+0.1% TFA)/95-5% Water (+0.1% TFA) in 10 min, 1 mL/min, $t_R = 8.6$ min.

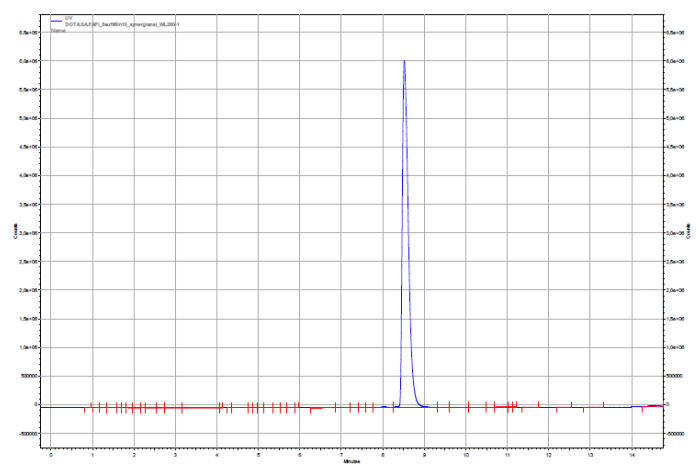


Fig. S2 HPLC spectra of DATA^{5m}.SA.FAPi with linear gradient condition of 5-95% MeCN (+0.1% TFA)/95-5% Water (+0.1% TFA) in 10 min, 1 mL/min, $t_R = 8.5$ min.

Radiolabeling

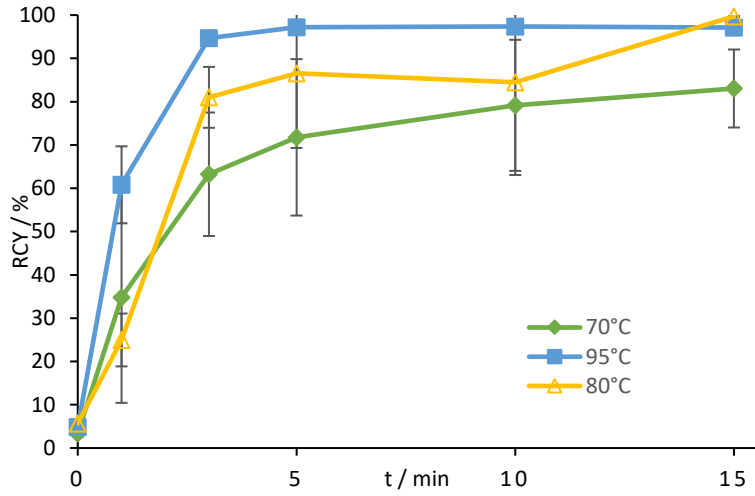


Fig. S3 radiolabeling kinetics at different temperatures of $[^{68}\text{Ga}]\text{Ga-DOTA.SA.FAPi}$ complex.

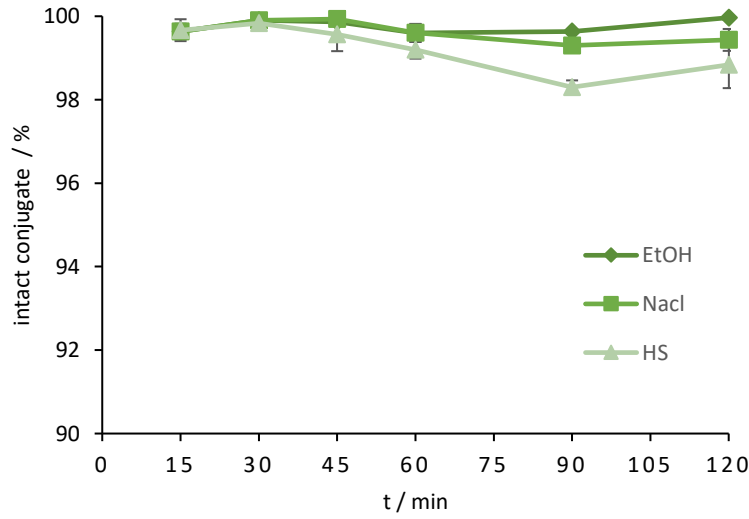


Fig. S4 Stability studies for $[^{68}\text{Ga}]\text{Ga-DOTA.SA.FAPi}$ complex in human serum, Ethanol and 0.9% isotone NaCl-solution in % of intact conjugate at different time points.

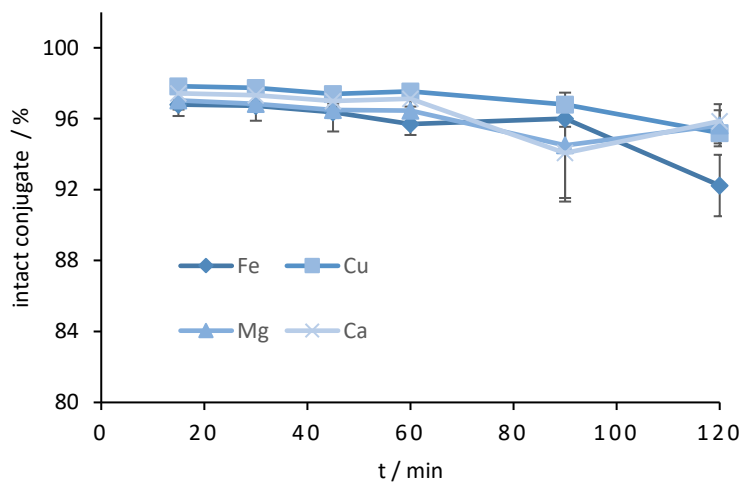


Fig. S5 Stability studies for $[^{68}\text{Ga}]\text{Ga-DOTA.SA.FAPI}$ complex against transmetallation (Fe, Cu, Mg and Ca) in % of intact conjugate at different time points.

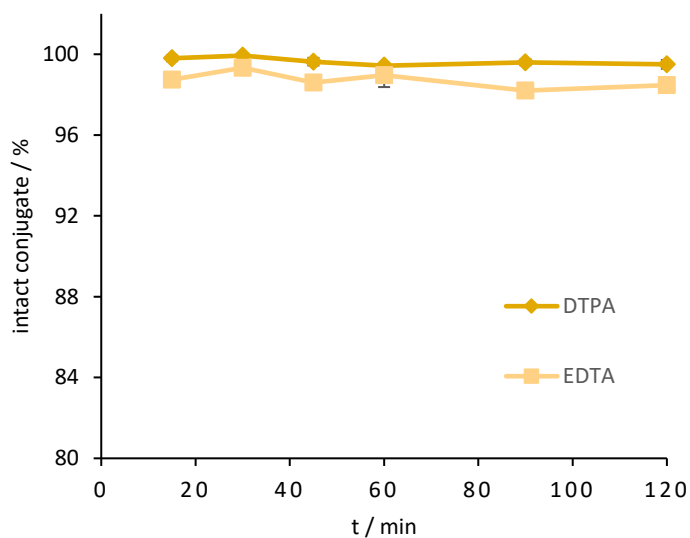


Fig. S6 Stability studies for $[^{68}\text{Ga}]\text{Ga-DOTA.SA.FAPI}$ complex against transchelation (DTPA and EDTA) in % of intact conjugate at different time points.

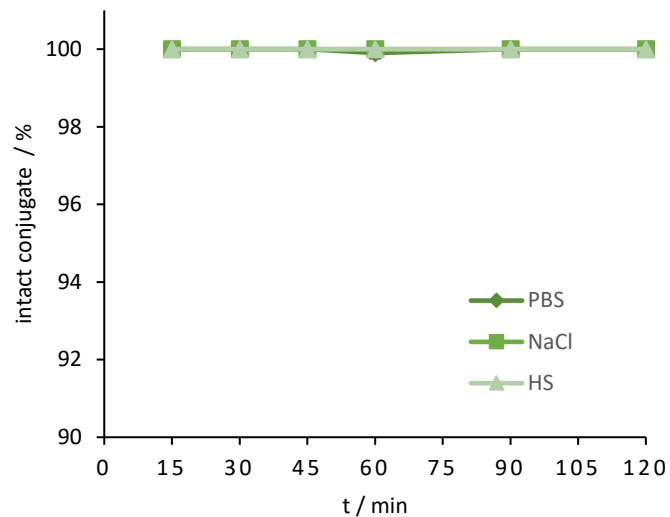


Fig. S7 Stability studies for $[^{68}\text{Ga}]\text{Ga-DOTA}^{5\text{m}}.\text{SA.FAPI}$ complex in HS, PBS and 0.9% isotone NaCl-solution in % of intact conjugate at different time points.

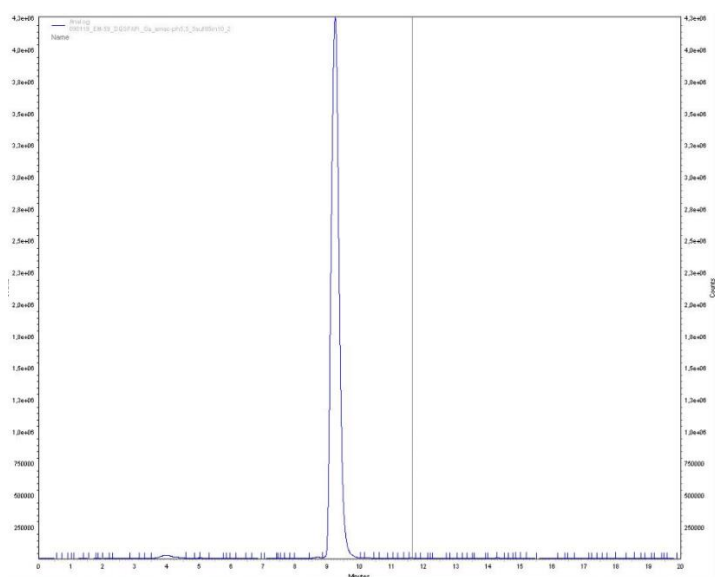


Fig. S8 radio-HPLC spectra of DOTA.SA.FAPI with linear gradient condition of 5-95% MeCN (+0.1% TFA)/95-5% Water (+0.1% TFA) in 8 min, 1 mL/min, $t_R = 9.1$ min.

Inhibition assays

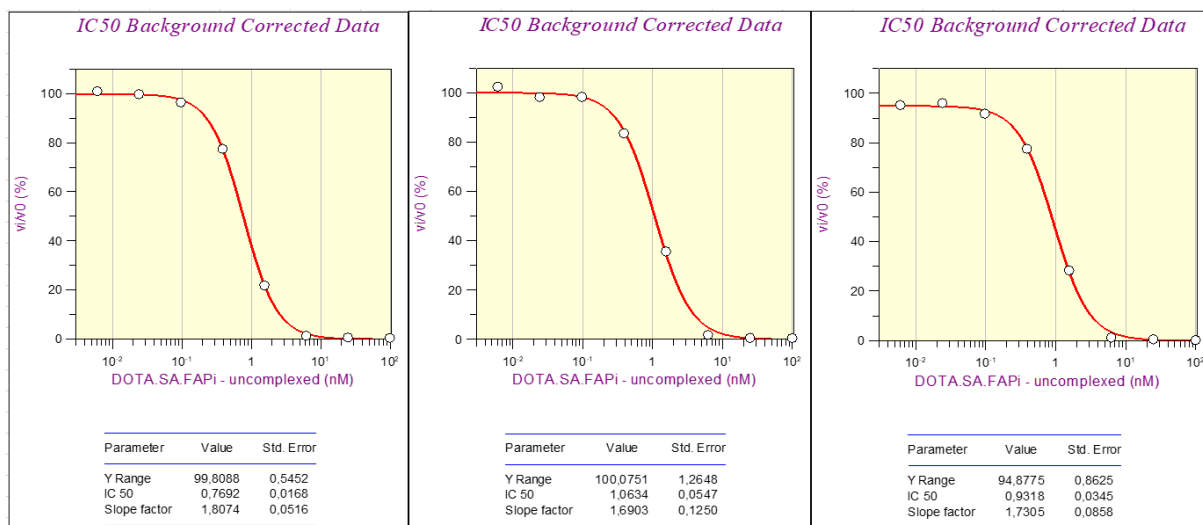


Fig. S9 Inhibition assay graph and calculated IC₅₀-data for DOTA.SA.FAPi (n=3) with regard to FAP.

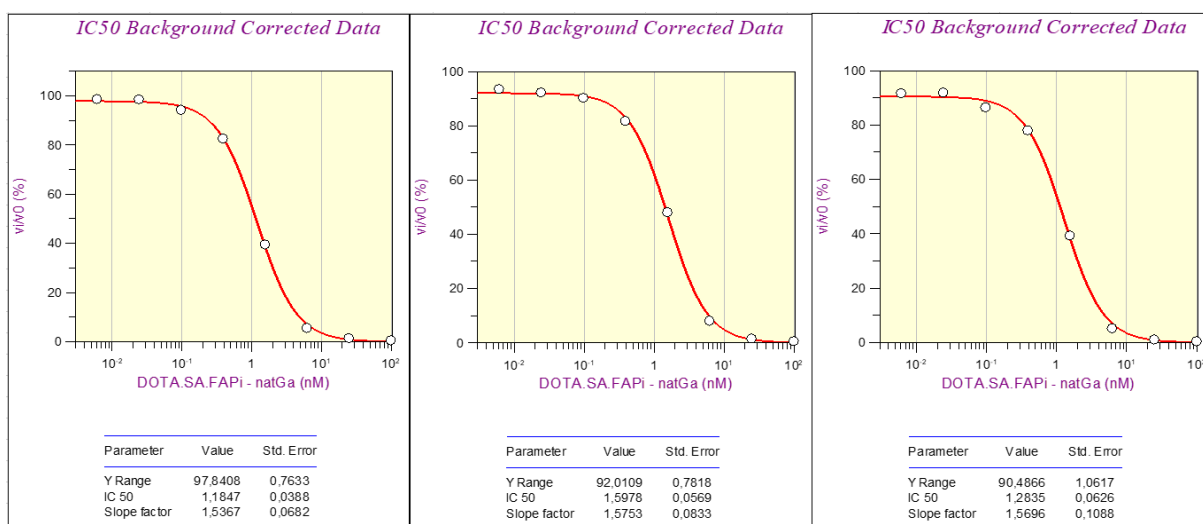


Fig. S10 Inhibition assay graph and calculated IC₅₀-data for ^{nat}Ga-DOTA.SA.FAPi (n=3) with regard to FAP.

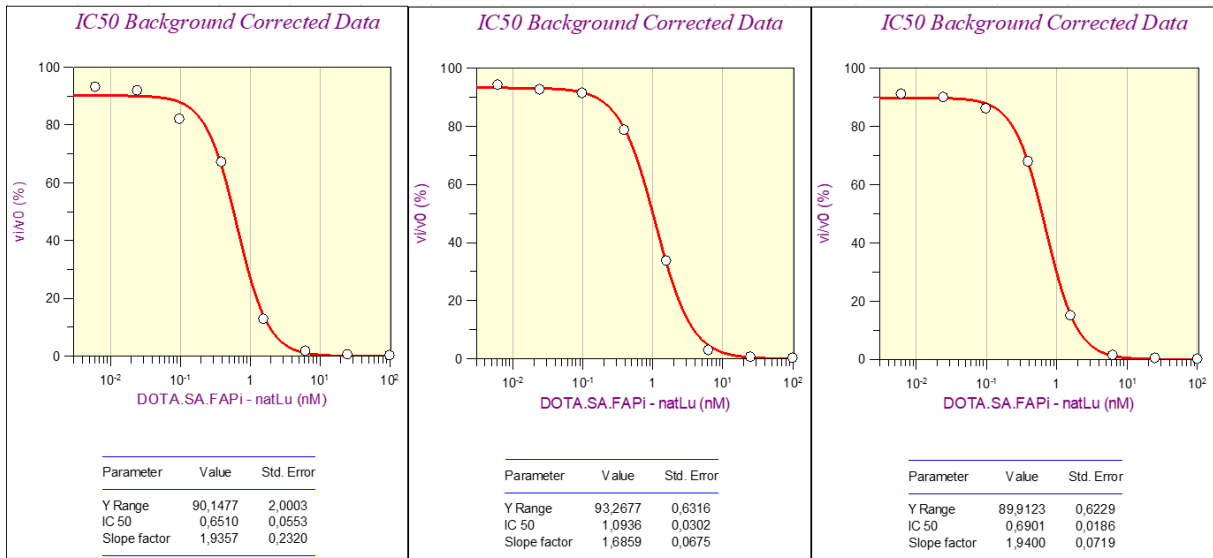


Fig. S11 Inhibition assay graph and calculated IC₅₀-data for ^{nat}Lu-DOTA.SA.FAPI (n=3) with regard to FAP.

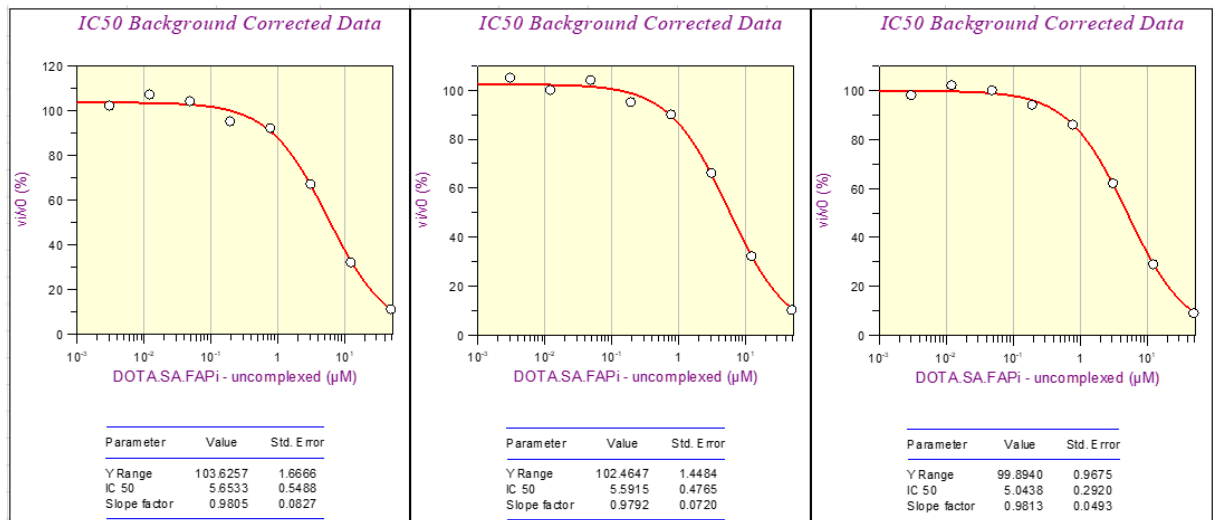


Fig. S12 Inhibition assay graph and calculated IC₅₀-data for DOTA.SA.FAPI (n=3) with regard to PREP.

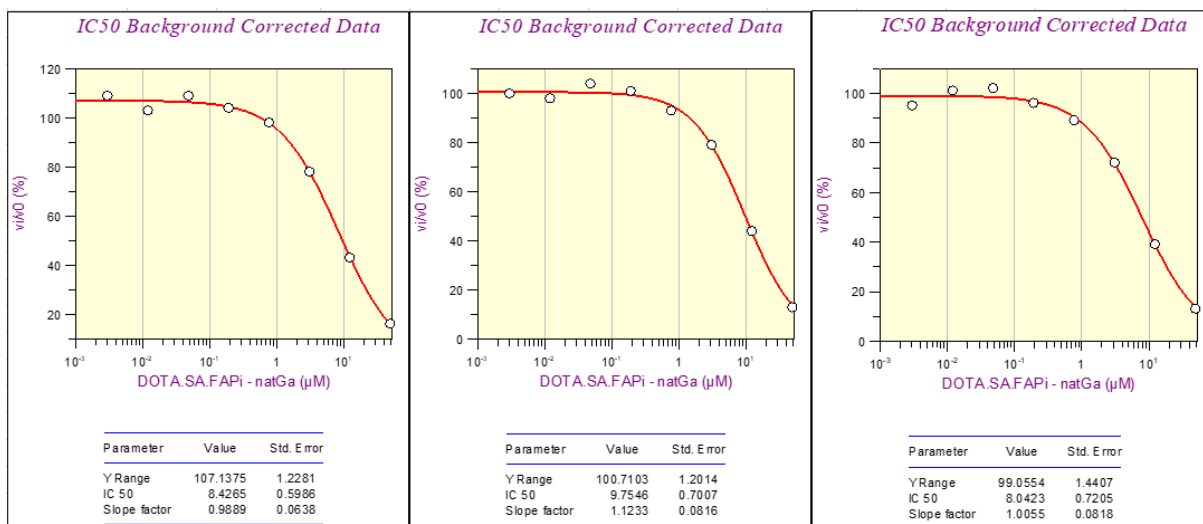


Fig. S13 Inhibition assay graph and calculated IC₅₀-data for ^{nat}Ga-DOTA.SA.FAPi (n=3) with regard to PREP.

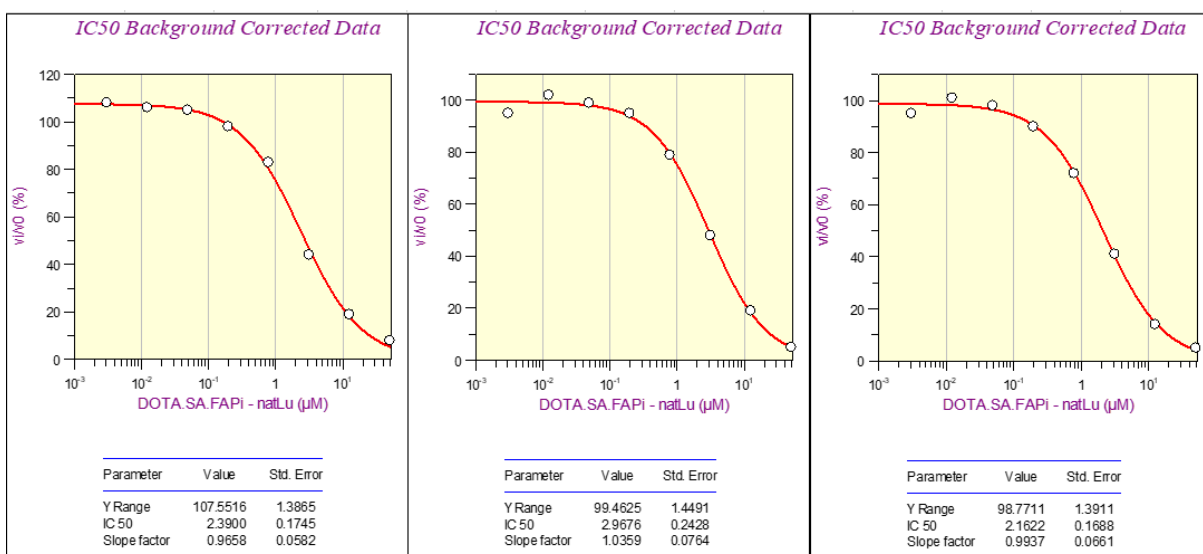


Fig. S14 Inhibition assay graph and calculated IC₅₀-data for ^{nat}Lu-DOTA.SA.FAPi (n=3) with regard to PREP.

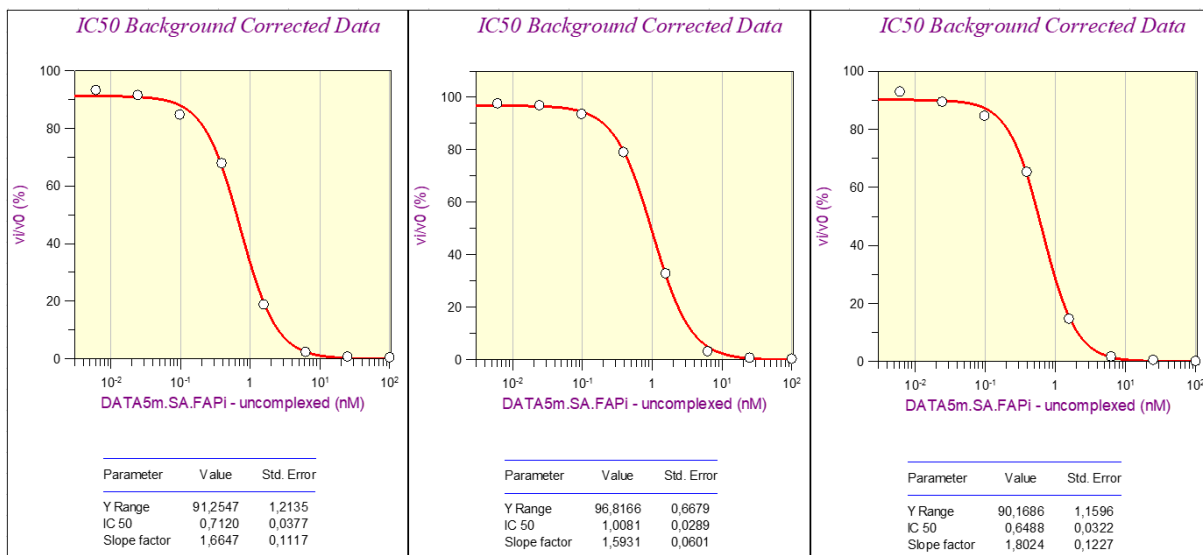


Fig. S15 Inhibition assay graph and calculated IC₅₀-data for DATA^{5m}.SA.FAPI (n=3) with regard to FAP.

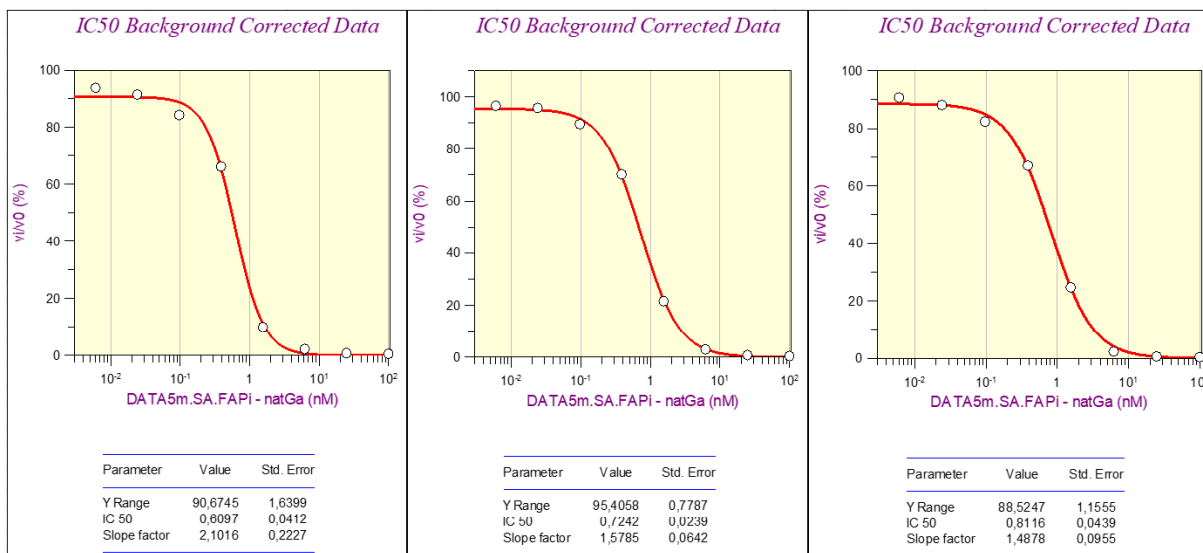


Fig. S16 Inhibition assay graph and calculated IC₅₀-data for ^{nat}Ga- DATA^{5m}.SA.FAPI (n=3) with regard to FAP.

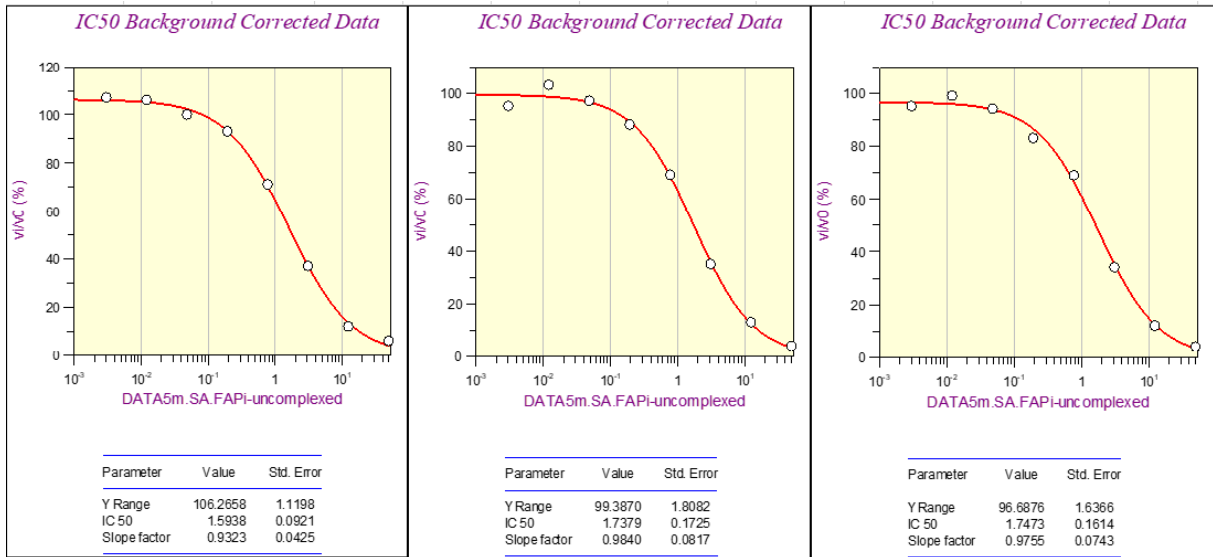


Fig. S17 Inhibition assay graph and calculated IC₅₀-data for DATA^{5m}.SA.FAPI (n=3) with regard to PREP.

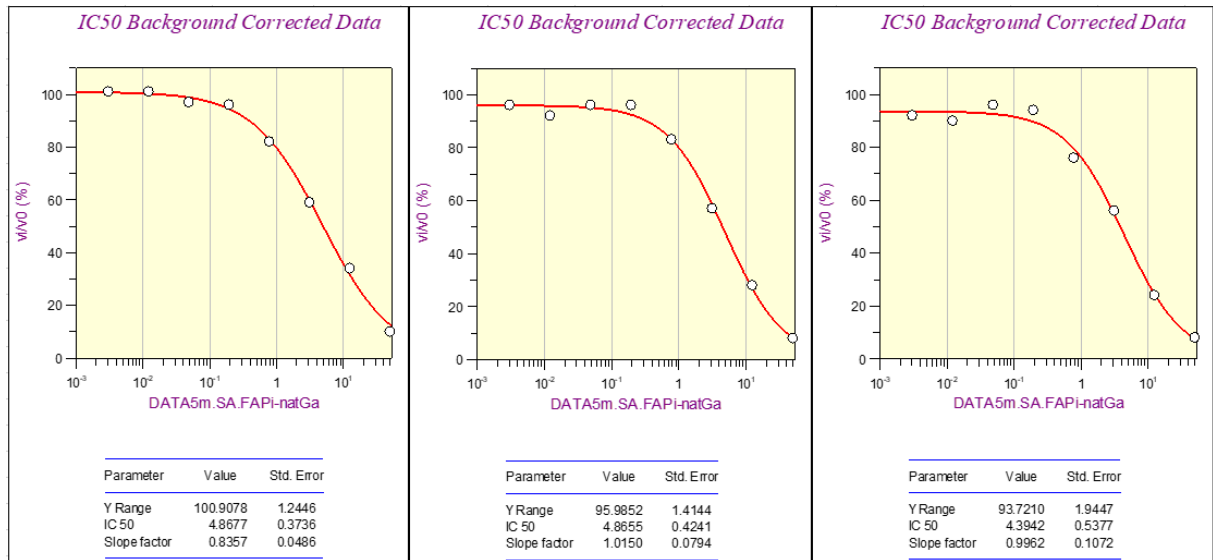


Fig. S18 Inhibition assay graph and calculated IC₅₀-data for natGa-DATA^{5m}.SA.FAPI (n=3) with regard to PREP.

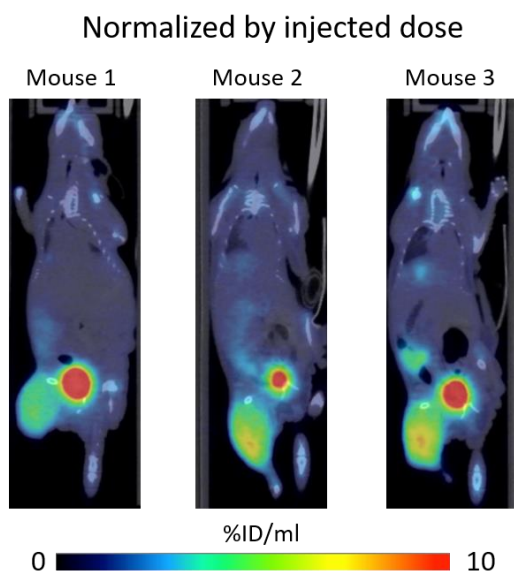


Fig. S19 [⁶⁸Ga]Ga-DOTA.SA.FAPi uptake in a HT-29 xenograft mouse model. Coronal 2D-fused PET/CT image (normalized by injected dose) 60 min after injection of [⁶⁸Ga]Ga-DOTA.SA.FAPi.

Ex vivo biodistribution

Tab. S1 Ex vivo biodistribution data of [⁶⁸Ga]Ga-DOTA.SA.FAPi at 1 h p.i. (N=3).

Ex vivo biodistribution (in %ID/g)		
Organ	Average	SD
Blood	0.56	0.06
Heart	0.22	0.01
Lungs	0.33	0.04
Liver	0.70	0.19
Spleen	0.23	0.03
Pancreas	0.51	0.13
Stomach	0.21	0.04
Small Intestine	1.81	0.49
Large Intestine	0.21	0.01
Kidneys	1.77	0.37
Bladder	0.96	0.10
Muscle	0.45	0.09
Fat	0.38	0.29
Bone	3.56	0.34
Skin	0.04	0.00
Brain	1.27	0.50
Tumor	5.20	0.21

A.1. [⁶⁸Ga]Ga-DATA^{5m}.SA.FAPi PET/CT: Specific Tracer-uptake in Focal Nodular Hyperplasia and potential Role in Liver Tumor Imaging

Veröffentlicht in *Nuklearmedizin* **2020**, 59, 387–389.

mit Genehmigung von © Thieme, Georg Thieme Verlag KG, Stuttgart

[⁶⁸Ga]Ga-DATA^{5m}.SA.FAPi PET/CT: Specific Tracer-uptake in Focal Nodular Hyperplasia and potential Role in Liver Tumor Imaging

[REDACTED]
[REDACTED] Euy Sung Moon⁵,
[REDACTED]

¹ Department of Nuclear Medicine, University Medical Center Bonn, Bonn, Germany

² Department of Radiology, University Medical Center Bonn, Bonn, Germany

³ Department of Pathology, University Medical Center Bonn, Bonn, Germany

⁴ Department of Internal Medicine III, University Medical Center Bonn, Bonn, Germany

⁵ Department of Chemistry, Johannes Gutenberg University, Mainz, Germany

⁶ Department of Pharmaceutical Sciences, Laboratory of Medical Biochemistry, University of Antwerp, Wilrijk, Belgium

*Corresponding author: [REDACTED]

Abstract

Fibroblast activating protein (FAP) is a membrane bound serine protease increased in activated fibroblasts occurring during tissue remodeling in benign and malignant diseases. Carcinoma-associated fibroblasts (CAF) contribute to the formation of tumor stroma promoting tumor growth, angiogenesis as well as immune-escape. Quinoline-based FAP-specific enzyme inhibitors (FAPis) labeled with ^{68}Ga were recently introduced as novel, highly effective PET-tracers for tumor imaging. Here we report about a thyroid carcinoma patient with increased Tg level without ^{131}I -positive lesions. A [^{68}Ga]Ga-DATA^{5m}.SA.FAPi-PET/CT was performed to detect resectable metastases. We found no metastases but a focal tracer-accumulation in the liver. Histology revealed that the tracer-accumulation corresponded to focal nodular hyperplasia expressing FAPi in fibrous septa. The case presented indicated that FAPi-PET helps to detect fibrous remodeling in benign and malignant tumors. This may be helpful especially in differential diagnosis of liver tumors.

Keywords: FAPi, PET/CT, fibroblast activating protein (FAP), focal nodular hyperplasia (FNH), metastasized thyroid carcinoma

Background

Fibroblast activating protein (FAP) is a membrane bound serine protease up-regulated in activated fibroblasts. These are essential for tissue remodeling in wound healing, chronic inflammation as well as in carcinoma associated fibroblasts (CAF) in several types of cancer [1,2,5,8,9,11]. Subject of recent developments are new ⁶⁸Ga-labelled PET tracers that operate as FAP-specific enzyme inhibitors (FAPi). The inhibitor is a small molecule based on a 4,4-difluoroproline-quinoline motif with a carbonitrile warhead that binds to FAP and blocks its chemical reaction. This highly potent inhibitor, referred to as UAMC 1110, combines high affinity respectively high inhibition ability to FAP and in opposite towards DPPs and PREP [6]. Various tumors and proliferating tissue show an uptake of this tracer. FAPi shows rapid washout from normal tissue facilitating high-contrast images. This is particularly advantageous as the sensitivity of FDG-PET is low in regions with high or inhomogenous glucose metabolism such as brain, heart or the liver [4]. Therefore, FAPi-PET may be superior to FDG-PET in these regions. The new class of FAPi-radiopharmaceuticals utilizes a squaric acid (SA) motif as part of the structure connecting the inhibitor moiety UAMC 1110 with various chelators such as DOTA and DATA, yielding precursors of type DOTA.SA.FAPi or DATA^{5m}.SA.FAPi. All compounds are of low nanomolar binding affinity to FAP and excellent selectivity towards other proteases [3].

Focal nodular hyperplasia (FNH) is the second most common benign liver tumor. The development is based on non-specific hyperplasia in response to a vascular transformation. In addition, an association with the intake of contraceptives containing estrogen is suspected. Diagnosis is usually based on sonography, contrast-enhanced CT or MRI. FNH is frequently an accidental finding. Therapy is usually not necessary. In difficult cases, however, a biopsy may also be necessary to rule out hepatocellular adenoma or carcinoma as well as metastases from extrahepatic tumors [7,10].

Case presentation

We report about a 44-year old female with thyroid carcinoma initially metastasized to the lung. The primary tumor was first diagnosed in 1998 and treated with surgery and 8 cycles of ^{131}I radiotherapy. As the tumormarker Tg was rising and ^{131}I whole body scans were negative, we decided to perform a ^{68}Ga]Ga-DATA^{5m}.SA.FAPi PET/CT for restaging to potentially find tumor manifestations accessible to resection.

In the present study we used the DATA^{5m}.SA.FAPi option because of its slightly better IC₅₀ values (0.7 nM for Ga-DATA^{5m}.SA.FAPi vs. 1.4 for Ga-DOTA.SA.FAPi) and because of its ease of preparation in an instant kit-type protocol. Radiolabeling of ^{68}Ga]Ga-DATA^{5m}.SA.FAPi (obtained from the Department of Chemistry, JGU Mainz, Germany) was carried out in 3.34 ± 0.04 mL 0.08 M ammonium acetate buffer (ABX advanced biochemical compounds GmbH, Radeberg, Germany) pH= 3.6, with ^{68}Ga obtained from a 1.85 GBq $^{68}\text{Ge}/^{68}\text{Ga}$ -generator. Manual synthesis was carried out in a thermo shaker at a temperature of 50 °C for 8 min. Radiochemical yield was $\geq 92\%$, radiochemical purity $\geq 97\%$.

The patient was intravenously administered with 210 MBq ^{68}Ga]Ga-FAPi. Whole body static imaging was performed 82 minutes p.i. with an acquisition time of 4 min per bed position using a Siemens Biograph 2 PET/CT machine.

PET/CT images did not show increased tracer-uptake in the neck region or in pulmonary lesions, but a focal tracer-enrichment in liver segment 8 corresponding to a faint hypodense lesion in native low-dose computed tomography (CT) (Figure 1). For further work-up, a MRI scan was performed and a CT-guided biopsy was taken. MRI shows a typical pattern of FNH (Figure 2). Histopathological examination using microscopy and immunohistochemistry (FAP, glutamin synthetase and cytokeratin 7) showed evidence of FNH. The sections stained positive for FAP in immunohistochemistry (Figure 3).

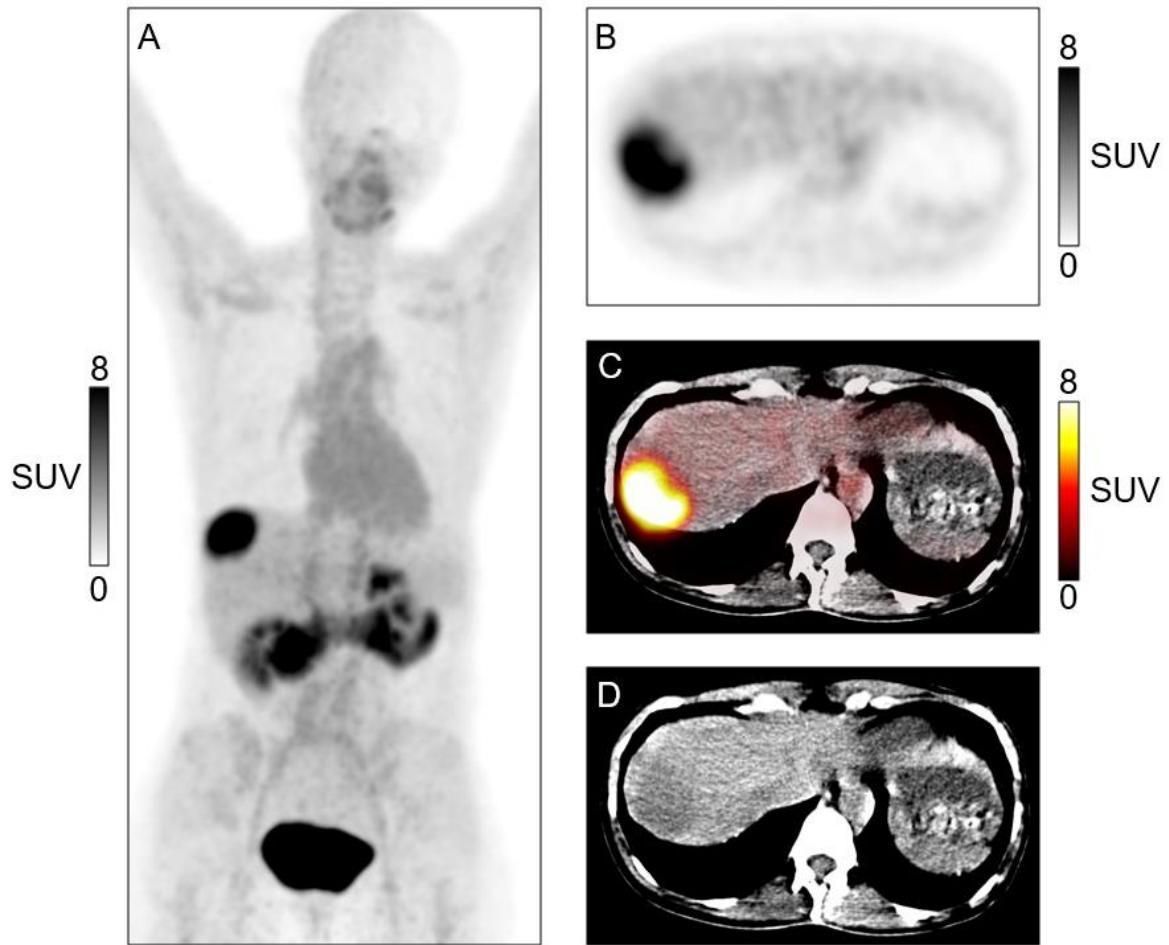


Fig. 1 FAPI-PET/CT. Intensive tracer uptake in liver segment 8 (SUVmax 9,4). In low-dose CT-technique without contrast medium there is only a faint hypodense lesion.

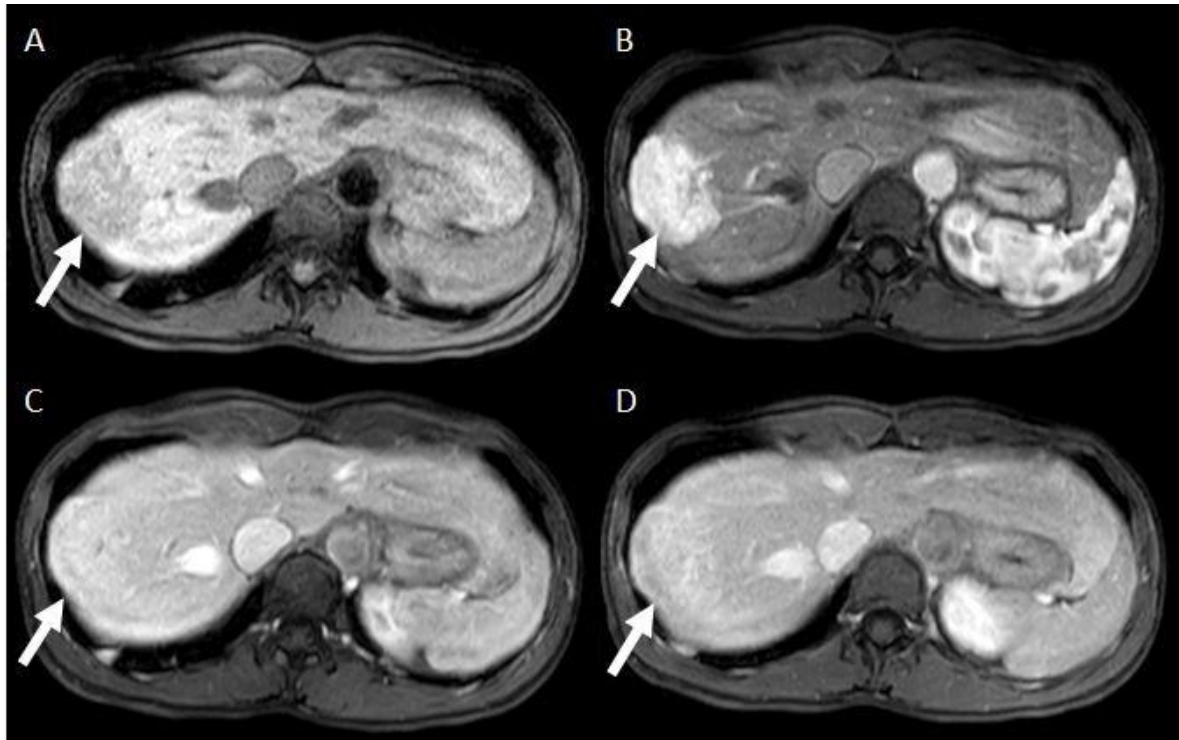


Fig. 2 MRI of the liver. MR-images demonstrate T1-weighted native (A) and contrast-enhanced (B-D postcontrast dynamic) sequences in a transversal plane of 44-year old female patient with an incidental finding of a big unclear focal liver lesion at the right liver lobe. **A** On the native T1-weighted image the liver mass (white arrow) at the right liver lobe appears hypointense compared to the surrounding normal liver. **B** The liver lesion shows an intense early homogeneous contrast enhancement on the arterial phase and is more hyperintense than the liver parenchyma. **C,D** The liver lesion is almost isointense to the surrounding liver parenchyma on portal venous **C** and venous **D** phase with no central fibrotic scar seen. The mass cannot be clearly distinguished from the liver parenchyma.

Discussion and conclusions

The case presented here demonstrates that FAPI-PET/CT may be helpful to characterize a variety of malignant and benign tumors. In addition, the present case also provides indications of possible pitfalls, which should be taken into account when interpreting FAPI-PET. It seems surprising to us that activated fibroblasts are present in FNH suggesting a functional role for growth of this tumor type. It will be important to see whether other benign liver tumors such as adenomas or hemangiomas also harbor activated fibroblasts detectable by PET-imaging. In our opinion it is very likely that most malignant liver tumors show high FAPI-accumulation. Possibly, also tissue remodeling in cirrhosis leads to activation of fibroblasts resulting in FAPI-uptake. In this case, FAPI-PET may be useful to detect active progression of cirrhosis. Finally, FAPI-PET may be helpful for radiation therapy planning in liver tumors as FDG-PET

has a high background in the liver hampering target volume definition. FAPi-PET may also play a role in planning of checkpoint-inhibitor treatment of hepatocellular carcinoma in the future, as activated fibroblasts modulate immune cell functions in tumor stroma. We propose that FAPi-PET will play a vital role in diagnosis and molecular characterization of liver tumors in the future.

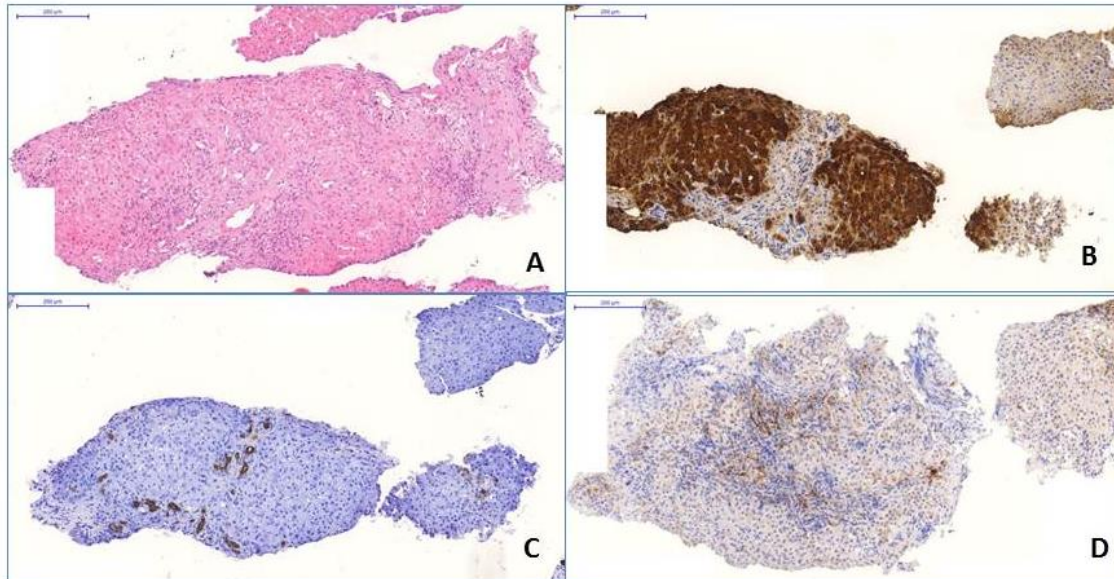


Fig. 3 Histopathology of the FAPi-positive lesion. **A** HE-staining. Liver tissue with nodular structured benign hepatocytes, separated by fibrous septa. Large dystrophic vessels appear in the fibrous septa. **B** FAP-immunohistochemistry. FAP-positive fibroblasts are present in the fibrous septa. **C** Glutaminsynthetase-immunohistochemistry. Large areas of hepatocytes expressing Glutaminsynthetase. **D** Cytokeratin 7-immunohistochemistry. Proliferating neoductuli in the fibrous septa.

Declarations

Conflict of Interest: The authors declare that they have no conflict of interest.

References

1. Acharya, P.S.; Zukas, A.; Chandan, V.; Katzenstein, A.-L.A.; Puré, E. Fibroblast activation protein: a serine protease expressed at the remodeling interface in idiopathic pulmonary fibrosis. *Hum. Pathol.* **2006**, *37*, 352–360, doi:10.1016/j.humpath.2005.11.020.
2. Egger, C.; Cannet, C.; Gérard, C.; Suply, T.; Ksiazek, I.; Jarman, E.; Beckmann, N. Effects of the fibroblast activation protein inhibitor, PT100, in a murine model of pulmonary fibrosis. *Eur. J. Pharmacol.* **2017**, *809*, 64–72, doi:10.1016/j.ejphar.2017.05.022.
3. Moon, E.S.; Elvas, F.; Vliegen, G.; De Lombaerde, S.; Vangestel, C.; De Bruycker, S.; Bracke, A.; Eppard, E.; Greifenstein, G.; Klasen, B.; Kramer, V.; Staelens, S.; De Meester, I.; Van der Veken, P.; Roesch, F. Targeting fibroblast activation protein (FAP): next generation PET radiotracers using squaramide coupled bifunctional DOTA and DATA^{5m} chelators. *EJNMMI Radiopharm. Chem.* **2020**, *5*, 19, doi:10.1186/s41181-020-00102-z.
4. Giesel, F.L.; Kratochwil, C.; Lindner, T.; Marschalek, M.M.; Loktev, A.; Lehnert, W.; Debus, J.; Jäger, D.; Flechsig, P.; Altmann, A.; et al. ⁶⁸Ga-FAPI PET/CT: Biodistribution and preliminary dosimetry estimate of 2 DOTA-containing FAP-targeting agents in patients with various cancers. *J. Nucl. Med.* **2019**, *60*, 386–392, doi:10.2967/jnumed.118.215913.
5. Giuffrida, P.; Pinzani, M.; Corazza, G.R.; Di Sabatino, A. Biomarkers of intestinal fibrosis - one step towards clinical trials for stricturing inflammatory bowel disease. *United European Gastroenterol J.* **2016**, *4*, 523–530, doi:10.1177/2050640616640160.
6. Jansen, K.; Heirbaut, L.; Verkerk, R.; Cheng, J.D.; Joossens, J.; Cos, P.; Maes, L.; Lambeir, A.M.; De Meester, I.; Augustyns, K.; et al. Extended structure-activity relationship and pharmacokinetic investigation of (4-quinolinoyl)glycyl-2-cyanopyrrolidine inhibitors of fibroblast activation protein (FAP). *J. Med. Chem.* **2014**, *57*, 3053–3074, doi:10.1021/jm500031w.
7. Koehne de Gonzalez, A.K.; Salomao, M.A.; Lagana, S.M. Current concepts in the immunohistochemical evaluation of liver tumors. *World J. Hepatol.* **2015**, *7*, 1403–1411, doi:10.4254/wjh.v7.i10.1403.
8. Levy, M.T.; McCaughan, G.W.; Abbott, C.A.; Cunningham, A.M.; Müller, E.; Rettig, W.J.; Gorrell, M.D. Fibroblast activation protein: a cell surface dipeptidyl peptidase and gelatinase expressed by stellate cells at the tissue remodelling interface in human cirrhosis. *Hepatology* **1999**, *29*, 1768–1778, doi:10.1002/hep.510290631.
9. López, J.I.; Errarte, P.; Erramuzpe, A.; Guarch, R.; Cortés, J.M.; Angulo, J.C.; Pulido, R.; Irazusta, J.; Llarena, R.; Larrinaga, G. Fibroblast activation protein predicts prognosis in clear cell renal cell carcinoma. *Hum. Pathol.* **2016**, *54*, 100–105, doi:10.1016/j.humpath.2016.03.009.
10. Rebouissou, S.; Bioulac-Sage, P.; Zucman-Rossi, J. Molecular pathogenesis of focal nodular hyperplasia and hepatocellular adenoma. *J. Hepatol.* **2008**, *48*, 163–170, doi:10.1016/j.jhep.2007.10.003.
11. Rovedatti, L.; Di Sabatino, A.; Knowles, C.H.; Sengupta, N.; Biancheri, P.; Corazza, G.R.; MacDonald T.T. Fibroblast activation protein expression in Crohn's disease strictures. *Inflamm. Bowel. Dis.* **2011**, *17*, 1251–1253, doi:10.1002/ibd.21446.

A.2. Fibroblast activation protein inhibitor (FAPI) positive tumour fraction on PET/CT correlates with Ki-67 in liver metastases of neuroendocrine tumours

Veröffentlicht in *Nuklearmedizin* **2021**, 60, 344–354.

mit Genehmigung von © Thieme, Georg Thieme Verlag KG, Stuttgart

Fibroblast activation protein inhibitor (FAPI) positive tumour fraction on PET/CT correlates with Ki-67 in liver metastases of neuroendocrine tumours

[REDACTED]
Euy Sung Moon⁴, [REDACTED]
[REDACTED]

¹ Department of Nuclear Medicine, University Medical Center Bonn, Bonn, Germany

² Department of Internal Medicine I, University Hospital Bonn, Bonn, Germany

³ Department of Internal Medicine III, University Hospital Bonn, Bonn, Germany

⁴ Department of Chemistry, Johannes Gutenberg University, Mainz, Germany

⁵ Department of Radiology, University Hospital Bonn, Bonn, Germany

⁶ Institute of Pathology, University Hospital Bonn, Bonn, Germany

⁷ Klinik und Poliklinik für Nuklearmedizin, Universitätsklinikum Bonn, Bonn, Germany

*Corresponding author: [REDACTED]

Abstract

Aim: Gallium-68-labelled inhibitors of the fibroblast activation protein (FAPi) enable positron emission tomography / computed tomography (PET/CT) imaging of fibroblast activation. We evaluated if [⁶⁸Ga]Ga-DATA^{5m}.SA.FAPi PET/CT is related to Ki-67 as a marker of tumour aggressiveness in patients with liver metastases of NET.

Methods: Thirteen patients with liver metastases of a histologically confirmed NET who underwent PET/CT with [⁶⁸Ga]Ga-DATA^{5m}.SA.FAPi, [¹⁸F]FDG and [⁶⁸Ga]Ga-DOTA-TOC were retrospectively analyzed. PET-positive liver tumour volumes were segmented for calculation of volume, SUVmax and PET-positive tumour fraction (TF). PET parameters were correlated with Ki-67.

Results: FDG-SUVmax correlated positively ($\rho = 0.543$, $p < 0.05$) and DOTATOC-SUVmax correlated negatively ($\rho = -0.618$, $p < 0.05$) with Ki-67, the correlation coefficients were in the moderate range. There was no significant correlation between FAPi-SUVmax and Ki-67 ($\rho = 0.382$, $p > 0.05$). FAPi-TF correlated positively ($\rho = 0.770$, $p < 0.01$) and DOTATOC-TF correlated negatively ($\rho = -0.828$, $p < 0.01$) with Ki-67, both significantly with high correlation coefficients. FDG-TF also correlated significantly with Ki-67, with a moderate correlation coefficient ($\rho = 0.524$, $p < 0.05$). The ratio FAPi-VOL:DOTATOC-VOL showed a significant and strong correlation with Ki-67 ($\rho = 0.808$, $p < 0.01$).

Conclusion: The ratio FAPi-VOL:DOTATOC-VOL might serve as a clinical parameter for the assessment of dedifferentiation and aggressiveness of liver metastases in patients with NET. [⁶⁸Ga]Ga-DATA^{5m}.SA.FAPi might hold potential for identification of high-risk patients. Further studies are warranted to evaluate its prognostic significance in comparison to [¹⁸F]FDG in patients with NET.

Keywords: fibroblast activation protein inhibitor (FAPi), Gallium-68 PET/CT, neuroendocrine tumours (NET), proliferation index, Ki-67, grading

Introduction

Neuroendocrine tumours (NET) are tumours derived from neuroendocrine cells which are distributed throughout the body and can develop in many different locations. These tumours mostly occur in the gastrointestinal system (gastro-entero-pancreatic neuroendocrine tumours, GEP-NET) and in the lungs [1].

A key feature of NET is overexpression of somatostatin receptors (SSTR) on the surface of the tumour cells, especially in well differentiated (G1 and G2) NET. SSTR expression enables tumour imaging by scintigraphy, single photon emission tomography (SPECT) and positron emission tomography (PET) [2]. A number of different somatostatin analogs labelled with gallium-68 have been successfully evaluated and are in clinical use for SSTR PET-imaging, such as [⁶⁸Ga]Ga-DOTA-TOC, [⁶⁸Ga]Ga-DOTA-TATE and [⁶⁸Ga]Ga-DOTA-NOC. SSTR PET/CT has been shown to be crucial in NET patient management [3].

The prognosis of patients with NET is strongly related to the tumour grade, which (in GEP-NET) is defined by the proliferation index Ki-67. Whereas well-differentiated G1 tumours (Ki-67 ≤ 2%) may exhibit an indolent behavior over many years, poorly differentiated G3 tumours (Ki-67 > 20%) may show rapid progression. During the course of disease, initially well-differentiated NET may show incremental dedifferentiation and transform into phenotypes that are more aggressive. Dedifferentiation is typically accompanied by diminished expression of the SSTR and increased glucose metabolism, leading to a reduced signal on SSTR PET and an increased uptake on [¹⁸F]fluorodeoxyglucose ([¹⁸F]FDG) PET. Positivity on [¹⁸F]FDG PET has been shown to correlate with poor clinical outcome [2].

Fibrosis is another characteristic hallmark of NET, which may develop locally or at distant sites [4]. Up to 40% of patients with carcinoid syndrome develop carcinoid heart disease (CHD) with formation of fibrotic endocardial plaques which may lead to valvular dysfunction and heart failure. Mesenteric fibrosis can be observed in up to 50% of small bowel NET, potentially leading to serious complications such as bowel ischemia, obstruction, volvulus, venous ischemia and ascites. Both CHD and mesenteric fibrosis are associated with poor survival [4]. The mechanisms leading to NET-associated fibrosis are not completely understood. Probably a complex interaction between tumour cells and cancer-associated fibroblasts leads to pathological remodeling of the extracellular matrix, fibrosis and finally desmoplasia. Serotonin, transforming growth factor, connective tissue growth factor, platelet-derived growth factor, insulin-like growth factor, epithelial growth factor, fibroblast growth factor, vascular endothelial growth factor, and kinins, amongst other peptides, are discussed as potential mediators in this interaction [4].

The overexpression of fibroblast activation protein (FAP), a type II membrane-bound glycoprotein of the dipeptidyl peptidase 4 family, is a distinguishing feature of cancer-associated fibroblasts. In adult normal tissue, FAP is not expressed in significant amounts and it therefore poses a promising molecular target for tumour imaging [5]. A relationship between high FAP expression and poor prognosis has already been reported in several types of cancer [6–11]. Gallium-68-labelled FAP-specific inhibitors (FAPi) have been suggested for tumour staging and characterization, as they can show high uptake in several highly prevalent cancers, such as breast cancer, lung cancer and esophageal cancer, amongst others [12].

Due to the known phenomenon of frequent desmoplastic reactions associated with NET and their association with poor survival, [⁶⁸Ga]Ga-DATA^{5m}.SA.FAPi PET/CT [13] poses a potential imaging biomarker for tumour grading and monitoring of tumour dedifferentiation in patients with NET. However, to our knowledge, no data is available to date regarding FAP expression or molecular imaging of FAP in NET and its possible correlation with tumour grading or clinical prognosis.

Early and accurate diagnosis of tumour dedifferentiation and prediction of tumour behavior and aggressiveness, preferably by non-invasive imaging, is desirable for optimized management of patients with NET in terms of personalized medicine. In the current study, we investigated if [⁶⁸Ga]Ga-DATA^{5m}.SA.FAPi PET/CT is related to Ki-67 as a marker of tumour proliferation, grading and aggressiveness in patients with liver metastases of NET.

Methods

Patient selection

Patients who underwent [⁶⁸Ga]Ga-DATA^{5m}.SA.FAPi, [¹⁸F]FDG and [⁶⁸Ga]Ga-DOTA-TOC PET/CT in our institution with histologically proven NET were retrospectively analyzed. The indication for the PET examinations was restaging due to tumour progression with suspicion of dedifferentiation. As this study is focused on liver metastases, patients without tumour involvement of the liver were excluded from the analysis. Also, patients in whom histological information on Ki-67 was more than 3 years old were excluded.

Radiochemical synthesis of [⁶⁸Ga]Ga-DATA^{5m}.SA.FAPi and [⁶⁸Ga]Ga-DOTA-TOC

Gallium-68 was obtained from a germanium-68/gallium-68 generator (EZAG, Berlin, Germany). Standard fluidic and reagent kit for gallium-68 radiolabelling of peptides (ABX advanced biochemical compounds GmbH, Radeberg, Germany) were employed. The standard strong cation exchanger (SCX) provided by the reagent kit was exchanged for a 200 mg STRATA SCX (Phenomenex, Torrance, USA). DATA^{5m}.SA.FAPi was obtained from the Rösch group [13] and diluted with TraceSelect water (Merck, Darmstadt, Germany) to 1 mg/ml. An automated cassette module (GAIA; Elysia-Raytest, Straubenhardt, Germany) was equipped with 30.0 ± 5.0 µg DATA^{5m}.SA.FAPi, 450 µl eluent, 3.36 ml ammonium acetate buffer (pH 4.5) and 200 µl ethanol Ph. Eur. (Merck, Darmstadt, Germany). After radiolabelling at 40 ± 5 °C for 8.0 min, the reaction mixture was purified through C-18 solid phase extraction and the final product was obtained in isotonic NaCl.

Radiochemical purity was determined using glass microfiber chromatography paper impregnated with silica-gel (iTLC-SG, Agilent Technologies, Santa Clara, USA) and analyzed with a single trace radioTLC-scanner (PET-miniGita, Elysia-Raytest, Straubenhardt, Germany). iTLC-strips were developed in 0.1 M citric buffer (pH 4; Merck, Darmstadt, Germany) and 1 M ammonium acetate/methanol (1:1). RadioHPLC was performed utilizing the Agilent 1260 Infinity II reverse phase HPLC system (Agilent Technologies, Santa Clara, USA) equipped with Gabi γ-HPLC flow detector (Elysia-Raytest, Straubenhardt, Germany) and a PC interface running Gina Star (Elysia-Raytest, Straubenhardt, Germany). A Nucleodur 100-3 C18 ec 125/4 column (Macherey-Nagel GmbH & Co. KG, Düren, Germany) was applied. The gradient utilized mobile phase A (deionized water + 0.01% TFA) and mobile phase B (acetonitrile + 0.01% TFA) at a flow rate of 0.7 ml/min starting with 100% A/0% B to 0% A/100% B within 20 min. Non-decay corrected (AY) and decay corrected radiochemical yields were calculated by the activity trapped on the SCX, on C-18 and remaining activity on C-18 after final formulation.

The synthesis of [⁶⁸Ga]Ga-DOTA-TOC was performed as previously described [14].

PET imaging

In the case of [⁶⁸Ga]Ga-DOTA-TOC PET/CT, long-acting somatostatin analogs were discontinued 4 weeks before PET/CT and patients were injected with 20 mg furosemide before tracer injection. Mean injected activities were 184 ± 22 MBq for [⁶⁸Ga]Ga-DATA^{5m}.SA.FAPi, 267 ± 56 MBq for [¹⁸F]FDG and 161 ± 18 MBq for [⁶⁸Ga]Ga-DOTA-TOC. Mean time intervals from tracer injection to image acquisition were 79 ± 34 min for [⁶⁸Ga]Ga-DATA^{5m}.SA.FAPi, 74 ± 17 min for [¹⁸F]FDG and 42 ± 16 min for [⁶⁸Ga]Ga-DOTA-TOC. PET/CT examinations were performed on a Biograph 2 PET/CT scanner (Siemens Medical Solutions, Erlangen, Germany), on a Gemini GXL 16 PET/CT scanner (Philips Healthcare, Eindhoven,

Netherlands) and on a GE Discovery STE 16 (GE Healthcare, Milwaukee, USA). Emission times per bed position were 4 min for Siemens, 2 min for Philips and 3 min for GE. A non-contrast-enhanced CT was acquired for attenuation correction purposes (Siemens: 16 mAs, 130 kV, CareDose; Philips: 80 mAs, 120 kV, DoseRight; GE: 100 mAs, 120 kV, DoseCheck). PET data were reconstructed iteratively, including scatter, random and decay correction (Siemens: OSEM, 4 iterations, 8 subsets; Philips: RAMLA 3D, 2 iterations, 0.05 relaxation; GE: iterative, 2 iterations, 20 subsets). Reconstructed PET images were subsequently smoothed using a 5 mm Gaussian filter.

Image analysis

Visual analysis of tracer uptake in liver metastases was performed by consensus reading of two board-certified nuclear medicine physicians. Uptake intensity of [⁶⁸Ga]Ga-DATA^{5m}.SA.FAPi, [¹⁸F]FDG and [⁶⁸Ga]Ga-DOTA-TOC was rated visually using a scoring system from 0 – 3 (0: no uptake, 1: faint uptake, 2: moderate uptake, 3: intense uptake). For each tracer, tumour uptake was categorized into three different patterns: peripheral (pronounced uptake in the lesion periphery), central (pronounced uptake in the center of the lesion) and diffuse (lesions without pronounced peripheral or central uptake).

Semi-quantitative analysis of PET data was performed on a Philips Imalytics workstation (Version 3.2 Rev 6515(64), Philips Healthcare, Eindhoven, Netherlands). For each patient, the [⁶⁸Ga]Ga-DOTA-TOC and [¹⁸F]FDG PET/CT datasets were coregistered to the [⁶⁸Ga]Ga-DATA^{5m}.SA.FAPi PET/CT dataset by manual rigid registration with emphasis on liver coregistration. The liver volumes were segmented manually on the low-dose CT dataset. On each PET dataset, background activity (mean and standard deviation) in normal liver tissue was measured using a 2D circular region of interest (ROI) with 4 cm diameter. In PET datasets, 3D tumour volumes of interest (VOI) were generated using a threshold algorithm confined to the boundaries of the liver volume. For segmentation of tumour volumes, the threshold was set to the mean liver background activity plus 6 times the standard deviation. Care was taken to exclude adjacent extrahepatic activity, e.g., the kidneys. This resulted in the tumour volumes FAPi_{VOL}, FDG_{VOL} and DOTATOC_{VOL} for each patient. SUV_{max} was measured in each tumour volume, resulting in FAPi_{SUVmax}, FDG_{SUVmax} and DOTATOC_{SUVmax}. For each patient, using the coregistered PET datasets, a set union VOI was calculated from the [⁶⁸Ga]Ga-DATA^{5m}.SA.FAPi-, [¹⁸F]FDG- and [⁶⁸Ga]Ga-DOTA-TOC-positive VOIs, resulting in one PET-positive whole tumour volume for each patient. For each tracer, the PET-positive tumour fraction (TF) was calculated by division of the tracer-positive volume by the PET-positive whole tumour volume, resulting in the PET-positive tumour fractions FAPi_{TF}, FDG_{TF} and DOTATOC_{TF}.

Statistical analysis

Statistical analysis was performed using IBM SPSS Statistics (Version 25, International Business Machines Corporation, Armonk, NY, USA). For correlation of two variables, the Spearman's rank correlation coefficient (ρ) was calculated. Correlations with $p < 0.05$ were regarded as statistically significant. Differences in mean values between groups of variables were tested for statistical significance using the Mann-Whitney-U test. Differences with $p < 0.05$ were regarded as significant.

Ethics Committee Approval and Patient Consent

Ethical approval was waived by the institutional ethics committee in view of the retrospective nature of the study and all procedures being performed were part of routine care. All procedures performed involving patients were in accordance with the ethical standards of the institutional and/or national research committee and with the principles of the 1964 Declaration of Helsinki and its later amendments or comparable ethical standards. [^{68}Ga]Ga-DATA^{5m}.SA.FAPi and [^{68}Ga]Ga-DOTA-TOC were administered in compliance with The German Medicinal Products Act, AMG §13 2b, and in accordance with the responsible regulatory body.

Informed consent was obtained from all patients before undergoing PET/CT imaging. Patients gave consent for retrospective data analysis. No identifying details of the patients are being published.

Results

Patient characteristics

Thirteen patients were included in this retrospective analysis (8 male, 5 female). The mean patient age at the time of [^{68}Ga]Ga-DATA^{5m}.SA.FAPi PET/CT was 66.8 ± 9.8 years. In all patients, [^{68}Ga]Ga-DATA^{5m}.SA.FAPi, [^{18}F]FDG and [^{68}Ga]Ga-DOTA-TOC PET/CT were performed in a time period of 57 ± 39 days. No change of treatment was initiated between the three PET scans. Patients undergoing biotherapy on the first scan continued biotherapy until the third scan. No other cancer specific treatments were performed between the three scans. The proliferation index Ki-67 was available either from liver biopsies (8/13 patients) or from primary tumor histology (5/13 patients). Information about Ki-67 was 0.9 ± 1.3 years old. Mean Ki-67 was $20.4 \pm 21.9\%$. Three patients had NET G1, 6 patients G2 and 4 patients G3 tumours. Eight patients had pancreatic NET, 2 patients small intestinal NET,

2 patients NET of unknown primary and 1 patient had a NET of the appendix. Detailed patient data are presented in Tab. 1.

Tab. 1 Patient characteristics.

Number of patients	13	
Gender	Male	8 (62%)
	Female	5 (38%)
Patient age	66.8 ± 9.8 years	(43 – 81 years)
Time from initial diagnosis to FAPI PET/CT	3.5 ± 3.1 years	(0 – 10 years)
Ki-67	20.4 ± 21.9%	(1 – 60%)
Ki-67 age	0.9 ± 1.3 years	(0 – 3 years)
Ki-67 assessment	Liver biopsy	8 (62%)
	Primary tumour	5 (38%)
Tumour grade	G1	3 (23%)
	G2	6 (46%)
	G3	4 (31%)
Tumour entity	Pancreatic NET	8 (62%)
	Small intestinal NET	2 (15%)
	NET of unknown primary	2 (15%)
	Appendix NET	1 (8%)
Tumour involvement	Liver metastases (inclusion criterion)	13 (100%)
	Lymph node metastases	9 (69%)
	Primary tumour in situ	7 (54%)
	Bone metastases	5 (38%)
	Lung metastases	2 (15%)
	Peritoneal metastases	2 (15%)
Previous therapies	Biotherapy (currently ongoing)	10 (77%)
	Biotherapy (not currently ongoing)	1 (8%)
	Peptide Receptor Radiotherapy (PRRT)	8 (62%)
	Surgery	5 (38%)
	Chemotherapy	5 (38%)
	Everolimus	3 (23%)
	Radiotherapy	1 (8%)

Radiosynthesis of [⁶⁸Ga]Ga-DATA^{5m}.SA.FAPi

Radiosynthesis of [⁶⁸Ga]Ga-DATA^{5m}.SA.FAPi with 1.23 ± 0.25 GBq gallium-68 revealed a decay corrected radiochemical yield of $99.29 \pm 3.56\%$ ($84.29 \pm 3.02\%$ AY), a volume activity of 96.99 ± 20.65 MBq/ml and an apparent molar activity of 39.86 ± 15.43 MBq/nmol. This resulted in an injected amount of peptide of about 5 – 10 µg per patient. Radiochemical purity was > 95%.

Visual analysis of tracer uptake in liver metastases

Overall, 12/13 patients were categorized as visually positive for uptake of [⁶⁸Ga]Ga-DATA^{5m}.SA.FAPi in liver metastases. Uptake pattern was peripheral in 9/12 cases (75%) and diffuse in 3/12 cases (25%). No central uptake pattern was observed. No significant differences in mean Ki-67 were observed between the groups of patients with peripheral and diffuse uptake ($p > 0.05$). No significant correlation was observed between visual scoring of [⁶⁸Ga]Ga-DATA^{5m}.SA.FAPi uptake intensity and Ki-67.

Regarding [¹⁸F]FDG, 8/13 patients were visually rated as positive for uptake in liver metastases. Uptake pattern was central in 6/8 cases (75%) and diffuse in 2/8 cases (25%). No peripheral uptake pattern was observed. No significant differences in mean Ki-67 were observed between the groups of patients with central and diffuse uptake ($p > 0.05$). Visual uptake intensity of [¹⁸F]FDG correlated significantly and positively with Ki-67 ($\rho = 0.580$, $p < 0.05$).

Using [⁶⁸Ga]Ga-DOTA-TOC, 12/13 patients were visually rated as positive for tracer uptake in liver metastases. Uptake pattern was diffuse in 7/12 cases (58%), central in 3/12 cases (25%) and peripheral in 2/12 cases (17%). No significant differences in mean Ki-67 were observed between the groups of different uptake patterns ($p > 0.05$). Visual uptake intensity of [⁶⁸Ga]Ga-DOTA-TOC correlated significantly and negatively with Ki-67 ($\rho = -0.603$, $p < 0.05$).

The results of visual analysis are summarized in Tab. 2.

Tab. 2 Visual analysis of tracer uptake of [⁶⁸Ga]Ga-DATA^{5m}.SA.FAPi, [¹⁸F]FDG and [⁶⁸Ga]Ga-DOTA-TOC in liver metastases.

		[⁶⁸ Ga]Ga-DATA ^{5m} .SA.FAPi	[¹⁸ F]FDG	[⁶⁸ Ga]Ga-DOTA-TOC
PET positivity	positive	12 (92%)	8 (62%)	12 (92%)
	negative	1 (8%)	5 (38%)	1 (8%)
Uptake intensity score	0: none	1 (8%)	5 (38%)	1 (8%)
	1: faint	2 (15%)	1 (8%)	0
	2: moderate	3 (23%)	3 (23%)	2 (15%)
	3: intense	7 (54%)	4 (31%)	10 (77%)
Uptake pattern	central	0	6 (75%)	3 (25%)
	diffuse	3 (25%)	2 (25%)	7 (58%)
	peripheral	9 (75%)	0	2 (17%)
Correlation of visual intensity with Ki-67	Spearman's rho	0.226	0.580	-0.603
	<i>p</i>	0.229	0.019*	0.015*
	N	13	13	13

*: *p* < 0.05

Semi-quantitative analysis of tracer uptake in normal liver tissue and liver metastases

SUV_{mean} in normal liver tissue was 2.43 ± 0.42 for [⁶⁸Ga]Ga-DATA^{5m}.SA.FAPi, 2.66 ± 0.70 for [¹⁸F]FDG and 4.01 ± 1.55 for [⁶⁸Ga]Ga-DOTA-TOC. The resulting thresholds for tumour segmentation were 4.26 ± 1.12 for [⁶⁸Ga]Ga-DATA^{5m}.SA.FAPi, 3.98 ± 1.44 for [¹⁸F]FDG and 6.80 ± 2.35 for [⁶⁸Ga]Ga-DOTA-TOC.

SUV_{max} in the [⁶⁸Ga]Ga-DATA^{5m}.SA.FAPi-positive tumour volume (FAPi_{SUVmax}) was 9.09 ± 3.35 (range 3.79 – 14.07), the [⁶⁸Ga]Ga-DATA^{5m}.SA.FAPi-positive tumour volume (FAPi_{VOL}) was 270 ml ± 419 ml (range 0.19 ml – 1524 ml) and the [⁶⁸Ga]Ga-DATA^{5m}.SA.FAPi-positive tumour fraction (FAPi_{TF}) was 52.3% ± 29.7% (range 2.0% – 97.4%).

In the [¹⁸F]FDG-positive tumour volume, FDG_{SUVmax} was 6.87 ± 2.08 (range 3.57 – 11.02), FDG_{VOL} was 122 ml ± 191 ml (range 0.05 ml – 584 ml) and FDG_{TF} was 15.5% ± 17.6% (range 0.03% – 60.9%).

In the [⁶⁸Ga]Ga-DOTA-TOC-positive tumour volume, DOTATOC_{SUVmax} was 22.31 ± 11.41 (range 10.00 – 44.93), DOTATOC_{VOL} was 240 ml ± 320 ml (range 9.1 ml – 837 ml) and DOTATOC_{TF} was 56.9% ± 29.1% (range 6.7% – 98.0%).

Correlation of SUV_{max} with Ki-67

There was a significant positive correlation between $FDG_{SUV_{max}}$ and Ki-67, the correlation coefficient was in the moderate range ($\rho = 0.543$, $p < 0.05$). Conversely, Ki-67 correlated negatively with $DOTATOC_{SUV_{max}}$, which was significant ($\rho = -0.618$, $p < 0.05$). There was no significant correlation between $FAPi_{SUV_{max}}$ and Ki-67 ($\rho = 0.382$, $p > 0.05$), though the correlation coefficient showed a trend for a positive correlation. Details are listed in Tab. 3 and graphical representations are shown in Fig. 1.

Tab. 3 Correlation of Ki-67 with SUV_{max} of $[^{68}Ga]Ga-DATA^{5m}.SA.FAPi$, $[^{18}F]FDG$ and $[^{68}Ga]Ga-DOTA-TOC$ PET/CT.

	Ki-67 – $FAPi_{SUV_{max}}$	Ki-67 – $FDG_{SUV_{max}}$	Ki-67 – $DOTATOC_{SUV_{max}}$
Spearman's rho	0.382	0.543	-0.618
<i>p</i>	0.099	0.028*	0.012*
N	13	13	13

*: $p < 0.05$

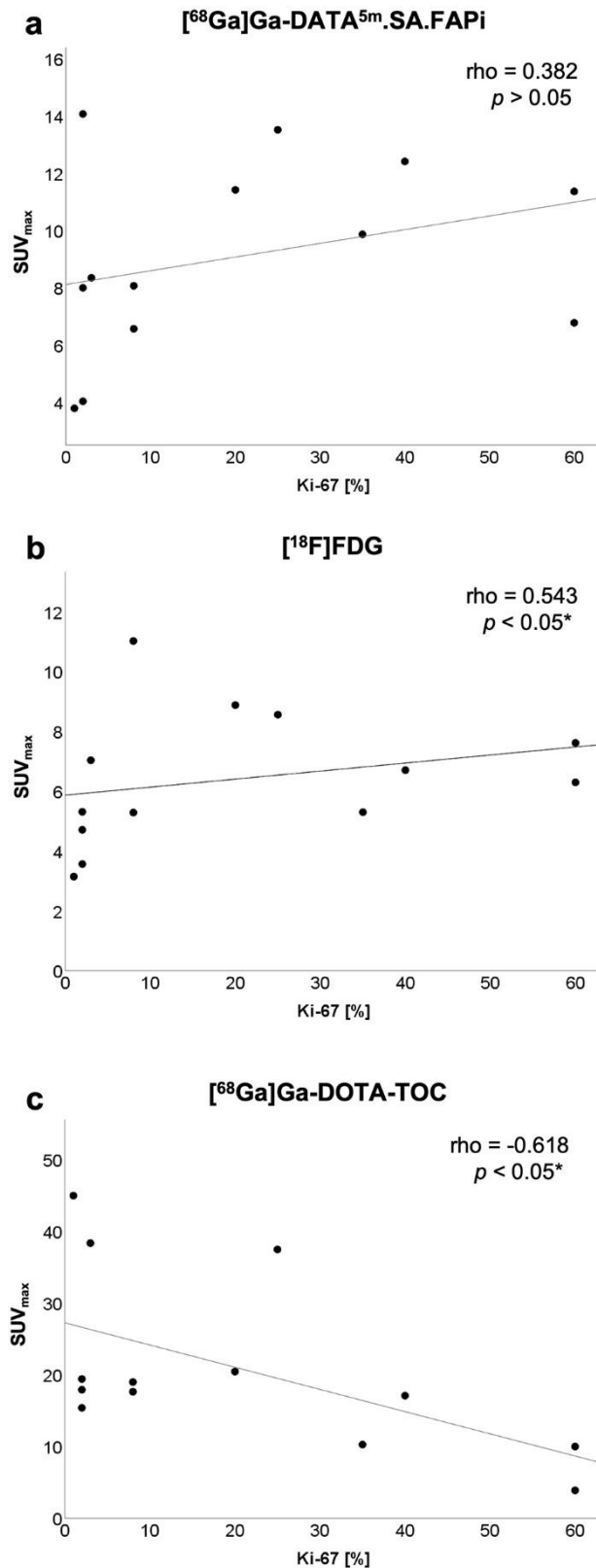


Fig. 1 Correlation between Ki-67 and SUV_{max} of (a) $[^{68}\text{Ga}]\text{Ga-DATA}^{5\text{m}}.\text{SA.FAPi}$, (b) $[^{18}\text{F}]\text{FDG}$ and (c) $[^{68}\text{Ga}]\text{Ga-DOTA-TOC}$ PET/CT. $\text{FAPi}_{\text{SUV}_{\text{max}}}$ showed no significant correlation with Ki-67, whereas $\text{FDG}_{\text{SUV}_{\text{max}}}$ and $\text{DOTATOC}_{\text{SUV}_{\text{max}}}$ showed a significant correlation with moderate correlation coefficients.

FAPi_{SUVmax} correlated significantly with FDG_{SUVmax}, with a low correlation coefficient ($\rho = 0.484$, $p < 0.05$). There were no significant correlations of FAPi_{SUVmax} with DOTATOC_{SUVmax}, or FDG_{SUVmax} with DOTATOC_{SUVmax}, respectively ($p > 0.05$), details are listed in Tab. 4.

Tab. 4 Correlation of SUV_{max} between [⁶⁸Ga]Ga-DATA^{5m}.SA.FAPi, [¹⁸F]FDG and [⁶⁸Ga]Ga-DOTA-TOC PET/CT.

	FAPi _{SUVmax} – FDG _{SUVmax}	FAPi _{SUVmax} – DOTATOC _{SUVmax}	FDG _{SUVmax} – DOTATOC _{SUVmax}
Spearman's rho	0.484	-0.231	-0.060
p	0.047*	0.224	0.422
N	13	13	13

*: $p < 0.05$

Correlation of PET-positive tumour fractions with Ki-67

The [⁶⁸Ga]Ga-DATA^{5m}.SA.FAPi-positive tumour fraction (FAPi_{TF}) showed a significant and strong positive correlation with Ki-67 ($\rho = 0.770$, $p < 0.01$). Also, FDG_{TF} showed a significant correlation with Ki-67, however the correlation coefficient was only in the moderate range ($\rho = 0.524$, $p < 0.05$). On the other hand, DOTATOC_{TF} showed a significant and strong negative correlation with Ki-67 ($\rho = -0.828$, $p < 0.01$). Details are listed in Tab. 5 and graphical representations are shown in Fig. 2.

Tab. 5 Correlation of Ki-67 with PET-positive tumour fractions of [⁶⁸Ga]Ga-DATA^{5m}.SA.FAPi, [¹⁸F]FDG and [⁶⁸Ga]Ga-DOTA-TOC PET/CT.

	Ki-67 – FAPi _{TF}	Ki-67 – FDG _{TF}	Ki-67 – DOTATOC _{TF}
Spearman's rho	0.770	0.524	-0.828
p	0.001**	0.033*	0.000**
N	13	13	13

*: $p < 0.05$; **: $p < 0.01$

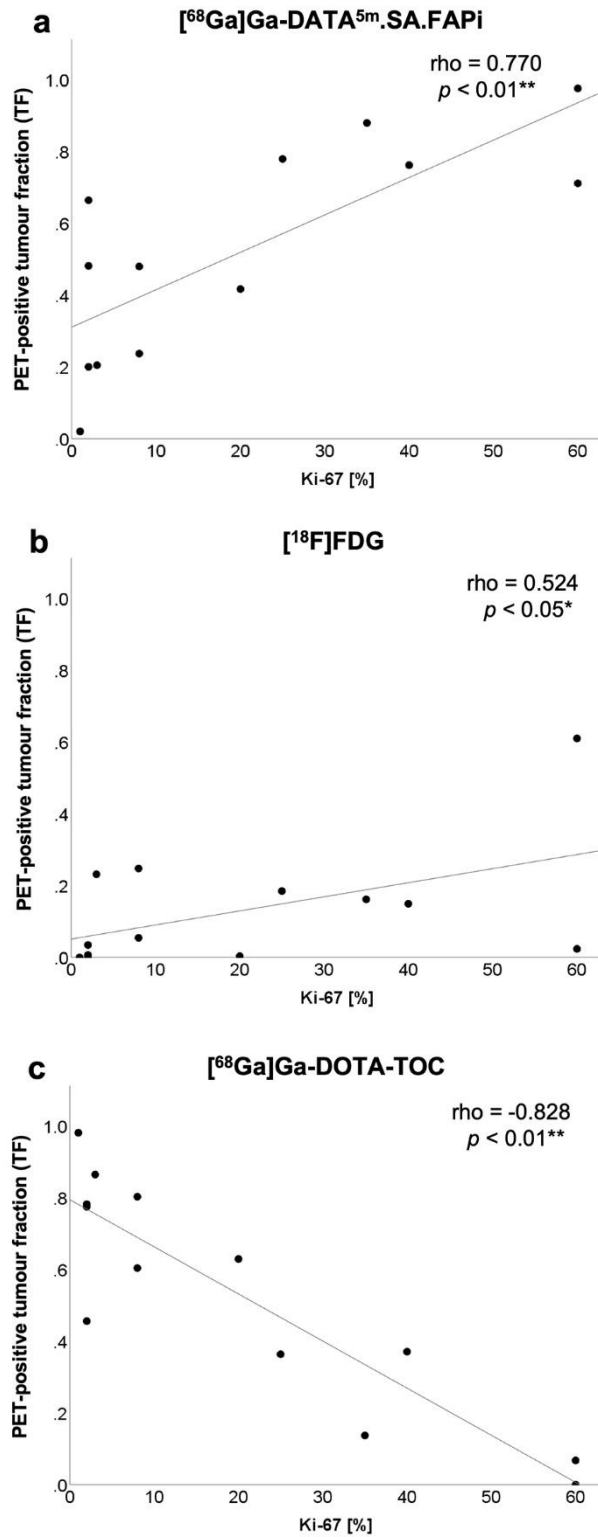


Fig. 2 Correlation between Ki-67 and PET-positive tumour fractions (TF) of (a) $[^{68}\text{Ga}]\text{Ga-DATA}^{5\text{m}}.\text{SA.FAPi}$, (b) $[^{18}\text{F}]\text{FDG}$ and (c) $[^{68}\text{Ga}]\text{Ga-DOTA-TOC}$ PET/CT. FAPi_{TF} and $\text{DOTATOC}_{\text{TF}}$ showed a strong and significant correlation with Ki-67, whereas FDG_{TF} only showed a moderate correlation coefficient.

There was a strong negative correlation between FAPi_{TF} and $\text{DOTATOC}_{\text{TF}}$ ($\rho = -0.912$, $p < 0.01$). No significant correlations were observed between FDG_{TF} and FAPi_{TF} ($p > 0.05$) or between FDG_{TF} and $\text{DOTATOC}_{\text{TF}}$ ($p > 0.05$), details are listed in Tab. 6.

Tab. 6 Correlation between PET-positive tumour fractions of $[^{68}\text{Ga}]\text{Ga-DATA}^{5\text{m}}.\text{SA.FAPi}$, $[^{18}\text{F}]\text{FDG}$ and $[^{68}\text{Ga}]\text{Ga-DOTA-TOC PET/CT}$.

	$\text{FAPi}_{\text{TF}} - \text{FDG}_{\text{TF}}$	$\text{FAPi}_{\text{TF}} - \text{DOTATOC}_{\text{TF}}$	$\text{FDG}_{\text{TF}} - \text{DOTATOC}_{\text{TF}}$
Spearman's rho	0.300	-0.912	-0.371
<i>p</i>	0.160	0.000**	0.106
N	13	13	13

** : $p < 0.01$

Correlation of PET-positive tumour volumes with Ki-67

The $[^{68}\text{Ga}]\text{Ga-DATA}^{5\text{m}}.\text{SA.FAPi}$ -positive tumour volume (FAPi_{VOL}) correlated significantly with Ki-67, with a moderate correlation coefficient ($\rho = 0.510$, $p < 0.05$). No significant correlations were observed between Ki-67 and FDG_{VOL} or $\text{DOTATOC}_{\text{VOL}}$, respectively ($p > 0.05$), details are listed in Tab. 7.

Tab. 7 Correlation of Ki-67 with PET-positive tumour volumes [ml] of $[^{68}\text{Ga}]\text{Ga-DATA}^{5\text{m}}.\text{SA.FAPi}$, $[^{18}\text{F}]\text{FDG}$ and $[^{68}\text{Ga}]\text{Ga-DOTA-TOC PET/CT}$.

	$\text{Ki-67} - \text{FAPi}_{\text{VOL}}$	$\text{Ki-67} - \text{FDG}_{\text{VOL}}$	$\text{Ki-67} - \text{DOTATOC}_{\text{VOL}}$
Spearman's rho	0.510	0.463	-0.288
<i>p</i>	0.038*	0.055	0.170
N	13	13	13

* : $p < 0.05$

The ratio of the PET-positive tumour volumes of $\text{FAPi}_{\text{VOL}}:\text{DOTATOC}_{\text{VOL}}$ showed a significant and strong correlation with Ki-67 ($\rho = 0.808$, $p < 0.01$), see Fig. 3.

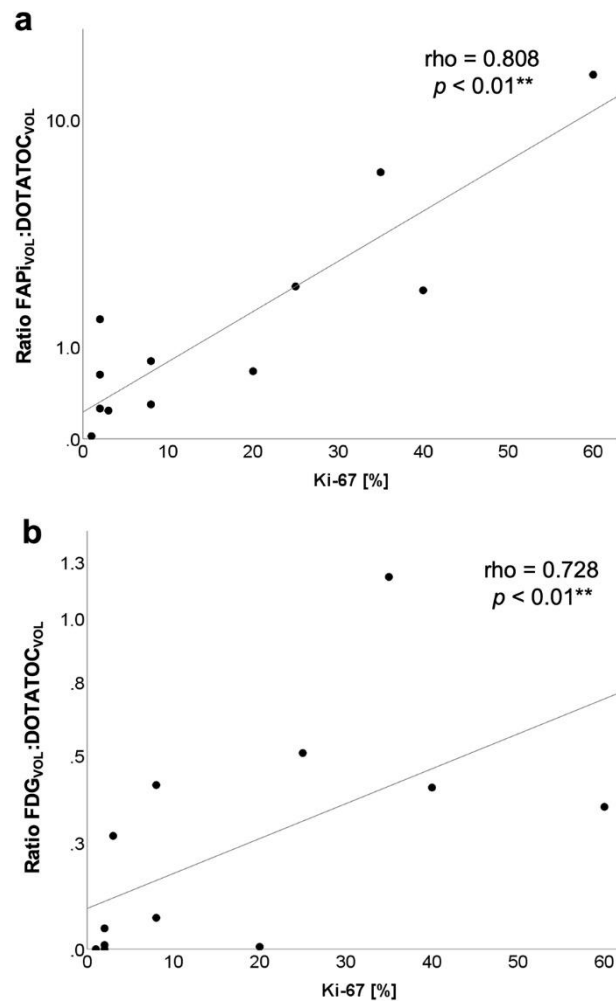


Fig. 3 (a) The ratio FAPI_{vol}:DOTATOC_{vol} showed a strong and significant correlation with Ki-67 (logarithmic scale on the y-axis). All patients with Ki-67 ≤ 20% had a FAPI_{vol}:DOTATOC_{vol} ratio < 1.5 and patients with Ki-67 > 55% had a FAPI_{vol}:DOTATOC_{vol} ratio > 10.0 (including one FAPI-positive patient with an incalculable ratio due to DOTATOC_{vol} being 0 ml). (b) Also, the ratio FDG_{vol}:DOTATOC_{vol} showed a significant, but less pronounced correlation with Ki-67 compared to FAPI_{vol}:DOTATOC_{vol} (logarithmic scale on the y-axis). No clear thresholds could be determined between patients with Ki-67 ≤ 20%, 20% - 55% and > 55%.

Also, the ratio FDG_{vol}:DOTATOC_{vol} correlated significantly with Ki-67 (rho = 0.728, p < 0.01), with a slightly lower correlation coefficient. Representative examples of patients with high and low Ki-67 are shown with corresponding PET parameters in Fig. 4. The corresponding non-fused PET and CT images are shown in supplemental figures Fig. S1 and Fig. S2, respectively.

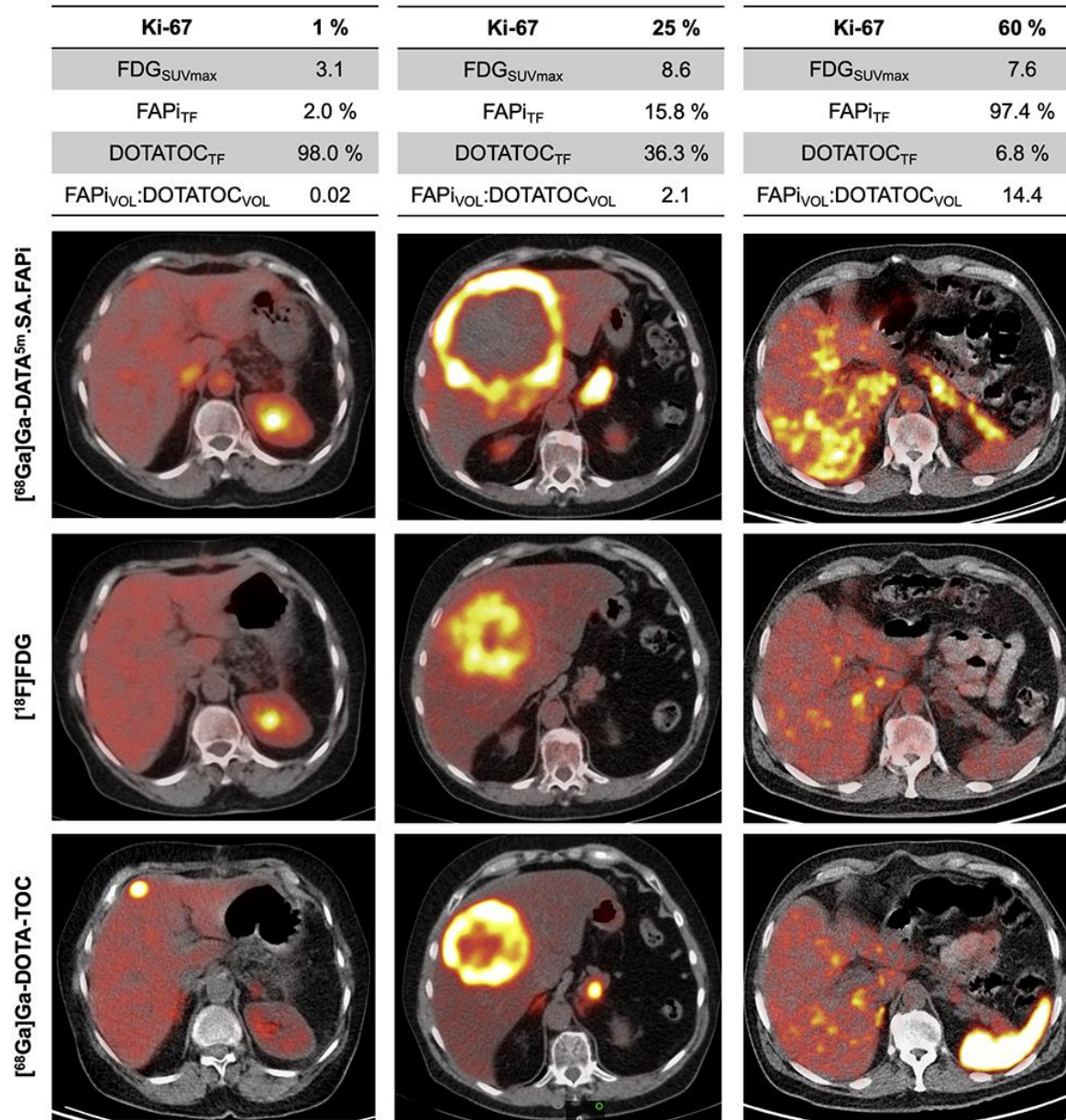


Fig. 4 Representative examples of PET/CT examinations of patients with low (left column), medium (middle column) and high (right column) Ki-67. The ratio FAPi_{VOL}:DOTATOC_{VOL} shows a steady increase from low to high Ki-67. FDG_{SUVmax} also shows a rising trend with increasing Ki-67. Corresponding non-fused PET images are shown in supplemental figure S1 and non-fused CT images are shown in supplemental figure S2.

Discussion

Patients with metastasized neuroendocrine tumours often exhibit a progressive tumour dedifferentiation over the course of disease. Re-assessment of the proliferation index may be indicated in patients with signs of progression and / or dedifferentiation to guide therapy decisions [15,16].

It is well documented that highly differentiated neuroendocrine tumours typically show a low glucose metabolism and [¹⁸F]FDG PET/CT can be a useful predictor of dedifferentiation. A study proposing a metabolic grading system for NET based on [¹⁸F]FDG PET/CT showed a significant positive correlation between Ki-67 and SUV_{max} of [¹⁸F]FDG with a correlation coefficient in the moderate range in a retrospective analysis of 89 patients [17]. Also, Panagiotidis et al. observed a similar positive correlation between Ki-67 and [¹⁸F]FDG SUV_{max} with a moderate correlation coefficient [18]. Our study is in line with these results, as a moderate positive correlation of [¹⁸F]FDG SUV_{max} with Ki-67 was also observed, reaching the level of significance. In 2017, Chan et al proposed the NETPET score, integrating information from SSTR PET/CT and [¹⁸F]FDG PET/CT into a clinical parameter with prognostic significance regarding overall survival [19].

Currently we observed that the [⁶⁸Ga]Ga-DATA^{5m}.SA.FAPi-positive tumour fraction (FAPi_{TF}) showed a strong and positive correlation with Ki-67 in liver metastases of NET. The correlation coefficient of FAPi_{TF} with Ki-67 was even higher compared to FDG_{SUVmax}, making FAPi_{TF} a potentially valuable predictor for Ki-67. However, as the calculation of FAPi_{TF} in our current analysis is based on the PET-positive whole tumour volume, which requires calculation of the set union of the coregistered [⁶⁸Ga]Ga-DATA^{5m}.SA.FAPi-, [¹⁸F]FDG- and [⁶⁸Ga]Ga-DOTA-TOC-positive tumour volumes, assessment of this parameter is time-consuming and does not seem feasible for clinical use.

Similar to FAPi_{TF}, also DOTATOC_{TF} showed a significant and strong, but negative correlation with Ki-67. Therefore, also the ratio FAPi_{TF}:DOTATOC_{TF} correlates very well with Ki-67. Mathematically, the ratio of the PET-positive tumour fractions FAPi_{TF}:DOTATOC_{TF} is not different from the ratio of the PET-positive tumour volumes FAPi_{VOL}:DOTATOC_{VOL}, which therefore also shows a strong positive correlation with Ki-67 ($\rho = 0.808$, $p < 0.01$, see Fig. 3a). This ratio can be calculated in a straightforward manner from segmentation of the PET-positive tumour volumes from [⁶⁸Ga]Ga-DOTA-TOC- and [⁶⁸Ga]Ga-DATA^{5m}.SA.FAPi PET/CT and it might be feasible for application in the clinical routine as a parameter predictive for Ki-67 in liver metastases of NET in case of clinical suspicion of dedifferentiation.

A Ki-67 index of 20% is the threshold to histologically distinguish NET G2 from G3. A Ki-67 of 20% seems to correspond to a FAPi_{VOL}:DOTATOC_{VOL} ratio of about 1.5 – 2.0. In our current study, 7/13 patients had

a ratio of less than 1.5, all of them had a Ki-67 of $\leq 20\%$ (NET G1 / G2). The remaining 6/13 patients all had a ratio of more than 2.0 (including one FAPI-positive patient with an incalculable ratio due to DOTATOC_{VOL} being 0 ml) and a Ki-67 of 25% or higher (NET G3).

In the clinical management of patients with metastasized NET, evidence of Ki-67 of $> 20\%$ may point to peptide-receptor-radionuclide therapy (PRRT) with [¹⁷⁷Lu]Lu-DOTA-TATE alone not being adequate for tumour growth control and chemotherapy or a combination of PRRT with chemotherapy might improve therapy efficacy [20–22]. A FAPI_{VOL}:DOTATOC_{VOL} ratio of more than 1.5 might be an indicator for the potential need of cytotoxic chemotherapy.

With further dedifferentiation, the use of platinum-based chemotherapy regimen may be indicated, especially when Ki-67 exceeds 55% / neuroendocrine carcinoma NEC G3 [20,23,24]. In our patient collective, 2/13 patients had a Ki-67 of more than 55% (both had a histological result of Ki-67 60%). In both patients, the ratio of FAPI_{VOL}:DOTATOC_{VOL} was greater than 10.0. The ratio of one patient was 14.4, the other patient had an incalculable ratio due to DOTATOC_{VOL} being 0 ml. The remaining 11/13 patients had a Ki-67 of $< 55\%$ (max. 40%), with a maximum FAPI_{VOL}:DOTATOC_{VOL} ratio of 6.4. Though the number of patients in our study is limited, we suspect that a FAPI_{VOL}:DOTATOC_{VOL} ratio of > 10.0 indicates a high probability for a Ki-67 of more than 55% / NEC G3.

Similar to FAPI_{VOL}:DOTATOC_{VOL}, also the ratio FDG_{VOL}:DOTATOC_{VOL} showed a significant correlation with Ki-67. However in the case of FDG_{VOL}:DOTATOC_{VOL}, the correlation with Ki-67 is mainly based on the negative correlation of DOTATOC_{TF} with Ki-67 and less on FDG_{TF}. This results in a higher scatter and lower correlation coefficient for FDG_{VOL}:DOTATOC_{VOL} compared to FAPI_{VOL}:DOTATOC_{VOL} (see Fig. 3b). In contrast to FAPI_{VOL}:DOTATOC_{VOL}, the FDG-based parameters FDG_{VOL}:DOTATOC_{VOL} and FDG_{SUVmax} did not show apparent thresholds differentiating NET G1/G2 from NET G3 or patients with Ki-67 $> 55\%$ in our patient collective.

Both [¹⁸F]FDG and [⁶⁸Ga]Ga-DATA^{5m}.SA.FAPI PET/CT correlate with Ki-67 in NET. Obviously, there are fundamental differences between these two imaging approaches. Using [¹⁸F]FDG PET, the signal is generated by tracer uptake of the tumour cells themselves, dependent on glucose metabolism. On the other hand, it is assumed that the signal of [⁶⁸Ga]Ga-DATA^{5m}.SA.FAPI PET is mostly generated by FAP-expression of cancer associated fibroblasts in the tumour stroma, although it has been described that FAP may also be expressed by certain transformed cells of malignant tissues [25,26]. These fundamental differences in imaging methodology between [¹⁸F]FDG PET and [⁶⁸Ga]Ga-DATA^{5m}.SA.FAPI PET are also reflected by the results of our current study. Whereas in [¹⁸F]FDG PET, SUV_{max} of hot-spots in the tumour volume as well as the volume-based parameter FDG_{TF} are related to Ki-67. Using

[⁶⁸Ga]Ga-DATA^{5m}.SA.FAPi, only the volume-based metric FAP_{iTF} was significantly correlated with Ki-67, but not SUV_{max}.

Differences between [⁶⁸Ga]Ga-DATA^{5m}.SA.FAPi and [¹⁸F]FDG were also observed regarding the tracer uptake patterns in tumour lesions. Whereas for [¹⁸F]FDG, predominantly the lesion center shows increased glucose metabolism PET-positive lesions, uptake of [⁶⁸Ga]Ga-DATA^{5m}.SA.FAPi was more often evident in the lesion periphery (a representative example is shown in Fig. 4, middle column). Wikberg et al. made a similar observation in tissue samples of colorectal cancer, describing a more pronounced FAP expression in the tumour front compared to the tumour center [6].

Overall, [¹⁸F]FDG and [⁶⁸Ga]Ga-DATA^{5m}.SA.FAPi seem to deliver a different quality of information in patients with NET, which is corroborated by the observation that there is only a weak correlation between FAP_{iSUVmax} and FDG_{SUVmax}, no correlation between FAP_{iTF} and FDG_{TF} and the obvious differences in visual uptake patterns of the two tracers.

There are limitations to our study. Though we obtained first results that the ratio FAP_{iVOL}:DOTATOC_{VOL} might enable prediction of Ki-67 in liver metastases of patients with NET, due to the currently limited number of patients in our analysis, it is too early to draw a definite conclusion. Further data is needed in a higher number of patients and including prognostic clinical information. Due to the mostly slow course of the disease in patients with NET, sufficient survival data is not yet available in our patient collective. The prognostic significance of FAP_{iVOL}:DOTATOC_{VOL} regarding progression free survival and overall survival needs to be evaluated in future studies in comparison to [¹⁸F]FDG-based parameters.

Due to the retrospective nature of our study, biopsy locations for assessment of Ki-67 were heterogeneous (liver metastases and primary tumours) and in some cases, biopsies were not performed in our institution. This also prevents correlation of Ki-67 with SUV at the exact site of biopsy in our patient collective.

Most of the patients in our collective received ongoing biotherapy with long-acting somatostatin analogs. It is currently unknown whether ongoing biotherapy or other previous therapy modalities may affect FAP expression or uptake of [⁶⁸Ga]Ga-DATA^{5m}.SA.FAPi.

For this initial study, we put the focus on liver metastases, as coregistration of PET data obtained at three different time points is feasible in the liver, while other sites of metastases, especially mesenteric lymph nodes and bone metastases are prone to errors due to misregistration using rigid coregistration methods. Furthermore, the liver is a common site of metastatic spread of advanced NET and liver metastases are a typical target for re-assessment of Ki-67 in patients with suspicion of dedifferentiation.

Lastly, the safety and effectiveness of [⁶⁸Ga]Ga-DATA^{5m}.SA.FAPi for imaging of fibroblast activation has not been evaluated so far and needs to be tested in future studies.

Conclusion

We found that the [⁶⁸Ga]Ga-DATA^{5m}.SA.FAPi-positive tumour fraction in liver metastases shows a strong correlation with Ki-67 in patients with metastasized NET. The ratio FAPi_{VOL}:DOTATOC_{VOL} correlates with Ki-67 with a high correlation coefficient and might serve as a clinical parameter for the assessment of dedifferentiation and aggressiveness of liver metastases in NET patients with clinical suspicion of dedifferentiation. [⁶⁸Ga]Ga-DATA^{5m}.SA.FAPi PET/CT holds potential for identification of high-risk patients with dedifferentiated tumour portions who might benefit from histological re-assessment of Ki-67 to guide therapy decisions.

Declarations

Conflict of Interest: Financial interests: ■■■ is a consultant for Bayer Healthcare (Leverkusen, Germany) and Eisai GmbH (Frankfurt, Germany). ■■■ has received speaker honorarium from Mediso Medical Imaging Systems Ltd., (Budapest, Hungary). ■■■ is a consultant to Bayer, Novartis, Eisai and Ipsen. Non-financial interests: ■■■ has a non-commercial research agreement with Mediso Medical Imaging Systems Ltd., (Budapest, Hungary). Funding: The authors did not receive support from any organization for the submitted work.

References

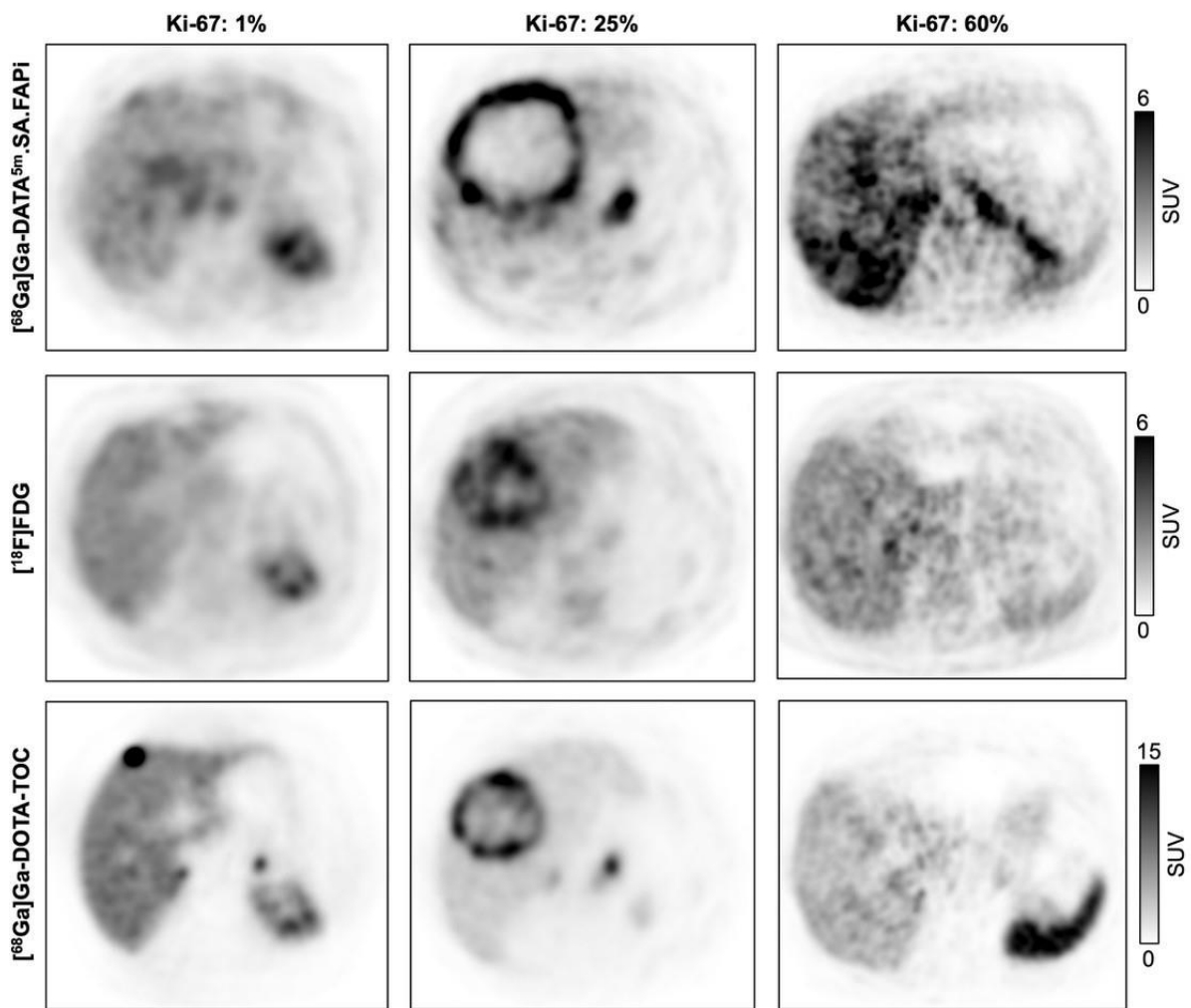
1. Pavel, M.; Öberg, K.; Falconi, M.; Krenning, E.P.; Sundin, A.; Perren, A.; Berruti, A. Gastroenteropancreatic neuroendocrine neoplasms: ESMO Clinical Practice Guidelines for diagnosis, treatment and follow-up. *Ann. Oncol.* **2020**, *31*, 844–860, doi:10.1016/j.annonc.2020.03.304.
2. Carideo, L.; Prospero, D.; Panzuto, F.; Magi, L.; Pratesi, M.S.; Rinzivillo, M.; Annibale, B.; Signore, A. Role of combined [⁶⁸Ga]Ga-DOTA-SST analogues and [¹⁸F]FDG PET/CT in the management of GEP-NENs: A systematic review. *J. Clin. Med.* **2019**, *8*, 1032, doi:10.3390/jcm8071032.
3. Barrio, M.; Czernin, J.; Fanti, S.; Ambrosini, V.; Binse, I.; Du, L.; Eiber, M.; Herrmann, K.; Fendler, W.P. The impact of somatostatin receptor-directed PET/CT on the management of patients with neuroendocrine tumor: A systematic review and meta-analysis. *J. Nucl. Med.* **2017**, *58*, 756–761, doi:10.2967/jnumed.116.185587.
4. Laskaratos, F.M.; Rombouts, K.; Caplin, M.; Toumpanakis, C.; Thirlwell, C.; Mandair, D. Neuroendocrine tumors and fibrosis: An unsolved mystery? *Cancer* **2017**, *123*, 4770–4790, doi:10.1002/cncr.31079.
5. Loktev, A.; Lindner, T.; Mier, W.; Debus, J.; Altmann, A.; Jaeger, D.; Giesel, F.; Kratochwil, C.; Barthe, P.; Roumestand, C.; Haberkorn, U. A Tumor-Imaging Method Targeting Cancer-Associated Fibroblasts. *J. Nucl. Med.* **2018**, *59*, 1423–1429, doi:10.2967/jnumed.118.210435.
6. Wikberg, M.L.; Edin, S.; Lundberg, I. V.; Van Guelpen, B.; Dahlin, A.M.; Rutegård, J.; Stenling, R.; Öberg, Å.; Palmqvist, R. High intratumoral expression of fibroblast activation protein (FAP) in colon cancer is associated with poorer patient prognosis. *Tumor Biol.* **2013**, *34*, 1013–1020, doi:10.1007/s13277-012-0638-2.
7. Henry, L.R.; Lee, H.O.; Lee, J.S.; Klein-Szanto, A.; Watts, P.; Ross, E.A.; Chen, W.T.; Cheng, J.D. Clinical implications of fibroblast activation protein in patients with colon cancer. *Clin. Cancer Res.* **2007**, *13*, 1736–1741, doi:10.1158/1078-0432.CCR-06-1746.
8. Saigusa, S.; Toiyama, Y.; Tanaka, K.; Yokoe, T.; Okugawa, Y.; Fujikawa, H.; Matsusita, K.; Kawamura, M.; Inoue, Y.; Miki, C.; et al. Cancer-associated fibroblasts correlate with poor prognosis in rectal cancer after chemoradiotherapy. *Int. J. Oncol.* **2011**, *38*, 655–663, doi:10.3892/ijo.2011.906.
9. Li, M.; Cheng, X.; Rong, R.; Gao, Y.; Tang, X.; Chen, Y. High expression of fibroblast activation protein (FAP) predicts poor outcome in high-grade serous ovarian cancer. *BMC Cancer* **2020**, *20*, 1032, doi:10.1186/s12885-020-07541-6.
10. Coto-Llerena, M.; Ercan, C.; Kancherla, V.; Taha-Mehlitz, S.; Eppenberger-Castori, S.; Soysal, S.D.; Ng, C.K.Y.; Bolli, M.; von Flüe, M.; Nicolas, G.P.; et al. High expression of FAP in colorectal cancer is associated with angiogenesis and immunoregulation processes. *Front. Oncol.* **2020**, *10*, 979, doi:10.3389/fonc.2020.00979.
11. Solano-Iturri, J.D.; Beitia, M.; Errarte, P.; Calvete-Candenas, J.; Etxezarraga, M.C.; Loizate, A.; Echevarria, E.; Badiola, I.; Larrinaga, G. Altered expression of fibroblast activation protein- α (FAP) in colorectal adenoma-carcinoma sequence and in lymph node and liver metastases. *Aging* **2020**, *12*, 10337–10358, doi:10.18632/aging.103261.
12. Kratochwil, C.; Flechsig, P.; Lindner, T.; Abderrahim, L.; Altmann, A.; Mier, W.; Adeberg, S.; Rathke, H.; Röhrich, M.; Winter, H.; et al. ⁶⁸Ga-FAPI PET/CT: Tracer uptake in 28 different kinds

- of cancer. *J. Nucl. Med.* **2019**, *60*, 801–805, doi:10.2967/jnumed.119.227967.
13. Kreppel, B.; Gärtner, F.C.; Marinova, M.; Attenberger, U.; Meisenheimer, M.; Toma, M.; Kristiansen, G.; Feldmann, G.; Moon, E.S.; Roesch, F.; et al. [⁶⁸Ga]Ga-DATA^{5m}.SA.FAPi PET/CT: Specific tracer-uptake in focal nodular hyperplasia and potential role in liver tumor imaging. *Nuklearmedizin* **2020**, *59*, 387–389, doi:10.1055/a-1164-5667.
 14. Gaertner, F.C.; Plum, T.; Kreppel, B.; Eppard, E.; Meisenheimer, M.; Strunk, H.; Bundschuh, R.A.; Sinnes, J.P.; Rösch, F.; Essler, M. Clinical evaluation of [⁶⁸Ga]Ga-DATA-TOC in comparison to [⁶⁸Ga]Ga-DOTA-TOC in patients with neuroendocrine tumours. *Nucl. Med. Biol.* **2019**, *76–77*, 1–9, doi:10.1016/j.nucmedbio.2019.08.006.
 15. Singh, S.; Hallet, J.; Rowsell, C.; Law, C.H.L. Variability of Ki67 labeling index in multiple neuroendocrine tumors specimens over the course of the disease. *Eur. J. Surg. Oncol.* **2014**, *40*, 1517–1522, doi:10.1016/j.ejso.2014.06.016.
 16. Shi, H.; Zhang, Q.; Han, C.; Zhen, D.; Lin, R. Variability of the Ki-67 proliferation index in gastroenteropancreatic neuroendocrine neoplasms - a single-center retrospective study. *BMC Endocr. Disord.* **2018**, *18*, 51, doi:10.1186/s12902-018-0274-y.
 17. Ezziddin, S.; Adler, L.; Sabet, A.; Pöppel, T.D.; Grabellus, F.; Yüce, A.; Fischer, H.P.; Simon, B.; Höller, T.; Biersack, H.J.; et al. Prognostic stratification of metastatic gastroenteropancreatic neuroendocrine neoplasms by ¹⁸F-FDG PET: Feasibility of a metabolic grading system. *J. Nucl. Med.* **2014**, *55*, 1260–1266, doi:10.2967/jnumed.114.137166.
 18. Panagiotidis, E.; Alshammari, A.; Michopoulou, S.; Skoura, E.; Naik, K.; Maragkoudakis, E.; Mohmaduvesh, M.; Al-Harbi, M.; Belda, M.; Caplin, M.E.; et al. Comparison of the impact of ⁶⁸Ga-DOTATATE and ¹⁸F-FDG PET/CT on clinical management in patients with neuroendocrine tumors. *J. Nucl. Med.* **2017**, *58*, 91–96, doi:10.2967/jnumed.116.178095.
 19. Chan, D.L.H.; Pavlakis, N.; Schembri, G.P.; Bernard, E.J.; Hsiao, E.; Hayes, A.; Barnes, T.; Diakos, C.; Khasraw, M.; Samra, J.; et al. Dual somatostatin receptor/FDG PET/CT imaging in metastatic neuroendocrine tumours: Proposal for a novel grading scheme with prognostic significance. *Theranostics* **2017**, *7*, 1149–1158, doi:10.7150/thno.18068.
 20. Gress, T.M.; Albert, J.; Alfke, H.; Amthauer, H.; Anlauf, M.; Arnold, R.; Baum, R.; Denecke, T.; Ezziddin, S.; Fendrich, V.; et al. Practice guideline neuroendocrine tumors: AWMF-Reg021-27. *Z. Gastroenterol.* **2018**, *56*, 583–681, doi:10.1055/a-0604-2924.
 21. Zaknun, J.J.; Bodei, L.; Mueller-Brand, J.; Pavel, M.E.; Baum, R.P.; Hörsch, D.; O’Dorisio, M.S.; O’Dorisio, T.M.; Howe, J.R.; Cremonesi, M.; et al. The joint IAEA, EANM, and SNMMI practical guidance on peptide receptor radionuclide therapy (PRRT) in neuroendocrine tumours. *Eur. J. Nucl. Med. Mol. Imaging* **2013**, *40*, 800–816, doi:10.1007/s00259-012-2330-6.
 22. Ezziddin, S.; Opitz, M.; Attassi, M.; Biermann, K.; Sabet, A.; Guhlke, S.; Brockmann, H.; Willinek, W.; Wardelmann, E.; Biersack, H.-J.; et al. Impact of the Ki-67 proliferation index on response to peptide receptor radionuclide therapy. *Eur. J. Nucl. Med. Mol. Imaging* **2011**, *38*, 459–466, doi:10.1007/s00259-010-1610-2.
 23. Sorbye, H.; Welin, S.; Langer, S.W.; Vestermark, L.W.; Holt, N.; Osterlund, P.; Dueland, S.; Hofsl, E.; Guren, M.G.; Ohrling, K.; et al. Predictive and prognostic factors for treatment and survival in 305 patients with advanced gastrointestinal neuroendocrine carcinoma (WHO G3): The NORDIC NEC study. *Ann. Oncol.* **2013**, *24*, 152–160, doi:10.1093/annonc/mds276.
 24. Rinke, A.; Gress, T.M. Neuroendocrine cancer, therapeutic strategies in G3 cancers. *Digestion* **2017**, *95*, 109–114, doi:10.1159/000454761.
 25. Altmann, A.; Haberkorn, U.; Siveke, J. The latest developments in imaging of fibroblast

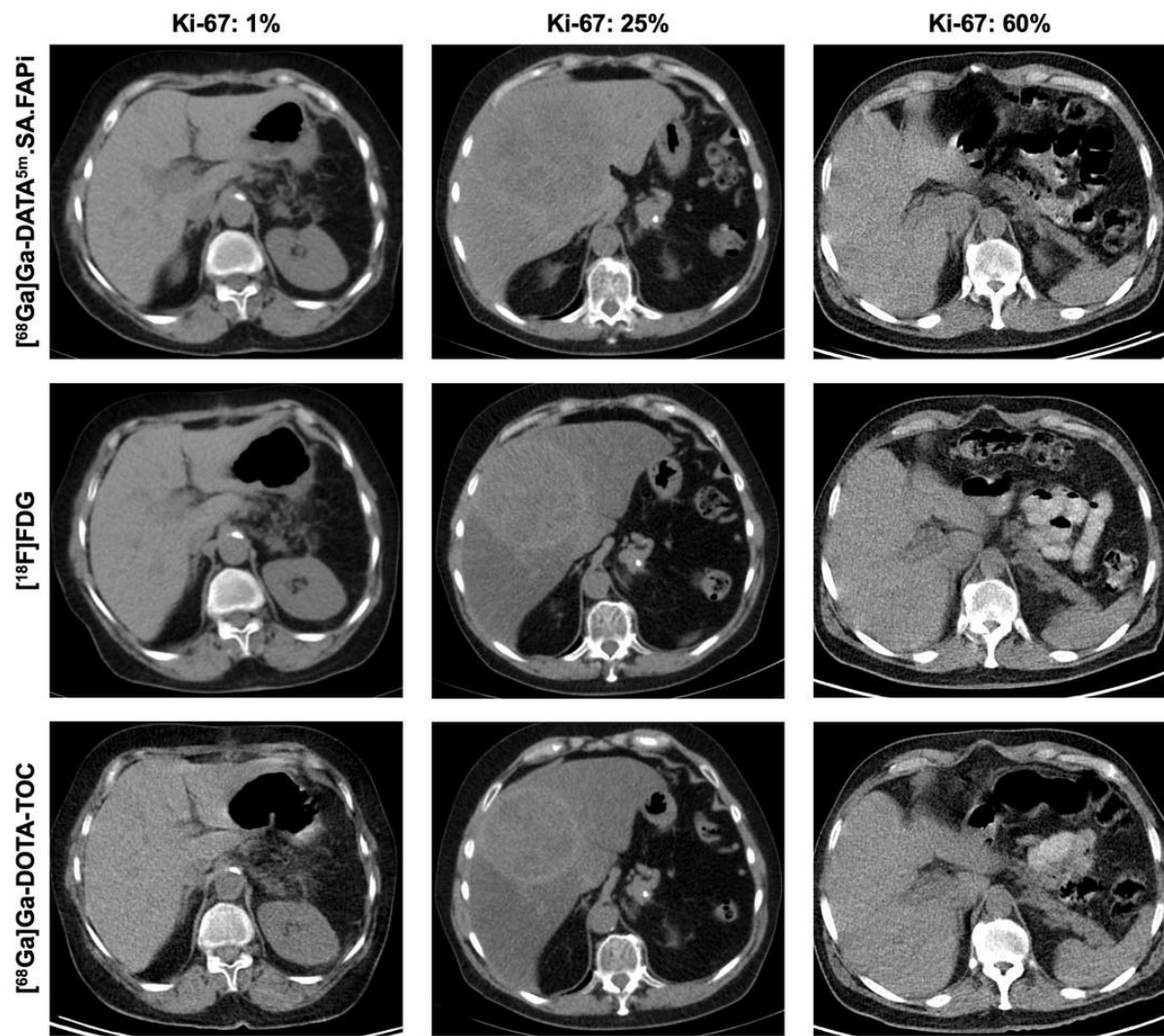
activation protein. *J. Nucl. Med.* **2021**, *62*, 160–167, doi:10.2967/jnumed.120.244806.

26. Hicks, R.J.; Roselt, P.J.; Kallur, K.G.; Tothill, R.W.; Mileskin, L. FAPI PET/CT: Will It End the Hegemony of ¹⁸F-FDG in Oncology? *J. Nucl. Med.* **2021**, *62*, 296–302, doi:10.2967/jnumed.120.256271.

Supporting Information



Supplemental fig. S1 Non-fused PET images corresponding to the fused images on fig. 4.



Supplemental fig. S2 Non-fused CT images corresponding to the fused images on fig. 4.

A.3. Biodistribution, pharmacokinetics, dosimetry of [⁶⁸Ga]Ga-DOTA.SA.FAPi and the head-to-head comparison with [¹⁸F]F-FDG PET/CT in patients with various cancers

Veröffentlicht in *European Journal of Nuclear Medicine and Molecular Imaging* **2021**, *48*, 1915–1931.

mit Genehmigung von © Springer Nature Switzerland AG, Springer Nature

Biodistribution, pharmacokinetics, dosimetry of [⁶⁸Ga]Ga-DOTA.SA.FAPi and the head-to-head comparison with [¹⁸F]F-FDG PET/CT in patients with various cancers

[REDACTED] Euy Sung Moon², [REDACTED]
[REDACTED]
[REDACTED]

¹ Department of Nuclear Medicine, AIIMS, Ansari Nagar, New Delhi, India

² Department of Chemistry, Johannes Gutenberg University, Mainz, Germany

³ PositronPharma SA, Santiago, Chile

Authors contributed equally

*Corresponding author: [REDACTED]

Abstract

Purpose: [⁶⁸Ga]Ga-labelled fibroblast-activation-protein inhibitors ([⁶⁸Ga]Ga-FAPi) have shown promising preclinical and clinical results in PET imaging. The present study aimed to evaluate the biodistribution, pharmacokinetics, dosimetry of [⁶⁸Ga]Ga-DOTA.SA.FAPi, another modified FAPi tracer, and performed a head-to-head comparison with [¹⁸F]F-FDG PET/CT scans in patients with various cancers.

Methods: In this prospective study, patients underwent both [¹⁸F]F-FDG and [⁶⁸Ga]Ga-DOTA.SA.FAPi PET/CT scans 60 minutes post-injection (p.i.). Dosimetry studies were conducted in three patients using [⁶⁸Ga]Ga-DOTA.SA.FAPi serial time-point imaging. The absorbed dose was calculated using OLINDA/EXM 2.2 software. Quantification of the uptake of the tracers were assessed using standardized uptake values corrected for lean body mass (SUL).

Results: Fifty-four patients (mean age; 48.4 years) with 14 types of cancers involving 37% breast, 24% lung, 7.4% head and neck (H&N), and remaining 31.6% patients with other histologies were evaluated prospectively. Physiological uptake of [⁶⁸Ga]Ga-DOTA.SA.FAPi were observed in the liver, kidneys, pancreas, heart contents, and to a lesser extent in the lacrimals, oral mucosa, salivary glands, and thyroid glands. Uptake in the target lesions on [⁶⁸Ga]Ga-DOTA.SA.FAPi scan was initiated at 10 minutes, and no additional lesions were detected in the delayed acquisition time-points. Pancreas was the organ with the highest absorbed dose (5.46E-02 mSv/MBq). While, patient-based comparison between the radiotracers revealed complete concordance in the detection of primary, pleural thickening, bone and liver metastases, and second primary malignancy, discordant findings were observed in the detection of lymph node (7.5%), lung nodules (5.6%), and brain metastases (2%). According to the site of primary disease, patients with H&N cancers demonstrated the highest SULpeak and average (avg) values on [⁶⁸Ga]Ga-DOTA.SAFAPi which was similar to the values of [¹⁸F]F-FDG [(SULpeak:15.4 vs. 14.2; P-0.680) (SULavg: 8.3 vs. 7.9; P-0.783)]. The lowest uptake was observed in lung cancers with both the radiotracers [(SULpeak: 5.8 vs. 7.4; P-0.238) (SULavg: 4.9 vs. 5.3; P-0.313)]. A significantly higher SULpeak and SULavg for brain metastases to normal brain parenchyma ratios were observed on [⁶⁸Ga]Ga-DOTA.SA.FAPi in contrast to the [¹⁸F]F-FDG values {SULpeak: median: 59.3 (IQR: 33.5 – 130.8) versus 1.5 (1 – 2.3); P-0.028}. Except for brain metastases, comparable SULpeak and average values were noted between the radiotracers in all other regions of metastases with no significant difference.

Conclusion: [⁶⁸Ga]Ga-DOTA.SA.FAPi is a promising alternative among the FAPI class of molecules and performed well as compared to standard-of-care radiotracer [¹⁸F]F-FDG in the diagnosis of various cancers.

Keywords: [⁶⁸Ga]Ga-DOTA.SA.FAPi PET/CT; Biodistribution; Dosimetry; Pharmacokinetics; Diagnosis

Introduction

To date, [¹⁸F]F-FDG PET/CT is the standard-of-care imaging modality in diagnosing various cancers and is based on the principle of the Warburg effect [1]. However, FDG has its own limitations such as low specificity, inability to detect small volume tumors, or lack of uptake in certain cancers, namely mucin-secreting epithelial malignancies, lepidic adenocarcinomas, well-differentiated neuroendocrine tumors, well-differentiated endocrine gland malignancies, etc. [2,3].

Currently, unlike [¹⁸F]-FDG, which is a non-specific metabolic tracer, targeted molecular imaging is experiencing a paradigm shift towards more specific radiotracer imaging. This receptor-specific targeted approach enables the practice of theranostics and likely to achieve the 'hallowed goal' of precision oncology. Imaging the tumor microenvironment beyond the glucose or amino acid or fatty acid metabolism is a new norm for understanding the in vivo tumor biology and probably, translating it to clinical oncology practice.

An in-depth understanding of the tumor microenvironment [4] leads to a new player, namely cancer-associated fibroblasts (CAFs). These CAFs are involved in producing growth factors that promote tumor growth, upregulate angiogenesis, mobilize pro-tumorigenic cells, promote immunosuppression and invasion. Fibroblast activation protein (FAP) is a growth factor that selectively overexpressed by CAFs and pericytes rather than the tumor cells in more than 90% of the human epithelial malignancies [5]. FAP α is a type II transmembrane glycoprotein that belongs to the superfamily of serine protease; consisting of a primary chain of 760 amino acids with a small intracellular component or a short cytoplasmic tail (6 amino acids), a transmembrane component (19 amino acids) and a large extracellular component [6]. The monomeric form of FAP α is inactive and is activated by dimerization, either homodimer FAP α /FAP α or heterodimer FAP α /FAP β . This membrane-bound protein is one of the crucial components of the extracellular matrix (ECM) and modulates or remodels the tumor microenvironment.

Fibroblast activating protein inhibitor (FAPi) is a class of biologic probes just at the verge of exploration. The enzymatic activity of FAP provides a therapeutic target in a variety of human malignancies. Therefore, it is an important development for selecting FAP inhibitors (FAPi) in targeting FAP overexpression by CAFs [7].

Based on the concept of a quinoline-based FAP-specific inhibitor(4-Quinolinoyl)glycyl-2-cyano-4,4-difluoropyrrolidine, referred to as UAMC1110, [8]; currently, a new class of molecules such as FAPI-02 [9,10], FAPI-04 [9,10], FAPI-46 [11] and other inhibitory-ligands are designed, synthesized and

evaluated both preclinically and clinically. These imaging probes are highly promising molecular targets when labelled with gallium-68 [9–12] because, the biological half-life of these probes is suitably matched with physical half-life of gallium-68. However, for therapeutic applications, whether with Lu-177 or Ac-225, the biological half-life of these above-mentioned probes are not suitable. The search is ongoing to have a molecule that will be true both for imaging and therapy.

Recently, another novel FAP inhibitor (Figure 1), with further improvised structural changes based on the introduction of squaric acid (SA) motif, namely ^{68}Ga -labelled-DOTA.SA.FAPi, has been introduced and evaluated in animal models [13].

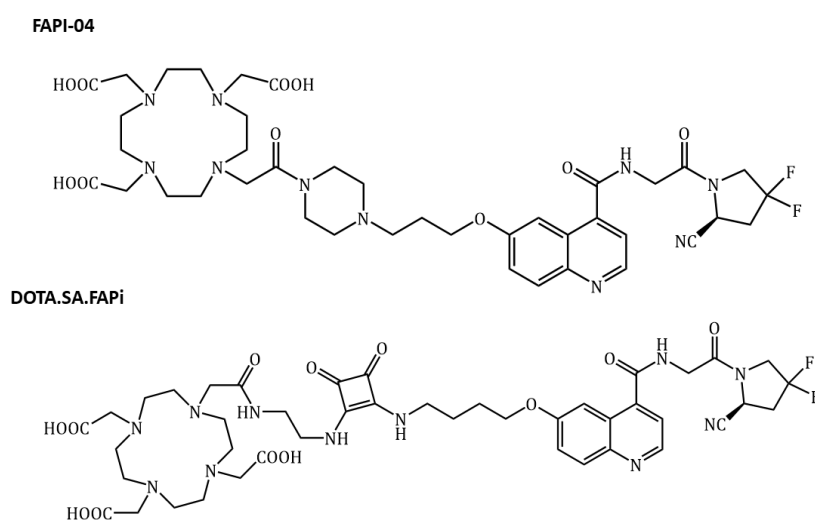


Figure 1: Molecular structure of FAPI-04 and DOTA.SA.FAPi.

The simple coupling chemistry of squaric acid motif increases the biological half-life of the probe which has been shown by our group in an animal study and in theranostic applications [13]. The preclinical data on ^{68}Ga -DOTA.SA.FAPi and ^{177}Lu -DOTA.SA.FAPi has been studied in an HT-29 human colorectal cancer xenograft mouse model and reveals encouraging results with high target-to-background ratios (TBR), longer biological half-life, and improved pharmacokinetic properties have been reported. The in vitro binding affinities, excellent in vivo, and ex vivo data are already published [13].

Additionally, DOTA.SA.FAPi demonstrates higher tumor-to-background ratios, and the macrocyclic bifunctional DOTA chelator facilitates radiolabelling with both gallium-68 and lutetium-177/yttrium-90/bismuth-213/actinium-225 which makes the DOTA.SA.FAPi molecule promising and applicable to both imaging and therapy. As a proof-of-principle, our group has applied a theranostic concept of ^{68}Ga -guided ^{177}Lu -DOTA.SA.FAPi therapy in an advanced-stage breast cancer patient who was

refractory all lines of treatment. The patient experienced immediate relief in pain and improvement in the quality of life. This radio-ligand therapy concept is adding a new milestone in precision oncology. However, the findings are preliminary, and the detailed pharmacokinetics and dosimetry data are evolving [14].

To the best of our knowledge, there is no large scale published human data on the biodistribution and pharmacokinetics of [⁶⁸Ga]Ga-DOTA.SA.FAPi. Hence, in this collaborative study, we have attempted to assess the biodistribution, pharmacokinetics, dosimetry, and the diagnostic value of [⁶⁸Ga]Ga-DOTA.SA.FAPi PET/CT, and head-to-head compared with the standard of the care imaging agent, namely the [¹⁸F]F-FDG PET/CT in patients having various cancers.

Methodology

Patient Recruitment

This prospective study was approved by the Ethics Committee of All India Institute of Medical Sciences (IECPG-22/2020) and was conducted between January 2020 and September 2020.

Patient Selection

The patients were scrutinized using the following eligibility criteria: age >18 years, histologically confirmed cases of any carcinoma or unknown primary with histological confirmation after PET/CT scans, patients referred to the Nuclear Medicine Department for both [¹⁸F]F-FDG and [⁶⁸Ga]Ga-DOTA.SA.FAPi PET/CT scans and were willing to give written informed consent to participate in this study were included. Exclusion criteria involved patients who denied to undergo [⁶⁸Ga]Ga-DOTA.SA.FAPi PET/CT imaging, pregnant and lactating females. Based on the above criteria, 54 patients were included in this study.

Synthesis of [⁶⁸Ga]Ga-DOTA.SA.FAPi

The DOTA.SA.FAPi molecule was synthesized by Moon et al. [13] under the supervision of Prof. Dr. F. Roesch from the Department of Chemistry, Johannes Gutenberg University of Mainz, Germany, and procured as a part of a collaborative project with Prof. Dr. C. S. Bal, AIIMS, New Delhi, India. The eluted ⁶⁸GaCl₃ solution (~925 MBq) was added to the reaction vial containing DOTA.SA.FAPi and ammonium

acetate and heated at 95 °C for 20 minutes. The radiolabelled product was eluted through a Sepak C18 cartridge with 50% ethanol followed by 10 ml normal saline. Quality control of the labelled product was performed by high-performance liquid chromatography (Radio-HPLC) and radiochemical purity of > 94% was accepted for patient injection.

Image Acquisition and Analysis

All the cans were acquired on a dedicated GE Discovery 710* 128 Slice PET/CT Scanner, with a 40-mm detector at 0.35sec rotation speed and 128 slice CT scanner. The images were corrected for random and scatter counts, decay correction, and dead time correction. The PET images were reconstructed with iterative reconstruction using ordered subset expectation maximization algorithm (OSEM) (21 subsets 3 iterations). The images were processed and analyzed with a dedicated commercially available workstation (GE Xeleris).

Image Acquisition and Analysis for Dosimetry

Acquisition Protocol

Three patients took part in the dosimetry study. As a prerequisite for imaging, the patient was instructed to void before the [⁶⁸Ga]Ga-DOTA.SA.FAPi injection. Following the administration of [⁶⁸Ga]Ga-DOTA.SA.FAPi (mean injected activity: 174 MBq), serial whole-body PET studies were acquired at 0.16, 1, 2, and 3 h post-injection (p.i.). For acquisition, the patient was positioned in a supine position. The acquisition protocol constituted an initial scout image to define the field of view of the acquisition required, followed by a CT scan, and PET acquired at 2 minutes per bed. A total of two CT scans were acquired for 4 PET image acquisitions. The first CT involved a diagnostic dose CT with 300–350 mAs, 120kVp, slice thickness-5 mm, pitch 1. The second CT scan was used only for attenuation correction purposes, which included a low-dose CT protocol of 180mAs, 80kVp, 5 mm slice thickness, and pitch 1.

Image Analysis

Source organs for analysis included pancreas, kidneys, liver, spleen, heart contents, L2–L4 lumbar vertebrae for red marrow dosimetry, and urinary bladder and its contents. To analyze the absorbed dose, the first step involved the region of interest (ROI) analysis of the above organs. The ROIs for the

above organs were drawn on the initial [⁶⁸Ga]Ga-DOTA.SA.FAPi PET/CT scan (0.16 h) and was appended/cloned to the consecutive sequential time points.

Three-dimensional (3D) ROIs, rectangular, elliptical or freehand ROIs were chosen according to the shape of the organ. For organs like the liver and spleen, to prevent to spill-in of activity from the kidneys and other adjacent organs, a two-dimensional ROI was drawn on one slice and stacked to all the slice base on the CT anatomy to deduce the 3D volume. The activity concentration in all the organs was assumed uniform and hence, were derived in the form of Bq/cm³. The activity per centimeter cube was multiplied by the total mass of the corresponding organ. The mass of various source organs was adopted from the anthropomorphic phantom data reported in the Annals of ICRP 89 [15].

Calculation of percentage of injected activity, residence times, and the mean absorbed dose

The ratio of mean activity in a source organ to the injected activity multiplied by 100 was defined as the percentage of injected activity (%IA). OLINDA/EXM 2.2 dosimetric software was used to calculate the residence times/number of disintegrations of each source organ. The %IA at time points 0.16, 1, 2, and 3 h for each source organ were entered in the kinetic input model of OLINDA/EXM 1.0, and the mono or biexponential curve fitting parameters were applied to derive the best curve fit for the residence time of activity in the source organ. As the blood sampling method was not a feasible option in the heavily pre-treated chemotherapy patients, red bone marrow dosimetry was done by image-based 3D volumetric analysis of L2–L4 vertebrae, which is considered to constitute 6.7% of the total bone marrow [16].

The patient was instructed to urinate just before the injection of [⁶⁸Ga]Ga-DOTA.SA.FAPi and advised not to void during the serial dosimetric acquisition of PET/CT images. It was to prevent any biologic mode of excretion of tracer from the body and to assume only physical decay of activity.

Once all the organ residence times were derived from the kinetic input model, they were entered in the adult female model data that derived the absorbed doses to all the organs, including the whole-body effective dose, and generated in mSv/MBq and rem/mCi. The time-activity graphs of various organs were generated using GraphPad Prism software.

Image Acquisition and Analysis for [¹⁸F]F-FDG and [⁶⁸Ga]Ga-DOTA.SA.FAPi PET/CT Qualitative and Quantitative Comparison

Fifty-four patients underwent [¹⁸F]F-FDG and [⁶⁸Ga]Ga-DOTA.SA.FAPi PET/CT for biodistribution and a head-to-head intra-individual comparison between the traces.

Acquisition Protocol

While, for [¹⁸F]F-FDG PET/CT, patients were advised to fast for at least 4-6 hours prior to injection, no such preparation was required for a [⁶⁸Ga]Ga-DOTA.SA.FAPi scan. The mean injected activities were 271 MBq (range: 185 MBq to 370 MBq) and 144.3 MBq (range; 59.2 to 296 MBq), for [¹⁸F]F-FDG, and [⁶⁸Ga]Ga-DOTA.SA.FAPi radiotracers, respectively. Patients underwent [⁶⁸Ga]Ga-DOTA.SA.FAPi PET/CT scans within a one-week interval of [¹⁸F]F-FDG PET/CT. The same parameters for acquisition were followed as stated above in the dosimetry acquisition section but were acquired only approximately at 1 h p.i. using diagnostic CT parameters. Spot views were acquired for brain metastases patients with a slice thickness of 3mm on CT at 120 kVp, 100 mAs, and a pitch of 0.6.

Image Analysis

[¹⁸F]F-FDG and [⁶⁸Ga]Ga-DOTA.SA.FAPi PET/CT scans were loaded simultaneously and co-registered using carina as anatomical landmark registration technique. Scan interpretations was conducted by 2 experienced Nuclear Medicine physicians. Any disagreement in the reports was reviewed by a third observer.

Qualitative analysis

Qualitative interpretations of both the scans were made to compare the visual expression and the concordance of the uptake between the tracers. The uptake in both the tracers was finally matched to the corresponding lesion morphology on CT. Any discordance was reconfirmed either by histopathological correlation or by MR imaging. Disease foci were divided into four anatomical sites: local disease (primary/residual tumor), nodal metastases, distant metastases (pulmonary, skeletal, liver, brain, etc.), and other metastatic or malignant sites not known earlier (new site).

Quantitative Analysis

For the quantitative comparison, ROIs were drawn according to the PET Response Criteria in Solid Tumors (PERCIST 1.0) [17]. The ROI for various organs and lesions were drawn on [¹⁸F]F-FDG PET/CT scan and cloned on to the [⁶⁸Ga]Ga-DOTA.SA.FAPi PET/CT scan. The ROIs were presented as standardized uptake value (SUV) corrected for lean body mass, SULpeak, and SULavg to quantitatively compare the uptake in the normal organs and cancer involved regions.

To calculate the SUL in normal organs, ROIs of 1.2 cm were drawn in order to produce a 1cm³ volume in the mediastinal blood pool, pancreas, left psoas major muscle, myocardium, spleen, salivary glands, thyroid, duodenum, normal parenchyma of the brain and spherical ROIs of 3 cm diameter were drawn in the right lobe of the liver. To compare the uptake in the lesions, a 3D auto contour ROI at a 40% threshold of SULpeak was carefully drawn around the site of [¹⁸F]F-FDG/[⁶⁸Ga]Ga-DOTA.SA.FAPi expressing lesions. TBRs were also calculated according to the site of the lesion and with various combination of backgrounds such as liver, spleen, pancreas, blood pool and muscle uptake.

Statistical analysis

The data were analyzed for the normality using D'Agostino-Pearson Test. Mean, median, standard deviation (SD), range, and interquartile range (IQR) were calculated for all continuous variables based on the distribution of data. The analysis was done on an intra-individual basis. The concordance and discordance were presented in the form of a percentage. Weighted kappa statistics were used to assess the level of agreement between the two observers in assessing the [⁶⁸Ga]Ga-DOTA.SA.FAPi PET/CT scan. It was calculated as follows: $(PO - Pe)/(1 - Pe)$, where PO is the observed agreement, Pe is the agreement by chance, and $(1 - Pe)$ is the proportion of the cases for which would predict disagreement between the raters. Kappa values <0.4 meant poor agreement, values between 0.4 and 0.75 indicate fair to good agreement, and values of 0.75 and higher represent excellent agreement [18]. Paired Student's t-test or Wilcoxon signed-rank test was used to compare the organ and lesion uptake values between and [¹⁸F]F-FDG and [⁶⁸Ga]Ga-DOTA.SA.FAPi PET/CT scans. P-value < 0.05 was considered statistically significant. Statistical analysis was performed using MedCalc statistical software.

Results

Patients

The detailed clinical history and extent of cancer spread of 54 patients (mean age; 48.4 ± 12.4 , 19 – 72 years) are depicted in Table 1.

Across the patients referred, three had unknown primaries that were diagnosed on both [^{18}F]F-FDG and [^{68}Ga]Ga-DOTA.SA.FAPi PET/CT and later confirmed on histopathology as infiltrating duct carcinoma of the breast, squamous cell carcinoma (SCC) of the base of the tongue, and SCC of the neck, respectively.

Among the various primary malignancies, breast cancer (37%, 20/54) followed by lung cancer (24%, 13/54) constituted the major sub-categories of the patients included (Table 1). The [^{68}Ga]Ga-DOTA.SA.FAPi injection was well-tolerated, and no adverse events were observed throughout the scanning procedure.

Table 1: Detailed demographics and extent of disease of patients

Patient No	Age/ Gender	Type of cancer	Extent of cancer
1	48/M	Olfactory neuroblastoma	Primary
2	25/M	Colon cancer	Primary, lymph node
3	48/F	Right Breast cancer ER +, PR +, Her2neu -	Liver, lung, brain
4	72/M	Pleural mesothelioma	Primary, lymph node, pleural thickening
5	40/F	Adenoid cystic carcinoma of liver	Primary, lymph node
6	65/M	Non-small cell lung cancer	Primary, lymph node
7	32/F	Right breast cancer ER+, PR+, Her2neu -	Lymph node, liver, skeletal
8	66/F	Breast cancer, triple negative	Lymph node, lung,
9	45/M	Left buccal mucosa squamous cell carcinoma	Primary, lymph node
10	45/F	Colon cancer	Primary, lymph node, lung
11	63/F	Rectal cancer	Krukenberg metastases
12	48/F	Right breast Cancer, ER+ PR+Her2neu -	Liver, lung, brain, pleural thickening, stomach second primary
13	41/F	Left breast Cancer, TNBC	Liver, skeletal, Krukenberg metastases
14	37/F	Gallbladder cancer	Primary
15	50/F	Right breast Cancer, ER+, PR+, Her2neu-	Primary, Lung, skeletal
16	56/F	Bilateral breast cancer, ER- PR - Her2neu +	Lymph node, brain
17	54/F	Left breast cancer, ER+, PR+, Her2neu-	Lymph node, skeletal, brain
18	30/F	Bilateral breast cancer ER-, PR-, Her2neu+	Primary, lymph nodes, lung, skeletal, liver, brain
19	45/F	Right breast cancer ER-, PR-, Her2neu+	Primary, lymph nodes, lung, liver
20	43/F	Non-small cell lung cancer	Primary, lymph nodes, lung, pleural thickening
21	45/F	Breast cancer, ER- PR- Her2neu+ Invasive ductal carcinoma	Primary, lymph node, lung, liver
22	38/F	Left breast cancer, TNBC, invasive ductal carcinoma	Primary, lymph node, lung
23	50/F	Right breast cancer, TNBC	Lung, skeletal
24	62/F	Breast cancer, ER+ PR+ Her2neu-	Primary, lymph node, lung, pleural thickening
25	54/M	Right lung cancer, NSCLC (adenocarcinoma)	Primary, lymph node, lung
26	37/F	Left breast cancer, TNBC	Primary, lymph node, liver, muscle
27	36/M	Lung cancer adenocarcinoma	Primary, lymph node, pleural thickening, brain
28	15/F	Non-Hodgkin's lymphoma-B-cell of the ovary	Skeletal metastases

29	56/M	Unknown primary <i>Post FAPI and FDG PET scans followed by Bx: (squamous cell carcinoma of the neck)</i>	Primary, lymph node, brain, muscle
30	67/F	Multiple myeloma	Primary, lymph node
31	46/F	Mesenteric carcinoid	Primary, lymph nodes, lung, liver, adrenals
32	61/F	Right lung cancer, NSCLC (adenocarcinoma)	Primary, lymph node
33	41/F	B/L Ovarian carcinoma	Primary, lymph nodes, serosal and omental deposits
34	47/F	<i>Non-small cell lung cancer (squamous cell carcinoma)</i>	<i>Primary, lymph nodes, lung</i>
35	37/M	Hodgkin's lymphoma	Lymph node
36	54/F	B/L breast cancer ER- PR- Her2neu+	Lymph node, lung, Skeletal, liver, brain
37	10/M	Glioblastoma multiforme	Primary
38	48/M	Olfactory neurofibroma	Primary
39	48/F	adenocarcinoma lung	Primary, lymph node, lung, pleural thickening, liver, brain
40	54/F	Unknown primary <i>Post FAPI and FDG PET scans followed by Bx: (left breast cancer)</i>	Lymph node, liver, lung mass, skeletal
41	57/F	Ovarian cancer	Primary, lymph node
42	69/M	Right lung cancer NSCLC (SCC)	Primary, lymph node, lung
43	52/M	Right lung cancer NSCLC (adenocarcinoma)	Primary, lymph node, lung
44	45/M	Multiple myeloma	Lymph node, lung, liver, skeletal, brain, B/L adrenals, omental nodules
45	42/F	Right breast cancer ER- PR+ Her2neu +	Brain metastases
46	33/F	Right breast cancer TNBC	Lymph node, lung, pleural thickening, skeletal, muscle
47	66/M	Unknown primary <i>Post FAPI and FDG PET scans followed by Bx: (base of tongue, squamous cell carcinoma)</i>	Primary, lymph node
48	58/F	Right lung cancer NSCLC (adenocarcinoma)	Primary, lymph nodes, lung, skeletal, liver, thyroid cartilage, adrenals
49	45/M	Glottic cancer, squamous cell carcinoma	Primary, lymph nodes
50	60/M	Right lung cancer NSCLC (adenocarcinoma)	Primary, lymph nodes, lung, pleural thickening, lymph node, brain
51	33/F	Right breast cancer	Lymph node, lung, lung mass, liver, skeletal, brain, adrenals
52	56/M	Gall bladder cancer	Primary, lung
53	66/M	Right lung cancer, sarcomatous ca with focal squamous cell differentiation	Primary, lymph node, lung, pleural thickening, skeletal, liver, adrenals
54	60/M	Left lung cancer NSCLC (modified differentiated SCC)	Primary, lymph node, lung, pleural thickening

M: Male; F: Female; ER: Estrogen receptor; PR: Progesterone receptor; Her2neu: Human epidermal growth factor receptor 2; TNBC: Triple negative breast cancer; NSCLC: Non-small cell lung cancer; SCC: Squamous cell carcinoma

Biodistribution and Pharmacokinetics of [⁶⁸Ga]Ga-DOTA.SA.FAPi

Dosimetry was conducted in 3 female patients (2 breast cancer and 1 lung cancer patient) with a mean age of 45 ± 6 years (38 – 50). The physiological biodistribution of [⁶⁸Ga]Ga-DOTA.SA.FAPi involved the pancreas, liver, heart contents, spleen, kidneys, urinary bladder, and to a lesser extent, in the lacrimals, oral mucosa, salivary glands, and thyroid glands. Visual analysis revealed the pancreas as the organ of the highest uptake. Figure 2 demonstrates serial images that depict the normal biodistribution and expression of [⁶⁸Ga]Ga-DOTA.SA.FAPi in a patient with carcinoma of breast showing extensive metastases to various organs (Figure 2).

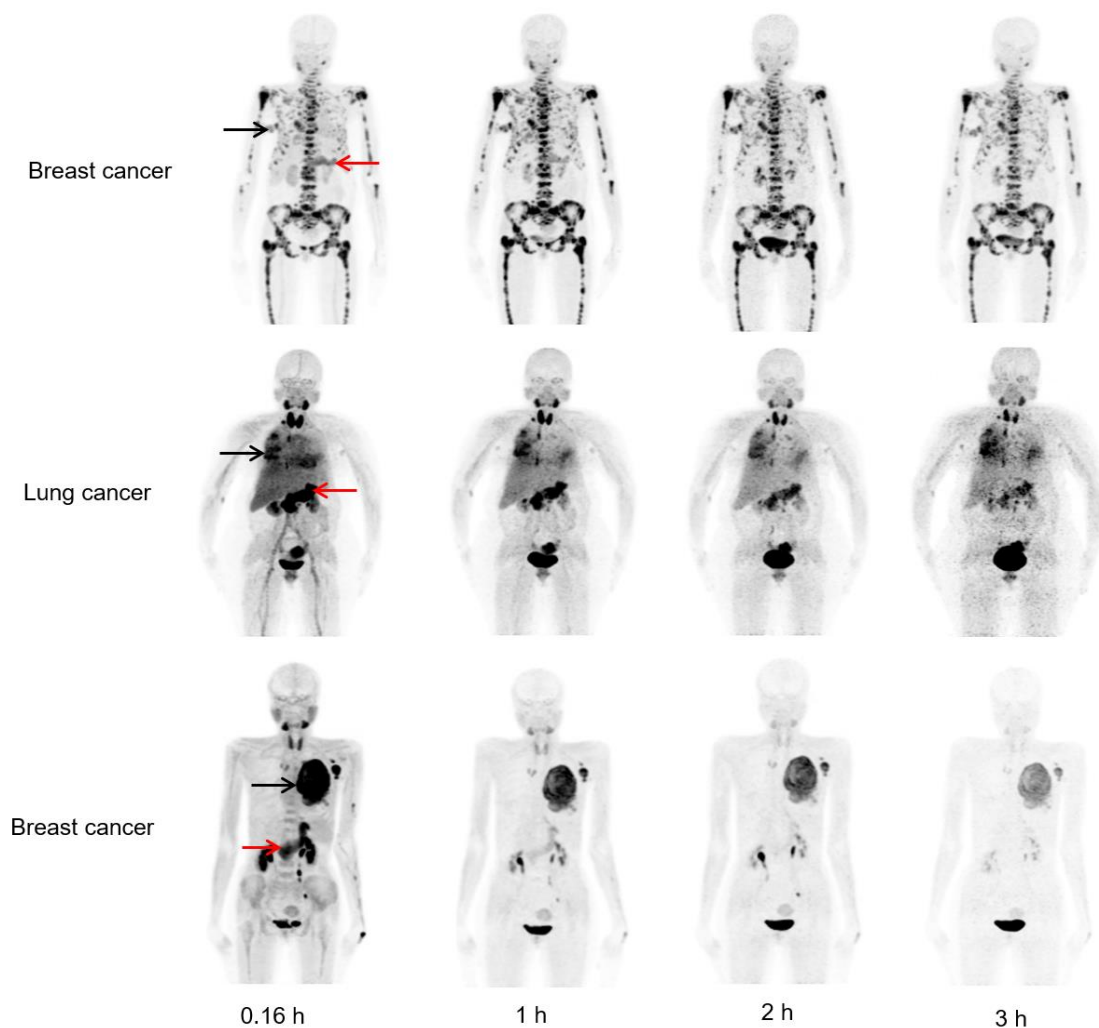


Figure 2: Biodistribution of [⁶⁸Ga]Ga-DOTA.SA.FAPi at serial time-points in a breast and lung cancer patients with primary lesions (black arrow) and metastases involving lymph nodes, liver, and bone. There is rapid accumulation of tracer seen in the 10 minute image with retention till 3 hours images. Radiotracer accumulation is also seen in the pancreas (red arrows), salivary glands. Steady clearance of blood pool activity with visualization of kidneys, ureter and urinary bladder noted in serial images.

Uptake in the normal organs, primary tumor, and the metastases was detectable as early as 10 min p.i. and remained visible up to 3 hours of imaging (Figure 2). All the organs showed an exponential decrease in the activity which was fitted using either mono-exponential or bi-exponential curve fitting. The washout of the radiotracer from the bone marrow was rapid, with a decrease in the %IA to > 50% of its initial value at 60 min p.i. (Figure 3a). Similarly, the washout in the remaining organs with normal physiological uptake (Figure 3a) and the remainder of the body (Figure 3b) was rapid all throughout the time span of 3 hours.

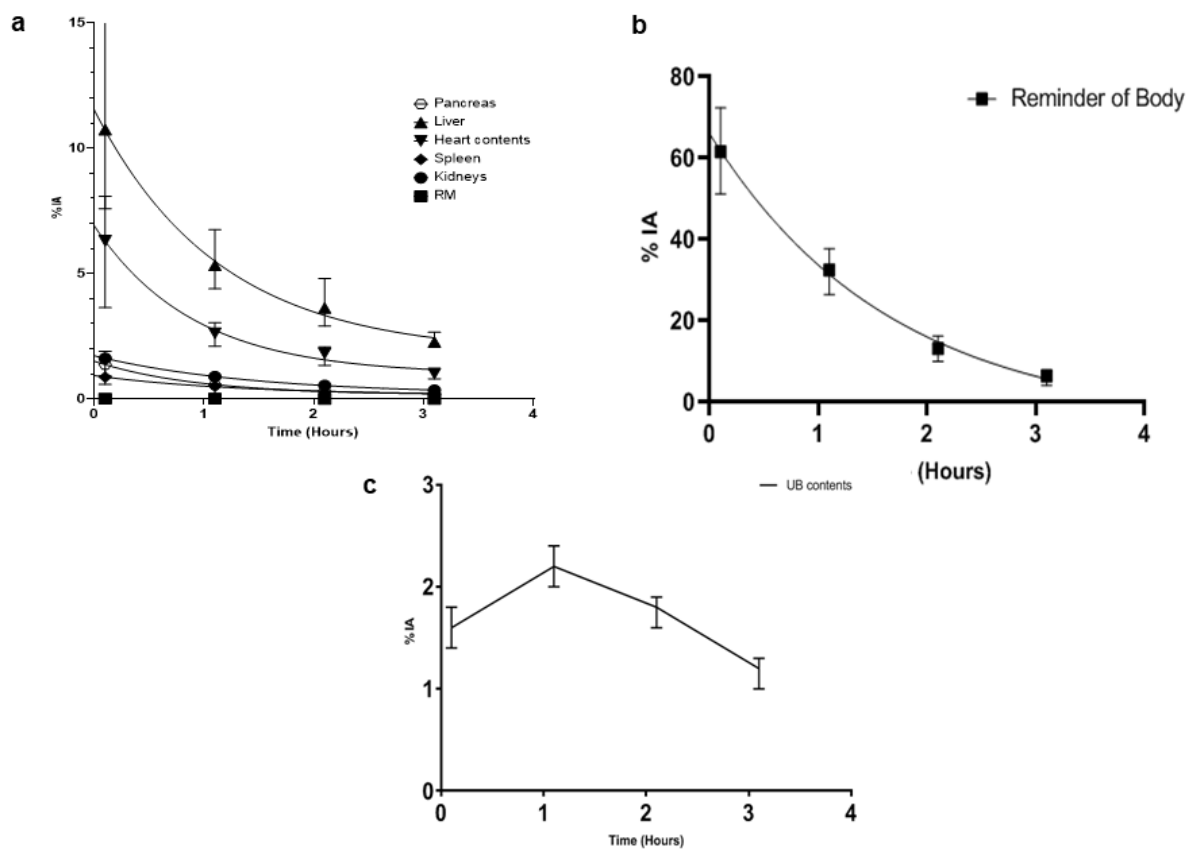


Figure 3: Percentage of injected activity (IA) of $[^{68}\text{Ga}]\text{Ga-DOTA.SA.FAPi}$ in organs with normal physiological uptake (a), %IA in the remainder of the body (b), and % IA in the urinary bladder without voiding (no biological excretion) (c).

Interestingly, the uptake in all the lesions initially showed a decrease from the 10 min to the 1 h time-point but remained relatively stable with only a mild decrease throughout up to 3 h p.i. (Figure 4).

In contrast to a subtle decrease in the SULavg values in the lesions, there is a rapid washout of the radiotracer from the normal organs such as the liver, pancreas, blood pool, left psoas muscle (Figure 4 and Table 2). Accordingly, the maximum target-to-background ratio (TBR) in the lesions steadily

increased over time, even up to 3 hours of the scan with a steady and significant decrease in the background activity. The highest TBR uptake was observed using the lesion to psoas muscle ratio.

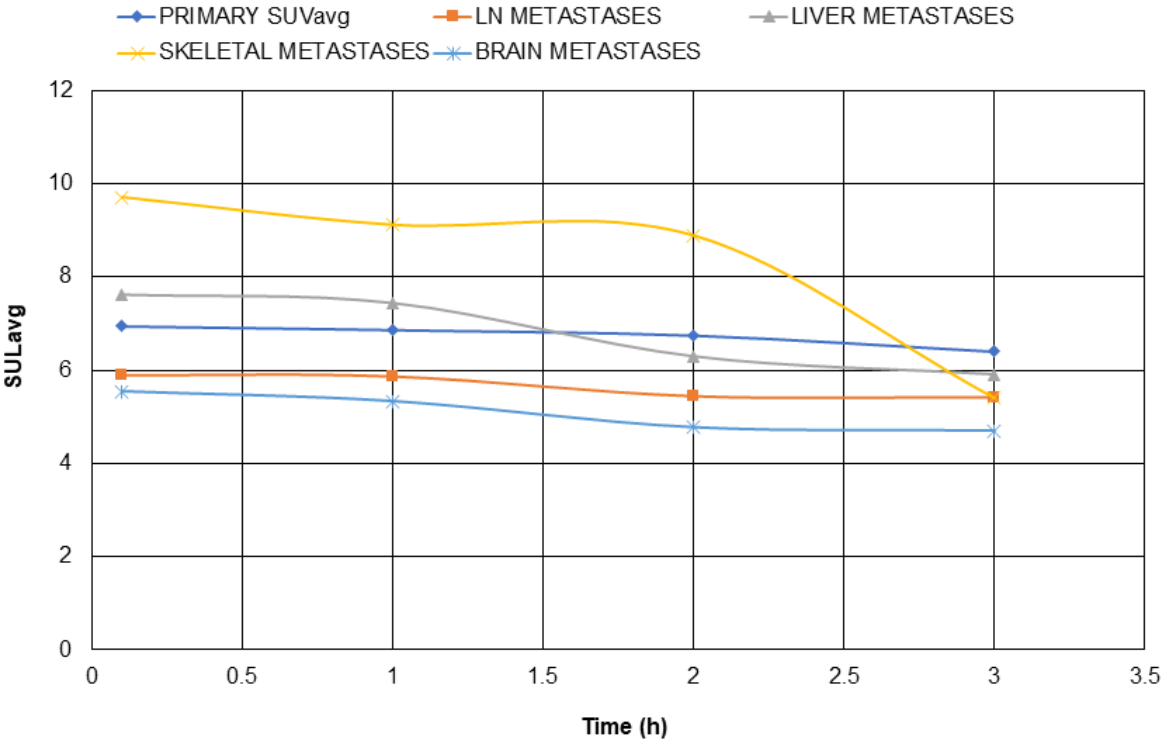


Figure 4: Mean standardized uptake value patterns of $[^{68}\text{Ga}]\text{Ga-DOTA.SA.FAPI}$ in lesions in 3 patients at various time-points. The highest SULavg values were observed is skeletal metastases.

Among the categories of lesions, the highest lesion-to-psoas muscle ratio was observed in skeletal metastases wherein the TBR was 9.33 at 10 min and 7.6 at 3 h with an 18% drop from its initial value. The next highest TBR was found in liver, followed by blood pool, and pancreas decreasing order. (Table 2).

Table 2: Target-to-background ratios of [⁶⁸Ga]Ga-DOTA.SA.FAPI at various time-points post-injection in three patients.

Primary tumor				
Time-point (h)	Primary tumor / liver Bkg	Primary tumor /Psoas muscle Bkg	Primary tumor /pancreas Bkg	Primary tumor /blood pool Bkg
0.16	2.27	6.68	1.01	1.12
1	2.28	6.80	1.32	1.32
2	3.05	7.84	1.50	2.63
3	3.15	9.01	2.46	3.55
Lymph node metastases				
Time-point (h)	LNmetastases /liver Bkg	LN metastases /Psoas muscle Bkg	LN metastases /pancreas Bkg	LN metastases /blood pool Bkg
0.16	1.93	5.66	0.85	0.95
1	1.94	5.80	1.12	1.12
2	2.46	6.32	1.20	2.12
3	2.66	7.63	2.08	3.01
Liver metastases				
Time-point (h)	Liver metastases/liver Bkg	Liver metastases /Psoas muscle Bkg	Liver metastases /pancreas Bkg	Liver metastases/blood pool Bkg
0.16	2.49	7.32	1.11	1.22
1	2.47	7.36	1.43	1.43
2	2.84	7.31	1.39	2.45
3	2.90	8.30	2.26	3.27
Skeletal metastases				
Time-point (h)	Skeletal metastases/liver Bkg	Skeletal metastases /Psoas muscle Bkg	Skeletal metastases /pancreas Bkg	Skeletal metastases/blood pool Bkg
0.16	3.18	9.33	1.41	1.56
1	3.02	9.02	1.75	1.75
2	4.02	10.33	1.97	3.47
3	2.66	7.60	2.07	3
Brain metastases				
Time -point (h)	Brain metastases / liver Bkg	Brain metastases /Psoas muscle Bkg	Brain metastases /pancreas Bkg	Brain metastases metastases/blood pool Bkg
0.16	1.81	5.32	0.80	0.89
1	1.77	5.27	1.02	1.02
2	2.15	5.54	1.06	1.86
3	2.31	6.61	1.80	2.61

Bkg: Background, LN: lymph node metastases.

A detailed comparison of SULavg uptake values in various types of cancer lesions at 10 min and 3 h post [⁶⁸Ga]Ga-DOTA.SA.FAPI injection, revealed a decline in the radiotracer uptake by 7.9% (SULavg: 6.95 to 6.6), 6.8% (SULavg: 5.89 to 5.42), 22.6% (SULavg: 7.62 to 5.9), 44.3% (SULavg: 9.7 to 5.4) and 14.7% (SULavg: 5.5 to 4.7) in the primary tumor, LN metastases, liver metastases, skeletal metastases, and brain metastases, respectively (Figure 4). Another interesting finding was that the number of lesions detected in the 1st time-point (i.e. 0.16 h p.i. scan) did not differ from the other time-point scans.

The mean fraction of activity excreted into the urinary bladder was double in the first 60 minutes. Figure 3c depicts the %IA in the urinary bladder contents without voiding between the scans derived from curve-fitting. Considering that no biological excretion took place during the temporal acquisition period, the %IA curve of the urinary bladder demonstrated an initial increase in the activity followed by a decreasing trend reflecting the collection and the physical decay of activity in the urinary bladder.

Dosimetry

The mean residence times in source organs, such as the heart contents, kidneys, liver, pancreas, red marrow, spleen, urinary bladder contents, and the remainder of the body were 4.20E-02, 1.41E-02, 1.01E-01, 9.76E-03, 8.53E-04, 7.93E-03, 3.03E-02, and, 4.86E-01 MBq-h/MBq, respectively. Table 3 details the dosimetry estimate of absorbed dose in each organ, effective dose equivalent, and the effective dose. The organ with the highest radiation absorbed dose were the pancreas (5.46E-02 mGy/MBq) followed by the urinary bladder wall (5.21E-02mGy/MBq), Liver (3.84E-02 mGy/MBq), Heart wall (3.16E-02 mS/MBq), spleen (2.68E-02 mGy/MBq) and Kidneys (2.62E-02 mGy/MBq). The mean effective dose equivalent (EDE) was (1.64E-02 mSv/MBq). The estimated mean effective dose was 0.011 mSv/MBq. The mean effective dose from 185 MBq of [⁶⁸Ga]Ga-DOTA.SA.FAPI is estimated to be 2mSv.

Table 3: Absorbed dose estimate of [⁶⁸Ga]Ga-DOTA.SA.FAPi.

Organ	Mean absorbed doses (mSv/MBq)	Mean absorbed doses (rem/mCi)
Adrenals	7.77E-03	2.87E-02
Brain	5.06E-03	1.87E-02
Breasts	5.48E-03	2.03E-02
Gallbladder Wall	8.37E-03	3.10E-02
LLI Wall	6.41E-03	2.37E-02
Small Intestine	6.26E-03	2.32E-02
Stomach Wall	6.93E-03	2.56E-02
ULI Wall	6.65E-03	2.46E-02
Heart Wall	3.16E-02	1.17E-01
Kidneys	2.62E-02	9.68E-02
Liver	3.84E-02	1.42E-01
Lungs	6.62E-03	2.45E-02
Muscle	5.79E-03	2.14E-02
Ovaries	6.48E-03	2.40E-02
Pancreas	5.46E-02	2.02E-01
Red Marrow	4.80E-03	1.78E-02
Osteogenic Cells	8.66E-03	3.20E-02
Skin	4.96E-03	1.83E-02
Spleen	2.68E-02	9.91E-02
Thymus	6.56E-03	2.43E-02
Thyroid	5.34E-03	1.97E-02
Urinary Bladder Wall	5.21E-02	1.93E-01
Uterus	6.98E-03	2.58E-02
Total Body	7.05E-03	2.61E-02
Effective Dose Equivalent	1.64E-02	6.08E-02
Effective Dose	1.11E-02	4.10E-02

LLI: Lower large intestine; ULI: Upper large intestine.

Comparison between and [¹⁸F]F-FDG and [⁶⁸Ga]Ga-DOTA-SA-FAPi PET/CT scans

There was a complete inter-observer agreement for all organs with physiological biodistribution on [⁶⁸Ga]Ga-DOTA-SA-FAPi PET/CT. Similarly, on the [⁶⁸Ga]Ga-DOTA-SA-FAPi PET/CT scans, for uptake in the lesions situated in the primary, pleural thickening, bone metastases, liver, brain, and second primary malignancies, the degree of inter-observer agreement was 1. Though there was disagreement between the observers in detecting the lymph node and lung metastases, the agreement level was high: 0.82 and 0.87, respectively.

Normal Organ Uptake comparison

Except for uptake in the pancreas which showed a significantly higher uptake of [⁶⁸Ga]Ga-DOTA-SA-FAPi when compared to [¹⁸F]F-FDG, all other organs showed similarities in both tracers' physiological uptake (Figure 5a & b, Supplementary Table 1). Despite the similarities, a significantly high SULpeak and average uptake values were noted in the pancreas, salivary glands, thyroid and the psoas muscle on [⁶⁸Ga]Ga-DOTA-SA-FAPi PET/CT scans in contrast to [¹⁸F]F-FDG PET/CT (Figure 5a & b, Supplementary Table 1). Both the tracers demonstrated low blood pool activity across all the scans. In organs such as spleen, duodenum, vertebrae, and extremities like femur, the quantitative uptake was slightly higher on the [¹⁸F]F-FDG PET/CT scans. Contrary to the avid uptake of [¹⁸F]F-FDG in the normal brain parenchyma, an outstandingly negligible uptake was quantified on [⁶⁸Ga]Ga-FAPi PET/CT scan aiding a better diagnosis of the brain metastases (Figure 5a & b, Supplementary Table 1).

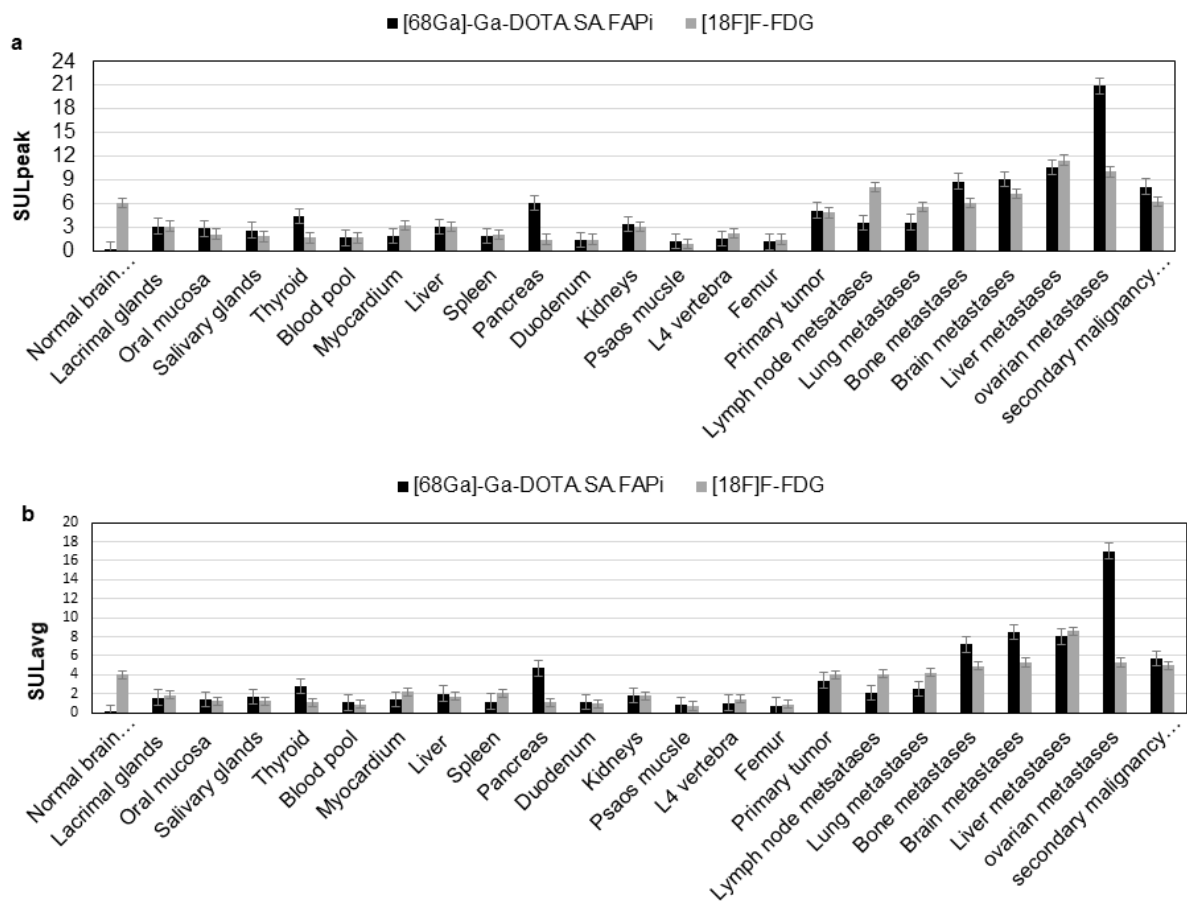


Figure 5: Comparison of SULpeak (a) and the SULavg (b) values between $[^{18}\text{F}]\text{F-FDG}$ and $[^{68}\text{Ga}]\text{Ga-DOTA.SA.FAPi}$ radiotracers in 20 patients at 1 hour after injection.

Comparison according to the site of malignancy or metastases

Patient-based Analysis

A comprehensive comparison of median SULpeak and SULavg values amidst the tracers in various primary disease sites and metastases are detailed in Table 4, 5 & Supplementary Table 3, respectively.

Table 5: Comparison of SUL values according to the site of primary tumor.

Site of primary cancer	SULpeak [⁶⁸ Ga]Ga-DOTA.SA.FAPi PET/CT (mean ± SD, range)	SULpeak [¹⁸ F]F-FDG PET/CT (mean ± SD, range)	P-value	SULavg [⁶⁸ Ga]Ga-DOTA.SA.FAPi PET/CT (mean ± SD, range)	SULavg [¹⁸ F]F-FDG PET/CT (mean ± SD, range)	P-value
Breast	6.5 ± 3.3 (3.3 - 12.5)	6.2 ± 1.6 (1.2 - 16.9)	0.921	4.9 ± 2.5 (2.2 - 9)	4.7 ± 2 (1 - 12.7)	0.911
Lung	5.8 ± 2.4 (1.2 - 9.6)	7.4 ± 3.8 (1.9 - 14.4)	0.238	4.9 ± 2.3 (2.2 - 9.9)	5.3 ± 3 (0.9 - 10.9)	0.313
Head and neck	15.4 ± 5.4 (8.6 - 21.2)	14.2 ± 6.7 (9.3 - 23.7)	0.680	8.3 ± 2.3 (5.4 - 10.9)	7.9 ± 2.9 (5.5 - 11.8)	0.783
Gall bladder	12.3	8.1	-	27	7.9	-
Ovary	8.9 ± 0.84 (7.9 - 9.6)	6.7 ± 1.5 (5.1 - 8.2)	0.199	6.8 ± 0.39 (6.3 - 7.1)	5.3 ± 1.2 (4.1 - 6.6)	0.108
Others	9.2 ± 2.5 (7.9 - 11.6)	9.9 ± 2 (4.7 - 12.8)	0.618	2.76 ± 2.5 (1.8 - 4.6)	5.85 ± 2.8 (3.5 - 7.1)	0.071

SULpeak and avg: Standardised uptake value corrected for lean body mass; IQR: Interquartile range.

Primary tumor

Thirty-seven patients were detected with primary residual tumor uptake, and a complete concordance was observed between both tracers. Referring to the intensity of the tracer accumulation in the primary/residual tumor site, the median SUL values were comparable between the tracers {[¹⁸F]F-FDG: 6.1; (IQR: 3.5 – 7.4) vs [⁶⁸Ga]Ga- DOTA.SA.FAPi: 4.4; (IQR: 2.8 – 8.7), P-0.843} (Table 4). Furthermore, a sub-categorical analysis was conducted according to primary cancer, and comparable results were noted between the two tracers (Table 5).

Lymph node

Concordance for detection of lymph node metastases between [⁶⁸Ga]Ga-DOTA.SA.FAPi and [¹⁸F]F-FDG PET/CT scan was 92.5% (50/54). Regarding the intensity of tracer accumulated in the lymph nodes, the SULpeak was higher for [¹⁸F]F-FDG PET/CT than the [⁶⁸Ga]Ga-DOTA.SA.FAPi, however, the difference was not significant [5 (IQR: 1.7 – 9.6) vs. 3.7 (IQR: 1.9 – 6.8), P=0.672] (Table 4). Among the 4 patients with discordant LN metastases findings, [⁶⁸Ga]Ga-DOTA.SA.FAPi scan was false negative in 2 cases, and [¹⁸F]F-FDG was false positive in two cases, respectively (Supplementary Table 3) (Figure 6 & 7).

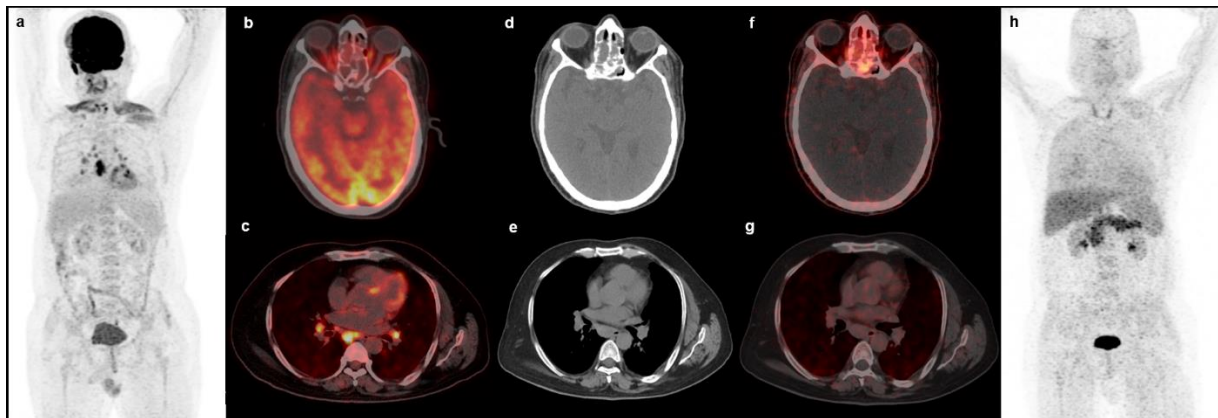


Figure 6: In a 48-year-old man with olfactory neuroblastoma involving sphenoid fossa and ethmoidal air cells, [¹⁸F]F-FDG PET/CT (a- maximum intensity projection, b,c –fused PET/CT images) and non-contrast Computed tomography (d,e) revealed increased FDG uptake in the primary tumor involving the ethmoid air cells (b), sub-carinal and bilateral hilar lymph nodes. [⁶⁸Ga]Ga-DOTA.SA.FAPi PET/CT images (f,g– fused PET/CT, H-maximum intensity projection) showing increased radiotracer uptake in the primary tumor only. FDG avid mediastinal lymph nodes do not show increased [⁶⁸Ga]Ga-DOTA.SA.FAPi uptake. He underwent endobronchial ultrasound guided biopsy from the sub-carinal lymph node, which showed only inflammatory infiltrate.

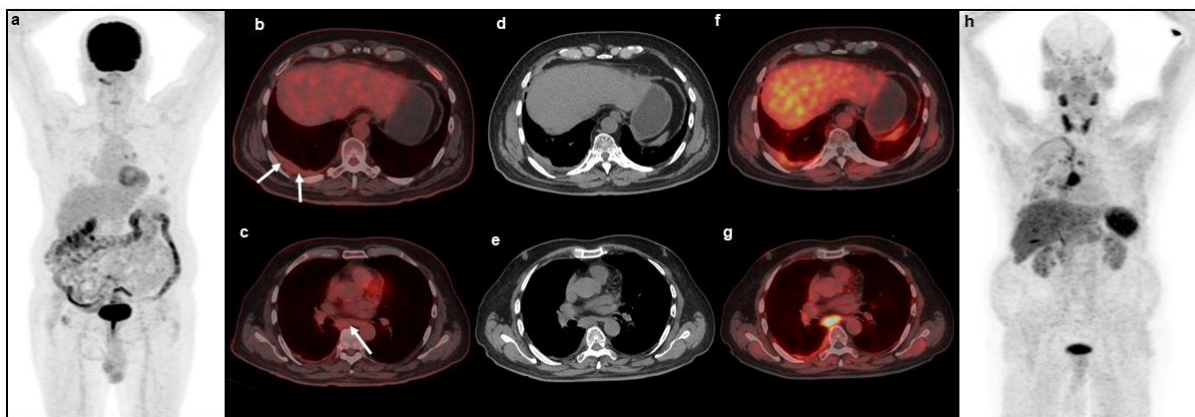


Figure 7: 72-year-old man, known case of Type 2 diabetes mellitus and a diagnosed case of mesothelioma of right pleura underwent both [^{18}F]F-FDG PET/CT and [^{68}Ga]Ga-DOTA.SA.FAPI PET/CT for staging. [^{18}F]F-FDG PET/CT images (a,b,c) and corresponding non contrast CT images (d, e) showing only mild FDG uptake in the irregular right pleural thickening and sub-carinal lymph node (arrows). [^{68}Ga]Ga-DOTA.SA.FAPI PET/CT images (f,g- fused PET/CT, h- maximum intensity projection) showing intense [^{68}Ga]Ga-DOTA.SA.FAPI uptake in the right pleural thickening and sub-carinal lymph node. Physiological uptake of [^{68}Ga]Ga-DOTA.SA.FAPI is seen in liver, spleen, pancreas, thyroid glands, salivary glands, lacrimal glands, kidney and urinary bladder. Also noted mild diffuse [^{68}Ga]Ga-DOTA.SA.FAPI uptake in the visualised skeletal muscles. Biopsy from the sub-carinal lymph node revealed metastases from mesothelioma.

Lung related lesions and liver metastases

While, 51 (94.4%) patients showed agreement between the detection of lung metastases, [^{68}Ga]Ga-DOTA.SA.FAPI proved superior in three patients, among whom 2 were falsely positive, and 1 was false negative on [^{18}F]F-FDG. A complete concordance was demonstrated in patients with pleural thickening. Similar radiotracer uptake values were noted between the two agents (Table 4, 5 & Supplementary Table 3). A complete concordance was noticed between the tracers for liver metastases with no significant difference in the uptake values (Table 4, 5 & Supplementary Table 3).

Skeletal Metastases

Both the tracers identified all sites of skeletal metastases in all patients (Supplementary Table 3). Despite the visual resemblance, when quantified, a marginally higher uptake was documented on [^{68}Ga]Ga-DOTA.SA.FAPI scans compared to [^{18}F]F-FDG scans, but was not significant {SULpeak: [7.9 (5.4 – 10.9) vs.4.5 (3 – 6.8), P-0.125], SULavg [6 (3.2 – 8.8) vs 3.5(2.2 – 5.1), P-0.225]} (Table 4).

Brain Metastases

Both the tracers identified brain metastatic lesions in 12 patients. Five patients demonstrated multiple brain metastases, but [^{18}F]F-FDG PET/CT failed to identify all the brain lesions in one patient (Figure 8). On quantification of tracer uptake, a remarkably higher SULpeak and SULavg brain metastases-to-brain normal parenchyma ratios were observed on [^{68}Ga]Ga-DOTA.SA.FAPi in contrast to the [^{18}F]F-FDG values. {SULpeak: [^{68}Ga]Ga-DOTA.SA.FAPi; median: 83.2 (IQR: 34.2 – 249.3) vs. [^{18}F]F-FDG; 1.5 (1 – 2.3); P-0.028} and {SULavg: [^{68}Ga]Ga-DOTA.SA.FAPi; median: 59.3 (IQR: 33.5 – 130.8) versus [^{18}F]F-FDG; 1.2 (1 – 2.3); P-0.029}. (Figure 8).

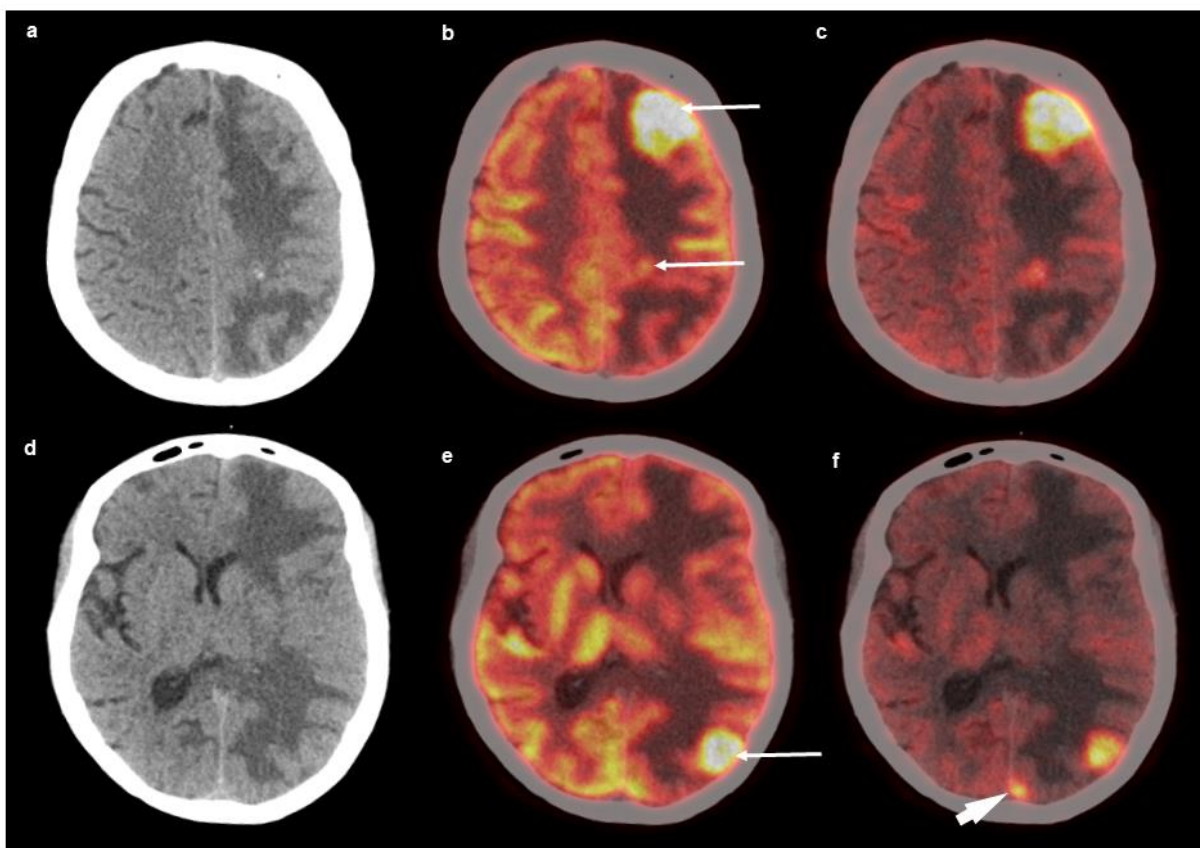


Figure 8: A 66-year-old woman known case of carcinoma breast with brain metastases underwent both [^{68}Ga]Ga-DOTA.SA.FAPi PET/CT (a,c,g) and [^{18}F]F-FDG PET/CT (e,d,h) for restaging. Maximum intensity projection images (a,e) showing multiple foci of intense tracer uptake in both PET/CT. Axial sections of non-contrast computed tomography images revealed ill-defined iso dense lesions in the left frontal, parietal and occipital lobes with perilesional edema (b,f). Corresponding fused PET/CT images of both PET/CT scans showing increased FDG uptake in these lesions (c,d,g,h-arrows). [^{68}Ga]Ga-DOTA.SA.FAPi PET/CT images also revealed small occult lesions in the left parietal and left occipital lobe (c,g-arrow head).

Metastases to other sites

In two patients with breast cancer as the primary, krukemberg metastases were detected, but an outstandingly high uptake was noted on [⁶⁸Ga]Ga-DOTA.SA.FAPi PET/CT scans compared to the [¹⁸F]F-FDG PET/CT scans ($P < 0.0001$). One patient was detected with avid uptake in the stomach on both scans. The biopsy report revealed adenocarcinoma of the stomach and confirmed it as a second primary malignancy (Table 4).

Discussion

This study provides the first comprehensive assessment of the biodistribution, pharmacokinetics, and dosimetry of [⁶⁸Ga]Ga-DOTA.SA.FAPi and additionally performed a head-to-head comparison of uptake patterns between [⁶⁸Ga]Ga-DOTA.SA.FAPi and [¹⁸F]F-FDG PET/CT.

Previously, FAP inhibitor like FAPI-02 and FAPI-04 have been developed, and the first results on the role of these agents were revealed by Giesel et al. [9] and Kratochwil et al. [10]. Among the two ⁶⁸Ga-labelled radiopharmaceuticals, though both agents are rapidly taken up in the lesions with almost complete internalization after 1 h in the tumor cells, and have shown similar effective doses, Giesel et al. [9] found [⁶⁸Ga]Ga-FAPI-04 to exhibit a longer residence time of the radiotracer compared to FAPI-02 in the lesions attributed by the structural modification in the proline ring (4,4-difluoroproline) of FAPI-04.

To make an ideal radio-ligand, particularly for theranostic use, one has to match the biological half-life of a pharmaceutical agent with that of the physical half-life of radionuclide in order to deliver maximum radiation absorbed dose to the desired targets. Further research has been carried out by Loktev et al. [12] who explored 15 novel linker variations in the UAMC1110-based FAP inhibitor labelled with gallium-68 and lutetium-177 in HT-1080-FAP tumor-bearing mice and compared them with FAPI-04 molecule. Among the FAPI compounds developed by the Heidelberg group, FAPI-21 and FAPI-46 exhibited the highest tumor-to-background ratios. Moon et al. [13] attempted to focus on better tumor retention and introduced a squaric acid (SA) motif into the linker of the FAP inhibitor UAMC1110-based structures, yielding DATA^{5m}.SA.FAPi and DOTA.SA.FAPi products. The groups at Antwerp [8] and Mainz [13] confirmed extraordinarily high binding affinities in FAP binding assays in vitro at the nanomolar level combined with more than 1000-fold selectivity against other proteases. They conducted a radiochemical evaluation with gallium-68 and lutetium-177 and confirmed high

tumor uptake and good tumor-to-background ratios in their *in vivo* microPET and *ex vivo* biodistribution studies on xenograft models. Following the above results, we consequently initiated a clinical study by labelling the FAP inhibitor tracer molecule DOTA.SA.FAPi with gallium-68. The next logical step was to test the new molecule, in a large number of cancer patients, its suitability as a theranostic vector.

Uptake

Similar to the *ex vivo* results of Moon et al. [13] we observed rapid uptake of [⁶⁸Ga] Ga-DOTA.SA.FAPi in all the organs, including the malignant lesions, within 10 min of intravenous injection. We observed that the maximum TBR in the lesions increased over time up to 3 h time-point scan, reflecting the stable uptake in the lesions with imperceptible washout and rapid clearance of radiotracer from the non-target organs, and hence, reducing the radiation burden to the normal organs. A rapid accumulation of activity was observed in the urinary bladder with twice the increase in the activity at 60 min p.i., indicating rapid renal clearance which is reconfirmed with the minimal absorbed dose estimate to the kidneys (2.62E-02 mSv/MBq). Although TBR improved over time, there were no additional benefits in delayed imaging, thus, diagnostic level scans could be acquired as early as 10 min p.i.

Kinetics

Well, in line with previous studies on various FAPi tracers [9,11], a similar pattern of radiotracer kinetics has been obtained with [⁶⁸Ga] Ga-DOTA.SA.FAPi wherein, the radiotracer washout from the non-target organs is rapid, thus, giving superior image contrast.

Blood clearances: Meyer et al. [11] using [⁶⁸Ga]Ga-FAPi-46 showed a 50% decrease in the activity from the blood at 1 h p.i.; similarly, we observed a 40% decrease of [⁶⁸Ga]Ga-DOTA.SA.FAPi at 60 min p.i. from the baseline scan, and both studies observed an exponential drop in the %IA at three hours.

Though the pancreas received the highest radiation absorbed dose, the %IA sharply dropped from 1.4% to 0.5% (60% drop) at 1 h p.i. and further reduced to 0.1% (93% decrease) at 3 h of p.i. These findings clearly indicate that the accelerated washout from the critical organ reduces the radiation burden on the pancreas. These imaging results are encouraging from the point of view of exploring ¹⁷⁷Lu/⁹⁰Y/²²⁵Ac-labelled DOTA.SA-FAP inhibitor for therapy perspective.

Even though there were variations in the kidney absorbed doses when compared to other studies, the findings remained consistent that a similar %IA from the kidneys was excreted at 3 h p.i. We observed

a 45% of the activity in the kidneys to clear at 1 h and an 80% washout by 3 h p.i. When comparing our results to that of Meyer et al. [11] in FAPI-46, it must be pointed out that though the authors observed a larger component of radiotracer (70%) washout at the initial 1 h, however, by 3 h similar to our report, they observed up to 80% decline in the %IA.

In our study, the SUV kinetics of the lesions suggested a rapid uptake, greater percentage of retention in the tumors/lesions compared to the normal organs. Meyer et al. [11] observed a 14% decrease in the SUV_{avg} uptake in the tumor at 60 min p.i. Unlike Meyer et al., we sub-categorized SUV kinetics according to various cancer involvement sites and compared the 0.16 h and the 3 h SUL_{peak} and avg values. Our findings revealed the percentage decrease in the mean SUL values ranged between 5.4 to 44.3%, with the maximum difference observed in the skeletal metastases.

Giesel et al. [9] observed a 75% and 25% decline in the tumor uptake from 1 h to 3 h with FAPI-02 and FAPI-04 compounds, respectively. The discrepancies pointed out the evolution of the FAPI molecules to improve tumor retention. Compared to the available studies on the SUV kinetics in tumor lesion, but similar to FAPI-46, [⁶⁸Ga]Ga-DOTA.SA.FAPi showed a superior tumor retention time. The difference in the retention time is no doubt due to the modification in the quinoline based structures.

One of the significant findings that emerged from this study was that in patients with extensive tumor uptake, lesser radiotracer was available for uptake in the background organs (Figure 2); while patients with lessor tumor burden showed higher background tracer uptake, that is quite logical (Figure 6, 7).

Doses

The effective dose equivalent and effective dose from [⁶⁸Ga]Ga-DOTA.SA.FAPi were 1.64E-02 and 1.1E-02 mSv/MBq, respectively, and well in line with that of [⁶⁸Ga]Ga-labelled FAPI-02, and FAPI-04 and FAPI-46 radiopharmaceuticals [9] (Supplementary Table 2).

The pancreas is the critical organ that received the highest radiation absorbed dose. It is because the highest uptake was observed in the pancreas of [⁶⁸Ga]Ga-DOTA.SA.FAPi scan at 0.16 h p.i. Busek et al. [19] conducted an enzymatic assay in adult pancreatic tissue, and demonstrated homologous proteases FAP in the islets of Langerhans. The pancreatic islets constitute 1–2% of the pancreas volume; however, they receive 10–15% of its blood flow. This expression could probably relate to the avid uptake of [⁶⁸Ga]Ga-DOTA.SA.FAPi in the pancreas.

In concordance with the biodistribution of [⁶⁸Ga]Ga-FAPI-21 [12], we observed a high expression of DOTA.SA.FAPi in the salivary thyroid glands and, to a less extent, in the lacrimal glands and in the oral

mucosa. The synthetic modifications in the FAPi molecule could attribute to its variability in the biodistribution pattern.

FAPi vs. FDG

In our study, while the highest uptake of [⁶⁸Ga]Ga-DOTA-SA-FAPi (SUL > 10) was found in head and neck cancers followed by gall bladder carcinoma, an uptake > 5 was observed in all other cancers. Though there was a similarity in the visual analysis between FAPi-02, FAPi-04, and DOTA-SA-FAPi in various cancers, Kratochwil et al. [10] reported the highest intensity of FAPi-04 uptake in lung cancer followed by breast, oesophageal cancer, cholangiocellular carcinoma; and sarcoma. On the other hand, Chen et al. [20] observed the highest uptake of [⁶⁸Ga]Ga-DOTA-FAPi-04 in pancreatic cancer, liver cancer (including cholangiocarcinoma and hepatocellular carcinoma), sarcoma, oesophageal cancer, and gastric cancer.

While, in our study, the average SUL_{peak} uptake for patients with breast cancer ranged between 3.3 – 12.5 on [⁶⁸Ga]Ga-DOTA-SA-FAPi, Kratochwil et al. [10] observed an average SUV_{max} of >12 in breast cancer patients, but, in agreement, both the tracers demonstrated a high agreement with the [¹⁸F]F-FDG in the detection of lesions. The variation in the histopathology of breast cancer, the method of SUV measurements adopted in the study, and the tissue changes due to the effects of previous treatment may probably cause the variation of the SUV value. Hence, uptake in terms of SUV and residence time depends on individual tumors and on individual expression of a given disease. It is also an important aspect that the biological probe should match the radionuclide physical half-life for therapy to give the best result; thus, SUV is not the only criterion on which theranostic agent is chosen. In this regard, our group has reported proof-of-principle work on [⁶⁸Ga]Ga-DOTA-SA-FAPi PET/CT-guided [¹⁷⁷Lu]Lu-DOTA-SA-FAPi radionuclide therapy in an end-stage breast cancer patient, which has proved the potential to open new applications for cancer therapeutics [14]. Garin and colleagues [5] best characterized FAP expression in the breast tissue where the authors demonstrated FAP expression exclusively in the stroma of the breast cancer, and interestingly, neither the malignant epithelial cells nor in the stroma of the adjacent normal breast tissue expressed FAPs.

We analyzed 13 patients with NSCLC, and the number of lesions correlated well between both tracers, except in one patient where [⁶⁸Ga]Ga-DOTA-SA-FAPi was not expressed in the lymph nodes. Liao et al. [21] illustrated the expression of FAP in paraffin-embedded primary NSCLC specimens of 50 NSCLC. The results provided important insights regarding the high expression of FAP as a prognostic indicator of poor survival.

Both [⁶⁸Ga]Ga-DOTA.SA.FAPi PET/CT and [¹⁸F]F-FDG PET/CT demonstrated equivalent and high SUL uptake values in the primary site of head and neck cancers. In this context Wang et al. [22] have shown a selective expression of FAP in oral squamous cell carcinoma patients. However, we studied only a small patient cohort with oral SCC; hence, it is too early to comment on the role of [⁶⁸Ga]Ga-DOTA.SA.FAPi in the above histological category of patients.

Among our series of patients, in two patients, the [⁶⁸Ga]Ga-DOTA.SA.FAPi identified additional lesions in the brain that could not be detected on [¹⁸F]F-FDG PET/CT. The distinctly lower brain parenchyma uptake of [⁶⁸Ga]Ga-DOTA.SA.FAPi scan makes it as an ideal tracer to detect brain metastases, and needless to mention is far superior to [¹⁸F]F-FDG PET/CT in detecting brain tumors.

Krukenberg tumors were detected in two patients who had primary breast carcinomas. A significantly avid expression was observed with [⁶⁸Ga]Ga-DOTA.SA.FAPi, in contrast to the [¹⁸F]F-FDG uptake. While no data regarding the expression of FAP has been recorded in literature until now, studies have shown stromal positivity in 92% of ovarian cancer tissues with extremely rare FAP expression in malignant cells [23].

Interestingly, Chen et al. [20] studied 12 different cancers in 75 patients and reported a superior detection rate of [⁶⁸Ga]Ga-FAPi-04 PET/CT over conventional [¹⁸F]F-FDG PET/CT (98.2% vs. 82.1%) in the diagnosis of various primary tumors, however, we could not show that great difference in our head-to-head comparative study. The underlying reason for this difference is that unlike Chen et al., who studied various cancers where FDG plays a limited role, in our study, a significant percentage of patients constituted breast cancer and lung cancers where FDG is avidly expressed. The results may vary in the wider population in different clinical settings. Our results were in close agreement with the study of Kratochwil et al. [10]. Further studies on head-to-head comparison with various FAP inhibitor tracers in the same patients will need to be carried out in order to examine the ideal molecule for FAPi imaging. Accurate characterization of each type of cancer and its association with FAP expression should be studied to fully understand the implications of [⁶⁸Ga]Ga-FAPi PET/CT in oncologic imaging. Follow-up studies with interim [⁶⁸Ga]Ga-DOTA.SA.FAPi PET/CT scans could help our understanding of the role of FAPi as a prognostic indicator of treatment response and survival.

There is no one-stop-shop in oncology; it is envisaged that in the future both FDG and FAPi-based tumor imaging shall complement each other to cover a greater number of cancers under its banner and minimize the false positive and false negative findings.

Limitations

This study is accompanied by certain limitations. The sample size of the patients with different kinds of histopathology was small. This investigation must be conducted in a large population of patients to study the variability of FAPi expression and its retention in different cancers.

Conclusions

This is the first clinical study on the biodistribution and pharmacokinetics of [⁶⁸Ga]Ga-DOTA.SA.FAPi and demonstrates a high target-to-background ratio in various types of cancers. The mean absorbed dose to various organs and the mean effective dose from 185 MBq of [⁶⁸Ga]Ga-DOTA.SA.FAPi was approximately 2 mSv, which was within the safe admissible limits. [⁶⁸Ga]Ga-DOTA.SA.FAPi PET/CT imaging can be conducted as early as 10 minutes post-injection of the radiotracer. The diagnostic accuracy of [⁶⁸Ga]Ga-DOTA.SA.FAPi PET/CT closely matched to the standard of care imaging [¹⁸F]F-FDG-PET/CT. The findings clearly indicate the selective expression of [⁶⁸Ga]Ga-DOTA.SA.FAPi in various cancers makes a contribution to the current literature on FAP inhibitor molecular imaging. It provides an additional role of FAPi in the field of theranostics. In future, large scale multicentre studies with a homogenous patient population in different cancer types should be tested with a head-to-head comparison with the FAPi-02, 04, DOTA.SA.FAPi and FAPi-46 molecules to best comment on the superiority of the tracers.

Compliance with ethical standards

Conflict of interest: The authors declare that they have no conflict of interest.

Ethical clearance: Ref. No IECPG-22/2020.

Informed consent: we obtained written informed consent from all the patients before commencing the investigational PET/CT Scan.

Disclaimer: The current work has not been submitted for review or is not under acceptance for publication in any journal.

References

1. Warburg, O.; Wind, F.; Negelein, E. The metabolism of tumors in the body. *J. Gen. Physiol.* **1927**, *8*, 519–530, doi:10.1085/jgp.8.6.519.
2. Mankoff, D.A.; Eary, J.F.; Link, J.M.; Muzi, M.; Rajendran, J.G.; Spence, A.M.; Krohn, K.A. Tumor-Specific Positron Emission Tomography Imaging in Patients: [¹⁸F]Fluorodeoxyglucose and Beyond. *Clin Cancer Res.* **2007**, *13*, 3460–3469, doi:10.1158/1078-0432.CCR-07-0074.
3. Chang, J.M.; Lee, H.J.; Goo, J.M.; Lee, H.Y.; Lee, J.J.; Chung, J.K.; Im, J.G. False positive and false negative FDG-PET scans in various thoracic diseases. *Korean J. Radiol.* **2006**, *7*, 57–69, doi:10.3348/kjr.2006.7.1.57.
4. Davidson, B.; Trope, C.G.; Reich, R. The role of the tumor stroma in ovarian cancer. *Front Oncol.* **2014**, *4*, 104, doi: 10.3389/fonc.2014.00104.
5. Garin-Chesa, P.; Old, L.J.; Rettig, W.J. Cell surface glycoprotein of reactive stromal fibroblasts as a potential antibody target in human epithelial cancers. *Proc. Natl. Acad. Sci.* **1990**, *87*, 7235–7239, doi:10.1073/pnas.87.18.7235.
6. Cheng, J.D.; Dunbrack, R.L.; Valianou, M.; Rogatko, A.; Alpaugh, R.K.; Weiner, L.M. Promotion of tumor growth by murine fibroblast activation protein, a serine protease, in an animal model. *Cancer Res.* **2002**, *62*, 4767–4772.
7. Liu, R.; Li, H.; Liu, L.; Yu, J.; Ren, X. Fibroblast activation protein: A potential therapeutic target in cancer. *Cancer Biol Ther.* **2012**, *13*, 123–129, doi:10.4161/cbt.13.3.18696.
8. Jansen, K.; Heirbaut, L.; Verkerk, R.; Cheng, J.D.; Joossens, J.; Cos, P.; Maes, L.; Lambeir, A.M.; De Meester, I.; Augustyns, K.; et al. Extended structure-activity relationship and pharmacokinetic investigation of (4-quinolinoyl)glycyl-2-cyanopyrrolidine inhibitors of fibroblast activation protein (FAP). *J. Med. Chem.* **2014**, *57*, 3053–3074, doi:10.1021/jm500031w.
9. Giesel, F.L.; Kratochwil, C.; Lindner, T.; Marschalek, M.M.; Loktev, A.; Lehnert, W.; Debus, J.; Jäger, D.; Flechsig, P.; Altmann, A.; et al. ⁶⁸Ga-FAPI PET/CT: Biodistribution and preliminary dosimetry estimate of 2 DOTA-containing FAP-targeting agents in patients with various cancers. *J. Nucl. Med.* **2019**, *60*, 386–392, doi:10.2967/jnumed.118.215913.
10. Kratochwil, C.; Flechsig, P.; Lindner, T.; Abderrahim, L.; Altmann, A.; Mier, W.; Adebeg, S.; Rathke, H.; Röhrich, M.; Winter, H.; et al. ⁶⁸Ga-FAPI PET/CT: Tracer uptake in 28 different kinds of cancer. *J. Nucl. Med.* **2019**, *60*, 801–805, doi:10.2967/jnumed.119.227967.
11. Meyer, C.; Dahlbom, M.; Lindner, T.; Vauclin, S.; Mona, C.; Slavik, R.; Czernin, J.; Haberkorn, U.; Calais, J. Radiation Dosimetry and Biodistribution of ⁶⁸Ga-FAPI-46 PET Imaging in Cancer Patients. *J. Nucl. Med.* **2020**, *6*, 1171–1177, doi:10.2967/jnumed.119.236786.
12. Loktev, A.; Lindner, T.; Burger, E.M.; Altmann, A.; Giesel, F.; Kratochwil, C.; Debus, J.; Marmé, F.; Jäger, D.; Mier, W.; et al. Development of fibroblast activation protein-targeted radiotracers with improved tumor retention. *J. Nucl. Med.* **2019**, *60*, 1421–1429, doi:10.2967/jnumed.118.224469.
13. Moon, E.S.; Elvas, F.; Vliegen, G.; De Lombaerde, S.; Vangestel, C.; De Bruycker, S.; Bracke, A.; Eppard, E.; Greifenstein, G.; Klasen, B.; Kramer, V.; Staelens, S.; De Meester, I.; Van der Veken, P.; Roesch, F. Targeting fibroblast activation protein (FAP): next generation PET radiotracers

- using squaramide coupled bifunctional DOTA and DATA^{5m} chelators. *EJNMMI Radiopharm. Chem.* **2020**, *5*, 19, doi:10.1186/s41181-020-00102-z.
14. Ballal, S.; Yadav, M.P.; Kramer, V.; Moon, E.S.; Roesch, F.; Tripathi, M.; Mallick, S.; ArunRaj, S.T.; Bal, C. A theranostic approach of [⁶⁸Ga]Ga-DOTA.SA.FAPi PET/CT-guided [¹⁷⁷Lu]Lu-DOTA.SA.FAPi radionuclide therapy in an end-stage breast cancer patient: new frontier in targeted radionuclide therapy. *Eur. J. Nucl. Med. Mol. Imaging* **2021**, *48*, 942–944, doi:10.1007/s00259-020-04990-w.
 15. Valentin J. Basic anatomical and physiological data for use in radiological protection: reference values. A report of age- and gender-related differences in the anatomical and physiological characteristics of reference individuals. ICRP Publication 89. *Ann ICRP.* **2002**, *32*, 5–265.
 16. Ferrer, L.; Kraeber-Bodere, F.; Bodet-Milin, C.; Rousseau, C.; Gouill, S.L.; Wegener, W.A.; Goldenberg, D.M.; Bardiès, M. Three methods assessing redmarrow dosimetry in lymphoma patients treated with radioimmunotherapy. *Cancer* **2010**, *116*, 1093–1100, doi:10.1002/cncr.24797.
 17. Wahl, R.L.; Jacene, H.; Kasamon, Y.; Lodge, M.A. From RECIST to PERCIST: evolving considerations for PET response criteria in solid tumors. *J. Nucl. Med.* **2009**, *50*, 122–150, doi:10.2967/jnumed.108.057307
 18. Mandrekar, J.N. Measures of interrater agreement. *J. Thorac Oncol.* **2011**, *6*, 6–7, doi:10.1097/JTO.0b013e318200f983.
 19. Busek, P.; Hrabal, P.; Fric, P.; Sedo, A. Co-expression of the homologous proteases fibroblast activation protein and dipeptidyl peptidase-IV in the adult human Langerhans islets. *Histochem. Cell Biol.* **2015**, *143*, 497–504, doi:10.1007/s00418-014-1292-0.
 20. Chen, H.; Pang, Y.; Wu, J.; Zhao, L.; Hao, B.; Wu, J.; Wei, J.; Wu, S.; Zhao, L.; Luo, Z.; Lin, X. et al. Comparison of [⁶⁸Ga]Ga-DOTA-FAPi-04 and [¹⁸F]FDG PET/CT for the diagnosis of primary and metastatic lesions in patients with various types of cancer. *Eur. J. Nucl. Med. Mol. Imaging* **2020**, *47*, 1820–1832, doi:10.1007/s00259-020-04769-z.
 21. Liao, Y.; Ni, Y.; He, R.; Liu, W.; Du, J. Clinical implications of fibroblast activation protein- α in non-small cell lung cancer after curative resection: a new predictor for prognosis. *J. Cancer Res. Clin. Oncol.* **2013**, *139*, 1523–1528, doi:10.1007/s00432-013-1471-8.
 22. Wang, H.; Wu, Q.; Liu, Z.; Luo, X.; Fan, Y.; Liu, Y.; Zhang, Y.; Hua, S.; Fu, Q.; Zhao, M.; Chen, Y.; Fang, W.; Lv, X. Downregulation of FAP suppresses cell proliferation and metastasis through PTEN/PI3K/AKT and Ras-ERK signaling in oral squamous cell carcinoma. *Cell Death Dis.* **2014**, *5*, 1155, doi:10.1038/cddis.2014.122.
 23. Zhang, Y.; Tang, H.; Cai, J.; Zhang, T.; Guo, J.; Feng, D.; Wang, Z. Ovarian cancer-associated fibroblasts contribute to epithelial ovarian carcinoma metastasis by promoting angiogenesis, lymphangiogenesis and tumor cell invasion. *Cancer Lett.* **2011**, *303*, 47–55, doi:10.1016/j.canlet.2011.01.011.

Supporting Information

Supplementary Table 1: Comparison of SUL vales between [⁶⁸Ga]Ga-DOTA.SA.FAPi and [¹⁸F]F-FDG PET/CT in various organs.

Organs	SULpeak [⁶⁸ Ga]Ga- DOTA.SA.FAPi PET/CT median (IQR)	SULpeak [¹⁸ F]F-FDG PET/CT median (IQR)	P value	SULavg [⁶⁸ Ga]Ga- DOTA.SA.FAPi PET/CT median (IQR)	SULavg [¹⁸ F]F-FDG PET/CT median (IQR)	P value
Lacrimal glands	3.2 (2.9 - 3.6)	2.6 (2.3–3.1)	0.3125	1.4 (1.1 - 1.7)	1.8 (1.7–1.8)	0.078
Oral mucosa	2.3 (1.2 - 2.9)	2.5 (1.8 - 3)	0.5459	1.27 (0.77 - 1.6)	1.4 (1 - 1.7)	0.468
*Salivary glands	2.8 ± 0.8 (0.8 - 4)	1.7 ± 0.9 (0.4 - 4)	0.014	1.7 ± 0.5 (0.5 - 2.6)	1.3 ± 0.6 (0.29 - 2.84)	0.055
Thyroid	4.3 (3.3 - 5.6)	1.7 (1.3 - 1.8)	0.0001	2.6 (1.2–3.9)	1.08 (0.7 - 1.3)	0.0007
*Blood pool superior vena cava	1.7 ± 0.6 (0.7 - 3)	1.7 ± 0.6 (0.5 - 2.6)	0.501	1.07 ± 0.4 (0.4 - 1.9)	0.9 ± 0.3 (0.3 - 1.5)	0.599
*Myocardium	1.9 ± 1.0 (0.5 - 2.8)	3.5 ± 2.7 (1.0 - 9.9)	0.391	1.4 ± 0.7 (0.4 - 2.5)	2.2 ± 1.7 (0.7 - 5.2)	0.363
Liver	3.25 (2.4 - 3.6)	3 (2.8 - 3.6)	0.926	1.9 (1.2 - 2.3)	1.7 (1.5 - 2)	0.746
Spleen	1.7 (1.0 - 2.6)	2.06 (1.87 - 2.6)	0.401	1.1 (0.7 - 1.5)	2 (1.25 - 1.9)	0.402
Pancreas	7 (3.3 - 10.8)	1.7 (1.2 - 2.5)	0.0017	4.8 (1.3 - 8.05)	1.1 (0.8 - 1.4)	0.001
Duodenum	1.3 (1 - 1.8)	1.42 (1.32 - 1.58)	0.568	1.1 (0.9 - 1.34)	1 (0.52 - 1.2)	0.678
Kidneys	3 (2 - 5.4)	3.1 (2.3 - 5)	0.490	1.8 (1 - 2.9)	1.9 (1.5 - 2.5)	0.517
Psaos Muscle	1.2 (1.02 - 1.6)	0.9 (0.77 - 1.0)	0.005	0.8 (0.5 - 1.0)	0.7 (0.5 - 0.8)	0.098
Bone (L4 vertebrae)	1.5 (1.1 - 2.2)	2.2 (1.7 - 2.6)	0.080	1.06 (0.7 - 1.2)	1.46 (1.1 - 1.9)	0.032
*Femur	1 ± 0.5 (0.5 - 1.0)	1.3 ± 0.6 (0.5 - 2.7)	0.224	0.75 ± 0.4 (0.2 - 1.37)	0.9 ± 0.4 (0.42 - 1.7)	0.254
Brain normal parenchyma	0.2 (0.07 - 0.6)	7.5 (4.1 - 8.9)	<0.0001	0.05 (0.01 - 0.1)	4.4 (2.5 - 6.8)	<0.0001

SULpeak and avg: Standardised uptake value corrected for lean body mass; IQR: Interquartile range;

*values represented in the form of mean ± standard deviation (SD) and range.

Supplementary Table 2: Comparison of the Absorbed dose estimate among various [⁶⁸Ga]Ga-FAPI radiotracers

Site	Mean absorbed doses (mSv/MBq)			
	[⁶⁸ Ga]Ga-FAPI-02 Giesel et al. [9]	[⁶⁸ Ga]Ga-FAPI-04 Giesel et al. [9]	[⁶⁸ Ga]Ga-FAPI-46 Meyer et al. [11]	[⁶⁸ Ga]Ga- DOTA.SA.FAPI Current study
Adrenals	1.23E-02	1.12E-02	5.60E-03	7.77E-03
Brain	9.54E-03	9.11E-03	4.59E-03	5.06E-03
Breasts	9.58E-03	8.88E-03	4.55E-03	5.48E-03
Gallbladder wall	1.19E-02	1.13E-02	5.62E-03	8.37E-03
Lower large intestine wall	1.23E-02	1.17E-02	5.72E-03	6.41E-03
Small intestine	1.19E-02	1.13E-02	5.48E-03	6.26E-03
Stomach wall	1.13E-02	1.06E-02	5.32E-03	6.93E-03
Upper large intestine wall	1.17E-02	1.11E-02	5.47E-03	6.65E-03
Heart wall	4.73E-02	2.02E-02	1.11E-02	3.16E-02
Kidneys	4.45E-02	4.43E-02	1.60E-02	2.62E-02
Liver	1.51E-02	1.46E-02	1.01E-02	3.84E-02
Lungs	1.09E-02	9.89E-03	5.02E-03	6.62E-03
Muscle	1.04E-02	9.91E-03	4.96E-03	5.79E-03
Ovaries	1.24E-02	1.19E-02	5.76E-03	6.48E-03
Pancreas	1.23E-02	1.13E-02	5.69E-03	5.46E-02
Red marrow	3.28E-02	2.08E-02	7.08E-03	4.80E-03
Osteogenic cells	2.94E-02	2.16E-02	9.38E-03	8.66E-03
Skin	9.01E-03	8.63E-03	4.41E-03	4.96E-03
Spleen	2.62E-02	1.05E-02	6.96E-03	2.68E-02
Testes	1.04E-02	1.01E-02	4.88E-03	*
Thymus	1.15E-02	1.01E-02	5.10E-03	6.56E-03
Thyroid	1.03E-02	9.82E-03	4.84E-03	5.34E-03
Urinary bladder wall	8.89E-02	9.91E-02	4.83E-02	5.21E-02
Uterus	1.33E-02	1.30E-02	9.54E-03	6.98E-03

Total body	1.19E-02	1.09E-02	5.82E-03	7.05E-03
Effective dose (mSv/MBq)	1.80E-02	1.64E-02	7.80E-03	1.11E-02

LLI: Lower large intestine ULI:Upper large intestine, *Testes absorbed dose not derived as all the three patients included for the dosimetric analysis were females.

Supplementary Table 3: Patient-wise visual comparison between [⁶⁸Ga]Ga-DOTA.SA.FAPi and [¹⁸F]F-FDG PET/CT scans.

Site of the cancer	[⁶⁸ Ga]Ga-DOTA.SA.FAPi PET/CT (N)				[¹⁸ F]F-FDG PET/CT (N)				Discordance (%)
	TP	TN	FP	FN	TP	TN	FP	FN	
Primary disease	36	18	0	0	36	18	0	0	0%
Lymph node metastases	39	13	0	2	41	11	2	0	7.5%
Lung metastases	28	25	0	1	26	24	2	2	5.6%
Pleural thickening	10	44	0	0	10	44	0	0	0%
Bone metastases	14	40	0	0	14	40	0	0	0%
Liver metastases	16	38	0	0	16	38	0	0	0%
Brain metastases	13	41	0	0	12	41	0	1	2%
Second primary malignancy	1	53	0	0	1	53	0	0	0%

TP: true positive; TN: true negative; FP: false positive; FN: false negative

B. In Vitro Evaluation of the Squaramide-Conjugated Fibroblast Activation Protein Inhibitor-Based Agents AAZTA⁵.SA.FAPi and DOTA.SA.FAPi

Veröffentlicht in *Molecules* **2021**, *26*, 3482.

mit Genehmigung von © MDPI (Basel, Switzerland)

In Vitro Evaluation of the Squaramide-Conjugated Fibroblast Activation Protein Inhibitor-Based Agents AAZTA⁵.SA.FAPi and DOTA.SA.FAPi

Euy Sung Moon¹, [REDACTED]
[REDACTED]

¹ Department of Chemistry – TRIGA, Johannes Gutenberg University Mainz, Mainz, Germany

² Laboratory of Medical Biochemistry, Department of Pharmaceutical Sciences, University of Antwerp, Wilrijk, Belgium

³ Laboratory of Medical Chemistry, Department of Pharmaceutical Sciences, University of Antwerp, Wilrijk, Belgium

*Corresponding author: [REDACTED]

Abstract

Recently, the first squaramide-(SA) containing FAP inhibitor-derived radiotracers were introduced. DATA^{5m}.SA.FAPi and DOTA.SA.FAPi with their non-radioactive complexes showed high affinity and selectivity for FAP. After a successful preclinical study with [⁶⁸Ga]Ga-DOTA.SA.FAPi, the first patient studies were realized for both compounds. Here, we present a new squaramide-containing compound targeting FAP, based on the AAZTA⁵ chelator 1,4-bis-(carboxymethyl)-6-[bis-(carboxymethyl)-amino-6-pentanoic-acid]-perhydro-1,4-diazepine.

For this molecule (AAZTA⁵.SA.FAPi), complexation with radionuclides such as gallium-68, scandium-44, and lutetium-177 was investigated, and the in vitro properties of the complexes were characterized and compared with those of DOTA.SA.FAPi. AAZTA⁵.SA.FAPi and its derivatives labelled with non-radioactive isotopes demonstrated similar excellent inhibitory potencies compared to the previously published SA.FAPi ligands, i.e., sub-nanomolar IC₅₀ values for FAP and high selectivity indices over the serine proteases PREP and DPPs. Labeling with all three radiometals was easier and faster with AAZTA⁵.SA.FAPi compared to the corresponding DOTA analogue at ambient temperature. Especially, scandium-44 labeling with the AAZTA derivative resulted in higher specific activities. Both DOTA.SA.FAPi and AAZTA⁵.SA.FAPi showed sufficiently high stability in different media. Therefore, these FAP inhibitor agents could be promising for theranostic approaches targeting FAP.

Keywords: AAZTA; scandium-44; lutetium-177; FAP; SA; DPP; PREP

Introduction

Fibroblast activation protein (FAP) is a post-prolyl proteolytic enzyme that belongs to the S9 family of serine proteases [1]. In addition to FAP, this S9 family includes other proline-specific serine proteases, such as prolyl oligopeptidase (PREP) and the dipeptidyl peptidases 4, 8, and 9 (DPP4, DPP8, and DPP9). Targeting fibroblast activation protein (FAP), overexpressed selectively in cancer-associated fibroblasts (CAFs), has recently become an attractive goal for diagnostic imaging and first therapeutic trials. FAP is involved in the promotion and development of tumor growth and is typically overexpressed in activated fibroblasts in the tumor stroma, whereas it is absent in most normal healthy tissues. Furthermore, FAP is overexpressed in several pathological tissue sites that are characterized by active remodeling [2–5]. Expression of FAP is found in CAFs in approximately 90% of epithelial carcinomas such as breast, pancreatic, colon, and prostate tumors. [6–8]. These properties make FAP a very interesting and universally applicable tumor target for a variety of tumor types.

PET tracers that operate as FAP-specific enzyme inhibitors (FAPI), have first been published by Lindner and Loktev et al. [9–11]. The FAP inhibitor used is a small molecule with an N-acylated glycyyl(2-cyano-4,4-difluoropyrrolidine) that binds to FAP active site and blocks its enzymatic activity. This highly potent inhibitor, referred to as UAMC1110, shows high affinity for FAP but not for the DPPs and PREP [12]. Meanwhile, many clinical trials have been initiated with related PET tracers based on the same FAP inhibitor [13–21]. Lindner and Loktev et al. developed DOTA-based FAP inhibitor conjugates with heterocyclic units as spacer. The most prominent are FAPI-04 and FAPI-46, with piperazine between chelator and inhibitor. Other examples include a glycosylated fluorine-18 derivative and tracers for SPECT applications with technetium-99 and rhenium-188 introduced by tricarbonyl ligands with piperazine linker systems [22–23]. Recently, we developed FAP inhibitor agents using squaramide-combined bifunctional chelators [24]. The use of a squaramide linker facilitated the synthetic work and delivered compounds with good pharmacological properties. The latter results were illustrated by the excellent in vitro affinity of these products for FAP and by their in vivo behavior in preclinical and clinical applications. With respect to clinical studies, the DATA^{5m}.SA.FAPI derivative showed specific tracer uptake in focal nodular hyperplasia via ⁶⁸Ga-PET/CT [25]. The DOTA.SA.FAPI tracer displayed a high target-to-background ratio during ⁶⁸Ga-PET/CT studies in patients with various cancers [26].

The advantageous properties of gallium-68, such as its high positron energy with $\beta^+ = 89\%$ and $E_{\beta,avg} = 830$ keV and its good accessibility due to the availability of ⁶⁸Ge/⁶⁸Ga generators, make it a commonly used PET radionuclide [27]. However, the short physical half-life of the nuclide (1.1 h) may impede focusing on longer-lasting physiological processes in PET/CT measurements. Scandium-44, which is

also characterized by a high branching ratio of $\beta^+ = 94\%$ and $E_{\beta, \text{avg}} = 632 \text{ keV}$, could be a valuable alternative with a $t_{1/2}$ of 4.0 h. There are two ways to produce scandium-44: one uses a cyclotron via the $^{44}\text{Ca}(p,n)^{44}\text{Sc}$ reaction, and the other, that we chose, uses a $^{44}\text{Ti}/^{44}\text{Sc}$ generator [27–29]. An established post-processing elution protocol provides carrier-free scandium-44 from a 185 MBq generator, with ~90% elution efficiency and a titanium-44 breakthrough of only $< 7 \text{ MBq}$ [30]. Due to its four-time longer half-life than gallium-68, the β^+ -emitter scandium-44 could be better suited for pretherapeutic PET/CT measurements resulting in individual dosimetric calculations in endoradiotherapy with longer-lived therapy nuclides such as yttrium-90, lutetium-177, or scandium-47. Scandium-44 has already been used in both preclinical and clinical applications [31–35]. In particular, the first in human PET measurements in metastasized castrate-resistant prostate cancer with $[^{44}\text{Sc}]\text{Sc-PSMA-617}$ indicated its potential as PET nuclide and pre-therapeutic agent [36]. Furthermore, the β^- -emitter lutetium-177, with a half-life of 6.7 days, is nowadays a very commonly used radionuclide in radioendotherapy. It is clinically used for neuroendocrine tumors in the somatostatin analogues $[^{177}\text{Lu}]\text{Lu-DOTATOC}$ and $[^{177}\text{Lu}]\text{Lu-DOTATATE}$ for peptide-mediated radioreceptor therapy and for treatment of prostate carcinomas by means of lutetium-177-PSMA therapy with PSMA derivatives such as PSMA-617 and PSMA-I&T [37–43].

In this work, we introduce a novel FAP inhibitor agent called AAZTA⁵.SA.FAPi. AAZTA chelators allow fast and quantitative complexation under mild conditions and display high stability. This is in particular relevant for radionuclides with high needs of coordination capacity, such as scandium-44 and lutetium-177.

Together with the recently published DOTA.SA.FAPi, both precursors were radiochemically investigated in terms of labeling and stability with gallium-68, scandium-44, and lutetium-177 and tested for their in vitro properties.

Results and Discussion

Synthesis of Chelator Conjugates

For AAZTA⁵.SA.FAPi, we first synthesized AAZTA⁵(^tBu)₄. The coupling of squaric acid to the terminal carboxyl group and the subsequent binding to the FAP inhibitor was performed in the same way as for the previously described DATA^{5m}.SA.FAPi [24]. Figure 1 shows the synthesis route of AAZTA⁵.SA.FAPi, following the protocol of Sinnes et al. and Greifenstein et al. [44,45].

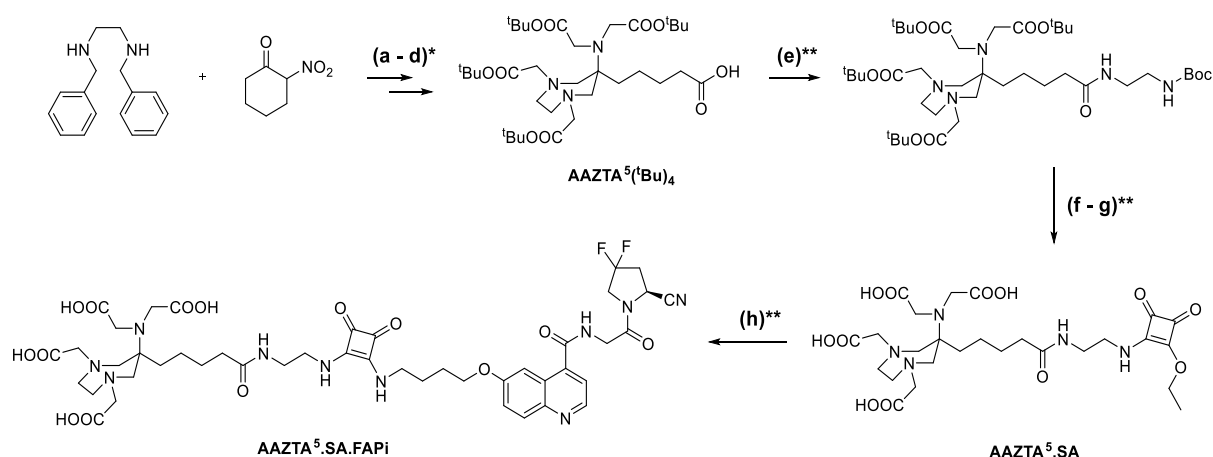


Figure 1. Synthesis of AAZTA⁵.SA.FAPi via AAZTA⁵(tBu)₄ and AAZTA⁵.SA: (a) 2-nitrocyclohexanone, Amberlyst A21, paraformaldehyde, methanol, 80 °C, 16 h; (b) palladium hydroxide/C, acetic acid, hydrogen, ethanol, 25 °C, 16 h; (c) tert-butyl bromoacetate, potassium carbonate, potassium iodide, acetonitrile, 40 °C, 48-72 h; (d) 1 M lithium hydroxide, 1,4-dioxane/water (2:1), 25 °C, 16 h; (e) N-Boc-ethylenediamine, HATU, HOBT, DIPEA, acetonitrile, 25 °C, 16 h; (f) dichloromethane/TFA (80:20)%, 25 °C, 7 h; (g) 3,4-diethoxycyclobut-3-ene-1,2-dione, 0.5 M phosphate buffer pH= 7, 25 °C, 16 h; (h) NH₂-UAMC1110, 0.5 M phosphate buffer pH= 9, 25 °C, 16 h; (*) as reported [44,45]; (**) as reported [24]. DOTA.SA.FAPi was synthesized as previously described [24].

Figure 2 shows the structures of the FAP inhibitor probes DOTA.SA.FAPi and AAZTA⁵.SA.FAPi.

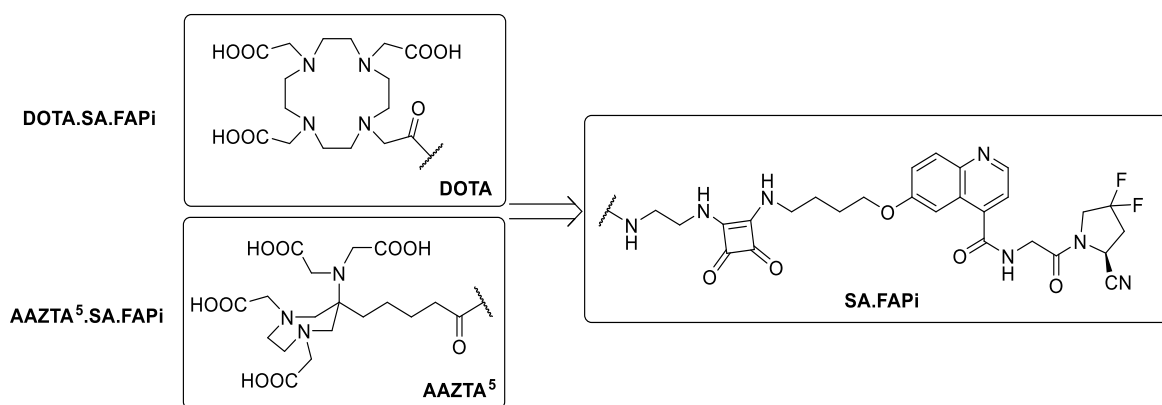


Figure 2. Structures of DOTA.SA.FAPi and AAZTA⁵.SA.FAPi.

In Vitro Inhibition Measurements

The IC₅₀ values for FAP, PREP, and the DPPs of the hybrid chelator conjugate AAZTA⁵.SA.FAPi compared to those of DOTA.SA.FAPi are shown in Table 1. The IC₅₀ values of AAZTA⁵.SA.FAPi as well as those of its non-radioactive complexes [^{nat}Sc]Sc-AAZTA⁵.SA.FAPi and [^{nat}Lu]Lu-AAZTA⁵.SA.FAPi for FAP appeared to be in the low nanomolar range (0.55–0.57 nM), whereas the IC₅₀ values for PREP resulted

in the low micromolar range (2.4–3.6 μM). Screening against DPP4 and DPP9 for both SA.FAPi complexes revealed that the remaining activity was more than 50% at a final concentration of 1 μM . Hence, the IC_{50} values for the DPPs were reported as >1 μM . The absence of a basic amine in the FAP inhibitor is known to result in an enormous increase of selectivity for the target molecule FAP, whereas the affinity for the DPPs can be drastically reduced. [12,46]. The IC_{50} values for FAP and PREP were in the same order of magnitude of those for the previously reported SA.FAPi compounds, i.e., indicating high inhibition potency and excellent FAP-to-PREP selectivity indices. In addition, high selectivity towards DPP4 and DPP9 was achieved.

Table 1. IC_{50} values of AAZTA⁵.SA.FAPi and DOTA.SA.FAPi derivatives for FAP and the related proteases DPPs and PREP. Data are presented as the mean with standard deviation ($n = 3$ for FAP and PREP and $n = 2$ for the DPPs).

Compound	DPPs	PREP	FAP	Selectivity Index (FAP/PREP)
	IC_{50} (μM)	IC_{50} (μM)	IC_{50} (nM)	
AAZTA ⁵ .SA.FAPi	>1	2.4 ± 0.4	0.56 ± 0.02	4286
[^{nat} Sc]Sc-AAZTA ⁵ .SA.FAPi	>1	3.6 ± 0.8	0.57 ± 0.04	6316
[^{nat} Lu]Lu-AAZTA ⁵ .SA.FAPi	>1	3.2 ± 0.6	0.55 ± 0.04	5818
DOTA.SA.FAPi	n.d.	5.4 ± 0.3^a	0.9 ± 0.1^a	6000
[^{nat} Ga]Ga-DOTA.SA.FAPi	>1	8.7 ± 0.9^a	1.4 ± 0.2^a	6214
[^{nat} Lu]Lu DOTA.SA.FAPi	>1	2.5 ± 0.4^a	0.8 ± 0.2^a	3125
DATA ^{5m} .SA.FAPi	n.d.	1.7 ± 0.1^a	0.8 ± 0.2^a	2113
[^{nat} Ga]Ga-DATA ^{5m} .SA.FAPi	>1	4.7 ± 0.3^a	0.7 ± 0.1^a	6714
UAMC1110-FAP inhibitor	>10	1.8 ± 0.01^b	0.43 ± 0.07^a	4186

^a data from Moon et al. [24]; ^b data from Jansen et al. [12]; n.d. not determined.

Radiolabeling and in Vitro Stability in Complex with Gallium-68, Scandium-44, and Lutetium-177

Gallium-68: DOTA.SA.FAPi complexed with gallium-68 showed very high kinetics in quantitative radiochemical yields (RCYs) in our previous work [24]. Gallium labeling of AAZTA⁵.SA.FAPi with diverse precursor amounts (10, 15 and 20 nmol) was performed at room temperature (Figure 3a). [⁶⁸Ga]Ga-AAZTA⁵.SA.FAPi displayed quantitative complexation already after 3–5 min (Figure 3a, Figure S1).

Compared to the DOTA derivative, complexation led to very high RCYs for tracer amounts ≥ 10 nmol, even at ambient temperature. In the case of the previously reported DOTA.SA.FAPi, high RCYs could only be achieved with an amount ≥ 15 nmol and at a high temperature of 95 °C. The stability of $[^{68}\text{Ga}]\text{Ga-AAZTA}^5\text{.SA.FAPi}$ in human serum (HS), ethanol (EtOH), and saline (NaCl) was excellent, with $> 99.9\%$ intact complexes over a measured time period of 2 h (Figure 3b, Figure S2–S4).

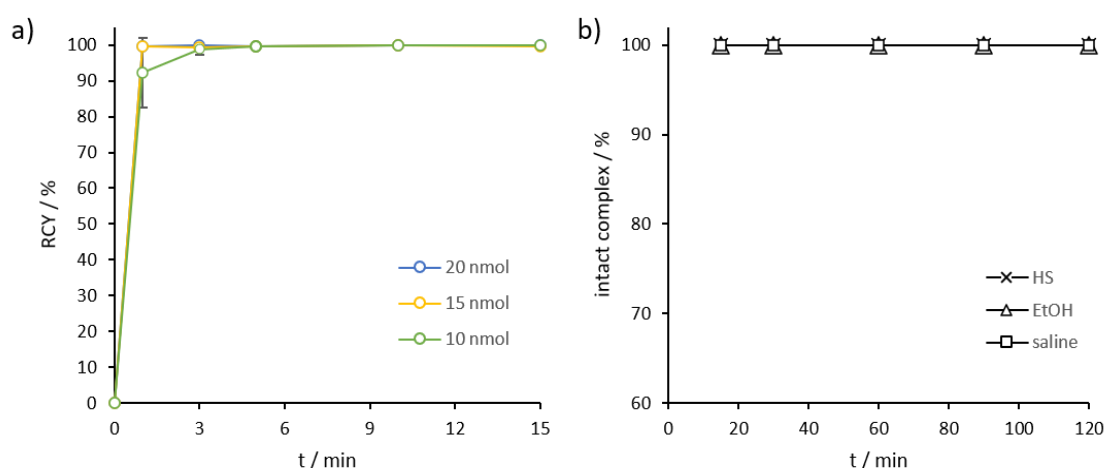


Figure 3. (a) Kinetics of $[^{68}\text{Ga}]\text{Ga-AAZTA}^5\text{.SA.FAPi}$ at RT for tracer amounts ≥ 10 nmol ($n = 3$); (b) Stability of $[^{68}\text{Ga}]\text{Ga-AAZTA}^5\text{.SA.FAPi}$ at 37 °C in HS, EtOH, and NaCl over a period of 120 min ($n = 3$).

Scandium-44: AAZTA⁵.SA.FAPi demonstrated excellent complexation with scandium-44 even at RT. We tested 5–20 nmol of precursor, which resulted in quantitative labeling already after 5 min for all amounts (Figure 4a, Figure S5). Stability was tested in HS, phosphate-buffered saline (PBS), and NaCl at 37 °C, demonstrating in highly satisfactory values in all three media (Figure 4b, Figure S6–S11). After 1 h, $[^{44}\text{Sc}]\text{Sc-AAZTA}^5\text{.SA.FAPi}$ conjugates were stable, with $> 99\%$ intact conjugate in all three media. Even up to the end of the measurement (8 h), the intact conjugates were stable in PBS and saline ($> 99\%$) and in HS ($> 97\%$) (Figure 4b).

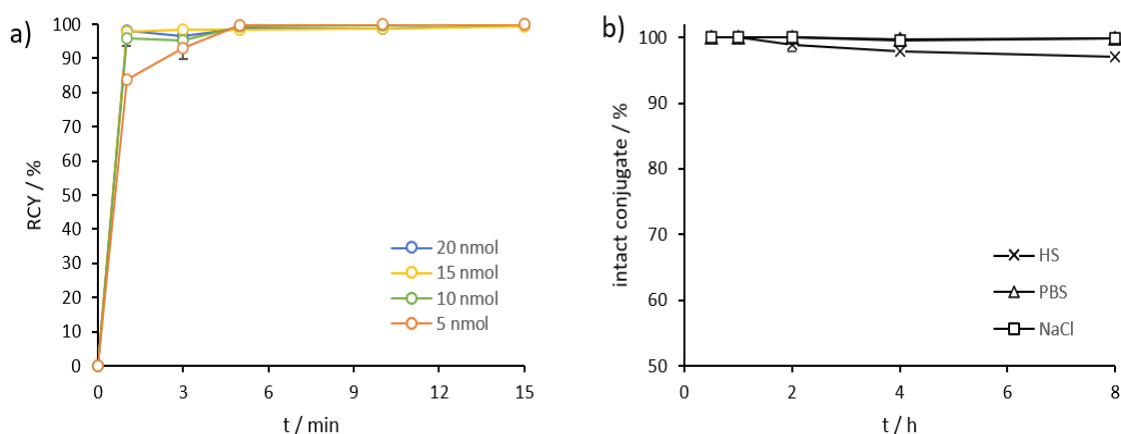


Figure 4. (a) Kinetics of [^{44}Sc]Sc-AAZTA⁵.SA.FAPi at RT for tracer amounts ≥ 5 nmol ($n = 3$ for 10; $n = 1$ for 5, 15, and 20 nmol); (b) Stability of [^{44}Sc]Sc-AAZTA⁵.SA.FAPi at 37 °C in HS, PBS, and NaCl over a period of 8 h ($n = 3$).

DOTA.SA.FAPi also showed good complexation with scandium-44. However, whereas [^{44}Sc]Sc-AAZTA⁵.SA.FAPi already displayed quantitative RCYs with 5 nmol (GBq/ 0.17 μmol) of precursors, [^{44}Sc]Sc-DOTA.SA.FAPi showed very low complexation with 20 nmol. Only with a quantity of 30 nmol, DOTA.SA.FAPi high yields with scandium-44 were reached, with RCYs $> 83\%$ and $> 95\%$, when, respectively, 30 and 40 nmol (GBq/ 1.33 μmol) were used (Figure 5a). Stability in HS, PBS, and NaCl were high over the measured period of 8 h, resulting in $> 97\%$ intact complexes with ^{44}Sc in all three medias (Figure 5b).

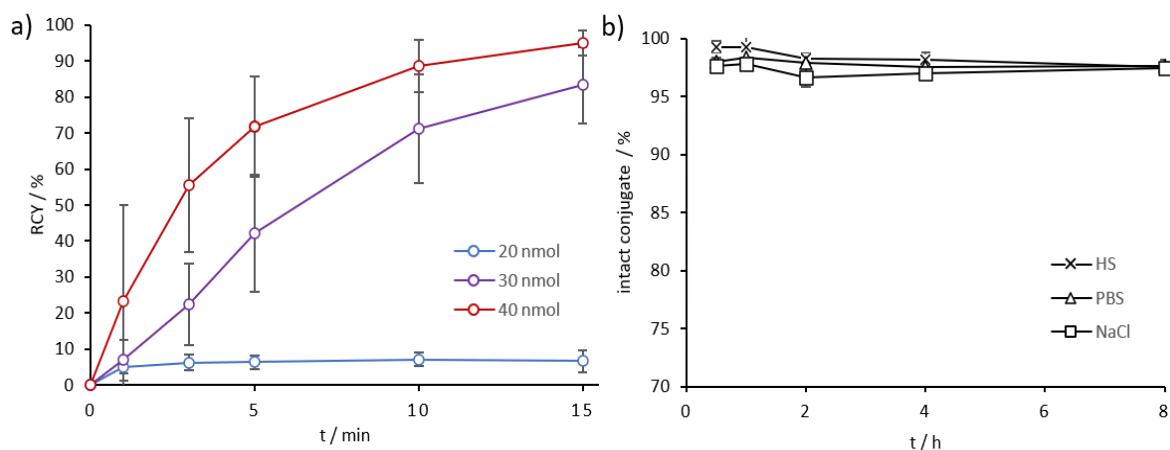


Figure 5. (a) Kinetics of [^{44}Sc]Sc-DOTA.SA.FAPi at 95 °C for tracer amounts ≥ 20 nmol ($n = 5$ for 20–40 nmol); (b) Stability of [^{44}Sc]Sc-DOTA.SA.FAPi at 37 °C in HS, PBS, and NaCl over a period of 8 h ($n = 3$).

Lutetium-177: For both DOTA.SA.FAPi and AAZTA⁵.SA.FAPi, precursors at a concentration of 20 nmol were used for labeling with lutetium-177. Both derivatives presented quantitative complexations with the radiometal after 60 min (Figure 6, Figure S12). The ^{177}Lu -AAZTA derivative showed $> 99\%$ RCY

already after 1 min at RT, whereas the ^{177}Lu -DOTA derivative reached > 99% complexation after 15 min at 95 °C (Figure 6).

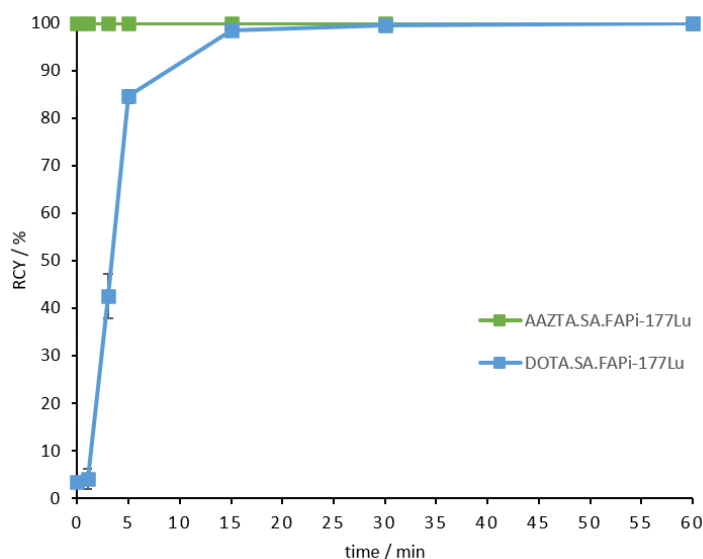


Figure 6. Kinetic measurements for ^{177}Lu -AAZTA⁵.SA.FAPi up to 60 min (green); Kinetic measurements for ^{177}Lu -DOTA.SA.FAPi up to 60 min (blue); ($n = 3$, 20 nmol for both conjugates).

Stability studies of both conjugates were performed in HS, PBS, and saline over a period of 10 days at 37 °C. In PBS and NaCl, very high stability values could be achieved for ^{177}Lu -AAZTA⁵.SA.FAPi, with > 99% after 2 d, > 98% after 3 d, and > 95% intact conjugates after 10 days. In HS, the ^{177}Lu -AAZTA complex showed > 99% of stability after 1 h, > 98% after 3 h, and > 96% after 6 h. However, the stability decreased significantly with time. After 1 d, the remaining stability of ^{177}Lu -AAZTA⁵.SA.FAPi in HS was > 83%, after 2 d it was > 64%, and after 3 d it was > 55% (Figure. 7a). Nevertheless, the stability of ^{177}Lu -AAZTA⁵.SA.FAPi in HS was satisfactory, with > 95% intact conjugate after 6 h. If it is assumed that small molecules accumulate in the target tissue within the first few hours, and therefore their stability in HS over a long period is not relevant. ^{177}Lu -DOTA.SA.FAPi showed very high stability, with > 99% of intact conjugate in HS within the measured time period of 10 days. In PBS and NaCl, the stability was high, i.e., > 98 % after 3 d and still > 93 % after 10 d (Figure 7b).

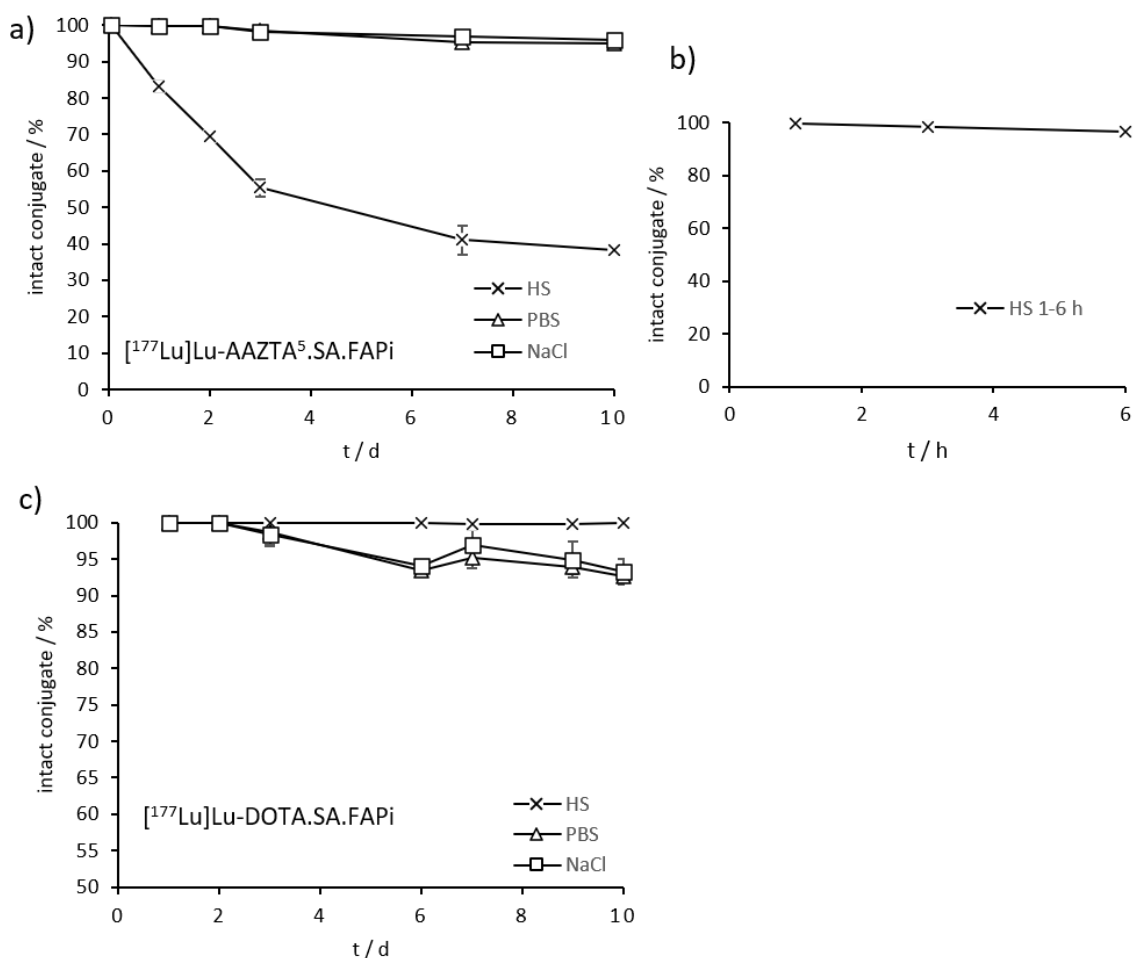


Figure 7. (a) Stability of $[^{177}\text{Lu}]\text{Lu-AAZTA}^5\text{.SA.FAPi}$ at 37 °C in HS, PBS, and NaCl over a period of 10 d ($n = 3$); (b) Stability of $[^{177}\text{Lu}]\text{Lu-AAZTA}^5\text{.SA.FAPi}$ at 37 °C in HS after 1, 3, and 6 h ($n = 3$); (c) Stability measurements of $[^{177}\text{Lu}]\text{Lu-DOTA.SA.FAPi}$ at 37 °C in HS, PBS, and NaCl during 10 d ($n = 3$).

Lipophilicity Measurements

Lipophilicity (logD value) was determined via the “shake-flask” method. For both precursors AAZTA⁵.SA.FAPi and DOTA.SA.FAPi logD (pH= 7.4), values were measured for the ⁶⁸Ga- and ⁴⁴Sc complexes. Table 2 shows the logD values for the respective radiotracers.

Table 2. LogD values (pH = 7.4) of $[^{68}\text{Ga}]\text{Ga-AAZTA}^5\text{.SA.FAPi}$, $[^{44}\text{Sc}]\text{Sc-AAZTA}^5\text{.SA.FAPi}$ and $[^{68}\text{Ga}]\text{Ga-DOTA.SA.FAPi}$.

Compound	LogD _{7.4}
$[^{68}\text{Ga}]\text{Ga-AAZTA}^5\text{.SA.FAPi}$	-2.53 ± 0.13
$[^{44}\text{Sc}]\text{Sc-AAZTA}^5\text{.SA.FAPi}$	-2.50 ± 0.11
$[^{68}\text{Ga}]\text{Ga-DOTA.SA.FAPi}$	-2.68 ± 0.06

The lipophilicity of the radiolabeled compounds [^{68}Ga]Ga-AAZTA⁵.SA.FAPi, [^{68}Ga]Ga-AAZTA⁵.SA.FAPi and [^{44}Sc]Sc-AAZTA⁵.SA.FAPi resulted located in hydrophilic ranges. Both gallium-68 derivatives [^{68}Ga]Ga-DOTA.SA.FAPi and [^{68}Ga]Ga-AAZTA⁵.SA.FAPi showed almost identical logD values of -2.68 and -2.53 , respectively. The carboxyl groups and the ionic bonds between chelator and radiometal favor the hydrophilic character of these radiotracers. The logD value of FAPI-04 is reported in the literature as -2.4 ± 0.28 , confirming the hydrophilic character of ^{68}Ga -DOTA complexes [22]. [^{44}Sc]Sc-AAZTA⁵.SA.FAPi display a similar logD value of -2.50 compared to gallium-68 derivatives. There seems to be no great influence of the DOTA and AAZTA chelators in the presence of gallium-68 and scandium-44 radiometals on the lipophilicity of the FAPi radiopharmaceuticals.

Materials and Methods

General

All basic chemicals were purchased from Merck KGaA (Darmstadt, Germany), TCI Deutschland GmbH (Eschborn, Germany), Fisher Scientific GmbH (Schwerte, Germany), Thermo Fisher GmbH (Kandel, Germany) and VWR International GmbH (Darmstadt, Germany) and used without further purification. (S)-6-(4-aminobutoxy)-N-(2-(2-cyano-4,4-difluoropyrrolidin-1-yl)-2-oxoethyl)-quinoline-4-carboxamide (called NH₂-UAMC1110) was purchased from KE Biochem Co. (Shanghai, China). Thin-layer chromatography was performed with silica gel 60 F254-coated aluminum plates that were acquired from Merck KGaA (Darmstadt, Germany). Detection was carried out by fluorescence extinction at $\lambda = 254$ nm and by staining with potassium permanganate. The LC/MS spectra were measured on an Agilent Technologies 1220 Infinity LC system coupled to an Agilent Technologies 6130B Single Quadrupole LC/MS system. NMR measurements were performed at 400 MHz (400 MHz FT NMR spectrometer AC 400, Bruker Analytik GmbH). For HPLC (high-performance liquid chromatography) a 7000 series Hitachi LaChrom with a Hitachi L7100 pump, an L7400 UV detector, and a Phenomenex Synergi C18 (250 x 10 mm, 4 μ) column (Aschaffenburg, Germany) were used.

Organic Synthesis

Synthesis of DOTA.SA.FAPi was reported recently [24]. Synthesis of AAZTA⁵.SA.FAPi was realized by first generating AAZTA⁵(^tBu)₄ according to the procedure by Sinnes et al. and Greifenstein et al. [44,45]. Subsequent coupling to the SA.FAPi conjugate was performed using the protocol published earlier for

the analogous DATA^{5m}.SA.FAPi precursor [24]. After HPLC purification with a gradient of 10–20% MeCN (+0.1% TFA)/90–80% water (+0.1% TFA) in 20 min., AAZTA⁵.SA.FAPi was obtained as a yellowish solid (16.8 mg; 0.02 mmol; 41%). MS (ESI⁺): 500.3 (M+2H²⁺); 999.3 (M+H⁺); calculated for C₄₅H₅₆F₂N₁₀O₁₄: 998.40.

Non-Radioactive Compounds and in Vitro Inhibition Studies

^{nat}Sc/^{nat}Lu-AAZTA⁵.SA.FAPi were synthesized by reaction of 5.0 mg (5 μmol) AAZTA⁵.SA.FAPi with 1.5 eq ^{nat}ScCl₃ and ^{nat}LuCl₃, respectively, in 500 μL 0.5 M NaAc buffer pH 4.5 for 2 h at room temperature. Complexation was confirmed by ESI–MS, and HPLC purification was performed with a flow rate 5 mL/min, H₂O (+0,1% TFA)/MeCN (+0,1% TFA), with a linear gradient condition of 5–95% MeCN in 10 min. The products (4.1 mg; 3.9 μmol; 79% for ^{nat}Sc-complex and 4.2 mg; 3.6 μmol; 72%) were obtained as a yellowish powder. MS (ESI⁺) for ^{nat}Sc-complex: m/z (%): 521.3 (M+2H)²⁺; 1041.4 (M+H)⁺ calculated for C₄₅H₅₂F₂ScN₁₀O₁₄: 1039.9 and ^{nat}Lu-complex: m/z (%): 586.2 (M+2H)²⁺; 1171.4 (M+H)⁺ calculated for C₄₅H₅₂F₂LuN₁₀O₁₄: 1169.9

Inhibition Assays

Enzymes: Recombinant human FAP and PREP were expressed and purified as published [24]. Recombinant human dipeptidyl 9 (DPP9) was purified as described by De Decker et al. [46]. Human dipeptidyl peptidase 4 was purified from seminal plasma as published [47].

IC₅₀ measurements and counter-screening: IC₅₀-measurements of the probes for FAP and PREP were carried out as published, using, respectively, Z-Gly-Pro-AMC and Suc-Gly-Pro-AMC as the substrate [24]. IC₅₀ experiments were repeated in triplicate, and the results are presented as mean ± standard deviation. Methods and data fitting were performed as published earlier [24]. Screening against DPP4 and DPP9 was performed at final probe concentrations of 10 μM and 1 μM using Ala-Pro-*paranitro*anilide (pNA) as the substrate at the respective final concentrations of 25 μM (DPP4) and 150 μM (DPP9) at pH 7.4 (0.05 M HEPES-NaOH buffer with 0.1% Tween-20, 0.1 mg/mL BSA, and 150 mM NaCl). Probes were pre-incubated with the respective enzyme for 15 min at 37 °C; afterwards, the substrate was added, and the velocities of pNA release were measured kinetically at 405 nm for at least 10 min at 37 °C. Measurements were executed using the Infinite 200 (Tecan Group Ltd.), and the Magellan software was used to process the data. If the remaining activity was more than 50% at 1 μM, the IC₅₀ values for the DPPs were reported as > 1 μM.

Radiolabeling and Stability Measurements

Gallium-68: $^{68}\text{Ge}/^{68}\text{Ga}$ generators (ITG Garching, Germany) were used with ethanol-based post-processing evaluated by Eppard et al. [48]. Elution of gallium-68 was performed with 0.05 M HCl trapped on a micro-chromatography CEX column AG 50W-X4. The column was washed with 80% EtOH/0.15 M HCl, and $^{68}\text{Ga}^{3+}$ was eluted with 90% EtOH/0.9 M HCl.

Scandium-44: Scandium-44 was obtained by a $^{44}\text{Sc}/^{44}\text{Ti}$ generator [29,30,36]. A solution of 0.005 M $\text{H}_2\text{C}_2\text{O}_4$ /0.07 M HCl was eluted through the $^{44}\text{Ti}/^{44}\text{Sc}$ generator to adsorb $^{44}\text{Sc}^{3+}$ onto the cation exchanger AG 50 W-X8. Elution of scandium-44 was executed with 0.25 M ammonium acetate buffer pH 4.

Lutetium-177: n.c.a. ^{177}Lu]LuCl₃ in 0.04 M HCl was provided by ITG Garching, Germany.

Radioactivity was measured using a PC-based dose calibrator (ISOMED 2010, Nuklear Medizintechnik Dresden GmbH). Reaction controls were done using radio-TLC, with 0.1 M citrate buffer pH 4 and an analytical HPLC 7000 series Hitachi LaChrom with a Phenomenex Luna C18 column (250 x 4.6 mm, 5 μ), linear gradient of 5–95% MeCN (+0.1% TFA)/H₂O (+0.1% TFA), flow rate 1 mL/min in 10 min. TLCs were measured in a CR-35 Bio Test-Imager from Duerr-ndt (Bietigheim-Bissingen, Germany) with the analysis software AIDA Elysia-Raytest (Straubenhardt, Germany).

Labeling was carried out with 100–150 MBq gallium-68 in 300 μ L of 1 M ammonium acetate (AmAc) buffer pH 5.5 and with 30–40 MBq scandium-44 in 1 mL of 0.25 M AmAc pH 4.0, and aliquots were taken at 1, 3, 5, 10, and 15 min. For lutetium-177, activity of 30–40 MBq in 300 μ L of 1 M AmAc pH 5.5 was used, and aliquots were taken at 1, 3, 5, 15, 30 and 60 min. Stability was tested in 500 μ L of human serum, phosphate-buffered saline, ethanol, and saline (0.9 % isotonic NaCl solution) using ~5 MBq of tracer solution with > 95% radiochemical purity. The measured time points were adjusted to the physical half-lives, i.e., gallium-68 (15, 30, 60, 90, 120 min), scandium-44 (0.5, 1, 2, 4, 8 h), and lutetium-177 (1–6 h, 1, 2, 3, 7, 10 d). HS (human male AB plasma, USA origin) and PBS were purchased from Sigma Aldrich, and 0.9% saline from B. Braun Melsungen AG (Melsungen, Germany).

Lipophilicity Determination

Lipophilicity of ^{68}Ga]Ga-AAZTA⁵.SA.FAPi, ^{44}Sc]Sc-AAZTA⁵.SA.FAPi and ^{68}Ga]Ga-DOTA.SA.FAPi was determined using the “shake-flask” methodology. After reaction of the precursor with the respective radionuclide, the reaction solution was adjusted to pH 7.4 with NaOH. Aliquots of ~5 MBq for the ^{68}Ga complexes and of ~3 MBq for the ^{44}Sc -complexed were taken and adjusted to a total volume of 700 μ L with PBS ($n = 4$). 700 μ L 1-octanol was added, and the solution was shaken for 2 min (1500 rpm).

Afterwards, each tube was centrifuged for 2 min. 400 μL of the octanol- and PBS phases were pipetted in new tubes, and aliquots of each phase (3 μL of the PBS phase and 6 μL of the octanol phase) were measured via radio-TLC. The PBS phases were adjusted to 700 μL , and 700 μL octanol was added to each tube. The procedure was repeated twice. LogD values were calculated as the logarithm of the octanol/PBS ratio.

Conclusions

In this work, a new squaramide FAPi conjugate to the AAZTA chelator is introduced. After successful preparative synthesis, the complex was tested for its *in vitro* binding characteristics and compared to the analogue DOTA.SA.FAPi derivative, published recently [24]. The inhibitory potency studies of AAZTA⁵.SA.FAPi showed excellent sub-nanomolar affinities for FAP, in the same order of magnitude of those of the already published SA.FAPi monomeric structures DATA^{5m}.SA.FAPi and DOTA.SA.FAPi. Furthermore, high selectivity against PREP and the DPPs was achieved. AAZTA⁵.SA.FAPi labeling with gallium-68, scandium-44, and lutetium-177, as well DOTA.SA.FAPi complexation with scandium-44 and lutetium-177, were successfully performed. Remarkably, for AAZTA⁵.SA.FAPi, compared to the DOTA derivative, [⁴⁴Sc]Sc-AAZTA.SA.FAPi required significantly less precursor for quantitative labeling, resulting in higher specific activities, and performed complete complexation at ambient temperatures. The stability of the radiometal-complexed AAZTA⁵.SA.FAPi in various media was excellent, as demonstrated by the presence of highly intact conjugates. Complexation with the β^+ -emitting scandium-44 may offer a good alternative to gallium-68 usage in diagnosis due to the longer half-life of 4 h and the favorable traits of this nuclide. Interesting is also the remarkable labeling and stability with lutetium-177, allowing therapeutical application. A first theranostic approach of DOTA.SA.FAPi was reported by Ballal et al. [49]. Therefore, the new FAP inhibitor-based probes DOTA.SA.FAPi and AAZTA⁵.SA.FAPi, complexed with gallium-68, scandium-44, and lutetium-177, are promising radiopharmaceuticals for use in a theranostic settings.

Declarations

Author Contributions: Conceptualization, [REDACTED] methodology, E.S.M., [REDACTED] validation, E.S.M., [REDACTED] formal analysis, E.S.M., [REDACTED] investigation, E.S.M., [REDACTED] resources, [REDACTED] data curation, E.S.M., [REDACTED] writing—original draft preparation, E.S.M.; writing—review and editing, E.S.M., [REDACTED] supervision and project administration, [REDACTED]. All authors have read and agreed to the published version of the manuscript.

Funding: This work was supported by the Fonds Wetenschappelijk Onderzoek Vlaanderen (FWO, Grant 1S64220N); [REDACTED] is a SB PhD fellow at FWO. This project also received funding from the Agentschap Innoveren en Ondernemen (VLAIO HCB 2019. 2446).

Institutional Review Board Statement: Not applicable

Informed Consent Statement: Not applicable.

Data Availability Statement: The study did not report any data.

Acknowledgments: Lutetium-177 (n.c.a. [¹⁷⁷Lu]LuCl₃ in 0.04 M HCl) was kindly provided by ITG Garching, Germany.

Conflicts of Interest: The authors declare no conflict of interest.

References

1. Rawlings, N.D.; Barrett, A.J.; Thomas, P.D.; Huang, X.; Bateman, A.; Finn, R.D. The MEROPS database of proteolytic enzymes, their substrates and inhibitors in 2017 and a comparison with peptidases in the PANTHER database. *Nucleic Acids Res.* **2018**, *46*, D624–D632, doi:10.1093/nar/gkx1134.
2. Huang, Y.; Simms, A.E.; Mazur, A.; Wang, S.; León, N.R.; Jones, B.; Aziz, N.; Kelly, T. Fibroblast activation protein- α promotes tumor growth and invasion of breast cancer cells through non-enzymatic functions. *Clin. Exp. Metastasis* **2011**, *28*, 567–579, doi:10.1007/s10585-011-9392-x.
3. Liu, R.; Li, H.; Liu, L.; Yu, J.; Ren, X. Fibroblast activation protein: A potential therapeutic target in cancer. *Cancer Biol. Ther.* **2012**, *13*, 123–129, doi:10.4161/cbt.13.3.18696.
4. Liu, T.; Zhou, L.; Li, D.; Andl, T.; Zhang, Y. Cancer-associated fibroblasts build and secure the tumor microenvironment. *Front. Cell Dev. Biol.* **2019**, *7*, 1–14, doi:10.3389/fcell.2019.00060.
5. De Vlieghe, E.; Verset, L.; Demetter, P.; Bracke, M.; De Wever, O. Cancer-associated fibroblasts as target and tool in cancer therapeutics and diagnostics. *Virchows Arch.* **2015**, *467*, 367–382, doi:10.1007/s00428-015-1818-4.
6. Tao, L.; Huang, G.; Song, H.; Chen, Y.; Chen, L. Cancer associated fibroblasts: An essential role in the tumor microenvironment (review). *Oncol. Lett.* **2017**, *14*, 2611–2620, doi:10.3892/ol.2017.6497.
7. Lindner, T.; Loktev, A.; Giesel, F.; Kratochwil, C.; Altmann, A.; Haberkorn, U. Targeting of activated fibroblasts for imaging and therapy. *EJNMMI Radiopharm. Chem.* **2019**, *4*, 1–15, doi:10.1186/s41181-019-0069-0.
8. Busek, P.; Mateu, R.; Zubal, M.; Kotackova, L.; Sedo, A. Targeting Fibroblast activation protein in cancer—Prospects and caveats. *Front. Biosci. Landmark* **2018**, *23*, 1933–1968, doi:10.2741/4682.
9. Loktev, A.; Lindner, T.; Mier, W.; Debus, J.; Altmann, A.; Jaeger, D.; Giesel, F.; Kratochwil, C.; Barthe, P.; Roumestand, C.; et al. A Tumor-Imaging Method Targeting Cancer-Associated Fibroblasts. *J. Nucl. Med.* **2018**, *59*, 1423–1429, doi:10.2967/jnumed.118.210435.
10. Lindner, T.; Loktev, A.; Altmann, A.; Giesel, F.; Kratochwil, C.; Debus, J.; Jäger, D.; Mier, W.; Haberkorn, U. Development of Quinoline-Based Theranostic Ligands for the Targeting of Fibroblast Activation Protein. *J. Nucl. Med.* **2018**, *59*, 1415–1422, doi:10.2967/jnumed.118.210443.
11. Loktev, A.; Lindner, T.; Burger, E.M.; Altmann, A.; Giesel, F.; Kratochwil, C.; Debus, J.; Marmé, F.; Jäger, D.; Mier, W.; et al. Development of fibroblast activation protein-targeted radiotracers with improved tumor retention. *J. Nucl. Med.* **2019**, *60*, 1421–1429, doi:10.2967/jnumed.118.224469.
12. Jansen, K.; Heirbaut, L.; Verkerk, R.; Cheng, J.D.; Joossens, J.; Cos, P.; Maes, L.; Lambeir, A.M.; De Meester, I.; Augustyns, K.; et al. Extended structure-activity relationship and pharmacokinetic investigation of (4-quinolinoyl)glycyl-2-cyanopyrrolidine inhibitors of

- fibroblast activation protein (FAP). *J. Med. Chem.* **2014**, *57*, 3053–3074, doi:10.1021/jm-500031w.
13. Kratochwil, C.; Flechsig, P.; Lindner, T.; Abderrahim, L.; Altmann, A.; Mier, W.; Adeberg, S.; Rathke, H.; Röhrich, M.; Winter, H.; et al. ^{68}Ga -FAPI PET/CT: Tracer uptake in 28 different kinds of cancer. *J. Nucl. Med.* **2019**, *60*, 801–805, doi:10.2967/jnumed.119.227967.
 14. Giesel, F.L.; Kratochwil, C.; Lindner, T.; Marschalek, M.M.; Loktev, A.; Lehnert, W.; Debus, J.; Jäger, D.; Flechsig, P.; Altmann, A.; et al. ^{68}Ga -FAPI PET/CT: Biodistribution and preliminary dosimetry estimate of 2 DOTA-containing FAP-targeting agents in patients with various cancers. *J. Nucl. Med.* **2019**, *60*, 386–392, doi:10.2967/jnumed.118.215913.
 15. Shi, X.; Xing, H.; Yang, X.; Li, F.; Yao, S.; Zhang, H.; Zhao, H.; Hacker, M.; Huo, L.; Li, X. Fibroblast imaging of hepatic carcinoma with ^{68}Ga -FAPI-04 PET/CT: A pilot study in patients with suspected hepatic nodules. *Eur. J. Nucl. Med. Mol. Imaging* **2021**, *48*, 196–203, doi:10.1007/s00259-020-04882-z.
 16. Luo, Y.; Pan, Q.; Zhang, W.; Li, F. Intense FAPI Uptake in Inflammation May Mask the Tumor Activity of Pancreatic Cancer in ^{68}Ga -FAPI PET/CT. *Clin. Nucl. Med.* **2020**, *45*, 310–311, doi:10.1097/RLU.0000000000002914.
 17. Khreish, F.; Rosar, F.; Kratochwil, C.; Giesel, F.L.; Haberkorn, U.; Ezziddin, S. Positive FAPI-PET/CT in a metastatic castration-resistant prostate cancer patient with PSMA-negative/FDG-positive disease. *Eur. J. Nucl. Med. Mol. Imaging* **2020**, *47*, 2040–2041, doi:10.1007/s00259-019-04623-x.
 18. Chen, H.; Pang, Y.; Wu, J.; Zhao, L.; Hao, B.; Wu, J.; Wei, J.; Wu, S.; Zhao, L.; Luo, Z.; et al. Comparison of [^{68}Ga]Ga-DOTA-FAPI-04 and [^{18}F]FDG PET/CT for the diagnosis of primary and metastatic lesions in patients with various types of cancer. *Eur. J. Nucl. Med. Mol. Imaging* **2020**, *47*, 1820–1832, doi:10.1007/s00259-020-04769-z.
 19. Chen, H.; Zhao, L.; Ruan, D.; Pang, Y.; Hao, B.; Dai, Y.; Wu, X.; Guo, W.; Fan, C.; Wu, J.; et al. Usefulness of [^{68}Ga]Ga-DOTA-FAPI-04 PET/CT in patients presenting with inconclusive [^{18}F]FDG PET/CT findings. *Eur. J. Nucl. Med. Mol. Imaging* **2021**, *48*, 73–86, doi:10.1007/s00259-020-04940-6.
 20. Varasteh, Z.; Mohanta, S.; Robu, S.; Braeuer, M.; Li, Y.; Omidvari, N.; Topping, G.; Sun, T.; Nekolla, S.G.; Richter, A.; et al. Molecular imaging of fibroblast activity after myocardial infarction using a ^{68}Ga -labeled fibroblast activation protein inhibitor, FAPI-04. *J. Nucl. Med.* **2019**, *60*, 1743–1749, doi:10.2967/jnumed.119.226993.
 21. Koerber, S.A.; Staudinger, F.; Kratochwil, C.; Adeberg, S.; Haefner, M.F.; Ungerechts, G.; Rathke, H.; Winter, E.; Lindner, T.; Syed, M.; et al. The role of FAPI-PET/CT for patients with malignancies of the lower gastrointestinal tract—First clinical experience. *J. Nucl. Med.* **2020**, *61*, 1331–1336, doi:10.2967/jnumed.119.237016.
 22. Toms, J.; Kogler, J.; Maschauer, S.; Daniel, C.; Schmidkonz, C.; Kuwert, T.; Prante, O. Targeting Fibroblast Activation Protein: Radiosynthesis and Preclinical Evaluation of an ^{18}F -labeled FAP Inhibitor. *J. Nucl. Med.* **2020**, *61*, 1806–1813, doi:10.2967/jnumed.120.242958.
 23. Lindner, T.; Altmann, A.; Kraemer, S.; Kleist, C.; Loktev, A.; Kratochwil, C.; Giesel, F.; Mier, W.; Marme, F.; Debus, J.; et al. Design and development of $^{99\text{m}}\text{Tc}$ labeled FAPI-tracers for SPECT-

- imaging and ^{188}Re therapy. *J. Nucl. Med.* **2020**, *61*, 1507–1513, doi:10.2967/jnu-med.119.239731.
24. Moon, E.S.; Elvas, F.; Gwendolyn, V.; De Lombaerde, S.; Vangestel, C.; De Bruycker, S.; Bracke, A.; Eppard, E.; Greifenstein, L.; Klasen, B.; et al. Targeting fibroblast activation protein (FAP): next generation PET radiotracers using squaramide coupled bifunctional DOTA and DATA^{5m} chelators. *EJNMMI Radiopharm. Chem.* **2020**, *5*, 19 doi:10.1186/s41181-020-00102-z.
 25. Kreppel, B.; Gärtner, F.; Marinova, M.; Attenberger, U.; Meisenheimer, M.; Toma, M.; Kristiansen, G.; Feldmann, G.; Moon, E.; Roesch, F.; et al. [^{68}Ga]Ga-DOTA^{5m}.SA.FAPi PET/CT : Specific Tracer-uptake in Focal Nodular Hyperplasia and potential Role in Liver Tumor Imaging. *Nuklearmedizin* **2020**, *59*, 387–389, doi:10.1055/a-1164-5667.
 26. Ballal, S.; Yadav, M.P.; Moon, E.S.; Kramer, V.S.; Roesch, F.; Kumari, S.; Tripathi, M.; ArunRaj, S.T.; Sarswat, S.; Bal, C. Biodistribution, pharmacokinetics, dosimetry of [^{68}Ga]Ga-DOTA.SA.FAPi, and the head-to-head comparison with [^{18}F]F-FDG PET/CT in patients with various cancers. *Eur. J. Nucl. Med. Mol. Imaging* **2021**, *48*, 1915–1931, doi:10.1007/s00259-020-05132-y.
 27. Kostelnik, T.I.; Orvig, C. Radioactive Main Group and Rare Earth Metals for Imaging and Therapy. *Chem. Rev.* **2019**, *119*, 902–956, doi:10.1021/acs.chemrev.8b00294.
 28. Roesch, F. Scandium-44: Benefits of a Long-Lived PET Radionuclide Available from the $^{44}\text{Ti}/^{44}\text{Sc}$ Generator System. *Curr. Radiopharm.* **2012**, *5*, 187–201, doi:10.2174/1874471011205030187.
 29. Filosofov, D.V.; Loktionova, N.S.; Rösch, F. A $^{44}\text{Ti}/^{44}\text{Sc}$ radionuclide generator for potential application of ^{44}Sc -based PET-radiopharmaceuticals. *Radiochim. Acta* **2010**, *98*, 149–156, doi:10.1524/ract.2010.1701.
 30. Pruszyński, M.; Loktionova, N.S.; Filosofov, D.V.; Rösch, F. Post-elution processing of $^{44}\text{Ti}/^{44}\text{Sc}$ generator-derived ^{44}Sc for clinical application. *Appl. Radiat. Isot.* **2010**, *68*, 1636–1641, doi:10.1016/j.apradiso.2010.04.003.
 31. Hernandez, R.; Valdovinos, H.; Yang, Y.; Chakravarty, R.; Hong, H.; Barnhart, T.; Cai, W. ^{44}Sc : An Attractive Isotope for Peptide-Based PET Imaging. *Mol. Pharm.* **2014**, *11*, 2954–2961, doi:10.1021/mp500343j.
 32. Koumarianou, E.; Loktionova, N.S.; Fellner, M.; Roesch, F.; Thews, O.; Pawlak, D.; Archimandritis, S.C.; Mikolajczak, R. ^{44}Sc -DOTA-BN[2–14]NH₂ in comparison to ^{68}Ga -DOTA-BN[2–14]NH₂ in pre-clinical investigation. Is ^{44}Sc a potential radionuclide for PET? *Appl. Radiat. Isot.* **2012**, *70*, 2669–2676, doi:10.1016/j.apradiso.2012.08.004.
 33. Domnanich, K.A.; Müller, C.; Farkas, R.; Schmid, R.M.; Ponsard, B.; Schibli, R.; Türlér, A.; van der Meulen, N.P. ^{44}Sc for labeling of DOTA- and NODAGA-functionalized peptides: Preclinical in vitro and in vivo investigations. *EJNMMI Radiopharm. Chem.* **2017**, *1*, 1–19, doi:10.1186/s41181-016-0013-5.
 34. Umbricht, C.A.; Benešová, M.; Schmid, R.M.; Türlér, A.; Schibli, R.; van der Meulen, N.P.; Müller, C. ^{44}Sc -PSMA-617 for radiotheragnostics in tandem with ^{177}Lu -PSMA-617—preclinical investigations in comparison with ^{68}Ga -PSMA-11 and ^{68}Ga -PSMA-617. *EJNMMI Res.* **2017**, *7*, 1–10, doi:10.1186/s13550-017-0257-4.
 35. Thorp-Greenwood, F.L.; Coogan, M.P. Multimodal radio- (PET/SPECT) and fluorescence imaging agents based on metallo-radioisotopes: Current applications and prospects for

- development of new agents. *J. Chem. Soc. Dalton Trans.* **2011**, *40*, 6129–6143, doi:10.1039/c0-dt01398f.
36. Eppard, E.; de la Fuente, A.; Benešová, M.; Khawar, A.; Bundschuh, R.A.; Gärtner, F.C.; Kreppel, B.; Kopka, K.; Essler, M.; Rösch, F. Clinical translation and first in-human use of [⁴⁴Sc]Sc-PSMA-617 for pet imaging of metastasized castrate-resistant prostate cancer. *Theranostics* **2017**, *7*, 4359–4369, doi:10.7150/thno.20586.
 37. Fröss-Baron, K.; Garske-Román, U.; Welin, S.; Granberg, D.; Eriksson, B.; Khan, T.; Sandström, M.; Sundin, A. ¹⁷⁷Lu-DOTATATE therapy of advanced pancreatic neuroendocrine tumors heavily pretreated with chemotherapy; analysis of outcome, safety and their determinants. *Neuroendocrinology* **2020**, *111*, 330–334, doi:10.1159/000506746.
 38. Forrer, F.; Uusijärvi, H.; Storch, D.; Maecke, H.R.; Mueller-Brand, J. Treatment with ¹⁷⁷Lu-DOTATOC of patients with relapse of neuroendocrine tumors after treatment with ⁹⁰Y-DOTATOC. *J. Nucl. Med.* **2005**, *46*, 1310–1316.
 39. Baum, R.P.; Kluge, A.W.; Kulkarni, H.; Schorr-Neufing, U.; Niepsch, K.; Bitterlich, N.; van Echteld, C.J.A. [¹⁷⁷Lu-DOTA]0-D-Phe1-Tyr3-Octreotide (¹⁷⁷Lu-DOTATOC) for peptide receptor radiotherapy in patients with advanced neuroendocrine tumours: A Phase-II study. *Theranostics* **2016**, *6*, 501–510, doi:10.7150/thno.13702.
 40. Baum, R.P.; Kulkarni, H.R.; Schuchardt, C.; Singh, A.; Wirtz, M.; Wiessalla, S.; Schottelius, M.; Mueller, D.; Klette, I.; Wester, H.J. ¹⁷⁷Lu-labeled prostate-specific membrane antigen radioligand therapy of metastatic castration-resistant prostate cancer: Safety and efficacy. *J. Nucl. Med.* **2016**, *57*, 1006–1013, doi:10.2967/jnumed.115.168443.
 41. Iravani, A.; Violet, J.; Azad, A.; Hofman, M.S. Lutetium-177 prostate-specific membrane antigen (PSMA) theranostics: Practical nuances and intricacies. *Prostate Cancer Prostatic Dis.* **2020**, *23*, 38–52, doi:10.1038/s41391-019-0174-x.
 42. Heck, M.M.; Retz, M.; Tauber, R.; Knorr, K.; Kratochwil, C.; Eiber, M. Radionuklidtherapie des Prostatakarzinoms mittels PSMA-Lutetium. *Urologe* **2017**, *56*, 32–39, doi:10.1007/s00120-016-0274-3.
 43. Heck, M.M.; Tauber, R.; Schwaiger, S.; Retz, M.; D'Alessandria, C.; Maurer, T.; Gafita, A.; Wester, H.J.; Gschwend, J.E.; Weber, W.A.; et al. Treatment Outcome, Toxicity, and Predictive Factors for Radioligand Therapy with ¹⁷⁷Lu-PSMA-I&T in Metastatic Castration-resistant Prostate Cancer. *Eur. Urol.* **2019**, *75*, 920–926, doi:10.1016/j.eururo.2018.11.016.
 44. Sinnes, J.; Nagel, J.; Rösch, F. AAZTA⁵/AAZTA⁵-TOC: Synthesis and radiochemical evaluation with ⁶⁸Ga, ⁴⁴Sc and ¹⁷⁷Lu. *EJNMMI Radiopharm. Chem.* **2019**, *4*, 1–10, doi:10.1186/s41181-019-0068-1.
 45. Greifenstein, L.; Grus, T.; Nagel, J.; Sinnes, J.P.; Rösch, F. Synthesis and labeling of a squaric acid containing PSMA-inhibitor coupled to AAZTA⁵ for versatile labeling with ⁴⁴Sc, ⁶⁴Cu, ⁶⁸Ga and ¹⁷⁷Lu. *Appl. Radiat. Isot.* **2020**, *156*, 108867, doi:10.1016/j.apradiso.2019.108867.
 46. De Decker, A.; Vliegen, G.; Van Rompaey, D.; Peeraer, A.; Bracke, A.; Verckist, L.; Jansen, K.; Geiss-Friedlander, R.; Augustyns, K.; De Winter, H.; et al. Novel Small Molecule-Derived, Highly Selective Substrates for Fibroblast Activation Protein (FAP). *ACS Med. Chem. Lett.* **2019**, *10*, 1173–1179, doi:10.1021/acsmchemlett.9b00191.

47. De Meester, I.; Vanhoof, G.; Lambeir, A.M.; Scharpé, S. Use of immobilized adenosine deaminase (EC 3.5.4.4) for the rapid purification of native human CD26/dipeptidyl peptidase IV (EC 3.4.14.5). *J. Immunol. Methods* **1996**, *189*, 99–105, doi:10.1016/0022-1759(95)00239-1.
48. Eppard, E.; Wuttke, M.; Nicodemus, P.L.; Rösch, F. Ethanol-based post-processing of generator-derived ⁶⁸Ga Toward kit-type preparation of ⁶⁸Ga-radiopharmaceuticals. *J. Nucl. Med.* **2014**, *55*, 1023–1028, doi:10.2967/jnumed.113.133041.
49. Ballal, S.; Yadav, M.P.; Kramer, V.; Moon, E.S.; Roesch, F.; Tripathi, M.; Mallick, S.; ArunRaj, S.T.; Bal, C. A theranostic approach of [⁶⁸Ga]Ga-DOTA.SA.FAPi PET/CT-guided [¹⁷⁷Lu]Lu-DOTA.SA.FAPi radionuclide therapy in an end-stage breast cancer patient: New frontier in targeted radionuclide therapy. *Eur. J. Nucl. Med. Mol. Imaging* **2021**, *48*, 942–944, doi:10.1007/s00259-020-04990-w.

Supporting Information

Radiolabeling

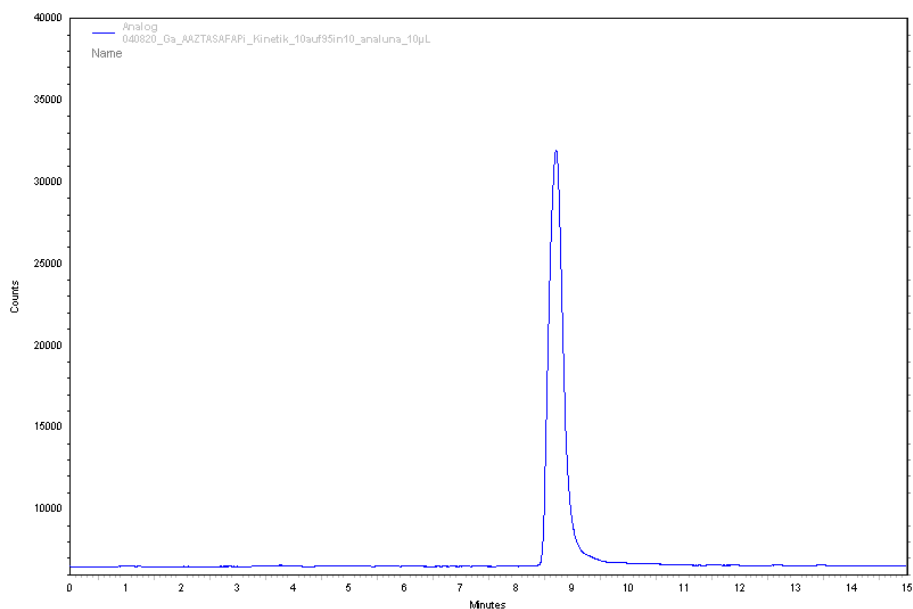


Figure S1. radio-HPLC spectra of [^{68}Ga]Ga-AAZTA⁵.SA.FAPi after reaction of 15 min. with linear gradient condition of 10-95% MeCN (+0.1% TFA)/95-10% Water (+0.1% TFA) in 10 min, 1 mL/min, t_R = 8.4 min.

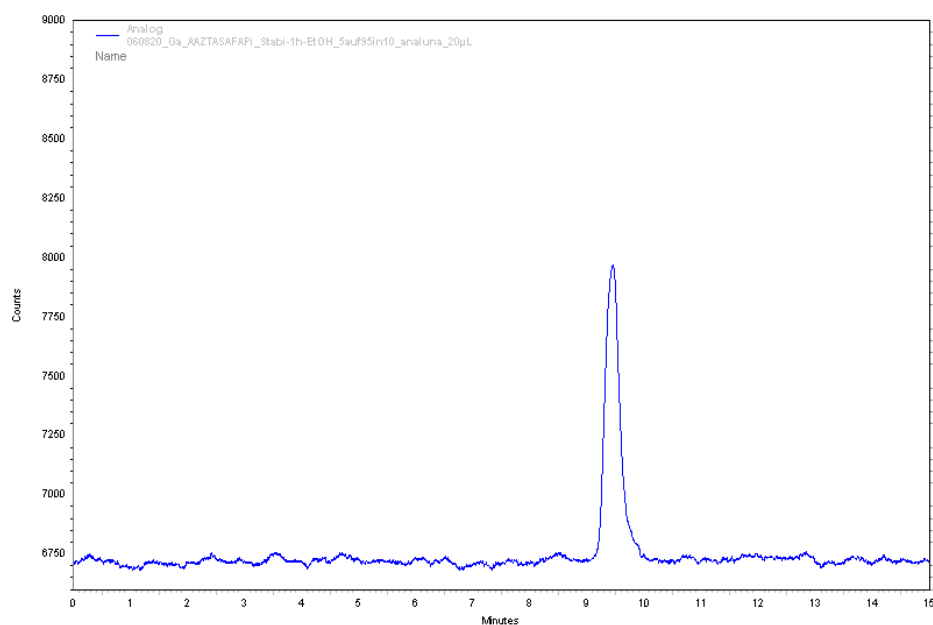


Figure S2. Stability test: radio-HPLC spectra of [^{68}Ga]Ga-AAZTA⁵.SA.FAPi in Ethanol after 1 h with linear gradient condition of 5-95% MeCN (+0.1% TFA)/95-5% Water (+0.1% TFA) in 10 min, 1 mL/min, t_R = 9.1 min.

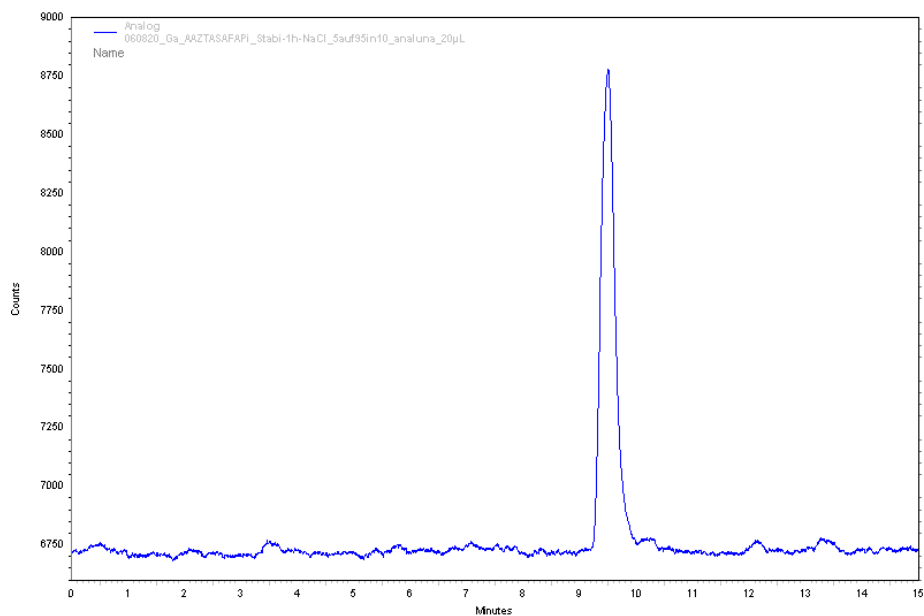


Figure S3. Stability test: radio-HPLC spectra of $[^{68}\text{Ga}]\text{Ga-AAZTA}^5\text{.SA.FAPI}$ in saline after 1 h with linear gradient condition of 5-95% MeCN (+0.1% TFA)/95-5% Water (+0.1% TFA) in 10 min, 1 mL/min, $t_R=9.1$ min.

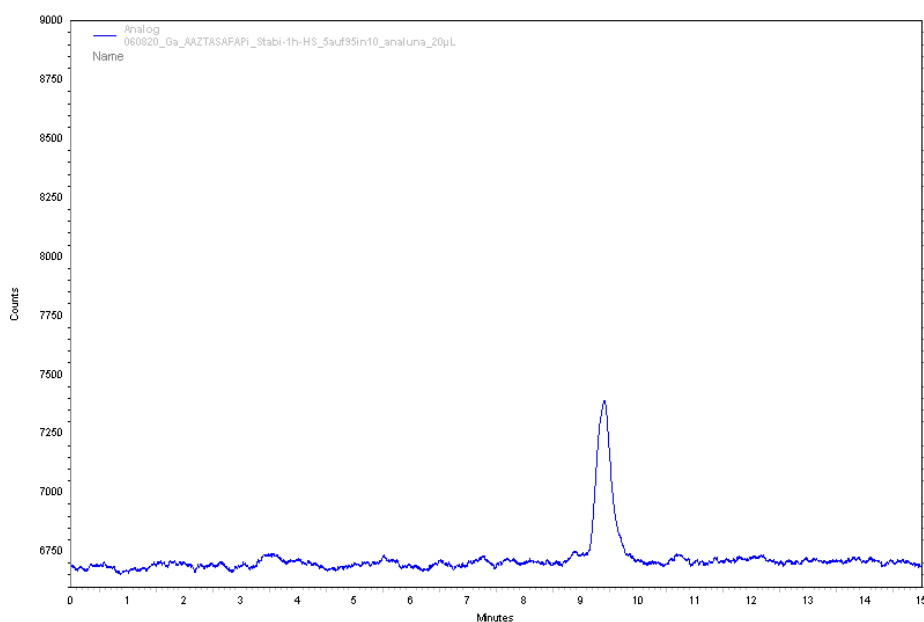


Figure S4. Stability test: radio-HPLC spectra of $[^{68}\text{Ga}]\text{Ga-AAZTA}^5\text{.SA.FAPI}$ in human serum after 1 h with linear gradient condition of 5-95% MeCN (+0.1% TFA)/95-5% Water (+0.1% TFA) in 10 min, 1 mL/min, $t_R=9.1$ min.

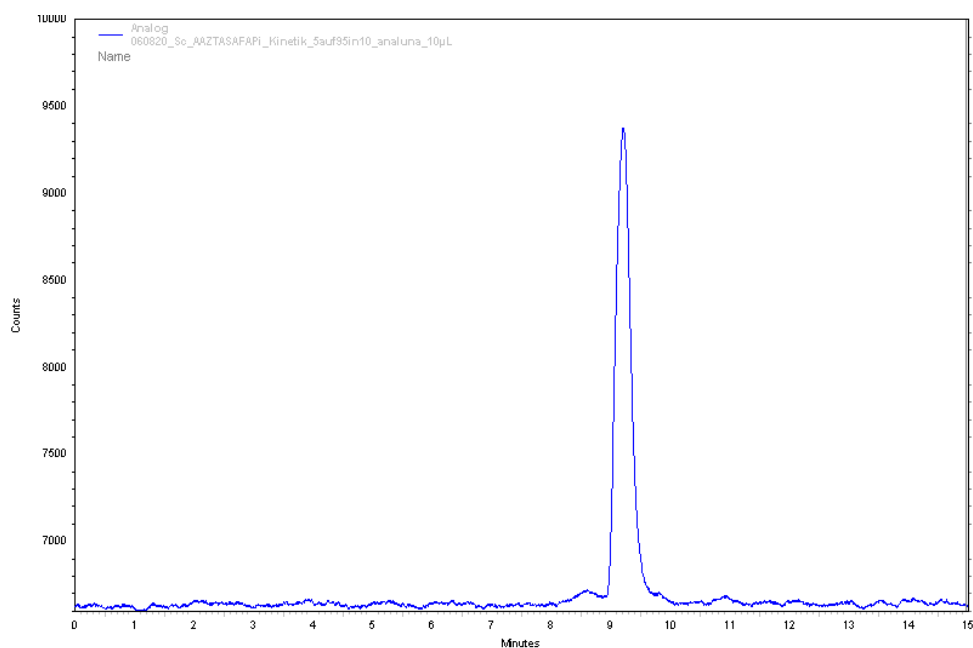


Figure S5. radio-HPLC spectra of $[^{44}\text{Sc}]\text{Sc-AAZTA}^5\text{.SA.FAPi}$ after 15 min. reaction with linear gradient condition of 5-95% MeCN (+0.1% TFA)/95-5% Water (+0.1% TFA) in 10 min, 1 mL/min, $t_R= 8.9$ min.

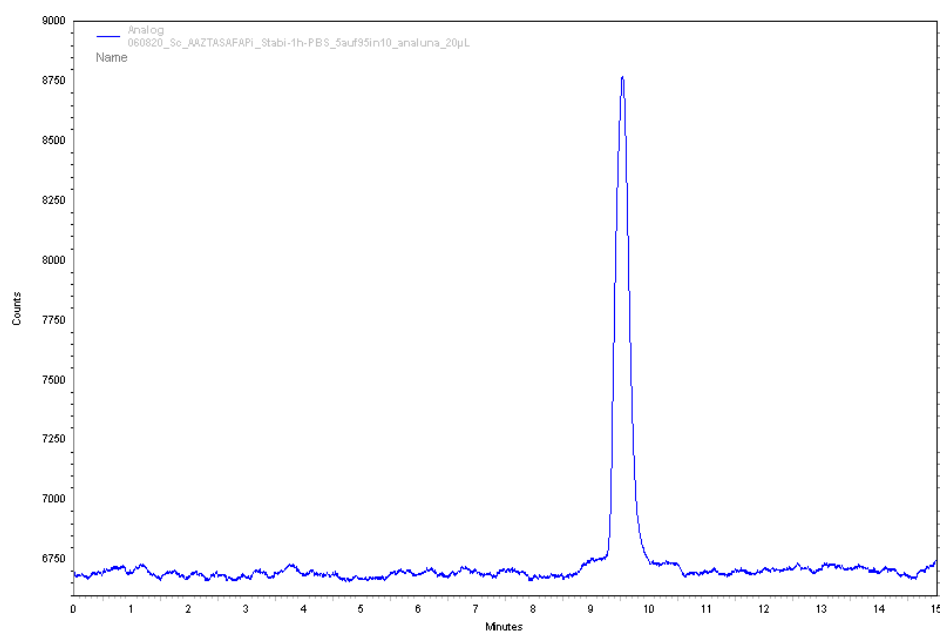


Figure S6. Stability test: radio-HPLC spectra of $[^{44}\text{Sc}]\text{Sc-AAZTA}^5\text{.SA.FAPi}$ in phosphate buffered saline after 1 h with linear gradient condition of 5-95% MeCN (+0.1% TFA)/95-5% Water (+0.1% TFA) in 10 min, 1 mL/min, $t_R= 9.3$ min.

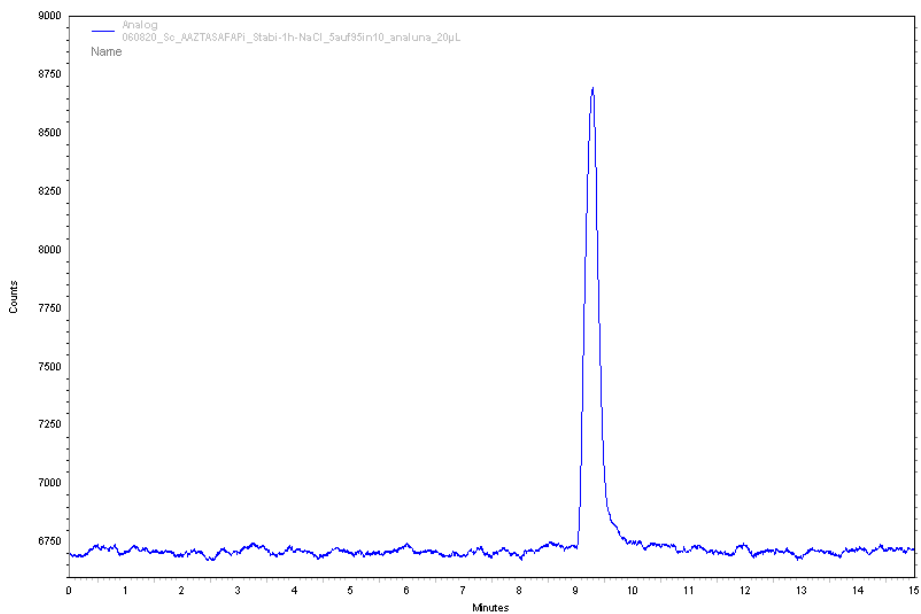


Figure S7. Stability test: radio-HPLC spectra of $[^{44}\text{Sc}]\text{Sc-AAZTA}^5\text{.SA.FAPi}$ in saline after 1 h with linear gradient condition of 5-95% MeCN (+0.1% TFA)/95-5% Water (+0.1% TFA) in 10 min, 1 mL/min, $t_R = 9.1$ min.

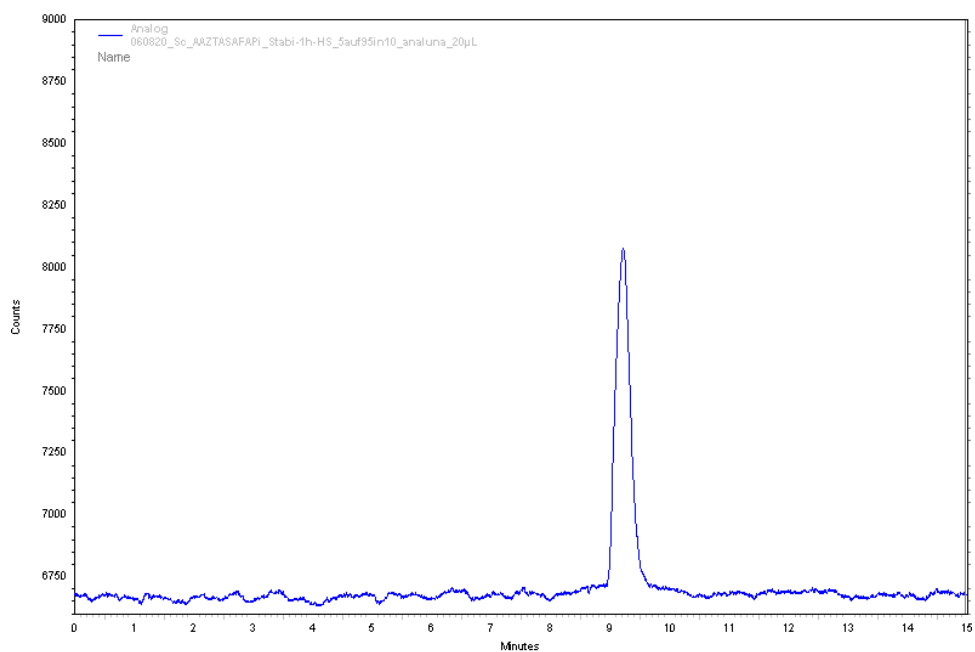


Figure S8. Stability test: radio-HPLC spectra of $[^{44}\text{Sc}]\text{Sc-AAZTA}^5\text{.SA.FAPi}$ in human serum after 1 h with linear gradient condition of 5-95% MeCN (+0.1% TFA)/95-5% Water (+0.1% TFA) in 10 min, 1 mL/min, $t_R = 9.1$ min.

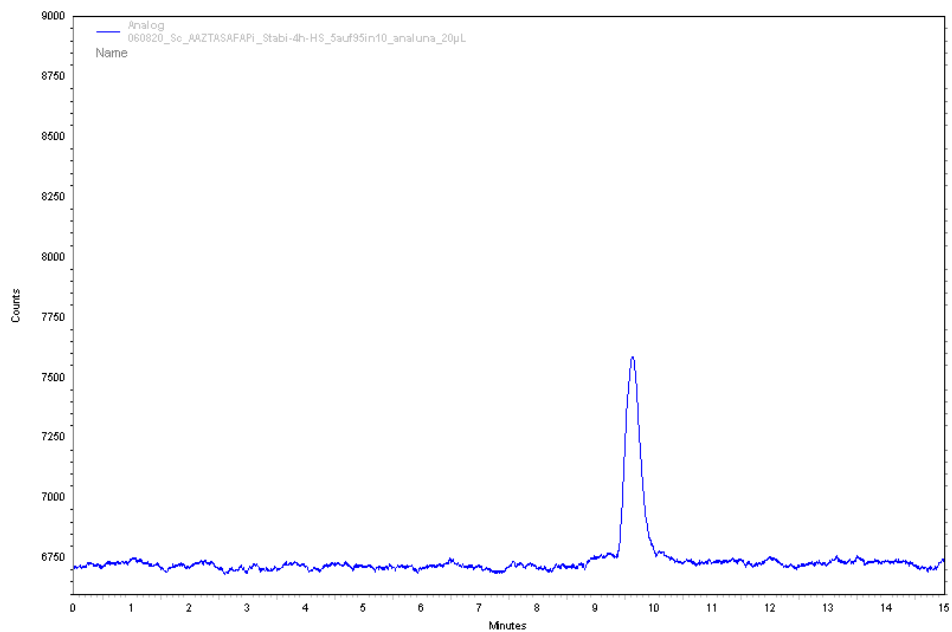


Figure S9. Stability test: radio-HPLC spectra of [⁴⁴Sc]Sc-AAZTA⁵.SA.FAPi in human serum after 4 h with linear gradient condition of 5-95% MeCN (+0.1% TFA)/95-5% Water (+0.1% TFA) in 10 min, 1 mL/min, t_R = 9.5 min.

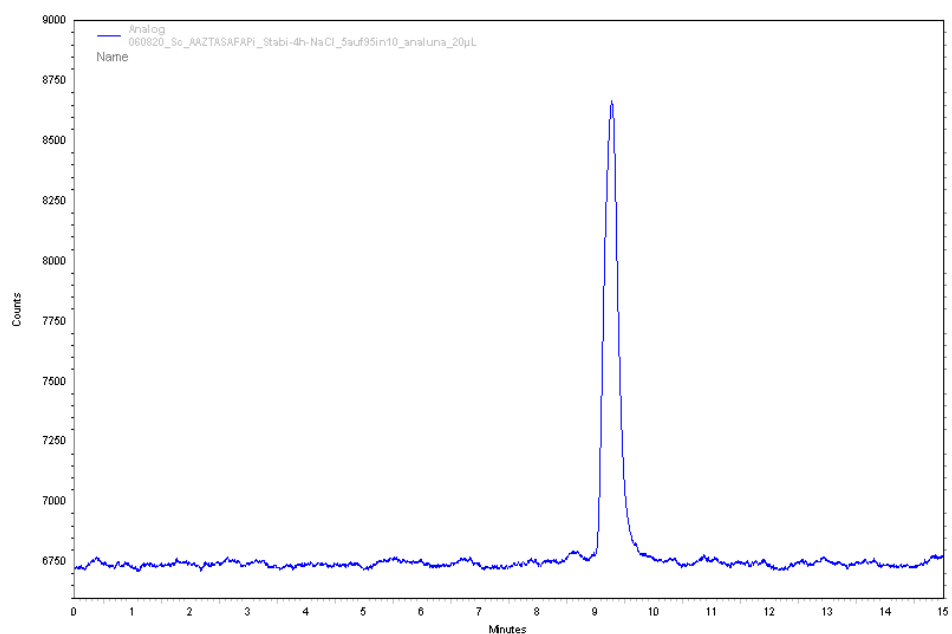


Figure S10. Stability test: radio-HPLC spectra of [⁴⁴Sc]Sc-AAZTA⁵.SA.FAPi in saline after 4 h with linear gradient condition of 5-95% MeCN (+0.1% TFA)/95-5% Water (+0.1% TFA) in 10 min, 1 mL/min, t_R = 9.3 min.

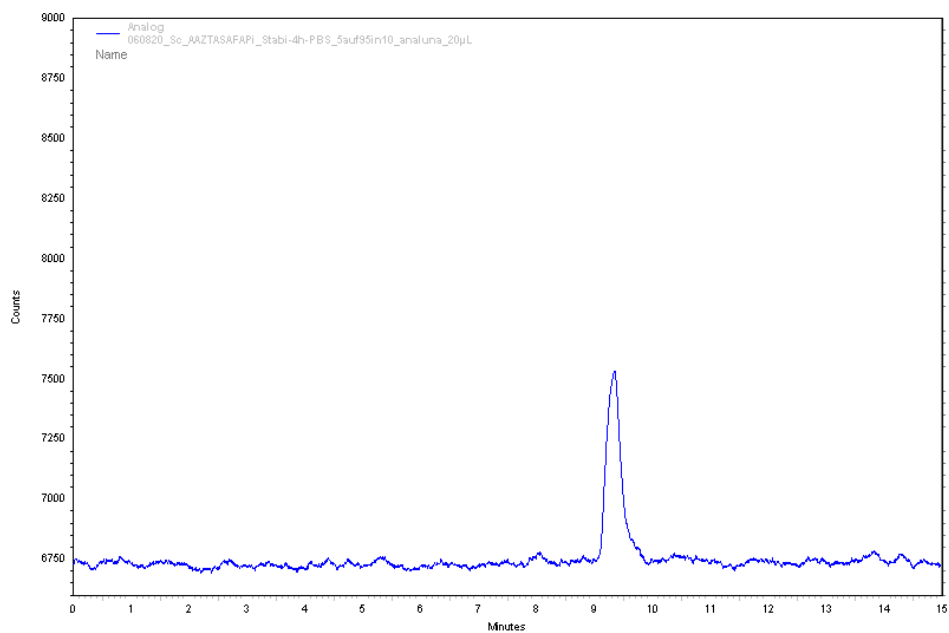


Figure S11. Stability test: radio-HPLC spectra of [⁴⁴Sc]Sc-AAZTA⁵.SA.FAPi in phosphate buffered saline after 4 h with linear gradient condition of 5-95% MeCN (+0.1% TFA)/95-5% Water (+0.1% TFA) in 10 min, 1 mL/min, t_R= 9.1 min.

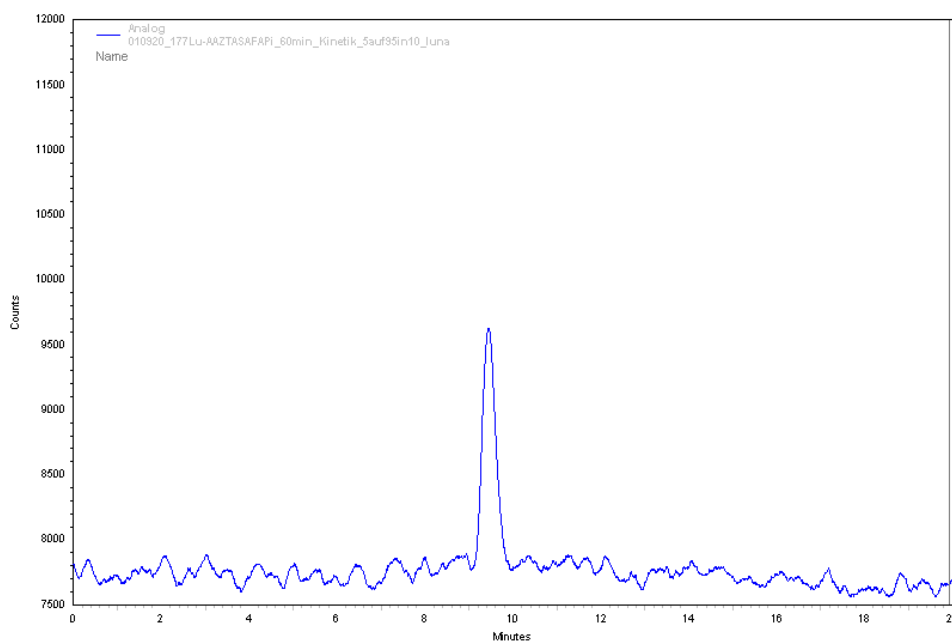


Figure S12. radio-HPLC spectra of [¹⁷⁷Lu]Lu-AAZTA⁵.SA.FAPi after 60 min. reaction with linear gradient condition of 5-95% MeCN (+0.1% TFA)/95-5% Water (+0.1% TFA) in 10 min, 1 mL/min, t_R= 9.1 min.

- C. Fibroblast Activation Protein (FAP) targeting homodimeric FAP inhibitor radiotheranostics: A step to improve tumor uptake and retention time

Akzeptiert in *AJNMMI*, **2021**.

mit Genehmigung von © AJNMMI, e-Century Publishing Corporation

Fibroblast Activation Protein (FAP) targeting homodimeric FAP inhibitor radiotheranostics: A step to improve tumor uptake and retention time

Euy Sung Moon¹, [REDACTED]
[REDACTED]

¹ Department of Chemistry – TRIGA site, Johannes Gutenberg University Mainz, Mainz, Germany

² Department of Nuclear Medicine, All India Institute of Medical Sciences, New Delhi, India

³ Department of Pharmaceutical Sciences, Laboratory of Medical Biochemistry, University of Antwerp, Wilrijk, Belgium

⁴ Department of Pharmaceutical Sciences, Laboratory of Medicinal Chemistry, University of Antwerp, Wilrijk, Belgium

*Corresponding author: [REDACTED]

Abstract

Several radiopharmaceuticals targeting fibroblast activation protein (FAP) based on the highly potent FAP inhibitor UAMC1110 are currently under investigation. Pre-clinical as well as clinical research exhibited the potential of these imaging agents. However, the monomeric small molecules seemed to have a short retention time in the tumor in combination with fast renal clearance. Therefore, our strategy was to develop homodimeric systems having two FAP inhibitors to improve residence time and tumor accumulation. The homodimers with two squaramide coupled FAP inhibitor conjugates DOTA.(SA.FAPi)₂ and DOTAGA.(SA.FAPi)₂ were synthesized, radiochemically evaluated with gallium-68. [⁶⁸Ga]Ga-DOTAGA.(SA.FAPi)₂ was tested for its *in vitro* stability, lipophilicity and affinity properties. In addition, human PET/CT scans were performed for [⁶⁸Ga]Ga-DOTAGA.(SA.FAPi)₂ with a head-to-head comparison with [⁶⁸Ga]Ga-DOTA.SA.FAPi and [¹⁸F]FDG. Labeling with gallium-68 demonstrated high radiochemical purities. Inhibition measurements revealed excellent affinity and selectivity with low nanomolar IC₅₀ values for FAP. In PET/CT human studies, significantly higher tumor uptake as well as longer tumor retention could be observed for [⁶⁸Ga]Ga-DOTAGA.(SA.FAPi)₂ compared to [⁶⁸Ga]Ga-DOTA.SA.FAPi. Therefore, the introduction of the dimer led to an advance in human PET imaging indicated by increased tumor accumulation and prolonged retention times *in vivo* and thus, the use of dimeric structures could be the next step towards prolonged uptake of FAP inhibitors resulting in radiotherapeutic analogs of FAP inhibitors.

Keywords: Fibroblast activation protein, homodimer, gallium-68, lutetium-177, DOTA, DOTAGA, squaric acid, squaramide

Introduction

Fibroblast activation protein (FAP) is a member of the S9 family of serine proteases. In addition to FAP this S9 family includes other closely related proline-specific serine proteases, such as prolyl oligopeptidase (PREP) and the dipeptidyl peptidases 4, 8, and 9 (DPP4, DPP8, and DPP9) [1]. FAP, a specific marker of myofibroblasts, has become a target of great interest, especially in the field of cancer diagnostics. Many radiotracers based on the highly selective FAP inhibitor UAMC1110 were developed and already used in different (pre-)clinical trials [2–9]. Recently, our group reported FAP inhibitor (FAPi) PET tracers containing squaramide (SA) as a linker moiety coupled on bifunctional DOTA and DATA^{5m} chelators [10]. These precursors and their non-radioactive metal (^{nat}Ga and ^{nat}Lu) complexes demonstrated very potent *in vitro* inhibition of FAP in combination with a high selectivity with respect to prolyl endopeptidase (PREP). A preclinical μ PET study and *ex vivo* biodistribution indicated high accumulation in tumor and overall, very low background activity at 1 h p.i. in HT-29 colon cancer tumor-bearing mice. Both [⁶⁸Ga]Ga-DATA^{5m}.SA.FAPi and [⁶⁸Ga]Ga-DOTA.SA.FAPi were examined in clinical PET/CT studies. Kreppel et al. showed specific uptake of [⁶⁸Ga]Ga-DATA^{5m}.SA.FAPi in focal nodular hyperplasia [11]. Ballal and Yadav et al. executed clinical trials with [⁶⁸Ga]Ga-DOTA.SA.FAPi in patients holding various end-stage cancer types [12]. The same authors have performed a first theranostic approach of [⁶⁸Ga]Ga-DOTA.SA.FAPi PET/CT and [¹⁷⁷Lu]Lu-DOTA.SA.FAPi radiotherapy in an end-stage breast cancer patient [13]. Yet, prolongation of residence times in stroma tissue appears to be one of the key challenges to turn FAP inhibitors into radiotherapeutics.

An approach to improve tumor accumulation as well as retention time is the formation of dimeric derivatives. Already in 2009 our group reported DOTA-based homodimers containing two separated tyrosine units [14,15]. Later, Chauhan et al. published bivalent chalcones bound to DTPA to diagnose Alzheimer's disease [16]. This homodimeric PET tracer displayed high affinity towards A β aggregates and high brain uptake *in vivo*. Later, the same group also published another chalcone- containing homodimeric tracer labeled with carbon-11. A higher binding affinity and higher brain uptake were observed for the latter compared to the corresponding monomeric tracer [17]. Liolios et al. observed comparable *in vivo* behavior and slightly better *in vitro* cell binding for dimeric HBED-CC coupled bombesin GRPR-antagonists, when compared to the monomeric analogs [18]. In 2019, Zia et al. published PSMA targeting mono- and bivalent PET tracers equipped with a sarcophagine chelator. They reported significantly increased tumor uptake with low background and retention for a homodimeric, copper-64 complexed structure than the corresponding monomeric analogue [19].

These desirable effects of bivalent structures with regard to the increased tumor accumulation and prolonged tumor retention time have led us to develop the two homodimeric structures DOTA.(SA.FAPi)₂ and DOTAGA.(SA.FAPi)₂ with squaramide-conjugated FAP inhibitors (**Figure 1**). The SA.FAPi moieties are connected via a central, bifunctional DOTA or DOTAGA chelator, respectively. As common substructure, they contain the SA.FAPi monomer that we reported earlier [10]. Non-radioactive complexes [^{nat}Ga]Ga-DOTA.(SA.FAPi)₂, [^{nat}Ga]Ga-DOTAGA.(SA.FAPi)₂ and [^{nat}Lu]Lu-DOTAGA.(SA.FAPi)₂ were synthesized and tested *in vitro* for their inhibitory potential to FAP and their selectivity against the DPPs and PREP. Radiolabeling and stability tests were determined with gallium-68 for DOTA.(SA.FAPi)₂ and DOTAGA.(SA.FAPi)₂. Lipophilicity comparison was determined with [⁶⁸Ga]Ga-DOTAGA.(SA.FAPi)₂ and the monomer [⁶⁸Ga]Ga-DOTA.SA.FAPi. Furthermore, clinical investigations were carried out including a head-to-head comparison with the DOTA.SA.FAPi monomer and the homodimer DOTAGA.(SA.FAPi)₂ addressing both absolute tumor accumulation and kinetics uptake.

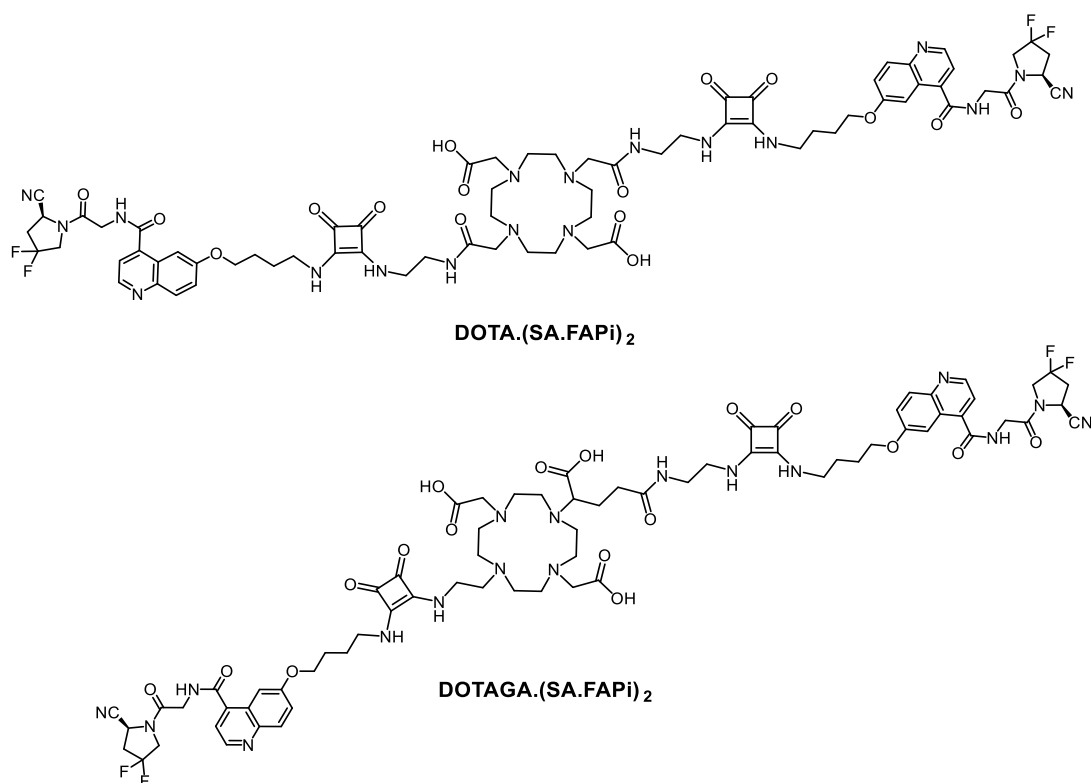


Figure 1 DOTA.(SA.FAPi)₂ and DOTAGA.(SA.FAPi)₂

Materials and Methods

General reagents and instrumentations

All basic chemicals were bought by Acros Organics (Schwerte, Germany), Alfa Aesar by Thermo Fisher Scientific (Kandel, Germany), Merck and Sigma-Aldrich (Darmstadt, Germany), TCI (Eschborn, Germany) ABCR (Karlsruhe, Germany) and VWR (Bruchsal, Germany) and used without further purification. Dry solvents were purchased from Merck and VWR and deuterated solvents from Deutero (Kastellaun, Germany). The chelators 2,2'-(4,10-bis(2-(*tert*-butoxy)-2-oxoethyl)-1,4,7,10-tetraaza-cyclodo-decane-1,7-diyl)diacetic acid [DOTA-di(^tBu)ester] and 5-benzyl-1-*tert*-butyl-2-(4,10-bis(2-(*tert*-butoxy)-2-oxoethyl)-1,4,7,10-tetraazacyclododecan-1-yl)pentanedioate [DO2A(^tBu)-GABz] were acquired from CheMatech (Dijon, France). (*S*)-6-(4-aminobutoxy)-N-(2-(2-cyano-4,4-difluoro-pyrrolidin-1-yl)-2-oxoethyl)-quinoline-4-carboxamide [NH₂-FAPI] was purchased from KE Biochem Co. (Shanghai, China). Reaction controls and determination of the product masses were measured on an Agilent Technologies (Waldbronn, Germany) 1220 Infinity LC System connected to an Agilent Technologies 6130B Single Quadrupole LC/MS system. Thin layer chromatography plates coated with silica gel 60 F254 were acquired from Merck. All analysis controls were detected with a UV lamp (254 nm) and by staining with potassium permanganate. For column chromatography, silica gel 60 (0.063 nm–0.200 nm) from Macherey-Nagel (Düren, Germany) was used. Semi-preparative HPLC was performed on a Hitachi LaChrom 7000 series with a Phenomenex (Aschaffenburg, Germany) Synergi C18 (250 x 10 mm, 4 μ) column. Characterization of compounds were performed by ¹H NMR on a Bruker Avance III HD 300 spectrometer (300 MHz, 5mm BBFO probe head with z-gradient and ATM and BACS 60 sample changer) and an Avance II 400 spectrometer (400 MHz, 5mm BBFO sample head with z-gradient and ATM and SampleXPress 60-sample changer).

Organic synthesis

Synthesis of DOTA.(SA.FAPI)₂

Di-tert-butyl-2,2'-(4,10-bis(2-((2-((tert-butoxycarbonyl)amino)ethyl)amino)-2-oxoethyl)-1,4,7,10-tetraazacyclododecane-1,7-diyl)diacetate [DOTA-(COO^tBu)₂(N-Boc-en)₂] (2)

Commercially available DOTA-di(^tBu)ester (1) (75.2 mg, 0.15 mmol), HATU (84.3 mg, 0.22 mmol), DIPEA (74 μL, 0.44 mmol) and HOBt (29.2 mg, 0.22 mmol) were dissolved in dry MeCN (2 mL). After 30 min at RT, *tert*-butyl-N-(2-aminoethyl)carbamate (60 μL, 0.38 mmol) was added and the mixture stirred for 24 h at RT. Afterwards, *tert*-butyl-N-(2-aminoethyl)carbamate (85 μL, 0.54 mmol), HATU (54.2 mg, 0.14

mmol), DIPEA (25 μ L, 0.14 mmol) and HOBt (19.1 mg, 0.14 mmol) were added in portions and the mixture was stirred for 24 h at RT. After the reaction was completed, the solvent was removed under reduced pressure and the residue purified by column chromatography (CHCl₃: MeOH/ 20:1, R_f = 0.3). Compound (2) (83.7 mg, 0.10 mmol, 72%) was obtained as yellowish oil. ¹H-NMR (300 MHz, CDCl₃): δ [ppm] = 3.44-3.28 (m, 16H), 1.47-1.43 (m, 36H), 1.42-1.39 (m, 10H), 1.33-1.21 (m, 3H), 0.92-0.83 (m, 3H). MS (ESI⁺): m/z = 802 [M+H]⁺, calculated M_{mi} for C₃₈H₇₂N₈O₁₀: 800.5.

2,2'-(4,10-bis(2-((2-((2-ethoxy-3,4-dioxocyclobut-1-en-1-yl)amino)ethyl)amino)-2-oxoethyl)-1,4,7,10-tetraazacyclododecane-1,7-diyl)diacetic acid [DOTA.(SA)₂] (4)

(2) (75.2 mg, 0.09 mmol) was dissolved in dry DCM (500 μ L) and TFA (500 μ L) was added. Under RT, the solution was stirred overnight and the solvents were removed at reduced pressure. Deprotected intermediate (3) was obtained as a yellowish oil and used without further purification processing. MS (ESI⁺): m/z = 489 [M+H]⁺, calculated M_{mi} for C₂₀H₄₀N₈O₆: 488.3. The intermediate (3) was dissolved in 0.5 M Na₂HPO₄/ NaH₂PO₄ phosphate buffer (pH 7, 1 mL). Afterwards, 3,4-diethoxycyclobut-3-ene-1,2-dione (SADE) (26 μ L, 0.18 mmol) was added and the pH value was adjusted with 1 M NaOH to 7 again. The reaction was stirred for 24 h at RT and then the solvent was removed by lyophilization. The colorless product (4) was processed without any further purification. MS (ESI⁺): m/z = 737 [M+H]⁺, calculated M_{mi} for C₃₂H₄₈N₈O₁₂: 736.3.

2,2'-(4,10-bis(2-((2-((4-((4-((S)-2-cyano-4,4-difluoropyrrolidin-1-yl)-2-oxoethyl)carbamoyl)-quinolin-6-yl)oxy)butyl)amino)-3,4-dioxocyclobut-1-en-1-yl)amino)ethyl)amino)-2-oxoethyl)-1,4,7,10-tetraazacyclododecane-1,7-diyl) diacetic acid [DOTA.(SA.FAPi)₂] (5)

(4) was suspended in 0.5 M phosphate buffer pH 9 (500 μ L). NH₂-FAPi (25.8 mg, 0.06 mmol) was then added and the pH adjusted with 1 M NaOH to pH 9. After 24 h at RT, the solvent was removed by lyophilization and the product was purified via HPLC purification (Phenomenex® Synergi® 10 μ m C18(2) 100 Å), flow rate 5 mL/min, H₂O (+0,1% TFA)/ MeCN (+0,1% TFA) with a linear gradient condition of 20-24% MeCN in 20 min. The final ligand (5) (11.6 mg, 0.01 mmol, 17%) could be obtained as a yellowish powder. MS (ESI⁺): m/z = 754 [M+2H]²⁺, calculated M_{mi} for C₇₀H₈₂F₄N₁₈O₁₆: 1506.5.

Synthesis of DOTAGA.(SA.FAPi)₂

5-benzyl-1-tert-butyl-2-(4,10-bis(2-(tert-butoxy)-2-oxoethyl)-7-(2-((tert-butoxycarbonyl)amino)ethyl)-1,4,7,10-tetraazacyclododecan-1-yl)pentanedioate [DOTAGA-(COO^tBu)₃-(NHBoc)-GABz] (7)

First, *tert*-butyl-(2-chloroethyl)carbamate (6a) was synthesized. 2-Chloroethylamine hydrochloride (500 mg, 4.31 mmol) was dissolved in TEA (0.6 mL, 4.31 mmol) and suspended in dry DCM (11 mL). Di-

tert-butyldicarbonate (941 mg, 4.31 mmol) was added in portions within 45 min and then the mixture stirred for 24 h at RT. The solution was washed three times with a H₂O-1 M NaCl-solution (1:1) and the organic phase dried over magnesium sulphate and the solvent removed under reduced pressure. (6a) (271 mg, 1.51 mmol, 35%) was obtained as yellowish oil. ¹H-NMR (400 MHz, CDCl₃): δ [ppm] = 4.97 (s, 1H), 3.63-3.60 (t, J= 6.0 Hz, 3H), 3.51-3.46 (t, J= 8.0 Hz, 3H), 1.47 (s, 9H). MS (ESI⁺): *m/z*= 202 [M+Na]⁺, calculated M_{mi} for C₇H₁₄ClNO₂: 179.64 [M].

(6a) (271 mg, 1.51 mmol) was combined with potassium carbonate (147 mg, 1.06 mmol) and DO2A(^tBu)-GABz (6) (400 mg, 0.59 mmol) in dry MeCN (12 mL) and the mixture stirred at 90 °C. After 24 h, 100 mg of (6a) was added and stirred for another 24 h. The solvent was removed under reduced pressure and the residue purified by column chromatography with ethyl acetate/*n*-hexane (1:1, 3% TEA, R_f = 0.34). Product (7) (145 mg, 0.18 mmol, 30%) could be achieved as a yellowish oil. ¹H-NMR (400 MHz, CDCl₃): δ [ppm] = 7.39 - 7.34 (m, 5H, H-6), 5.13 (d, J = 4.3 Hz, 2H), 3.44 (d, J = 7.3 Hz, 1H), 3.23 (dd, J = 14.3 Hz, 8.9 Hz, 6H), 2.98 - 2.60 (m, 16H), 2.06 (s, 2H), 2.05 - 1.98 (m, 2H), 1.89 - 1.79 (m, 2H), 1.50 - 1.24 (m, 26H). MS (ESI⁺): *m/z*= 411 [M+2H]²⁺, 821 [M+H]⁺, 843 [M+Na]⁺, calculated M_{mi} for C₄₃H₇₃N₅O₁₀: 819.5.

4-(4,10-bis(2-(tert-butoxy)-2-oxoethyl)-7-(2-((tert-butoxycarbonyl)amino)ethyl)-1,4,7,10-tetraazacyclododecan-1-yl)-5-(tert-butoxy)-5-oxopentanoic acid [DOTAGA(COO^tBu)₃(NHBoc)] (8)

(7) (870 mg, 1.06 mmol) was dissolved in MeOH (11 mL) and Pd on activated charcoal (27 mg, 0.25 mmol, 10 wt%) was added to the solution. Stirring at RT was carried out overnight under a hydrogen atmosphere. The suspension was filtered through Celite and the solvent was removed under reduced pressure. Compound (8) as yellowish oil (798 mg, 1.09 mmol, 100%) was obtained which was used without further purification. ¹H-NMR (400 MHz, CDCl₃): δ [ppm] = 6.82 (s, 1H), 3.46 - 2.75 (m, 21H), 2.63 - 2.30 (m, 4H), 2.05 - 1.74 (m, 2H), 1.44 (s, 9H), 1.44 (s, 18H), 1.44 (s, 9H), 1.34 - 1.20 (m, 2H). MS (ESI⁺): *m/z*= 366 [M+2H]²⁺, 730 [M+H]⁺, 753 [M+Na]⁺, calculated M_{mi} for C₃₆H₆₇N₅O₁₀: 729.4.

Di-tert-butyl-2,2'-(4-(2-((tert-butoxycarbonyl)amino)ethyl)-10-(2,2,15,15-tetramethyl-4,9,13-trioxo-3,14-dioxo-5,8-diazahexadecan-12-yl)-1,4,7,10-tetraazacyclododecane-1,7-diyl)diacetate [DOTAGA(COO^tBu)₃(NHBoc)(N-Boc-ethylendiamin)] (9)

(8) (171 mg, 0.23 mmol), HATU (136 mg, 0.47 mmol), DIPEA (120 μL, 0.70 mmol) and HOBt (47.6 mg, 0.35 mmol) were dissolved in dry MeCN (2 mL). *Tert*-butyl-N-(2-amino-ethyl)-carbamate (74 μL, 0.47 mmol) was added within 30 min and the mixture was stirred for 24 h at RT. The residue was removed under reduced pressure and purified by column chromatography with chloroform/ methanol (10:1, R_f = 0.25). (9) could be received as yellowish oil (88.2 mg, 0.10 mmol, 43%). ¹H-NMR (400 MHz, CDCl₃): δ [ppm] = 5.35 (s, 2H), 3.40 (q, J= 3.4 Hz, 2H), 3.33 (t, J=6.5 Hz, 7H), 3.29 (s, 2H), 2.98-2.23 (m,

18H), 2.19-1.89 (m, 4H), 1.45 (q, $J=1.9$ Hz, 45H). MS (ESI⁺): $m/z= 437 [M+2H]^{2+}$, $873 [M+H]^+$, calculated M_{mi} for $C_{43}H_{81}N_7O_{11}$: 871.6.

2,2'-(4-(1-carboxy-4-((2-((2-ethoxy-3,4-dioxocyclobut-1-en-1-yl)amino)ethyl)amino)-4-oxobutyl)-10-(2-((2-ethoxy-3,4-dioxocyclobut-1-en-1-yl)amino)ethyl)-1,4,7,10-tetraazacyclododecane-1,7-diyl)-diacetic acid [DOTAGA.(SA)₂] (11)

(9) (88.2 mg, 0.10 mmol) was dissolved in dry DCM (200 μ L) and TFA (800 μ L). The solution was stirred at RT for 24 h and the solvent was removed under reduced pressure. Deprotected intermediate (10) was identified as yellowish oil and used without further processing. MS (ESI⁺): $m/z= 504 [M+H]^+$, calculated M_{mi} for $C_{21}H_{41}N_7O_7$: 503.3. Deprotected (10) was dissolved in 0.5 M phosphate buffer (pH 7, 2 mL). Afterwards SADE (36,6 μ L, 0.25 mmol) was added and the reaction was stirred at pH 7 for 24 h at RT. The solvent was removed by lyophilization and the colorless precursor (11) was used without further purification. MS (ESI⁺): $m/z= 752 [M+H]^+$, calculated M_{mi} for $C_{33}H_{49}N_7O_{13}$: 751.3.

2,2'-(4-(1-carboxy-4-((2-((4-((4-((S)-2-cyano-4,4-difluoropyrrolidin-1-yl)-2-oxoethyl)carbamoyl)-quinolin-6-yl)oxy)butyl)amino)-3,4-dioxocyclobut-1-en-1-yl)amino)ethyl)amino)-4-oxobutyl)-10-(2-((2-((4-((4-((S)-2-cyano-4,4-difluoropyrrolidin-1-yl)-2-oxoethyl)carbamoyl)quinolin-6-yl)oxy)butyl)-amino)-3,4-dioxocyclobut-1-en-1-yl)amino)ethyl)-1,4,7,10-tetraazacyclododecane-1,7-diyl)diacetic acid [DOTAGA.(SA.FAPi)₂] (12)

(11) was dissolved in 0.5 M phosphate buffer pH 9 (1.5 mL). NH₂-FAPi (41.3 mg, 0.10 mmol) was added and the pH was adjusted with 1 M NaOH to pH 9 again. The mixture was shaken for 24 h at RT and after the reaction was completed, the solvent was removed by lyophilization. The residue was purified via HPLC (Phenomenex[®] Synergi[®] 10 μ m C18(2) 100 \AA), flow rate 5 mL/min, H₂O (+0,1% TFA)/ MeCN (+0,1% TFA) with a linear gradient of 20-25% MeCN in 20 min. The final ligand (12) (18.1 mg, 0.01 mmol, 12%) was obtained as a yellowish powder. MS (ESI⁺): $m/z= 762 [M+2H]^{2+}$, calculated M_{mi} for $C_{71}H_{83}F_4N_{17}O_{17}$: 1521.6.

^{nat}Ga/^{nat}Lu-complexes

DOTA.(SA.FAPi)₂ (4.8 mg, 3.1 μ mol) was reacted with ^{nat}Ga(NO₃)₂ (2 eq.) in 0.5 M sodium acetate buffer pH 4.5 (500 μ L). After the solution was stirred for 6 h at 95 °C, the ^{nat}Ga complexes [^{nat}Ga]Ga-DOTA.(SA.FAPi)₂ were obtained. Complexation was confirmed by ESI-MS and the precursor was purified via HPLC (Phenomenex Synergi[®] 10 μ m C18(2) 100 \AA), flow rate 5 mL/min, H₂O (+0,1% TFA)/ MeCN (+0,1% TFA) with a linear gradient condition of 5-95% MeCN in 10 min. The product was

obtained as yellowish powder (4.4 mg, 2.8 μmol , 90%). MS (ESI⁺): m/z = 525.4 [M+3H]³⁺, 787.4, 787.9, 788.3 [M+2H]²⁺; calculated M_{mi} for $\text{C}_{70}\text{H}_{80}\text{F}_4\text{GaN}_{18}\text{O}_{16}$: 1573.5

[^{nat}Ga]Ga-DOTAGA.(SA.FAPi)₂ (5.5 mg, 3.6 μmol) and [^{nat}Lu]Lu-DOTAGA.-(SA.FAPi)₂ (5.1 mg, 3.3 μmol) could be generated analogously to the ^{nat}Ga-DOTA derivative with ^{nat}Ga(NO₃)₂ resp. ^{nat}LuCl₃. [^{nat}Ga]Ga-DOTAGA.(SA.FAPi)₂ was obtained as yellowish powder (5.1 mg, 3.2 μmol , 89%). MS (ESI⁺): m/z = 530.4 [M+3H]³⁺, 794.9, 795.4, 795.8 [M+2H]²⁺; calculated M_{mi} for $\text{C}_{71}\text{H}_{81}\text{F}_4\text{GaN}_{17}\text{O}_{17}$: 1588.5 and [^{nat}Lu]Lu-DOTAGA.(SA.FAPi)₂ was obtained as yellowish powder (4.7 mg, 2.8 μmol , 85%). MS (ESI⁺): m/z = 565.7 [M+3H]³⁺, 847.8, 848.3 [M+2H]²⁺; calculated M_{mi} for $\text{C}_{71}\text{H}_{80}\text{F}_4\text{LuN}_{17}\text{O}_{17}$: 1693.5

Radiocomplexes with gallium-68

Gallium-68 elution was performed using ethanol-based post-processing from a ⁶⁸Ge/⁶⁸Ga-generator (ITG Garching, Germany) following the procedure by Eppard et al. [20].

Reaction controls for radiochemical yields (RCY) was executed using radio-TLC (TLC Silica gel 60 F₂₅₄ Merck) with 0.1 M citrate buffer pH 4. TLC's were measured in TLC imager CR-35 Bio Test-Imager from Duerr-ndt (Bietigheim-Bissingen, Germany) with the analysis software AIDA Elysia-Raytest (Straubenhardt, Germany).

Stability studies in human serum (HS), phosphate buffered saline (PBS) and saline (0.9% isotonic NaCl-solution): ~5 MBq of the radionuclide tracer solution after > 95% radiochemical purity was added to 500 μL of the respective media and stirred at 37 °C. Aliquots were taken at the measured time points for gallium-68 were 15, 30, 60, 90, 120 min. HS (human male AB plasma, USA origin) was bought from Sigma Aldrich, PBS was purchased from Sigma Aldrich and 0.9% saline from B. Braun Melsungen AG (Melsungen, Germany). Radiochemical yields was determined with radio-TLC and evaluated by a TLC imager.

Lipophilicity measurement

The shake-flask method was carried out to determine the lipophilicity. After completion of radiolabeling with a RCP > 95%, the tracer solution was adjusted to pH 7.4 with 2 M NaOH. ~5 MBq was taken from the solution and adjusted to a total volume of 700 μL with PBS (n=4). 700 μL 1-octanol was added to each PBS solution and stirred for 2 min (1500 rpm). Subsequently, each tube was centrifuged for 1–2 min. 400 μL of the octanol- and PBS phases were pipetted into new tubes and aliquots of each phase (3 μL of the PBS phase and 6 μL of the octanol phase) were measured via radio-

TLC. The PBS phases were adjusted up to 700 μ L and 700 μ L octanol was added to each tube. The procedure was repeated twice more. $\text{LogD}_{7.4}$ values were calculated as the logarithm of the octanol/PBS ratio measured by a TLC imager CR-35 Bio Test-Imager from Duerr-ndt (Bietigheim-Bissingen, Germany) and the software AIDA Elysia-Raytest (Straubenhardt, Germany).

Inhibition assays

Recombinant human FAP, PREP, DPP8 and DPP9 were expressed and purified as described earlier [10]. Human DPP 4 was purified from seminal plasma as published [21]. IC_{50} -measurements of the probes for FAP and PREP were carried out as using respectively Z-Gly-Pro-AMC (50 μ M) and Suc-Gly-Pro-AMC (250 μ M) as the substrate [10].

Patient studies

The detailed clinical history of the six patients is shown in **Table 1**.

Table 1 Clinical details of the 6 included patients (RAI: Radioiodine, ER: the estrogen receptor, PR: progesterone receptor, HER2/neu: human epidermal growth factor receptor-2, LAR: long-acting).

S.No	Age/Gender	Histopathology	Prior treatments
1	45/F	Papillary thyroid cancer (RAI refractory)	Disease progression on sorafenib, radiotherapy and lenvatinib
2	63/F	Papillary thyroid cancer (RAI refractory)	Disease progression on sorafenib, radiotherapy and lenvatinib
3	46/F	Papillary thyroid cancer (RAI refractory)	Disease progression on sorafenib and lenvatinib
4	56/F	ER-, PR- HER2/neu- left breast cancer	Surgery, radiotherapy and chemotherapy
5	46/M	Pancreatic neuroendocrine cancer	Sandostatin LAR, capecitabine
6	58/M	Duodenal neuroendocrine cancer	Sandostatin LAR, [^{177}Lu]Lu-DOTATATE+capecitabine

Clinical image Acquisition and Analysis

Scans were acquired on a dedicated GE Discovery 710* 128 Slice PET/CT Scanner, with a 40-mm detector at a rotation speed of 0.35 sec. The mean injected activities were 74 MBq (range: 48.1 MBq to 88.8 MBq), 122.1 MBq (range; 74 to 185 MBq), 296 MBq (range; 259 to 333 MBq) and 130 MBq for [⁶⁸Ga]Ga-DOTAGA.(SA.FAPi)₂, [⁶⁸Ga]Ga-DOTA.SA.FAPi, [¹⁸F]FDG radiotracers and [⁶⁸Ga]Ga-DOTANOC respectively. While, in all cancers, a head-to-head comparison was performed between the [¹⁸F]FDG and [⁶⁸Ga]Ga-DOTA.SA.FAPi monomer and [⁶⁸Ga]Ga-DOTAGA.(SA.FAPi)₂ dimer, in patients with an additional [⁶⁸Ga]Ga-DOTANOC PET/CT was also performed to visualize the somatostatin receptor expression. The PET/CT acquisition parameters and post processing were similar to that of [¹⁸F]FDG and [⁶⁸Ga]Ga-FAPi PET/CT.

All scans were acquired within a time interval of one week. For all the three radiotracers, whole-body PET/CT studies were acquired at 1-hour post-injection. The acquisition protocol constituted an initial scout image, followed by a CT scan, and PET acquired at 2 minutes per bed. A diagnostic whole-body CT scan parameter included 300-350 mAs, 120kVp, slice thickness 5 mm, pitch 1 was acquired.

[¹⁸F]FDG, [⁶⁸Ga]Ga-DOTA.SA.FAPi and [⁶⁸Ga]Ga-DOTAGA.(SA.FAPi)₂ PET/CT scans were loaded simultaneously and co-registered using carina as an anatomical landmark registration technique. Two experienced Nuclear Medicine physicians conducted scan interpretations and disagreement in the reports was reviewed by a third physician. For the quantitative comparison, ROIs were drawn according to the PET Response Criteria in Solid Tumors (PERCIST 1.0). The quantitative assessment of standardized uptake values (SUV) corrected for lean body mass was done using a 3D auto-contour ROI at a 40% threshold of SULpeak technique.

The clinical section of this study was approved by the Institute Ethics committee, All India Institute of Medical Sciences, (IECPG-22/27.02.2020). All patients gave their written informed consent.

Results and Discussion

Synthesis of DOTA.(SA.FAPi)₂

DOTA.(SA.FAPi)₂ was synthesized starting with the commercially available DOTA-di(^tBu)ester (1) in a 4-step route according to **Figure 2**. In the first step, (1) was reacted with N-Boc-ethylenediamine using the base DIPEA and the coupling agents HATU and HOBt. The obtained compound DOTA-(COO^tBu)₂(N-

Boc-en_2 (2) was treated with trifluoroacetic acid to remove the Boc- and *tert*-butyl protective groups. In the next step, amidations were carried out with squaric acid diethyl ester (SADE) to get DOTA.(SA)₂ (4). In the last synthesis stage, the formed squaric diester was bound to NH₂-FAPi at basic pH to obtain DOTA.(SA.FAPi)₂ (5).

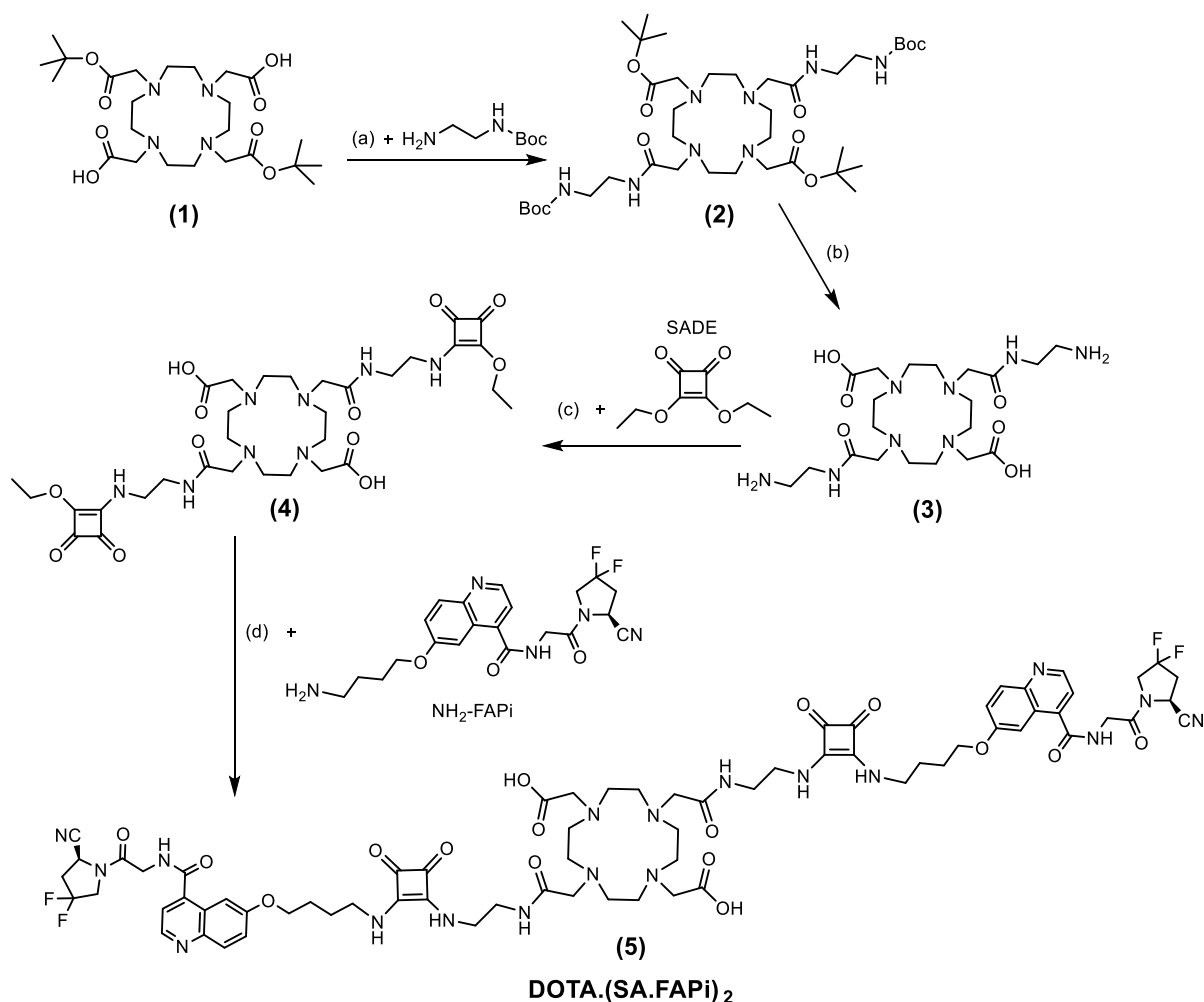


Figure 2 Four-step synthetic route of DOTA.(SA.FAPi)₂ (5): (a) HATU, HOBT, DIPEA, MeCN, RT, 48 h, 72%; (b) DCM/TFA (1:1), RT, 16 h; (c) 0.5 M phosphate buffer pH= 7, RT, 16 h; (d) 0.5 M phosphate buffer pH= 9, RT, 16 h, 17%.

Synthesis of DOTAGA.(SA.FAPi)₂

DOTAGA.(SA.FAPi)₂ could be obtained in a 7-step synthesis route according to **Figure 3**. First, the 2-chloroethylamine hydrochloride was protected with a Boc group by means of triethylamine and di-*tert*-butyl dicarbonate. The formed *tert*-butyl-(2-chloroethyl)-carbamate (6a) was introduced to the commercially available DO2A(^tBu)-GABz (6) via nucleophilic substitution. This resulted in DOTAGA(COO^tBu)₃(NHBoc)-GABz (7). Deprotection of the benzyl protective group was achieved by hydrogenolysis using Pd(OH)₂ on active charcoal to receive the product DOTAGA(COO^tBu)₃(NHBoc) (8).

Subsequently, commercially available N-Boc-ethylenediamine was bound to the standalone carboxylic acid with the coupling agents HATU, HOBT and the base DIPEA analogously to the DOTA derivative. In the next step, the protecting groups Boc and *tert*-butyl of DOTAGA(COO^tBu)₃(NHBoc)(N-Boc-en) (10) were cleaved with TFA in DCM and two identical SADE substituents were coupled to the terminal amines of the DOTAGA derivative at neutral pH. The esters of the obtained DOTAGA.(SA)₂ (11) were amidated with two NH₂-FAPi molecules at basic conditions. DOTAGA.(SA.FAPi)₂ (12) could be isolated via HPLC purification.

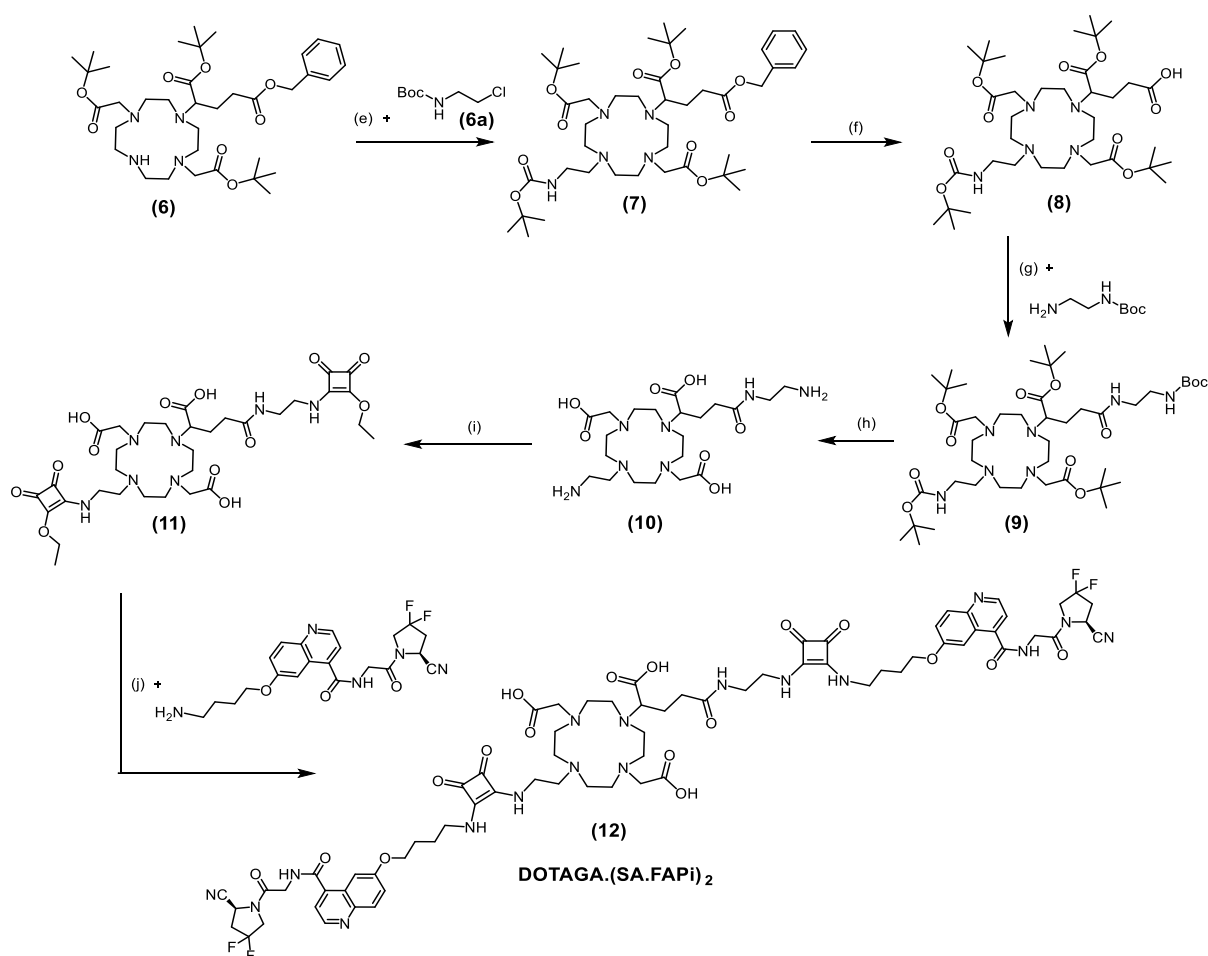


Figure 3 Seven-step synthesis route of DOTAGA.(SA.FAPi)₂ (12): (e) MeCN, K₂CO₃, 90 °C, 48 h, 30%; (f) Pd/C (10%), MeOH, H₂, RT, 16 h, 100%; (g) HATU, HOBT, DIPEA, MeCN, RT, 24 h, 43%; (h) DCM/ TFA (20:80)%, RT, 48 h; (i) SADE, 0.5 M phosphate buffer pH= 7, RT, 48 h; (j) 0.5 M phosphate buffer pH= 9, RT, 24 h, 12%.

Synthesis of non-radioactive complexes

The non-radioactive complexes [^{nat}Ga]Ga-DOTA.(SA.FAPi)₂, [^{nat}Ga]Ga-DOTAGA.(SA.FAPi)₂ and [^{nat}Lu]Lu-DOTAGA.(SA.FAPi)₂ were synthesized by treating the corresponding precursors with gallium (III) nitrate and lutetium (III) chloride, respectively. The reactions were executed in 0.2 M sodium acetate buffer pH 4.5 at 95 °C. After lyophilization of the reaction solution, the residue was purified via HPLC to obtain the final metal-complexed derivatives.

In vitro enzyme inhibition measurements

Confirming the selectivity of the FAPi compounds against the closely related serine proteases of the S9 family (PREP, DPP4, DPP8 and DPP9) is crucial for considering their applicability in *in vivo* studies. These related proteases are ubiquitously expressed: If DPP or PREP affinity would be present, this could significantly discount on the tumor selectivity of the FAPi compounds. IC₅₀ measurements for FAP, PREP and DPPs (DPP4, DPP8 and DPP9) of both dimeric systems with their ^{nat}Ga/^{nat}Lu metal complexes were measured. **Table 2** shows the IC₅₀ values for the five compounds DOTA.(SA.FAPi)₂, [^{nat}Ga]Ga-DOTA.(SA.FAPi)₂, DOTAGA.(SA.FAPi)₂, [^{nat}Ga]Ga-DOTAGA.(SA.FAPi)₂ and [^{nat}Lu]Lu-DOTAGA.(SA.FAPi)₂ compared to the reference FAP inhibitor UAMC1110 and the monomeric probes [^{nat}Ga]Ga-DOTA.SA.FAPi and [^{nat}Lu]Lu-DOTA.SA.FAPi. The IC₅₀ values for FAP of all dimeric tracers were in the same order of magnitude compared to the reference compound UAMC1110 and the monomers ^{nat}Ga/^{nat}Lu-DOTA.SA.FAPi and are within the subnanomolar to low nanomolar range (0.78–1.54 nM).

For all dimeric derivatives, the affinity for PREP was in the μM range (IC₅₀s 0.42–1.60 μM) resulting in high FAP/PREP selectivity indices in favor of FAP targeting. Additionally, IC₅₀ values of the dimeric compounds against DPPs were within the low micromolar ranges. Compared to the reference compound UAMC1110, the selectivity towards DPP4, DPP8 and DPP9 is slightly decreased. In summary, selectivity against the DPPs and PREP are high and sufficient for all five dimeric compounds. Furthermore, excellent affinity for the target enzyme FAP was achieved.

Table 2 IC₅₀ values of the FAPI probes against FAP and the related serine proteases (PREP, DPP4, DPP8, DPP9). Data are described as the mean with standard deviation (n = 3 for FAP and n = 2 for PREP and the DPPs).

Compound	IC ₅₀ (μM)				IC ₅₀ (nM)
	DPP4	DPP8	DPP9	PREP	FAP
DOTA.(SA.FAPi) ₂	0.44 ± 0.06	1.33 ± 0.11	0.96 ± 0.15	0.42 ± 0.02	0.78 ± 0.05
[^{nat} Ga]Ga-DOTA.(SA.FAPi) ₂	0.51 ± 0.09	1.44 ± 0.16	0.78 ± 0.07	0.92 ± 0.07	1.05 ± 0.07
DOTAGA.(SA.FAPi) ₂	0.40 ± 0.07	0.42 ± 0.04	0.16 ± 0.02	0.39 ± 0.02	0.92 ± 0.06
[^{nat} Ga]Ga-DOTAGA.(SA.FAPi) ₂	0.70 ± 0.11	0.87 ± 0.08	0.19 ± 0.01	1.60 ± 0.16	0.90 ± 0.06
[^{nat} Lu]Lu-DOTAGA.(SA.FAPi) ₂	0.63 ± 0.07	0.41 ± 0.03	0.18 ± 0.02	0.56 ± 0.04	1.54 ± 0.15
[^{nat} Ga]Ga-DOTA.SA.FAPi	> 1	N/A	> 1	8.7 ± 0.9 ^a	1.4 ± 0.2 ^a
[^{nat} Lu]Lu-DOTA.SA.FAPi	> 1	N/A	> 1	2.5 ± 0.4 ^a	0.8 ± 0.2 ^a
UAMC1110	> 10	10.1 ± 0.6 ^b	4.7 ± 0.4 ^b	1.8 ± 0.01	0.43 ± 0.02 ^a

^a IC₅₀ for FAP and PREP from Moon et al.[10]

^b The IC₅₀ value of UAMC-1110 for DPP9 (4.7 ± 0.4 μM) is slightly lower compared to what was published before (> 12 μM)[2]. This is due to introducing of a new measurement method in combination with new human recombinant DPP9 (instead of bovine DPP9). The IC₅₀ of UAMC1110 for DPP8 was determined as a part of this study.

Labeling kinetics with gallium-68

DOTA.(SA.FAPi)₂ was labeled with gallium-68 under various buffer conditions. Ammonium acetate (AmAc), sodium acetate (NaAc) and N-2-hydroxyethyl piperazine-N'-2-ethanesulfonic acid (HEPES) buffer were used. **Figure 4** compares the radiochemical yields (RCY) of the DOTA dimer precursor in the three different buffer systems with identical buffer molarity, pH, volume, reaction temperature, activity and ligand amount (1 M, pH 5.5, 300 μL, 95 °C, 100–150 MBq and 20 nmol). The RCY are analyzed by radio-TLC and evaluated with a TLC imager. Initially, radiolabeling was performed in AmAc buffer, analogous to our recently published DOTA.SA.FAPi monomer. However, in contrast to the monomer which led to quantitative yields, DOTA dimer showed an RCY of only 9% after 10 min.

Thereupon, labeling was performed in NaAc and HEPES buffer. In both, NaAc and HEPES buffer, complexation with gallium-68 could be obtained with RCY of 87% within 10 min.

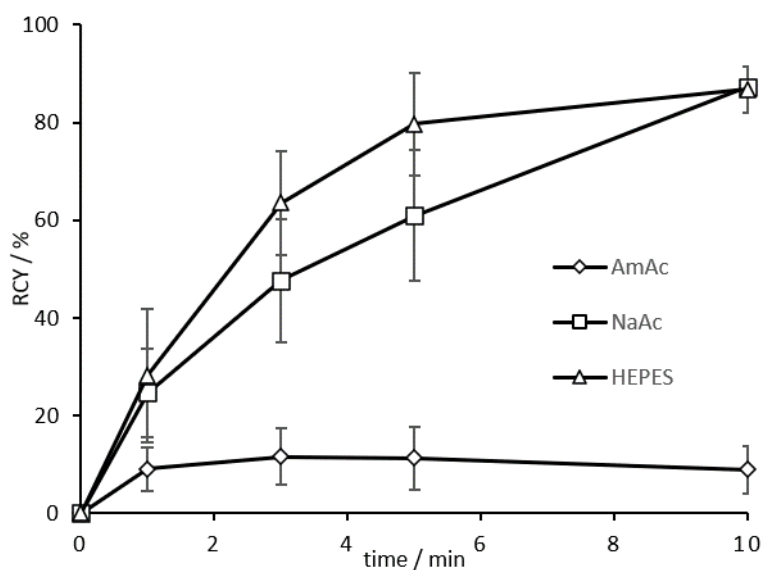


Figure 4 RCY (in %) of 20 nmol [^{68}Ga]Ga-DOTA.(SA.FAPi) $_2$ in 1 M AmAc, NaAc and HEPES buffers after 10 min at 95 °C (n = 2 for AmAc and NaAc, n = 3 for HEPES; pH 5.5, A(^{68}Ga)= 100–150 MBq).

Afterwards, labeling was performed in 1 M HEPES buffer with different precursor amounts of 10–40 nmol (**Figure 5**). RCY of more than 80% was achieved for precursor quantity of ≥ 20 nmol. At 10 nmol ligand amount only a RCY of 50% could be observed. Complexation with gallium-68 with 20–40 nmol was comparably good in a range of 80–90% RCY. Compared to DOTA.SA.FAPi, no quantitative yields could be attained. Due to the linear arrangement of the bifunctional conjugates, coordination of gallium-68 to the central DOTA core might be sterically difficult.

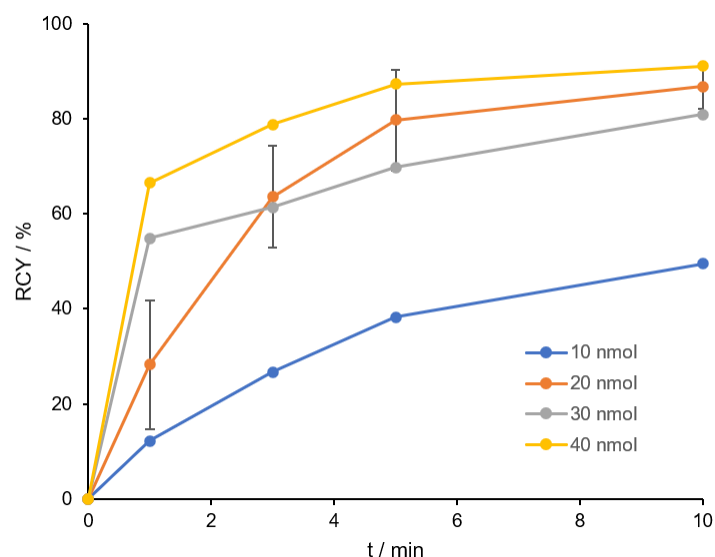


Figure 5 RCY (in %) of 10-40 nmol $[^{68}\text{Ga}]\text{Ga-DOTA}(\text{SA.FAPi})_2$ in 1 M HEPES buffer pH 5.5 after 10 min at 95 °C (n = 3 for 20 nmol, n = 1 for 10, 30 and 40 nmol), $A(^{68}\text{Ga}) = 100\text{-}150$ MBq.

For synthesis of $[^{68}\text{Ga}]\text{Ga-DOTAGA}(\text{SA.FAPi})_2$, identical conditions as for the $[^{68}\text{Ga}]\text{Ga-DOTA}(\text{SA.FAPi})_2$ derivative were used. **Figure 6** shows the kinetics of three precursor concentrations (5, 10 and 20 nmol) in 1 M HEPES pH 5.5 at 95 °C. In comparison to the DOTA dimer, quantitative yields > 99% were obtained after a reaction time of 10 minutes. Even a precursor quantity of 10 nmol led to excellent complexation and at 5 nmol, a RCY of > 90% was still obtained. This may confirm the previous statement, since the DOTAGA chelator provides an additional coordination option that might facilitate the faster and better complexation with gallium-68.

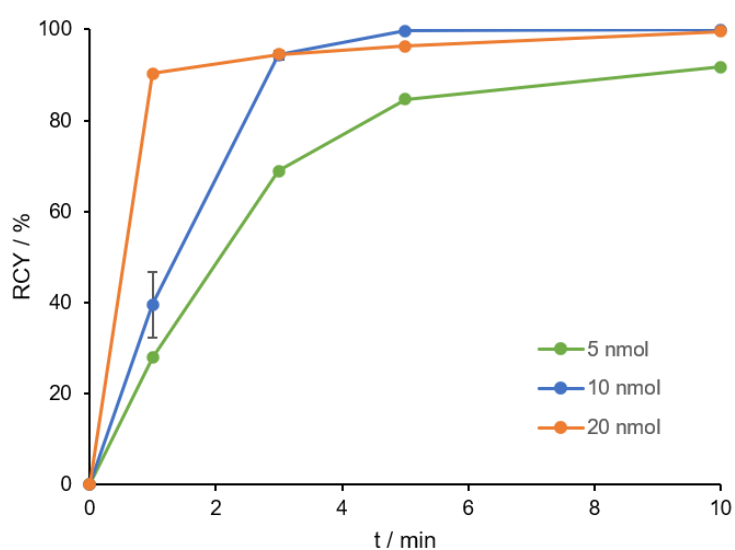


Figure 6 RCY (in %) of 5, 10 and 20 nmol $[^{68}\text{Ga}]\text{Ga-DOTAGA}(\text{SA.FAPi})_2$ in 1 M HEPES buffer pH 5.5 in 10 min at 95 °C (n = 3 for 10 nmol, n = 1 for 5 and 20 nmol), $A(^{68}\text{Ga}) = 100\text{-}150$ MBq.

In vitro stability of ⁶⁸Ga-labeled derivatives

[⁶⁸Ga]Ga-DOTAGA.(SA.FAPi)₂ was tested for its stability in different media: HS, PBS and saline at different time points (15-120 min) at 37 °C. The RCY of the intact conjugates are analyzed by radio-TLC and evaluated with a TLC imager. *In vitro* stabilities in HS and in NaCl were > 98% and in PBS > 91%, respectively, after 120 min (**Figure 7**).

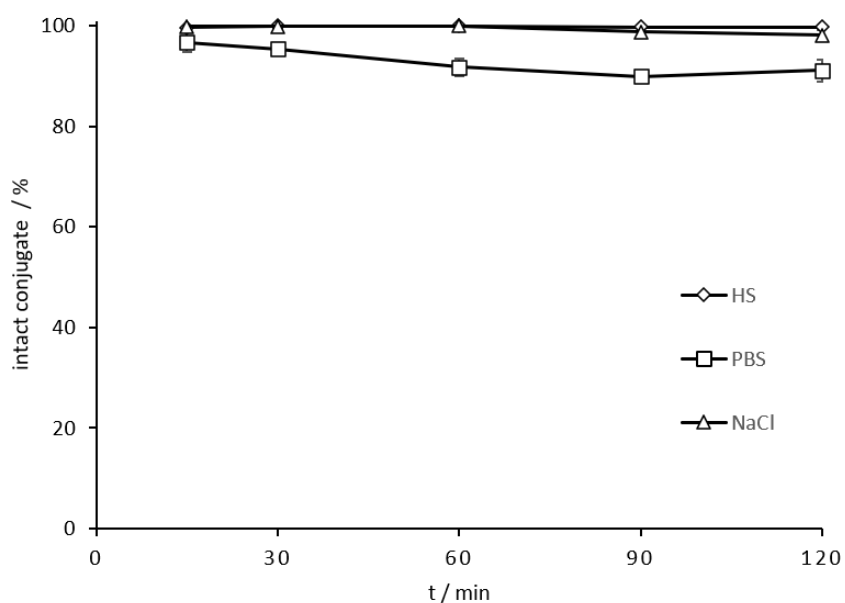


Figure 7 *In vitro* stability of [⁶⁸Ga]Ga-DOTAGA.(SA.FAPi)₂ (in % intact conjugates) in HS, PBS and saline during a period of 15-120 min at 37 °C (n = 3 for all media).

Lipophilicity comparison [⁶⁸Ga]Ga-DOTA.SA.FAPi vs. [⁶⁸Ga]Ga-DOTAGA.(SA.FAPi)₂

Lipophilicity (logD_{7.4} value) was performed via “shake-flask” method for the dimer [⁶⁸Ga]Ga-DOTAGA.(SA.FAPi)₂ and compared to those of the monomer [⁶⁸Ga]Ga-DOTA.SA.FAPi from [22] (**Table 3**).

Table 3 LogD values (pH=7.4) of [⁶⁸Ga]Ga-DOTA.SA.FAPi and [⁶⁸Ga]Ga-DOTAGA.(SA.FAPi)₂ (n = 3)

[⁶⁸ Ga]Ga-complex	LogD _{7.4} value
[⁶⁸ Ga]Ga-DOTA.SA.FAPi	-2.68 ± 0.06 ^a
[⁶⁸ Ga]Ga-DOTAGA.(SA.FAPi) ₂	-2.02 ± 0.06

^a LogD_{7.4} from Moon et al. [22]

The lipophilicity of [⁶⁸Ga]Ga-DOTA.SA.FAPi was already published in our recent work [22] with a logD_{7.4} of -2.68. [⁶⁸Ga]Ga-DOTAGA.(SA.FAPi)₂ displayed a slightly higher lipophilicity with a logD_{7.4} value of -2.02. Both derivatives have strong hydrophilic characteristics however the dimer showed a more lipophilic character due to the additional linker-targeting vector conjugate.

Clinical studies

Six patients (4 females, 2 males, mean age 52.3 ± 7.6 years; range 45–63 years) who had progressed on all the available cancer treatment options were referred to the Department of Nuclear Medicine at AIIMS. None of the patients experienced adverse events from the radiotracers. The detailed clinical history of the six patients is mentioned in **Table 1**.

Organ distribution of [⁶⁸Ga]Ga-DOTA.SA.FAPi vs. [⁶⁸Ga]Ga-DOTAGA.(SA.FAPi)₂

The physiological biodistribution of [⁶⁸Ga]Ga-DOTA.SA.FAPi involved the pancreas, liver, heart, spleen, kidneys, gut, bladder, and to a lesser extent, lacrimals, oral mucosa, salivary glands, and thyroid glands. The biodistribution of [⁶⁸Ga]Ga-DOTAGA.(SA.FAPi)₂ was similar to that of [⁶⁸Ga]Ga-DOTA.SA.FAPi, yet the intensity of uptake in the corresponding organs varied (**Figure 8, Table S3.1**). Visual analysis revealed the pancreas as the organ of the highest uptake on both the radiotracers.

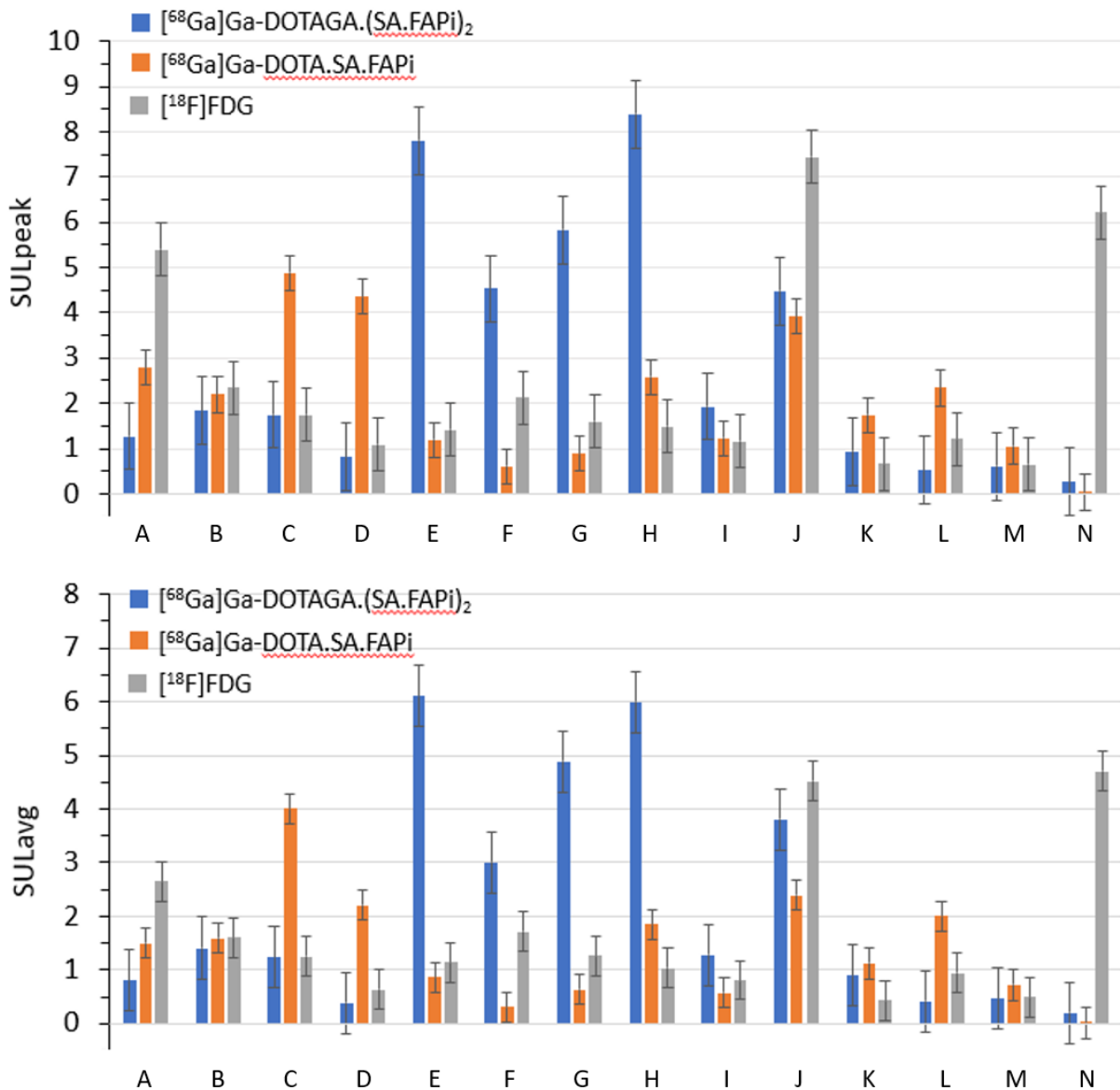


Figure 8 Comparison of SUL (standardized uptake value (SUV) normalized to lean body mass) values among various radiotracers in six patients; above: SUL_{peak} of [⁶⁸Ga]Ga-DOTAGA.(SA.FAPi)₂ (blue), [⁶⁸Ga]Ga-DOTA.SA.FAPi (orange) and [¹⁸F]FDG (grey); below: SUL_{avg} of [⁶⁸Ga]Ga-DOTAGA.(SA.FAPi)₂ (blue), [⁶⁸Ga]Ga-DOTA.SA.FAPi (orange) and [¹⁸F]FDG (grey).; A: lacrimal glands; B: oral mucosa; C: salivary glands; D: thyroid; E: heart contents/ blood pool; F: liver; G: spleen; H: pancreas; I: duodenum; J: kidneys; K: psoas muscle; L: bone (L4 vertebrae); M: femur; N: brain normal parenchyma.

Normal Organ Uptake

On quantitative analysis, variable, higher SUL (standardized uptake value (SUV) normalized to lean body mass) peak and higher average uptake values were noted in the blood pool, liver, spleen, pancreas, salivary glands, thyroid and the psoas muscle on [⁶⁸Ga]Ga-DOTAGA.(SA.FAPi)₂ compared to [⁶⁸Ga]Ga-DOTA.SA.FAPi PET/CT scans (**Figure 8–10, Table S3.1**). The main reason for higher uptake in normal tissues are not known yet. However, the change in the structure from a monomer to a dimeric

system and thus the introduction of an additional linker-TV unit and the increase of molecular weight have shown an influence to a slightly higher lipophilicity, which could be a reason for the higher retention. The delayed blood pool from [⁶⁸Ga]Ga-DOTAGA.(SA.FAPi)₂ in some patients is of concern and may contribute a relatively high bone marrow toxicity, but detailed pharmacokinetic and dosimetry data is warranted to validate the findings. However, while the dosimetry results on [⁶⁸Ga]Ga-DOTA.SA.FAPi are reported and are proven safe for diagnostic use [11], pharmacokinetic data on [⁶⁸Ga]Ga-DOTAGA.(SA.FAPi)₂, [¹⁷⁷Lu]Lu-DOTA.SA.FAPi, and [¹⁷⁷Lu]Lu-DOTAGA.(SA.FAPi)₂ are underway. Contrary to the avid uptake of [¹⁸F]FDG in the normal brain parenchyma, outstanding negligible uptake was quantified on [⁶⁸Ga]Ga-DOTAGA.(SA.FAPi)₂ and [⁶⁸Ga]Ga-DOTA.SA.FAPi PET/CT scans (**Figure 8 and 10, Table S3.1**).

Case reports

(I) In a case of the 63-year-old female diagnosed with papillary thyroid cancer (PET/CT scans maximum intensity projection (MIP) of [⁶⁸Ga]Ga-DOTA.SA.FAPi and [⁶⁸Ga]Ga-DOTAGA.(SA.FAPi)₂ in **Figure 9, Table S3.2**), the DOTAGA dimer probe showed increased tumor uptake (SUL_{avg}: 9.93 in L2 vertebra tumor, 8.9 in right ischium and 8.9 in the left femur) with overall higher tumor-to-background ratios than the DOTA monomer (SUL_{avg}: 7.44 in L2 vertebra, 6.7 in right ischium and 1.42 in the left femur) after 1 h p.i. High retention of [⁶⁸Ga]Ga-DOTAGA.(SA.FAPi)₂ were shown after 3 h p.i. with SUL_{avg}: 10.3 in L2 vertebra, 8.4 in right ischium and 8.5 in the left femur, respectively. Yet, higher uptake in the blood-pool with retention duration up to 3 h p.i. was observed.

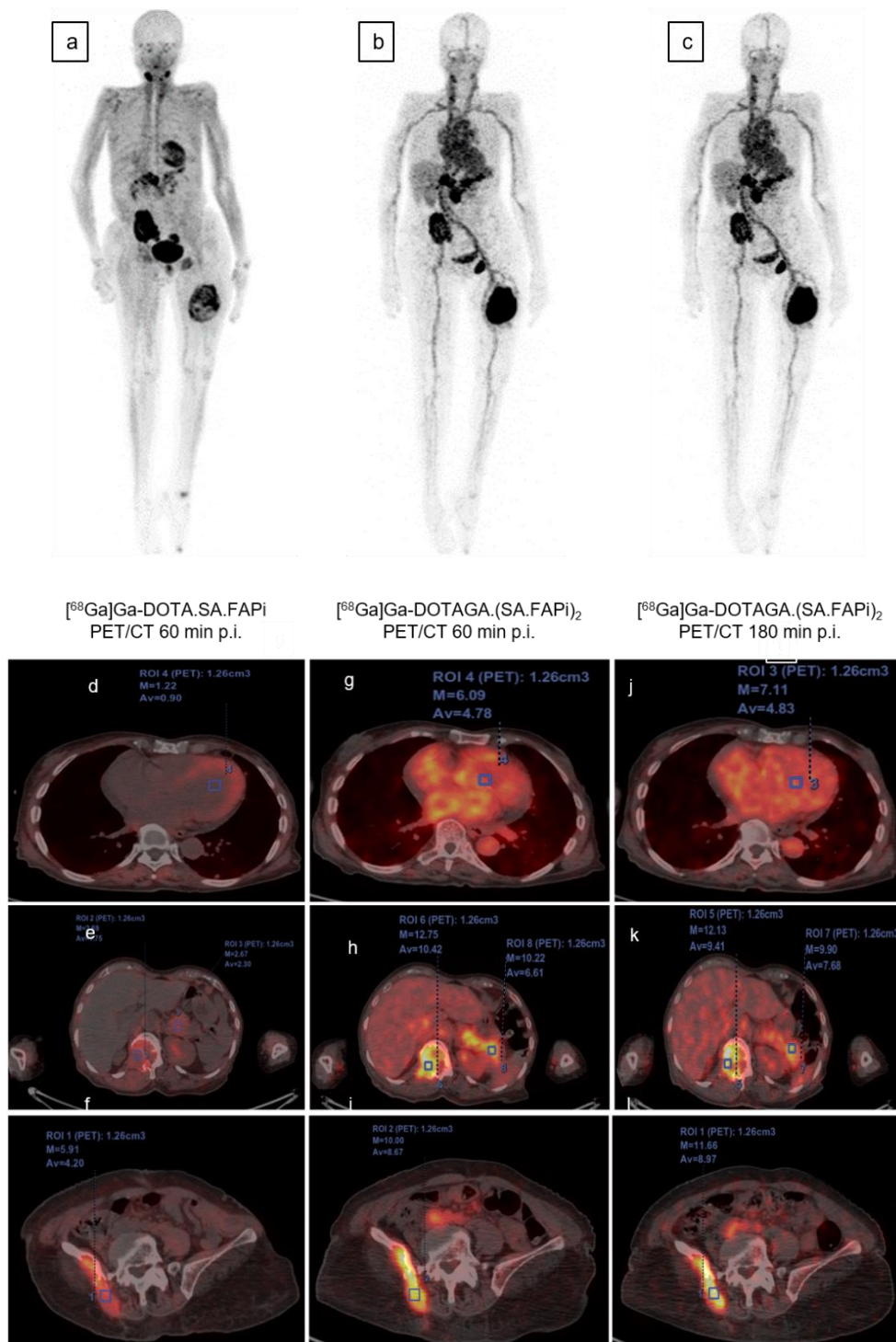


Figure 9 63-year-old female diagnosed with papillary thyroid cancer; (a) PET/CT MIP of $[^{68}\text{Ga}]\text{Ga-DOTA.SA.FAPi}$: normal distribution in the salivary glands, pancreas and myocardium; avid skeletal lesions in the right ilium, left ischial tuberosity, and left femur; (b,c) PET/CT MIP of $[^{68}\text{Ga}]\text{Ga-DOTAGA.(SA.FAPi)}_2$: normal biodistribution in the pancreas, and liver; concordance of tracer avidity in all the lesions compared to $[^{68}\text{Ga}]\text{Ga-DOTA.SA.FAPi}$ but demonstrated higher tumor-to-background ratios and avidity in the tumor lesions; higher retention duration of $[^{68}\text{Ga}]\text{Ga-DOTAGA.(SA.FAPi)}_2$ in the blood-pool with retention up to 3 h p.i. compared to $[^{68}\text{Ga}]\text{Ga-DOTA.SA.FAPi}$; fused axial PET/CT images demonstrate higher standardized uptake values for $[^{68}\text{Ga}]\text{Ga-DOTAGA.(SA.FAPi)}_2$ in both normal organs (g,h) and lesions (h,i) compared to $[^{68}\text{Ga}]\text{Ga-DOTA.SA.FAPi}$ PET/CT (d,e,f) which remained stable even up to 3 h p.i. (j,k,l).

(II) A 36-year-old male was diagnosed with grade III pancreatic neuroendocrine tumor (**Figure 10**). Due to the neuroendocrine origin and Ki-67 index of > 20%, patient underwent [⁶⁸Ga]Ga-DOTANOC (a,b), [¹⁸F]FDG (c,d) PET/CT's, followed by and [⁶⁸Ga]Ga-DOTAGA.(SA.FAPi)₂ (e,f), and [⁶⁸Ga]Ga-DOTA.SA.FAPi (g,h), PET/CT scans. The MIP and PET/CT fused axial images of [⁶⁸Ga]Ga-DOTANOC (a,b), [¹⁸F]FDG (c,d), [⁶⁸Ga]Ga-DOTAGA.(SA.FAPi)₂ (e,f) and [⁶⁸Ga]Ga-DOTA.SA.FAPi (g,h) revealed highest uptake on [⁶⁸Ga]Ga-DOTA.SA.FAPi PET/CT (SUVmax: 30.84) (h) followed by [⁶⁸Ga]Ga-DOTAGA.(SA.FAPi)₂ (SUVmax: 27.22) (f) in the primary tumor (pancreas).

All the agents, except [¹⁸F]FDG (c,d), demonstrated similar biodistribution and showed increased radiotracer uptake in the primary pancreatic tumor. On the other hand, the left supraclavicular lymph node was only remarkably visible on the [⁶⁸Ga]Ga-DOTAGA.(SA.FAPi)₂ (e) and [⁶⁸Ga]Ga-DOTA.SA.FAPi (g) PET MIP images. Unlike the high blood pool activity noted on the [⁶⁸Ga]Ga-DOTAGA.(SA.FAPi)₂ images of the patient described in **Figure 9**, no or minimal blood pool uptake was observed in this patient (**Figure 10 e,f**).

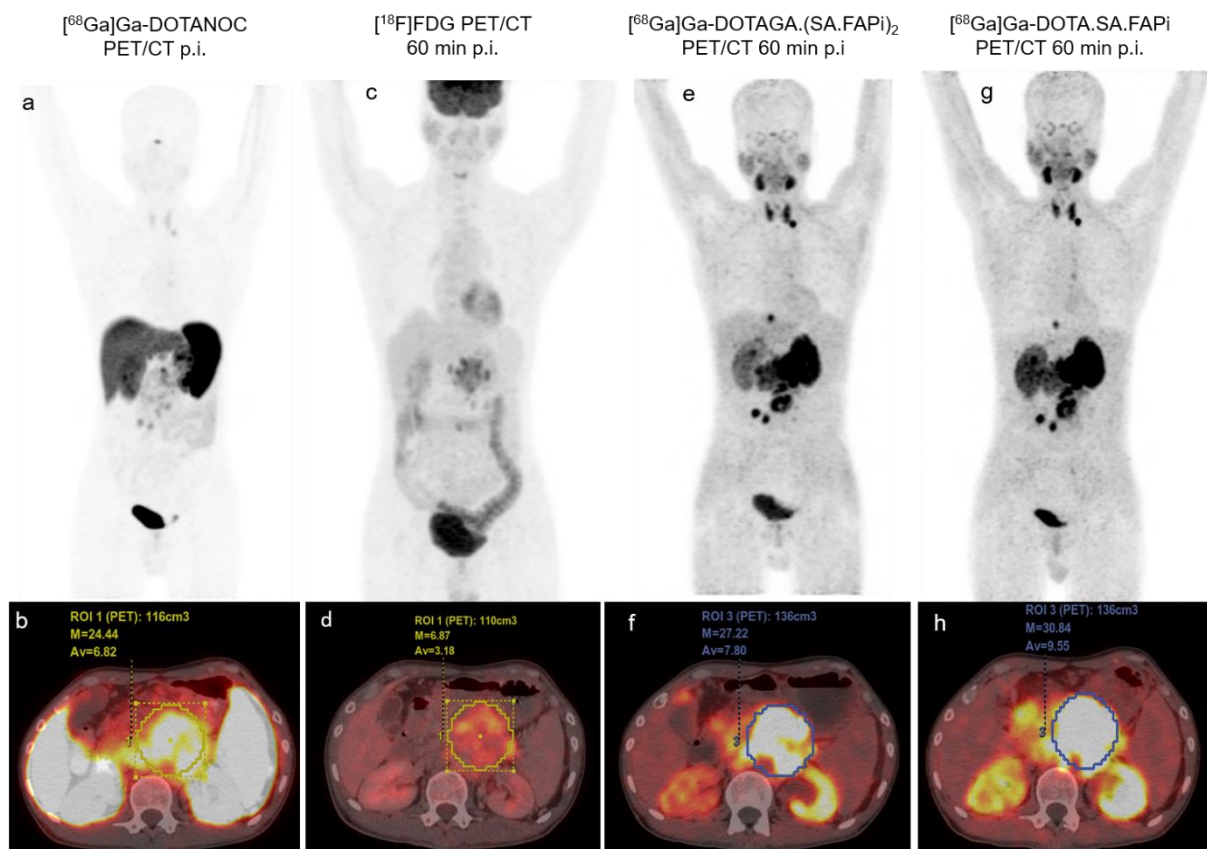


Figure 10 36-year-old male diagnosed with grade III pancreatic neuroendocrine tumor, the extent of cancer involved primary tumor in the pancreas and left supra clavicular lymph node. MIP and PET/CT fused axial images 1 h p.i. of (a,b) [⁶⁸Ga]Ga-DOTANOC; (c,d) [¹⁸F]FDG; (e,f) [⁶⁸Ga]Ga-DOTAGA.(SA.FAPi)₂ and (g,h) [⁶⁸Ga]Ga-DOTA.SA.FAPi. Highest primary tumor uptake in pancreas: (h) [⁶⁸Ga]Ga-DOTA.SA.FAPi PET/CT (SUVmax: 30.84); (f) [⁶⁸Ga]Ga-DOTAGA.(SA.FAPi)₂ (SUVmax: 27.22). Left supraclavicular visible on (e) [⁶⁸Ga]Ga-DOTAGA.(SA.FAPi)₂ and (g) [⁶⁸Ga]Ga-DOTA.SA.FAPi.

In case II, it seems that the DOTA.SA.FAPi monomer performed better than the DOTAGA.(SA.FAPi)₂ dimer. However, the mainstay goal was to design a molecule that can be multifaceted and exploited as a theranostic option for both imaging and treatment. The DOTA.SA.FAPi monomer labeled with ¹⁷⁷Lu though, the uptake in the tumors was instant, the washout from the lesion were rapid and hence was not an ideal agent for therapy. This led to the re-designing of the monomer to dimer with an aim to improve the tumor retention. The dimer DOTAGA.(SA.FAPi)₂ was further labelled with ⁶⁸Ga. Unfortunately, as demonstrated in **Figure 10**, despite the tumor retention, there was also a proportional retention in the normal organs and blood pool. Despite the high blood-pool activity, the DOTAGA.(SA.FAPi)₂ was labeled with ¹⁷⁷Lu, and interestingly a drastically low blood-pool activity was observed with [¹⁷⁷Lu]Lu-DOTAGA.(SA.FAPi)₂. Hence, after several attempts to improvise the biodistribution pattern of [⁶⁸Ga]Ga-DOTAGA.(SA.FAPi)₂ dimer, but due to its inherent drawbacks in terms of high radiation burden to normal organs, and the wide variability in the biodistribution pattern across the patients (**Figure 9** vs. **Figure 10**), the conclusion was that the best approach and the right direction to treat patients is to adopt monomer guided dimer treatment i.e. [⁶⁸Ga]Ga-DOTA.SA.FAPi monomer guided [¹⁷⁷Lu]Lu-DOTAGA.(SA.FAPi)₂ dimer treatment. This current approach has been now adopted routinely at our clinic to treat patients.

Comparison according to the site of malignancy

Though a complete concordance was observed between the tracers in detecting the site of the primary tumor, the intensity of the tracer accumulation in the primary/residual tumor site was highest for [⁶⁸Ga]Ga-DOTAGA.(SA.FAPi)₂. However, there was no significant difference in the median SUL peak (P-0.3488) and average values (P-0.3828) between [⁶⁸Ga]Ga-DOTAGA.(SA.FAPi)₂ and [⁶⁸Ga]Ga-DOTA.SA.FAPi radiotracers (**Table 4**). Similarly, the SUL peak and average values did not differ between [⁶⁸Ga]Ga-DOTAGA.(SA.FAPi)₂ and [¹⁸F]FDG radiotracers.

Table 4 Comparison of lesion SUL values between the radiotracers 1 h p.i. for all six patients (Comparison between variable was done by paired sample t-test), Comparison of SULpeak of metastases and lesions in Table S4.

Radiotracer	SULpeak (mean ± SD, range)	P-value	SULavg (mean ± SD, range)	P-value
[⁶⁸ Ga]Ga-DOTAGA.(SA.FAPi) ₂	12 ± 3.9 (9.5 - 12.5)	0.3488	7.6 ± 2.7 (3.6 - 9.8)	0.3828
[⁶⁸ Ga]Ga-DOTA.SA.FAPi	9.5 ± 3 (5.4 - 14.6)		5.7 ± 3 (2.5 - 8.9)	
[¹⁸ F]FDG	7.8 ± 5.4 (4.2 - 10.9)	0.1535*	4.2 ± 2.9 (2.2 - 8)	0.0619*

*P-values derived by comparing the SUL peak and average values between [⁶⁸Ga]Ga-DOTAGA.(SA.FAPi)₂ and [¹⁸F]FDG.

Conclusion

Here, we reported two novel PET radiopharmaceuticals based on a homodimer system with DOTA and DOTAGA as chelators. Both were conjugated via squaramide to a FAP inhibitor for targeting the tumor microenvironment. Synthesis of the DOTA dimer derivative was faster and easier to realize, however, complexation with gallium-68 was better and more efficient using the DOTAGA derivative. *In vitro* affinity studies showed that the formation of bivalent structures with an additional linker-target vector unit has no negative influence regarding the affinity and inhibition potency towards FAP relative to the monomeric derivatives. As a result, IC₅₀ values in the low nanomolar range were obtained, similar to the IC₅₀ values of the monomeric structures reported earlier [10].

In first clinical investigations, [⁶⁸Ga]Ga-DOTAGA.(SA.FAPi)₂ demonstrated first of all that relative to the monomer, tumor uptake increased at 1 h p.i. time points and secondly, that even at 3 h p.i. the accumulation in tumor tissue increased compared to the 1 h p.i. time point. In our opinion, this verifies the hypothesis that dimeric FAPi derivatives can function as an approach towards increasing tumor stroma residence times. However, [⁶⁸Ga]Ga-DOTAGA.(SA.FAPi)₂ is accompanied by high, delayed, and heterogeneous blood pool uptake across the patients, thereby attributing to a risk of increased radiation dose to the non-target organs. Yet, showing promising pharmaceutical profiles both *in vitro* and *in vivo*, DOTAGA.(SA.FAPi)₂ and related compounds could be a suitable PET imaging probe for diagnostic approaches targeting FAP in the tumor stroma. In future work, our focus is on the performance of [¹⁷⁷Lu]Lu-labeled DOTAGA.(SA.FAPi)₂, which will be investigated *in vivo*.

Abbreviations: DOTAGA: 1:4,7,10-tetraazacyclododecane,1-(glutaric acid)-4,7,10-triacetic acid; IC₅₀: half maximal inhibitory concentration; DATA^{5m}: 2,2'-(6-(4carboxybutyl)-6-((carboxymethyl)(methyl)amino)-1,4-diazepane-1,4-diyl)diacetic acid; PET/CT: positron emission tomography/computed tomography; DTPA: Diethylenetriaminepentaacetic acid; HBED: 2,2'-(1,2-Ethanediybis[(2-hydroxy-benzyl)imino]]-diacetic acid; GRPR: gastrin-releasing peptide receptor; PSMA: prostate specific membrane antigen; HPLC: High pressure liquid chromatography; n.c.a.: non carrier added; TLC: thin layer chromatography; p.i.: post injection; SUL: standardized uptake value (SUV) normalized to lean body mass; RCY: radio chemical yield; FDG: fluorodeoxyglucose; MIP: maximum intensity projection

Supplementary Materials: Figure S1. Analytical HPLC profile of DOTA.(SA.FAPi)₂ [Compound 5], linear gradient condition of 10-90% MeCN (+0.1% TFA)/ 90-10% Water (+0.1% TFA) in 10 min, 1 mL/min.; **Figure S2.** Analytical HPLC profile of DOTAGA.(SA.FAPi)₂ [Compound 12], linear gradient condition of 10-90% MeCN (+0.1% TFA)/ 90-10% Water (+0.1% TFA) in 10 min, 1 mL/min.; **S3.** Methodology for patient studies: Radiolabeling of [⁶⁸Ga]Ga-DOTAGA.(SA.FAPi)₂; Radiochemical purity; Radiolabeling of [⁶⁸Ga]Ga-DOTANOC; **Table S3.1.** Comparison of SUL values among various radiotracers in six patients (The values are given as median and interquartile range (IQR)); **Table S3.2.** Comparison of SUL values of the regions of interest for [⁶⁸Ga]Ga-DOTA.SA.FAPi and [⁶⁸Ga]Ga-DOTAGA.(SA.FAPi)₂ related to the 63-year old female patient (related to Figure 11). **Table S4.** Comparison of SULpeak of metastases and lesions (related to Table 4) for the different radiotracers.

Declarations

Funding: This work was funded by the Fonds Wetenschappelijk Onderzoek Vlaanderen (FWO, Grant 1S64220N), [REDACTED] is a SB PhD fellow at FWO. This project also received funding from the Agentschap Innoveren en Ondernemen (VLAIO HCB 2019. 2446).

Institutional Review Board Statement: Ethical review and approval was obtained for the clinical part of this study: Institute Ethics Committee of All India Institute of Medical Sciences, (IECPG-22/27.02.2020).

Informed Consent Statement: All patients gave their written informed consent IECPG-22/27.02.2020, Institute Ethics committee, All India Institute of Medical Sciences.

References

1. Rawlings, N.D.; Barrett, A.J.; Thomas, P.D.; Huang, X.; Bateman, A.; Finn, R.D. The MEROPS database of proteolytic enzymes, their substrates and inhibitors in 2017 and a comparison with peptidases in the PANTHER database. *Nucleic Acids Res.* **2018**, *46*, D624–D632, doi:10.1093/nar/gkx1134.
2. Jansen, K.; Heirbaut, L.; Verkerk, R.; Cheng, J.D.; Joossens, J.; Cos, P.; Maes, L.; Lambeir, A.M.; De Meester, I.; Augustyns, K.; et al. Extended structure-activity relationship and pharmacokinetic investigation of (4-quinolinoyl)glycyl-2-cyanopyrrolidine inhibitors of fibroblast activation protein (FAP). *J. Med. Chem.* **2014**, *57*, 3053–3074, doi:10.1021/jm500-031w.
3. Loktev, A.; Lindner, T.; Burger, E.M.; Altmann, A.; Giesel, F.; Kratochwil, C.; Debus, J.; Marmé, F.; Jäger, D.; Mier, W.; et al. Development of fibroblast activation protein-targeted radiotracers with improved tumor retention. *J. Nucl. Med.* **2019**, *60*, 1421–1429, doi:10.2967/jnumed.11-8.224469.
4. Kratochwil, C.; Flechsig, P.; Lindner, T.; Abderrahim, L.; Altmann, A.; Mier, W.; Adebeg, S.; Rathke, H.; Röhrich, M.; Winter, H.; et al. ⁶⁸Ga-FAPI PET/CT: Tracer uptake in 28 different kinds of cancer. *J. Nucl. Med.* **2019**, *60*, 801–805, doi:10.2967/jnumed.119.227967.
5. Giesel, F.L.; Kratochwil, C.; Lindner, T.; Marschalek, M.M.; Loktev, A.; Lehnert, W.; Debus, J.; Jäger, D.; Flechsig, P.; Altmann, A.; et al. ⁶⁸Ga-FAPI PET/CT: Biodistribution and preliminary dosimetry estimate of 2 DOTA-containing FAP-targeting agents in patients with various cancers. *J. Nucl. Med.* **2019**, *60*, 386–392, doi:10.2967/jnumed.118.215913.
6. Chen, H.; Pang, Y.; Wu, J.; Zhao, L.; Hao, B.; Wu, J.; Wei, J.; Wu, S.; Zhao, L.; Luo, Z.; et al. Comparison of [⁶⁸Ga]Ga-DOTA-FAPI-04 and [¹⁸F]FDG PET/CT for the diagnosis of primary and metastatic lesions in patients with various types of cancer. *Eur. J. Nucl. Med. Mol. Imaging* **2020**, *47*, 1820–1832, doi:10.1007/s00259-020-04769-z.
7. Chen, H.; Zhao, L.; Ruan, D.; Pang, Y.; Hao, B.; Dai, Y.; Wu, X.; Guo, W.; Fan, C.; Wu, J.; Huang, W.; Lin, Q.; Sun, L.; Wu, H. Usefulness of [⁶⁸Ga]Ga-DOTA-FAPI-04 PET CT in patients presenting with inconclusive [¹⁸F]FDG PET/CT findings. *Eur. J. Nucl. Med. Mol. Imaging* **2021**, *48*, 73–86, doi:10.1007/s00259-020-04940-6.
8. Meyer, C.; Dahlbom, M.; Lindner, T.; Vauclin, S.; Mona, C.; Slavik, R.; Czernin, J.; Haberkorn, U.; Calais, J. Radiation dosimetry and biodistribution of ⁶⁸Ga-FAPI-46 PET imaging in cancer patients. *J. Nucl. Med.* **2020**, *61*, 1171–1177, doi:10.2967/jnumed.119.236786.
9. Syed, M.; Flechsig, P.; Liermann, J.; Windisch, P.; Staudinger, F.; Akbaba, S.; Koerber, S.A.; Freudsperger, C.; Plinkert, P.K.; Debus, J.; et al. Fibroblast activation protein inhibitor (FAPI) PET for diagnostics and advanced targeted radiotherapy in head and neck cancers. *Eur. J. Nucl. Med. Mol. Imaging* **2020**, *47*, 2836–2845, doi:10.1007/s00259-020-04859-y.
10. Moon, E.S.; Elvas, F.; Vliegen, G.; De Lombaerde, S.; Vangestel, C.; De Bruycker, S.; Bracke, A.; Eppard, E.; Greifenstein, G.; Klasen, B.; Kramer, V.; Staelens, S.; De Meester, I.; Van der Veken, P.; Roesch, F. Targeting fibroblast activation protein (FAP): next generation PET radiotracers using squaramide coupled bifunctional DOTA and DATA^{5m} chelators. *EJNMMI Radiopharm. Chem.* **2020**, *5*, 19, doi:10.1186/s41181-020-00102-z.
11. Kreppel, B.; Gärtner, F.; Marinova, M.; Attenberger, U.; Meisenheimer, M.; Toma, M.; Kristiansen, G.; Feldmann, G.; Moon, E.; Roesch, F.; et al. [⁶⁸Ga]Ga-DATA^{5m}.SA .FAPI PET/CT :

Specific Tracer-uptake in Focal Nodular Hyperplasia and potential Role in Liver Tumor Imaging. *Nuklearmedizin* **2020**, *59*, 387–389, doi: 10.1055/a-1164-5667.

12. Ballal, S.; Yadav, M.P.; Moon, E.S.; Kramer, V.S.; Roesch, F.; Kumari, S.; Tripathi, M.; ArunRaj, S.T.; Sarswat, S.; Bal, C. Biodistribution, pharmacokinetics, dosimetry of [⁶⁸Ga]Ga-DOTA.SA.FAPI, and the head-to-head comparison with [¹⁸F]F-FDG PET/CT in patients with various cancers. *Eur. J. Nucl. Med. Mol. Imaging* **2021**, *48*, 1915–1931, doi:10.1007/s00259-020-05132-y.
13. Ballal, S.; Yadav, M.P.; Kramer, V.; Moon, E.S.; Roesch, F.; Tripathi, M.; Mallick, S.; ArunRaj, S.T.; Bal, C. A theranostic approach of [⁶⁸Ga]Ga-DOTA.SA.FAPI PET/CT-guided [¹⁷⁷Lu]Lu-DOTA.SA.FAPI radionuclide therapy in an end-stage breast cancer patient: new frontier in targeted radionuclide therapy. *Eur. J. Nucl. Med. Mol. Imaging* **2021**, *48*, 942–944, doi:10.1007/s00259-020-04990-w.
14. Burchardt, C.; Riss, P.J.; Zoller, F.; Maschauer, S.; Prante, O.; Kuwert, T.; Roesch, F. [⁶⁸Ga]Ga-DO2A-(OBu-I-tyr)₂: Synthesis, ⁶⁸Ga-radiolabeling and in vitro studies of a novel ⁶⁸Ga-DO2A-tyrosine conjugate as potential tumor tracer for PET. *Bioorganic Med. Chem. Lett.* **2009**, *19*, 3498–3501, doi:10.1016/j.bmcl.2009.05.001.
15. Riss, P.J.; Burchardt, C.; Roesch, F. A methodical ⁶⁸Ga-labelling study of DO2A-(butyl-I-tyrosine)₂ with cation-exchanger post-processed ⁶⁸Ga: Practical aspects of radiolabelling. *Contrast Media Mol. Imaging* **2011**, *6*, 492–498, doi:10.1002/cmml.451.
16. Chauhan, K.; Datta, A.; Adhikari, A.; Chuttani, K.; Kumar Singh, A.; Mishra, A.K. ⁶⁸Ga based probe for Alzheimer's disease: Synthesis and preclinical evaluation of homodimeric chalcone in β-amyloid imaging. *Org. Biomol. Chem.* **2014**, *12*, 7328–7337, doi:10.1039/c4ob00941j.
17. Chauhan, K.; Tiwari, A.K.; Chadha, N.; Kaul, A.; Singh, A.K.; Datta, A. Chalcone Based Homodimeric PET Agent, ¹¹C-(Chal)₂DEA-Me, for Beta Amyloid Imaging: Synthesis and Bioevaluation. *Mol. Pharm.* **2018**, *15*, 1515–1525, doi:10.1021/acs.molpharmaceut.7b01070.
18. Liolios, C.; Buchmuller, B.; Bauder-Wüst, U.; Schäfer, M.; Leotta, K.; Haberkorn, U.; Eder, M.; Kopka, K. Monomeric and Dimeric ⁶⁸Ga-Labeled Bombesin Analogues for Positron Emission Tomography (PET) Imaging of Tumors Expressing Gastrin-Releasing Peptide Receptors (GRPrs). *J. Med. Chem.* **2018**, *61*, 2062–2074, doi:10.1021/acs.jmedchem.7b01856.
19. Zia, N.A.; Cullinane, C.; Van Zuylekom, J.K.; Waldeck, K.; McInnes, L.E.; Buncic, G.; Haskali, M.B.; Roselt, P.D.; Hicks, R.J.; Donnelly, P.S. A Bivalent Inhibitor of Prostate Specific Membrane Antigen Radiolabeled with Copper-64 with High Tumor Uptake and Retention. *Angew. Chemie - Int. Ed.* **2019**, *58*, 14991–14994, doi:10.1002/anie.201908964.
20. Eppard, E.; Wuttke, M.; Nicodemus, P.L.; Rösch, F. Ethanol-based post-processing of generator-derived ⁶⁸Ga Toward kit-type preparation of ⁶⁸Ga-radiopharmaceuticals. *J. Nucl. Med.* **2014**, *55*, 1023–1028, doi:10.2967/jnumed.113.133041.
21. De Meester, I.; Vanhoof, G.; Lambeir, A.M.; Scharpé, S. Use of immobilized adenosine deaminase (EC 3.5.4.4) for the rapid purification of native human CD26/dipeptidyl peptidase IV (EC 3.4.14.5). *J. Immunol. Methods* **1996**, *189*, 99–105, doi:10.1016/0022-1759(95)00239-1.
22. Moon, E.S.; Rymenant, Y. Van; Battan, S.; Loose, J. De; Bracke, A.; Van der Veken, P.; De Meester, I.; Rösch, F. In Vitro Evaluation of the Squaramide-Conjugated Fibroblast Activation Protein Inhibitor-Based Agents AAZTA⁵.SA.FAPI and DOTA.SA.FAPI. *Molecules* **2021**, *26*, 3482, doi:10.3390/molecules26123482.

Supporting Information

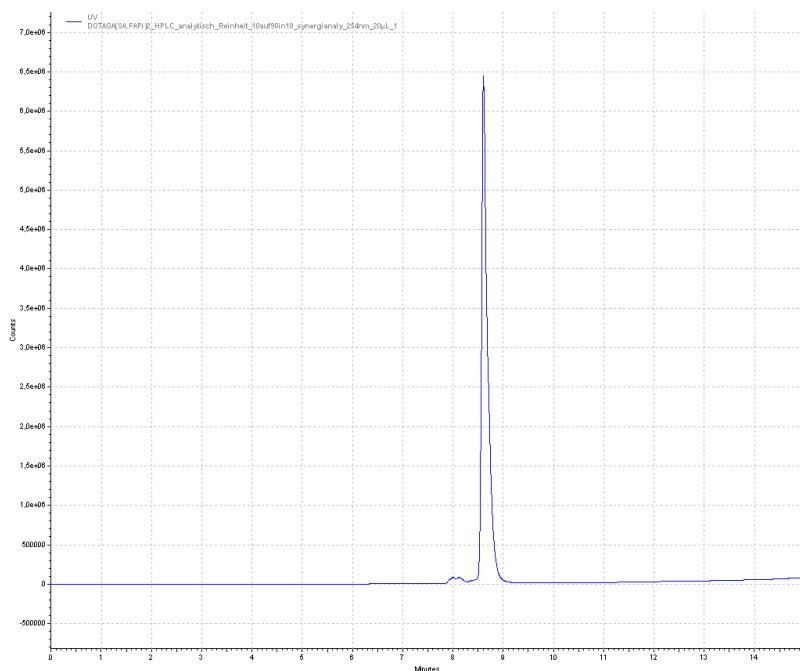


Figure S1 Analytical HPLC profile of DOTA.(SA.FAPi)₂ [Compound 5], linear gradient condition of 10-90% MeCN (+0.1% TFA)/ 90-10% Water (+0.1 % TFA) in 10 min, 1 mL/min.

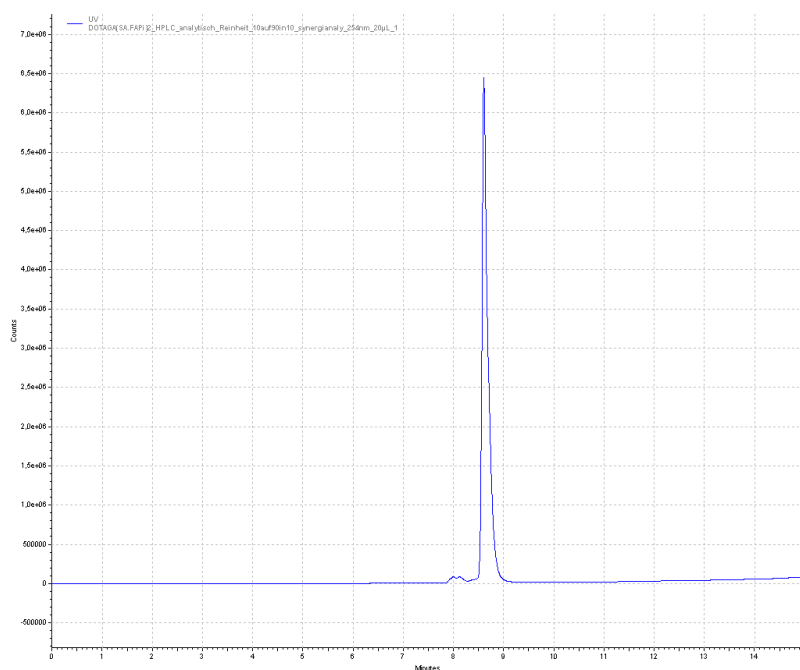


Figure S2 Analytical HPLC profile of DOTAGA.(SA.FAPi)₂ [Compound 12], linear gradient condition of 10-90% MeCN (+0.1% TFA)/ 90-10% Water (+0.1% TFA) in 10 min, 1 mL/min.

S3 Methodology for patient studies:

Radiolabeling of [⁶⁸Ga]Ga-DOTAGA.(SA.FAPi)₂

All the procedures were performed in sterile conditions in a laminar flow to maintain sterility. For the [⁶⁸Ga]Ga-DOTAGA.(SA.FAPi)₂ radiolabeling, the required amount of the buffers such as 1 mL 0.4 M sodium acetate, pH 4 or 0.6–1 mL of 1 M HEPES buffer, pH 5.5 were used. Different ligand-to-radionuclide ratios were investigated across nine batches of radiolabelling to evaluate the most suitable ligand: radionuclide ratio (L:R).

The ⁶⁸GaCl₃ solution (~ 925 MBq) was eluted from the ⁶⁸Ge/⁶⁸Ga-generator (ITG Garching, Germany) using 0.05 M HCl and added to the vial containing the buffer-peptide mixture and incubated at 95 °C for 10 minutes. The light C18 cartridge (Sep-Pak Plus Light C18) required for purification was preconditioned by 5 mL of ethanol followed by air and then rinsed with 10 mL of Ultrapure water. After heating, the radiolabelled product was passed through the pre-conditioned cartridge and purged with air followed by water and air to dryness and the effluent was collected in a waste vial for free ⁶⁸GaCl₃.

The radiolabeled DOTA.SA.FAPi retained in the C18 cartridge was eluted with 1 mL of 50% ethanol. The cartridge was purged with 10 mL of 0.9% saline solution and air to dryness. The preparation was subjected to Millipore filtration prior to the administration to the patient and was delivered as 10 mL solution with the saline. The product was visually checked and pH was determined using the pH paper.

Radiochemical purity

Radiochemical purity (RCP) of [⁶⁸Ga]Ga-DOTAGA.(SA.FAPi)₂ was determined by ITLC after the radiopharmaceutical purification. Sodium citrate buffer (0.1 M), pH 4 was used as mobile phase and Silica gel impregnated aluminium strips (ITLC-SG strips) were used as stationary phase. The developed TLC strip was read in the TLC scanner (Bioscan) to determine the radiochemical purity using proportional counter.

Radiolabeling of [⁶⁸Ga]Ga-DOTANOC

⁶⁸Ga (1,110–1,850 MBq [30–50 mCi]) was eluted from a ⁶⁸Ge/⁶⁸Ga generator (ITG) using 0.1 M HCl. The eluent was loaded on a miniaturized column of organic cation-exchanger STRATA X C column to pre-concentrate (using 80% acetone/0.15 M HCl). The processed ⁶⁸Ga was directly eluted with 97.7% acetone/0.05 M HCl into the reaction vial containing 30–50 mg of DOTANOC. Synthesis was performed at approximately 95 °C for 10–15 min, followed by transferring of product from the reaction vessel on

to the C-18 cartridge. The labelled product from the C-18 cartridge is eluted finally by 70% ethanol and further rinsed with 10 ml normal saline.

Table S3.1 Comparison of SUL values among various radiotracers in six patients (The values are given as median and interquartile range (IQR)).

Organs	SUL _{peak} [⁶⁸ Ga]Ga- DOTAGA. (SA.FAPi) ₂	SUL _{avg} [⁶⁸ Ga]Ga- DOTAGA. (SA.FAPi) ₂	SUL _{peak} [⁶⁸ Ga]Ga- DOTA.SA. FAPi	SUL _{avg} [⁶⁸ Ga]Ga- DOTA.SA. FAPi	SUL _{peak} [¹⁸ F]F-FDG	SUL _{avg} [¹⁸ F]F-FDG
Lacrimal glands	1.275 0.935 - 2.235	0.8 0.460 - 1.300	2.78 1.220 - 4.340	1.505 0.580 - 2.430	5.385 1.930 - 8.840	2.655 1.150 - 4.160
Oral mucosa	1.84 1.710 - 2.005	1.415 1.355 - 1.490	2.185 1.590 - 2.780	1.595 1.360 - 1.830	2.34 1.850 - 2.830	1.6 1.240 - 1.960
Salivary glands	1.745 1.150 - 2.340	1.235 0.780 - 1.690	4.88 4.720 - 5.405	4.015 3.075 - 4.695	1.745 1.290 - 2.200	1.255 0.960 - 1.550
Thyroid	0.81 0.470 - 1.150	0.395 0.210 - 0.580	4.365 3.510 - 5.320	2.21 1.885 - 3.375	1.09 0.890 - 1.290	0.633 0.510 - 0.760
Heart contents /blood pool	7.8 6.680 - 9.025	6.1 5.705 - 7.310	1.19 0.840 - 1.540	0.86 0.640 - 1.080	1.425 1.340 - 1.510	1.145 1.060 - 1.230
Liver	4.535 4.025 - 4.655	3.015 2.620 - 3.120	0.605 0.380 - 0.830	0.3 0.250 - 0.350	2.125 2.060 - 2.190	1.715 1.600 - 1.830
Spleen	5.83 5.805 - 7.345	4.88 4.720 - 5.405	0.885 0.790 - 0.980	0.64 0.590 - 0.690	1.605 1.420 - 1.790	1.275 1.150 - 1.400
Pan-creas	8.38 6.270 - 9.740	5.99 3.800 - 6.975	2.585 2.570 - 2.600	1.85 1.770 - 1.930	1.48 1.430 - 1.530	1.03 0.960 - 1.100
Duo-denum	1.935 1.210 - 2.655	1.285 0.725 - 1.890	1.235 1.100 - 1.370	0.575 0.510 - 0.640	1.15 0.770 - 1.530	0.81 0.460 - 1.160
Kidneys	4.48 4.335 - 5.930	3.815 3.630 - 5.115	3.92 2.000 - 5.840	2.39 1.330 - 3.450	7.445 2.240 - 12.65	4.525 1.740 - 7.310
Psoas Muscle	0.93 0.620 - 1.240	0.905 0.880 - 0.930	1.74 0.960 - 3.235	1.12 0.745 - 1.930	0.66 0.560 - 0.760	0.435 0.300 - 0.570

Bone (L4 vertebrae)	0.525 0.520 - 0.530	0.425 0.410 - 0.440	2.345 1.595 - 2.735	2 1.465 - 2.055	1.215 1.180 - 1.250	0.94 0.870 - 1.010
Femur	0.6 0.590 - 0.610	0.46 0.430 - 0.490	1.105 1.060 - 1.355	0.72 0.620 - 0.985	0.64 0.600 - 0.680	0.495 0.440 - 0.550
Brain normal parenchyma	0.265 0.122 - 0.335	0.205 0.160 - 0.230	0.035 0.020 - 0.050	0.015 0.010 - 0.020	6.22 4.290 - 8.150	4.745 3.220 - 6.270

Table S3.2 Comparison of SUL values of the regions of interest for [⁶⁸Ga]Ga-DOTA.SA.FAPi and [⁶⁸Ga]Ga-DOTAGA.(SA.FAPi)₂ related to the 63-year old female patient (related to Figure 11)

Regions of Interest	[⁶⁸ Ga]Ga-DOTA.SA.FAPi 1 h p.i.		[⁶⁸ Ga]Ga-DOTAGA.(SA.FAPi) ₂ 1 h p.i.		[⁶⁸ Ga]Ga-DOTAGA.(SA.FAPi) ₂ 3 h p.i.	
	SUL _{max}	SUL _{avg}	SUL _{max}	SUL _{avg}	SUL _{max}	SUL _{avg}
Heart contents (blood pool)	1.2	0.9	6.9	5.2	6.3	4.56
Pancreas	2.94	2.5	10.18	8.9	9.3	8
L2 vertebra tumor	10.18	7.44	12.03	9.93	12.69	10.3
Right ischium	8.4	6.7	10.68	8.9	11.66	8.4
Left femur	1.78	1.42	9.08	8.9	9.4	8.5

Table S4 Comparison of SULpeak of metastases and lesions (related to Table 4) for the different radiotracers.

S. No	Site of metastases	[⁶⁸ Ga]Ga-DOTA.SA.FAPi SULpeak	[⁶⁸ Ga]Ga-DOTAGA.(SA.FAPi) ₂ SULpeak	[¹⁸ F]FDG SULpeak	[⁶⁸ Ga]Ga-DOTANOC SULpeak
1	Pelvic bone	6.9	8.6	4.8	NA
2	Iliac bone	5.9	11.6	4.8	NA
3	Neck node	7.6	8.9	5.4	NA
4	Lung mass	3.7	7.7	2.8	NA
5	Neck node	8.6	12.8	1.2	1.6
6	Lumbar vertebra	8.6	12	1.9	3.6

NA: not assessed

C.1. First-in-human results on the Biodistribution, Pharmacokinetics, and Dosimetry of [¹⁷⁷Lu]Lu-DOTA.SA.FAPi and [¹⁷⁷Lu]Lu-DOTAGA.(SA.FAPi)₂ in Patients with Various End-stage Cancers

Eingereicht in *Pharmaceuticals*, **2021**.

Abstract

Purpose: The present study aimed to evaluate and compare the biodistribution, pharmacokinetics, dosimetry of [¹⁷⁷Lu]Lu-DOTA.SA.FAPi, and [¹⁷⁷Lu]Lu-DOTAGA.(SA.FAPi)₂ in patients with various cancers.

Methods: The FAPi agents, [¹⁷⁷Lu]Lu-DOTA.SA.FAPi and [¹⁷⁷Lu]Lu-DOTAGA.(SA.FAPi)₂ were administered in two different groups of patients. Three patients (mean age; 50 years) were treated with a median cumulative activity of 2.96 GBq (IQR: 2.2 – 3 GBq) [¹⁷⁷Lu]Lu-DOTA.SA.FAPi and seven (mean age; 51 years) were treated with 1.48 GBq (IQR: 0.6 – 1.5) of [¹⁷⁷Lu]Lu-DOTAGA.(SA.FAPi)₂. Patients in both the groups underwent serial imaging whole-body planar and SPECT/CT scans that were acquired between 1 hour and 168 hours post-injection (p.i.). The residence time and absorbed dose estimate in the source organs and tumor were calculated using OLINDA/EXM 2.2 software. Time versus activity graphs were plotted to determine the effective half-life (Te) in the whole body and lesions for both the radiotracers.

Results: Physiological uptake of [¹⁷⁷Lu]Lu-DOTA.SA.FAPi was observed in the kidneys, colon, pancreas, liver, gall bladder, oral mucosa, lacrimal glands, and urinary bladder contents. Physiological biodistribution of [¹⁷⁷Lu]Lu-DOTAGA.(SA.FAPi)₂ involved liver, gall bladder, colon, pancreas, kidneys, and urinary bladder contents, lacrimal glands, oral mucosa, and salivary glands. The whole body effective dose for [¹⁷⁷Lu]Lu-DOTAGA.(SA.FAPi)₂ was significantly higher than [¹⁷⁷Lu]Lu-DOTA.SA.FAPi [2.26E-01 ± 1.24E-01; vs. 6.22E-02 ± 9.96E-03 mSv/MBq, P=0.058]. In the [¹⁷⁷Lu]Lu-DOTA.SA.FAPi group, the highest absorbed dose were noted in the Kidneys (0.618 ± 0.015 Gy/GBq), followed by a colon (right colon: 0.472 Gy/GBq and left colon: 0.43 Gy/GBq). In the [¹⁷⁷Lu]Lu-DOTAGA.(SA.FAPi)₂ group, the colon received the highest absorbed dose (right colon: 1.16 Gy/GBq and left colon: 2.87 Gy/GBq), and demonstrated a significantly higher mean absorbed dose than [¹⁷⁷Lu]Lu-DOTA.SA.FAPi (P < 0.011). [¹⁷⁷Lu]Lu-DOTAGA.(SA.FAPi)₂ had significantly longer median whole-body Te compared to that of [¹⁷⁷Lu]Lu-DOTA.SA.FAPi [46.2 h (IQR: 38.5 – 70.1) vs. 23.1 h (IQR: 17.8 – 31.5); P=0.0167]. The median absorbed doses to the lesions were 6.03E-01 (IQR: 2.30E-01 - 1.81E+00) Gy/GBq and 6.70E+00 (IQR: 3.40E+00 – 4.9E+01) Gy/GBq dose per cycle in the [¹⁷⁷Lu]Lu-DOTA.SA.FAPi, and [¹⁷⁷Lu]Lu-DOTAGA.(SA.FAPi)₂ groups, respectively.

Conclusion: The first clinical dosimetry study demonstrated significantly higher tumor absorbed doses with [¹⁷⁷Lu]Lu-DOTAGA.(SA.FAPi)₂ compared to [¹⁷⁷Lu]Lu-DOTA.SA.FAPi. [¹⁷⁷Lu]Lu-DOTAGA.(SA.FAPi)₂ is safe and unveiled new frontiers to treat various end-stage cancer patients with a theranostic approach.

Keywords: [⁶⁸Ga]Ga-DOTA.SA.FAPi PET/CT; [¹⁷⁷Lu]Lu-DOTA.SA.FAPi; [¹⁷⁷Lu]Lu-DOTAGA.(SA.FAPi)₂; Biodistribution; Dosimetry; Pharmacokinetics; absorbed dose estimates, effective half-life

Introduction

The tumor microenvironment (TME) plays a crucial role in tumor remodeling and is an important contributor to tumor growth and promoting drug resistance. Within the TME, cancer-associated fibroblasts (CAFs) have a multifaceted function and are major contributors to TME remodeling. The high abundance of CAFs in a wide range of tumors offers important implications to target various cancers.

The fibroblast activation protein (FAP α), a type II transmembrane serine protease, is highly expressed in CAFs. Histopathologic studies reported the prevalence of FAP-positive cancer-associated fibroblasts in ~90% of epithelial tumors [1]. The ubiquitous expression of fibroblast activation protein (FAP) makes it an interesting target for imaging and therapy of a wide spectrum of malignancies [1]. FAP promotes tumor growth, proliferation, and angiogenesis [2]. Hence, targeting this protein with several probes, including antibodies, immunoconjugates, and small molecular FAP inhibitors, may be an interesting approach for tumor detection and suppression.

Although FAP imaging is in the early developmental stage, several FAP inhibitor based small molecules (chelator-linker-FAP inhibitor conjugates) have been developed. Mostly, heterocyclic linker units between chelator and inhibitor were introduced by piperazine series [3,4] and squaramide based [5–7] FAP-inhibitor precursors, all based on the highly affine and selective inhibitor lead structure UAMC1110 as described by van der Veken's group [8,9] have been developed for diagnostic and therapeutic use (Figure 1).

Haberkorn's group reported a series of piperazine-based FAP-inhibitors labeled with the positron emitter gallium-68, which were successfully used for imaging various cancers [3,4], particularly when utilizing the most prominent molecules among their structures such as FAPI-04, FAPI-21, and FAPI-46 [4].

Roesch's group, in collaboration with our group, introduced a modified ligand keeping the pharmacophore intact as new FAPI PET tracers. The critical subunits constituted the squaramide (SA) linker unit coupled with the DOTA/ DATA^{5m} bifunctional chelators and a FAP inhibitor targeting moiety. Both agents were coupled with generator produced gallium-68 and revealed promising imaging and theranostic benefits on in vitro, preclinical, and clinical studies [5,6]. It is well established now that these FAP inhibitors show expression in various cancers [5–7,10]. The monomeric DOTA.SA.FAPI labelled with gallium-68 showed the most favorable properties from the imaging point of view which includes high tumor-to-background ratios [TBR], and demonstrates a great applicability for theranostic treatment approach of various cancers.

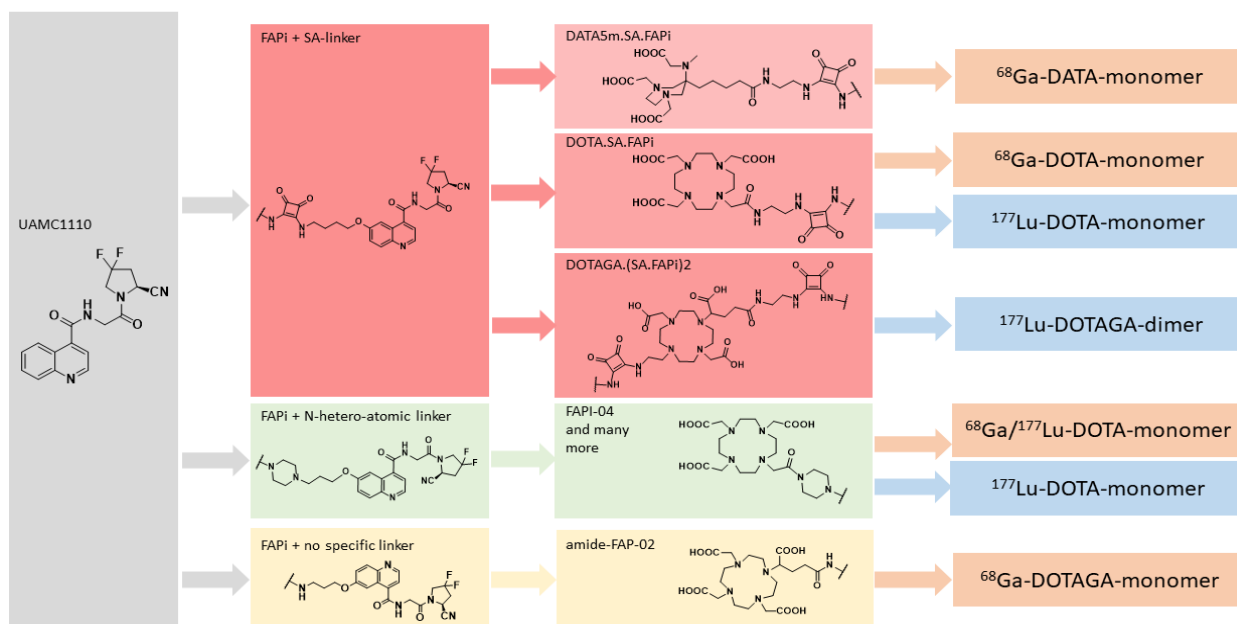


Figure 1: Generations of chelator-linker FAP inhibitor conjugates, a step towards development of FAP-targeted theranostics.

We applied a theranostic approach of [^{68}Ga]Ga guided [^{177}Lu]Lu-DOTA.SA.FAPi therapy in an advanced stage breast cancer (histology status: ER⁻,PR⁻,HER2/neu⁺) patient who failed multiple lines of treatment, and demonstrated a promising improvement in the quality of life. This radio-ligand therapy concept unveiled a new milestone in precision oncology. However, the findings were preliminary, and the detailed pharmacokinetics and dosimetry data were underway [7]. On visual analysis, we noticed early washout of [^{177}Lu]Lu-DOTA.SA.FAPi radiotracer. To overcome this problem, in consultation with our group, Moon et al., [11] modified the structure and introduced dimeric systems for prolonged tumor retention. Using the SA.FAPi monomer as the base, they developed two homodimeric structures such as DOTA(SA.FAPi)₂ and DOTAGA (SA.FAPi)₂ (Figure 1).

The DOTAGA.(SA.FAPi)₂ is based on the monomeric DOTA.SA.FAPi structure, but unlike the monomer, two identical SA.FAPi units are bound to a trifunctional DOTAGA chelator forming a homodimeric system. Additionally, for the possibility of complexing radiometals such as lutetium-177 or actinium-225, at least seven coordination's are required; hence, DOTAGA as chelator was used in the case of the dimer (Figure 1).

Various derivatives were investigated in *in vitro* binding assays to FAP, DPPs (proline-specific enzymes dipeptidyl peptidases), and PREP (prolyl oligopeptidase), and revealed high affinity and protease selectivity to FAP and towards DPPs and PREP (Table 1).

Table 1: IC₅₀ values for FAP and the related serine proteases (PREP, DPP4, DPP8, DPP9). (Data from reference 5 and 11).

Compound	IC ₅₀ (μM)				IC ₅₀ (nM)
	DPP4	DPP8	DPP9	PREP	FAP
DOTAGA.(SA.FAPi) ₂	0.40 ± 0.07	0.42 ± 0.04	0.16 ± 0.02	0.39 ± 0.02	0.92 ± 0.06
[^{nat} Lu]Lu-DOTAGA.(SA.FAPi) ₂	0.63 ± 0.07	0.41 ± 0.03	0.18 ± 0.02	0.56 ± 0.04	1.54 ± 0.15
[^{nat} Ga]Ga-DOTA.SA.FAPi	> 1	N/A	> 1	8.7 ± 0.9	1.4 ± 0.2
[^{nat} Lu]Lu-DOTA.SA.FAPi	> 1	N/A	> 1	2.5 ± 0.4	0.8 ± 0.2

FAP Fibroblast Activation Protein; DPPs Proline-specific enzymes Dipeptidyl Peptidases; PREP Prolyl Oligopeptidase.

It is of interest to know whether in vitro results of homodimers still hold true from the clinical aspect; therefore, the aim of the present study was to compare the in vivo biodistribution, pharmacokinetics, absorbed dose estimates, and effective half-lives of [¹⁷⁷Lu]Lu-DOTA.SA.FAPi monomer and [¹⁷⁷Lu]Lu-DOTAGA.(SA.FAPi)₂ dimer in cancer patients.

Materials and Methods

Patient recruitment

The study was duly approved by the ethics committee of the All India Institute of Medical Sciences, New Delhi. Patients were included for [¹⁷⁷Lu]Lu-DOTA.SA.FAPi or [¹⁷⁷Lu]Lu-DOTAGA.(SA.FAPi)₂ treatment if they had histologically confirmed carcinoma, documented radiological/molecular or biochemical disease progression on previous lines of treatment, and have exhausted all lines of treatments, ECOG status up to 4, cancers that demonstrated high FAPi expression on [⁶⁸Ga]Ga-DOTA.SA.FAPi PET/CT scan (SUVmax > 3), and patients who signed the informed consent form.

Patients who received prior anti-cancer therapy in less than four weeks' time, patients with Hb < 9 g/dL, leukocyte counts less than 4.0 × 10⁹/L, platelet counts less than 75,000 per mL, inadequate liver function parameters, serum creatinine > 1.2 mg/dL were excluded from the study.

The study was first initiated using [¹⁷⁷Lu]Lu-DOTA.SA.FAPi, but after the preliminary qualitative results of serial imaging, we observed low radiotracer retention at about 1 to 2 days p.i. in the target lesions. To improve the radiotracer's retention time, further modifications of the radiopharmaceutical's design led to the development of DOTAGA.(SA.FAPi)₂ homo-dimer.

Pertaining to the time difference in chemical modifications in the molecule, the recruiting time-points in both patient groups were different. A total of 3 patients (mean: 50 ± 17.2 (31 – 63) years, 3 females) were recruited from May 2020 to August 2020 in the [¹⁷⁷Lu]Lu-DOTA.SA.FAPi group. Seven patients (mean: 51 ± 12.7 (26 – 63) years, 4 males and 3 females) were recruited between November 2020 to March 2021 in the [¹⁷⁷Lu]Lu-DOTAGA.(SA.FAPi)₂ group. Dosimetry analysis was conducted, compared, and analyzed between patients treated with [¹⁷⁷Lu]Lu-DOTA.SA.FAPi and [¹⁷⁷Lu]Lu-DOTAGA.(SA.FAPi)₂.

[⁶⁸Ga]Ga-DOTA.SA.FAPi PET/CT imaging

Scans were obtained on a dedicated GE Discovery 710* 128 Slice PET/CT Scanner, with a 40-mm detector at a rotation speed of 0.35 seconds. Whole-body PET/CT scans were acquired 1 hour after the administration of [⁶⁸Ga]Ga-DOTA.SA.FAPi (mean injected activity: 148 MBq). Patients were positioned in a supine position, and an initial scout was acquired, followed by a diagnostic dose CT with 300–350 mAs, 120 kVp, slice thickness 5 mm, and pitch 1 and PET acquisition with 2 minutes per bed.

The images were subjected to dead-time, random, scatter, and decay correction. The PET image reconstruction was performed using an ordered subset expectation maximization algorithm (OSEM) (21 subsets 3 iterations). All images were processed and analyzed on the GE Xeleris workstation.

[¹⁷⁷Lu]Lu-DOTA.SA.FAPi and [¹⁷⁷Lu]Lu-DOTAGA.(SA.FAPi)₂ radiolabelling

25 nmol of [¹⁷⁷Lu]Lu-DOTA.SA.FAPi and DOTAGA.(SA.FAPi)₂ were radiolabelled with [¹⁷⁷Lu]LuCl₃ which was obtained from BRIT, India, in sodium acetate buffer, pH 4, in 0.01 M supra pure HCl. The radiolabelled solution was heated at 95 °C for 30 min. Radiochemical quality control was carried out using the instant thin-layer chromatography method with sodium citrate buffer as the solvent and radiolabelled products with > 90% purity was administered.

Post-therapy [¹⁷⁷Lu]Lu-DOTA.SA.FAPi and [¹⁷⁷Lu]Lu-DOTAGA.(SA.FAPi)₂ whole body scintigraphy

The planar acquisition of whole-body scans was performed using a dual-headed gamma camera (GE, Discovery NM/CT 670). The camera was equipped with a high-energy general-purpose (HEGP) parallel-hole collimator, and the energy peak was centered at 113 keV and 208 keV with a 10% window width.

Dual-energy Scatter corrections were applied at 90 keV and 170 keV with a window width of 10%. Serial whole-body emission scans were performed at 1 (pre-void), 6, 24, 48, and 144 hours (h) after treatment for the [¹⁷⁷Lu]Lu-DOTA.SA.FAPi group and at 1 (pre-void), 4-6, 24, 48, 96, and 144 to 168 h in the [¹⁷⁷Lu]Lu-DOTAGA.(SA.FAPi)₂ group. Simultaneous anterior and posterior emission scans were acquired at a speed of 15 cm/min and a matrix size of 256 x 1024. Delayed images were acquired up to 168 h post-injection to prevent the overestimation of doses.

Similarly, SPECT/CT scans of the abdomen and the lesions were acquired in both the radiotracer groups at serial time points but were mainly used to demarcate the overlapping gut and kidney activity and to calculate the volume of the tumor. SPECT/CT acquisition parameters included a total angular range of 360 degrees, an angle view of 6 degrees, acquired at 25 seconds per view, and a matrix size of 512 x 512.

Image analysis

In the dosimetry analysis, salivary glands, kidneys, pancreas, liver, gall bladder, right colon, left colon, tumor lesions, and whole body were included for dose calculation. The first whole-body image post-injection before voiding was considered to include 100% of injected activity. The region of interests (ROI's) was drawn on the source organs showing uptake of [¹⁷⁷Lu]Lu-DOTA.SA.FAPi and [¹⁷⁷Lu]Lu-DOTAGA.(SA.FAPi)₂ on both anterior (A) and posterior images (P). The ROI of the initial scan was cloned to the subsequent serial time-point images of the patient.

Background counts were obtained from the thigh region. For overlapping organs such as the right kidney had overlapping intestinal uptake, the counts were considered to the left kidney. The corresponding time-point Tx-SPECT/CT scans were also referred to prevent overlap. Background correction of lesion counts was done by subtracting counts in background ROI of the similar area drawn close to the lesions.

Finally, attenuated, background, and scatter corrected percentage injected activity (%IA) in each source organ including salivary glands (parotid and submandibular glands), kidney, liver, gall bladder, pancreas, right and left colon, and the tumor was calculated according to the equation 3.

$$\% IA_{uncorr} = \frac{Ct_{ROI} / pixel}{Ct_{WB} / pixel} \times 100 \quad (1)$$

Where: %IA_{unCorr}: Uncorrected Percentage of injected activity, Ct_{ROI/pixel}: counts/pixel in a region of interest, Ct_{WB/pixel}: counts in the whole-body image

$$\%IA_{Corr} = \frac{Ct_{ROI} / pixel}{Ct_{WB} / pixel} \times DF \times 100 \quad (2)$$

where: %IA_{Corr}: Corrected Percentage of injected activity (Corrected with Decay factor), Ct_{ROI/pixel}: counts/pixel in the region of interest, Ct_{WB/pixel}: counts/pixel in Whole-body image, DF: decay factor (¹⁷⁷Lu- 0.9 for 24 hrs)

Internal dose estimation

The percentage injected activities against time were entered in the kinetic input model of the OLINDA/EXM v2.2 software to calculate the area under the curve that represented the number of disintegrations or residence time or cumulative activity in each source organ. The residence times were input to the ICRP-89 female and male models to derive absorbed doses of organs and whole-body effective doses.

Tumor dosimetry

For the tumor dosimetry, a sphere model implemented within OLINDA/EXM v2.2 was used. For each considered lesion, the volume was evaluated on pre-therapy [⁶⁸Ga]Ga-DOTA.SA.FAPi PET/CT and Tx SPECT-CT of the area of interest using the commercially available workstation (GE Xeleris).

For the estimation of tumor absorbed dose, the dose equation based on the MIRD formalism is expressed below [12,13] (Equation 3).

$$D = \tilde{A} * S = A_0 * \tau * S \quad (3)$$

Here, τ is the residence time, \tilde{A} is the cumulated activity, A_0 is the patient's administered activity, and S is the mean absorbed dose per unit cumulated activity.

Finally, the residence times of source organs and tumors were entered in the adult female or male ICRP 89 model for normal organs and the sphere model, respectively, that derived the organ absorbed doses, effective dose for each organ as per the ICRP 103 model, and whole-body effective dose, in terms of mSv/MBq. The time-activity graphs and effective half-lives (T_e) of various organs and tumors were generated using GraphPad Prism software (v9.1).

Blood dosimetry

Blood dosimetry was conducted in all patients belonging to the [¹⁷⁷Lu]Lu-DOTA.SA.FAPi and was feasible only in three patients in the [¹⁷⁷Lu]Lu-DOTAGA.(SA.FAPi)₂ group. One millilitre of venous blood sample was taken at 0.5 (prevoid), 3.5, 24, 48, 72, 96, 120, 144 and 168 h after injection from each patient. The marrow dose was derived using the method of Sgouros [14].

Safety

Safety was assessed by dosimetry and adverse events assessment according to the National Cancer Institute's Common Toxicity Criteria (NCI-CTCAE) version 5.0.

Statistical analysis

The D'Agostino Pearson test was used to check for the normal distribution of data. Based on the distribution, summary statistics were obtained in terms of mean, median, standard deviation (SD), range, and interquartile range (IQR) were calculated for all continuous variables based on the distribution of data. Mann-Whitney test for independent samples used to compare the organ, tumor absorbed doses, and the T_e between the radiotracers. P-value < 0.05 was considered statistically significant. Statistical analysis was performed with MedCalc statistical software version 12.

Results

Patients

[¹⁷⁷Lu]Lu-DOTA.SA.FAPi and [¹⁷⁷Lu]Lu-DOTAGA.(SA.FAPi)₂ were administered as a therapy after pretherapeutic confirmation of adequate FAP expression (SUV_{max} > 3) of the metastases on [⁶⁸Ga]Ga-DOTA.SA.FAPi-PET/CT. The mean SUV_{max} values and tumor-to-background (pancreas) ratios in both groups were 8.1 ± 0.8 (6.7 – 9), 4 ± 0.5 (3.3 – 4.8), and 10.2 ± 2.1 (7.2 – 14.2), 4.347 ± 1.1 (2.7 – 6.7), respectively (Supplementary Table 1 & Table 2).

The demographics of patients treated with [¹⁷⁷Lu]Lu-DOTA.SA.FAPi and [¹⁷⁷Lu]Lu-DOTAGA.(SA.FAPi)₂ are mentioned in Table 2.

A complete concordance was observed in the FAPi expression of lesions between pre-therapy Dx-^{[68Ga]Ga-DOTA.SA.FAPi} PET/CT and post-therapeutic ^{[177Lu]Lu-DOTA.SA.FAPi/ [177Lu]-DOTAGA.(SA.FAPi)₂} scans (Table 2).

Table 2: Patient demographics

Parameters	^{[177Lu]Lu-DOTA.SA.FAPi}	^{[177Lu]Lu-DOTAGA.(SA.FAPi)₂}
Number of patients	3	7
Age (years) [mean ± SD; range]	50 ± 17.2 (31 – 63)	51 ± 12.7 (26 – 63)
Gender		
Male	0	4
Female	3	3
Type of cancer		
Breast cancer	3	1
Thyroid cancer	0	5
Paraganglioma	0	1
The extent of disease on ^{[68Ga]Ga-DOTA.SA.FAPi} PET/CT scan		
Primary	1	0
Lymph nodes	1	3
Skeletal metastases	3	4
Brain metastases	1	0
Liver metastases	1	1
Lung mass	0	1
Injected activity (GBq; IQR)	2.96 GBq (IQR: 2.2 – 3)	1.48 GBq (IQR: 0.6 – 1.5)

Three breast cancer patients from the ^{[177Lu]Lu-DOTA.SA.FAPi} group (mean age ± SD: 50 ± 17.2 years; range: 31 – 63 years) were injected with a median cumulative activity of 2.96 GBq (IQR: 2.2 – 3 GBq). In the ^{[177Lu]Lu-DOTAGA.(SA.FAPi)₂} group, seven patients (mean age ± SD: 51 ± 12.7 years; range: 26 – 63 years) were injected with a median dosage of 1.48 GBq (IQR: 0.6 – 1.5 GBq) at the first cycle of treatment. While patients in ^{[177Lu]Lu-DOTA.SA.FAPi} group received only one treatment cycle; patients in the ^{[177Lu]Lu-DOTAGA.(SA.FAPi)₂} dimer group received two cycles of treatment at a median interval of 2 months.

Safety

[¹⁷⁷Lu]Lu-DOTA.SA.FAPi and [¹⁷⁷Lu]Lu-DOTAGA.(SA.FAPi)₂ doses were well tolerated. None of the patients experienced any early adverse events after the administration of the agents. One patient with extensive skeletal metastases and pre-existing grade I anaemia experienced grade III and grade I anaemia and thrombocytopenia, respectively. No other grade III/IV toxicities were noted. Table 3 summarizes the median pre-treatment and 6 months post-treatment hematological, kidney, and liver function parameters that showed that both radiotracers were well endured.

Table 3: Comparison of hematological, renal and liver function parameters pre and at median of 6 months post-treatment.

[¹⁷⁷Lu]Lu-DOTA.SA.FAPi group				[¹⁷⁷Lu]Lu-DOTAGA.(SA.FAPi)₂ group		
Parameters	Baseline (Mean, 95% CI of mean)	Post- treatment (Mean, 95% CI of mean)	P value	Baseline (Mean, 95% CI of mean)	Post- treatment (Mean, 95% CI of mean)	P value
Haemoglobin (g/dL)	10.9 (8.9 - 11.7)	11.0 (8.7 - 11.6)	-	10.8 (9.1 - 11.9)	10.1 (6.9 - 11)	0.112
Platelets (lakhs/ μ L)	199 (178 - 201)	199 (188 - 201)	-	225 (156 - 295)	198 (81 - 239)	0.255
Leukocytes 109/L	6500 (5600 -7800)	7700 (6780-7877)	-	6782 (4216 - 9348)	6947 (5239 - 8655)	0.857
Creatinine (mg/dL)	0.8 (0.67 - 0.9)	0.77 (0.7 - 0.9)	-	0.70 (0.17 - 1.2)	0.50 (0.36 - 0.64)	0.385
ALP	212 (168-225)	188 (160 - 234)	-	98.3 (73.4 - 123)	90.5 (70.6 - 110)	0.304

(-): P value cannot be estimated due to low sample size

Biodistribution and pharmacokinetics of normal organs

[¹⁷⁷Lu]Lu-DOTA.SA.FAPi

On qualitative analysis, maximum normal physiological uptake was observed in the kidneys, followed by the colon/large intestines (ascending, transverse, and descending colon). Other organs included the liver, pancreas, gall bladder, oral mucosa, lacrimal gland, and urinary bladder contents. Time-activity curves were derived by either mono or biexponential curve fitting. [¹⁷⁷Lu]Lu-DOTA.SA.FAPi is excreted via both renal excretion and hepatobiliary clearance. A combined wash-in and washout trend of the radiotracer in the kidneys were observed in all patients. The wash-in of radiotracer in the kidneys was

initiated as early as 6 h p.i. and continued up to 144 h after treatment. Pure washout of the trend was observed for lacrimal glands, oral mucosa, liver, and pancreas (Figure 2).

Transit of radiotracer in the gut (ascending and descending colon) was first observed at 24 h post-injection and reached its peak uptake at 48 h. At 144 h p.i. a complete washout of the radiotracer was observed from the gut. Figure 2 shows the $[^{177}\text{Lu}]\text{Lu-DOTA.SA.FAPi}$ serial whole-body scintigraphy images obtained up to 144 h of breast cancer patients with extensive skeletal metastases. The image demonstrates the biodistribution of FAPi in various organs. The graphical representation details the pattern of clearance of $[^{177}\text{Lu}]\text{Lu-DOTA.SA.FAPi}$ from the organs and whole-body, which was predominantly bi-phasic (Figure 2).

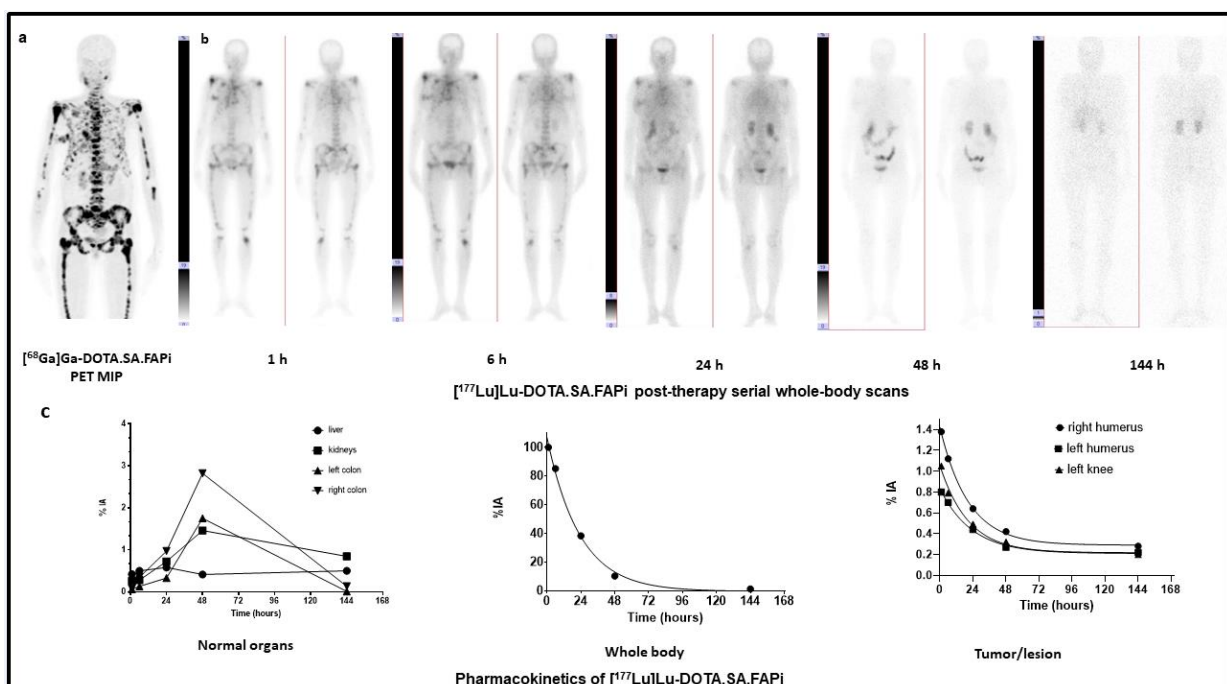


Figure 2: a. $[^{68}\text{Ga}]\text{Ga-DOTA.SA.FAPi}$ PET/CT images of a 49-year-old woman with breast cancer shows biodistribution in the oral mucosa, pancreas, and kidneys and intense expression of DOTA.SA.FAPi in extensive skeletal metastases. b. Serial $[^{177}\text{Lu}]\text{Lu-DOTA.SA.FAPi}$ whole body scintigraphic images for dosimetry, after intravenous injection of 50 mCi of radiotracer, demonstrates normal and minimal biodistribution in the oral mucosa, salivary glands, liver, kidneys and intestines. b. Accumulation in the metastatic sites were observed at 1 and 6 h p.i. and decreased significantly by 24 h p.i., and nearly complete washout by 48 h p.i. c. Time–activity curves for whole body, organs that were easily discernible and metastatic sites generated from region of interest placed on whole-body scintigraphic images.

$[^{177}\text{Lu}]\text{Lu-DOTAGA}(\text{SA.FAPi})_2$

Physiological biodistribution of $[^{177}\text{Lu}]\text{Lu-DOTAGA}(\text{SA.FAPi})_2$ involved liver, gall bladder, large intestines (transverse, ascending, and descending colon), pancreas, kidneys, urinary bladder contents, and to a lesser extent in the lacrimal glands, oral mucosa, salivary glands (Figure 3). Visual analysis

revealed the colon as the organ with the highest FAP uptake. Route of excretion was predominantly via biliary followed by renal excretion. A pure washout trend was observed by the kidneys, and a combined wash-in and washout trend of radiotracer was observed by the biliary route and fitted with bi-exponential curves. Kidney excretion was seen as early as 1 h p.i. continued up to 168 h (Figure 3).

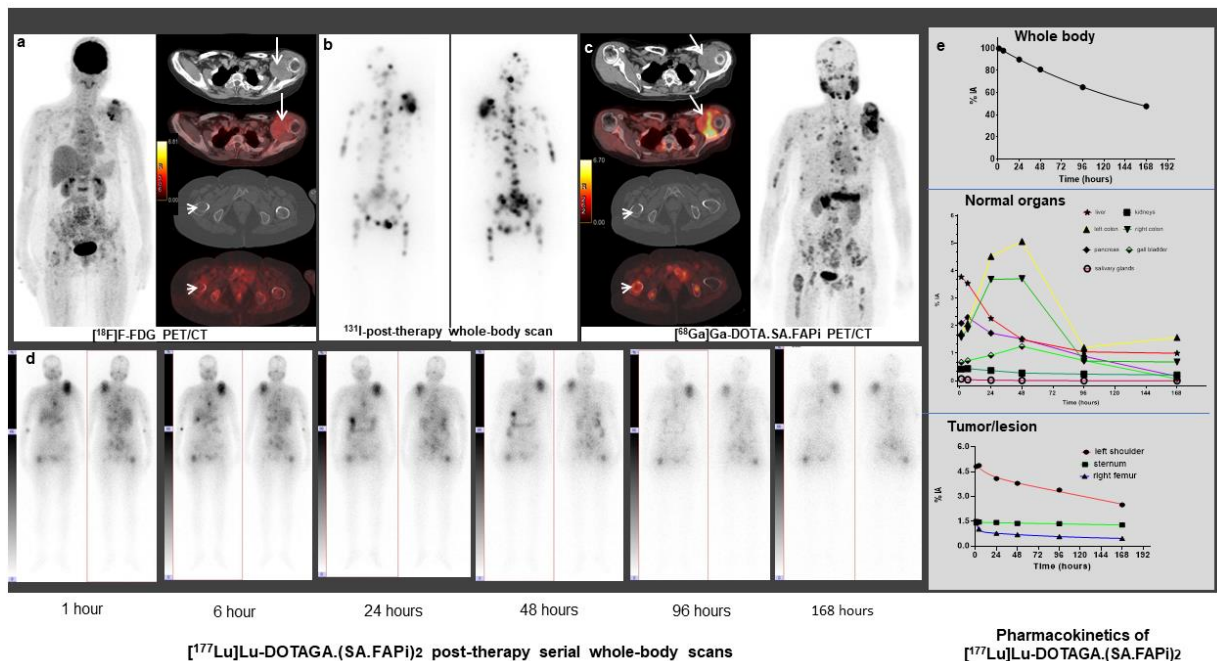


Figure 3: a. $[^{18}\text{F}]\text{F}$ -Fluorodeoxyglucose (FDG) PET/CT images of a 50-year-old woman with follicular variant of papillary carcinoma, post radioiodine therapy (cumulative dose of 22.2 GBq) showing soft tissue density mass in left shoulder (arrows) and multiple skeletal lesions. b. Whole body scintigraphy done after additional 7.4 GBq of radioiodine therapy, showing multiple foci of tracer accumulation suggestive of disease progression and was started on Sorafenib (400 mg OD). c. $[^{68}\text{Ga}]\text{Ga-DOTA.SA.FAPI}$ PET/CT images (done after 6 months of Sorafenib therapy as part of ongoing clinical study when the patient had clinically progressive disease with thyroglobulin 3,00,000 ng/mL) show normal biodistribution in the oral mucosa, salivary glands, liver, pancreas, gall bladder, colon, and kidneys. Intense accumulation of radiotracer in the soft tissue mass (arrows) and multiple skeletal sites (right femur-arrow head). d. Serial $[^{177}\text{Lu}]\text{Lu-DOTAGA}(\text{SA.FAPI})_2$ whole body scintigraphic images for dosimetry, after intravenous injection of 40 mCi of radiotracer, showing radiotracer retention in the metastatic sites till 168-hours delayed images. e. Time–activity curves for whole body, organs that were easily discernible and metastatic sites generated from region of interest placed on whole-body scintigraphic images. Accumulation in the normal organs peaked during the 24-48 hours and decreased significantly by 96 hours post injection. Left shoulder, sternum and right femur shows persistent retention till 168-hour delayed images. Patient received two cycles of $[^{177}\text{Lu}]\text{Lu-DOTAGA}(\text{SA.FAPI})_2$ therapy and showed significant clinical improvement with a decrease of thyroglobulin levels to 27,000 ng/mL. The patient also showed significant decrease in the VASmax score from 10 to 5 in a follow-up of 4.5 months.

Excretion of radiotracer from the hepatobiliary system/liver was initiated 4 h p.i. and rapidly reduced by 50% at 24 h p.i. (5.2% - 1 h p.i. to 2.4% - 24 h p.i.); further reached negligible concentration at 168 h p.i. (1% IA). The radiotracer concentration in the colon was observed at 24 h p.i. (mean %IA: 14%) and showed the maximum uptake at 48 h p.i. (%IA: 17.8%) and washed out to as low as 3% at 168 h post-

infusion. Clearance of gut activity by approximately 7.4-fold was observed between 96 h and 168 h. However, the radiotracer concentration in the gut widely varied among the patients depending on the tumor burden, intestinal motility, and excretion. Patients with a high tumor burden received lower absorbed doses to the colon and kidneys due to the "tumor-sink" effect.

Dosimetry estimate and Te of normal organs

The mean absorbed doses and the whole body effective dose of [¹⁷⁷Lu]Lu-DOTA.SA.FAPi and [¹⁷⁷Lu]Lu-DOTAGA.(SA.FAPi)₂ are mentioned in Table 4. The whole body effective dose for [¹⁷⁷Lu]Lu-DOTAGA.(SA.FAPi)₂ was significantly higher than [¹⁷⁷Lu]Lu-DOTA.SA.FAPi [2.26E-01 ± 1.24E-01; vs. 6.22E-02 ± 9.96E-03 mSv/MBq, P=0.058).

Table 4: Absorbed dose and effective dose estimate of [¹⁷⁷Lu]Lu-DOTA.SA.FAPi and [¹⁷⁷Lu]Lu-DOTAGA.(SA.FAPi)₂.

¹⁷⁷ Lu]Lu-DOTA.SA.FAPi			¹⁷⁷ Lu]Lu-DOTAGA.(SA.FAPi) ₂		
Organ	Mean absorbed doses (mSv/MBq)	ED ICRP-103 (mSv/MBq)	Organ	Mean absorbed doses (mSv/MBq)	ED ICRP-103 (mSv/MBq)
Adrenals	7.79E-03 ± 3.69E-04	7.19E-05 ± 3.42E-06	Adrenals	1.27E-02 ± 4.63E-03	1.19E-04 ± 4.05E-05
Brain	2.06E-05 ± 2.09E-05	2.06E-07 ± 2.09E-07	Brain	1.17E-04 ± 3.93E-05	1.17E-06 ± 3.93E-07
Breasts	4.39E-04 ± 2.64E-04	5.27E-05 ± 3.16E-05	Breasts	6.39E-04 ± 5.30E-05	7.67E-05 ± 6.37E-06
Esophagus	1.80E-03 ± 9.12E-04	7.19E-05 ± 3.65E-05	Esophagus	3.07E-03 ± 6.35E-04	1.23E-04 ± 2.55E-05
Eyes	2.13E-05 ± 2.04E-05	0	Eyes	9.96E-05 ± 4.11E-05	0
Gallbladder Wall	6.06E-03 ± 1.91E-04	5.59E-05 ± 1.80E-06	Gallbladder Wall	7.95E-01 ± 2.58E-01	7.34E-03 ± 2.39E-03
Left colon	4.30E-01 ± 9.40E-02	2.08E-02 ± 4.58E-03	Left colon	2.87E+00 ± 1.74E+00	1.39E-01 ± 8.43E-02
Small Intestine	2.71E-03 ± 1.74E-04	2.50E-05 ± 1.55E-06	Small Intestine	9.24E-03 ± 4.92E-03	8.53E-05 ± 4.53E-05
Stomach Wall	2.03E-03 ± 3.74E-04	2.43E-04 ± 4.48E-05	Stomach Wall	6.62E-03 ± 1.84E-03	7.96E-04 ± 2.23E-04
Right Colon	4.72E-01 ± 3.93E-02	2.29E-02 ± 1.91E-03	Right Colon	1.16E+00 ± 8.58E-01	5.64E-02 ± 4.18E-02
Rectum	5.08E-04 ± 5.31E-05	1.17E-05 ± 1.25E-06	Rectum	2.02E-03 ± 1.04E-03	4.69E-05 ± 2.46E-05
Heart Wall	1.40E-03 ± 1.09E-03	1.29E-05 ± 1.01E-05	Heart Wall	2.57E-03 ± 1.39E-03	2.37E-05 ± 1.28E-05
Kidneys	6.18E-01 ± 1.54E-02	5.70E-03 ± 1.42E-04	Kidneys	3.74E-01 ± 2.57E-01	3.45E-03 ± 2.37E-03
Liver	1.15E-01 ± 9.02E-03	4.61E-03 ± 3.56E-04	Liver	2.09E-01 ± 2.38E-02	8.36E-03 ± 9.57E-04
Lungs	6.10E-02 ± 1.04E-01	7.31E-03 ± 1.2E-02	Lungs	2.21E-03 ± 5.66E-04	2.67E-04 ± 7.03E-05

Ovaries	9.08E-04 ± 7.3E-05	3.63E-05 ± 2.94E-06	Ovaries	2.23E-03 ± 2.50E-04	8.55E-05 ± 1.4E-05
Pancreas	3.69E-03 ± 2.33E-04	3.41E-05 ± 2.16E-06	Pancreas	6.51E-01 ± 1.37E-01	6.01E-03 ± 1.26E-03
Prostate	-	-	Prostate	2.57E-03 ± 1.35E-03	1.19E-05 ± 6.24E-06
Salivary glands	6.56E-05 ± 6.79E-05	6.56E-07 ± 6.79E-07	Salivary glands	1.17E-01 ± 9.53E-03	1.17E-03 ± 9.53E-05
Red Marrow	9.84E-04 ± 2.58E-04	1.18E-04 ± 3.07E-05	Red Marrow	1.73E-02 ± 1.82E-02	2.08E-03 ± 2.18E-03
Osteogenic Cells	1.18E-03 ± 2.89E-04	1.18E-05 ± 2.89E-03	Osteogenic Cells	8.57E-03 ± 6.95E-03	3.33E-04 ± 6.48E-04
Spleen	3.99E-03 ± 2.18E-04	3.68E-05 ± 2.01E-06	Spleen	6.36E-03 ± 1.52E-03	5.87E-05 ± 1.40E-05
Testes	-	-	Testes	1.71E-04 ± 9.97E-05	6.87E-06 ± 3.99E-06
Thymus	1.22E-03 ± 1.49E-03	1.13E-05 ± 1.37E-05	Thymus	1.00E-03 ± 3.09E-04	9.24E-06 ± 2.85E-06
Thyroid	4.53E-04 ± 5.25E-04	1.81E-05 ± 2.10E-05	Thyroid	3.98E-04 ± 8.53E-05	1.59E-05 ± 3.40E-06
Urinary Bladder Wall	4.05E-04 ± 4.12E-05	1.62E-05 ± 1.65E-06	Urinary Bladder Wall	1.28E-03 ± 4.29E-04	5.01E-05 ± 1.73E-05
Uterus	7.84E-04 ± 7.47E-04	3.62E-06 ± 3.44E-07	Uterus	2.18E-03 ± 2.70E-04	9.77E-05 ± 1.58E-05
Total Body	1.10E-02 ± 1.72E-03	0	Total Body	2.33E-02 ± 6.15E-03	0
Effective Dose Equivalent			Effective Dose Equivalent		
Effective Dose		6.22E-02 ± 9.96E-03	Effective Dose		2.26E-01 ± 1.24E-01

All values are mentioned as mean ± SD

In the [¹⁷⁷Lu]Lu-DOTA.SA.FAPi group, the non-target organs with the highest absorbed dose, were noted in kidneys (0.618 ± 0.015 Gy/GBq), followed by a colon (right colon: 0.472 Gy/GBq and left colon: 0.43 Gy/GBq). On the other hand, with [¹⁷⁷Lu]Lu-DOTAGA.(SA.FAPi)₂ colon received the highest absorbed dose right colon: 1.16 Gy/GBq and left colon: 2.87 Gy/GBq and demonstrated a significantly higher mean absorbed dose than [¹⁷⁷Lu]Lu-DOTA.SA.FAPi (P < 0.011). The marrow dose was 9.84E-04 ± 2.58E-04 and 1.73E-02 ± 1.82E-02 Gy/GBq for the [¹⁷⁷Lu]Lu-DOTA.SA.FAPi, and [¹⁷⁷Lu]Lu-DOTAGA.(SA.FAPi)₂ groups, respectively.

Contrary to [¹⁷⁷Lu]Lu-DOTA.SA.FAPi, which showed mono-exponential whole-body clearance, [¹⁷⁷Lu]Lu-DOTAGA.(SA.FAPi)₂ radiotracer followed a bi-exponential clearance. [¹⁷⁷Lu]Lu-DOTAGA.(SA.FAPi)₂ had significantly longer median whole-body T_e compared to that of [¹⁷⁷Lu]Lu-DOTA.SA.FAPi [46.2 h (IQR: 38.5 – 70.1) vs. 23.1 h (IQR: 17.8 – 31.5); P=0.0167].

Tumor pharmacokinetics, effective half-lives, and absorbed dose estimate

The values for the corresponding absorbed doses for various tumor lesions for [¹⁷⁷Lu]Lu-DOTA.SA.FAPi and [¹⁷⁷Lu]Lu-DOTAGA.(SA.FAPi)₂ are presented in Tables 5 & 6. The median masses of the lesions in the [¹⁷⁷Lu]Lu-DOTA.SA.FAPi and [¹⁷⁷Lu]Lu-DOTAGA.(SA.FAPi)₂ groups were similar; 32 grams (IQR:16.8 – 43.3) and 31.7 grams (9.630 - 118.000), P=0.8658, respectively.

Table 5: Effective half-life (T_e) and Dosimetry estimate of tumor lesions with [¹⁷⁷Lu]Lu-DOTA.SA.FAPi.

Patient S.No	Cancer type	Site of lesion	T _e in tumor (hours)	No of disintegrations or Residence time	Mass of lesion (grams)	Absorbed dose mGy/MBq
1.	Right breast cancer	Right breast primary tumor	17	2.44E+00	800	2.52E-01
		Right shoulder skeletal lesion	13.7	3.09E-01	46.1	5.40E-01
2.	B/L breast cancer	Right shoulder skeletal lesion	14	4.30E-01	22	1.57E+00
		Left shoulder skeletal lesion	16	3.54E-01	15	1.89E+00
		Left knee skeletal lesion	14	0.41E-01	15	2.13E+00
3.	Right breast cancer	Ileum	12.6	2.80E -01	32	6.03E-01
		Pubis	12	1.02E-01	35	2.34E-01
Total number of lesions		7				
Median (IQR)			14 (12.8 – 15.5)	3.00E-01 (1.46E-01 - 4.11E-01)	32 (16.8 – 43.3)	6.03E-01 (2.30E-01 – 1.81E+00)

All lesions that showed expression on [⁶⁸Ga]Ga-DOTA.SA.FAPi PET/CT scans were visualized on both [¹⁷⁷Lu]Lu-DOTA.SA.FAPi and [¹⁷⁷Lu]Lu-DOTAGA.(SA.FAPi)₂ post-therapy scans. Uptake in the tumor and metastases was detectable as early as 1 h p.i. for both radiotracers. Interestingly, on qualitative analysis, despite the early and avid uptake of [¹⁷⁷Lu]Lu-DOTA.SA.FAPi in the tumor lesions, a rapid washout was observed with only minimal uptake in the lesion at 24 h and no uptake at 48 h post-treatment. In contrast, there were combined wash-in and washout trends observed in the lesions of [¹⁷⁷Lu]Lu-DOTAGA.(SA.FAPi)₂ group where lesions demonstrated avid uptake even up to 168 h post-treatment. Similar to the clearance pattern from the whole body, a rapid mono-exponential clearance was observed with [¹⁷⁷Lu]Lu-DOTA.SA.FAPi radiotracer compared to the significantly slow and bi-phasic clearance of [¹⁷⁷Lu]Lu-DOTAGA.(SA.FAPi)₂ radiotracer.

In total, all lesions received a median absorbed dose of 6.03E-01 (IQR: 2.30E-01 – 1.81E+00) Gy/GBq in the [¹⁷⁷Lu]Lu-DOTA.SA.FAPi group and patients belonging to the [¹⁷⁷Lu]Lu-DOTAGA.(SA.FAPi)₂ group received a significantly higher absorbed dose of 6.70E+00 (IQR: 3.40E+00 - 4.9E+01) Gy/GBq dose per cycle (Table 5 & 6).

Table 6: Effective half-life (T_e) and Dosimetry estimate of tumor lesions with [¹⁷⁷Lu]Lu-DOTAGA.(SA.FAPi)₂.

Patient S.No	Cancer type	Site of lesion	Te in tumor (hours)	Number of disintegrations or Residence time	Mass of lesion (grams)	Absorbed dose mGy/MBq
1	Radioiodine refractory follicular thyroid cancer	Right ileum skeletal lesion	99	3.37E+00	65.4	4.16E+00
		Femur bone lesion	231	9.80E+00	158	7.99E+00
2	Triple negative breast cancer	Right lung mass	40.7	3.47E+00	50.7	5.51E+00
3	Radioiodine refractory papillary thyroid cancer	Right lung nodule	86.6	6.02E+00	1.5	3.17E+02
4	Radioiodine refractory papillary thyroid cancer	Left shoulder bone lesion	86.62	6.41E+00	189	2.64E+00
		Sternum	89.5	4.47E+00	3.96	8.97E+01
		Right head of femur lesion	48.6	3.97E+00	23.2	1.37E+01
5	Paraganglioma	Skull	27.7	1.82E-01	6.04	2.40E+00
		Anterior rib lesion	27.9	6.48E-01	5.57	9.33E+00
		Posterior rib lesion	23.9	8.51E-01	30	2.28E+00
6	Anaplastic thyroid cancer	Right neck mass	90.2	1.54E+01	250	5.02E+00
7	Medullary thyroid cancer	Liver lesion	115.5	3.51E+01	33.4	8.44E+01
Total number of lesions		N =12				
Median (IQR)			86.6 (34.3 – 94.6)	4.22E+00 (2.11E+00 – 8.10 E+00)	31.7 (5.8 – 111.7)	6.70E+00 (3.40E+00 to 4.9E+01)

The T_e of tumors in both groups reflected the uptake pattern. Unlike $[^{177}\text{Lu}]\text{Lu-DOTA.SA.FAPi}$, a remarkably higher tumor T_e was observed in the patient group treated with $[^{177}\text{Lu}]\text{Lu-DOTAGA.(SA.FAPi)}_2$. (Table 7).

Table 7: Comparison of T_e between $[^{177}\text{Lu}]\text{Lu-DOTA.SA.FAPi}$ and $[^{177}\text{Lu}]\text{Lu-DOTAGA.(SA.FAPi)}_2$ post-therapy scans.

Te	$[^{177}\text{Lu}]\text{-DOTA.SA.FAPi}$	$[^{177}\text{Lu}]\text{Lu-DOTAGA.(SA.FAPi)}_2$	P value
Whole body T_e	N = 3 patients	N = 7 patients	
Median (IQR)	23.1 (17.8 – 31.5)	46.2 (38.5 – 70.1)	0.0167
Tumor T_e			
	N = 7 lesions	N = 12 lesions	
Median (IQR)	14 (12.8 – 15.5)	86.6 (34.3 – 94.6)	0.0004

The absorbed dose to the bone lesions of $[^{177}\text{Lu}]\text{Lu-DOTAGA.(SA.FAPi)}_2$ group was about 5.6-fold higher than that in the $[^{177}\text{Lu}]\text{Lu-DOTA.SA.FAPi}$ group, 6.0750 (2.5200 – 11.5150) Gy/GBq with 8 lesions vs. 1.0865 (0.5400 – 1.8900) Gy/GBq with 6 lesions, P=0.0019). Due to the difference in the type of cancer and the low sample size, the comparison was not possible for other categories of lesions such as primary tumor, lymph nodes, and visceral metastases.

Response assessment

Patients in the $[^{177}\text{Lu}]\text{Lu-DOTA.SA.FAPi}$ group were administered only a single cycle of treatment, hence one hematological and clinical response was assessed. Though patients showed initial response which remained for up to 6 weeks post treatment, they demonstrated relapse in the clinical symptoms. Two patients in this group died.

On the contrary, all patients in the $[^{177}\text{Lu}]\text{Lu-DOTAGA.(SA.FAPi)}_2$ have demonstrated clinical response, have completed a median of 3 cycles of treatment and are alive.

Discussion

The expression of cancer-associated FAP in a broad spectrum of cancers offers an optimal target for various molecular-based FAP inhibitor imaging and therapies [6,7,15]

Based on the synthesis of a potent FAP inhibitor UAMC1110 [8,9], Moon et al. [5] introduced a squaramide linker containing bifunctional DATA^{5m} and DOTA chelators and a FAP targeting moiety abbreviated as DATA^{5m}.SA.FAPi and DOTA.SA.FAPi were labeled with gallium-68. Both show sufficient in vitro affinity in nanomolar IC₅₀ values for FAP and low affinity in μM IC₅₀ ranges for DPPs and PREP. Selectivity to FAP and accordingly towards DPPs and PREP is an important aspect for efficacy targeting FAP. Research on [⁶⁸Ga]Ga-DOTA.SA.FAPi in an HT-29 human colorectal cancer xenograft mouse model revealed excellent in vivo and ex vivo results [5].

Subsequently, we conducted clinical studies comparing [⁶⁸Ga]Ga-DOTA.SA.FAPi with [¹⁸F]F-FDG in various cancers and demonstrated comparable results and complimentary benefits to [¹⁸F]F-FDG PET/CT reporting and demonstrated a scope for [⁶⁸Ga]Ga-DOTA.SA.FAPi guided theranostic approach for the treatment of various cancers [6].

Ballal et al. further carried out a theranostic approach of [⁶⁸Ga]Ga-DOTA.SA.FAPi PET/CT guided [¹⁷⁷Lu]Lu-DOTA.SA.SA.FAPi radionuclide therapy in an ER⁻, PR⁻, Her2neu⁺ end-stage breast cancer patient [7]. Though, visual analysis on PTx-[¹⁷⁷Lu]Lu-DOTA.SA.SA.FAPi whole-body scan demonstrated a high tumor affinity, early washout of the radiotracer, which was completely eliminated by 48 h p.i. which was the major drawback of the molecule. Despite the short-tumor retention time, the patient experienced an improvement in the clinical status.

Among the various FAP targeted molecules, owing to its superior tumor retention and fast clearance from the kidneys, Haberkorn's group [3] evaluated FAPI-04 as a theranostic tool. Preclinical studies in cells expressing human and murine FAP and CD26 resulted in an increased half-life of 3.0 h for [¹⁷⁷Lu]Lu-FAPi-04, versus 1.7 h [¹⁷⁷Lu]Lu-FAPi-02 in the tumor. Further, they attempted a theranostic approach of [⁶⁸Ga]Ga-FAPi-04 guided [⁹⁰Y]Y-FAPi-04 therapy in an end-stage breast cancer patient. Though the tumor absorbed dose for [⁹⁰Y]Y-FAPi-04 was not conclusive; however, the patient experienced a reduction in pain with no significant toxicities [3].

From the reports of previous studies [3,7], it is evident that the main challenge for the potential therapeutic application of the FAP tracers was to optimize its tumor retention time. To design an ideal radiotracer for theranostic use and deliver a maximum radiation dose to the desired target lesions, the biological half-life of the FAPI agent should match the physical half-life of the radiometal.

Small-molecule inhibitors with a shorter-biological half-life could be labelled with shorter physical half-life therapeutic radionuclides such as $^{90}\text{Y}/^{188}\text{Re}/^{213}\text{Bi}$, and similar molecules with longer half-life could be tagged to long-lived therapeutic radionuclides like $^{177}\text{Lu}/^{225}\text{Ac}$, etc.

This problem received substantial interest and an approach to improve tumor affinity as well as tumor retention led to the evolution from monomers to dimeric systems such as DOTA based homodimeric structures [DOTA.(SA.FAPi)₂ and DOTAGA.(SA.FAPi)₂] by Moon et al. [11]. Unlike monomeric precursors, the bifunctional chelator at the centre is linked to two squaramide linker/target vector units. The coupling of squaramide linker-target vector (FAP inhibitor) to dimers significantly increases tumor uptake, tumor retention, and low background. DOTA.(SA.FAPi)₂ and DOTAGA.(SA.FAPi)₂ were synthesized, tested for stability in vitro, and complexed with gallium-68 and lutetium-177. As evident from the reports of Moon et al. [11] the homodimers display very high in vitro affinity for FAP similar to the monomeric structures (similar low nM IC₅₀ values). The use of the DOTAGA chelator for the dimeric version allows to have the same coordination sites as the DOTA monomer structure attributing to the better chelation with heavy radiometals such as lutetium-177, yttrium-90, rhenium-188, actinium-225, bismuth-213, etc. It increases the tumor retention time by several folds. Interestingly, the homodimeric structure had significantly increased tumor uptake and retention with a low background at 24 h p.i. compared to the monomer.

To introduce the homodimers from bench to bedside, the systematic clinical trials focusing on head-to-head comparisons of the homo-dimers addressing the pharmacokinetics in normal organ and tumor lesions are warranted.

Both radiotracers were well tolerated in all patients with minimal toxicities. While the dose-limiting organ with [^{177}Lu]Lu-DOTA.SA.FAPi was the kidney, followed by a colon, the highest estimated absorbed radiation dose by [^{177}Lu]Lu-DOTAGA.(SA.FAPi)₂ dimer was observed in the colon, followed by gall bladder, pancreas, and kidneys.

To achieve a safe limit of 28 Gy [16] to the kidneys, a calculated maximum cumulative activity of 45 GBq [^{177}Lu]Lu-DOTA.SA.FAPi and ~10 GBq [^{177}Lu]Lu-DOTAGA.(SA.FAPi)₂ can be safely administered. A study by Bodei et al. [17] has followed patients post-PRRT in NET patients and revealed that long-term kidney toxicities are minimal. The safe, tolerable limit of [^{177}Lu]Lu-DOTATATE or [^{90}Y]Y-DOTATOC could reach up to 40 Gy in patients who have no prior risks factor, co-morbidities or previous history of impaired kidney function.

Based on the maximum tolerable dose limit of 38 Gy in the colon based on the stereotactic body radiation therapy (SBRT) data [18], patients can be injected with as much as 84 GBq of [^{177}Lu]Lu-DOTA.SA.FAPi and approximately 20 GBq of [^{177}Lu]Lu-DOTAGA.(SA.FAPi)₂. Among our patient series in

the [^{177}Lu]Lu-DOTAGA.(SA.FAPI) $_2$ group, one patient with paraganglioma suffered from constipation with the persistence of activity in the gut even up to 168 h p.i. and hence received a relatively higher absorbed to the colon (Figure 4). The physiological uptake in the gut/intestines varied widely across the patients and was majorly dependent on intestinal motility. Efforts to reduce the risk to the colon and reduce the absorption might be facilitated by suggesting high fatty food to accelerate the washout from the gall bladder and administrating laxatives to accelerate the washout of the radiotracer from the gut may be beneficial. However, the effect of the above methods cannot be deduced from the current study results, and it mandates a proper execution and investigation.

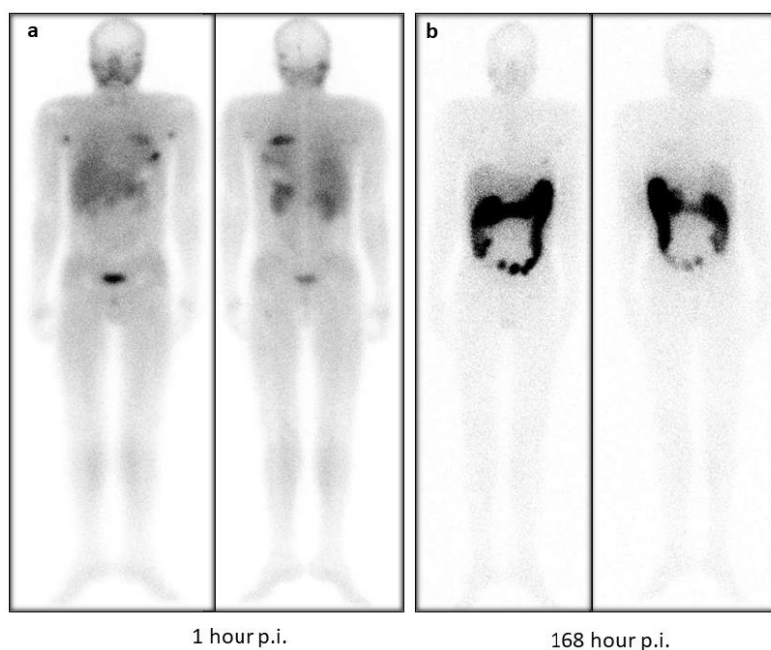


Figure 4: a. A 27-year old male diagnosed with paraganglioma was treated with [^{177}Lu]Lu-DOTAGA.(SA.FAPI) $_2$ treatment and the 1 h scan post-treatment showed (a) normal and minimal biodistribution of radiotracer in the oral mucosa, salivary glands, liver, pancreas, and kidneys. At 1 h p.i. intense accumulation of radiotracer was observed in the skull, and rib lesions. The patient has a history of constipation and hence demonstrated persistent and intense uptake of [^{177}Lu]Lu-DOTAGA.(SA.FAPI) $_2$ radiotracer in the gut due to reduced intestinal motility even at 168 h (b) post-treatment reflecting higher radiation absorbed dose to the colon compared to the other patients such the patient treated in Figure 3.

The whole body effective dose was significantly higher for [^{177}Lu]Lu-DOTAGA.(SA.FAPI) $_2$ group compared to [^{177}Lu]Lu-DOTA.SA.FAPI. A similar pattern of the whole-body effective dose was observed with [^{177}Lu]Lu-EB-PSMA-617 (0.1 mSv/MBq) [19] and [^{177}Lu]Lu-PSMA-ALB-56 (0.2 Gy/GBq) [20] radiotracers that were introduced to improve the pharmacokinetic profile of the PSMA ligands in treating mCRPC patients. The findings go hand-in-hand with the significantly higher tumor effective half-lives in patients treated with [^{177}Lu]Lu-DOTAGA.(SA.FAPI) $_2$. Our median absorbed doses to the tumor lesions was 6.7 Gy/GBq in patients injected with [^{177}Lu]Lu-DOTAGA.(SA.FAPI) $_2$, which was

5.16-folds higher than that deposited by [¹⁷⁷Lu]-DOTA.SA.FAPi (0.67Gy/GBq). Comparable tumor absorbed doses of 6.64 Gy/GBq were obtained by Kramer et al. [20]. The high absorbed doses from [¹⁷⁷Lu]Lu-DOTAGA.(SA.FAPi)₂ were in concordance with the high survival rate of advanced stage disease in our patient cohort.

[¹⁷⁷Lu]Lu-DOTAGA.(SA.FAPi)₂ demonstrates rapid internalization, high tumor uptake, prolonged tumor effective half-life, delivers high radiation dose to the tumors even with lower dosages of lutetium. However, along with providing promisingly high tumor doses, [¹⁷⁷Lu]Lu-DOTAGA.(SA.FAPi)₂ also attributes higher absorbed dose to the whole body, including other organs at risk as to the gall bladder, pancreas, kidneys, and liver.

It should be underlined that the benefit-to-risk ratio should be weighed for each patient taking into account factors such as tumor burden, the bowel emptying time of each patient, history of hepatobiliary obstruction. Additionally, dose fractionation protocols by inducing small doses of [¹⁷⁷Lu]Lu-DOTAGA.(SA.FAPi)₂ per treatment cycle at longer treatment intervals may cover a descent treatment period and at the same time induce tumor regression and provide a window for recovery of vital and clinical toxicities.

Limitations

The current administered activities to patients were arbitrary as no data on the dosimetry estimates were available for any therapeutic FAPi tracer in the literature.

Pertaining to the heterogeneity in the type of cancers and difference in the tumor burdens of the patients between the two radiotracer groups, it is not ideal for conducting a head-to-head comparison. The serial time-point of the acquisition was not uniform due to the differences in the pharmacokinetics between the radiotracers. An inherent drawback of planar dosimetry is the overestimation of dose due to overlap of abdominal organs, but efforts were made to reduce the error by applying appropriate subtraction techniques. The effect of laxatives to promote the early washout of radiotracers and the reduction of radiation burden to the large intestine was out of the scope of this paper.

Future prospects

Based on the current results, we have initiated a dose-escalation study to evaluate the maximum tolerated absorbed dose to critical organs for [¹⁷⁷Lu]Lu-DOTAGA.(SA.FAPi)₂; thereby, we expect to achieve the best objective response and minimal toxicities at an optimal dosage of lutetium-177.

From the molecular perspective, we intend to reconstruct/improvise the molecule further, improve its pharmacokinetics to promote minimum uptake in the non-target organs by reducing the percentage of injected activity to the dose-limiting organs (hepatobiliary and large bowels), and enhancing tumor internalization and greater "tumor-sink" effect.

Conclusion

Compared to [¹⁷⁷Lu]Lu-DOTA.SA.FAPi monomer, [¹⁷⁷Lu]Lu-DOTAGA.(SA.FAPi)₂ homodimer demonstrated longer tumor retention significantly; however, later uptakes in colon and kidneys are higher than the former but are well tolerated. The desired qualities like rapid internalization, higher affinity, longer tumor retention, faster clearance from the non-target organs with [¹⁷⁷Lu]Lu-DOTAGA.(SA.FAPi)₂ unveiled new frontiers for the treatment of various end-stage cancer patients with a theranostic approach.

Declarations

Compliance with Ethical Standards

Ethical Clearance: Ref. No IEC/PG-22/2020 for the clinical use of [⁶⁸Ga]Ga-DOTA.SA.FAPi, and Ref. No. IEC/1054/5/2020 for the clinical use of [¹⁷⁷Lu]Lu-labelled FAPi radiotracers

Funding: None

Conflict of Interest: All the authors included in this manuscript state no conflict of interest.

Availability of data and material: The data and material are available

Informed Consent: Written informed consent was obtained from all patients to participate in the study

Disclaimer: The current work has not been submitted for review or is not under acceptance for publication in any journal.

References

1. Jiang, G.M.; Xu, W.; Du, J.; Zhang, K.S.; Zhang, Q.G.; Wang, X.W.; Liu, Z.G.; et al. The application of the fibroblast activation protein α -targeted immunotherapy strategy. *Oncotarget* **2016**, *7*, 33472–33482, doi:10.18632/oncotarget.8098.
2. Hamson, E.J.; Keane, F.M.; Tholen, S.; Schilling, O.; Gorrell, M.D.; Understanding fibroblast activation protein (FAP): substrates, activities, expression, and targeting for cancer therapy. *Proteomics Clin. Appl.* **2014**, *8*, 454–463, doi:10.1002/prca.201300095.
3. Lindner, T.; Loktev, A.; Altmann, A.; Giesel, F.; Kratochwil, C.; Debus, J.; Jäger, D.; Mier, W.; Haberkorn, U. Development of Quinoline-Based Theranostic Ligands for the Targeting of Fibroblast Activation Protein. *J. Nucl. Med.* **2018**, *59*, 1415–1422, doi:10.2967/jnu-med.118.210443.
4. Loktev, A.; Lindner, T.; Burger, E.M.; Altmann, A.; Giesel, F.; Kratochwil, C.; Debus, J.; Marmé, F.; Jäger, D.; Mier, W.; et al. Development of fibroblast activation protein-targeted radiotracers with improved tumor retention. *J. Nucl. Med.* **2019**, *60*, 1421–1429, doi:10.2967/jnu-med.118.224469.
5. Moon, E.S.; Elvas, F.; Vliegen, G.; De Lombaerde, S.; Vangestel, C.; De Bruycker, S.; Bracke, A.; Eppard, E.; Greifenstein, G.; Klasen, B.; Kramer, V.; Staelens, S.; De Meester, I.; Van der Veken, P.; Roesch, F. Targeting fibroblast activation protein (FAP): next generation PET radiotracers using squaramide coupled bifunctional DOTA and DATA^{5m} chelators. *EJNMMI Radiopharm. Chem.* **2020**, *5*, 19, doi:10.1186/s41181-020-00102-z.
6. Ballal, S.; Yadav, M.P.; Moon, E.S.; Kramer, V.S.; Roesch, F.; Kumari, S.; Tripathi, M.; ArunRaj, S.T.; Sarswat, S.; Bal, C. Biodistribution, pharmacokinetics, dosimetry of [⁶⁸Ga]Ga-DOTA.SA.FAPi, and the head-to-head comparison with [¹⁸F]F-FDG PET/CT in patients with various cancers. *Eur. J. Nucl. Med. Mol. Imaging* **2021**, *48*, 1915–1931, doi:10.1007/s00259-020-05132-y.
7. Ballal, S.; Yadav, M.P.; Kramer, V.; Moon, E.S.; Roesch, F.; Tripathi, M.; Mallick, S.; ArunRaj, S.T.; Bal, C. A theranostic approach of [⁶⁸Ga]Ga-DOTA.SA.FAPi PET/CT-guided [¹⁷⁷Lu]Lu-DOTA.SA.FAPi radionuclide therapy in an end-stage breast cancer patient: new frontier in targeted radionuclide therapy. *Eur. J. Nucl. Med. Mol. Imaging* **2021**, *48*, 942–944, doi:10.1007/s00259-020-04990-w.
8. Jansen, K.; De Winter, H.; Heirbaut, L.; Cheng, J.D.; Joossens, J.; Lambeir, A.M.; De Meester, I.; Augustyns, K.; Van Der Veken, P. Selective inhibitors of fibroblast activation protein (FAP) with a xanthine scaffold. *Medchemcomm* **2014**, *5*, 1700–1707, doi:10.1039/c4md00167b.
9. Jansen, K.; Heirbaut, L.; Verkerk, R.; Cheng, J.D.; Joossens, J.; Cos, P.; Maes, L.; Lambeir, A.M.; De Meester, I.; Augustyns, K.; et al. Extended structure-activity relationship and pharmacokinetic investigation of (4-quinolinoyl)glycyl-2-cyanopyrrolidine inhibitors of fibroblast activation protein (FAP). *J. Med. Chem.* **2014**, *57*, 3053–3074, doi:10.1021/jm500-031w.
10. Kreppel, B.; Gärtner, F.; Marinova, M.; Attenberger, U.; Meisenheimer, M.; Toma, M.; Kristiansen, G.; Feldmann, G.; Moon, E.; Roesch, F.; et al. [⁶⁸Ga]Ga-DOTA^{5m}.SA .FAPi PET/CT : Specific Tracer-uptake in Focal Nodular Hyperplasia and potential Role in Liver Tumor Imaging. *Nuklearmedizin* **2020**, *59*, 387–389, doi: 10.1055/a-1164-5667.
11. Moon, E.S.; Ballal, S.; Yadav, M.P.; Bal, C.; Van Rymentant, Y.; Stephan, S.; Bracke, A.; Van der Veken, P.; De Meester, I.; Roesch, F. Fibroblast Activation Protein (FAP) targeting homodimeric

- FAP inhibitor radiotheranostics: A step to improve tumor uptake and retention time. *AJNMMI* **2021**, accepted.
12. Stabin, M.G. MIRDOSE: personal computer software for internal dose assessment in nuclear medicine. *J. Nucl. Med.* **1996**, *37*, 538–546.
 13. Howard, D.M.; Kearfott, K.J.; Wilderman, S.J.; Dewaraja, Y.K. Comparison of I-131 radioimmunotherapy tumor dosimetry: unit density sphere model versus patient-specific Monte Carlo calculations. *Cancer Biother. Radiopharm.* **2011**, *26*, 615–621, doi:10.1089/cbr.2011.0965.
 14. Sgouros, G. Bone marrow dosimetry for radioimmunotherapy: theoretical considerations. *J. Nucl. Med.* **1993**, *34*, 689–694.
 15. Koustoulidou, S.; Hoorens, M.W.H.; Dalm, S.U.; Mahajan, S.; Debets, R.; Seimbille, Y.; de Jong, M. Cancer-Associated Fibroblasts as Players in Cancer Development and Progression and Their Role in targeted Radionuclide Imaging and Therapy. *Cancers* **2021**, *13*, 1100, doi:10.3390/cancers13051100.
 16. Emami, B.; Lyman, J.; Brown, A.; Goitein, M.; Munzenrider, J.E.; Shank, B.; Solin, L.J.; Wesson, M. Tolerance of normal tissue to therapeutic irradiation. *Int. J. Radiat. Oncol. Biol. Phys.* **1991**, *21*, 109–122, doi:10.1016/0360-3016(91)90171-y.
 17. Bodei, L.; Cremonesi, M.; Ferrari, M.; Pacifici, M.; Grana, C.M.; Bartolomei, M.; Baio, S.M.; Sansovini, M.; Paganelli, G. Long-term evaluation of renal toxicity after peptide receptor radionuclide therapy with ⁹⁰Y-DOTATOC and ¹⁷⁷Lu-DOTATATE: the role of associated risk factors. *Eur. J. Nucl. Med. Mol. Imaging* **2008**, *35*, 1847–1856, doi:10.1007/s00259-008-0778-1.
 18. Grimm, J.; LaCouture, T.; Croce, R.; Yeo, I.; Zhu, Y.; Xue, J. Dose tolerance limits and dose volume histogram evaluation for stereotactic body radiotherapy. *J. Appl. Clin. Med. Phys.* **2011**, *12*, 3368, doi:10.1120/jacmp.v12i2.3368.
 19. Zang, J.; Fan, X.; Wang, H.; Liu, Q.; Wang, J.; Li, H.; Fang, L.; Jacobson, O.; Niu, G.; Zhu, Z.; Chen, X. First-in-human study of ¹⁷⁷Lu-EB-PSMA-617 in patients with metastatic castration-resistant prostate cancer. *Eur. J. Nucl. Med. Mol. Imaging* **2019**, *46*, 148–158, doi:10.1007/s00259-018-4096-y.
 20. Kramer, V.; Fernández, R.; Lehnert, W.; Jiménez-Franco, L.D.; Soza-Ried, C.; Eppard, E.; Matias, C.; Meckel, M.; et al. Biodistribution and dosimetry of a single dose of albumin-binding ligand [¹⁷⁷Lu]Lu-PSMA-ALB-56 in patients with mCRPC. *Eur. J. Nucl. Med. Mol. Imaging* **2021**, *48*, 893–903, doi:10.1007/s00259-020-05022-3.

Supporting Information

Supplementary Table 1: SUVmax of tumor lesions on the baseline [⁶⁸Ga]Ga-DOTA.SA.FAPi PET/CT in the [¹⁷⁷Lu]Lu-DOTA.SA.FAPi group.

Patient S.No	Cancer type	Site of lesion	SUVmax	Tumor-to-pancreas ratio
1.	Right breast cancer	Right breast primary tumor	12.5	4.8
		Right shoulder skeletal lesion	8.7	3.34
2.	B/L breast cancer	Right shoulder skeletal lesion	7.8	3.9
		Left shoulder skeletal lesion	8.8	4.4
		Left knee skeletal lesion	6.7	3.4
3.	Right breast cancer	Ileum	8.1	4
		Pubis	9.08	4.54
Total number of lesions		7		
Mean±SD (Range)			8.1 ± 0.8 (6.7 – 9)	4 ± 0.5 (3.3 – 4.8)

Supplementary Table 2: SUVmax of tumor lesions on the baseline [⁶⁸Ga]Ga-DOTA.SA.FAPi PET/CT in the [¹⁷⁷Lu]Lu-DOTAGA.(SA.FAPi)₂ group.

Patient S.No	Cancer type	Site of lesion	SUVmax	Tumor-to-pancreas ratio
1	Radioiodine refractory follicular thyroid cancer	Right ileum skeletal lesion	10	3.85
		Femur bone lesion	12.8	6
2	Triple negative breast cancer	Right lung mass	11.1	4.6
3	Radioiodine refractory papillary thyroid cancer	Right lung nodule	14.2	6.76
4	Radioiodine refractory papillary thyroid cancer	Left shoulder bone lesion	9.21	4.6
		Sternum	8.9	4.2
		Right head of femur lesion	7.6	3.8
5	Paraganglioma	Skull	12	4.6
		Anterior rib lesion	8.7	3.3
		Posterior rib lesion	7.2	2.7
6	Anaplastic thyroid cancer	Right Neck mass	9.8	3.68
7	Medullary thyroid cancer	Liver lesion	11.8	4.08
Total number of lesions		N = 12		
Mean ± SD (Range)			10.2 ± 2.1 (7.2 – 14.2)	4.347 ± 1.1 (2.7 – 6.7)

C.2. Novel Fibroblast Activation Protein Inhibitor-Based targeted Theranostics for Radioiodine Refractory differentiated Thyroid Cancer Patients: A Pilot Study

Veröffentlicht in *Thyroid*, **2021**.

mit Genehmigung von © Mary Ann Liebert, Inc.

Novel Fibroblast Activation Protein Inhibitor-Based targeted Theranostics for Radioiodine Refractory differentiated Thyroid Cancer Patients: A Pilot Study

[REDACTED] Euy Sung Moon², [REDACTED]
[REDACTED]
[REDACTED]

¹ Department of Nuclear Medicine, All India Institute of Medical Sciences, New Delhi, India

² Department of Chemistry - TRIGA, Johannes Gutenberg University, Mainz, Germany

³ Department of Pathology, All India Institute of Medical Sciences, New Delhi, India

⁴ Department of Medical Oncology, All India Institute of Medical Sciences, New Delhi, India

* These authors contributed equally

Corresponding author: [REDACTED]

Abstract

Background: This exploratory study was to assess clinical and safety data with a novel fibroblast activation protein inhibitor-based targeted theranostics as a salvage treatment option in radioiodine-refractory differentiated thyroid cancer (RR-DTC) patients who had progressed on tyrosine kinase inhibitors (TKI).

Methods: Patients with metastatic RR-DTC who progressed on sorafenib/lenvatinib were prospectively recruited. If [⁶⁸Ga]Ga-DOTA.SA.FAPI PET/CT scan demonstrated moderate-to-excellent uptake in metastases, and patients given informed consents, they received intravenous [¹⁷⁷Lu]Lu-DOTAGA.(SA.FAPI)₂ as therapy at eight-weekly intervals. The primary endpoints were thyroglobulin (Tg) response, and functional imaging response. Secondary endpoints were visual analog score (VAS) and Eastern Cooperative Oncology Group performance status (ECOG). The grading of toxicities was performed using Common Terminology Criteria for Adverse Events (CTCAEV5.0). The sequential images were acquired by a dual-headed gamma camera, and dosimetric calculations were performed using OLINDA/EXM V2.1.

Results: Fifteen patients were recruited [Age: 55 ± 9 years (range: 39 – 67)]. [¹⁷⁷Lu]Lu-DOTAGA.(SA.FAPI)₂ had median whole-body Teff of 88.06 h (IQR: 86.6 - 99). The colon was identified as critical organ. The whole-body effective dose was 1.62E-01 ± 1.53E-02 mSv/MBq. A total of 45 cycles were administered and the median cumulative administered activity was 8.2 ± 2.7 GBq (range 5.5 – 14 GBq). The median absorbed doses to the tumor lesions were 1.08E+01 (IQR: 4.16E+00 to 8.97E+01) mSv/MBq per cycle. The Serum Tg level significantly decreased after treatment [(median Tg: baseline-10549 ng/mL (IQR: 3066.5 to 39450) vs. at the time of assessment: 5649 ng/mL (IQR:939.5 to 17099), P=0.0005)]. Molecular response assessment revealed, no CR, however, PR was documented in 4, and SD in 3 patients. The VASmax scores [pre-therapy: 9 (IQR:8 to 10) vs. follow-up: 6 (3 to 6) (P-0.0001)], and ECOG [3, (IQR: 2 – 3) vs. 2, (IQR: 2 – 3) (P-0.0078)] performance scores significantly improved after treatment. None of the patients experienced grade III/IV hematological, renal or hepatotoxicity.

Conclusion: This preliminary data suggest novel molecule [¹⁷⁷Lu]Lu-DOTAGA.(SA.FAPI)₂ is safe; seems effective, and most importantly opens up a new avenue for the treatment of aggressive RR-DTC patients who have exhausted all standard line of treatments.

Keywords: Radioiodine Refractory differentiated Thyroid Cancer; Fibroblast activation protein inhibitors; [¹⁷⁷Lu]Lu-DOTAGA.(SA.FAPI)₂

Introduction

Radioiodine (RAI) treatment is the mainstay adjuvant treatment option in the management of intermediate and high-risk differentiated thyroid cancer (DTC). However, approximately 5 to 15% of locoregional DTC and 40 – 50% of metastatic DTCs are refractory to RAI treatment [1–3]. It is a well-known fact that radioiodine refractoriness is associated with poor outcome, leading to cancer specific mortality at 5-years of 60% to 70% [4]. Moreover, patients with radioiodine refractory metastatic DTC are associated with the worst outcome with a 10-year survival probability of 10% [5].

In recent years, a better understanding of molecular pathways involved in the tumorigenesis, the dysfunction of Na⁺/I⁻ symporter (NIS) system, and abnormal tyrosine kinase pathways have led to the development of multikinase inhibitors (MKIs). Among the various MKIs, sorafenib based on DECISION trial [6] and lenvatinib based on SELECT trial [7] have been Food and Drug Administration (FDA) approved for the use in RAI-refractory DTC (RR-DTC) patients. Lenvatinib significantly prolonged PFS as compared to placebo group (*18.3 months in Lenvatinib group vs. 3.6 months in the placebo group*). However, 23.9% of patients with skeletal metastases progressed on lenvatinib; overall 75.9% had treatment related adverse events (AE) that were grade III or higher. In either of the scenario's patients cannot further continue MKI treatment and have depleted all lines of treatment.

Apart from the genetic alterations that contribute to the management of aggressiveness of DTC, recent investigations have uncovered the contributions of tumor microenvironment (TME) in the growth and progression of the disease [8]. Cancer associated fibroblasts (CAFs) are the key component of TME, and play a key role in the progression of varieties of human cancers, including abnormally high fibroblast activating proteins (FAPs) expression in thyroid cancer [9–11]. The FAP inhibitors (FAPi), recently developed as small molecule radioligands, both for positron emission tomographic (PET) imaging and as radioligand therapy option are being explored in many cancers. The literature is sparse regarding the use of FAPi radioligand therapies in RR-DTC. A couple of publications in small number of patients have shown that the presence of CAFs in PTC patients were associated with increased frequency of lymph nodal metastases [12]. Sun et al. [13] have reported a strong relationship between the prevalence of BRAF V600E mutation and the high expression of FAP in human PTCs. Authors also revealed the high stromal reactivity was associated with a shorter overall survival. Targeting CAF to treat thyroid cancer with an aim to arrest or interfere the activation of CAFs and thereby inhibit CAF functions is a new strategy in precision oncology.

Recently, several FAP inhibitor molecules such as [⁶⁸Ga]Ga-labelled FAPI-02 [14], -04 [14], -46 [15] and DOTA.SA.FAPi [16,17] have been introduced and are highly promising molecular targets from the

imaging point of view. FAP inhibitors introduced via bifunctional chelate DOTA [18] have been used for imaging in last 3–4 years. Recently, our collaborators from Mainz developed a new concept of FAPi small molecules having a dimeric system (under review). A bifunctional DOTAGA chelator was used to combine two SA.FAPi conjugates. Our group compared and contrasted the pharmacokinetics, absorbed dose estimates to the normal organs, and tumor lesions between [¹⁷⁷Lu]Lu-DOTA.SA.FAPi and [¹⁷⁷Lu]Lu-DOTAGA.(SA.FAPi)₂ and demonstrated significantly higher tumor absorbed doses with the dimer [¹⁷⁷Lu]Lu-DOTAGA.(SA.FAPi)₂, compared to the monomer [¹⁷⁷Lu]Lu-DOTA.SA.FAPi (under review) [19].

Encouraged by the promising dosimetry results and the need for safe and effective treatment strategies in RR-DTC, this pilot study was under taken to share the clinical experience with [¹⁷⁷Lu]Lu-DOTAGA.(SA.FAPi)₂ therapy as a salvage treatment option in advanced stage RR-DTC patients.

Materials and Methods

This prospective study for the treatment of RR-DTC patients with [¹⁷⁷Lu]Lu-DOTAGA.(SA.FAPi)₂ treatment was approved by the ethics committee of All India Institute of Medical Sciences, New Delhi on compassionate grounds in patients who have failed standard treatment options.

Eligibility Criteria

Eligibility criteria for [¹⁷⁷Lu]Lu-DOTAGA.(SA.FAPi)₂ treatment included: >18 years of age, histologically (HPE) confirmed differentiated thyroid cancer, documented radiological/molecular or biochemical disease progression on previous lines of treatment, documented as RR-DTC, ECOG status up to 4, cancers that demonstrated high FAPi expression on [⁶⁸Ga]Ga-DOTA.SA.FAPi PET/CT scan, patients with greater or equal number of lesions that were positive on [⁶⁸Ga]Ga-DOTA.SA.FAPi PET/CT scan compared to the corresponding [¹⁸F]F-FDG PET/CT scan, and patients who signed the informed consent form.

Patients who received prior anti-cancer therapy in less than four weeks' time, pregnant or lactating women, patients with Hb < 9 g/dL, leukocyte counts < 4.0 × 10⁹/L, platelet counts < 75,000 per mL, inadequate liver function parameters, serum creatinine >1.2 mg/dL at the baseline were excluded from the study.

Initially, among 19 patients who underwent [⁶⁸Ga]Ga-DOTA.SA.FAPi and [¹⁸F]F-FDG PET/CT scans, four were excluded, among whom two demonstrated lesser number of lesions on [⁶⁸Ga]Ga-DOTA.SA.FAPi and the remaining two showed mild FAPi expression contrary to the avid uptake on FDG (Figure 1).

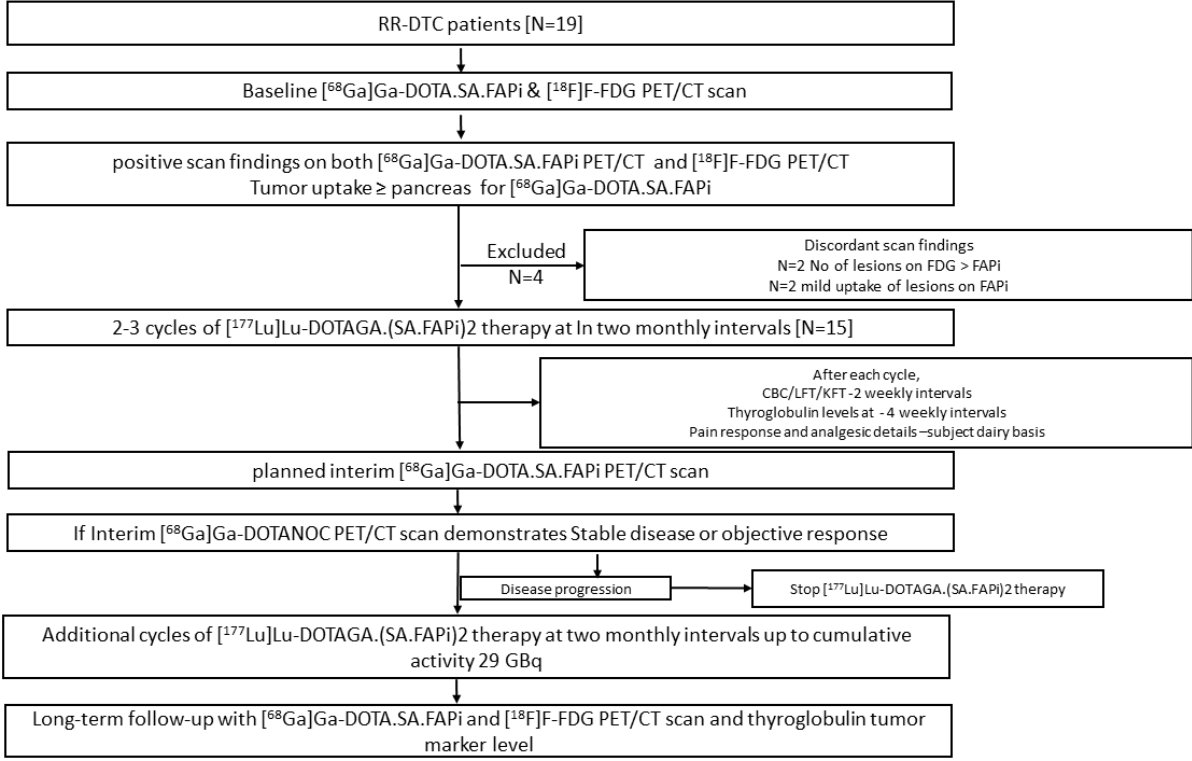


Figure 1: Flow chart depicting the [¹⁷⁷Lu]Lu-DOTAGA.(SA.FAPi)₂ treatment planning and follow-up protocol.

Finally, our analysis included 15 eligible patients with advanced RR-DTC who progressed from multikinase inhibitors, and were treated with [¹⁷⁷Lu]Lu-DOTAGA.(SA.FAPi)₂. Patients were followed-up between October 2020 and September, 4th 2021 with a median follow-up duration of 7.2 (IQR: 6.3 – 8.1) months. Among them three patients participated in the dosimetry study (No. 1, 4, and 7) at their first cycle of [¹⁷⁷Lu]Lu-DOTAGA.(SA.FAPi)₂ treatment.

Definition of RR-DTC

The definition of RR-DTC was adopted as per ATA 2015 Guidelines, namely structural progressive disease according to RECIST1.1 [20], with no further indication for RAI treatment, because of a partial or complete lack of RAI uptake, or evidence of progression despite RAI avidity at the time of treatment or after receiving cumulative RAI activity ≥ 22.2 GBq (600 mCi) [21].

Image Acquisition, Analysis for [¹⁸F]F-FDG and [⁶⁸Ga]Ga-DOTA.SA.FAPi PET/CT

In all patients, baseline [¹⁸F]F-FDG and [⁶⁸Ga]Ga-DOTA.SA.FAPi PET/CT scans were acquired before the initiation of treatment to compare the sites of lesion uptake between both the radiotracers. During follow-up, as solely patients with FAPi findings (number of lesions) \geq FDG at the baseline were treated, only [⁶⁸Ga]Ga-DOTA.SA.FAPi PET/CT scan was performed to minimize frequent unwanted radiation exposure.

Acquisition Protocol

Scans were obtained on a dedicated GE Discovery 710* 128 Slice PET/CT Scanner, with a 40-mm detector at a rotation speed of 0.35 seconds. While, for [¹⁸F]F-FDG PET/CT, patients were advised to fast for at least 4-6 hours prior to injection, no such preparation was required for a [⁶⁸Ga]Ga-DOTA.SA.FAPi scan. The mean injected activities were 251.6 ± 61.42 (range: 118.4 – 333) MBq and 200 ± 74 (range: 111 – 285) MBq, for [¹⁸F]F-FDG, and [⁶⁸Ga]Ga-DOTA.SA.FAPi radiotracers, respectively. The time interval between [⁶⁸Ga]Ga-DOTA.SA.FAPi and [¹⁸F]F-FDG PET/CT scans were no more than 10 days. For the acquisition, an initial scout image followed by CT, and PET scans were acquired at 2 minutes per bed. The diagnostic CT parameters involved, 300–350 mAs, 120 kVp, slice thickness- 5 mm, and a pitch of 1.

Image Analysis

For the head-head comparison, both [¹⁸F]F-FDG and [⁶⁸Ga]Ga-DOTA.SA.FAPi PET/CT scans were loaded simultaneously and co-registered using carina as anatomical landmark registration technique. Scan interpretations was conducted by 2 experienced Nuclear Medicine physicians. Any disagreement in the reports was reviewed by a third observer.

Qualitative analysis

For qualitative interpretations, the visual interpretation method was adopted to compare the concordance or discordance in the uptake between the tracers and compared to the morphological findings on CT. Any disagreement in the findings were reconfirmed either by histopathological correlation or by other imaging modalities. For the ease of analysis, the lesions were interpreted according to four anatomical sites: local disease (primary/residual tumor), nodal metastases, distant metastases (pulmonary, skeletal, liver, brain, etc.), and other metastatic sites.

Quantitative Analysis

Quantitative analysis and comparison were conducted according to the ROI methods prescribed by PERCIST 1 criteria [22]. In brief, both PET/CT scans were linked followed by placing ROIs on normal organs and lesions on [¹⁸F]F-FDG PET/CT scan which was cloned on the [⁶⁸Ga]Ga-DOTA.SA.FAPi PET/CT scan. The values in the respective ROIs were presented as standardized uptake value (SUV) corrected for lean body mass, SULpeak, and SULavg. To compare the uptake in the lesions, a 3D auto contour ROI at a 40% threshold of SULpeak was carefully drawn around the site of [¹⁸F]F-FDG/[⁶⁸Ga]Ga-DOTA.SA.FAPi expressing lesions.

[¹⁷⁷Lu]Lu-DOTAGA.(SA.FAPi)₂ synthesis

DOTAGA.(SA.FAPi)₂ was provided by our collaborators from University of Mainz, Germany. FAPi dimer of 30 μg was radiolabeled [¹⁷⁷Lu]LuCl₃, which was obtained from BRIT, India, in sodium acetate buffer, pH 4, in 0.01 M supra pure HCl. The radiolabeled solution was heated at 95 °C for 30 min. The radiolabeled product of > 90% purity was administered to the patients.

Treatment protocol

The detailed patient recruitment and therapy protocol in the form of flow chart is depicted in figure 1. [¹⁷⁷Lu]Lu-DOTAGA.(SA.FAPi)₂ infusion involved a dilution in 30 mL normal saline (0.9%), which was administered intravenously over 10 min, with subsequent flushing of 10 mL normal saline. The entire process was performed on an in-patient basis, and patients were discharged in a few hours of observation if they did not show any adverse reaction. In the later phases of the study after understanding the biodistribution and pharmacokinetics of the [¹⁷⁷Lu]Lu-DOTAGA.(SA.FAPi)₂ radiotracer, patients were instructed to have high fatty food diet and prescribed laxative syrup for the first 72 hours post-treatment to increase the liver-gallbladder excretion and bowel transit of the radiotracer.

Post-therapy [¹⁷⁷Lu]Lu-DOTAGA.(SA.FAPi)₂ whole body scintigraphy

The whole body and organ dosimetry were performed as per the methodology detailed in the supplementary data. In brief, the planar acquisition of post-therapy whole-body scans (PTx-WBS) were performed using a dual-headed gamma camera (GE, Discovery NM/CT 670). The camera was equipped with a high-energy general-purpose (HEGP) parallel-hole collimator, and the energy peak was centered

at 113 keV and 208 keV with a 10% window width. Serial anterior and posterior PTx-WBS emission scans were performed at 1 (pre-void), 4-6, 24, 48, 96, and 144 to 168 h. p.i., in three patients and in the remaining scans were conducted at 24–48 h p.i.

Similarly, SPECT/CT scans of the abdomen and the lesions were acquired. The SPECT/CT acquisition parameters included a total angular range of 360 degrees, an angle view of 6 degrees, acquired at 25 seconds per view, and a matrix size of 512 X 512.

Tumor Dosimetry

For the tumor dosimetry, a sphere model implemented within OLINDA/EXM v2.1 was used. For each considered lesion, the volume was evaluated on pre-therapy [⁶⁸Ga]Ga-DOTA.SA.FAPi PET/CT and PTx SPECT-CT of the area of interest using the commercially available workstation (GE Xeleris).

For the estimation of tumor absorbed dose, the dose equation based on the MIRD formalism (23, 24) is expressed below.

$$D = \tilde{A} * S = A_0 * \tau * S$$

Here, τ is the residence time, \tilde{A} is the cumulated activity, A_0 is the patient's administered activity, and S is the mean absorbed dose per unit cumulated activity.

Finally, the residence times of source organs and tumors were entered in the adult female or male ICRP 89 model for normal organs and the sphere model, respectively, that derived the organ absorbed doses, effective dose for each organ as per the ICRP 103 model, and whole-body effective dose, in terms of mSv/MBq. The time-activity graphs and effective half-lives (T_e) of various organs and tumors were generated using GraphPad Prism software (v9.1).

Blood dosimetry

Blood dosimetry was feasible only in three patients. One millilitre of venous blood sample was taken at 0.5 (prevoid), 3.5, 24, 48, 72, 96, 120, 144 and 168 h after injection from each patient. The marrow dose was derived using the method of Sgouros [25].

Follow-up

Safety evaluation, based on physical examination and laboratory testing including complete blood counts (CBC), kidney function tests (KFT), liver function tests (LFT), serum thyrotropin-stimulating hormone (TSH), thyroxine (T4), and thyroglobulin (Tg) were determined every month. Patients were suggested to maintain a subject diary to document the pain score and information on adverse event experienced and were reviewed on weekly basis. Interim [⁶⁸Ga]Ga-DOTA.SA.FAPi PET/CT scans were performed 6–8 weeks after the 2 to 3 cycles of [¹⁷⁷Lu]Lu-DOTAGA.(SA.FAPi)₂ therapy and evaluated by a single Nuclear Medicine physician.

Treatment response assessment

The study aimed to evaluate the preliminary efficacy and safety of [¹⁷⁷Lu]Lu-DOTAGA.(SA.FAPi)₂ therapy.

Primary outcome endpoint

The primary outcome endpoint was biochemical and functional imaging response assessment by serum thyroglobulin assay and [⁶⁸Ga]Ga-DOTA.SA.FAPi PET/CT scans.

At the end of analysis on September, 4th 2021, we classified the response of patient based on our clinic set criteria into complete response, partial response, persistent disease and disease progression.

Complete response was defined as negative imaging, and either nsTg <0.1 or sTg <1 ng/ml with negative structural and functional imaging findings. Partial response was defined continuous decreasing levels of nsTg or sTg with or concurrent decrease in the uptake values on PET/CT or structural imaging. Increase in the structural size or appearance of new lesions with rising trend in the nsTg or sTg values was classified as disease progression.

Secondary outcome endpoints

Other clinical response assessment parameters involved visual analog score (VAS) [26], Analgesic score, global pain assessment (GPA) [27], Eastern Cooperative Oncology Group (ECOG) performance status, and adverse event profile. Detailed definitions are mentioned in the supplementary data.

Safety Assessment

Safety was assessed by dosimetry and adverse events graded according to the National Cancer Institute’s Common Terminology Criteria for Adverse Event (NCI-CTCAE) version 5.0. [28].

Statistical Analysis

The data were examined for normality using the D’Agostino–Pearson test. Paired sample t-test (parametric test) or Wilcoxon signed-rank test (nonparametric test) was executed to compare parameters at pre- and post-treatment time points. MedCalc statistical software version 12 was used for statistical analyses. P values ≤ 0.05 were considered significant.

Results

Fifteen RR-DTC patients (4 males and 11 females) with a mean age of 55 ± 9 years (range: 39 – 67) were recruited after demonstrating moderate to high uptake in [^{68}Ga]Ga-DOTA.SA.FAPi PET/CT imaging and all lesions were in consonance and exhibited comparable uptake with [^{18}F]F-FDG PET/CT scans (Table 1). Subsequently patients were administered [^{177}Lu]Lu-DOTAGA.(SA.FAPi)₂ therapy and PTx-WBS also revealed equivalent visual uptake in all the lesions corresponding to the [^{68}Ga]Ga-DOTA.SA.FAPi and [^{18}F]F-FDG PET/CT scans.

Table 1: Comparison of uptake values between baseline [^{68}Ga]Ga-DOTA.SA.FAPi and [^{18}F]F-FDG PET/CT scans

Patient ID	Site of Lesion	[^{68}Ga]Ga-DOTA.SA.FAPi SULpeak	[^{18}F]F-FDG SULpeak
1			
	Right ileum skeletal lesion	10	11.8
	Femur bone lesion	12.8	14.6
2			
	Right lung nodule	3.5	4.6
3			
	Right lung nodule	14.2	16.8
4			
	Lymph node	10	14.2

	Right lung nodule	3.9	2.5
5			
	Left lung nodule	2.58	1.78
6			
	Left iliac bone	13.7	15
7			
	Left shoulder bone lesion	9.21	8.56
	Sternum	8.9	9.87
	Right head of femur lesion	7.6	8.5
8			
	Neck mass	14.8	16.1
9			
	Sternal mass	17.8	20.5
10			
	Femoral lesion	7.8	
11			
	Liver metastases	8.9	7.8
12			
	Left Shoulder	7.9	8.7
13			
	Neck mass	12.9	14.6
14			
	Left Lung nodule	7.6	5.4
15			
	Left femur mass	4.5	5.2

Table 2 summarizes the baseline demographic profile of the patients. All the patients had undergone a minimum of two lines of prior treatments. Out of ten patients who underwent lenvatinib treatment, eight demonstrated disease progression, and two patients discontinued lenvatinib due to treatment-related adverse events. While three (20%) patients were on morphine medications at the baseline, 66.6% (10/15) were either on atypical opioids, non-morphine opioids, or other NSAIDs, and the remaining two patients did not encounter constant pain, and hence, were analgesic naïve.

Table 2: Demographic and clinical details of patients

Patient No	Age/Gender	HPE	Type of RR-DTC	Prior Treatments				Extent of cancer on [⁶⁸ Ga]Ga-DOTA.SA.FAPi PET/CT	Baseline Tg ng/ml
				Surgery	TKI/13-CRA	Pain palliation	Analgesics		
1	67/F	FCT	>22.2 GBq RAI Tx & PD	TT	Sorafenib 400 mg	EBRT	Tramadol	Bone, liver	48900
2	67/M	FVPTC	>22.2 GBq RAI Tx & PD	TT+ B/L MRND	Sorafenib 400 mg, Lenvatinib	EBRT	Tramadol	Remnant, bone, lung	5146
3	58/F	PCT	Mixed RAI uptake	TT+ Lt MRND	Sorafenib, Lenvatinib	No	None	Lymph nodes, lung	3.4
4	62/F	PCT	>22.2 GBq RAI Tx	TT	Sorafenib	No	None	Lymph nodes, lung	19659
5	57/F	FVPTC	RAI negative	TT+B/L MRND	Sorafenib	No	Tramadol	Remnant, lymph nodes, bone, lung	4
6	46/F	FVPTC	>22.2 GBq RAI Tx & PD	TT+ CND	Lenvatinib	EBRT, [¹⁷⁷ Lu]Lu-DOTAZO L	Tramadol	Bone	54690
7	50/F	FVPTC	>22.2 GBq of RAI Tx & PD	TT	Lenvatinib	EBRT	Morphine	Lymph nodes, bone	300000
8	49/M	PCT	Mixed RAI uptake	TT+ CND	Lenvatinib	EBRT	Tramadol	Remnant, lymph nodes, bone, lung, brain, liver	10199
9	58/M	FVPTC	>22.2 GBq of RAI Tx & persistent disease	TT+ B/L MRND	Lenvatinib	EBRT	Tramadol	Bone	10900
10	47/F	PCT	RAI negative	TT+ Rt sub occipital craniotomy with excision of tumor	Lenvatinib	EBRT	Tramadol	Remnant, lymph nodes, bone, lung, liver	335
11	67/F	PCT	RAI negative	TT+ B/L MRND	13-cis-retinoic acid, sorafenib, Lenvatinib	No	Tramadol	Bone, lung, liver	3
12	46/F	PCT	>22.2 GBq RAI Tx & mixed RAI uptake in lesions	TT+ B/L MRND	13-cis-retinoic acid, sorafenib, Lenvatinib	EBRT	Tramadol	Bone	987
13	65/F	FCT	RAI negative	TT	13-cis-retinoic acid, sorafenib, Lenvatinib	EBRT	Morphine	Remnant, lymph nodes, bone, lung	7890
14	39/F	FCT	No RAI concentration	TT+CND+MRND	Sorafenib	No	Tramadol	Lymph nodes, lung, bone	30000
15	50/M	FCT	>22.2 GBq RAI Tx	TT	Sorafenib	EBRT	Morphine	Bone	789

HPE: histopathology; RR-DTC: radioiodine refractory differentiated thyroid cancer; PD: progressive disease; PCT: papillary carcinoma thyroid; FVPTC: Follicular variant papillary carcinoma of thyroid; FCT: follicular carcinoma of thyroid; RAI: radioiodine; Tx: therapy; TT: total thyroidectomy; CND: central neck dissection; MRND: modified radical neck dissection; 13-CRA: 13-cis-retenoic acid; EBRT: external beam radiotherapy.

Before the initiation of [¹⁷⁷Lu]Lu-DOTAGA.(SA.FAPi)₂ treatment, all patients presented with distant metastases with skeletal metastases detected in 86.6% (13/15), lung nodules in 60% (9/15), and liver metastases in 26.6% (4/15).

Prior to treatment, nsTg levels were elevated along with abnormal [¹⁸F]-FDG and [⁶⁸Ga]Ga-DOTA.SA.FAPi PET/CT scan findings in 12 patients. Interestingly, three patients had negligible Tg values (probably Tg “nonsecretor”), but on the contrary, demonstrated extensive disease on the PET/CT scans.

[¹⁷⁷Lu]Lu-DOTAGA.(SA.FAPi)₂ Treatment cycles

A total of 45 cycles were administered in fifteen patients, among whom, nine received three cycles each, three were treated with 4 cycles, and the remaining three received two cycles each. The mean cumulative activity administered was 8.2 ± 2.7 GBq (range 5.5 – 14 GBq) (221.6 ± 75 mCi; range 150 – 378 mCi). (Table 3)

Table 3: [¹⁷⁷Lu]Lu-DOTAGA.(SA.FAPi)₂ treatment details and outcomes

Patient No	Baseline Tg (ng/mL)	No of cycles Of [¹⁷⁷ Lu]Lu-DOTAGA.(SA.FAPi) ₂	Cumulative activity (GBq)	Tg at end of assessment (ng/mL)	Response on [⁶⁸ Ga]Ga-DOTA.SA.FAPi PET/CT	VASmax (baseline)	VASmax (end of assessment)	Base line AS	Post -Tx AS	Survival since [¹⁷⁷ Lu]Lu-DOTAGA.(SA.FAPi) ₂ (months)
1	48900	4	11.1	35152	PR	10	1	9	6	11
2	5146	3	7.8	4986	NA	9	6	9	9	9 (discontinued treatment)
3	3.4	2	6.6	2.3	NA (clinically PD)	5	2	0	0	9 (discontinued treatment)
4	19659	3	10.3	17658	NA	4	0	0	0	9
5	4	3	6.6	3.2	PR	8	7	6	3	8
6	54952	3	7.8	16540	SD	9	6	9	3	8.2
7	300000	4	10.3	6312	PR	10	3	20	6	6.5
8	10199	4	13	3700	PR	9	2	6	0	7
9	10900	3	10.4	6321	SD	8	5	9	6	6.3
10	335	3	6.6	192	NA	9	6	3	3	7.2
11	3	3	6.4	1	SD	9	4	6	0	7.2
12	987	3	6.6	878	NA	10	6	9	9	7.2
13	7890	3	6.3	1001	NA	10	6	16	0	7.2
14	30000	2	6	24897	NA	10	8	6	3	2.5
15	789	2	6	678	NA	8	7	20	16	2.5

Tg: thyroglobulin; AS: analgesic score; PR: partial response; SD: stable disease; NA: not assessed; Tx: therapy; PD; progressive disease.

Organ and Tumor Dosimetry

The mean organ and the tumor absorbed doses are enumerated in Table 4 & 5.

Table 4: Absorbed dose and effective dose estimate of [¹⁷⁷Lu]Lu-DOTAGA.(SA.FAPi)₂

[¹⁷⁷Lu]Lu-DOTAGA.(SA.FAPi)₂		
Organ	Mean absorbed doses (mSv/MBq)	ED ICRP-103 (mSv/MBq)
Adrenals	9.47E-03 ± 3.35E-03	9.03E-05 ± 2.75E-05
Brain	1.31E-04 ± 4.58E-05	1.31E-06 ± 4.58E-07
Breasts	6.40E-04 ± 6.49E-05	7.68E-05 ± 7.80E-06
Esophagus	2.75E-03 ± 3.63E-04	1.10E-04 ± 1.48E-05
Eyes	1.22E-04 ± 4.58E-05	0
Gallbladder Wall	7.09E-01 ± 1.12E-01	6.55E-03 ± 1.04E-03
Left colon	1.97E+00 ± 1.68E-01	9.56E-02 ± 8.19E-03
Small Intestine	6.66E-03 ± 8.19E-04	6.15E-05 ± 7.58E-06
Stomach Wall	5.44E-03 ± 5.39E-04	6.53E-04 ± 6.47E-05
Right Colon	7.56E-01 ± 1.15E-01	3.66E-02 ± 5.62E-03
Rectum	1.50E-03 ± 7.57E-05	3.46E-05 ± 1.84E-06
Heart Wall	1.72E-03 ± 2.03E-04	1.59E-05 ± 1.86E-06
Kidneys	3.02E-01 ± 2.86E-01	2.79E-03 ± 2.64E-03
Liver	2.11E-01 ± 3.24E-02	8.43E-03 ± 1.30E-03
Lungs	1.92E-03 ± 2.43E-04	2.31E-04 ± 2.89E-05
Ovaries	2.14E-03 ± 2.03E-04	8.54E-05 ± 8.27E-06
Pancreas	7.20E-01 ± 6.41E-02	6.64E-03 ± 5.86E-04
Salivary glands	1.11E-01 ± 2.52E-03	6.15E-05 ± 7.58E-06
Red Marrow	2.64E-02 ± 2.12E-02	3.18E-03 ± 2.55E-03
Osteogenic Cells	1.14E-02 ± 7.78E-03	6.09E-04 ± 9.04E-04
Spleen	5.73E-03 ± 1.58E-03	5.29E-05 ± 1.46E-05
Thymus	8.40E-04 ± 7.37E-05	7.75E-06 ± 6.82E-07
Thyroid	3.60E-04 ± 1.41E-05	1.44E-05 ± 5.51E-07
Urinary Bladder Wall	1.13E-03 ± 9.87E-05	1.42E+05 ± 2.45E+05
Uterus	2.07E-03 ± 2.00E-04	9.57E-06 ± 8.97E-07
Total Body	2.05E-02 ± 2.81E-03	0
Effective Dose		1.62E-01 ± 1.53E-02

All values are mentioned as mean ± SD

Table 5: Effective half-life (T_e) and Dosimetry estimate of tumor lesions with [^{177}Lu]Lu-DOTAGA.(SA.FAPi)₂

Patient S.No	Cancer type	Site of lesion	T_e in tumor (hours)	Number of disintegrations or Residence time	Mass of lesion (grams)	Absorbed dose mSv/MBq
1	Radioiodine refractory follicular thyroid cancer	Right ileum skeletal lesion	99	3.37E+00	65.4	4.16E+00
		Femur bone lesion	231	9.80E+00	158	7.99E+00
4	Radioiodine refractory papillary thyroid cancer	Right lung nodule	86.6	6.02E+00	1.5	3.17E+02
7	Radioiodine refractory papillary thyroid cancer	Left shoulder bone lesion	86.62	6.41E+00	189	2.64E+00
		Sternum	89.5	4.47E+00	3.96	8.97E+01
		Right head of femur lesion	48.6	3.97E+00	23.2	1.37E+01
Total number of lesions		N = 6				
Median (IQR)			88.06 (86.6 - 99)	5.25E+00 (3.97E+00 – 6.41E+00)	44.3 (3.960 – 158)	1.08E+01 (4.16E+00 to 8.97E+01)

Physiological biodistribution of [^{177}Lu]Lu-DOTAGA.(SA.FAPi)₂ involved liver, gall bladder, colon, pancreas, kidneys, and urinary bladder contents, lacrimal glands, oral mucosa, and salivary glands (Figure 2 & 3). The whole body effective dose for [^{177}Lu]Lu-DOTAGA.(SA.FAPi)₂ was $1.62\text{E-}01 \pm 1.53\text{E-}02$. The highest organ radiation dose was observed for colon (left colon: $1.97\text{E+}00 \pm 1.68\text{E-}01$ mSv/MBq, and right colon: $7.56\text{E-}01 \pm 1.15\text{E-}01$ mSv/MBq). Pancreas, gall bladder, kidneys, liver, and salivary glands received $7.20\text{E-}01 \pm 6.41\text{E-}02$ mSv/MBq, $7.09\text{E-}01 \pm 1.12\text{E-}01$ mSv/MBq, $3.02\text{E-}01 \pm 2.86\text{E-}01$ mSv/MBq, $2.11\text{E-}01 \pm 3.24\text{E-}02$ mSv/MBq, and $1.11\text{E-}01 \pm 2.52\text{E-}03$ mSv/MBq, respectively. [^{177}Lu]Lu-DOTAGA.(SA.FAPi)₂ had remarkably long/adequate median whole-body T_e 88.06 h (IQR: 86.6 – 99). The median absorbed doses to the tumor lesions were $1.08\text{E+}01$ (IQR: $4.16\text{E+}00$ to $8.97\text{E+}01$) mSv/MBq per cycle.

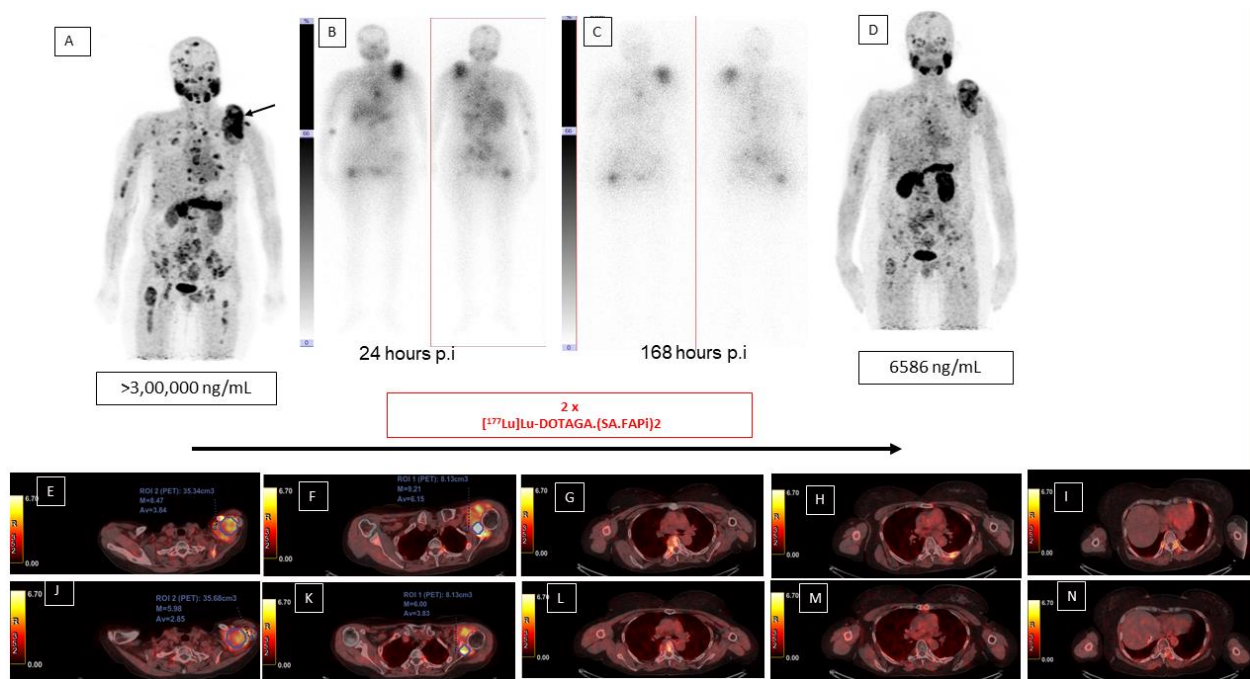


Figure 2: A 50-year-old woman with follicular variant of papillary carcinoma failed radioiodine therapy, Soranib and Lenvatinib. Patient had clinically progressive disease with thyroglobulin > 3,00,000 ng/mL. Baseline $[^{68}\text{Ga}]\text{Ga-DOTA.SA.FAPi}$ PET/CT MIP image (A), shows normal biodistribution in the oral mucosa, salivary glands, liver, pancreas, gall bladder, colon, and kidneys. Intense accumulation of radiotracer was in the soft tissue mass (black arrow) and multiple skeletal sites (A). Serial $[^{177}\text{Lu}]\text{Lu-DOTAGA}(\text{SA.FAPi})_2$ whole body scintigraphic images for dosimetry, after intravenous injection of 40 mCi of radiotracer, showed radiotracer retention in the metastatic sites till 168-hours delayed images (B, C). Patient received two cycles of $[^{177}\text{Lu}]\text{Lu-DOTAGA}(\text{SA.FAPi})_2$ therapy and showed significant clinical improvement with a decrease of thyroglobulin levels to 6586 ng/mL. The patient also showed significant decrease in the VASmax score from 10 to 4 in a follow-up of 9 months. The follow-up MIP $[^{68}\text{Ga}]\text{Ga-DOTA.SA.FAPi}$ PET/CT images (D), and fused axial images demonstrate the reduction in the SUVmax values after treatment (E, F vs. J, K). A Remarkable decrease in the FAPI expression was observed in all the lesions after treatment (A vs. D, and E-I vs. J-N).

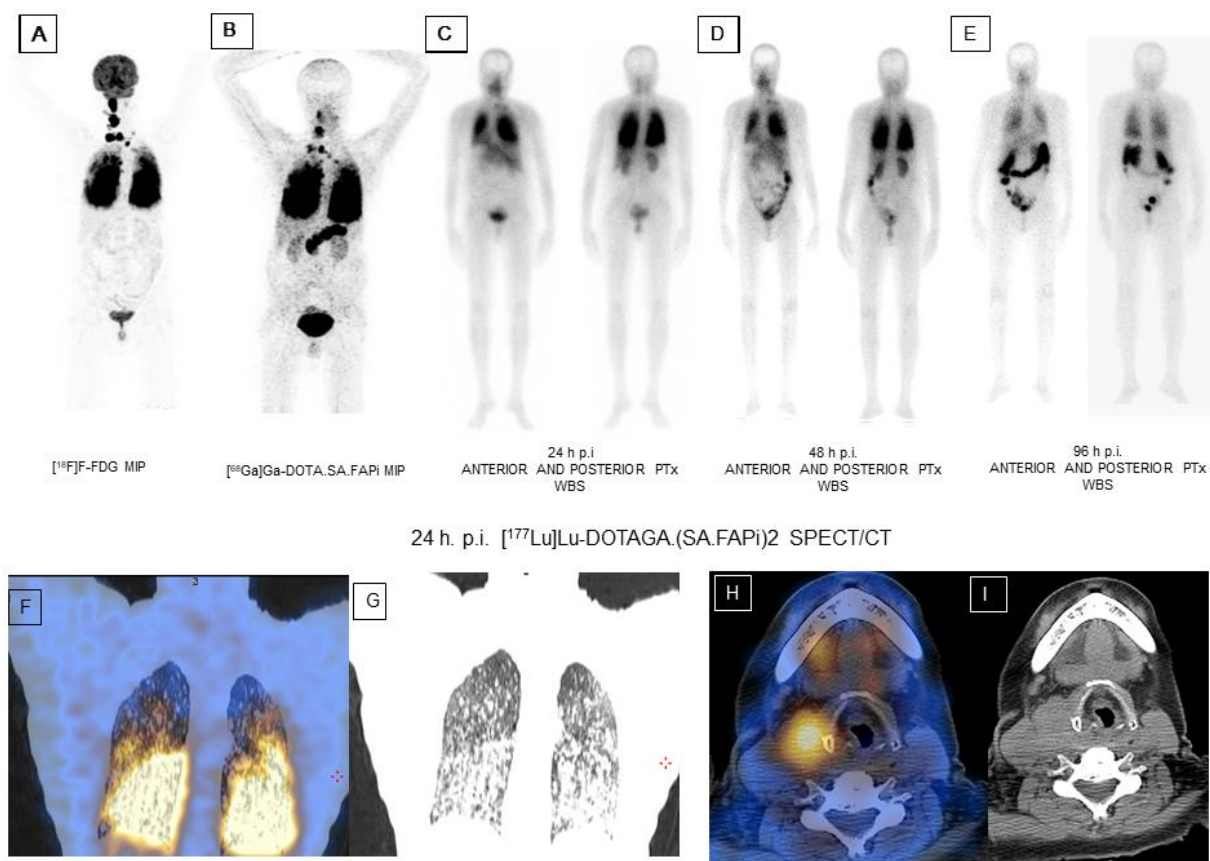


Figure 3: A 62-year-old female was diagnosed with papillary carcinoma of thyroid in 2018, and received > 22.2 GBq of RAI treatment followed by sorafenib treatment. Patient has multiple neck lymph nodes and extensive lung metastases which demonstrated intense FDG uptake (A, maximum intensity projection image (MIP) of FDG) and FAPi expression (B, MIP of FAPi) with a complete concordance between the PET/CT scans. A significant uptake and tumor retention were noted in all the lesions on the serial post-therapy $[^{177}\text{Lu}]\text{Lu-DOTAGA.(SA.FAPi)}_2$ whole-body scintigraphy scans in anterior and posterior views at 24 h (C), 48 h (D) and 96 h (E) post-treatment. The transverse fused 24 h SPECT/CT image (F, H) and their corresponding CT sections (G, I) also show a better clarity of the lung metastases and right neck lymph nodes, respectively.

Response Assessment

Biochemical and functional Imaging response

At the time of assessment (September 4th, 2021), Tg levels had decreased in all patients with a significant decrease in the Tg levels before treatment (median Tg: baseline-10549 ng/mL (IQR: 3066.5 to 39450) vs. at the time of assessment: 5649 ng/mL (IQR:939.5 to 17099), $P=0.0005$).

No patients in the series demonstrated CR. A continuous decrease in the Tg levels indicating biochemical response was observed in all patients. Among the seven patients who underwent an interim $[^{68}\text{Ga}]\text{Ga-DOTA.SA.FAPi}$ PET/CT scan, two patients (No. 5 and 11) belonged to the non-secretory group and the scan findings were suggestive of PR and SD, respectively. In the remaining 5 patients, three achieved both biochemical and molecular response (Table 3, Figure 2, Supplement

Figure 1), and two others observed a remarkable decrease in Tg levels but stable disease on molecular imaging assessment (Table 3 & 6). One patient No.3 with non-secreting Tg denied treatment after receiving 2 cycles, but on follow-up presented with clinical appearance of new neck node which was stony-hard on palpation with no symptoms of fever and was hence classified as clinically progressive disease. Patient 2 and 3 are alive, but discontinued further treatment. (Table 3).

Table 6: Efficacy Assessment

Biochemical Response category	Definition	Number of patients
Complete response		
	Negative thyroglobulin (<1.0 ng/mL unstimulated Tg) and negative structural and functional imaging	None
Partial response		
	Biochemical response (any level of Tg decrease)	12/12
	Biochemical response along with molecular response (>30% decrease in the SUVmax values)	3/5*
	Biochemical response and stable functional imaging	2/5*
	non-secretory Tg, molecular response	1/2 [#]
	non-secretory Tg, stable disease on functional imaging	1/2 [#]
Progressive disease	Appearance of new site of metastases or increase in the size of pre-existing lesions or clinically palpable disease	1 ^{\$}

Note: Seven patients underwent an interim [⁶⁸Ga]Ga-DOTA.SA.FAPi PET/CT scan. Among them 5(*) belonged to the Tg secretor group and 2([#]) from the Tg Non-secretor group. (^{\$}) clinical disease progression

Clinical Response assessment

The results of both VASmax and global pain assessment response criteria were in complete concordance with CR in 23% (3/13), PR in 38.4% (5/13), MR in 30.7% (4/13), and no response in one patient (patient 2) with an overall response rate (ORR) of 92%. (Table 7)

Table 7: Comparison of VAS and GPA response criteria with Analgesic scores.

Response category	VAS criteria	GPA criteria	Baseline AS (median, range)	Post-treatment AS (median, range)	P-value
CR	3	3	12.5 (9 – 16)	0	
PR	5	5	9 (6 – 20)	6 (3 – 6)	0.0625
MR	4	4	7.5 (3 – 20)	3 (1 – 9)	Not estimable
NR	1	1	9	9	-
Not assessed	2	2	0	0	-

Note: in 2 patients pain score criteria were not assessed as they did not take any pain medications.

VAS: visual analog score; GPA: global pain assessment criteria; AS: analgesic score; CR: complete response; PR: partial response; MR: minimal response; NR: no response

At a median follow-up of 7.2 months, there was a significant improvement in the VASmax scores [pre-therapy: 9 (IQR: 8 to 10) vs. follow-up: 6 (3 to 6) (P-0.0001)], and ECOG performance status [3, (IQR: 2 – 3) vs. 2, (IQR: 2 – 3) (P-0.0078)]. In concordance with the VASmax and GPA scores, there was a decrease in the intake of analgesics in the respective response groups (Table 7).

Interestingly, the median time for the initiation of pain relief was 6 days (IQR: 6 – 10 days). Patient 1 initially experienced complete pain relief after the first cycle, but showed recurrence in pain after 4 weeks of 2nd cycle, and hence, analgesics were resumed. Among the 13 patients on analgesics (Table 3), all patients except 3 experienced pain relief after the 1st cycle of treatment, and the remaining three patients experienced relief after the 2nd cycle. Only one patient (Patient No. 2) experienced < 20% decrease in the pain score from the baseline. Two patients, No. 12, and 15 experienced an initial flare in the pain after the 1st cycle, but both found relief after their second treatment cycle.

Safety and tolerability

None of the patients experienced grade III/IV hematological, renal or hepatotoxicity from [¹⁷⁷Lu]Lu-DOTAGA(SA.FAPi)₂ therapy (Table 8). No other treatment related toxicities were observed. Grade 1 diarrhea occurred in one patient after each cycle of her treatment which lasted up to 24 hours and was replenished by oral hydration solution. In three patients with Gr-I fatigue at the baseline a further increase in fatigue was observed which lasted for up to 3 days post- treatment.

Table 8: Laboratory parameters at baseline and post-treatment

Parameters	Baseline (Mean, 95% CI of mean)	Post-treatment (Mean, 95% CI of mean)	P-value
Hemoglobin (g/dL)	11 (10.0 to 11.6)	10.7 (9 to 11.4)	0.034
Platelets (lakhs/ μ L)	226 (171.4 to 280.1)	206.4 (177.8 to 235)	0.236
Leukocytes 10 ⁹ /L	6561 (4931 to 8190)	6951 (5930 to 7900)	0.646
Creatinine (mg/dL)	0.73 (0.41 to 1.04)	0.53 (0.44 to 0.62)	0.198
ALP (IU/L)	99 (74 to 124)	90.02 (69.7 to 111)	0.298

ALP: alkaline phosphatase

No patient in the series experienced any episodes of vomiting, nausea or fluctuations in the vital parameters during and after [¹⁷⁷Lu]Lu-DOTAGA.(SA.FAPi)₂ therapy. In two skeletal metastases patients who reported a flare in the pain after treatment, the symptoms subsided approximately after 1 week of treatment cycle.

At the time of recruitment, six patients presented with G1 and three G2 anemia, and one patient had G1 thrombocytopenia which did not deteriorate with treatment. Interestingly, in one patient with pre-existing renal insufficiency kidney function normalized after 6 weeks of first treatment where the creatinine values decreased gradually from 1.2 mg/dL to 0.5 mg/dL. No grade hepatotoxicity was observed.

Discussion

The pivotal role of radioiodine for the management of distant metastases from DTC in the last eight-decades, since its introduction in early 1940s by Seidlin et al. [29], is unparalleled in clinical oncology. The routine measurement of Tg and anti-Tg as tumor biomarkers, and generous use of ultrasonography, contrast enhanced computed tomography/magnetic resonance imaging, and [¹⁸F]F-FDG PET/CT imaging in the surveillance of DTC patients have resulted in diagnosing a higher percentage of RR-DTCs than in the earlier times. However, the definition of RR-DTC is itself controversial. ATA 2015 Guidelines have for the first time tried to define RR-DTC, but controversies in literature demand for further

refinement of the definition of RR-DTC [30]. Albeit, three facts are non-controversial: a) de novo absence of radioiodine uptake in metastatic sites, b) loss of the ability by the metastatic deposits over time for taking up radioiodine, or, c) moderate to high uptake of radioiodine in metastases but demonstrable progressive disease on conventional/functional imaging.

It was initially difficult to manage these so-called RR-DTC patients without safe and effective systemic therapy options. In the last-decade, two important drugs got Food and Drug Administration (FDA) approvals following the multicentric phase-III randomized trials, namely DECISION trial [6] for sorafenib and SELECT trial [7] for lenvatinib.

The object response rate (ORR) for sorafenib is about 12%, and for lenvatinib, it is significantly better which is about 65% but is accompanied with a higher grade III/IV AEs. Moreover, certain cohort of patients, approximately ~25% even fail to respond to sorafenib/lenvatinib. The high percentage drug-related toxicities interfere with the course of treatment and lead to the early discontinuation of the drug (34/207; 16.4%) in patients on sorafenib and approximately 37/261 (14%) with lenvatinib. In the current study, while, 7/15 (46.6%) patients exhausted both sorafenib and lenvatinib, the remaining patients were treated with TKIs at least once in their treatment tenure. Recently, a pivotal phase III COSMIC-311 trial [31] on cabozantinib in RR-DTC also revealed a promising progression-free survival that was not attained at the time of assessment, but at the same time a significantly high grade 3 or 4 toxicities in 57% and serious adverse events in 16 patients were observed.

This large percentage of early drop out from the treatment regimen strongly supports the unmet need of additional highly targeted salvage treatment options in this subset of aggressive thyroid cancers. Currently, there are sparse options available for them to manage, and thus, there is ongoing search for suitable, safe and effective therapeutic option for these heavily pretreated RR-DTC patients who have progressed on TKIs. Research has also been ongoing and have proved CRAs [31] beneficial in the re-differentiation of RR-DTC, but needs further large-scale research in each sub-category of RR-DTC patients as defined by ATA.

Recently, targeting FAP with various small molecule FAP inhibitors has gained momentum and extensive clinical research on its role in cancer therapeutics is ongoing. FAP inhibitor agents ($[^{68}\text{Ga}]\text{Ga-DOTA-FAPI-02}$ and FAPI-04) for imaging are well-established for a wide spectrum of cancers. However, a major challenge has remained on the therapeutic front pertaining to the early tumor washout and short tumor retention time, thereby delivering negligible tumor absorbed dose, and thus, limiting the therapeutic efficacy. For an effective radioligand therapy, it is critical that the biological half-life of pharmacophore must match the physical half-life of radionuclide to give best effective tumor half-life.

Lutetium-177 is nick-named as 'metallic iodine' with physical half-life 6.71 days and beta energy similar to Iodine-131.

Our department in collaboration with the Department of Chemistry at Mainz, Germany also observed the same pattern of untimely tracer washout with the one of the initially synthesized squaric acid linker-based molecule, DOTA.SA.FAPi when labelled with Lutetium-177 [16]. Further structural modifications of DOTA.SA.FAPi molecule led to the development of a dimer, DOTAGA.(SA.FAPi)₂ and unlike the monomer, showed a longer and promising tumor effective half-life that has been reported by our group that is currently under review [19].

The favorable dosimetry data encouraged us to use [¹⁷⁷Lu]Lu-DOTAGA.(SA.FAPi)₂ for therapeutic use, and in an interest to know whether the findings hold true from the therapeutic clinical aspect, we therefore studied the efficacy and safety of [¹⁷⁷Lu]Lu-DOTAGA.(SA.FAPi)₂ in RR-DTC patients. From our findings in this study, the first-in-human application confirmed [¹⁷⁷Lu]Lu-DOTAGA.(SA.FAPi)₂ therapy safe for the treatment of heavily pretreated advanced stage RR-DTC patients.

In our study, all patients demonstrated a positive uptake on the [⁶⁸Ga]Ga-DOTA.SA.FAPi PET/CT scan and [¹⁸F]F-FDG PET/CT scans. Similarly, the post-treatment serial biodistribution scan findings also corroborated with the PET/CT scan findings and additionally showed a promising tumor retention even up to 6 days after treatment. Unlike our findings, initial results on [¹⁷⁷Lu]Lu-FAPi-labelled compounds observed a rapid tumor washout and hence, suggested the use of a shorter half-life radionuclides such as Yttrium-90 with the FAPi molecule [33]. However, yttrium-90, attributing to its longer-range beta emission, might increase the risk of hematological toxicity. It is important to note that the present argument is based on only the physical characteristics of the radionuclide and this assumption can only be validated with longer follow-up high evidence-based prospective studies.

Our study recognized a variation in the administration of treatment doses across the patients which is apparently prevalent when investigating new radiopharmaceuticals where the biodistribution, pharmacokinetics and dosimetry data is unknown. While majority of the patients were administered with an average of 2 GBq per treatment cycle, in the later phases of recruitment, after we noted the treatment was safe from the clinical and dosimetry point of view, we escalated the dose to approximately 4 GBq. Consistent with the dosimetry findings, the rate of hematologic adverse events was minimal, transient and more importantly did not differ even in patient treated with higher doses.

Most remarkably, one patient (No. 7) with multiple extensive skeletal metastasis refractory to radioiodine, external beam radiotherapy, and lenvatinib demonstrated biochemical, molecular, and remarkable clinical response after two cycles of [¹⁷⁷Lu]Lu-DOTAGA.(SA.FAPi)₂ therapy (median activity 50 mCi/cycle) (Figure 2). In this patient the dose has been further escalated to 4GBq/cycle in the 3rd

and 4th cycle of treatment. The adequate effective-tumor half-life in this patient ranging between 48.6 to 89.5 hours reflects the promising response to treatment. (Table 5, patient 7)

Our dose estimates suggest a mean 1.36 mSv/MBq to the colon which is the critical organ. Hence, according the maximum safe limit of radiation dose to the colon which is 38 Gy as reported with external beam radiotherapy, a maximum tolerable cumulative dose of 29 GBq (780 mCi) can be administered safely.

The dose fractionation protocols and treatment intervals are yet to be studied based on the tumor burden, physiological radiotracer biodistribution, and transit aspects in the gut which widely varies from patient-to-patient. Despite the fact that there is no evidence regarding the use of intervention such as a high fatty food diet, and laxatives, to accelerate the excretion from liver-gall bladder and the administration of laxatives to hasten the intestinal motility, we incorporated a high fatty food diet and laxatives in patients for the first three days after the treatment. However, the effect of accelerating agents is not yet quantified and calls for a head-to-head dosimetry comparison between the intervention naïve and intervention groups. If the positive impact of intervention holds true, it can aid in lowering radiation dose to the liver and gut, provide a scope for administering larger cumulative doses of the radiotracer, and thereby achieve a better therapeutic effectiveness.

[¹⁷⁷Lu]Lu-DOTAGA.(SA.FAPi)₂ treatment induced clinical response as indicated by a significant reduction in the pain scores and the intake of analgesics with a similar trend of biochemical response to treatment was observed.

To the best of our knowledge, this study is the first comprehensive investigation to evaluate preliminary therapeutic efficacy and safety of [¹⁷⁷Lu]Lu-DOTAGA.(SA.FAPi)₂ therapy in RR-DTC patients after exhaustion of all standard line treatment options including sorafenib/lenvatinib. This pilot study has opened up a new avenue to be explored in the management of RR-DTC patients who have reached end of the road situation.

The major limitation of this study is the small patient number and the short follow-up duration. This was not a systematic dose-escalation study and heterogeneous activities were administered due to the unavailability of previous reports on the dosimetry of this radiotracer. However, the insights gained from this study may be of assistance to execute large scale, prospective clinical trials in RR-DTC patients particularly, who have progressed on TKIs.

The initial results of [¹⁷⁷Lu]Lu-DOTAGA.(SA.FAPi)₂ therapy are encouraging with significant biochemical and molecular response. This pilot study demonstrated promising results of FAP inhibitor-based targeted therapy in the aggressive cohort of thyroid cancer patients.

Authorship Contribution

████████████████████ conception, design, obtained ethical approval, acquisition, data collection, analysis interpretation, manuscript drafting and refinement

Euy Sung Moon, ██████████ molecule development, testing its invitro pharmacokinetics, standardization of radiolabelling

██████████ Dosimetry and PET/CT scan acquisition

██████████ Pathology review of the patients, manuscript refinement

████████████████████ Clinical data management, reviewing the PET/CT scans, recruitment of patients

██████████ Referring patients to Nuclear Medicine, conception, design

██████████ **(Corresponding author):** Design, Conception, recruitment, clinical follow-up, follow-up with adverse events, analysis, manuscript drafting, final approval

Authorship disclosure statements

Competing Interest: All the authors included in this manuscript have stated no financial or personal conflict of interest.

Funding: None

Employment: No Recent (within the past 5 years), current, or anticipated employment by an organization that may gain or lose financially from publication of the article.

Ethical Clearance: Ref. No IECPG-22/2020 for the clinical use of [⁶⁸Ga]Ga-DOTA.SA.FAPi, and Ref. No. IEC/1054/5/2020 for the clinical use of [¹⁷⁷Lu]Lu-labelled FAPi radiotracers in various cancers.

Informed Consent: Written informed consent was obtained from all patients to participate in the study

Disclaimer: The current work has not been submitted for review or is not under acceptance for publication in any journal.

References

1. Zarnegar, R.; Brunaud, L.; Kanauchi, H.; Wong, M.; Fung, M.; Ginzinger, D.; Duh, Q.; Clark, O.H. Increasing the effectiveness of radioactive iodine therapy in the treatment of thyroid cancer using Trichostatin A, a histone deacetylase inhibitor. *Surgery* **2002**, *132*, 984–990, doi:10.1067/msy.2002.128690.
2. Worden, F. Treatment strategies for radioactive iodine-refractory differentiated thyroid cancer. *Ther. Adv Med. Oncol.* **2014**, *6*, 267–279, doi:10.1177/1758834014548188.
3. Xing, M.; Haugen, B.R.; Schlumberger M. Progress in molecular-based management of differentiated thyroid cancer. *Lancet* **2013**, *381*, 1058–1069, doi: 10.1016/S0140-6736(13)60109-9.
4. Nixon I.J.; Whitcher M.M.; Palmer, F.L.; Tuttle, R.M.; Shaha, A.R.; Shah, J.P.; Patel, S.G.; Ganly, I. The Impact of Distant Metastases at Presentation on Prognosis in Patients with Differentiated Carcinoma of the Thyroid Gland. *Thyroid* **2012**, *22*, 884–889, doi:10.1089/thy.2011.0535.
5. Durante, C.; Haddy, N.; Baudin, E.; Leboulleux, S.; Hartl, D.; Travagli, J.P.; Caillou, B.; Ricard, M.; Lumbroso, J.D.; De Vathaire, F.; Schlumberger M. Long-Term Outcome of 444 Patients with Distant Metastases from Papillary and Follicular Thyroid Carcinoma: Benefits and Limits of Radioiodine Therapy. *J. Clin. Endocrinol. Metab.* **2016**, *91*, 2892–2899, doi:10.1210/jc.2005-2838.
6. Brose, M.S.; Nutting, C.M.; Jarzab, B.; Elisei, R.; Siena, S.; Bastholt, L.; De la Fouchardiere, C.; Pacini, F.; Paschke, R.; Shong, Y.K.; Sherman, S.I.; et al. Sorafenib in radioactive iodine-refractory, locally advanced or metastatic differentiated thyroid cancer: a randomised, double-blind, phase 3 trial. *Lancet* **2014**, *384*, 319–328, doi:10.1016/S0140-6736(14)60421-9.
7. Schlumberger, M.; Tahara, M.; Wirth, L.J.; Robinson, B.; Brose, M.S.; Elisei, R.; Habra, M.A.; Newbold, K.; Shah, M.H.; Hoff, A.O.; et al. Lenvatinib versus placebo in radioiodine-refractory thyroid cancer. *N. Engl. J. Med.* **2015**, *372*, 621–630, doi:10.1056/NEJMoa1406470.
8. Fozzatti, L.; Cheng, S.Y. Tumor Cells and Cancer-Associated Fibroblasts: A Synergistic Crosstalk to Promote Thyroid Cancer. *Endocrinol. Metab.* **2020**, *35*, 673–680, doi:10.3803/EnM.20-20.401.
9. Cirri, P.; Chiarugi, P. Cancer associated fibroblasts: the dark side of the coin. *Am. J. Cancer. Res.* **2011**, *1*, 482–497.
10. Ohlund, D.; Elyada, E.; Tuveson, D. Fibroblast heterogeneity in the cancer wound. *J. Exp. Med.* **2014**, *211*, 1503–1523, doi:10.1084/jem.20140692.
11. Kalluri, R. The biology and function of fibroblasts in cancer. *Nat. Rev. Cancer* **2016**, *16*, 582–598, doi:10.1038/nrc.2016.73.
12. Cho, J.G.; Byeon, H.K.; Oh, K.H.; Baek, S.K.; Kwon, S.Y.; Jung, K.Y.; Woo, J.S. Clinicopathological significance of cancer-associated fibroblasts in papillary thyroid carcinoma: a predictive marker of cervical lymph node metastasis. *Eur. Arch. Otorhinolaryngol* **2018**, *275*, 2355–2361.
13. Sun, W.Y.; Jung, W.H.; Koo, J.S.; Expression of cancer-associated fibroblast-related proteins in thyroid papillary carcinoma. *Tumour Biol.* **2016**, *37*, 8197–8207, doi:10.1007/s13277-015-4684-4.

14. Kratochwil, C.; Flechsig, P.; Lindner, T.; Abderrahim, L.; Altmann, A.; Mier, W.; Adebeg, S.; Rathke, H.; Röhrich, M.; Winter, H.; et al. ^{68}Ga -FAPI PET/CT: Tracer uptake in 28 different kinds of cancer. *J. Nucl. Med.* **2019**, *60*, 801–805, doi:10.2967/jnumed.119.227967.
15. Meyer, C.; Dahlbom, M.; Lindner, T.; Vauclin, S.; Mona, C.; Slavik, R.; Czernin, J.; Haberkorn, U.; Calais, J. Radiation dosimetry and biodistribution of ^{68}Ga -FAPI-46 PET imaging in cancer patients. *J. Nucl. Med.* **2020**, *61*, 1171–1177, doi:10.2967/jnumed.119.236786.
16. Moon, E.S.; Elvas, F.; Vliegen, G.; De Lombaerde, S.; Vangestel, C.; De Bruycker, S.; Bracke, A.; Eppard, E.; Greifenstein, G.; Klasen, B.; Kramer, V.; Staelens, S.; De Meester, I.; Van der Veken, P.; Roesch, F. Targeting fibroblast activation protein (FAP): next generation PET radiotracers using squaramide coupled bifunctional DOTA and DATA^{5m} chelators. *EJNMMI Radiopharm. Chem.* **2020**, *5*, 19, doi:10.1186/s41181-020-00102-z.
17. Ballal, S.; Yadav, M.P.; Moon, E.S.; Kramer, V.S.; Roesch, F.; Kumari, S.; Tripathi, M.; ArunRaj, S.T.; Sarswat, S.; Bal, C. Biodistribution, pharmacokinetics, dosimetry of [^{68}Ga]Ga-DOTA.SA.FAPi, and the head-to-head comparison with [^{18}F]F-FDG PET/CT in patients with various cancers. *Eur. J. Nucl. Med. Mol. Imaging* **2021**, *48*, 1915–1931, doi:10.1007/s00259-020-05132-y.
18. Ballal, S.; Yadav, M.P.; Kramer, V.; Moon, E.S.; Roesch, F.; Tripathi, M.; Mallick, S.; ArunRaj, S.T.; Bal, C. A theranostic approach of [^{68}Ga]Ga-DOTA.SA.FAPi PET/CT-guided [^{177}Lu]Lu-DOTA.SA.FAPi radionuclide therapy in an end-stage breast cancer patient: new frontier in targeted radionuclide therapy. *Eur. J. Nucl. Med. Mol. Imaging* **2021**, *48*, 942–944, doi:10.1007/s00259-020-04990-w.
19. Ballal, S.; Yadav, M.P.; Moon, E.S.; Roesch, F.; Kumari, S.; Bal, C. First-in-human results on the Biodistribution, Pharmacokinetics, and Dosimetry of [^{177}Lu]Lu-DOTA.SA.FAPi and [^{177}Lu]Lu-DOTAGA.(SA.FAPi)₂ in Patients with Various End-stage Cancers. *EJNMMI Research* **2021** (under review)
20. Eisenhauer, E.A.; Therasse, P.; Bogaerts, J.; Schwartz, L.H.; Sargent, D.; Ford, R.; Dancey, J.; Arbuck, S.; Gwyther, S.; Mooney, M.; Rubinstein, L.; et al. New response evaluation criteria in solid tumours: revised RECIST guideline (version 1.1). *Eur. J. Cancer* **2019**, *45*, 228–247, doi:10.1016/j.ejca.2008.10.026.
21. Schlumberger, M.; Brose, M.; Elisei, R.; Leboulleux, S.; Luster, M.; Pitoia, F.; Pacini, F. Definition and management of radioactive iodine-refractory differentiated thyroid cancer. *Lancet Diabetes Endocrinol.* **2014**, *2*, 356–358, doi:10.1016/S2213-8587(13)70215-8.
22. Wahl, R.L.; Jacene, H.; Kasamon, Y.; Lodge, M.A. From RECIST to PERCIST: evolving considerations for PET response criteria in solid tumors. *J. Nucl. Med.* **2019**, *1*, 122–150, doi:10.2967/jnumed.108.057307.
23. Stabin, M.G. MIRDOSE: personal computer software for internal dose assessment in nuclear medicine. *J. Nucl. Med.* **1996**, *37*, 538–546.
24. Howard, D.M.; Kearfott, K.J.; Wilderman, S.J.; Dewaraja, Y.K. Comparison of I-131 radioimmunotherapy tumor dosimetry: unit density sphere model versus patient specific Monte Carlo calculations. *Cancer Biother. Radiopharm.* **2011**, *26*, 615–621, doi:10.1089/cbr.2011.0965.
25. Sgouros, G. Bone marrow dosimetry for radioimmunotherapy: theoretical considerations. *J. Nucl. Med.* **1993**, *34*, 689–694.
26. McCafery, M.; Pasero, C. Pain: clinical manual. 2nd ed. St Louis: Mosby; **1999**.

27. Thapa, P.; Nikam, D.; Das, T.; Sonawane, G.; Agarwal, J.P.; Basu, S. Clinical efficacy and safety comparison of ¹⁷⁷Lu-EDTMP with ¹⁵³Sm-EDTMP on an equidose basis in patients with painful skeletal metastases. *J. Nucl. Med.* **2015**, *56*, 1513–1519, doi:10.2967/jnumed.115.155762.
28. Common Terminology Criteria for Adverse Events (CTCAE) v5.0. Publish Date: November 27, **2017**.
29. Seidlin, S.M.; Marinelli, L.D.; Oshry, E. Radioactive iodine therapy; effect on functioning metastases of adenocarcinoma of the thyroid. *J. Am. Med. Assoc.* **1946**, *132*, 838–847, doi:10.1001/jama.1946.02870490016004.
30. Tuttle, R.M.; Ahuja, S.; Avram, A.M.; Bernet, V.J.; Bourguet, P.; Daniels, G.H.; Dillehay, G.; Draganescu, C.; Flux, G.; Führer, D.; Giovanella, L.; et al. Controversies, Consensus, and Collaboration in the Use of ¹³¹I Therapy in Differentiated Thyroid Cancer: A Joint Statement from the American Thyroid Association, the European Association of Nuclear Medicine, the Society of Nuclear Medicine and Molecular Imaging, and the European Thyroid Association. *Thyroid* **2019**, *29*, 461–470, doi:10.1089/thy.2018.0597.
31. Brose, M.S.; Robinson, B.; Sherman, S.I.; Krajewska, J.; Lin, C.C.; Vaisman, F.; Hoff, A.O.; Hitre, E.; Bowles, D.W.; Hernando, J.; Faoro, L.; Banerjee, K.; Oliver, J.W.; Keam, B.; Capdevila, J. Cabozantinib for radioiodine-refractory differentiated thyroid cancer (COSMIC-311): a randomised, double-blind, placebo-controlled, phase 3 trial. *Lancet Oncol.* **2021**, *22*, 1126–1138, doi:10.1016/S1470-2045(21)00332-6.
32. Simon, D.; Koehrlé, J.; Reiners, C.; Boerner, A.R.; Schmutzler, C.; Mainz, K.; Goretzki, P.E.; Roeher, H.D. Redifferentiation therapy with retinoids: therapeutic option for advanced follicular and papillary thyroid carcinoma. *World J. Surg.* **1998**, *22*, 569–574, doi:10.1007/s002689900436.
33. Ferdinandus, J.; Fragoso Costa, P.; Kessler, L.; Weber, M.; Hirmas, N.; Kostbade, K.; Bauer, S.; Schuler, M.; Ahrens, M.; Schildhaus, H.U.; Rischpler, C.; Grafe, H.; Siveke, J.T.; Herrmann, K.; Fendler, W.; Hamacher, R. Initial clinical experience with ⁹⁰Y-FAPI-46 radioligand therapy for advanced stage solid tumors: a case series of nine patients. *J. Nucl. Med.* **2021**, doi:10.2967/jnumed.121.262468.

Supporting Information

Post-therapy [¹⁷⁷Lu]Lu-DOTAGA.(SA.FAPi)₂ whole body scintigraphy

The planar acquisition of whole-body scans was performed using a dual-headed gamma camera (GE, Discovery NM/CT 670). The camera was equipped with a high-energy general-purpose (HEGP) parallel-hole collimator, and the energy peak was centered at 113 keV and 208 keV with a 10% window width. Dual-energy Scatter corrections were applied at 90 KeV and 170 keV with a window width of 10%. Serial whole-body emission scans were performed at 1 (pre-void), 4-6, 24, 48, 96, and 144 to 168 h. Simultaneous anterior and posterior emission scans were acquired at a speed of 15 cm/min and a matrix size of 256 x 1024. Delayed images were acquired up to 168 h post-injection to prevent the overestimation of doses.

Similarly, SPECT/CT scans of the abdomen and the lesions were acquired in both the radiotracer groups at serial time points but were mainly used to demarcate the overlapping gut and kidney activity and to calculate the volume of the tumor. SPECT/CT acquisition parameters included a total angular range of 360 degrees, an angle view of 6 degrees, acquired at 25 seconds per view, and a matrix size of 512 x 512.

Image Analysis

In the dosimetry analysis, salivary glands, kidneys, pancreas, liver, gall bladder, right colon, left colon, tumor lesions, and whole body were included for dose calculation. The first whole-body image post-injection before voiding was considered to include 100% of injected activity. The region of interests (ROI's) was drawn on the source organs showing uptake of [¹⁷⁷Lu]Lu-DOTAGA.(SA.FAPi)₂ on both anterior (A) and posterior images (P). The ROI of the initial scan was cloned to the subsequent serial time-point images of the patient.

Background counts were obtained from the thigh region. For overlapping organs such as the right kidney had overlapping intestinal uptake, the counts were considered to the left kidney. The corresponding time-point Tx-SPECT/CT scans were also referred to prevent overlap. Background correction of lesion counts was done by subtracting counts in background ROI of the similar area drawn close to the lesions.

Finally, attenuated, background, and scatter corrected percentage injected activity (%IA) in each source organ including salivary glands (parotid and submandibular glands), kidney, liver, gall bladder, pancreas, right and left colon, and the tumor was calculated.

$$\%IA_{uncorr} = \frac{Ct_{ROI} / pixel}{Ct_{WB} / pixel} \times 100 \quad (1)$$

Where: %IA_{unCorr}: Uncorrected Percentage of injected activity, Ct_{ROI/pixel}: counts/pixel in a region of interest, Ct_{WB/pixel}: counts in the whole-body image

$$\%IA_{Corr} = \frac{Ct_{ROI} / pixel}{Ct_{WB} / pixel} \times DF \times 100 \quad (2)$$

where: %IA_{Corr}: Corrected Percentage of injected activity (Corrected with Decay factor), Ct_{ROI/pixel}: counts/pixel in the region of interest, Ct_{WB/pixel}: counts/pixel in Whole-body image, DF: decay factor (¹⁷⁷Lu- 0.9 for 24 hrs)

Internal Dose Estimation

The percentage injected activities against time were entered in the kinetic input model of the OLINDA/EXM v2.1 software to calculate the area under the curve that represented the number of disintegrations or residence time or cumulative activity in each source organ. The residence times were input to the ICRP-89 female and male models to derive absorbed doses of organs and whole-body effective doses.

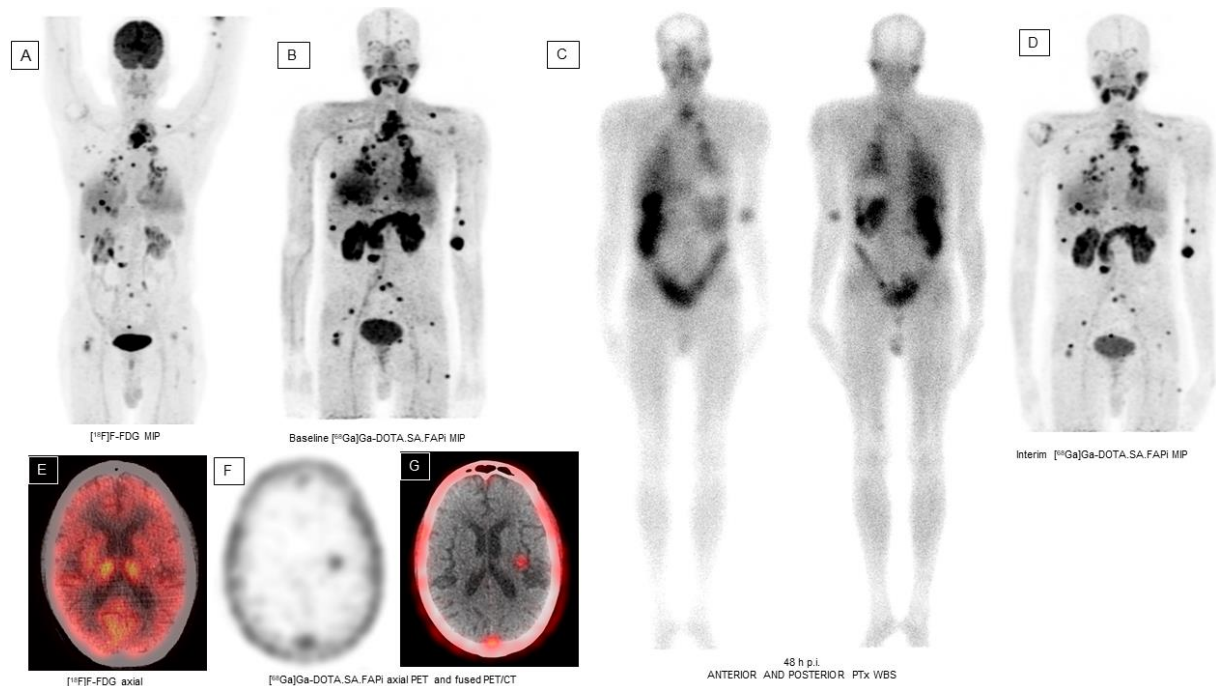
Detailed Definitions of Secondary outcome endpoints

According to VAS, complete response (CR), partial response (PR), minimal response (MR), and no response (NR) were categorized as > 70% reduction, 40–70% reduction, 20–40% reduction, and < 20% decrease in VAS or increase in pain, respectively [22].

The analgesic scoring was conducted as per the Urological Group of the European Organization of Research and Treatment of Cancer (EORTC, Protocol 30921). As per EORTC protocol, the analgesic score is the product of two five-point scales (the type of analgesic and the frequency of its administration). A decline in the analgesic score was documented as a response to treatment.

Additionally, global pain response assessment (GPA) was analyzed according to the criteria adopted by Thapa et al. [23] that considered changes in both VAS and analgesic scores (rather than a single

parameter). According to the criteria, the present study design considered post-therapy changes in both VAS and analgesic scores on a sliding scale. The global pain assessment criteria are accordingly complete (75% decrease in analgesic score with change in pain score), partial (50–75% decrease in analgesic score with a change in pain score), minimal (25–50% decrease in analgesic score with a change in pain score), or none (no change in pain score or, 25% decrease in the analgesic score). ECOG status ranged from 0 to 5.



Supplemental Figure 1: A 49-year-old male suffered from RAI refractory papillary carcinoma of thyroid and demonstrated intense expression of FDG (A, MIP) and FAPi (B, MIP) in the locoregional thyroid mass, multiple lung metastases, bone, liver, brain, and sub-cutaneous metastases (left forearm) on both [^{18}F]F-FDG and [^{68}Ga]Ga-DOTA.SA.FAPi PET/CT scans. A similar [^{177}Lu]Lu-DOTAGA.(SA.FAPi) $_2$ radiotracer concentration was also noted in all the lesions on the anterior and posterior 48 h post-treatment whole body scan (C). Interestingly, the patient had brain metastases which failed to be clearly delineated on [^{18}F]F-FDG PET/CT (E, fused axial), but was remarkably visualized on [^{68}Ga]Ga-DOTA.SA.FAPi on axial PET (F), and PET/CT (G) fused sections. In this patient after receiving 2 cycles of [^{177}Lu]Lu-DOTAGA.(SA.FAPi) $_2$ treatment, the interim [^{68}Ga]Ga-DOTA.SA.FAPi (D, MIP), demonstrated a reduction in the intensity of FAPi expression in all the pre-existing lesions and patient achieved partial molecular response.

- D. Development of DATA^{5m} chelator-based Fibroblast Activation Protein Inhibitor small molecules for PET imaging

In Vorbereitung zur Veröffentlichung.

**Development of DATA^{5m} chelator-based Fibroblast Activation Protein
Inhibitor small molecules for PET imaging**

Euy Sung Moon¹, [REDACTED]
[REDACTED]

¹ Department of Chemistry – TRIGA, Johannes Gutenberg University Mainz, Mainz, Germany

² Department of Pharmaceutical Sciences, Laboratory of Medical Biochemistry, University of Antwerp, Wilrijk, Belgium

³ Department of Pharmaceutical Sciences, Laboratory of Medicinal Chemistry, University of Antwerp, Wilrijk, Belgium

* Corresponding author: [REDACTED]

Abstract

Targeting fibroblast activation protein (FAP)-positive cancer-associated fibroblasts (CAFs) is currently a major topic in radiopharmaceutical chemistry and nuclear medicine. Many FAP inhibitor (FAPi) small molecules with a chelator-linker-FAPi construct were developed and already under multiple clinical studies, especially for ^{68}Ga -PET/CT diagnostic applications. Our squaramide FAPi (SA.FAPi) molecules, DOTA.SA.FAPi, AAZTA⁵.SA.FAPi and DATA^{5m}.SA.FAPi, also demonstrated very potent *in vitro* and *in vivo* characteristics and are part of several clinical applications. Here, we focused on the development of new DATA^{5m} based FAP-targeting radiopharmaceuticals (DATA^{5m}.NH.FAPi, DATA^{5m}.Pip.FAPi, DATA^{5m}.Pyr-N-CH₃.FAPi and DATA^{5m}.NH-Pyr.FAPi) differing in the linker units. The rationale is to provide lyophilized precursors easy to label at room temperature under instant kit protocols. The derivatives were synthesized, investigated for their labeling properties with gallium-68 and *in vitro* stabilities in different media. In addition, lipophilicity and *in vitro* inhibition efficacy measurements for FAP were carried out. All four novel compounds showed good labeling profiles with gallium-68 and except for DATA^{5m}.NH-Pyr.FAPi sufficient *in vitro* stabilities. The logD_{7.4} values displayed strong hydrophilic characteristics for all probes and magnificent affinity for FAP and against PREP (prolyl endopeptidase) resulting in high FAP selectivity.

Keywords: DATA^{5m}, FAP, PREP, gallium-68, NH, Pip, Pyr, SA, radiopharmaceuticals

Introduction

The fibroblast activation protein (FAP) is a type II transmembrane serine protease and present in > 90% of human epithelial tumors but low abundant in normal healthy tissues. The high expression in cancer associated fibroblasts (CAFs), representing a huge part of tumor stroma and surface, gives the attractive opportunity to address various cancers [1–5]. These FAP-positive CAFs have gained recently more and more interests in medicine, in particular in oncology and nuclear medicine [6–8]. Various FAP-targeted radiopharmaceuticals based on a highly potent and selective FAP inhibitor ((S)-N-(2-(2-cyano-4,4-difluoropyrrolidin-1-yl)-2-oxoethyl)quinoline-4-carboxamide, so-called “UAMC1110”) developed in the group of P. van der Veken at the University of Antwerp [9]. Since 2018, Lindner and Loktev et al. developed many chelator-conjugated FAPi based small molecules with a DOTA chelator and mostly piperazine modified spacer systems [10–12]. Among these, the so-called FAPI-04, FAPI-21 and FAPI-46 have emerged as the most promising combinations. Meanwhile, many (pre-)clinical studies with these FAPi have been performed, mostly for molecular PET/CT imaging with gallium-68 [13,14]. Additionally, first (pre-)clinical approaches with other radionuclides (^{18}F , ^{225}Ac , ^{64}Cu , ^{153}Sm , $^{99\text{m}}\text{Tc}$ and ^{188}Re) and the corresponding ligands have been initiated [15–19]. In parallel, we also developed FAPi agents containing a squaramide (SA) linker between chelator and inhibitor [20,21]. The three precursors DOTA.SA.FAPi, AAZTA⁵.SA.FAPi and DATA^{5m}.SA.FAPi showed excellent *in vitro* affinity for FAP. The AAZTA⁵ derivative AAZTA⁵.SA.FAPi demonstrated high complexation yields and stability with radionuclides such as gallium-68, scandium-44 and lutetium-177 [21]. Ballal et al. has shown great potential for [^{68}Ga]Ga-DOTA.SA.FAPi PET/CT imaging reported in fifty-four patients with various cancer types [22]. Additionally, [^{68}Ga]Ga-DATA^{5m}.SA.FAPi showed promising value by Kreppel et al. in a female patient with focal nodular hyperplasia [23]. Recently, the same group revealed a systematic correlation between the PET-positive tumor fraction of the [^{68}Ga]Ga-DATA^{5m}.SA.FAPi and the Ki-67 in liver metastases of neuroendocrine tumors (NET) [24].

The DATA chelator represents optimal conditions for complexing gallium-68. Due to the favorable N_3O_3 coordination with Ga^{3+} and the combination of a macro- and acyclic scaffold, DATA enables very fast complexation within few minutes at ambient temperatures and very sufficient *in vitro* stabilities [25–31]. The possibilities to provide so-called “kit-instant-type” labeling under mild conditions with bifunctional DATA chelators are very auspicious. The DATA^{5m} coupled somatostatin analogue DATA-TOC for ^{68}Ga -PET/CT imaging has already demonstrated excellent *in vitro* properties right up to preclinical and clinical translations [32,33]. Additionally, clinical comparisons with [^{68}Ga]Ga-DOTA-TOC and [^{68}Ga]Ga-DOTA-NOC displayed comparable and sufficient results showing the potential of the DATA analogue as instant-kit-alternatives in PET/CT of the established NET tracers [34-35].

In this work, we developed four new DATA^{5m} coupled FAP-targeting radiopharmaceuticals (DATA^{5m}.NH.FAPi, DATA^{5m}.Pip.FAPi, DATA^{5m}.Pyr-N-CH₃.FAPi and DATA^{5m}.NH-Pyr.FAPi) with multiple spacer variants. In case of the DATA^{5m}.NH.FAPi, DATA^{5m} was directly coupled to the NH₂-UAMC1110 FAPi without any heterocyclic linker in-between. DATA^{5m}.Pip.FAPi contains a piperazine as heterocyclic unit, DATA^{5m}.Pyr-N-CH₃.FAPi and DATA^{5m}.NH-Pyr.FAPi comprise modified pyrrolidine moieties. Both, the exo- and endo-site amine of the pyrrolidine were used for the respective coupling to chelator and the FAPi target vector scaffold. These novel radiotracers were labeled with gallium-68, investigated for their *in vitro* behavior regarding stability (in human serum, ethanol and saline) and inhibition potency for FAP and against PREP (prolyl endopeptidase). PREP is related in the same enzyme family as the FAP. They share both the endopeptidase activity and as PREP is ubiquitous in all organs and tissues, high FAP specificity is essential for potent FAP inhibitors.

Results

Synthesis of DATA^{5m}.NH.FAPi

DATA^{5m}.NH.FAPi was synthesized in a two-step route according to **Fig. 1**. Commercially available DATA^{5m}(^tBu)₃ and NH₂-FAPi were reacted with the coupling reagents HATU, HOBT and DIPEA. Via an amide bond, compound (1) was received. Subsequent deprotection of the ^tBu-groups using TFA/TIPS/H₂O resulted in DATA^{5m}.NH.FAPi (2).

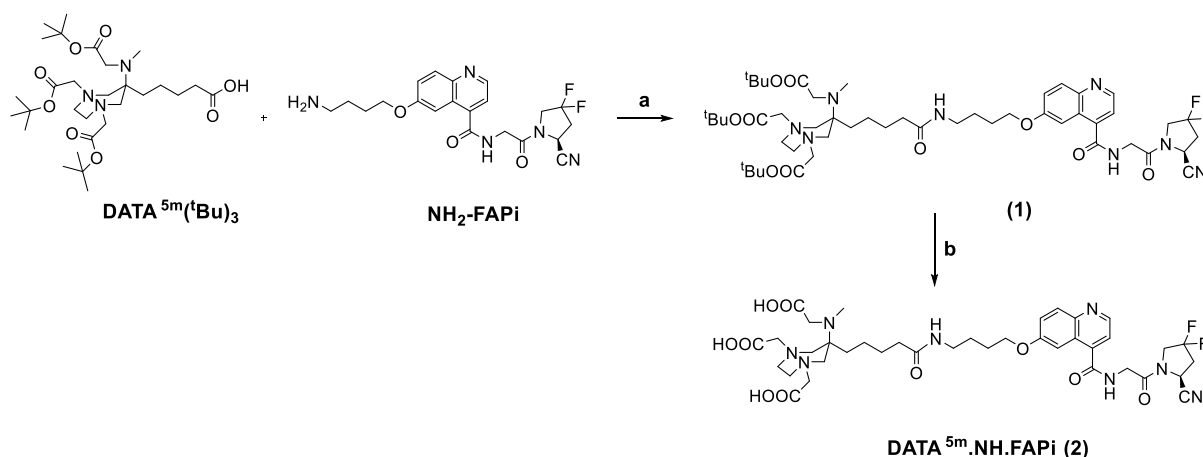


Fig. 1 Synthesis of DATA^{5m}.NH.FAPi: (a) HATU, HOBT, DIPEA, MeCN, RT, 16 h; (b) TFA/TIPS/H₂O (95/2.5/2.5), RT, 5 h.

Synthesis of DATA^{5m}.Pip.FAPi

DATA^{5m}.Pip.FAPi was synthesized in a six-step route (**Fig. 2**). Commercially available 1-Boc-piperazine and benzyl bromoacetate were alkylated with DIPEA to get (3). Deprotection of the Boc-group with 20% TFA resulted in (4), which was directly amidated with DATA^{5m}(^tBu)₃ and the coupling reagents HATU, HOBT and DIPEA. Afterwards, compound (5) was treated with Pd on activated charcoal in a hydrogen atmosphere to deprotect the benzyl group and receive (6). After reaction with NH₂-FAPi, forming an amide bond, deprotection of the ^tBu-groups on the DATA^{5m} chelator with TFA/TIPS/H₂O was carried out to form DATA^{5m}.Pip.FAPi (7).

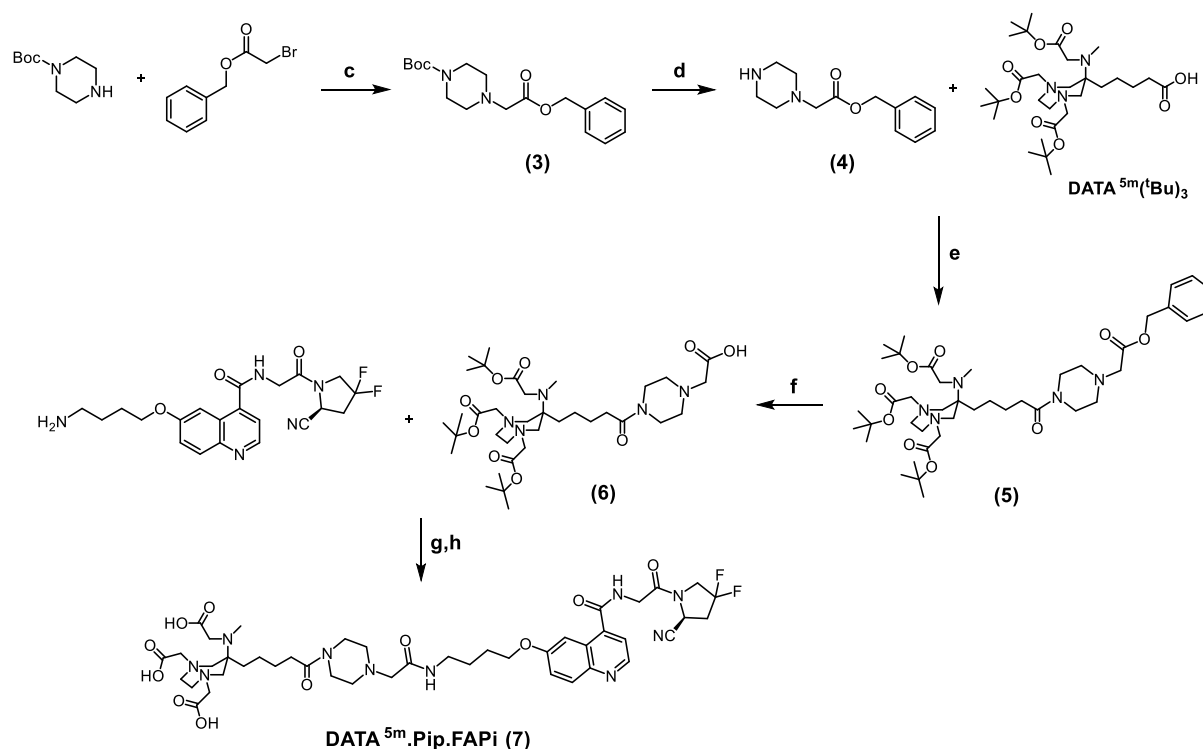


Fig. 2 Synthesis of DATA^{5m}.Pip.FAPi: (c) DIPEA, MeCN, RT, 16 h; (d) 20% TFA in DCM, RT, 4 h; (e) HATU, HOBT, DIPEA, MeCN, RT, 16 h; (f) Pd/C, H₂, MeOH, RT, 16 h; (g) HATU, HOBT, DIPEA, MeCN, RT, 16 h; (h) TFA/TIPS/H₂O (95/2.5/2.5), RT, 5 h.

Synthesis of DATA^{5m}.Pyr-N-CH₃.FAPi

Synthesis of DATA^{5m}.Pyr-N-CH₃.FAPi was achieved in seven-steps following the pathway given in Fig. 3. (S)-1-Boc-3-aminopyrrolidine and benzyl bromoacetate were alkylated forming (8). Then, the exo-amine was methylated to get (9) using the reagents formaldehyde solution 37 wt%, acetic acid and sodium borohydride. After deprotection of the Boc group, (10) was directly amidated with DATA^{5m}(^tBu)₃. The benzyl protecting groups of (11) were removed and (12) was reacted with NH₂-FAPi. The ^tBu-groups of the chelator were deprotected and DATA^{5m}.Pyr-N-CH₃.FAPi (13) was obtained.

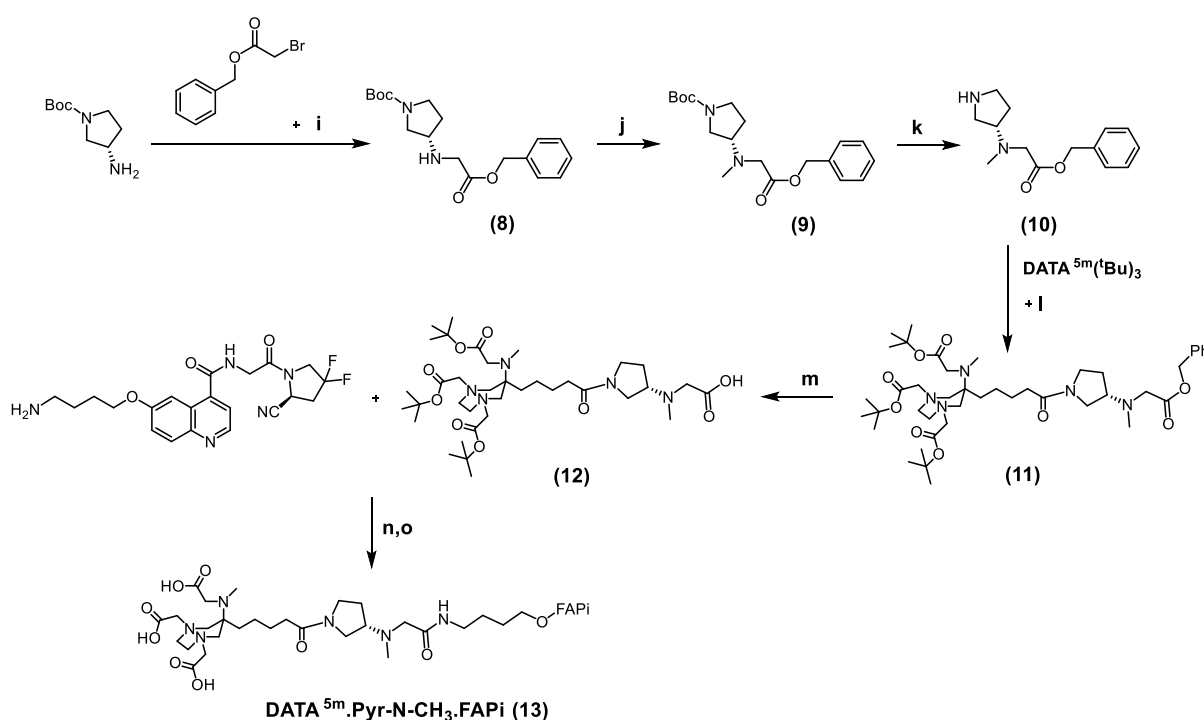


Fig. 3 Synthesis of DATA^{5m}.Pyr-N-CH₃.FAPi: (i) DIPEA, MeCN, RT, 1 h; (j) formaldehyde solution 37 wt%, acetic acid, sodium borohydride, MeCN, RT, 1 h; (k) 20% TFA in DCM, RT, 5 h; (l) HATU, HOBT, DIPEA, MeCN, RT, 20 h; (m) Pd/C, H₂, MeOH, RT, 16 h; (n) HATU, HOBT, DIPEA, MeCN, RT, 16 h; (o) 50% TFA in DCM, RT, 3 h.

Synthesis of DATA^{5m}.NH-Pyr.FAPi

DATA^{5m}.NH-Pyr.FAPi was obtained in an analogous procedure as DATA^{5m}.Pip.FAPi via a six-step synthesis (Fig. 4). Alkylation with (S)-3-(Boc-amino)pyrrolidine and benzyl bromoacetate were executed. The Boc group of (14) was deprotected (15) and after amidation with DATA^{5m}(^tBu)₃, compound (16) was obtained. After removing the benzyl protecting group (17) and amidation with NH₂-FAPi, the ^tBu groups of DATA^{5m} were deprotected and DATA^{5m}.NH-Pyr.FAPi (18) was received.

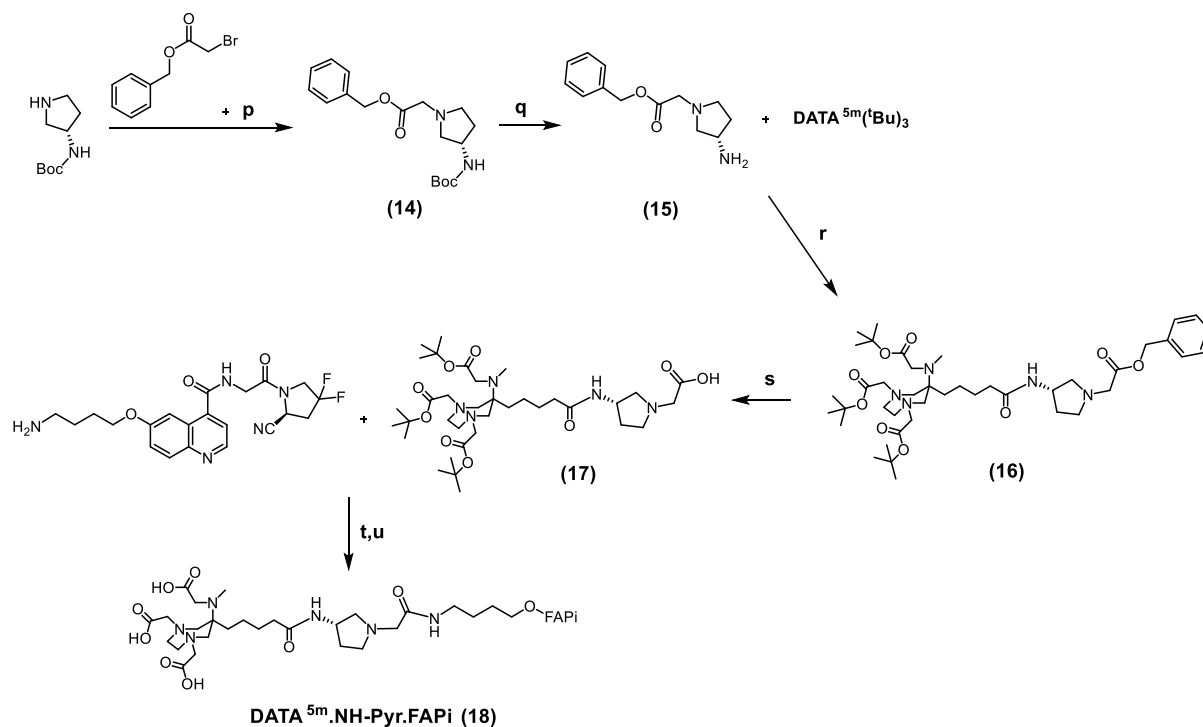


Fig. 4 Synthesis of DATA^{5m}.NH-Pyr.FAPi: (p) DIPEA, MeCN, RT, 2 h; (q) 20% TFA in DCM, RT, 4 h; (r) HATU, HOBT, DIPEA, MeCN, RT, 16 h; (s) Pd/C, H₂, MeOH, RT, 16 h; (t) HATU, HOBT, DIPEA, MeCN, RT, 16 h; (u) TFA/TIPS/H₂O (95/2.5/2.5), RT, 5 h.

Inhibition measurements

IC₅₀ values for FAP and for PREP were determined for the new compounds DATA^{5m}.NH.FAPi, DATA^{5m}.Pip.FAPi, DATA^{5m}.Pyr-N-CH₃.FAPi and DATA^{5m}.NH-Pyr.FAPi. The values were also compared to those of FAPi-04 (same assay) and DATA^{5m}.SA.FAPi (from Moon et al. [20]).

The IC₅₀ values for FAP of all four compounds lay in the same excellent order of magnitude (within the subnanomolar ranges of 0.27–0.31 nM) compared to the reference FAP inhibitor UAMC-1110 (**Tab. 1**). They also showed very high selectivity against PREP (in μM IC₅₀ range). FAPi-04 also displayed very sufficient inhibitory efficacy for FAP and very high selectivity against PREP.

Tab. 1 IC₅₀ measurements of the DATA^{5m}.X.FAPi (X=NH; Pip; Pyr-N-CH₃; NH-Pyr) derivatives for FAP and the related protease PREP. IC₅₀ values were compared to DATA^{5m}.SA.FAPi, FAPI-04 and the FAP inhibitor UAMC1110. Data are presented as the mean with standard deviation (n=3 for FAP and PREP).

Probes	PREP	FAP
	IC ₅₀ (μM)	IC ₅₀ (nM)
DATA ^{5m} .NH.FAPi	6.4 ± 0.4	0.27 ± 0.02
DATA ^{5m} .Pip.FAPi	1.5 ± 0.3	0.27 ± 0.01
DATA ^{5m} .Pyr-N-CH ₃ .FAPi	2.6 ± 0.3	0.31 ± 0.02
DATA ^{5m} .NH-Pyr.FAPi	3.3 ± 0.2	0.28 ± 0.02
DATA ^{5m} .SA.FAPi	1.7 ± 0.1 ^a	0.8 ± 0.2 ^a
FAPI-04	8.4 ± 1.6	0.21 ± 0.02
UAMC1110 inhibitor	1.8 ± 0.01	0.43 ± 0.02

^adata from Moon et al. [20]

Gallium-68 radiolabeling, stability studies and lipophilicity measurements

⁶⁸Ga-Radiolabeling

Gallium-68 radiolabeling was performed for all four new developed FAPi precursors, DATA^{5m} based -NH.FAPi, -Pip.FAPi, -Pyr-N-CH₃.FAPi and -NH-Pyr.FAPi. Labeling kinetics with different precursor quantities (10, 15 and 20 nmol) were investigated under the following conditions: A (⁶⁸Ga)= ~100 MBq, 300 μL 1 M ammonium acetate pH=5.5 buffer and 30 °C in time intervals of 1-15 minutes (**Fig. 5a-d and Fig. 6**).

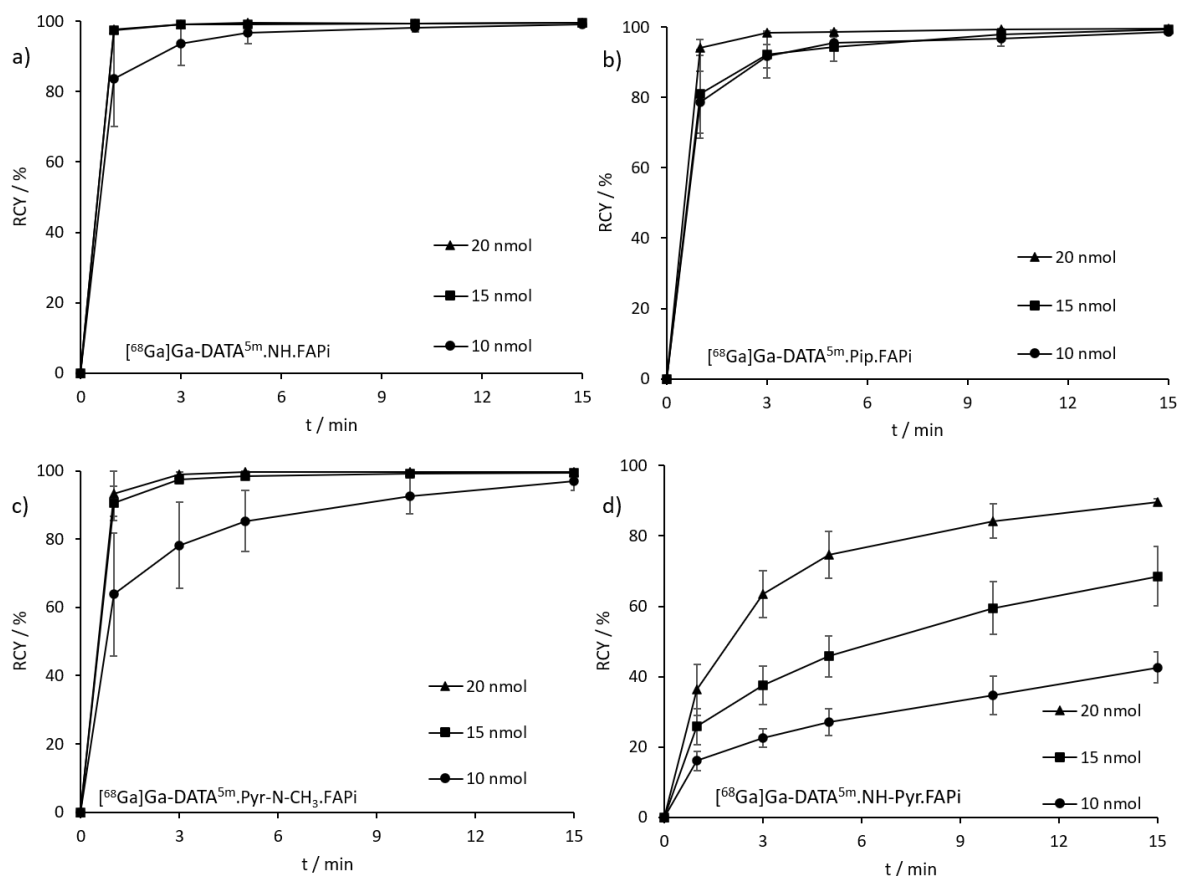


Fig. 5 Kinetic measurements of a) $[^{68}\text{Ga}]\text{Ga-DOTA}^{5\text{m}}.\text{NH.FAPi}$, b) $[^{68}\text{Ga}]\text{Ga-DOTA}^{5\text{m}}.\text{Pip.FAPi}$, c) $[^{68}\text{Ga}]\text{Ga-DOTA}^{5\text{m}}.\text{Pyr-N-CH}_3.\text{FAPi}$ and d) $[^{68}\text{Ga}]\text{Ga-DOTA}^{5\text{m}}.\text{NH-Pyr.FAPi}$, at 30 °C for precursor amounts 10, 15 and 20 nmol (n=3).

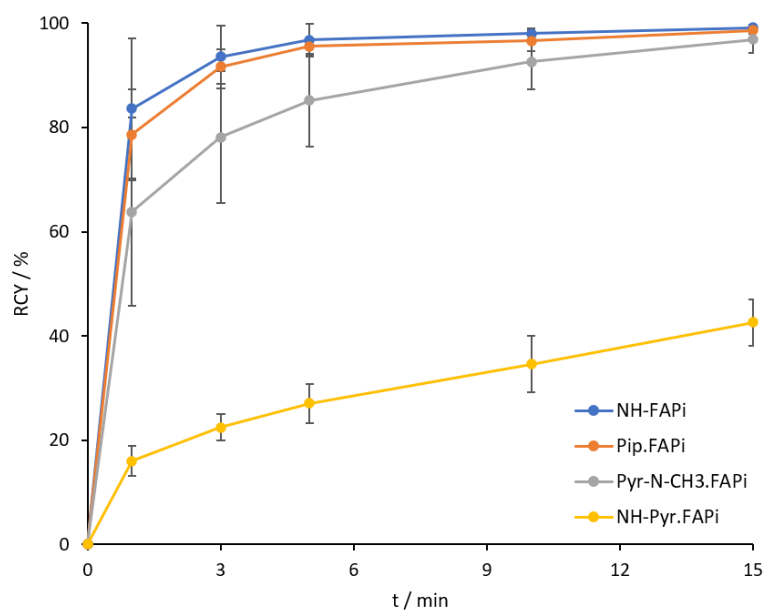


Fig. 6 ^{68}Ga labeling comparison between 10 nmol precursor: $[^{68}\text{Ga}]\text{Ga-DOTA}^{5\text{m}}.\text{NH.FAPi}$ (blue), $[^{68}\text{Ga}]\text{Ga-DOTA}^{5\text{m}}.\text{Pip.FAPi}$ (orange), $[^{68}\text{Ga}]\text{Ga-DOTA}^{5\text{m}}.\text{Pyr-N-CH}_3.\text{FAPi}$ (gray) and $[^{68}\text{Ga}]\text{Ga-DOTA}^{5\text{m}}.\text{NH-Pyr.FAPi}$ (yellow), at 30 °C.

[⁶⁸Ga]Ga-DATA^{5m}.NH.FAPi: DATA^{5m}.NH.FAPi displayed high radiochemical yields (RCYs) for all three precursor concentrations (10, 15 and 20 nmol) with gallium-68. 10 nmol showed after 5 min RCY of $\geq 95\%$ and for 15 and 20 nmol already after 3 min $\geq 99\%$ RCY. After 15 min all three concentrations could generate $\geq 99\%$ RCY.

[⁶⁸Ga]Ga-DATA^{5m}.Pip.FAPi: Gallium-68 labeling showed quantitative complexation $\geq 98\%$ RCY already after 3–5 min for 20 nmol of precursors. Complexation with 10 and 15 nmol were slower but after 10 min reaction time RCY were $\geq 97\%$ and after 15 min $\geq 99\%$.

[⁶⁸Ga]Ga-DATA^{5m}.Pyr-N-CH₃.FAPi: Kinetics for 10 nmol concentration led to $\geq 96\%$ RCY after 15 min of reaction time. Gallium complexation with 15 and 20 nmol were faster, after 5 min quantitative labeling $\geq 98\%$ and after 10 min $\geq 99\%$ RCY.

[⁶⁸Ga]Ga-DATA^{5m}.NH-Pyr.FAPi: DATA^{5m}.NH-Pyr.FAPi indicated low RCY with 10 and 20 nmol ligand concentrations. After 15 min, RCY for 10 nmol was 43% and for 15 nmol 69%. However, 20 nmol precursor amount pointed good complexation and after 15 min reaction the RCY was 90%.

In vitro stability

Stability studies of all four conjugates were performed in human serum (HS), absolute ethanol (EtOH) and saline (0.9% NaCl) (**Fig. 7a-d**). After 15 min radiolabeling, ~ 5 MBq of the tracer solution were taken and added to 500 μ L of each media (n=3) and measured within a time period of 0.5-2 h at 37 °C.

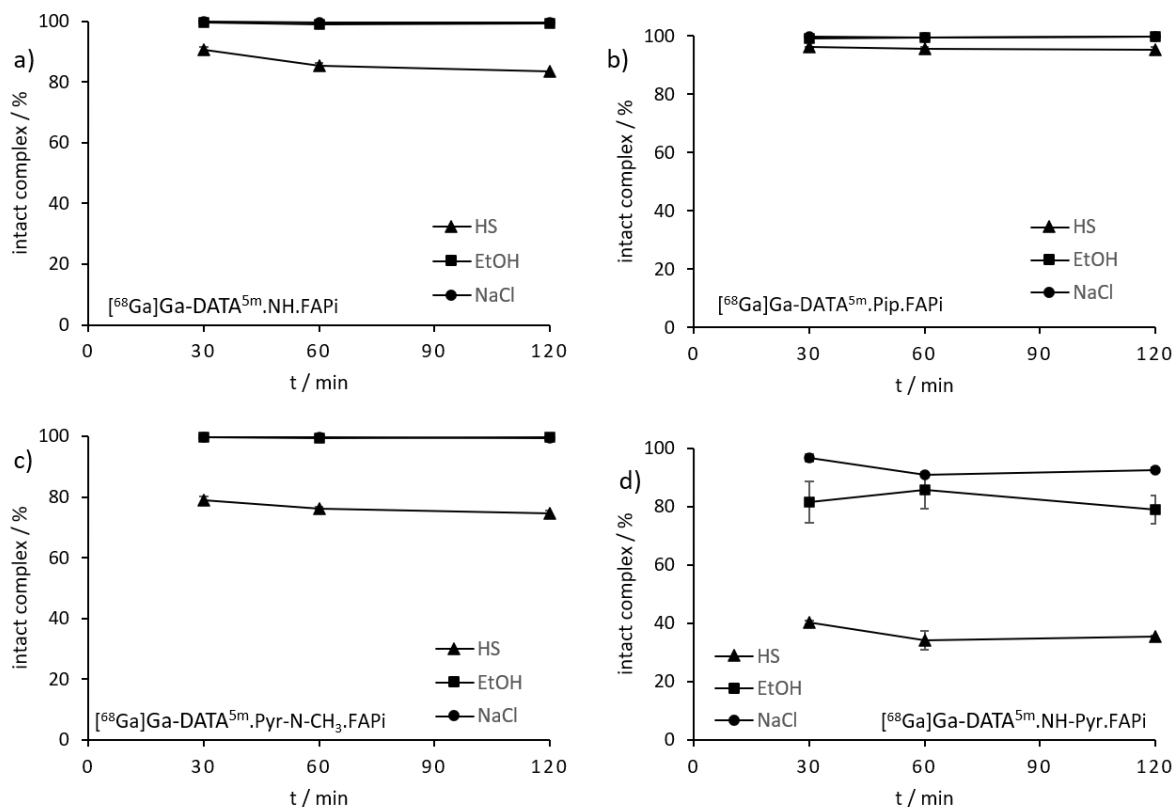


Fig. 7 Stability of a) $[^{68}\text{Ga}]\text{Ga-DATA}^{5m}.\text{NH.FAPi}$, b) $[^{68}\text{Ga}]\text{Ga-DATA}^{5m}.\text{Pip.FAPi}$, c) $[^{68}\text{Ga}]\text{Ga-DATA}^{5m}.\text{Pyr-N-CH}_3.\text{FAPi}$ and d) $[^{68}\text{Ga}]\text{Ga-DATA}^{5m}.\text{NH-Pyr.FAPi}$, at 37 °C in HS, EtOH and NaCl, time points 0.5, 1 and 2 h (n=3).

$[^{68}\text{Ga}]\text{Ga-DATA}^{5m}.\text{NH.FAPi}$: Stabilities in ethanol and saline were very high with $\geq 99\%$ intact conjugates after 2 h measured time. In human serum, the stability was $\geq 90\%$ after 0.5 h and $\geq 83\%$ after 2 h.

$[^{68}\text{Ga}]\text{Ga-DATA}^{5m}.\text{Pip.FAPi}$: $[^{68}\text{Ga}]\text{Ga-DATA}^{5m}.\text{Pip.FAPi}$ displayed high stabilities in HS, EtOH and NaCl. In HS, the stability was $\geq 95\%$ intact complex and in EtOH as well as in NaCl $\geq 99\%$ after the 2 h time point.

$[^{68}\text{Ga}]\text{Ga-DATA}^{5m}.\text{Pyr-N-CH}_3.\text{FAPi}$: The stability in EtOH and in NaCl was very sufficient with $\geq 99\%$ intact conjugates after 2 h. Stability in HS was 79% after 0.5 h and after 2 h at 75%.

$[^{68}\text{Ga}]\text{Ga-DATA}^{5m}.\text{NH-Pyr.FAPi}$: In saline, the stability of $[^{68}\text{Ga}]\text{Ga-DATA}^{5m}.\text{NH-Pyr.FAPi}$ was $\geq 96\%$ after 0.5 h reaction time and after 2 h at 93% intact complexes. The stability in ethanol was $\geq 81\%$ after 0.5 h and $\geq 79\%$ after 2 h. In human serum, the intact conjugates showed low stabilities of 40% after 0.5 h and 35% after 2 h measured time points.

Lipophilicity

Lipophilicity measurements ($\log D_{7.4}$ values) were performed for all derivatives, $[^{68}\text{Ga}]\text{Ga-DATA}^{5\text{m}}.\text{NH.FAPi}$, $[^{68}\text{Ga}]\text{Ga-DATA}^{5\text{m}}.\text{Pip.FAPi}$, $[^{68}\text{Ga}]\text{Ga-DATA}^{5\text{m}}.\text{Pyr-N-CH}_3.\text{FAPi}$ and $[^{68}\text{Ga}]\text{Ga-DATA}^{5\text{m}}.\text{NH-Pyr.FAPi}$ via the “shake-flask” method (**Tab. 2**). Additionally, $\log D_{7.4}$ of $[^{68}\text{Ga}]\text{Ga-DATA}^{5\text{m}}.\text{SA.FAPi}$ was determined for comparison.

Tab 2. LogD values (pH=7.4) of $[^{68}\text{Ga}]\text{Ga-DATA}^{5\text{m}}.\text{X.FAPi}$ (X=NH; Pip; Pyr-N-CH₃; NH-Pyr; SA) complexes.

Radiocomplex	LogD _{7.4}
$[^{68}\text{Ga}]\text{Ga-DATA}^{5\text{m}}.\text{NH.FAPi}$	-2.18 ± 0.05
$[^{68}\text{Ga}]\text{Ga-DATA}^{5\text{m}}.\text{Pip.FAPi}$	-2.29 ± 0.08
$[^{68}\text{Ga}]\text{Ga-DATA}^{5\text{m}}.\text{Pyr-N-CH}_3.\text{FAPi}$	-2.16 ± 0.03
$[^{68}\text{Ga}]\text{Ga-DATA}^{5\text{m}}.\text{NH-Pyr.FAPi}$	-2.22 ± 0.06
$[^{68}\text{Ga}]\text{Ga-DATA}^{5\text{m}}.\text{SA.FAPi}$	-2.25 ± 0.06

The lipophilicity of all measured derivatives, $[^{68}\text{Ga}]\text{Ga-DATA}^{5\text{m}}.\text{NH.FAPi}$, $[^{68}\text{Ga}]\text{Ga-DATA}^{5\text{m}}.\text{Pip.FAPi}$, $[^{68}\text{Ga}]\text{Ga-DATA}^{5\text{m}}.\text{Pyr-N-CH}_3.\text{FAPi}$, $[^{68}\text{Ga}]\text{Ga-DATA}^{5\text{m}}.\text{NH-Pyr.FAPi}$ and $[^{68}\text{Ga}]\text{Ga-DATA}^{5\text{m}}.\text{SA.FAPi}$ was in the same range between $\log D_{7.4}$ -2.16 to -2.29.

Discussion

Inhibition measurements

IC₅₀ values of all measured derivatives were in the low nM range (0.27–0.31 nM) demonstrating magnificent affinity for FAP. The new probes $\text{DATA}^{5\text{m}}.\text{NH.FAPi}$, $\text{DATA}^{5\text{m}}.\text{Pip.FAPi}$, $\text{DATA}^{5\text{m}}.\text{Pyr-N-CH}_3.\text{FAPi}$, $\text{DATA}^{5\text{m}}.\text{NH-Pyr.FAPi}$ and FAPi-04 had better selectivity for FAP compared to the reference inhibitor UAMC1110. In addition, $\text{DATA}^{5\text{m}}.\text{NH.FAPi}$, $\text{DATA}^{5\text{m}}.\text{Pyr-N-CH}_3.\text{FAPi}$, $\text{DATA}^{5\text{m}}.\text{NH-Pyr.FAPi}$ and FAPi-04 presented higher selectivity (selectivity indices FAP to PREP) than UAMC1110 and $\text{DATA}^{5\text{m}}.\text{Pip.FAPi}$ showed similar FAP/PREP selectivity compared to UAMC1110. By contrast, the IC₅₀ of $\text{DATA}^{5\text{m}}.\text{SA.FAPi}$, measured earlier (Moon et al. [20]), was 0.8 nM, however, still with an eminent inhibition efficacy for FAP and against PREP. In our opinion, all the analyzed chelator-conjugated FAPi derivatives show a very similar FAP binding affinity of 0.5 ± 0.3 . This is in the same order of magnitude then the FAP inhibitor itself.

⁶⁸Ga-Radiolabeling and in vitro stability

Radiolabeling with gallium-68 was fast and efficient for [⁶⁸Ga]Ga-DATA^{5m}.NH.FAPi, [⁶⁸Ga]Ga-DATA^{5m}.Pip.FAPi and [⁶⁸Ga]Ga-DATA^{5m}.Pyr-N-CH₃.FAPi, resulting in quantitative radiochemical yields after 15 min of complexation for 10, 15 and 20 nmol ligand concentrations at ambient temperature. [⁶⁸Ga]Ga-DATA^{5m}.NH-Pyr.FAPi, by contrast, showed low RCY with 10 and 15 nmol precursor concentrations. An adequate RCY of ≥ 90% after 15 min could be achieved with 20 nmol precursor amount. Nevertheless, the radiochemical conversion rates obviously seem to slightly depend on the way the DATA^{5m} chelator is linked to the spacer-FAPi component.

The *in vitro* stabilities in saline were very high for all four derivatives, ≥ 99% for [⁶⁸Ga]Ga-DATA^{5m}.NH.FAPi, [⁶⁸Ga]Ga-DATA^{5m}.Pip.FAPi and [⁶⁸Ga]Ga-DATA^{5m}.Pyr-N-CH₃.FAPi and ≥ 93% for [⁶⁸Ga]Ga-DATA^{5m}.NH-Pyr.FAPi. For -NH, -Pip and -Pyr-N-CH₃ linker units, stabilities in ethanol were also excellent with ≥ 99% intact conjugates after 2 h. The stability in EtOH for [⁶⁸Ga]Ga-DATA^{5m}.NH-Pyr.FAPi was less than the other respective complexes resulted in 79% after 2 h time. The situation in human serum was differing. [⁶⁸Ga]Ga-DATA^{5m}.Pip.FAPi had the best stability with ≥ 95%, next to [⁶⁸Ga]Ga-DATA^{5m}.NH.FAPi with ≥ 83% followed by [⁶⁸Ga]Ga-DATA^{5m}.Pyr-N-CH₃.FAPi ≥ 75% and lastly [⁶⁸Ga]Ga-DATA^{5m}.NH-Pyr.FAPi with ≥ 35% after 2 h period. While the stabilities for -NH, -Pip and -Pyr-N-CH₃ were sufficient, the stability of the -NH-Pyr complex was inadequate. In comparison, the stabilities in HS and NaCl for [⁶⁸Ga]Ga-DATA^{5m}.SA.FAPi were ≥ 99% intact conjugates and seem to have slightly better stability at least in human serum than the new DATA^{5m} derivatives [20].

Lipophilicity

The logD_{7.4} values of all ⁶⁸Ga-DATA^{5m} derivatives are similar. The lipophilicity is between -2.16 and -2.29. [⁶⁸Ga]Ga-DATA^{5m}.Pip.FAPi and [⁶⁸Ga]Ga-DATA^{5m}.SA.FAPi showed the most hydrophilic properties followed by [⁶⁸Ga]Ga-DATA^{5m}.NH-Pyr.FAPi, [⁶⁸Ga]Ga-DATA^{5m}.NH.FAPi and [⁶⁸Ga]Ga-DATA^{5m}.Pyr-N-CH₃.FAPi. The variation of the linker moiety seemed to have no influence in regard to lipophilicity. In comparison to [⁶⁸Ga]Ga-DOTA.SA.FAPi and [⁶⁸Ga]Ga-AAZTA⁵.SA.FAPi with logD values of -2.68 and -2.53, respectively [21], the ⁶⁸Ga-DATA^{5m} compounds displayed slightly more lipophilic characteristics. In coordination with gallium-68, the DOTA and AAZTA share one more free carboxyl group than the DATA chelator leading to a greater impact on hydrophilicity.

Materials and methods

General

Basic chemicals were purchased from Merck KGaA (Darmstadt, Germany), TCI Deutschland GmbH (Eschborn, Germany), Fisher Scientific GmbH (Schwerte, Germany), ABCR GmbH (Karlsruhe, Germany) VWR International GmbH (Darmstadt, Germany) and used without further purification. DATA^{5m}(^tBu)₃ was bought by ChiroBlock GmbH (Wolfen, Germany). (S)-6-(4-aminobutoxy)-N-(2-(2-cyano-4,4-difluoropyrrolidin-1-yl)-2-oxoethyl)-quinoline-4-carboxamide (NH₂-FAPi) was purchased from KE Biochem Co. (Shanghai, China). FAPI-04 was bought from MedChemTronica (Sollentuna, Sweden). Thin-layer chromatography (silica gel 60 F254 coated aluminum plates) were acquired from Merck KGaA (Darmstadt, Germany). LC/MS was measured on Agilent Technologies 1220 Infinity/Agilent Technologies 6130B Single Quadrupole. NMR measurements were performed at 400 MHz (400 MHz FT NMR spectrometer AC 400, Bruker Analytik GmbH). HPLC (High-performance liquid chromatography) on a 7000 series Hitachi LaChrom with a Hitachi L7100 pump, a L7400 UV-detector and a Phenomenex Synergi C18 (250 x 10 mm, 4 μ) and Synergi C18 (250 x 4.6 mm, 4 μ) column (Aschaffenburg, Germany) were used.

Organic Synthesis

Synthesis of DATA^{5m}.NH.FAPi

Di-tert-butyl-2,2'-(6-((2-(tert-butoxy)-2-oxoethyl)(methyl)amino)-6-(5-((4-((2-(2-cyano-4,4-difluoropyrrolidin-1-yl)-2-oxoethyl)carbamoyl)quinolin-6-yl)oxy)butyl)amino)-5-oxopentyl)-1,4-diazepane-1,4-diyl)(S)-diacetate (1)

DATA^{5m}(^tBu)₃ (22.3 mg, 0.04 mmol) was dissolved in 1 mL dry MeCN. HATU (22.2 mg, 0.06 mmol), HOBT (15.8 mg, 0.12 mmol) and DIPEA (20 μL, 0.12 mmol) were added to the solution and stirred for 30 minutes at RT. Afterwards, NH₂-FAPi (20.1 mg, 0.05 mmol) was added and the solution was stirred overnight at RT. After completion, the solvent was removed under vacuum and the residue (1) was used for further reaction without purification.

MS (ESI⁺): m/z = 493.4 [M+2H]²⁺, 985.5 [M+H]⁺, calculated for C₅₀H₇₄F₂N₈O₁₀: 984.6.

(S)-2,2'-(6-((carboxymethyl)(methyl)amino)-6-(5-((4-((4-((2-(2-cyano-4,4-difluoropyrrolidin-1-yl)-2-oxoethyl)carbonyl)quinolin-6-yl)oxy)butyl)amino)-5-oxopentyl)-1,4-diazepane-1,4-diyl)diacetic acid [DATA^{5m}.NH.FAPi] (2)

25 μ L TIPS and 25 μ L MilliQ H₂O was added to (1). Additionally, 950 μ L TFA was added and stirred for 5 h at RT. After completion, DCM was added to the solution and TFA/DCM was concentrated under vacuum. The residue was purified via HPLC (linear gradient 17-19% MeCN (+0.1% TFA)/ 83-81% H₂O (+0.1% TFA) in 20 min, 5 mL/min flow, 254 nm, t_R =14 min). After lyophilization, DATA^{5m}.NH.FAPi (2) was obtained as yellowish powder (12.8 mg, 0.02 mmol, 40 %).

MS (ESI⁺): m/z = 409.3 [M+2H]²⁺, 817.3 [M+H]⁺, calculated for C₃₈H₅₀F₂N₈O₁₀: 816.4.

Synthesis of DATA^{5m}.Pip.FAPi

Tert-butyl 4-(2-(benzyloxy)-2-oxoethyl)piperazine-1-carboxylate (3)

1-Boc-piperazine (158 mg, 0.85 mmol) was dissolved in 3 mL dry MeCN. DIPEA (217 μ L, 1.27 mmol) was added to the solution and stirred for 30 min at RT. Afterwards, benzyl bromoacetate (268 μ L, 1.70 mmol) was added and the solution was further stirred overnight at RT. After the reaction was complete, the solvent was concentrated under vacuum and the residue was purified via column chromatography (CHCl₃:MeOH, 20:1, R_f =0.3). The product (3) was obtained as a white solid (267 mg, 0.80 mmol, 94%).

¹H-NMR (CDCl₃, 400 MHz, δ [ppm]): 7.32-7.25 (m, 5 H); 5.08 (s, 2 H); 3.42 (t, J =5.1 Hz, 4H); 3.25 (s, 2H); 2.53 (t, J =5.1 Hz, 4H); 1.36 (s, 9H). MS (ESI⁺): m/z = 335.2 [M+H]⁺, calculated for C₁₈H₂₆N₂O₄: 334.2.

Benzyl 2-(piperazin-1-yl)acetate (4)

(3) (103 mg, 0.30 mmol) was solved in 800 μ L dry DCM and 200 μ L TFA. The reaction was completed after 3 h and DCM/TFA was removed under vacuum. The residue was used further without purification.

MS (ESI⁺): m/z = 235.1 [M+H]⁺, calculated for C₁₃H₁₈N₂O₂: 234.1.

Di-tert-butyl 2,2'-(6-(5-(4-(2-(benzyloxy)-2-oxoethyl)piperazin-1-yl)-5-oxopentyl)-6-((2-(tert-butoxy)-2-oxoethyl)(methyl)amino)-1,4-diazepane-1,4-diyl)diacetate (5)

DATA^{5m}(^tBu)₃ (69.7 mg, 0.12 mmol), HATU (70.0 mg, 0.18 mmol) and HOBt (49.5 mg, 0.37 mmol) were solved in 3 mL dry MeCN. DIPEA (62.4 μ L, 0.37 mmol) was added to the solution and stirred for 30 min at RT. After, (4) (81.8 mg, 0.24 mmol) was added and stirred overnight at RT. The solvent was

concentrated under vacuum and the residue was purified by column chromatography (CHCl₃:MeOH, 20:1, R_f=0.4). Compound (5) was received as a yellowish oil (80.4 mg, 0.10 mmol, 85%).

¹H-NMR (CDCl₃, 400 MHz, δ [ppm]): 7.37-7.32 (m, 5H); 5.16 (s, 2H); 3.65 (t, *J*=5.1 Hz, 3H); 3.47 (d, *J*=23.4 Hz, 4H); 3.26 (d, *J*=16.8 Hz, 5H); 2.80 (s, 5H); 2.67-2.44 (m, 6H); 2.29 (d, *J*=19.4 Hz, 4H); 1.51-1.48 (m, 13H); 1.45 (s, 22H). MS (ESI⁺): *m/z*= 394.8 [M+2H]²⁺, 788.5 [M+H]⁺, calculated for C₄₂H₆₉N₅O₉: 787.5.

2-(4-(5-(1,4-bis(2-(tert-butoxy)-2-oxoethyl)-6-((2-(tert-butoxy)-2-oxoethyl)(methyl)amino)-1,4-diazepan-6-yl)pentanoyl)piperazin-1-yl)acetic acid (6)

(5) (69.2 mg, 0.09 mmol) was dissolved in 3 mL dry MeOH. To the solution, catalytic amount of Pd on active charcoal 10 wt% was added. Subsequently, the flask was flushed under hydrogen atmosphere and stirred overnight at RT. The suspension was filtered through Celite and after the solvent was concentrated under vacuum. Product (6) was achieved as yellowish oil and used without further purification.

MS (ESI⁺): *m/z*= 349.8 [M+2H]²⁺, 698.4 [M+H]⁺, calculated for C₃₅H₆₃N₅O₉: 697.5.

(S)-2,2'-(6-((carboxymethyl)(methyl)amino)-6-(5-(4-(2-((4-((2-(2-cyano-4,4-difluoropyrrolidin-1-yl)-2-oxoethyl)carbamoyl)quinolin-6-yl)oxy)butyl)amino)-2-oxoethyl)piperazin-1-yl)-5-oxopentyl)-1,4-diazepane-1,4-diyl)diacetic acid [DATA^{5m}.Pip.FAPi] (7)

(6) (41.2 mg, 0.06 mmol), HATU (33.4 mg, 0.09 mmol) and HOBt (21.7 mg, 0.18 mmol) were solved in 2 mL dry MeCN. DIPEA (30.1 μL, 0.18 mmol) was added and stirred for 30 min at RT. Then, NH₂-FAPi (41.4 mg, 0.09 mmol) was added and the solution was stirred overnight. After completion and removing the solvent under reduced pressure, the residue was treated with TFA/TIPS/H₂O (95/2.5/2.5) and reacted for further 5 h. The solvent was concentrated and the residue was HPLC purified (linear gradient 15% MeCN (+0.1% TFA)/ 85% H₂O (+0.1% TFA) in 20 min, 5 mL/min flow, 254 nm, t_R=13 min). After lyophilization, DATA^{5m}.Pip.FAPi (7) was obtained as yellowish powder (16.1 mg, 0.02 mmol, 28%).

MS (ESI⁺): *m/z*= 472.8 [M+2H]²⁺, 943.4 [M+H]⁺, calculated for C₄₄H₆₀F₂N₁₀O₁₁: 942.4.

Synthesis of DATA^{5m}.Pyr-N-CH₃.FAPi

Tert-butyl (S)-3-((2-(benzyloxy)-2-oxoethyl)amino)pyrrolidine-1-carboxylate (8)

(S)-1-Boc-3-aminopyrrolidine (669 mg, 3.59 mmol) was dissolved in 4 mL dry MeCN. DIPEA (915 μL, 5.39 mmol) was admitted and the solution was stirred for 30 min at RT. Benzyl bromoacetate (898 μL, 5.68 mmol) was added and after 1 h the reaction was completed. The solvent was concentrated and

the residue was purified via column (CHCl₃:MeOH, 20:1, R_f=0.4). Product (8) was received as a yellowish oil (558 mg, 1.67 mmol, 46%).

¹H-NMR (CDCl₃, 400 MHz, δ [ppm]): 7.41-7.29 (m, 5H); 5.71 (s, 2H); 3.55-3.41 (m, 3H); 3.34 (p, J=5.6 Hz, 2H); 3.14 (ddd, J=31.2, 10.7, 4.7, 1H); 2.24 (s, 2H); 2.10-1.50 (m, 2H); 1.44 (s, 9H). MS (ESI⁺): m/z= 335.2 [M+H]⁺, calculated for C₁₈H₂₆N₂O₄: 334.2.

Tert-butyl (S)-3-((2-(benzyloxy)-2-oxoethyl)(methyl)amino)pyrrolidine-1-carboxylate (9)

(8) (155 mg, 0.46 mmol) was solved in 3 mL dry MeCN. Formaldehyde solution 37 wt% (128 μL, 4.64 mmol) and acetic acid (79.7 μL, 1.39 mmol) was added and stirred for 30 min at RT. Sodium borohydride (52.7 mg, 1.39 mmol) was admitted in portions to the solution and the suspension was stirred for 2 h. After the reaction was completed, 5 mL H₂O was added and the solution extracted 4-times with 5 mL CHCl₃ each. The collected organic phases were then extracted with 5 mL 1 M NaHCO₃ and dried with MgSO₄. The organic phase was reduced under vacuum and the residue purified with column chromatography (cyclohexane:ethylacetate, 2:1). (9) was obtained as yellowish solid (106 mg, 0.30 mmol, 66%).

¹H-NMR (CDCl₃, 400 MHz, δ [ppm]): 7.35 (d, J=3.9 Hz, 5H); 5.16 (t, J=1.8 Hz, 2H); 3.72-3.47 (m, 2H); 3.44-3.17 (m, 3H); 3.12 (d, J=9.1 Hz, 1H); 2.45 (s, 3H); 2.15-1.65 (m, 2H); 1.45 (s, 9H). MS (ESI⁺): m/z= 349.2 [M+H]⁺, calculated for C₁₉H₂₈N₂O₄: 348.2.

Benzyl (S)-N-methyl-N-(pyrrolidin-3-yl)glycinate (10)

(9) (92.8 mg, 0.27 mmol) was dissolved in 800 μL dry DCM and 200 μL TFA. The reaction was completed after 4 h and DCM/TFA was reduced under vacuum. The residue (10) was used further without purification.

MS (ESI⁺): m/z= 249.1 [M+H]⁺, calculated for C₁₄H₂₀N₂O₂: 248.2.

Di-tert-butyl 2,2'-(6-(5-(3-((2-(benzyloxy)-2-oxoethyl)(methyl)amino)pyrrolidin-1-yl)-5-oxopentyl)-6-((2-(tert-butoxy)-2-oxoethyl)(methyl)amino)-1,4-diazepane-1,4-diyl)(S)-diacetate (11)

DATA^{5m}(^tBu)₃ (69.2 mg, 0.12 mmol), HATU (92.2 mg, 0.24 mmol) and HOBt (49.0 mg, 0.36 mmol) were dissolved in 2 mL dry MeCN. DIPEA (81.7 μL, 0.48 mmol) was added to the solution and stirred for 30 min at RT. After (10) (85.1 mg, 0.24 mmol) was added, the solution was stirred further overnight. After completion, the solvent was concentrated and the residue was purified via column (CHCl₃:MeOH, 20:1, R_f=0.2). Substance (11) was attained as yellowish oil (81.5 mg, 0.10 mmol, 85%).

¹H-NMR (CHCl₃, 400 MHz, δ [ppm]): 7.39-7.31 (m, 5H); 5.18-5.12 (m, 2H); 3.87-3.08 (m, 6H); 2.80 (s, 4H); 2.43 (d, *J*=4.8 Hz, 4H); 2.37-1.49 (m, 8H); 1.46 (d, *J*=3.1 Hz, 29H); 1.43-1.21 (m, 12H). MS (ESI⁺): *m/z*= 401.9 [M+2H]²⁺, 802.5 [M+H]⁺, calculated for C₄₃H₇₁N₅O₉: 801.5.

(S)-N-(1-(5-(1,4-bis(2-(tert-butoxy)-2-oxoethyl)-6-((2-(tert-butoxy)-2-oxoethyl)(methyl)amino)-1,4-diazepan-6-yl)pentanoyl)pyrrolidin-3-yl)-N-methylglycine (12)

(11) (71.5 mg, 0.09 mmol) was dissolved in 3 mL dry MeOH. One spatula Pd/C was added and subsequently the flask was flushed with hydrogen. The suspension was stirred overnight at RT under hydrogen atmosphere and after completion, the suspension was filtered through Celite and the solvent concentrated under vacuum. Compound (12) was obtained as yellowish oil and used without further purification.

MS (ESI⁺): *m/z*= 356.9 [M+2H]²⁺, 712.5 [M+H]⁺, calculated for C₃₆H₆₅N₅O₉: 711.5.

2,2'-(6-((carboxymethyl)(methyl)amino)-6-(5-((S)-3-((2-((4-((4-((2-((S)-2-cyano-4,4-difluoropyrrolidin-1-yl)-2-oxoethyl)carbamoyl)quinolin-6-yl)oxy)butyl)amino)-2-oxoethyl)(methyl)amino)pyrrolidin-1-yl)-5-oxopentyl)-1,4-diazepane-1,4-diyl)diacetic acid [DATA^{5m}.Pyr-N-CH₃.FAPi] (13)

(12) (35.0 mg, 0.04 mmol), HATU (33.1 mg, 0.09 mmol) and HOBT (21.7 mg, 0.13 mmol) were dissolved in 2 mL dry MeCN. DIPEA (26.4 μL, 0.15 mmol) was added and stirred for 30 min at RT. Then, NH₂-FAPi (28.5 mg, 0.07 mmol) was added and the solution was stirred overnight. After completion and removing the solvent under reduced pressure, the residue was treated with 5 mL H₂O. The solution was extracted with each 5 mL ethyl acetate 5-times and the organic phases dried over MgSO₄. The solvent was removed under reduced pressure and the residue was treated with 50% TFA in DCM. After reaction of 3 h, TFA/DCM was concentrated and the residue was HPLC purified (linear gradient 15-17% MeCN (+0.1% TFA)/ 85-83% H₂O (+0.1% TFA) in 20 min, 5 mL/min flow, 254 nm, *t_R*=12 min). After lyophilization, DATA^{5m}.Pyr-N-CH₃.FAPi (13) was obtained as yellowish powder (9.5 mg, 0.01 mmol, 22%).

MS (ESI⁺): *m/z*= 319.9 [M+3H]³⁺, 479.3 [M+2H]²⁺, 957.4 [M+H]⁺, calculated for C₄₅H₆₂F₂N₁₀O₁₁: 956.5.

Synthesis of DATA^{5m}.NH-Pyr.FAPi

Benzyl-(S)-2-(3-((tert-butoxycarbonyl)amino)pyrrolidin-1-yl)acetate (14)

Tert-butyl-(*S*)-pyrrolidine-3-yl carbamate (563 mg, 3.02 mmol) was dissolved in 8 mL dry MeCN. DIPEA (770 μL, 4.54 mmol) was added and stirred for 30 min at RT. Benzyl bromoacetate (478 μL, 3.02 mmol)

was added and after 1 h the reaction was completed. The solvent was concentrated and the residue was purified via column (CHCl₃:MeOH, 30:1, R_f=0.4). Product (14) was received as a yellowish oil (912 mg, 2.73 mmol, 90%).

¹H-NMR (CDCl₃, 400 MHz, δ [ppm]): 7.41-7.28 (m, 5H); 5.16 (s, 2H); 4.20 (s, 1H), 3.40 (s, 2H); 3.01 (d, J=6.8 Hz, 1H); 2.78 (dd, J=14.6, 8.1 Hz, 2H); 2.50 (q, J=8.2 Hz, 1H); 2.38-2.12 (m, 1H); 1.68 (d, J=9.3 Hz, 1H); 1.43 (s, 9H). MS (ESI⁺): m/z= 335.2 [M+H]⁺, calculated for C₁₈H₂₆N₂O₄: 334.2.

Benzyl (S)-2-(3-aminopyrrolidin-1-yl)acetate (15)

(14) (150 mg, 0.45 mmol) was dissolved in 1.6 mL dry DCM and 500 μL TFA. The reaction was completed after 5 h and DCM/TFA was reduced under vacuum. The residue (15) was used further without purification.

MS (ESI⁺): m/z= 235.1 [M+H]⁺, calculated for C₁₃H₁₈N₂O₂: 234.1.

Di-tert-butyl 2,2'-(6-(5-((1-(2-(benzyloxy)-2-oxoethyl)pyrrolidin-3-yl)amino)-5-oxopentyl)-6-((2-(tert-butoxy)-2-oxoethyl)(methyl)amino)-1,4-diazepane-1,4-diyl)(S)-diacetate (16)

DATA^{5m}(^tBu)₃ (60.0 mg, 0.11 mmol), HATU (59.9 mg, 0.16 mmol) and HOBt (42.6 mg, 0.32 mmol) were dissolved in 2 mL dry MeCN. DIPEA (53.6 μL, 0.32 mmol) was added to the solution and stirred for 30 min at RT. After (15) (70.2 mg, 0.21 mmol) was added, the solution was stirred overnight at 30 °C. After completion, the solvent was concentrated and the residue was purified via column (CHCl₃:MeOH, 20:1, R_f=0.3). Compound (16) was attained as yellowish oil (63.0 mg, 0.08 mmol, 73%).

¹H-NMR (CDCl₃, 400 MHz, δ [ppm]): 7.37-7.31 (m, 5H); 5.13 (s, 2H); 3.67 (s, 2H), 3.44 (s, 2H); 3.30 (s, 4H); 3.02-2.71 (m, 6H); 2.51 (s, 3H); 2.28-2.12 (m, 3H); 1.74 (q, J=13.7, 9.7, 1H); 1.64-1.48 (m, 6H); 1.44 (d, J=1.8 Hz, 31H); 1.33-1.21 (m, 2H). MS (ESI⁺): m/z= 394.9 [M+2H]²⁺, 788.5 [M+H]⁺, calculated for C₄₂H₆₉N₅O₉: 787.5.

(S)-2-(3-(5-(1,4-bis(2-(tert-butoxy)-2-oxoethyl)-6-((2-(tert-butoxy)-2-oxoethyl)(methyl)amino)-1,4-diazepan-6-yl)pentanamido)pyrrolidin-1-yl)acetic acid (17)

(16) (63.0 mg, 0.08 mmol) was dissolved in 3 mL dry MeOH. Pd/C was added and the flask was flushed under hydrogen atmosphere. The suspension was stirred overnight at RT and after completion, the suspension was filtered through Celite and the solvent concentrated under vacuum. Compound (17) was obtained as yellowish oil and used without further purification.

MS (ESI⁺): m/z= 349.8 [M+2H]²⁺, 698.5 [M+H]⁺, calculated for C₃₅H₆₃N₅O₉: 697.5.

2,2'-(6-((carboxymethyl)(methyl)amino)-6-(5-(((S)-1-(2-((4-((4-((2-((S)-2-cyano-4,4-difluoropyrrolidin-1-yl)-2-oxoethyl)carbamoyl)quinolin-6-yl)oxy)butyl)amino)-2-oxoethyl)pyrrolidin-3-yl)amino)-5-oxopentyl)-1,4-diazepane-1,4-diyl)diacetic acid [DATA^{5m}.NH-Pyr.FAPi] (18)

(17) (25.0 mg, 0.03 mmol), HATU (23.9 mg, 0.06 mmol) and HOBt (12.8 mg, 0.09 mmol) were dissolved in 2 mL dry MeCN. DIPEA (16.2 μ L, 0.09 mmol) was added and stirred for 30 min at RT. NH₂-FAPi (20.7 mg, 0.05 mmol) was added and the solution was stirred overnight. After completion of the reaction, the solvent was concentrated under reduced pressure and the residue was treated with 1 mL TFA/TIPS/H₂O (95/2.5/2.5). After reaction of 4 h, the solvent was concentrated and the residue was HPLC purified (linear gradient 15-16% MeCN (+0.1% TFA)/ 85-84% H₂O (+0.1% TFA) in 20 min, 5 mL/min flow, 254 nm, t_R =14 min). After lyophilization, DATA^{5m}.NH-Pyr.FAPi (18) was obtained as yellowish powder (9.6 mg, 0.01 mmol, 34%).

MS (ESI⁺): m/z = 315.3 [M+3H]³⁺, 472.3 [M+2H]²⁺, 943.4 [M+H]⁺, calculated for C₄₄H₆₀F₂N₁₀O₁₁: 942.4.

Inhibition studies

Enzymes: A gateway-entry clone for human FAP was purchased from Dharmacon (Accession number DQ891423) and the human secretion signal was replaced with the HoneyBee mellitin secretion signal. For transfection and expression of FAP in Sf9 insect cells the C-terminal BaculoDirect kit from LifeTechnologies was used. The enzyme was purified from the supernatant of the insect cells using immobilized Ni-chelating chromatography (GE healthcare, Diegem, Belgium), followed by anion-exchange chromatography using a 1 mL HiTrap Q and size exclusion chromatography using the Superdex 200 column (GE healthcare, Diegem, Belgium). Human recombinant PREP was expressed in BL21(DE3) cells and purified using immobilized Co-chelating chromatography (GE healthcare), followed by anion-exchange chromatography on a 1 mL Mono Q column (GE healthcare).

IC₅₀ measurements: For FAP: IC₅₀ measurement of the probes was performed using Z-Gly-Pro-7-amino-4-methylcoumarine (AMC) as the substrate at a concentration of 50 μ M at pH 8 (0.05 M Tris-HCl buffer, with 0.1% glycerol, 1 mg/mL BSA and 140 mM NaCl). Eight concentrations of inhibitors/probe were tested. The final DMSO concentration was kept constant during the experiment to exclude any effects. Inhibitors were pre-incubated with the enzyme for 15 minutes at 37 °C, afterwards the substrate was added and the velocities of AMC release were measured kinetically at λ_{ex} = 380 nm, λ_{em} = 465 nm for at least 10 minutes at 37 °C. Measurements were executed on the Infinite 200 (Tecan Group Ltd.) and the Magellan software was used to process the data. For PREP: IC₅₀ measurements of the probes were carried out using N-succinyl-Gly-Pro-AMC as the substrate at a concentration of 250 μ M at pH 7.4 (0.1 M K-phosphate, 1 mM EDTA, 1 mM DTT and 1 mg/mL BSA). At least eight concentrations of

inhibitors were tested. The final DMSO concentration in kept constant during the experiment to exclude any effects. Inhibitors were pre-incubated with the enzyme for 15 minutes at 37 °C, afterwards the substrate was added and the velocities of AMC release were measured kinetically at $\lambda_{\text{ex}}= 380 \text{ nm}$, $\lambda_{\text{em}}= 465 \text{ nm}$ for at least 10 minutes at 37 °C. Measurements were done on the Infinite 200 (Tecan Group Ltd.) and the Magellan software was used to process the data.

⁶⁸Ga-Labeling and *in vitro* stability

⁶⁸Ge/⁶⁸Ga generator (ITG, Garching, Germany) was used to determine kinetics and stability studies. Gallium-68 was eluted with 0.05 M HCl trapped on a microchromatography CEX column AG 50W-X4 and purified via an ethanol post-processing, washed with 80% EtOH/0.15 M HCl and eluted with 90% EtOH/0.9 M HCl. Activity of gallium-68 was measured with a PC-based dose calibrator (ISOMED 2010, Nuklear Medizintechnik Dresden GmbH, Dresden, Germany). Reaction controls were performed with radio-TLC (0.1 M citrate buffer pH=4 and analytical radio-HPLC (7000 series Hitachi LaChrom, Phenomenex Luna C18 column (250 x 4.6 mm, 5 μ), linear gradient of 5-95% MeCN (+0.1% TFA)/ H₂O (+0.1% TFA), flow rate 1 mL/min in 10 min)). R-TLCs were measured by a TLC imager CR-35 Bio Test-Imager from Duerr-ndt (Bietigheim-Bissingen, Germany) and the software AIDA Elysia-Raytest (Straubenhardt, Germany).

⁶⁸Ga-Labeling was carried out with ~100 MBq. 300 μ L 1 M ammonium acetate buffer pH=5.5 was used with different precursor amounts (n=3 for each tracer), reacted in a thermoshaker at 30 °C. Aliquots were taken at 1, 3, 5, 10 and 15 minutes. Stabilities (n=3) were tested in 500 μ L human serum (human male AB plasma, USA origin), absolute ethanol (Merck KGaA, Darmstadt, Germany) and saline (0.9% isotone NaCl-solution, B. Braun Melsungen AG, Melsungen, Germany) using ~5 MBq of ⁶⁸Ga-tracer solution. Aliquots were taken at 30, 60 and 120 min.

Lipophilicity measurements

Lipophilicity was measured using the “shake-flask” method. The respective ⁶⁸Ga-FAPi tracer solution was adjusted to pH 7.4 with 2 M NaOH. ~5 MBq was taken from the solution and adjusted to a total volume of 700 μ L with PBS (n=4). 700 μ L 1-octanol was added to the PBS solution and stirred for 2 min (1500 rpm). Subsequently, each tube was centrifuged for 2 min. 400 μ L of the octanol- and PBS phases were abstracted into new tubes and aliquots of each phase (3 μ L of the PBS phase and 6 μ L of the octanol phase) were measured via radio-TLC. The PBS phases were adjusted up to 700 μ L and 700 μ L octanol was added to each tube. The whole procedure was repeated two times. LogD_{7.4} values were

calculated as the logarithm of the octanol/PBS ratio measured by a TLC imager CR-35 Bio Test-Imager from Duerr-ndt (Bietigheim-Bissingen, Germany) and the software AIDA Elysia-Raytest (Straubenhardt, Germany).

Conclusion

In this work, we designed the four new DATA^{5m} related FAPi small molecules, DATA^{5m}.NH.FAPi, DATA^{5m}.Pip.FAPi, DATA^{5m}.Pyr-N-CH₃.FAPi and DATA^{5m}.NH-Pyr.FAPi. The intention is to provide ⁶⁸Ga-labeled FAP inhibitors for PET/CT diagnoses, which can be labeled in an instant kit-type fashion at ambient temperatures similar to established ^{99m}Tc radiopharmaceuticals. Three compounds demonstrated promising characteristics in terms of ⁶⁸Ga-radiolabeling, lipophilicity, *in vitro* stability and inhibition properties for FAP and PREP. An exception is [⁶⁸Ga]Ga-DATA^{5m}.NH-Pyr.FAPi, which indicates an impact of the linker moiety arranged between the DATA^{5m} chelator and the FAPi targeting unit. Because the DATA^{5m}.NH.FAPi, DATA^{5m}.Pip.FAPi and DATA^{5m}.Pyr-N-CH₃.FAPi new agents all illustrate IC₅₀ values of 0.2–0.5 nmol, allow for almost quantitative ⁶⁸Ga radiolabeling at mild conditions, stay in hydrophilicity range of 2.1 (± 0.1) and are stable *in vitro*, they represent promising candidates for clinical application under instant kit-type conditions. *In vivo* evaluations will be reported soon.

Supplementary Materials: **Fig. S1** analytical-HPLC of DATA⁵.NH.FAPi with linear gradient condition of 10-95% MeCN (+0.1% TFA)/95-10% Water (+0.1% TFA) in 10 min, 1 mL/min flow, WL: 254 nm, Phenomenex Synergi C18 (250 x 4.6 mm, 4 μ) column.; **Fig. S2** analytical-HPLC of DATA⁵.Pip.FAPi with linear gradient condition of 10-95% MeCN (+0.1% TFA)/95-10% Water (+0.1% TFA) in 10 min, 1 mL/min flow, WL: 254 nm, Phenomenex Synergi C18 (250 x 4.6 mm, 4 μ) column.; **Fig. S3** analytical-HPLC of DATA⁵.Pyr-N-CH₃.FAPi with linear gradient condition of 10-95% MeCN (+0.1% TFA)/95-10% Water (+0.1% TFA) in 10 min, 1 mL/min flow, WL: 254 nm, Phenomenex Synergi C18 (250 x 4.6 mm, 4 μ) column.; **Fig. S4** analytical-HPLC of DATA⁵.NH-Pyr.FAPi with linear gradient condition of 10-95% MeCN (+0.1% TFA)/95-10% Water (+0.1% TFA) in 10 min, 1 mL/min flow, WL: 254 nm, Phenomenex Synergi C18 (250 x 4.6 mm, 4 μ) column.; **Fig. S5** radio-HPLCs of [⁶⁸Ga]Ga-DATA^{5m}.NH.FAPi a) after reaction of 15 min; stability measurements b) in ethanol after 1 h; c) in human serum; d) in saline. Linear gradient condition of 5-95% MeCN (+0.1% TFA)/95-5% Water (+0.1% TFA) in 10 min, 1 mL/min, Phenomenex Synergi C18 (250 x 4.6 mm, 4 μ) column.; **Fig. S6** radio-HPLCs of [⁶⁸Ga]Ga-DATA^{5m}.Pip.FAPi a) after reaction of 15 min; stability measurements b) in ethanol after 1 h; c) in human serum; d) in saline. Linear gradient condition of 5-95% MeCN (+0.1% TFA)/95-5% Water (+0.1% TFA) in 10 min, 1 mL/min, Phenomenex Synergi C18 (250 x 4.6 mm, 4 μ) column.; **Fig. S7** radio-HPLCs of [⁶⁸Ga]Ga-DATA^{5m}.Pyr-N-CH₃.FAPi a) after reaction of 15 min; stability measurements b) in ethanol after 1 h; c) in human serum; d) in saline. Linear gradient condition of 5-95% MeCN (+0.1% TFA)/95-5% Water (+0.1% TFA) in 10 min, 1 mL/min, Phenomenex Synergi C18 (250 x 4.6 mm, 4 μ) column.; **Fig. S8** radio-HPLCs of [⁶⁸Ga]Ga-DATA^{5m}.NH-Pyr.FAPi a) after reaction of 15 min; stability measurements b) in ethanol after 1 h; c) in human serum; d) in saline. Linear gradient condition of 5-95% MeCN (+0.1% TFA)/95-5% Water (+0.1% TFA) in 10 min, 1 mL/min, Phenomenex Synergi C18 (250 x 4.6 mm, 4 μ) column.

Declarations

Author Contributions: ESM did the conceptualization, preparative organic and radiochemical synthesis and validations, chemical separations, and analytics and wrote the manuscript. ■ carried out the *in vitro* inhibitory studies and ■ is responsible for the expression of FAP and PREP. ■ and ■ did the methodology, ■ was the project administrator and supervised the whole project.

Ethics approval and consent to participate: Not applicable

Consent for publication: Not applicable

Availability of data and materials: Contact corresponding author for reasonable data requests

Competing interests: No competing interests

Funding: This work was supported by the Fonds Wetenschappelijk Onderzoek Vlaanderen (FWO, Grant 1S64220N); ■ is a SB PhD fellow at FWO. This project also received funding from the Agentschap Innoveren en Ondernemen (VLAIO HCB 2019. 2446).

Acknowledgements: We thank ITM for providing us the ⁶⁸Ga-Generator.

References

1. Kalluri, R. The biology and function of fibroblasts in cancer. *Nat. Rev. Cancer* **2016**, *16*, 582–598, doi:10.1038/nrc.2016.73.
2. Chen, X.; Song, E. Turning foes to friends: targeting cancer-associated fibroblasts. *Nat. Rev. Drug Discov.* **2019**, *18*, 99–115, doi:10.1038/s41573-018-0004-1.
3. Brennen, W.N.; Isaacs, J.T.; Denmeade, S.R. Rationale behind targeting fibroblast activation protein-expressing carcinoma-associated fibroblasts as a novel chemotherapeutic strategy. *Mol. Cancer Ther.* **2012**, *11*, 257–266, doi:10.1158/1535-7163.MCT-11-0340.
4. Liu, T.; Zhou, L.; Li, D.; Andl, T.; Zhang, Y. Cancer-associated fibroblasts build and secure the tumor microenvironment. *Front. Cell Dev. Biol.* **2019**, *7*, 1–14, doi:10.3389/fcell.2019.00060.
5. Busek, P.; Mateu, R.; Zubal, M.; Kotackova, L.; Sedo, A. Targeting Fibroblast activation protein in cancer - Prospects and caveats. *Front. Biosci. - Landmark* **2018**, *23*, 1933–1968, doi:10.2741/4682.
6. Koustoulidou, S.; Hoorens, M.W.H.; Dalm, S.U.; Mahajan, S.; Debets, R.; Seimbille, Y.; de Jong, M. Cancer-associated fibroblasts as players in cancer development and progression and their role in targeted radionuclide imaging and therapy. *Cancers* **2021**, *13*, 1–19, doi:10.3390/cancers13051100.
7. Altmann, A.; Haberkorn, U.; Siveke, J. The Latest Developments in Imaging of Fibroblast Activation Protein. *J. Nucl. Med.* **2021**, *62*, 160–167, doi:10.2967/jnumed.120.244806.
8. Windisch, P.; Zwahlen, D.R.; Giesel, F.L.; Scholz, E.; Lugenbiel, P.; Debus, J.; Haberkorn, U.; Adeberg, S. Clinical results of fibroblast activation protein (FAP) specific PET for non-malignant indications: systematic review. *EJNMMI Res.* **2021**, *11*, doi:10.1186/s13550-021-00761-2.
9. Jansen, K.; Heirbaut, L.; Verkerk, R.; Cheng, J.D.; Joossens, J.; Cos, P.; Maes, L.; Lambeir, A.M.; De Meester, I.; Augustyns, K.; et al. Extended structure-activity relationship and pharmacokinetic investigation of (4-quinolinoyl)glycyl-2-cyanopyrrolidine inhibitors of fibroblast activation protein (FAP). *J. Med. Chem.* **2014**, *57*, 3053–3074, doi:10.1021/jm500031w.
10. Loktev, A.; Lindner, T.; Mier, W.; Debus, J.; Altmann, A.; Jaeger, D.; Giesel, F.; Kratochwil, C.; Barthe, P.; Roumestand, C.; et al. A Tumor-Imaging Method Targeting Cancer-Associated Fibroblasts. *J. Nucl. Med.* **2018**, *59*, 1423–1429, doi:10.2967/jnumed.118.210435.
11. Lindner, T.; Loktev, A.; Altmann, A.; Giesel, F.; Kratochwil, C.; Debus, J.; Jäger, D.; Mier, W.; Haberkorn, U. Development of Quinoline-Based Theranostic Ligands for the Targeting of Fibroblast Activation Protein. *J. Nucl. Med.* **2018**, *59*, 1415–1422, doi:10.2967/jnu-med.118.210443.
12. Loktev, A.; Lindner, T.; Burger, E.M.; Altmann, A.; Giesel, F.; Kratochwil, C.; Debus, J.; Marmé, F.; Jäger, D.; Mier, W.; et al. Development of fibroblast activation protein-targeted radiotracers with improved tumor retention. *J. Nucl. Med.* **2019**, *60*, 1421–1429, doi:10.2967/jnu-med.118.224469.
13. Altmann, A.; Haberkorn, U.; Siveke, J. The latest developments in imaging of fibroblast activation protein. *J. Nucl. Med.* **2021**, *62*, 160–167, doi:10.2967/jnumed.120.244806.
14. Windisch, P.; Zwahlen, D.R.; Giesel, F.L.; Scholz, E.; Lugenbiel, P.; Debus, J.; Haberkorn, U.;

- Adeberg, S. Clinical results of fibroblast activation protein (FAP) specific PET for non-malignant indications: systematic review. *EJNMMI Res.* **2021**, *11*, 18, doi:10.1186/s13550-021-00761-2.
15. Toms, J.; Kogler, J.; Maschauer, S.; Daniel, C.; Schmidkonz, C.; Kuwert, T.; Prante, O. Targeting Fibroblast Activation Protein: Radiosynthesis and Preclinical Evaluation of an ¹⁸F-labeled FAP Inhibitor. *J. Nucl. Med.* **2020**, *61*, 1806–1813, doi:10.2967/jnumed.120.242958.
 16. Giesel, F.L.; Adeberg, S.; Syed, M.; Lindner, T.; Jiménez-Franco, L.D.; Mavriopoulou, E.; Staudinger, F.; Tonndorf-Martini, E.; Regnery, S.; Rieken, S.; et al. FAPI-74 PET/CT Using Either ¹⁸F-AIF or Cold-Kit ⁶⁸Ga Labeling: Biodistribution, Radiation Dosimetry, and Tumor Delineation in Lung Cancer Patients. *J. Nucl. Med.* **2021**, *62*, 201–207, doi:10.2967/jnumed.120.245084.
 17. Watabe, T.; Liu, Y.; Kaneda-Nakashima, K.; Shirakami, Y.; Lindner, T.; Ooe, K.; Toyoshima, A.; Nagata, K.; Shimosegawa, E.; Haberkorn, U.; et al. Theranostics Targeting Fibroblast Activation Protein in the Tumor Stroma: ⁶⁴Cu- and ²²⁵Ac-Labeled FAPI-04 in Pancreatic Cancer Xenograft Mouse Models. *J. Nucl. Med.* **2020**, *61*, 563–569, doi:10.2967/jnumed.119.233122.
 18. Kratochwil, C.; Giesel, F.L.; Rathke, H.; Fink, R.; Dendl, K.; Debus, J.; Mier, W.; Jäger, D.; Lindner, T.; Haberkorn, U. [¹⁵³Sm]Samarium-labeled FAPI-46 radioligand therapy in a patient with lung metastases of a sarcoma. *Eur. J. Nucl. Med. Mol. Imaging* **2021**, *48*, 3011–3013, doi:10.1007/s00259-021-05273-8.
 19. Lindner, T.; Altmann, A.; Kraemer, S.; Kleist, C.; Loktev, A.; Kratochwil, C.; Giesel, F.; Mier, W.; Marme, F.; Debus, J.; et al. Design and development of ^{99m}Tc labeled FAPI-tracers for SPECT-imaging and ¹⁸⁸Re therapy. *J. Nucl. Med.* **2020**, *61*, 1507–1513, doi:10.2967/jnumed.119.239731.
 20. Moon, E.S.; Elvas, F.; Vliegen, G.; De Lombaerde, S.; Vangestel, C.; De Bruycker, S.; Bracke, A.; Eppard, E.; Greifenstein, G.; Klasen, B.; Kramer, V.; Staelens, S.; De Meester, I.; Van der Veken, P.; Roesch, F. Targeting fibroblast activation protein (FAP): next generation PET radiotracers using squaramide coupled bifunctional DOTA and DATA^{5m} chelators. *EJNMMI Radiopharm. Chem.* **2020**, *5*, 19, doi:10.1186/s41181-020-00102-z.
 21. Moon, E.S.; Rymentant, Y. Van; Battan, S.; Loose, J. De; Bracke, A.; Van der Veken, P.; De Meester, I.; Rösch, F. In Vitro Evaluation of the Squaramide-Conjugated Fibroblast Activation Protein Inhibitor-Based Agents AAZTA⁵.SA.FAPi and DOTA.SA.FAPi. *Molecules* **2021**, *26*, 3482, doi:10.3390/molecules26123482.
 22. Ballal, S.; Yadav, M.P.; Moon, E.S.; Kramer, V.S.; Roesch, F.; Kumari, S.; Tripathi, M.; ArunRaj, S.T.; Sarswat, S.; Bal, C. Biodistribution, pharmacokinetics, dosimetry of [⁶⁸Ga]Ga-DOTA.SA.FAPi, and the head-to-head comparison with [¹⁸F]F-FDG PET/CT in patients with various cancers. *Eur. J. Nucl. Med. Mol. Imaging* **2021**, *48*, 1915–1931, doi:10.1007/s00259-020-05132-y.
 23. Kreppel, B.; Gärtner, F.; Marinova, M.; Attenberger, U.; Meisenheimer, M.; Toma, M.; Kristiansen, G.; Feldmann, G.; Moon, E.; Roesch, F.; et al. [⁶⁸Ga]Ga-DOTA^{5m}.SA .FAPi PET/CT : Specific Tracer-uptake in Focal Nodular Hyperplasia and potential Role in Liver Tumor Imaging. *Nuklearmedizin* **2020**, *59*, 387–389, doi: 10.1055/a-1164-5667.
 24. Kreppel, B.; Gonzalez-carmona, M.A.; Feldmann, G.; Küppers, J.; Moon, E.S.; Marinova, M.; Gaertner, F.C. Fibroblast activation protein inhibitor (FAPi) positive tumour fraction on PET/CT correlates with Ki-67 in liver metastases of neuroendocrine tumours. *Nuklearmedizin* **2021**, *60*, 344–354, doi:10.1055/a-1521-8604.
 25. Waldron, B.P.; Parker, D.; Burchardt, C.; Yufit, D.S.; Zimny, M.; Roesch, F. Structure and stability of hexadentate complexes of ligands based on AAZTA for efficient PET labelling with gallium-68. *Chem. Commun.* **2013**, *49*, 579–581, doi:10.1039/c2cc37544c.

26. Parker, D.; Waldron, B.P. Conformational analysis and synthetic approaches to polydentate perhydro-diazepine ligands for the complexation of gallium(III). *Org. Biomol. Chem.* **2013**, *11*, 2827–2838, doi:10.1039/c3ob40287h.
27. Price, E.W.; Orvig, C. Matching chelators to radiometals for radiopharmaceuticals. *Chem. Soc. Rev.* **2014**, *43*, 260–290, doi:10.1039/c3cs60304k.
28. Farkas, E.; Nagel, J.; Waldron, B.P.; Parker, D.; Tóth, I.; Brücher, E.; Rösch, F.; Baranyai, Z. Equilibrium, Kinetic and Structural Properties of Gallium(III) and Some Divalent Metal Complexes Formed with the New DATA^m and DATA^{5m} Ligands. *Chem. - A Eur. J.* **2017**, *23*, 10358–10371, doi:10.1002/chem.201701508.
29. Seemann, J.; Waldron, B.P.; Roesch, F.; Parker, D. Approaching “kit-type” labelling with ⁶⁸Ga: The DATA chelators. *ChemMedChem* **2015**, *10*, 1019–1026, doi:10.1002/cmdc.201500092.
30. Seemann, J.; Eppard, E.; Waldron, B.P.; Ross, T.L.; Roesch, F. Cation exchange-based post-processing of ⁶⁸Ga-eluate: A comparison of three solvent systems for labelling of DOTATOC, NO2APBP and DATA^m. *Appl. Radiat. Isot.* **2015**, *98*, 54–59, doi:10.1016/j.apradiso.2015.01.023.
31. Seemann, J.; Waldron, B.; Parker, D.; Roesch, F. DATATOC: a novel conjugate for kit-type ⁶⁸Ga labelling of TOC at ambient temperature. *EJNMMI Radiopharm. Chem.* **2017**, *1*, 4, doi:10.1186/s41181-016-0007-3.
32. Nock, B.A.; Kaloudi, A.; Nagel, J.; Sinnes, J.P.; Roesch, F.; Maina, T. Novel bifunctional DATA chelator for quick access to site-directed PET ⁶⁸Ga-radiotracers: Preclinical proof-of-principle with [Tyr³]octreotide. *Dalt. Trans.* **2017**, *46*, 14584–14590, doi:10.1039/c7dt01684k.
33. Sinnes, J.P.; Nagel, J.; Waldron, B.P.; Maina, T.; Nock, B.A.; Bergmann, R.K.; Ullrich, M.; Pietzsch, J.; Bachmann, M.; Baum, R.P.; et al. Instant kit preparation of ⁶⁸Ga-radiopharmaceuticals via the hybrid chelator DATA: clinical translation of [⁶⁸Ga]Ga-DATA-TOC. *EJNMMI Res.* **2019**, *9*, 48, doi:10.1186/s13550-019-0516-7.
34. Gaertner, F.C.; Plum, T.; Kreppel, B.; Eppard, E.; Meisenheimer, M.; Strunk, H.; Bundschuh, R.A.; Sinnes, J.P.; Rösch, F.; Essler, M. Clinical evaluation of [⁶⁸Ga]Ga-DATA-TOC in comparison to [⁶⁸Ga]Ga-DOTA-TOC in patients with neuroendocrine tumours. *Nucl. Med. Biol.* **2019**, *76–77*, 1–9, doi:10.1016/j.nucmedbio.2019.08.006.
35. Yadav, D.; Ballal, S.; Yadav, M.P.; Tripathi, M.; Roesch, F.; Bal, C. Evaluation of [⁶⁸Ga]Ga-DATA-TOC for imaging of neuroendocrine tumours: comparison with [⁶⁸Ga]Ga-DOTA-NOC PET/CT. *Eur. J. Nucl. Med. Mol. Imaging* **2020**, *47*, 860–869, doi:10.1007/s00259-019-04611-1.

Supporting Information

Preparative Synthesis

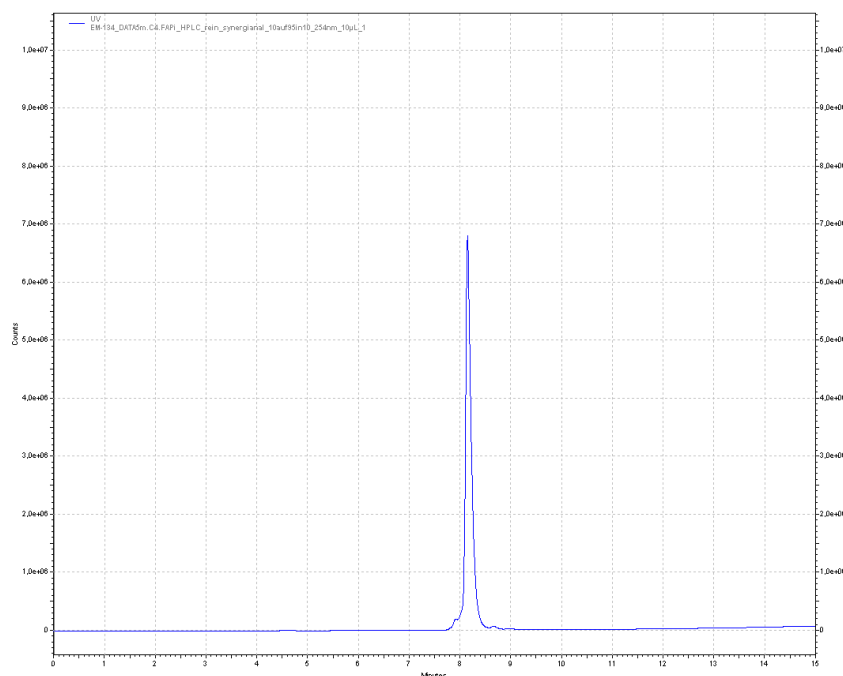


Fig. S1 analytical-HPLC of DATA⁵.NH.FAPi with linear gradient condition of 10-95% MeCN (+0.1% TFA)/95-10% Water (+0.1% TFA) in 10 min, 1 mL/min flow, WL: 254 nm, Phenomenex Synergi C18 (250 x 4.6 mm, 4 μ) column.

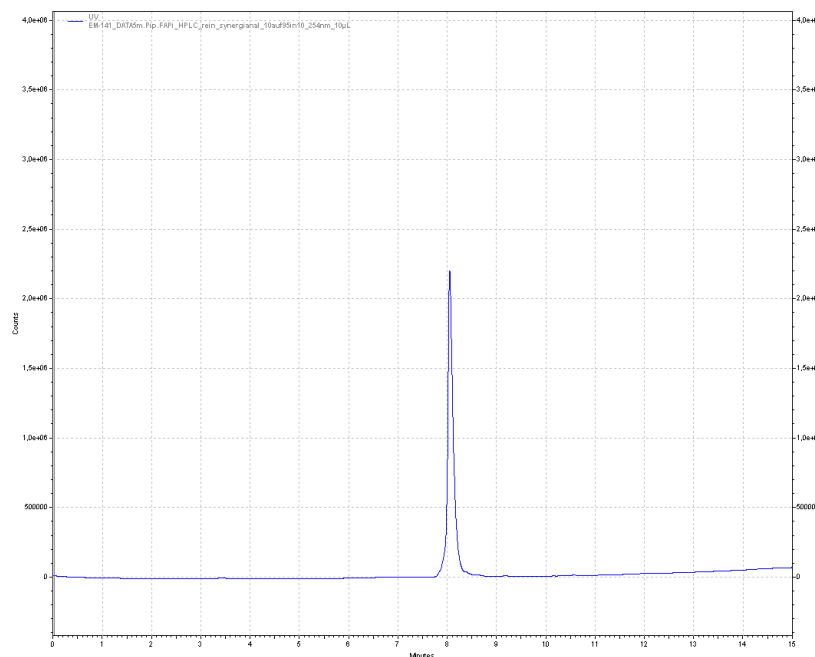


Fig. S2 analytical-HPLC of DATA⁵.Pip.FAPi with linear gradient condition of 10-95% MeCN (+0.1% TFA)/95-10% Water (+0.1% TFA) in 10 min, 1 mL/min flow, WL: 254 nm, Phenomenex Synergi C18 (250 x 4.6 mm, 4 μ) column.

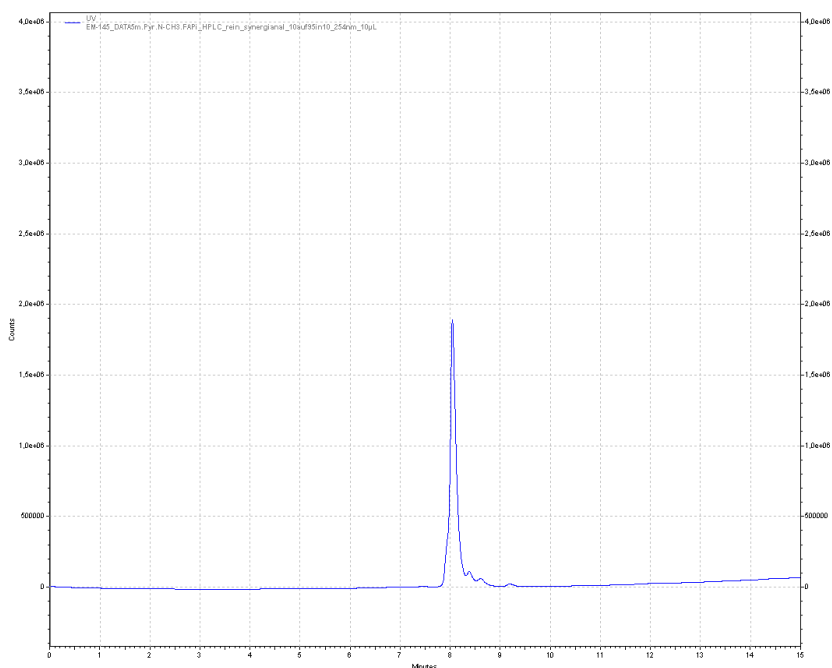


Fig. S3 analytical-HPLC of DATA⁵.Pyr-N-CH₃.FAPi with linear gradient condition of 10-95% MeCN (+0.1% TFA)/95-10% Water (+0.1% TFA) in 10 min, 1 mL/min flow, WL: 254 nm, Phenomenex Synergi C18 (250 x 4.6 mm, 4 μ) column.

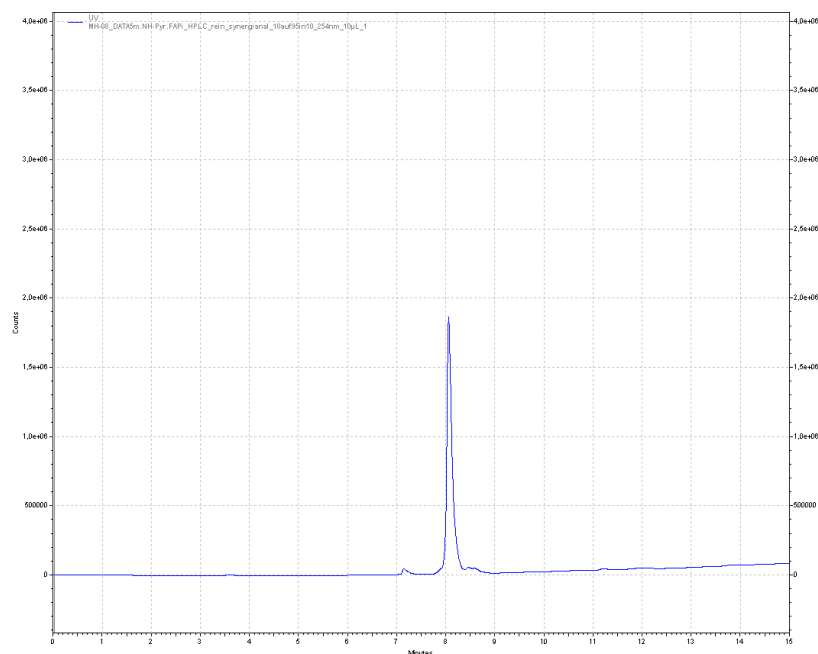


Fig. S4 analytical-HPLC of DATA⁵.NH-Pyr.FAPi with linear gradient condition of 10-95% MeCN (+0.1% TFA)/95-10% Water (+0.1% TFA) in 10 min, 1 mL/min flow, WL: 254 nm, Phenomenex Synergi C18 (250 x 4.6 mm, 4 μ) column.

Radiolabeling

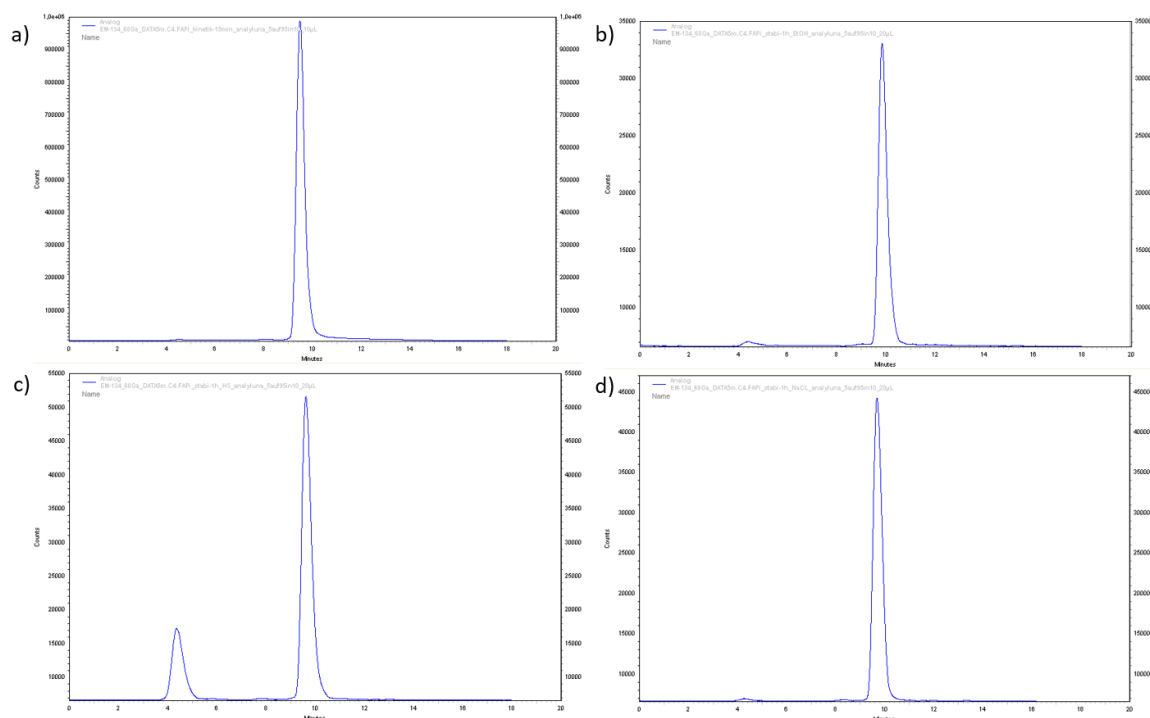


Fig. S5 radio-HPLCs of $[^{68}\text{Ga}]\text{Ga-DATA}^{5\text{m}}.\text{NH.FAPi}$ a) after reaction of 15 min; stability measurements b) in ethanol after 1 h; c) in human serum; d) in saline. Linear gradient condition of 5-95 % MeCN (+0.1% TFA)/95-5% Water (+0.1% TFA) in 10 min, 1 mL/min, Phenomenex Synergi C18 (250 x 4.6 mm, 4 μ) column.

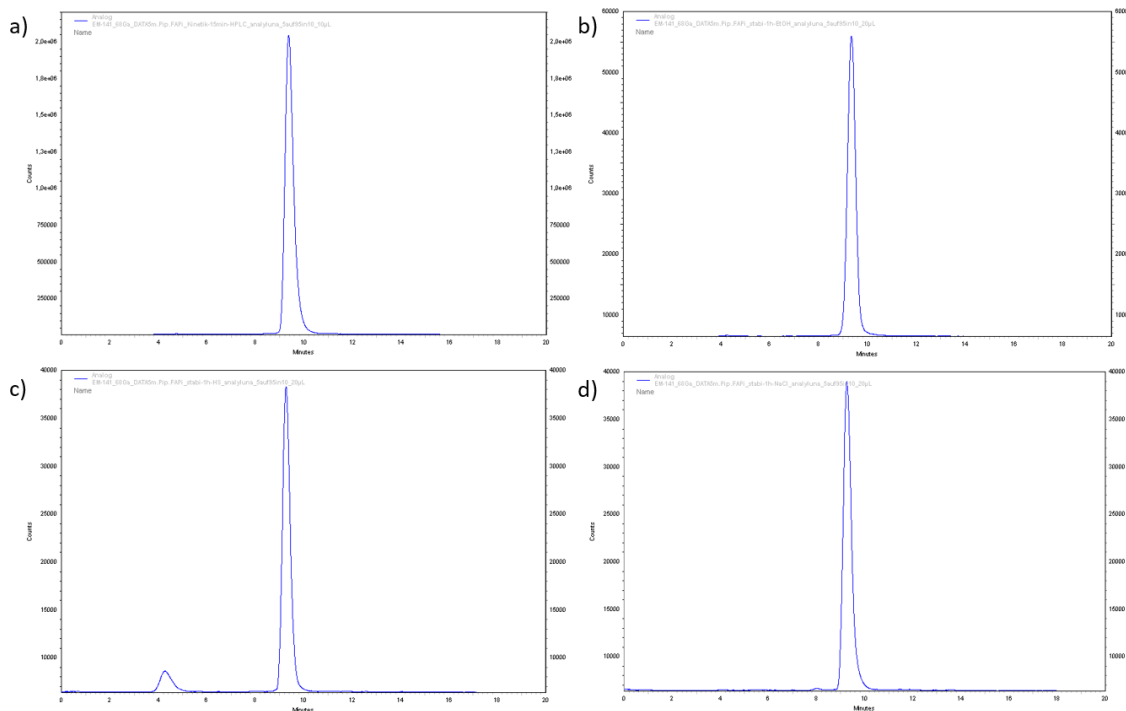


Fig. S6 radio-HPLCs of $[^{68}\text{Ga}]\text{Ga-DATA}^{5\text{m}}.\text{Pip.FAPi}$ a) after reaction of 15 min; stability measurements b) in ethanol after 1 h; c) in human serum; d) in saline. Linear gradient condition of 5-95% MeCN (+0.1 % TFA)/95-5% Water (+0.1% TFA) in 10 min, 1 mL/min, Phenomenex Synergi C18 (250 x 4.6 mm, 4 μ) column.

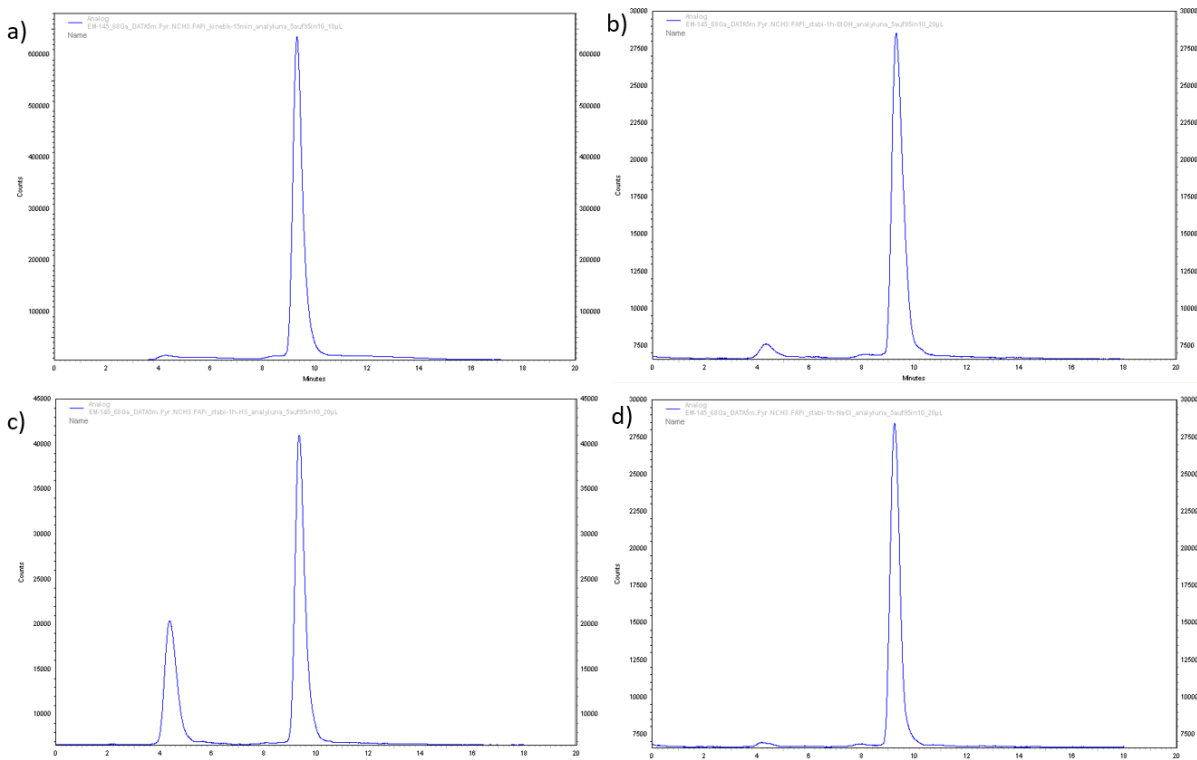


Fig. S7 radio-HPLCs of $[^{68}\text{Ga}]\text{Ga-DATA}^{5\text{m}}.\text{Pyr-N-CH}_3.\text{FAPi}$ a) after reaction of 15 min; stability measurements b) in ethanol after 1 h; c) in human serum; d) in saline. Linear gradient condition of 5-95% MeCN (+0.1% TFA)/95-5% Water (+0.1% TFA) in 10 min, 1 mL/min, Phenomenex Synergi C18 (250 x 4.6 mm, 4 μ) column.

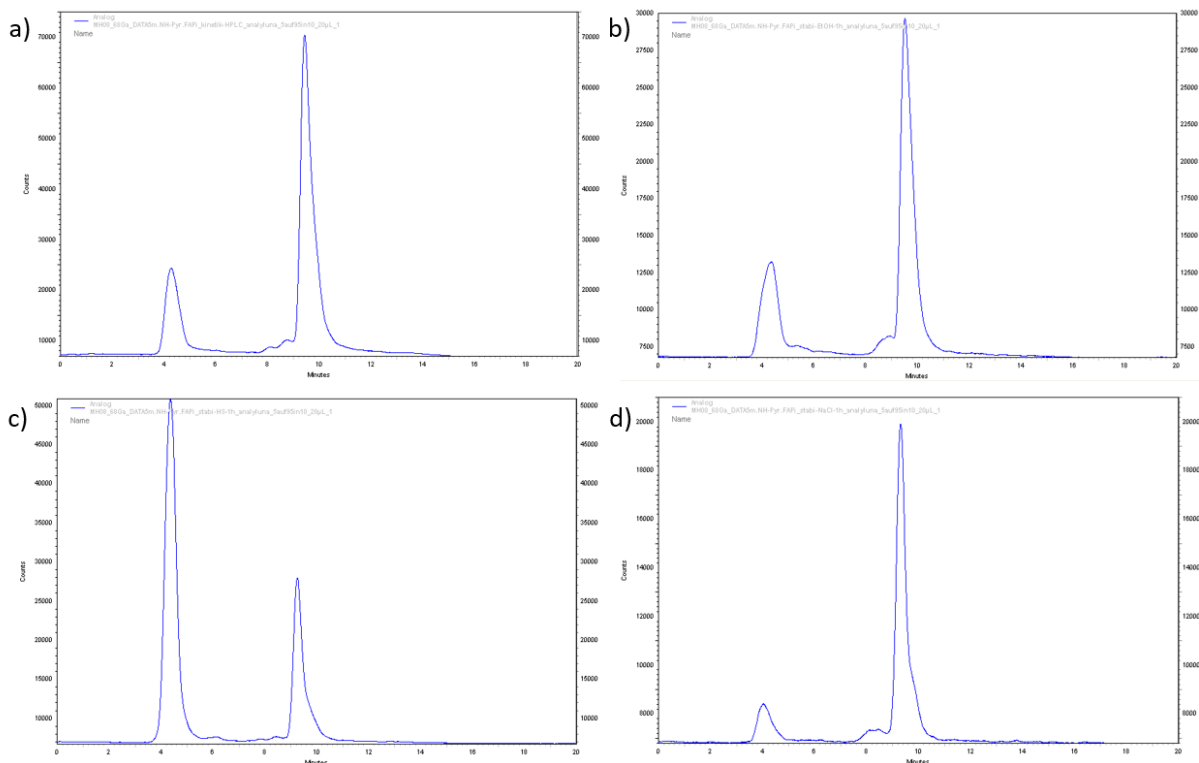


Fig. S8 radio-HPLCs of $[^{68}\text{Ga}]\text{Ga-DATA}^{5\text{m}}.\text{NH-Pyr.FAPi}$ a) after reaction of 15 min; stability measurements b) in ethanol after 1 h; c) in human serum; d) in saline. Linear gradient condition of 5-95% MeCN (+0.1% TFA)/95-5% Water (+0.1% TFA) in 10 min, 1 mL/min, Phenomenex Synergi C18 (250 x 4.6 mm, 4 μ) column.

4. Zusammenfassung und Ausblick

Das Fibroblasten-Aktivierungsprotein (FAP) als Target zur molekularen Bildgebung sowie zur therapeutischen Anwendung erlangt immer mehr Interesse und Bedeutung in der heutigen Nuklearmedizin. Als CAF (cancer-associated-fibroblasts)-Marker sind FAP⁺-CAFs im Tumorstroma in über 90% der humanen Epithelkarzinome überexprimiert und wiederum in dem meisten gesunden Gewebe so gut wie nicht anwesend. Das Tumorstroma kann unter Umständen den überwiegenden Anteil (bis zu 90%) der Tumormasse ausmachen. Da CAFs als wesentlicher Bestandteil im Tumorstroma vorzufinden sind, eignet sich das FAP besonders gut als biologisch aktives Zielmolekül für die nuklearmedizinische Theranostik.

In der vorliegenden Arbeit wurden, basierend auf dem hochaffinen und selektiven FAP-Inhibitor (FAPi) UAMC1110, verschiedene bifunktionelle Chelator-Linker-FAPi-Systeme synthetisiert und anschließend auf die radiochemischen und pharmakologischen Eigenschaften hin untersucht. Im Folgenden werden die einzelnen Hauptabschnitte der vorliegenden Arbeit näher erläutert.

Hauptabschnitt A

Dieses Kapitel umfasste die FAP adressierenden Radiopharmaka DOTA.SA.FAPi und DATA^{5m}.SA.FAPi. Die Chelatoren DOTA und DATA^{5m} sind über einen Quadratsäureamid-Linker mit dem FAPi verknüpft. Der makrozyklische DOTA Chelator ist als „Gold-Standard“ in der Nuklearmedizin in vielen Chelator-basierten Radiopharmaka vorzufinden. Die Quadratsäure (squaric acid, SA) als Linkereinheit bietet in präparativer Hinsicht den Vorteil einer einfachen Kopplung an verfügbare, freie Amine. Durch deren Selektivität gegenüber primären Aminen kann eine etwaige Schützung von Carboxylgruppen vernachlässigt werden und durch die pH-kontrollierte, sukzessive Amidierung wird eine zielgerichtete Anbindung an beide Esterseiten des Quadratsäurediethylesters ermöglicht. Weiterhin konnten in vorherigen Arbeiten pharmakologisch positive Einflüsse mit der Quadratsäure als Linkereinheit festgestellt werden [1,2]. Unter anderem zeigten die Quadratsäureamid-konjugierten PSMA-Derivate [⁶⁸Ga]Ga-NODAGA.SA.PSMA, [⁶⁸Ga]Ga-TRAM.SA.PSMA und [⁶⁸Ga]Ga-DOTAGA.SA.PSMA in präklinischen Studien vergleichbar gute Ergebnisse wie [⁶⁸Ga]Ga-PSMA-617 und [⁶⁸Ga]Ga-PSMA-11.

Im Rahmen des Projekts A „*Targeting fibroblast activation protein (FAP): next generation PET radiotracers using squaramide coupled bifunctional DOTA and DATA^{5m} chelators*“ wurden die zwei Chelator-SA-basierten FAPi-Derivate DATA^{5m}.SA.FAPi und DOTA.SA.FAPi synthetisiert. DOTA.SA.FAPi wurde ausgehend von DO3A^tBu-N-(2-aminoethyl) ethanamid in drei Stufen erfolgreich hergestellt. Für die Synthese von DATA^{5m}.SA.FAPi wurde zunächst der geschützte, bifunktionelle Chelator DATA^{5m}-^tBu₃ in fünf Stufen hergestellt. Die Bindung über eine Ethylendiaminbrücke an den Quadratsäurediethylester und die anschließende Verknüpfung an den FAP-Inhibitor wurde in weiteren drei Stufen realisiert.

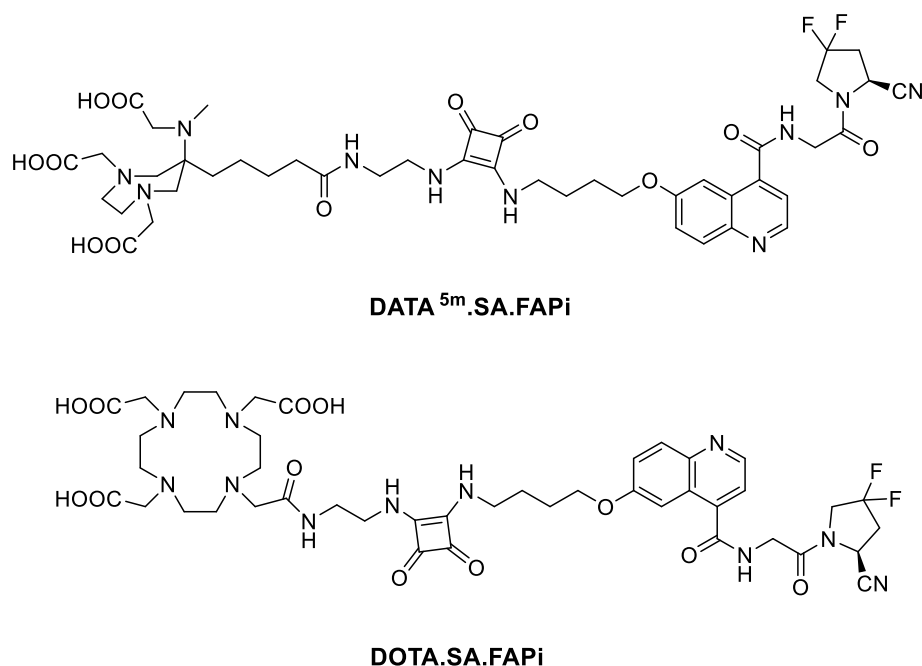


Abbildung 17: Strukturen von DATA^{5m}.SA.FAPi und DOTA.SA.FAPi

In radiochemischen Untersuchungen zeigten die beiden Vorläufer DOTA.SA.FAPi und DATA^{5m}.SA.FAPi schon nach 5 – 10 Minuten sehr gute, quantitative Komplexierungen mit dem Radiometall ⁶⁸Ga. Das [⁶⁸Ga]Ga-DATA^{5m}-Derivat erreichte vollständige radiochemische Umsätze (RCU) bereits bei Raumtemperatur, wohingegen der [⁶⁸Ga]Ga-DOTA-Komplex Temperaturen von 80 °C bis 95 °C benötigte. Beide Komplexe zeigten hohe Stabilitäten von > 95% nach zweistündiger Inkubation in den Medien HS, EtOH und isot. NaCl bei 37 °C.

In Affinitätsstudien zeigten DATA^{5m}.SA.FAPi und DOTA.SA.FAPi sowie deren ^{nat}Ga- und ^{nat}Lu-Komplexe eine sehr hohe Inhibitionseffizienz für FAP, resultierend in IC₅₀-Werten von 0,7 – 1,4 nM (Tabelle 3). Dazu konnte die Selektivität für FAP bestätigt werden, da die IC₅₀-Werte der Derivate gegenüber der Prolylendopeptidase PREP in µM-Bereichen (1,7 – 8,7 µM) lagen und dadurch hohe FAP zu PREP-Verhältnisse vorliegen. Zusätzlich zeigten alle gemessenen Verbindungen ähnlich gute Inhibitionswerte im Vergleich zum UAMC1110 FAP-Inhibitor selbst (FAP: 0,43 nM; PREP: 1,8 µM).

Tabelle 3: Affinitätsstudien für FAP und PREP: IC₅₀-Werte für DOTA.SA.FAPi und DATA^{5m}.SA.FAPi, sowie deren ^{nat}Ga bzw. ^{nat}Lu-Komplexe.

Verbindungen	IC ₅₀ FAP (nM)	IC ₅₀ PREP (μM)
DOTA.SA.FAPi	0.9 ± 0.1	5.4 ± 0.3
[^{nat} Ga]Ga-DOTA.SA.FAPi	1.4 ± 0.2	8.7 ± 0.9
[^{nat} Lu]Lu-DOTA.SA.FAPi	0.8 ± 0.2	2.5 ± 0.4
DATA ^{5m} .SA.FAPi	0.8 ± 0.2	1.7 ± 0.1
[^{nat} Ga]Ga-DATA ^{5m} .SA.FAPi	0.7 ± 0.1	4.7 ± 0.3
UAMC1110	0.43 ± 0.07	1.8 ± 0.2

Das [⁶⁸Ga]Ga-DOTA.SA.FAPi wurde in einer ersten präklinischen Tierstudie mit HT-29-Kolonkarzinom tragenden Tumormäusen untersucht. Die Tumoranreicherung war deutlich erkennbar und 60 min nach Injektion höher als die Anreicherung in allen anderen Organen (Abbildung 18). Die *ex vivo*-Biodistribution zeigte eine Tumoranreicherung von 5,2% ID/g und ein insgesamt gutes Tumor-zu-Organ-Verhältnis wie z.B. Tumor-zu-Blut (9,2 ± 1,1), Tumor-zu-Dickdarm (24,9 ± 1,7) und Tumor-zu-Muskel (11,5 ± 2,2).

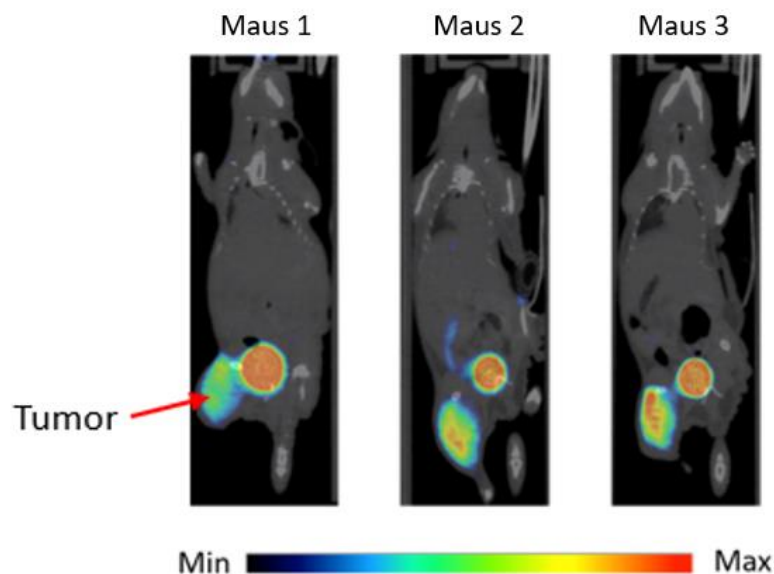


Abbildung 18: [⁶⁸Ga]Ga-DOTA.SA.FAPi-Anreicherung in HT-29 xenotransplantierten Tumormäusen (coronal PET/CT Aufnahmen (MIP)) 60 min nach Injektion.

Die erfolgreichen *in vitro*- und präklinischen Studien ermöglichten weitere klinische Anwendungen. Mit Kooperationspartnern aus Bonn und New Delhi konnten beide Radiotracer in humanen *in vivo*-Studien untersucht werden.

Im Abschnitt A.1. “[⁶⁸Ga]Ga-DATA^{5m}.SA.FAPi PET/CT: Specific Tracer-uptake in Focal Nodular Hyperplasia and potential Role in Liver Tumor Imaging“ wurde ein Fallbeispiel mit einer 44-jährigen Patientin mittels [⁶⁸Ga]Ga-DATA^{5m}.SA.FAPi-PET/CT diskutiert, wobei sich eine spezifische Aufnahme in fokaler nodulärer Hyperplasia zeigte.

In der klinischen Untersuchung A.2. “Fibroblast activation protein inhibitor (FAPi) positive tumour fraction on PET/CT correlates with Ki-67 in liver metastases of neuroendocrine tumours“ konnte in Patienten mit lebermetastasierenden neuroendokrinen Tumoren eine signifikante Korrelation zwischen FAPi-positiven Tumorfraktionen und Ki-67-Expression festgestellt werden (Abbildung 19). Die Korrelation war erheblicher als die von [¹⁸F]FDG mit Ki-67. Weiterhin konnte eine deutliche Korrelation zwischen FAPi-PET positiven Tumorumfängen und Ki-67 gemessen werden, welche bei [¹⁸F]FDG und [⁶⁸Ga]Ga-DOTATOC nicht festgestellt werden konnte. Das Indiz von einem positiven Verhältnis zwischen FAPi_{VOL} zu DOTATOC_{VOL} könnte für weitere Untersuchungen, auch hinsichtlich Therapie, ein wichtiger Anhaltspunkt sein.

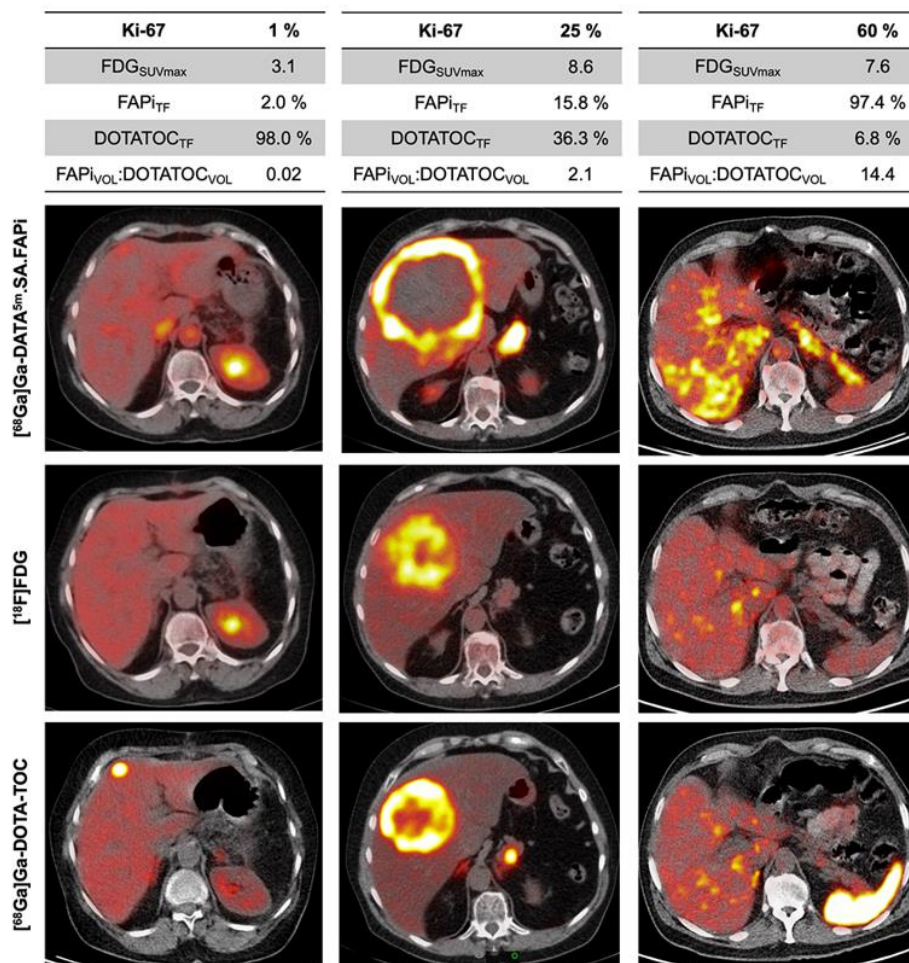


Abbildung 19: PET/CT Aufnahmen mit für [⁶⁸Ga]Ga-DATA^{5m}.SA.FAPi, [⁶⁸Ga]Ga-DOTA-TOC und [¹⁸F]FDG bei geringer (links), mittlerer (mitte) und hoher (rechts) Ki-67-Expression.

Im Abschnitt A.3. *“Biodistribution, pharmacokinetics, dosimetry of $[^{68}\text{Ga}]\text{Ga-DOTA.SA.FAPi}$, and the head-to-head comparison with $[^{18}\text{F}]\text{F-FDG}$ PET/CT in patients with various cancers”* wurde $[^{68}\text{Ga}]\text{Ga-DOTA.SA.FAPi}$ mittels PET/CT klinisch evaluiert. 54 Patienten mit 14 verschiedenen Krebsarten wurde $[^{68}\text{Ga}]\text{Ga-DOTA.SA.FAPi}$ injiziert und die Organverteilung, Pharmakokinetik sowie Dosimetrie im Vergleich mit $[^{18}\text{F}]\text{F-FDG}$ analysiert. Dosimetrie und Organverteilung wurden repräsentativ anhand von drei Patienten (zwei mit Brustkrebs und einem mit Lungenkrebs) untersucht (Abbildung 20). Die Tumoranreicherung von $[^{68}\text{Ga}]\text{Ga-DOTA.SA.FAPi}$ im primären Tumor und in Metastasen war sehr schnell und bereits 10 min nach Injektion bis hin zu 3 Stunden detektierbar. Physiologische Anreicherung konnte u.a. in Bauchspeicheldrüse, Leber, Herz, Milz, Nieren, Harnblase und Speicheldrüse gefunden werden. Die Ausscheidung des Radiotracers aus den gesunden Organen und dem gesamten Körper erfolgte schnell.

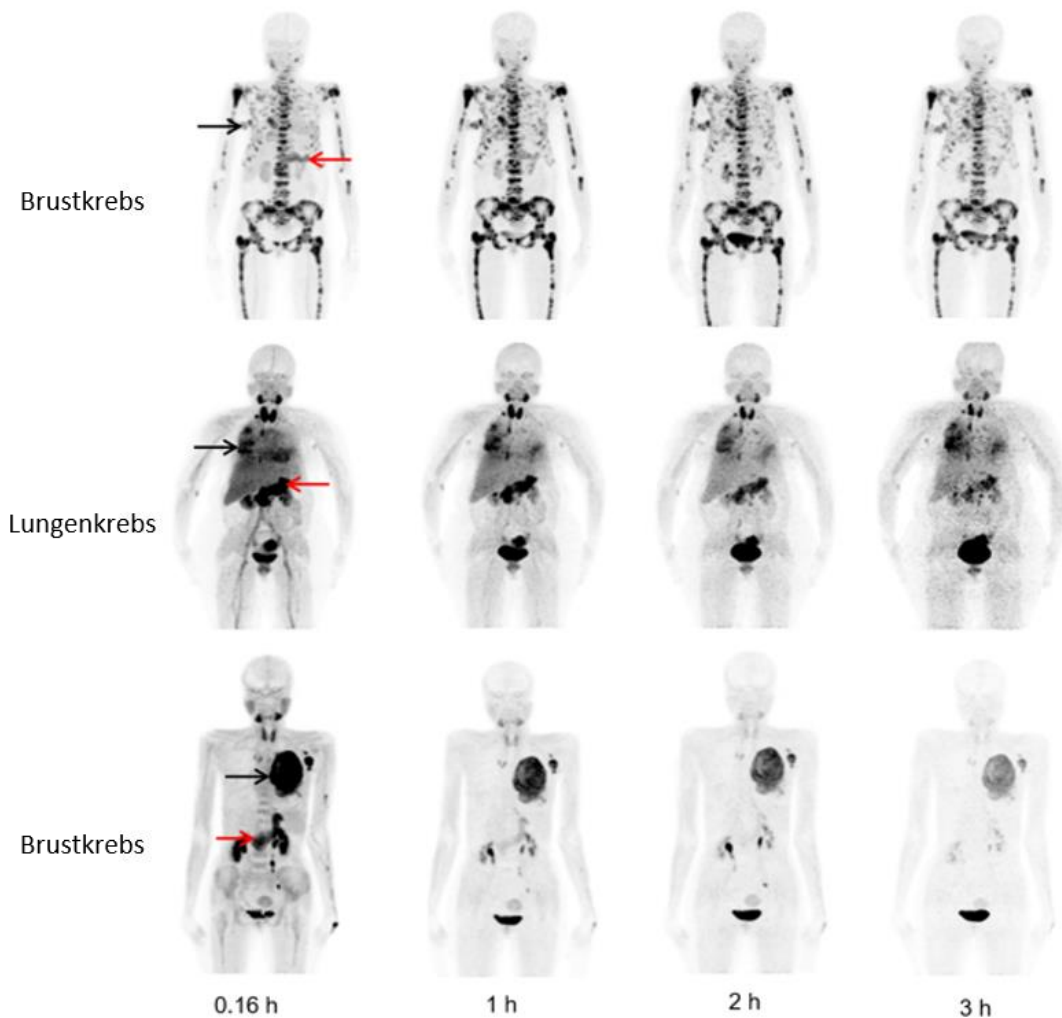


Abbildung 20: Organverteilung von $[^{68}\text{Ga}]\text{Ga-DOTA.SA.FAPi}$ zu bestimmten Zeitpunkten bei zwei Brustkrebs- und einem Lungenkrebspatienten; primäre Läsionen (schwarzer Pfeil) und Metastasen (Lymphknoten, Leber und Knochen). Unspezifische Anreicherung in der Bauchspeicheldrüse (roter Pfeil) und Speicheldrüsen.

Allgemein konnte in den primären Tumoren und Metastasen aller Patienten eine hohe Anreicherung des FAPi-Radiotracers festgestellt werden, immer in Übereinstimmung mit [^{18}F]FDG. Der höchste Tumoruptake von [^{68}Ga]Ga-DOTA.SA.FAPi konnte bei Hals- und Nackenkrebepatienten mit einem SUL-Wert > 10 , SUL-Werte mit mind. > 5 konnten bei allen anderen Patienten beobachtet werden.

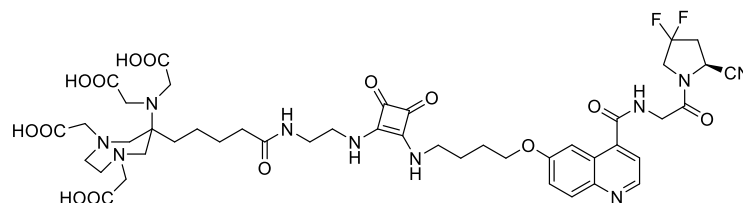
Sowohl die guten *in vitro*-, als auch die ersten präklinischen und klinischen *in vivo*-Anwendungen zeigten hohe FAP-Selektivitäten und Anreicherungen in verschiedenen Tumorarten für die Chelator-SA-FAPi-Konjugate DOTA.SA.FAPi und DATA^{5m}.SA.FAPi und ermöglichen die potenzielle Anwendung in der Diagnostik mittels ^{68}Ga -PET/CT als FAP-adressierende Radiopharmaka.

Hauptabschnitt B

Im Rahmen des Projekts B *“In Vitro Evaluation of the Squaramide-Conjugated Fibroblast Activation Protein Inhibitor-Based Agents AAZTA⁵.SA.FAPi and DOTA.SA.FAPi”* wurde das AAZTA⁵.SA.FAPi Derivat hergestellt und hinsichtlich seiner *in vitro*-Eigenschaften untersucht.

Der AAZTA-Chelator teilt das gleiche Grundgerüst des DATA-Chelators, besitzt allerdings am exozyklischen Amin eine zusätzliche Carboxylgruppe. Dadurch ermöglicht AAZTA die Koordination weiterer Radiometalle, wie z.B. das PET-Nuklid ^{44}Sc und das Therapienuklid ^{177}Lu mit Koordinationszahlen bis 7. Mit dem Hybridchelator sollte eine schnelle und effektive Radiomarkierung unter milden Bedingungen erreicht werden.

Der geschützte, bifunktionelle Chelator AAZTA⁵-^tBu₄ wurde in vier Stufen synthetisiert. Die anschließende Anbindung an den Quadratsäurediethylester über eine Ethylendiamin-Brücke und die sukzessive Amidierung des FAP-Inhibitors zur Bildung von AAZTA⁵.SA.FAPi erfolgte in weiteren vier Stufen.



AAZTA⁵.SA.FAPi

Abbildung 21: Struktur von AAZTA⁵.SA.FAPi.

Die Affinitäten zu FAP, DPPs (DPP4 und DPP9) und PREP wurden für AAZTA⁵.SA.FAPi und dessen ^{nat}Sc und ^{nat}Lu-Komplexe gemessen und mit denen von DOTA.SA.FAPi, ^{nat}Ga-, ^{nat}Lu-DOTA.SA.FAPi sowie mit DATA^{5m}.SA.FAPi und ^{nat}Ga-DATA^{5m}.SA.FAPi, aus Projekt A, verglichen. Die IC₅₀-Werte von AAZTA⁵.SA.FAPi und seinen natürlichen Komplexen betragen 0,55 – 0,57 nM und zeigten eine vergleichbar gute Inhibition von FAP wie DOTA.SA.FAPi und DATA^{5m}.SA.FAPi. Dazu lagen die IC₅₀-Werte für PREP und DPPs in µM-Bereichen (PREP: 2,4 – 3,6 µM; DPPs: > 1 µM), womit hohe Selektivität der AAZTA⁵-Derivate bzgl. FAP, analog zu den DOTA- und DATA^{5m}-Derivaten, demonstriert werden konnte (Tabelle 4).

Tabelle 4: Inhibitionsmessungen für FAP und die Proteasen DPPs und PREP: IC₅₀-Werte für AAZTA⁵.SA.FAPi, ^{nat}Sc und ^{nat}Lu-Komplexe.

Verbindungen	DPPs	PREP	FAP
	IC ₅₀ (µM)	IC ₅₀ (µM)	IC ₅₀ (nM)
AAZTA ⁵ .SA.FAPi	>1	2.4 ± 0.4	0.56 ± 0.02
[^{nat} Sc]Sc-AAZTA ⁵ .SA.FAPi	>1	3.6 ± 0.8	0.57 ± 0.04
[^{nat} Lu]Lu-AAZTA ⁵ .SA.FAPi	>1	3.2 ± 0.6	0.55 ± 0.04

AAZTA⁵.SA.FAPi wurde weiterhin radiochemisch mit ⁶⁸Ga, ⁴⁴Sc und ¹⁷⁷Lu analysiert. Parallel wurde DOTA.SA.FAPi ebenfalls mit den genannten Radiometallen markiert und die Komplexbildungskinetik und *in vitro*-Stabilität beider Präkursoren miteinander verglichen.

Die Komplexbildung mit ⁶⁸Ga zeigte für [⁶⁸Ga]Ga-AAZTA⁵.SA.FAPi quantitative RCU bereits nach 3 – 5 Minuten bei Raumtemperatur. [⁶⁸Ga]Ga-AAZTA⁵.SA.FAPi in HS, Ethanol und isot. Kochsalzlösung bei 37 °C zeigte ausgezeichnete Stabilitäten von > 99% über eine zweistündige Inkubationszeit.

Der [⁴⁴Sc]Sc-AAZTA⁵.SA.FAPi-Komplex bildete sich nach bereits 5 Minuten quantitativ. Im Vergleich dazu verlief die Komplexbildung von [⁴⁴Sc]Sc-DOTA.SA.FAPi deutlich langsamer mit geringerem RCU. Die Stabilitäten in HS, PBS und iso. NaCl waren bei beiden ⁴⁴Sc-Komplexen hoch mit > 97% innerhalb einer Messdauer von 8 Stunden.

Die ¹⁷⁷Lu-Markierung zeigte für AAZTA⁵.SA.FAPi als auch für DOTA.SA.FAPi quantitative RCU nach bereits einer Minute bei Raumtemperatur für [¹⁷⁷Lu]Lu-AAZTA⁵.SA.FAPi. Stabilitätsmessungen in HS, PBS und NaCl über einen Zeitraum von 10 Tagen zeigten sehr hohe Stabilitäten für [¹⁷⁷Lu]Lu-DOTA.SA.FAPi. Die Stabilitäten von [¹⁷⁷Lu]Lu-AAZTA⁵.SA.FAPi waren in PBS und NaCl vergleichbar zum DOTA-Derivat, im HS war der ¹⁷⁷Lu-AAZTA⁵-Komplex nach 6 Stunden > 95% stabil und nach einem Tag noch zu > 83%.

Die Lipophilien von AAZTA⁵.SA.FAPi und DOTA.SA.FAPi wurden mittels deren ⁶⁸Ga-Komplexe über die „shake-flask“-Methode gemessen. Beide Derivate weisen einen hydrophilen Charakter auf mit logD_{7,4}-Werten von $-2,5 \pm 0,2$.

Die *in vitro*-Studien von AAZTA⁵.SA.FAPi zeigen vielversprechende Ergebnisse und ermöglichen eine potentielle Nutzung für weitere *in vivo*-Versuche. Inhibitionseffizienzen für FAP sind vergleichbar gut wie die der DOTA.SA.FAPi- und DATA^{5m}.SA.FAPi-Konjugate. Hohe Komplexierungen und Stabilitäten unter milden Bedingungen konnten für alle drei verwendeten Radiometalle erzielt werden. Hinsichtlich des theranostischen Einsatzes erlaubt AAZTA⁵.SA.FAPi daher auch die potentielle Anwendung in der molekularen Bildgebung mit ⁶⁸Ga und ⁴⁴Sc sowie in der Therapie mit ¹⁷⁷Lu.

Hauptabschnitt C

In diesem Hauptabschnitt wurden, auf Basis der monomeren SA.FAPi Derivate, homodimere FAPi-Strukturen entwickelt. Durch die Verfügbarkeit von zwei FAP-Inhibitoren in einem Molekül soll die Avidität und dadurch sowohl die Tumoranreicherung erhöht als auch die Tumorverweildauer verlängert werden.

Der Abschnitt C *“Fibroblast Activation Protein (FAP) targeting homodimeric FAP inhibitor radiotheranostics: A step to improve tumor uptake and retention time”* beschreibt die Synthese der beiden Homodimere DOTA.(SA.FAPi)₂ und DOTAGA.(SA.FAPi)₂ sowie deren radiochemische, *in vitro*-Stabilitäts- und Affinitäts-Untersuchungen. Zusätzlich wurden mit [⁶⁸Ga]Ga-DOTAGA.(SA.FAPi)₂ erste Patienten mittels PET/CT klinisch untersucht.

Der symmetrische Aufbau von DOTA.(SA.FAPi)₂ wurde mit der Kopplung von zwei SA.FAPi-Einheiten über Ethylendiamin-Brücken in vier Stufen realisiert. Für die Synthese des DOTAGA.(SA.FAPi)₂-Konjugats wurde ausgehend von DO2A(^tBu)-GABz zunächst das sekundäre Amin im makrozyklischen Ring mit *tert*-butyl-(2-chloroethyl)carbammat alkyliert. Die weitere bifunktionelle Seite des DOTAGA Chelators wurde mit Ethylendiamin verknüpft. Die dadurch parallel angeordneten Amine konnten über zwei Quadratsäurediethylester und FAPi-Einheiten sukzessive gekoppelt werden. Das Dimer DOTAGA.(SA.FAPi)₂ wurde erfolgreich über sieben Stufen hergestellt.

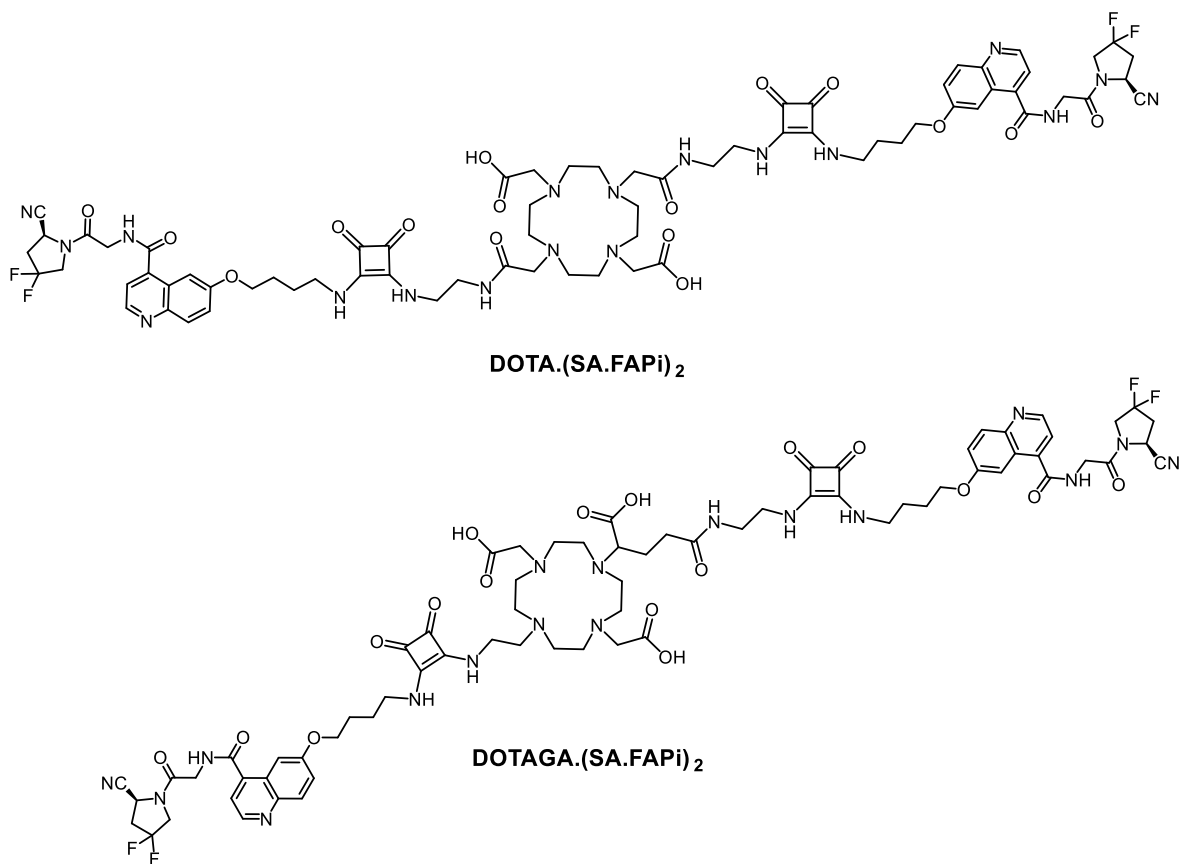


Abbildung 22: Strukturen von DOTA.(SA.FAPi)₂ und DOTAGA.(SA.FAPi)₂.

In Bindungsaffinitätsmessungen stellten sich für die homodimeren Derivate DOTA.(SA.FAPi)₂, DOTAGA.(SA.FAPi)₂ sowie deren natürliche Ga- und Lu-Komplexe sehr gute Affinitäten zu FAP heraus (IC₅₀ Werte von 0.78 – 1.54 nM), vergleichbar mit denen der monomeren SA.FAPi Strukturen und dem UAMC1110 FAP-Inhibitor. Zusätzlich konnte die Selektivität bzgl. FAP, gegenüber den verwandten Proteasen, bestätigt werden. Die Affinitäten für PREP lagen in μM IC₅₀-Bereich (0,42 – 1,60 μM) und für die DPPs (DPP4, DPP8 und DPP9) bei IC₅₀-Werten von 0,16 – 1,44 μM (Tabelle 5).

Tabelle 5: Inhibitionsmessungen für FAP und die Proteasen DPPs und PREP: IC₅₀-Werte für DOTA.(SA.FAPi)₂, DOTAGA.(SA.FAPi)₂ und deren ^{nat}Ga- und ^{nat}Lu-Komplexe.

Verbindungen	IC ₅₀ (μM)				IC ₅₀ (nM)
	DPP4	DPP8	DPP9	PREP	FAP
DOTA.(SA.FAPi) ₂	0.44 ± 0.06	1.33 ± 0.11	0.96 ± 0.15	0.42 ± 0.02	0.78 ± 0.05
[^{nat} Ga]Ga-DOTA.(SA.FAPi) ₂	0.51 ± 0.09	1.44 ± 0.16	0.78 ± 0.07	0.92 ± 0.07	1.05 ± 0.07
DOTAGA.(SA.FAPi) ₂	0.40 ± 0.07	0.42 ± 0.04	0.16 ± 0.02	0.39 ± 0.02	0.92 ± 0.06
[^{nat} Ga]Ga-DOTAGA.(SA.FAPi) ₂	0.70 ± 0.11	0.87 ± 0.08	0.19 ± 0.01	1.60 ± 0.16	0.90 ± 0.06
[^{nat} Lu]Lu-DOTAGA.(SA.FAPi) ₂	0.63 ± 0.07	0.41 ± 0.03	0.18 ± 0.02	0.56 ± 0.04	1.54 ± 0.15

Beide Vorläufer DOTA.(SA.FAPi)₂ und DOTAGA.(SA.FAPi)₂ wurden radiochemisch mit ⁶⁸Ga untersucht. Das [⁶⁸Ga]Ga-DOTA.(SA.FAPi)₂ wurde zunächst in verschiedenen Puffersystemen unter gleichen Reaktionsbedingungen getestet. Dabei stellte sich heraus, dass im Ammoniumacetat-Puffer, welcher bei den Monomeren FAPi-Strukturen als Reaktionsmedium genutzt wurde, die Komplexbildung minimal war mit > 9% RCU. Reaktion im Natriumacetat-Puffer und HEPES-Puffer verlief in höheren RCU von > 87%, eine quantitative radiochemische Ausbeute konnte nicht erzielt werden. Im Vergleich dazu erreichte das [⁶⁸Ga]Ga-DOTAGA.(SA.FAPi)₂ im HEPES-Puffer einen quantitativen RCU bei einer Reaktionsdauer von 10 min. [⁶⁸Ga]Ga-DOTAGA.(SA.FAPi)₂ zeigte in Stabilitätsmessungen sehr hohe Stabilitäten von > 98% in HS und NaCl, sowie > 91% in PBS nach zwei Stunden.

Die Lipophilie von [⁶⁸Ga]Ga-DOTAGA.(SA.FAPi)₂ wurde mit einem LogD_{7,4} von -2,02 bestimmt. Somit zeigte auch der DOTAGA-Dimer-Komplex einen hydrophilen Charakter, welcher jedoch weniger stark als der des monomeren [⁶⁸Ga]Ga-DOTA.SA.FAPi (LogD_{7,4} von -2,68) ist.

In einer ersten klinischen PET-Studie wurde [⁶⁸Ga]Ga-DOTAGA.(SA.FAPi)₂ bei sechs Patienten zur Diagnostik von verschiedenen Tumorarten angewendet. Außerdem wurde ein direkter Vergleich mit dem [⁶⁸Ga]Ga-DOTA.SA.FAPi Monomer hergestellt. Die physiologische Anreicherung in den gesunden Organen war zwischen Monomer und Dimer vergleichbar. Der höchste Uptake wurde bei beiden Derivaten in der Bauchspeicheldrüse detektiert.

Im Vergleich zur [⁶⁸Ga]Ga-DOTA.SA.FAPi-PET/CT wurden bei [⁶⁸Ga]Ga-DOTAGA.(SA.FAPi)₂ höhere SUL-Werte im Blut, in der Leber, der Milz, der Bauchspeicheldrüse, den Speicheldrüsen und der Schilddrüse festgestellt. Auffallend war die insgesamt höhere Tumoranreicherung des Dimers [⁶⁸Ga]Ga-DOTAGA.(SA.FAPi)₂ im Vergleich zum Monomer [⁶⁸Ga]Ga-DOTA.SA.FAPi. In einem Fallbeispiel einer

Patientin mit papillärem Schilddrüsenkrebs wurde ein höherer Uptake im Tumor (durchschn. SUL: 9,93 im L2-Wirbeltumor, 8,9 im rechten Sitzbein und 8,9 im linken Oberschenkelknochen) mit höheren Tumor-zu-Hintergrund-Verhältnissen als beim DOTA-Monomer (durchschn. SUL: 7,44 im L2-Wirbel, 6,7 im rechten Sitzbein und 1,4 im linken Oberschenkelknochen) nach 60 min p.i. detektiert (Abbildung 23). Zusätzlich konnte für das Dimer, ganz im Gegensatz zum Monomer, auch nach 180 min p.i. eine hohe, anhaltende Tumoranreicherung festgestellt werden (durchschn. SUL: 10,3 im L2-Wirbel, 8,4 im rechten Sitzbein und 8,5 im linken Oberschenkelknochen).

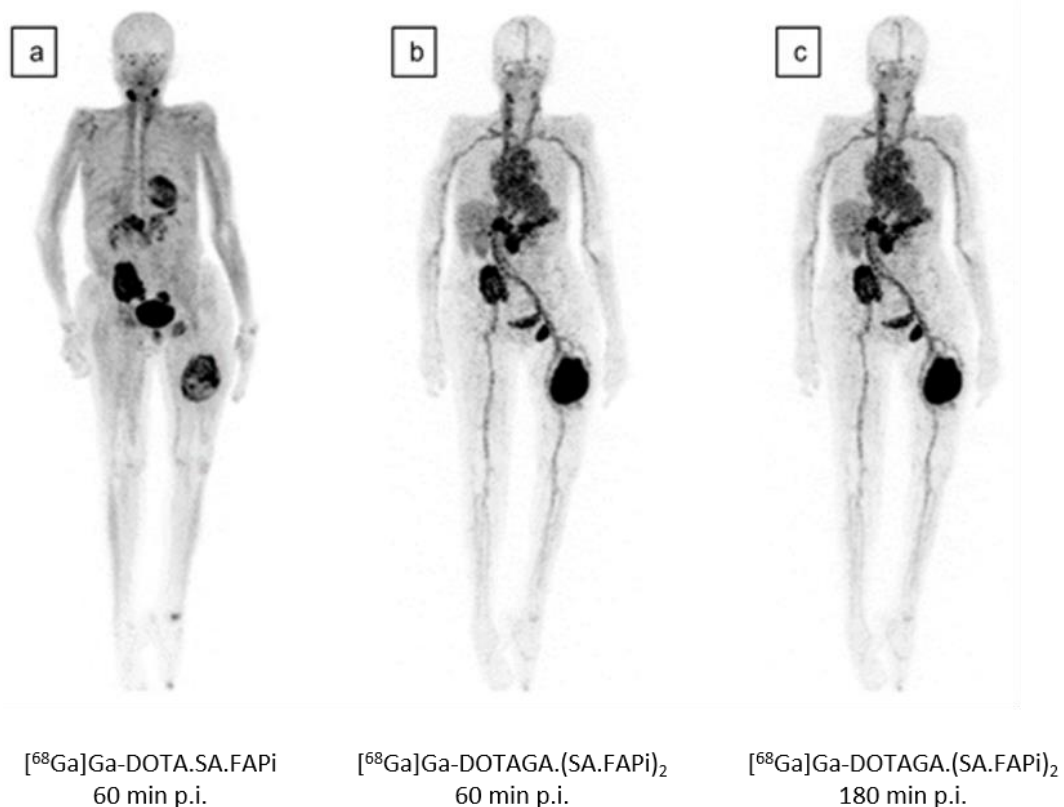


Abbildung 23: 63-jährige Patientin mit papillärem Schilddrüsenkarzinom: a) PET/CT MIP von $[^{68}\text{Ga}]\text{Ga-DOTA.SA.FAPI}$ 60 min nach Injektion; (b,c) PET/CT MIP von $[^{68}\text{Ga}]\text{Ga-DOTAGA.(SA.FAPI)}_2$ 60 min und 180 min p.i.: höherer Uptake in Tumorläsionen und Tumor-zu-Hintergrund-Verhältnis verglichen mit $[^{68}\text{Ga}]\text{Ga-DOTA.SA.FAPI}$, hohe Tumorretention bis zu 3 Stunden nach Injektion.

Die DOTAGA.(SA.FAPI)₂-Verbindung wurde in C.1. *“First-in-human results on the Biodistribution, Pharmacokinetics, and Dosimetry of $[^{177}\text{Lu}]\text{Lu-DOTA.SA.FAPI}$ and $[^{177}\text{Lu}]\text{Lu-DOTAGA.(SA.FAPI)}_2$ in Patients with Various End-stage Cancers”* mit ¹⁷⁷Lu klinisch in Hinblick auf die Organverteilung, Pharmakokinetik und Dosimetrie untersucht. Die Patienten wurden *via* $[^{68}\text{Ga}]\text{Ga-DOTA.SA.FAPI}$ -PET/CT diagnostiziert und mit entweder $[^{177}\text{Lu}]\text{Lu-DOTA.SA.FAPI}$ oder $[^{177}\text{Lu}]\text{Lu-DOTAGA.(SA.FAPI)}_2$ behandelt. Die mittlere absorbierte Dosis und effektive Ganzkörperdosis für $[^{177}\text{Lu}]\text{Lu-DOTAGA.(SA.FAPI)}_2$ war signifikant höher als für $[^{177}\text{Lu}]\text{Lu-DOTA.SA.FAPI}$. Interessanterweise wurde mit $[^{177}\text{Lu}]\text{Lu-$

DOTAGA.(SA.FAPI)₂ eine drastisch niedrige Blutaktivität im Vergleich zum [⁶⁸Ga]Ga-DOTAGA-Dimer beobachtet. Die Gründe dafür sind noch unbekannt und liegen vermutlich im unterschiedlichen Ladungsverhältnis der Radiokomplexe. Die Anreicherung in den Tumoren und in den Metastasen konnte sowohl beim Monomer als auch beim Dimer bereits nach 60 min p.i. beobachtet werden. Als wichtigste Erkenntnis zeigte sich, dass [¹⁷⁷Lu]Lu-DOTAGA.(SA.FAPI)₂ eine deutlich längere Tumoraufnahme und Retention von mind. 168 Stunden im Gegensatz zum Monomer und damit eine höhere effektive Halbwertszeit in den Läsionen aufwies (Abbildung 24).

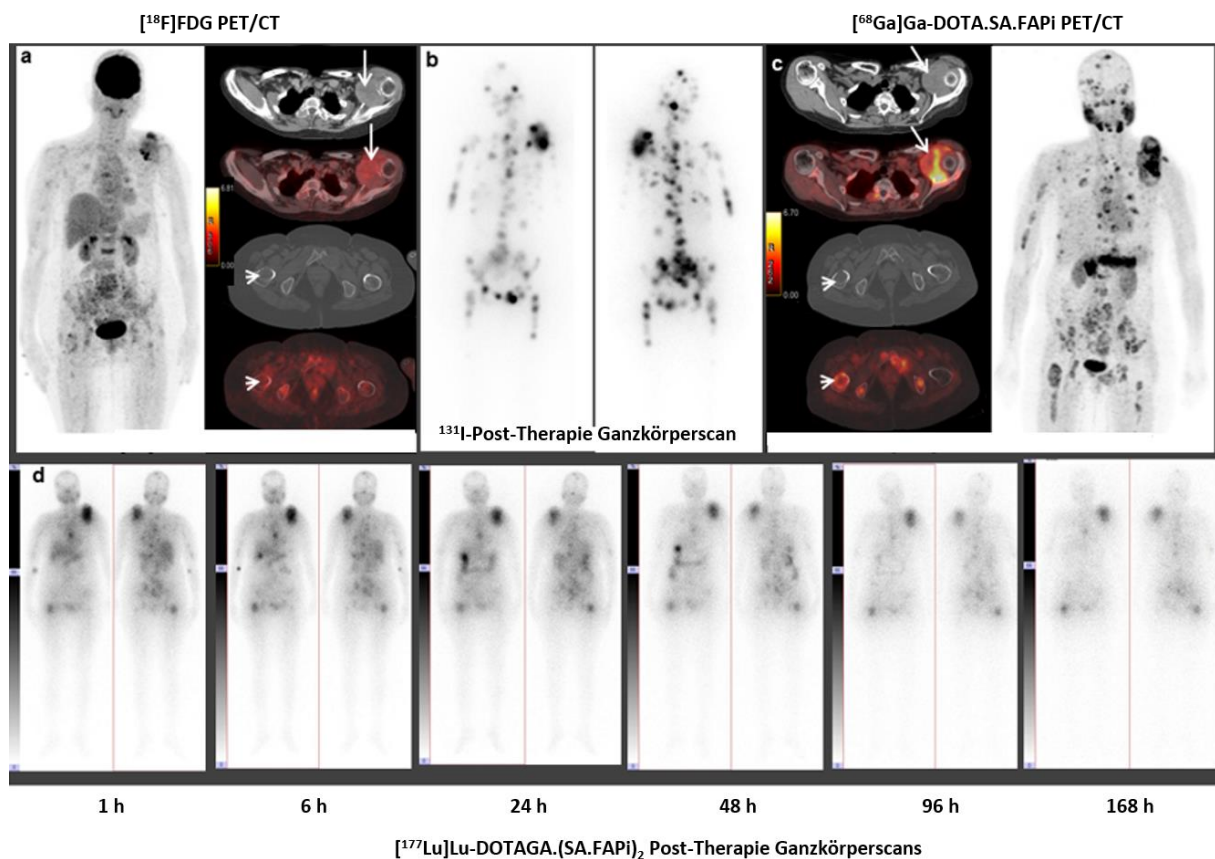


Abbildung 24: 50-jährige Patientin mit follikulärer Variante eines papillären Karzinoms: a) [¹⁸F]FDG PET/CT (dichte Weichteilmasse in der linken Schulter (Pfeile) und mehrere Skelettläsionen); b) Ganzkörperzintigraphie nach zusätzlicher Radiojodtherapie (Fortschreiten der Krankheit visualisierbar); c) [⁶⁸Ga]Ga-DOTA.SA.FAPI PET/CT: Hohe Anreicherung in der Weichteilmasse (Pfeile) und an mehreren Stellen des Skeletts (rechter Oberschenkelknochen - Pfeilspitze); d) [¹⁷⁷Lu]Lu-DOTAGA.(SA.FAPI)₂ Ganzkörperzintigraphie, Verweildauer in den Metastasen bis zu 168 Stunden.

Im nächsten Schritt wurde im Abschnitt C.2. *“Novel Fibroblast Activation Protein Inhibitor-Based targeted Theranostics for Radioiodine Refractory differentiated Thyroid Cancer Patients: A Pilot Study”* in einer Teststudie das [¹⁷⁷Lu]Lu-DOTAGA.(SA.FAPI)₂ zu therapeutischen Zwecken in 15 Patienten in verschiedenen Zyklen angewendet. Dabei wurden Patienten mit radiojodrefraktärem differenziertem Schilddrüsenkrebs (RR-DTC) im fortgeschrittenen Stadium auf die Sicherheit und die Wirksamkeit der Therapie untersucht. Die physiologische Organverteilung von [¹⁷⁷Lu]Lu-DOTAGA.(SA.FAPI)₂ war analog wie in C.1. Auch hier konnte der ¹⁷⁷Lu-Dimer-Komplex eine lange effektive Halbwertszeit (Median: 88 Stunden) bestätigen. Interessant war, dass die Thyreoglobulin (Tg)-Werte aller Patienten signifikant gesunken waren, mit einem medianen Tg-Ausgangswert von 10549 ng/ml und im Laufe der Behandlung einen medianen Tg-Wert von 5649 ng/ml. Eine signifikante Besserung in der visuellen Analogskala (VAS) von 9 vor Therapie auf 6 konnte nach einer medianen Zeit von 7,2 Monaten beobachtet werden und es kam zu einer reduzierten Einnahme von Analgetika bei den Patienten. Wichtig war vor allem, dass keiner der Patienten während der ¹⁷⁷Lu-Behandlung hämatologische, renale, Hepatotoxizität des Grades III/IV oder andere behandlungsbedingte Toxizitäten aufwies. Weiterhin kam es während der [¹⁷⁷Lu]Lu-DOTAGA.(SA.FAPI)₂-Therapie zu keinem Fortschreiten der Krankheit oder zum Tod.

Die *in vitro*- und die weiterführenden klinischen *in vivo*-Studien vom Homodimer DOTAGA.(SA.FAPI)₂ konnten einen vielversprechenden Ansatz zur Anwendung in der Theranostik aufweisen. Somit konnte ein signifikanter Fortschritt der Pharmakokinetik im Vergleich zum monomeren DOTA.SA.FAPI-Derivat dargestellt werden. Die molekulare Bildgebung mittels [⁶⁸Ga]Ga-DOTAGA.(SA.FAPI)₂-PET/CT konnte eine insgesamt höhere Tumoranreicherung und eine verlängerte Tumorretentionszeit aufweisen. Die höhere und verzögerte Aufnahme im Blut und in der Bauchspeicheldrüse sollte dennoch mit Vorsicht betrachtet werden. Erst kürzlich wurde eine Arbeit veröffentlicht, die auch einen dimeren Ansatz aufweist, mit einem DOTA Chelator verknüpft über eine zentrale Einheit via PEG₃ Linker an zwei FAPI-46 Bindungsmotiven [3]. Dort wurden neben einer höheren Tumoranreicherung und verlängerter Tumorverweildauer, auch eine erhöhte und verlängerte Blutaktivität sowie hoher Anreicherung in der Bauchspeicheldrüse im Vergleich zum Monomeren FAPI-46 bei Patienten beobachtet. Die Gründe dafür sind noch unbekannt; es bedarf weiterer Untersuchungen. Die klinische Untersuchung mit [¹⁷⁷Lu]Lu-DOTAGA.(SA.FAPI)₂ bestätigte die höhere Tumoranreicherung und absorbierte Dosis sowie die längere Tumorretention im Vergleich zum [¹⁷⁷Lu]Lu-DOTA.SA.FAPI. Die schnellere Ausscheidung des DOTA.SA.FAPI-Monomers bietet daher zwar keine optimale Voraussetzung für eine Therapieanwendung, dennoch eignet es sich gut für die Diagnostik mittels ⁶⁸Ga-PET/CT. Daher wurden [⁶⁸Ga]Ga-DOTA.SA.FAPI und [¹⁷⁷Lu]Lu-DOTAGA.(SA.FAPI)₂ als theranostisches Paar für die klinischen Studien verwendet. Die erste Pilotstudie bei RR-DTC-Patienten konnte erste Einblicke in der

therapeutischen Wirksamkeit und Sicherheit des Dimers $[^{177}\text{Lu}]\text{Lu-DOTAGA}(\text{SA.FAPi})_2$ geben. Die vielversprechenden ersten Ergebnisse geben die Möglichkeit für weiterführende Therapiestudien mittels $[^{177}\text{Lu}]\text{Lu-DOTAGA}(\text{SA.FAPi})_2$.

Hauptabschnitt D

Im Hauptabschnitt D *“Development of DATA^{5m} chelator-based fibroblast activation protein inhibitor small molecules for PET imaging”* wurden weitere DATA^{5m} basierte FAPi-Derivate synthetisiert und auf ihre *in vitro*-Eigenschaften getestet. Die entwickelten DATA^{5m}-FAPi-Derivate enthalten Variationen von Linkereinheiten. Durch die Änderung der heterozyklischen Linkersysteme können die FAP-adressierenden DATA^{5m}-Verbindungen, insbesondere auch mit dem SA.FAPi-Derivat, in deren radiochemischen und pharmakokinetischen Eigenschaften miteinander verglichen und dadurch weiter optimiert werden.

Der DATA-Chelator eignet sich besonders gut für die Komplexierung von ⁶⁸Ga, welches eine hexadentate Koordination mit der N₃O₃ Konformation des Chelators eingeht. Durch die schnelle und quantitative Komplexierung in wenigen Minuten unter milden Bedingungen ermöglicht der DATA-Chelator eine Art *“instant-kit”*-Markierung und -Anwendung. Daher bietet DATA eine Alternative zum DOTA, da durch die relativ harschen Komplexierungsbedingungen eine Kit-Anwendung beim DOTA erschwert wird. Das Octreotid-Derivat [⁶⁸Ga]Ga-DATATOC konnte bereits neben den guten *in vitro*-Eigenschaften auch bei ersten klinischen Untersuchungen Erfolg aufweisen [4–7].

Die Derivate DATA^{5m}.NH.FAPi, DATA^{5m}.Pip.FAPi, DATA^{5m}.Pyr-N-CH₃.FAPi und DATA^{5m}.NH-Pyr.FAPi wurden erfolgreich synthetisiert. DATA^{5m}.NH.FAPi beinhaltet eine direkte Kopplung des DATA^{5m}-Chelators zum FAPi-Targetvektor und konnte in zwei Stufen hergestellt werden. Die Synthese von DATA^{5m}.Pip.FAPi verlief in sechs Stufen und enthält eine Piperazin-Acetamid-Einheit als Linker. DATA^{5m}.Pyr-N-CH₃.FAPi wurde in sieben Stufen synthetisiert und beinhaltet als Linker eine Pyrrolidin-Methylamino-Acetamid-Einheit. Dabei fand die Amidkopplung der bifunktionellen Carboxygruppe des DATA^{5m} Chelators mit dem Stickstoff im Pyrrolidinring statt. Beim DATA^{5m}.NH-Pyr.FAPi wurde die Kopplung des Pyrrolidins umgekehrt durchgeführt, der Exo-Stickstoff des Pyrrolidins wurde mit der COOH-Gruppe des DATA^{5m} verbunden. Die Verbindung DATA^{5m}.NH-Pyr.FAPi mit dem Aminopyrrolidin-Acetamid-Linker konnte über sechs Stufen hergestellt werden.

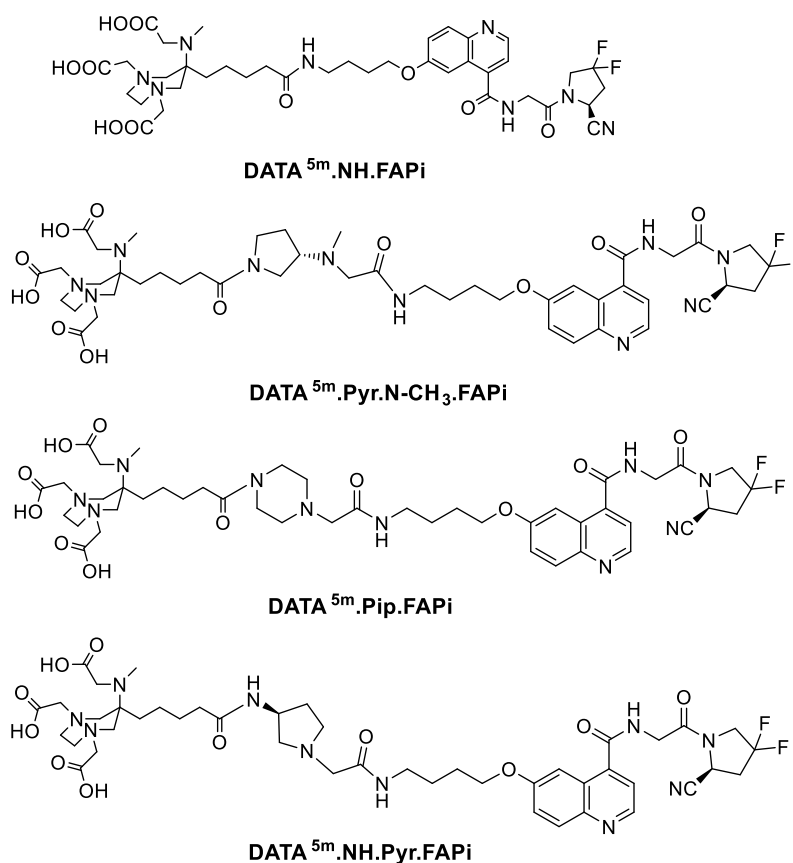


Abbildung 25: Strukturen von DATA^{5m}.NH.FAPi, DATA^{5m}.Pip.FAPi, DATA^{5m}.Pyr-N-CH₃.FAPi und DATA^{5m}.NH-Pyr.FAPi.

Alle vier Verbindungen wurden in Affinitätsstudien auf die Inhibitionseffizienz für FAP untersucht (Tabelle 6). Die IC₅₀-Werte befanden sich im Bereich 0,27 – 0,31 nM und lagen im selbigen IC₅₀-Bereich wie der UAMC1110 FAP-Inhibitor (0,4 nM) und DATA^{5m}.SA.FAPi (0,8 nM). Auch die Selektivität für FAP konnte dank der schlechten Affinität für PREP mit μM IC₅₀-Werten (1,5 – 6,4 μM) hervorgehoben werden.

Tabelle 6: IC₅₀-Werte für FAP und PREP von DATA^{5m}.X.FAPi (X=NH; Pip; Pyr-N-CH₃; NH-Pyr).

Verbindungen	PREP	FAP
	IC ₅₀ (μM)	IC ₅₀ (nM)
DATA ^{5m} .NH.FAPi	6.4 ± 0.4	0.27 ± 0.02
DATA ^{5m} .Pip.FAPi	1.5 ± 0.3	0.27 ± 0.01
DATA ^{5m} .Pyr-N-CH ₃ .FAPi	2.6 ± 0.3	0.31 ± 0.02
DATA ^{5m} .NH-Pyr.FAPi	3.3 ± 0.2	0.28 ± 0.02

Zusätzlich wurden alle vier DATA^{5m}-Markierungsvorläufer hinsichtlich der Radiokomplexierung mit ⁶⁸Ga und deren *in vitro*-Stabilitäten getestet. Die ⁶⁸Ga-Komplexierung erfolgte schnell und in quantitativen RCU nach 10–15 Minuten bei 30 °C für die drei Derivate [⁶⁸Ga]Ga-DATA^{5m}.NH.FAPi, [⁶⁸Ga]Ga-DATA^{5m}.Pip.FAPi und [⁶⁸Ga]Ga-DATA^{5m}.Pyr-N-CH₃.FAPi. Im Vergleich dazu konnte mit [⁶⁸Ga]Ga-DATA^{5m}.NH-Pyr.FAPi ein RCU von > 90% nach 15 Minuten erzielt werden.

Die *in vitro*-Stabilitäten in NaCl und Ethanol waren für [⁶⁸Ga]Ga-DATA^{5m}.NH.FAPi, [⁶⁸Ga]Ga-DATA^{5m}.Pip.FAPi und [⁶⁸Ga]Ga-DATA^{5m}.Pyr-N-CH₃.FAPi mit ≥ 99% nach zwei Stunden sehr hoch. [⁶⁸Ga]Ga-DATA^{5m}.NH-Pyr.FAPi war in NaCl zu > 93% und in EtOH zu > 79% stabil. Im HS zeichneten sich Stabilitätsunterschiede ab. Die stabilste Verbindung war [⁶⁸Ga]Ga-DATA^{5m}.Pip.FAPi mit ≥ 95%, gefolgt von [⁶⁸Ga]Ga-DATA^{5m}.NH.FAPi mit ≥ 83%, dann [⁶⁸Ga]Ga-DATA^{5m}.Pyr-N-CH₃.FAPi mit ≥ 75% und zuletzt [⁶⁸Ga]Ga-DATA^{5m}.NH-Pyr.FAPi mit ≥ 35% nach zweistündiger Inkubation. Im Hauptabschnitt A waren die Stabilitäten für [⁶⁸Ga]Ga-DATA^{5m}.SA.FAPi in allen drei Medien bei ≥ 95%. Von allen DATA^{5m}-FAPi Verbindungen scheint [⁶⁸Ga]Ga-DATA^{5m}.SA.FAPi die beste *in vitro* Stabilität aufzuweisen.

Die Lipophiliemessungen ergaben für die vier ⁶⁸Ga-DATA^{5m}-Derivate ähnliche logD_{7,4}-Werte zwischen -2,16 und -2,29. Auch das [⁶⁸Ga]Ga-DATA^{5m}.SA.FAPi, mit einem logD-Wert von -2,25, befand sich im selbigen hydrophilen Bereich. Die Variation des Linkers scheint daher keinen großen Einfluss auf die Gesamtlipophilie der FAPi Verbindungen zu nehmen.

Im Gesamten stellten sich die drei Verbindungen [⁶⁸Ga]Ga-DATA^{5m}.NH.FAPi, [⁶⁸Ga]Ga-DATA^{5m}.Pip.FAPi und [⁶⁸Ga]Ga-DATA^{5m}.Pyr-N-CH₃.FAPi als mögliche Kandidaten für weiterführenden *in vivo* Studien auf. Die radiochemischen Evaluierungen sowie die *in vitro*-Daten haben das Potential sich analog zum DATA^{5m}.SA.FAPi in der klinischen Anwendung zu etablieren. Interessant sein könnten vor allem die direkten pharmakokinetischen Vergleiche der DATA^{5m}-Derivate sowohl präklinisch als auch klinisch, um die vielversprechendsten Kandidaten für eine instant-kit Anwendung in der Diagnostik mittels PET/CT zu ermitteln.

Fazit

Im Rahmen der Promotion konnten Chelator-konjugierte FAP-Inhibitoren, verknüpft über verschiedene Linkereinheiten, entwickelt werden, die das Fibroblasten-Aktivierungsprotein (FAP) im Tumorstroma adressieren. Nach präparativer Synthese der sowohl monomeren als auch dimeren FAPI-Derivate wurden alle hergestellten Verbindungen *in vitro* untersucht und für einige dieser Verbindungen vielversprechende erste *in vivo*-Daten generiert. Die Tracer konnten somit vollständig „from-bench-to-beside“ transferiert, d.h. die Chronologie von Synthese der Vorläufer im Labor bis hin zur Translation und Applikation in der Klinik konnte erfolgreich dargestellt werden. Durch die Weiterentwicklung von monomeren zu dimeren Strukturen konnte die Pharmakokinetik *in vivo* erheblich verbessert werden. Auch erste Therapieansätze zeigen das Potential von dimeren FAPI-Verbindungen und finden bereits jetzt Anwendung im Gebiet der Theranostik durch unsere Kooperationspartner weltweit. Zukünftig könnten durch etwaige Veränderung der Linker die physiologischen und pharmakokinetischen Eigenschaften der FAP-adressierenden Radiopharmaka *in vivo* weiter optimiert werden.

Die entwickelten Chelator-basierten FAPI-Konjugate zeigten durch vielversprechende Studien das Potential FAP effektiv zu adressieren und damit viele verschiedene epitheliale Tumore zu visualisieren und zu therapieren. Die dabei erhaltenen Ergebnisse sind vielversprechend und geben Ansätze für die nuklearmedizinische Anwendung in fortgeschritteneren Studien vor.

Referenzen

1. Greifenstein, L.; Engelbogen, N.; Lahnif, H.; Sinnes, J.-P.; Bergmann, R.; Bachmann, M.; Rösch, F. Synthesis, labeling and preclinical evaluation of a squaric acid containing PSMA-inhibitor labeled with ^{68}Ga – a comparison with PSMA-11 and PSMA-617. *ChemMedChem* **2020**, *15*, 695–704, doi:10.1002/cmdc.201900559.
2. Grus, T.; Lahnif, H.; Klasen, B.; Moon, E.S.; Greifenstein, L.; Roesch, F. Squaric Acid-Based Radiopharmaceuticals for Tumor Imaging and Therapy. *Bioconjug. Chem.* **2021**, *32*, 1223–1231, doi:10.1021/acs.bioconjchem.1c00305.
3. Zhao, L.; Niu, B.; Fang, J.; Pang, Y.; Li, S.; Xie, C.; Sun, L.; Zhang, X.; Guo, Z.; Lin, Q.; et al. Synthesis, preclinical evaluation, and a pilot clinical PET imaging study of ^{68}Ga -labeled FAPI dimer. *J. Nucl. Med.* **2021**, doi:10.2967/jnumed.121.263016.
4. Seemann, J.; Waldron, B.; Parker, D.; Roesch, F. DATATOC: a novel conjugate for kit-type ^{68}Ga labelling of TOC at ambient temperature. *EJNMMI Radiopharm. Chem.* **2017**, *1*, 4, doi:10.1186/s41181-016-0007-3.
5. Sinnes, J.P.; Nagel, J.; Waldron, B.P.; Maina, T.; Nock, B.A.; Bergmann, R.K.; Ullrich, M.; Pietzsch, J.; Bachmann, M.; Baum, R.P.; et al. Instant kit preparation of ^{68}Ga -radiopharmaceuticals via the hybrid chelator DATA: clinical translation of [^{68}Ga]Ga-DATA-TOC. *EJNMMI Res.* **2019**, *9*, 48, doi:10.1186/s13550-019-0516-7.
6. Nock, B.A.; Kaloudi, A.; Nagel, J.; Sinnes, J.P.; Roesch, F.; Maina, T. Novel bifunctional DATA chelator for quick access to site-directed PET ^{68}Ga -radiotracers: Preclinical proof-of-principle with [Tyr3]octreotide. *Dalt. Trans.* **2017**, *46*, 14584–14590, doi:10.1039/c7dt01684k.
7. Gaertner, F.C.; Plum, T.; Kreppel, B.; Eppard, E.; Meisenheimer, M.; Strunk, H.; Bundschuh, R.A.; Sinnes, J.P.; Rösch, F.; Essler, M. Clinical evaluation of [^{68}Ga]Ga-DATA-TOC in comparison to [^{68}Ga]Ga-DOTA-TOC in patients with neuroendocrine tumours. *Nucl. Med. Biol.* **2019**, *76–77*, 1–9, doi:10.1016/j.nucmedbio.2019.08.006.

5. Liste der Publikationen

- 10/2021 **Fibroblast Activation Protein (FAP) targeting homodimeric FAP inhibitor radiotheranostics: A step to improve tumor uptake and retention time**
Moon, E.S.; [REDACTED]
[REDACTED]
AJNMMI 2021, akzeptiert.
- 10/2021 **Novel Fibroblast Activation Protein Inhibitor-Based targeted Theranostics for Radioiodine Refractory differentiated Thyroid Cancer Patients: A Pilot Study**
[REDACTED] Moon, E.S.; [REDACTED]
[REDACTED]
Thyroid 2021, doi:10.1089/thy.2021.0412.
- 10/2021 **New Frontiers in Cancer Imaging and Therapy Based on Radiolabeled Fibroblast Activation Protein Inhibitors : A Rational Review and Current Progress**
[REDACTED] Moon, E.S.; [REDACTED]
Pharmaceuticals 2021, 14, 1023, doi:10.3390/ph14101023.
- 07/2021 **Fibroblast activation protein inhibitor (FAPi) positive tumour fraction on PET/CT correlates with Ki-67 in liver metastases of neuroendocrine tumours**
[REDACTED] Moon, E.S.; [REDACTED]
[REDACTED]
Nuklearmedizin 2021, 60, 344–354, doi:10.1055/a-1521-8604.
- 06/2021 **Squaric Acid-Based Radiopharmaceuticals for Tumor Imaging and Therapy**
[REDACTED] Moon, E.S.; [REDACTED]
Bioconjug. Chem. 2021, 32, 1223–1231, doi:10.1021/acs.bioconjchem.1c00305.
- 06/2021 **In Vitro Evaluation of the Squaramide-Conjugated Fibroblast Activation Protein Inhibitor-Based Agents AAZTA⁵.SA.FAPi and DOTA.SA.FAPi**
Moon, E.S.; [REDACTED]
[REDACTED]
Molecules 2021, 26, 3482, doi:10.3390/molecules26123482.
- 03/2021 **AAZTA⁵-squaramide ester competing with DOTA-, DTPA- and CHX-A-DTPA-analogues: Promising tool for ¹⁷⁷Lu-labeling of monoclonal antibodies under mild conditions**
[REDACTED] Moon, E.S.; [REDACTED]
Nucl. Med. Biol. 2021, 96–97, 80–93, doi:10.1016/j.nucmedbio.2021.03.007.
- 01/2021 **Impact of prompt gamma emission of ⁴⁴Sc on quantification in preclinical and clinical PET systems**
[REDACTED] Moon, E.S.; [REDACTED]
[REDACTED]
Appl. Radiat. Isot. 2021, 170, 1–8, doi:10.1016/j.apradiso.2021.109599.

- 11/2020 **Effect of the versatile bifunctional chelator AAZTA⁵ on the radiometal labelling properties and the in vitro performance of a gastrin releasing peptide receptor antagonist**
[REDACTED] Moon, E.S.; [REDACTED]
EJNMMI Radiopharm. Chem. 2020, 5, 29, doi:10.1186/s41181-020-00115-8.
- 11/2020 **⁶⁸Ga, ⁴⁴Sc and ¹⁷⁷Lu-labeled AAZTA⁵-PSMA-617: synthesis, radiolabeling, stability and cell binding compared to DOTA-PSMA-617 analogues**
[REDACTED] Moon, E.S.; [REDACTED]
EJNMMI Radiopharm. Chem. 2020, 5, 28, doi:10.1186/s41181-020-00107-8.
- 11/2020 **Biodistribution, pharmacokinetics, dosimetry of [⁶⁸Ga]Ga-DOTA.SA.FAPi, and the head-to-head comparison with [¹⁸F]F-FDG PET/CT in patients with various cancers**
[REDACTED] Moon, E.S.; [REDACTED]
Eur. J. Nucl. Med. Mol. Imaging 2021, 48, 1915–1931, doi:10.1007/s00259-020-05132-y.
- 08/2020 **A theranostic approach of [⁶⁸Ga]Ga-DOTA.SA.FAPi PET/CT-guided [¹⁷⁷Lu]Lu-DOTA.SA.FAPi radionuclide therapy in an end-stage breast cancer patient: new frontier in targeted radionuclide therapy**
[REDACTED] Moon, E.S.; [REDACTED]
Eur. J. Nucl. Med. Mol. Imaging 2021, 48, 942–944, doi:10.1007/s00259-020-04990-w.
- 07/2020 **Targeting fibroblast activation protein (FAP): next generation PET radiotracers using squaramide coupled bifunctional DOTA and DATA^{5m} chelators**
Moon, E.S.; [REDACTED]
[REDACTED]
EJNMMI Radiopharm. Chem. 2020, 5, 19, doi:10.1186/s41181-020-00102-z.
- 05/2020 **[⁶⁸Ga]Ga-DATA^{5m}.SA.FAPi PET/CT: Specific Tracer-uptake in Focal Nodular Hyperplasia and potential Role in Liver Tumor Imaging**
[REDACTED]
[REDACTED] Moon, E.S.; [REDACTED]
Nuklearmedizin 2020, 59, 387–389, doi:10.1055/a-1164-5667.

Danksagung

[Redacted text block 1]

[Redacted text block 2]

[Redacted text block 3]

[Redacted text block 4]

[Redacted text block 5]

[Redacted text block 6]

Eidesstattliche Erklärung

Ich, Euy Sung Moon, versichere, dass ich die vorliegende Dissertation selbstständig verfasst und keine anderen als die angegebenen schriftlichen und elektronischen Quellen sowie andere Hilfsmittel benutzt habe.

Die vorliegende Arbeit wurde unter der Betreuung von [REDACTED] in der Zeit von September 2018 bis zum November 2021 am Department Chemie - TRIGA, ehem. Institut für Kernchemie der Johannes Gutenberg-Universität Mainz durchgeführt.

Mainz, den 02.11.2021

Euy Sung Moon

Curriculum Vitae

[Redacted text block]

[Redacted text block]

[Redacted text block]

[Redacted text block]

[Redacted text block]

[Redacted text block]

[Redacted text block]

[REDACTED]

[REDACTED]
[REDACTED]
[REDACTED]
[REDACTED]
[REDACTED]

[REDACTED]
[REDACTED]
[REDACTED]
[REDACTED]

[REDACTED]
[REDACTED]
[REDACTED]
[REDACTED]
[REDACTED]
[REDACTED]
[REDACTED]

[REDACTED]
[REDACTED]
[REDACTED]

[REDACTED]
[REDACTED]
[REDACTED]
[REDACTED]
[REDACTED]

[REDACTED]
[REDACTED]
[REDACTED]
[REDACTED]
[REDACTED]

[REDACTED]
[REDACTED]